A theory for x-ray-optical wavemixing with applications in spectroscopy and nonlinear crystallography

Dissertation
zur Erlangung des Doktorgrades
an der Fakultät für Mathematik, Informatik und Naturwissenschaften
Fachbereich Physik
der Universität Hamburg

vorgelegt von

Dietrich Krebs

Hamburg
2022

Gutachter/innen der Dissertation:	Prof. Dr. Nina Rohringer Dr. Mariana Rossi
Zusammensetzung der Prüfungskommission:	Prof. Dr. Nina Rohringer Dr. Mariana Rossi Prof. Dr. Michael Potthoff Prof. Dr. Ralf Röhlsberger Prof. Dr. Edgar Weckert
Vorsitzende/r der Prüfungskommission:	Prof. Dr. Michael Potthoff
Datum der Disputation:	10.02.2023
Vorsitzender des Fach-Promotionsausschusses PHYSIK:	Prof. Dr. Wolfgang J. Parak
Leiter des Fachbereichs PHYSIK:	Prof. Dr. Günter H. W. Sigl
Dekan der Fakultät MIN:	Prof. Dr.-Ing. Norbert Ritter

Abstract

In this treatise, we discuss the subject of parametric x-ray-optical wavemixing. We commence from a theoretical point of view, deriving a coherent framework for the description of wavemixing processes, such as x-ray-optical sum- and difference frequency generation as well as x-ray parametric down-conversion. In contrast to earlier, often classical, approaches, our framework is rooted in first-principles, non-relativistic Quantum Electrodynamics. It enables microscopic insights into the respective wavemixing processes and likewise allows for quantitative predictions of their nonlinear scattering yields. On the microscopic level, we could thereby identify the electronic observable, which underlies x-ray-optical wavemixing to lowest order, to be a density–current-density correlator of the electronic system. Quantitatively, we benchmark our framework against existing reports of wavemixing and, more importantly, engage in a series of experimental studies to validate our predictions. Among other things, we report the experimental observation of x-ray-optical difference frequency generation, which shows promise for application in nonlinear crystallography, and pursue tests of x-ray parametric down-conversion in two different regimes. For its second case, namely x-ray-to-XUV conversion, these experiments furthermore elucidate scattering features that have previously proven incomprehensible. Resolving the associated conundrum, we develop a polaritonic explanation of parametric down-conversion and present a simple model for its illustration.

Kurzfassung

In dieser Abhandlung widmen wir uns dem Thema parametrischer röntgen-optischer Mischprozesse. Ausgehend von Seiten der Theorie entwickeln wir eine systematische Beschreibung für eine Klasse von Wellenmischprozessen, die sowohl röntgen-optische Summen- und Differenzfrequenzerzeugung wie auch parametrische Abwärtskonvertierung von Röntgenstrahlung umfasst. Im Gegensatz zu vorhergehenden, zumeist klassischen, Beschreibungsansätzen entspringt unser Vorgehen aus fundamentalen Prinzipien der nichtrelativistischen Quantenelektrodynamik. Dieses Vorgehen eröffnet uns einerseits mikroskopische Einblicke in die jeweiligen Wellenmischprozesse und erlaubt uns andererseits, quantitative Vorhersagen über deren Verteilung nichtlinearer Streuwahrscheinlichkeiten zu treffen. Auf mikroskopischer Ebene konnten wir so die elektronische Observable, die der röntgen-optischen Wellenmischung in niedrigster Ordnung zugrunde liegt, als Dichte–Stromdichte-Korrelator des elektronischen Systems identifizieren. Quantitativ untersuchen wir die Genauigkeit unserer Beschreibung im Vergleich zu bereits bekannten Wellenmischexperimenten und, mehr noch, beteiligen uns an einer Reihe unabhängiger, experimenteller Studien, um unsere Vorhersagen zu validieren. Hieraus resultieren unter anderem die experimentelle Beobachtung der röntgen-optischen Differenzfrequenzerzeugung, die sich als vielversprechende Grundlage für nichtlineare Kristallographie erweist, und Tests der parametrischen Abwärtskonvertierung von Röntgenstrahlung in zwei verschiedenen Regimen. Im zweiten dieser Fälle, der Abwärtskonvertierung von Röntgenstrahlung in den XUV-Spektralbereich, klären diese Experimente darüber hinaus Streubilder auf, die zuvor nicht eindeutig verstanden waren. Um die hiermit verbundenen Fragen auch theoretisch zu adressieren, entwickeln wir eine polaritonische Anschauung der parametrischen Abwärtskonvertierung und führen ein einfaches Modell zum Zweck ihrer Veranschaulichung vor.

List of publications

As a result of—among other contributions—the research conducted for this thesis, the following article has been published:

- C. Boemer, D. Krebs, A. Benediktovitch, E. Rossi, S. Huotari, and N. Rohringer, *Towards novel probes for valence charges via x-ray optical wave mixing*, Faraday Discuss., **228**, 451 (2021).

In addition, two further manuscripts have been submitted to scientific journals, the latter still being under review for publication as of this writing:

- C. Boemer, D. Krebs, M. Diez, N. Rohringer, A. Galler, and C. Bressler, *X-ray parametric down-conversion: Challenging previous findings on the basis of improved experimental methods*, arXiv, 2002.12822 (2020),

- D. Krebs and N. Rohringer, *Theory of parametric x-ray optical wavemixing processes*, Phys Rev X (under review) (2022).

Additional manuscripts are in preparation.

Contents

Chapter 1

Introduction

1.1 What is wavemixing

Wavemixing is a nonlinear process, wherein multiple oscillating signals are compounded in such a way that new signals—most often at new frequencies—arise. The term 'mixing', hereunto, derives from radio-frequency applications, where 'mixer' or 'mixing stage' refers to an electronic circuit that, ideally, converts two signals at frequencies ω_1 and ω_2 into signals at their sum- and difference-frequency, $\omega_1+\omega_2$ and $|\omega_1-\omega_2|$, respectively [1, 2].

More generally, the concept of wavemixing has spread across the electromagnetic spectrum and is regularly applied with radio- and microwaves [3, 4], in infrared spectroscopy [5, 6] as well as using visible and UV laser-light by now [7, 8]. In a further extension, our aim within this treatise will be to investigate applications of wavemixing at even higher frequencies, namely in the x-ray regime.

In order to illustrate the fundamental working-principles of wavemixing, however, we think it is most instructive to consider a simple example from electro-technics first:
At its outset, let us assume two electrical signals given by oscillating voltages

$$U_1(t)=\sin(\omega_1 t) \qquad \text{and} \qquad U_2(t)=\sin(\omega_2 t), \tag{1.1}$$

which feature the aforementioned frequencies ω_1 and ω_2. In the following thought-experiment, we want to trace the modulation of these signals through two different models of (electronic) amplifiers, namely, a linear and a nonlinear one.

The linear amplifier is supposed to produce an output signal that is strictly proportional to its input:

$$U_{\text{out}}(t)=\chi^{(1)}\times U_{\text{in}}(t), \tag{1.2}$$

with a proportionality constant, i.e., amplification factor, $\chi^{(1)}$. We have further visualized its linear transfer-characteristic in Fig. 1.1 (a), where we use a straight line of slope $\chi^{(1)}$ to graphically construct the amplified signal.

Applying Eq. (1.2) to the sum of our model-signals, we generate a linear superposition of amplified signals, unsurprisingly

$$\begin{aligned} U_{\text{out}}(t) &= \chi^{(1)}\times\big(U_1(t)+U_2(t)\big) \\ &= \chi^{(1)}\times\sin(\omega_1 t)+\chi^{(1)}\times\sin(\omega_2 t). \end{aligned} \tag{1.3}$$

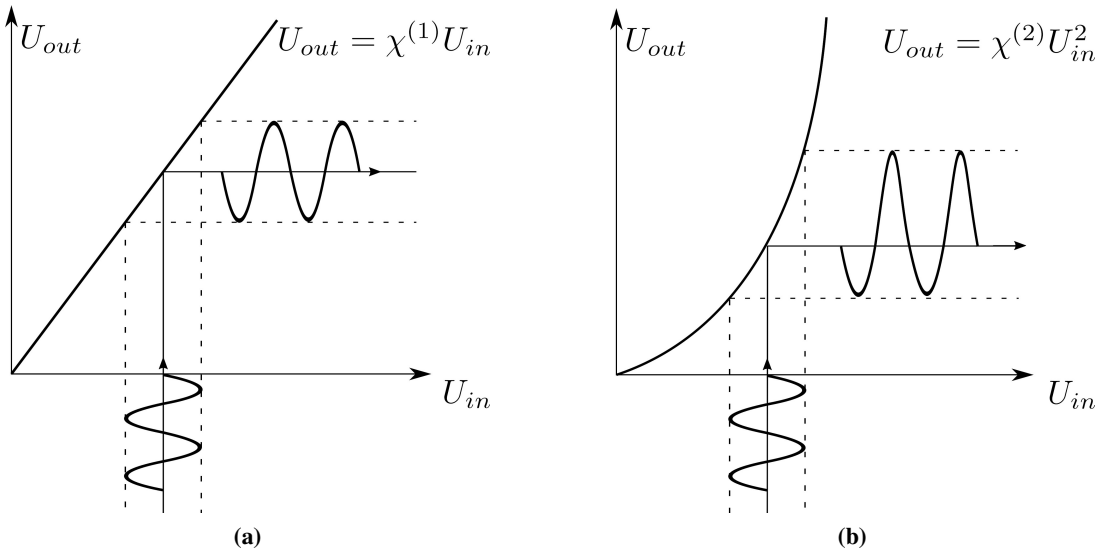

Figure 1.1: Illustration of trasmission-curves for: (a) a linear amplifier and (b) a nonlinear amplifier. For both cases the amplification of a sinusoidal signal is visualized. Its graphical construction proceeds by projecting the incident signal (U_{in}) onto the transmission-curve and extrapolating the associated output voltage (U_{out}) to the right. In the linear case (a) the output signal is fully proportional to the input signal, whereas in the nonlinear case (b), the transmitted signal exhibits significant distortion. Even though undesirable in a 'pure' amplifier, this capability to distort and cross-modulate signals will allow the nonlinear amplifier to act as a mixing stage ultimately. [We gratefully acknowledge Dr. Christina Bömer's help in rendering the above computer graphics.]

As the output does not contain any *new* frequency components vis-a-vis the input signals, we would not consider this to be a case of wavemixing yet.

The situation changes markedly, if we consider a *nonlinear* amplifier instead. For a minimal example, let us assume a device that features the following quadratic transmission behaviour:

$$U_{\text{out}}(t) = \chi^{(2)} \times \big(U_{\text{in}}(t)\big)^2. \tag{1.4}$$

Here, we choose to label the new proportionality constant $\chi^{(2)}$, with the small superscript $^{(2)}$ indicating its correspondence to the 2^{nd}-order of a polynomial in U_{in}. Analogous to the linear case, we have sketched the transmission characteristics of the nonlinear amplifier-model in Fig. 1.1 (b). From this visualization, it becomes apparent already that the bent transmission-curve will introduce distortions of the output signal compared to the linear alternative (a).

We shall see below, how these distortions translate into the mixing of frequencies, once Eq. (1.4) is itself applied to the sum of our model-signals:

$$\begin{aligned} U_{\text{out}}(t) &= \chi^{(2)} \times \big(U_1(t) + U_2(t)\big)^2 \\ &= \chi^{(2)} \times \big((U_1(t))^2 + 2U_1(t)U_2(t) + (U_2(t))^2\big) \\ &= \chi^{(2)} \times \big((\sin(\omega_1 t))^2 + 2\sin(\omega_1 t)\sin(\omega_2 t) + (\sin(\omega_2 t))^2\big) \\ &= \chi^{(2)} \times \Big(\frac{1}{2}\big[1 \underset{\text{DC}}{\uparrow} - \underbrace{\cos(2\omega_1 t)}_{\text{SHG}}\big] + \big[\underbrace{\cos((\omega_1-\omega_2)t)}_{\text{DFG}} - \underbrace{\cos((\omega_1+\omega_2)t)}_{\text{SFG}}\big] + \frac{1}{2}\big[1 \underset{\text{DC}}{\uparrow} - \underbrace{\cos(2\omega_2 t)}_{\text{SHG}}\big]\Big). \end{aligned} \tag{1.5}$$

In the last line, we have applied the well-known relations of powers and products of trigonometric functions [9] to expose the emergence of several new frequency components. In particular, we find:

- Constant contributions, which we have labelled DC for 'direct current'[1],
- Signal components, which have doubled in frequency, i.e., oscillating at $2\omega_1$ or $2\omega_2$. We label these SHG for 'second harmonic generation'.
- Finally, the cross-modulated terms DFG and SFG appear, which represent 'difference-' and 'sum-frequency generation' from the input signals, respectively. They oscillate at $\omega_1 - \omega_2$ or $\omega_1 + \omega_2$ and thereby fulfil our initial expectations for the output of an electronic mixing circuit.

We thus find that this simple, quadratic amplifier-model gives rise to a host of different phenomena already. In fact, it anticipates most of the wave mixing processes that we shall discuss in greater complexity later on. Most importantly, in our opinion, the model highlights the fact that wavemixing requires a *nonlinear* element, which functions as the mixer. Generalizing from the simple, quadratic curve of Eq. (1.4), we will ultimately investigate the nonlinear, quantum-mechanical response of electrons within crystalline materials to the external 'signals' provided by x-ray and optical light-fields.

Before addressing such x-ray-optical wavemixing directly, we want to note in closing that the model from Eq. (1.4) may gradually be extended towards greater complexity. As a first step, we could obviously include nonlinearities beyond the quadratic term, e.g.,

$$U_{\mathrm{out}}(t) = \chi^{(1)} \times U_{\mathrm{in}}(t) + \chi^{(2)} \times \left(U_{\mathrm{in}}(t)\right)^2 + \chi^{(3)} \times \left(U_{\mathrm{in}}(t)\right)^3 + ... \tag{1.6}$$

Here, we have written the output-response as a series expansion in U_{in}, with successive expansion coefficients $\chi^{(n)}$.

The next step—which is less obvious yet wide-spread in its application—would see us transfer the whole model from oscillating voltages to oscillating electric fields in general

$$\mathbf{P}(t) = \chi^{(1)} \cdot \mathbf{E}(t) + \chi^{(2)} : \mathbf{E}(t)\,\mathbf{E}(t) + \chi^{(3)} : \mathbf{E}(t)\,\mathbf{E}(t)\,\mathbf{E}(t) + ... \ . \tag{1.7}$$

In this largely analogous construction, the output of interest is the induced polarization $\mathbf{P}(t)$ that results from nonlinear combinations of driving electric fields $\mathbf{E}(t)$ inside a medium. The 'expansion coefficients' $\chi^{(n)}$ are referred to as n-th order (nonlinear) susceptibilities in this case and need to be of tensorial nature, because $\mathbf{E}(t)$ and $\mathbf{P}(t)$ are themselves vectors already. The colon-notation $\chi^{(2)} : \mathbf{EE}$ is meant to symbolize the respective tensor-vector multiplication (cf. Ref. [13]).

At this point, we have basically reached the foundations of modern nonlinear optics [11–14]. This in itself is a seminal and prolific field of research, which facilitated numerous advances across science and technology over the past decades and underpins many of today's spectroscopic techniques (cf. Refs. above as well as [15–20], for further examples).

Yet, as long as these techniques remain restricted to optical wavelengths, they will be fundamentally unsuited to provide microscopic *spatial* insights in addition to their *spectral* information. In order to lift this limitation and add atomic-scale resolution to wavemixing techniques, we shall study their extension into the x-ray-regime, where truly microscopic probes are available. Thus, we shall subsequently investigate **x-ray-optical wavemixing**.

[1] We note that the production of dc-voltages from alternating inputs is typically the task of so-called rectifiers in electrotechnics. It would hardly be economical to use a high-frequency mixer-circuit for the sole purpose of performing rectification. In a peculiar sleight of terminology-transfer, the nonlinear-optics community has, nevertheless, adopted this expression in the term 'optical rectification', when referring to the creation of DC-components as of Eq. (1.5) from optical wavemixing (cf., for examples, Refs. [10–12]).

1.2 Introduction to x-ray-optical wavemixing

Looking beyond the well-established forms of wavemixing, we seek to study its extension into the x-ray regime. More specifically, we shall address the combination of x-ray-*and*-optical wavemixing, which promises to combine the spectroscopic selectivity of optical techniques with unprecedented spatial resolution—provided via the diffractive imaging capabilities of x-rays.

Motivating this ansatz in greater depth, we shall present a short exposition of the subject's origin and context below. We note for reference that this equals verbatim our discussion in Ref. [21] to the same end.

"Since their discovery in 1895, x-rays have been used to obtain insights into the structure of material systems—with x-ray diffraction in particular serving as a microscopic probe of the electronic density [22, 23]. Backed by the continuous improvement of sources and detectors, it has become routinely possible nowadays, to reconstruct complicated protein structures from x-ray scattering measurements [24], for example.

Notwithstanding its broad success, regular x-ray diffraction becomes very challenging, if microscopic resolution of valence electron distributions is desired [25]. These weakly bound electrons, which are the most relevant in chemical and technological terms, are typically spread dilutely across the solid. As such, their scattering signal scales unfavorably compared to the well-localized (atomic) core electrons.

In order to circumvent this problem and obtain a valence selective scheme, Freund and Levine suggested to go beyond linear elastic scattering as early as 1970 [26]. Using nonlinear, parametric x-ray optical wavemixing processes (XOWM), one can leverage the spectral selectivity of an additional optical field to isolate the response of valence electrons. An example of this is the process of sum-frequency generation (SFG), wherein a sample is illuminated by both x-ray (ω_X) and optical (ω_O) photons, while the detection focuses on scattered photons at the sum-frequency $\omega_S = \omega_X + \omega_O$. As this frequency cannot be generated via elastic scattering, any measured signal thus provides a short-wavelength probe *conditional* on the simultaneous interaction with the optical admixture. Tuning the optical photons resonantly with valence excitations then establishes the desired selectivity.

Though promising in principle, x-ray wavemixing approaches were restricted to proof-of-principle tests for a long time, because they were stifled by low count rates and cumbersome detection [27, 28]. Yet, with the arrival of storage-ring based x-ray sources and x-ray free-electron lasers (XFEL), a wide range of nonlinear x-ray phenomena has become observable [29–45] and XOWM itself has attracted renewed experimental interest [46–51].

Complementing these experimental developments, we want to address the theoretical understanding of XOWM. To this end, we present a modern framework for its description, which we derive on the basis of nonrelativistic Quantum Electrodynamics (QED) [52, 53]. So far, interpretations of XOWM recurringly [46, 48, 54, 55] rely on the classical picture suggested by Eisenberger and McCall [27]. Their model, in turn, was developed for wavemixing solely within the x-ray domain and treats the electronic response in terms of free charges on classical trajectories. However, this treatment becomes invalid once optical frequencies are admixed, for which the electronic response is instead dominated by discrete, quantum mechanical transitions. These have to be incorporated from first principles, in order to obtain a microscopically accurate description of XOWM."

With our initial motivation thus reinforced, we will address our main goal of describing XOWM in the following chapters. In this, we reach beyond merely qualitative explanations or singular case-

studies and, instead, seek to establish a framework of broad applicability. Starting from first-principles, we shall derive a unified scattering expression for a class of XOWM processes, which covers sum- and difference-frequency generation as well as x-ray parametric down-conversion on equal footing.

Beyond proposing this theory, we likewise engage in benchmarking and applying it. In particular, we have sought several experimental applications ourselves—a fact that might be mildly obscured by the overtly theoretical title of this treatise—and will report on them at some length. We emphasize that—in our opinion—any theory is only as good as its applications and, as such, we are particularly grateful to numerous people and various circumstances that have allowed our theory to manifest itself experimentally.

In closing, we express our hope that, we can share some of our theoretical or experimental insights in the following chapters. For a more detailed guide to the work's structure, we refer the reader to the next section. We wish for a pleasant and, hopefully, informative reading.

1.3 Reader's guide

Following this introduction, the thesis is structured into four main chapters (2 - 5) followed by 'Extras' (6) and a concluding chapter (7).

In the course of the main part, we develop our theory for x-ray-optical wavemixing. To this end, we establish the basic theoretical formalism in Chpt. 2 and derive the essential scattering equations needed to describe parametric XOWM. From this point onwards, we pursue the evaluation of these equations under realistic conditions. This requires substantial modelling, both on the side of the nonlinear electronic response function and on the description of any electromagnetic field, which partakes in the mixing process. These subjects are addressed in detail within Chpts. 3 and 4, respectively. Converging onto our central objective, we combine our basic theoretical framework with the subsequently obtained models, in order to evaluate different XOWM scenarios quantitatively in Chpt. 5. In the pertaining discussion, we will likewise report on several experimental results, which were obtained during the course of this thesis-work.

For readers, who are interested primarily in these experimental results on XOWM and their comparison to theory, we note that they may skip ahead to said Chpt. 5 directly. The preceding development of the theoretical framework and, in particular, the detailed discussions of constituent correlation functions are not strictly required for its understanding.

Finally, we will present 'extra' work in Chpt. 6. While this chapter's content is connected to our main topic of XOWM, it already points beyond the scope of this thesis. In it, we will draw on concepts that we have established in the preceding chapters and address two outstanding issues. Thereby, the chapter provides an early outlook towards future research activities, before Chpt. 7 closes with a more general conclusion as well as a more general outlook.

Conventions In closing, we want to collate some conventions, which concern the units and notation used in the subsequent work. This collection is likely incomplete, yet we consider it a convenient starting point, nonetheless.

Atomic units: Throughout our derivations, we will employ the conventional system of atomic units, i.e., $\hbar = a_0 = m_\mathrm{e} = |e| = 1$. In this, the symbols refer to the reduced Planck constant, the Bohr radius as well as the mass and charge of an electron, respectively. Furthermore, we fix the speed of light in vacuo

in terms of the fine structure constant $c = 1/\alpha \approx 1/137$. The combination of these choices implies that the prefactor of Coulomb's law, i.e., $1/4\pi\varepsilon_0$, reduces to unity.

Vectorial notation: Throughout our treatise we shall employ bold typesetting to indicate vectorial quantities in $\mathbb{R}^3$. For example, $\mathbf{x}$ could be a position vector in real-space. In addition to this general notation, we reserve certain letters for specific purposes and (largely) adhere to this guideline. Thus, for spatial positions, we tend to employ $\mathbf{x}$ and $\mathbf{y}$. Special emphasis is put on lattice vectors of crystals (i.e., translations on the lattice), which we denote by $\mathbf{R}$. Momenta, instead, will usually be denoted by letters $\mathbf{k}$, $\mathbf{p}$, $\mathbf{q}$ or $\mathbf{Q}$. Once again, special emphasis is placed on momenta on the reciprocal lattice of a crystal, which we denote by $\mathbf{G}$. Regarding *unit vectors*, there is additional notation, which we explain next.

'Hat'-notation: We employ a 'hat'-notation on top of symbols to signify either of two things: Primarily, we shall indicate quantum-mechanical operator by the use of an added 'hat'-symbol, for example, $\hat{\mathbf{p}}$ indicates the momentum operator or $\hat{H}$ indicates a Hamiltonian operator. In the absence of quantum-mechanical operators, however, we employ the 'hat'-notation to signify unit vectors. As such $\hat{\mathbf{G}}$ denotes the unit vector parallel to $\mathbf{G}$. In case operators *and* unit vectors appear concurrently in a discussion, we shall resort to an alternative notation for the latter. This will see the letter $\mathbf{e}$ in bold face used for a unit vector—following the German word **E**inheit for unit.

Frequency nomenclature: Throughout this work, we will often make use of the symbol ω, whereby we refer to an angular frequency in the vast majority of cases. As an example consider the oscillation $\cos(\omega t)$, which is understood to feature a period of $T = 2\pi/\omega$. Diverging from the precise nomenclature, however, we shall mostly refer to this quantity ω in an abbreviated fashion as a 'frequency'. As a third option, we may employ the designation 'energy' for ω as well—owing to the fact that energy and *angular* frequency are interchangeable in atomic units $E = \hbar\omega \to \omega$ (see above).

Fourier transformations: We outline our Fourier conventions—both for continuous and bounded domains—in a dedicated Appendix A.2, along with more detailed follow-up sections.

Multiple integrals: During our initial derivation, we will—at times—encounter expressions, wherein integrations abound. Usually, these are cases of multiple Fourier transforms or similar. In order to keep these expressions readable, nonetheless, we seek to avoid printing accumulated integral signs individually. Instead, we will often opt for a 'multiplicative' notation that summarizes groups of integrals, which pertain to similar differentials, e.g.,

$$\int d^3k_L \int d^3k'_L \int d^3k_X \int d^3k'_X \to \int^{\times 4} d^3k_L\, d^3k'_L\, d^3k_X\, d^3k'_X. \tag{1.8}$$

Chapter 2

Theoretical framework for XOWM

In this chapter, we commence our efforts to formally describe x-ray-optical wavemixing (XOWM). Our primary aim will be the derivation of a unified scattering expression for a class of XOWM processes—comprising SFG, DFG as well as XPDC—which is amenable to quantitative, numerical evaluation later on (see Chpt. 5). To this end, we will lay the theoretical foundations in the upcoming sections.

First of all, we shall give a general exposition of the basic theoretical framework, upon which we will build our description of XOWM. In Sec. 2.1, we briefly outline the respective 'first principles', before we proceed to the core of our derivation.

In said core part, namely the bipartite Sec. 2.2, we will approach XOWM from the perspective of x-ray scattering: Initially (in Sec. 2.2.1), we derive an inelastic scattering expression, within the perturbative limit, that concerns only the interaction of x-rays with matter. Subsequently (in Sec. 2.2.2), we turn our attention towards the optical admixture, the effect of which we will include via further perturbative expansion[1].

After identifying the essential contributions to the desired XOWM signal, we process them into a compact expression for an XOWM-observable. This will be summarized in Sec. 2.3—both in real- and reciprocal-space.

[1] We note that at a far later stage of this treatise, we shall re-evaluate our purely perturbative tenet and explore non-perturbative effects within the scope of a model system (cf. Chpt. 6, Sec. 6.1).

2.1 Basic framework

At the outset of our discussion of XOWM, we shall introduce the theoretical framework, wherein our work will be rooted. We note up-front that the pertaining exposition will largely reproduce an analogous discussion from our manuscript [21]. Readers, who are either familiar with its preprint or familiar with works in related fields (such as Refs. [56–60], for instance), may consider to skip this section in its entirety and focus on the actual derivations, starting in Sec. 2.2.

We set our description of XOWM within the well-established framework of nonrelativistic Quantum-Electrodynamics (QED) [52, 53], wherein we closely follow the formalism outlined in Ref. [57]. Before we quantize this field-theory, we impose the Coulomb gauge upon the electromagnetic vector potential, i.e., $\nabla \cdot \mathbf{A}(\mathbf{x}) = 0$. Thereby, $\mathbf{A}(\mathbf{x})$ is rendered fully transverse, while any longitudinal coupling is relegated into the scalar potential[2] $\Phi(\mathbf{x})$.

For the quantized vector potential in free space, we adopt the expansion

$$\hat{\mathbf{A}}(\mathbf{x}) = \sum_{\mathbf{k},\lambda} \sqrt{\frac{2\pi}{V\omega_{\mathbf{k}}\alpha^2}} \left(\hat{a}_{\mathbf{k},\lambda}\ \boldsymbol{\varepsilon}_{\mathbf{k},\lambda}\ e^{\mathrm{i}\mathbf{k}\cdot\mathbf{x}} + \mathrm{h.c.}\right), \tag{2.1}$$

where $\hat{a}_{\mathbf{k},\lambda}$ ($\hat{a}^{\dagger}_{\mathbf{k},\lambda}$) is the annihilation (creation) operator for a photon of energy $\omega_{\mathbf{k}} = c\,|\mathbf{k}|$ in the plane wave mode of wave vector $\mathbf{k}$ and polarization $\boldsymbol{\varepsilon}_{\mathbf{k},\lambda}$. We use the index λ to enumerate two distinct polarization states, both of which satisfy the transversality condition $\boldsymbol{\varepsilon}_{\mathbf{k},\lambda} \cdot \mathbf{k} = 0$ as a consequence of the Coulomb gauge. The theoretical quantization volume is labelled by V for the time being, however, it will not feature in any *physical* observable (see discussion below).

Coupling the field to matter, we focus on the electronic charges and write the associated interaction Hamiltonian in the familiar minimal coupling form [3]:

$$\hat{H}_{\mathrm{INT}} = \int d^3x\, \hat{\psi}^{\dagger}(\mathbf{x}) \left(\alpha \mathbf{p} \cdot \hat{\mathbf{A}}(\mathbf{x}) + \frac{\alpha^2}{2}\hat{\mathbf{A}}^2(\mathbf{x})\right) \hat{\psi}(\mathbf{x}). \tag{2.2}$$

Here, the 2-component spinors $\hat{\psi}(\mathbf{x})$ ($\hat{\psi}^{\dagger}(\mathbf{x})$) are electronic field operators. Analogous to the action of $\hat{a}_{\mathbf{k},\lambda}$ ($\hat{a}^{\dagger}_{\mathbf{k},\lambda}$) on photons, their electronic counterparts annihilate (create) an electron of particular spin state at the position $\mathbf{x}$.

Apart from their interaction with the light-field, we shall not concern ourselves any further with the electrons' description at this point. Suffices to state that any material properties (including electrostatic interactions) will be captured by a pertaining Hamiltonian $\hat{H}_{\mathrm{MAT}}$. We shall elaborate further on its application (or approximation for that matter) in the later Chpt. 3. For the electromagnetic field itself, we adopt the standard mode-based formulation $\hat{H}_{\mathrm{EM}} = \sum_{\mathbf{k},\lambda} \omega_{\mathbf{k}} (\hat{a}^{\dagger}_{\mathbf{k},\lambda} \hat{a}_{\mathbf{k},\lambda} + 1/2)$. Together with Eq. (2.2), these render the Hamiltonian of the overall light-matter system tripartite:

$$\hat{H} = \hat{H}_{\mathrm{MAT}} + \hat{H}_{\mathrm{EM}} + \hat{H}_{\mathrm{INT}}. \tag{2.3}$$

[2] We note that, in the suggestively named 'Coulomb gauge', the scalar potential will take on the form of the well-known Coulomb potential, i.e., $\Phi(\mathbf{x}) = \sum_i \frac{q_i}{|\mathbf{x}-\mathbf{x}_i|} = \int d^3y\ \frac{\rho(\mathbf{y})}{|\mathbf{x}-\mathbf{y}|}$, for point charges or continuous charge distributions, respectively. We remark further that this choice of gauge—far from being unique—is highly advantageous, when it comes to the interoperability of our scattering theory with electronic structure methods later on. Most of these methods will rely on a basic Hamiltonian for the electronic system, which posits the above form of the Coulomb potential.

[3] We emphasize that the interaction Hamiltonian as shown in Eq. (2.2) neglects any couplings of $\hat{\mathbf{A}}(\mathbf{x})$ to nuclear charges and—more intricately—to the spin degrees of freedom, which are present in the material systems.

Based on this, we can formally account for the time-evolution of the full, coupled quantum-system using either the time-dependent Schrödinger equation (TDSE) for state-vectors $|\Psi(t)\rangle$

$$i\,\frac{\partial}{\partial t}\,|\Psi(t)\rangle = \hat{H}\,|\Psi(t)\rangle \tag{2.4}$$

or the Liouville-von Neumann equation for the system's density operator $\hat{\rho}(t)$

$$i\,\frac{\partial\,\hat{\rho}(t)}{\partial t} = [\hat{H},\hat{\rho}(t)]. \tag{2.5}$$

During the course of this work, we shall focus on the latter formulation, i.e., in terms of density operators. We do so, because we consider this formalism more conducive to the discussion of partially coherent systems—such as the light-fields emitted by synchrotron radiation sources or free-electron lasers.

In order to evaluate physically observable quantities, which are characterized by an operator $\hat{O}$, we will compute expectation values according to the prescription

$$\langle\hat{O}\rangle(t) = \mathrm{Tr}\,\{\hat{\rho}(t)\hat{O}\} = \mathrm{Tr}\,\{\hat{U}(t,t_0)\,\hat{\rho}(t_0)\,\hat{U}(t_0,t)\,\hat{O}\}\,. \tag{2.6}$$

Herein, we use the symbol $\mathrm{Tr}\,\{...\}$ to denote the trace over all operators enclosed by the curly brackets. Furthermore, we note the introduction of so-called time-evolution operators $\hat{U}(t,t_0)$. These unitary operators are constructed to satisfy the TDSE in place of a state-vector and may be used to formalize the temporal propagation of either $|\Psi(t)\rangle$ or $\hat{\rho}(t)$, as above. Within the upcoming Sec. 2.2, such operators $\hat{U}(t,t_0)$ will prove instrumental in the perturbative expansion of the time-evolution, which is driven by external light fields. For a more detailed review of their properties and applications, as well as an introduction to time-dependent perturbation theory itself, we refer the reader to an additional Appendix A.1.

Observable Recurring to Eq. (2.6), we emphasize the particular need to define an observable $\hat{O}$ that suitably captures XOWM. Given that all x-ray-optical wavemixing processes should effectively 'modify' the initial x-ray field—for instance by (up-)conversion of an x-ray photon $\omega_X \to \omega_{\mathrm{SFG}} = \omega_X + \omega_O$ during sum-frequency generation—we decide to focus on such 'modifications' for detection. More formally speaking, we adopt a scattering perspective and focus on the detection of x-ray photons that are scattered out of an incoming field distribution into initially unoccupied modes of the field (cf. Eq. (2.1)). For any such final mode $\mathbf{k}_f,\lambda_f$ we can determine the probability of a single photon being scattered into it by projecting onto the number state $|1\rangle_{\mathbf{k}_f,\lambda_f}$. Analogous procedures are widely used in the calculation of far-field diffraction patterns from weakly scattering samples (see for instance Refs. [58, 61–63]). We can write an according projection operator across the full radiative Fock-space as

$$\hat{\Pi}_{\mathbf{k}_f,\lambda_f} = \Big(\bigotimes_{\mathbf{k}\neq\mathbf{k}_f,\lambda\neq\lambda_f}\hat{\mathbb{1}}_{\mathbf{k},\lambda}\Big)\otimes|1\rangle\langle 1|_{\mathbf{k}_f,\lambda_f}\,. \tag{2.7}$$

Once again, this singles out the probability for a (new) photon being in mode $\mathbf{k}_f,\lambda_f$. Combining this with the identity on the material part, yields the desired observable for our purpose

$$\hat{O}_{\mathbf{k}_f,\lambda_f} := \hat{\Pi}_{\mathbf{k}_f,\lambda_f}\otimes\hat{\mathbb{1}}_{\mathrm{MAT}} = \Big(\bigotimes_{\mathbf{k}\neq\mathbf{k}_f,\lambda\neq\lambda_f}\hat{\mathbb{1}}_{\mathbf{k},\lambda}\Big)\otimes|1\rangle\langle 1|_{\mathbf{k}_f,\lambda_f}\otimes\hat{\mathbb{1}}_{\mathrm{MAT}}. \tag{2.8}$$

We point out that this choice of an observable does entail a range of shortcomings, even though it will prove very insightful for the scope of this work. Notable caveats to bear in mind comprise:

- The detection scheme, which is modelled by the photon-projector in Eq. (2.8), corresponds to an intensity-type observable. Hypothetical analysis of the electric field, or its phase in particular, are thus precluded a priori[4].
- By extension of the above point, the observable should only be applied to far-field detection schemes—avoiding scenarios of phase-contrast imaging or strong heterodyning fields.
- On the level of simple, intensity-based detection (i.e., photon counting), care should be taken to restrict the scattering signal to an appropriately low count per mode[5]. By construction, our observable would saturate for counts $\left\langle \hat{n}_{\mathbf{k}_f,\lambda_f} \right\rangle \gtrsim 1$.
- The above observable is, again by construction, wholly unsuited to the analysis of photon correlations. This would concern the (hypothetical[6]) emission or scattering of multiple photons, of which Eq. (2.8) could only capture one under any given circumstance.

As a final outlook towards the definition of more versatile observables, we note that a natural way forward would consist in the adoption of detection-models on the basis of field correlation functions. This was pioneered by Glauber [64] and has seen various extensions over time. For an example, on how to connect the intensity as an observable quantity to an underlying field correlator, see derivations in App. A.10. Regarding the application of Glauber-functions to the detection of correlated x-ray photons, a recent example can be found in Ref. [65].

***Physical* observable** In a final revision of the above, we have to ensure that any observable we compute is ultimately independent of our modelling parameters. For the present case, this concerns in particular the arbitrary quantization volume V, which we have introduced in the very beginning (cf. Eq. (2.1)). It determines the mode spacing of our quantized field and is implicitly imprinted in any expectation value $\langle \hat{O}_{\mathbf{k}_f,\lambda_f} \rangle$, which we could compute of the observable (Eq. (2.8)).

As a solution, we should take the continuum limit $V \to \infty$ (cf. analogously App. A.4) and consider the scattering probability into a differential mode-volume rather than a discrete, single mode. The corresponding prescription to convert the observable into a double differential scattering probability reads (cf. also Ref. [57]):

$$\frac{\mathrm{d}P_{\lambda_f}(\mathbf{k}_f)}{d\Omega_f d\omega_f} = \frac{V\alpha^3}{(2\pi)^3}\,\omega_f^2\,\langle \hat{O}_{\mathbf{k}_f,\lambda_f} \rangle. \tag{2.9}$$

[4] We comment that the restriction to intensity-based observables does not constitute a major impediment, as experimental x-ray detectors, to-date, are themselves restricted to intensity-based detection.

[5] We note that the formal limitation of the scattering yield to a single photon per mode, has not posed a restriction to practical applications yet.

[6] We note that an interest in photon correlations could indeed be justified. Considering, for instance, the process of x-ray parametric down-conversion, we are faced with the scattering of an x-ray photon and the *simultaneous* emission of a so-called 'idler'-photon at lower energies. Measuring their correlation experimentally could not yet be achieved for x-ray-optical scenarios, though.

2.2 Perturbative approach to XOWM

With the basic framework established, we focus our attention onto our main goal, i.e., the derivation of a description for (parametric) XOWM processes. Given that these processes are typically weak, we will rely on perturbative methods for their evaluation[7]. Overall, our description takes on a scattering perspective, for which we derive (i.e., expand) the pertaining observable (cf. Eq. (2.8)) in two successive steps:

1. In the first section, which follows below (Sec. 2.2.1), we will derive a perturbative expression for general (inelastic) x-ray scattering (IXS). Herein, we shall not impose any conditions on the *optical* light-matter interaction yet.

2. Subsequently (i.e., in Sec. 2.2.2), we will render the optical admixture explicit and include it at the next order of perturbation theory. This expansion will build upon our previous IXS result.

For readers, who are familiar with IXS from works such as Refs. [59, 61, 66], we note that they may skip the first part of our derivations (Sec. 2.2.1). The result recovers previous expressions [ibid.] and its expansion in the following does not rely on earlier steps.

2.2.1 Resolution of (inelastic) x-ray scattering

In order to formalize our understanding of x-ray-optical wavemixing, we adopt a scattering description. As such, we seek to describe the probability that an x-ray photon is scattered by the sample *under* the influence of an optical admixture.

Our first step to this end, will see us evaluate the x-ray scattering part quite generally, before addressing details of the optical interaction later (Sec. 2.2.2). We recall from our earlier discussion that we have already established an observable to measure x-ray scattering (Eq. (2.8)). In order to properly quantify the scattering probability during an actual diffraction process, however, we still need to evaluate its expectation value for the respective conditions. In general, we can write

$$\langle \hat{O}_{\mathbf{k}_f,\lambda_f} \rangle (t) = \mathrm{Tr}\left\{ \hat{U}(t,t_0)\hat{\rho}(t_0)\hat{U}(t_0,t)\hat{O}_{\mathbf{k}_f,\lambda_f} \right\}, \tag{2.10}$$

which is simply a combination of Eqs. (2.6) and (2.8). In here, we find the time-evolution operators $\hat{U}(t_0,t)$ that still pertain to the description (i.e., Hamiltonian) of the *full*, interacting light-matter system. Its exact treatment is notoriously infeasible for realistic systems, such that we have to approach it via a series of simplifications.

As pointed out earlier, we choose to employ (conventional) time-dependent perturbation theory (TDPT) as a means to reduce the complexity of the problem[8]. To this end, we assume the light-matter coupling—here for x-rays scattering off the sample—to be sufficiently weak, such as to allow the decomposition of the fully interacting problem into two almost independent subsystems. For their description, we can re-partition the overall Hamiltonian

$$\hat{H} = \underbrace{\hat{H}_{\mathrm{MAT}} + \hat{H}_{\mathrm{EM}}}_{\hat{H}_0} + \underbrace{\hat{H}_{\mathrm{INT}}}_{\downarrow\ \hat{H}_{\mathrm{INT\_X}}}. \tag{2.11}$$

[7] We note that the interested reader can find an exposition of the basic principles of time-dependent perturbation in the Appendix A.1.

[8] See above footnote.

into one part for the non-interacting light and matter systems and a second part for their interaction. For the moment, we shall ignore coupling to optical field components, which we can consider to be included with $\hat{H}_0$ for convenience. Moreover, we shall restrict our discussion of x-ray scattering to *non-resonant* scattering, which is dominantly mediated via the $\mathbf{A}^2$-part of Eq. (2.2), i.e.,

$$\begin{aligned}\hat{H}_{\text{INT\_X}} &\approx \frac{\alpha^2}{2}\int d^3x\, \hat{\psi}^\dagger(\mathbf{x})\hat{\mathbf{A}}^2(\mathbf{x})\hat{\psi}(\mathbf{x}) = \frac{\alpha^2}{2}\int d^3x\, \hat{n}(\mathbf{x})\,\hat{\mathbf{A}}^2(\mathbf{x}) \\ &= \frac{\alpha^2}{2}\int d^3x\, \hat{n}(\mathbf{x})\left[2\hat{\mathbf{A}}_{\text{x\_in}}(\mathbf{x})\hat{\mathbf{A}}_{\text{x\_out}}(\mathbf{x}) + \hat{\mathbf{A}}^2_{\text{x\_in}}(\mathbf{x}) + \hat{\mathbf{A}}^2_{\text{x\_out}}(\mathbf{x})\right]. \end{aligned} \tag{2.12}$$

In writing Eq. (2.12), we have identified $\hat{\psi}^\dagger(\mathbf{x})\hat{\psi}(\mathbf{x}) = \hat{n}(\mathbf{x})$ as the operator pertaining to the electronic density and further exploited its fully local nature to commute around $\hat{\mathbf{A}}(\mathbf{x})$. Regarding the vector potential itself: We have formally partitioned this into orthogonal components

$$\hat{\mathbf{A}}(\mathbf{x}) = \hat{\mathbf{A}}_{\text{x\_in}}(\mathbf{x}) + \hat{\mathbf{A}}_{\text{x\_out}}(\mathbf{x}) + \hat{\mathbf{A}}_{\text{opt}}(\mathbf{x}) + ..., \tag{2.13}$$

where the listed components pertain to incoming x-ray modes, scattered (or outgoing) x-ray modes as well as optical contributions to the electromagnetic field, respectively. The trailing '...' indicate a presently irrelevant remainder—for instance deep-IR modes, THz-waves or γ-rays.

To lowest order, the only relevant contribution to x-ray scattering—from incident into outgoing field modes—would obviously stem from the cross-term involving $\mathbf{A}_{\text{x\_in}} \cdot \mathbf{A}_{\text{x\_out}}$ inside $\hat{H}_{\text{INT\_X}}$. Thus, we shall only consider

$$\hat{H}^{\text{relev.}}_{\text{INT\_X}} = \alpha^2 \int d^3x\, \hat{n}(\mathbf{x})\hat{\mathbf{A}}_{\text{x\_in}}(\mathbf{x})\hat{\mathbf{A}}_{\text{x\_out}}(\mathbf{x}) \tag{2.14}$$

within the subsequent derivations.

Application of TDPT Acting on our premise that x-ray and matter subsystems should only interact weakly during scattering processes, we partition the time-evolution operators from Eq. (2.10) and approximate the interaction part in accordance with prescription (A.12)—cf. App. A.1

$$\hat{U}(t,t_0) = \hat{U}_0(t,t_0)\,\hat{U}_{\text{INT\_X}}(t,t_0) \tag{2.15}$$

$$\approx \hat{U}_0(t,t_0)\left(\hat{\mathbb{1}} - \mathrm{i}\int_{t_0}^{t} dt_1\, \hat{U}_0(t_0,t_1)\,\hat{H}^{\text{relev.}}_{\text{INT\_X}}\,\hat{U}_0(t_1,t_0)\right). \tag{2.16}$$

As the identity in above's equation does not contribute to any scattering processes, we may neglect it as well and write our approximate observable as[9]

$$\langle \hat{O}_{\mathbf{k}_f,\lambda_f}\rangle(t) \approx \mathrm{Tr}\left\{\Big(\int_{t_0}^{t} dt_1\; \hat{U}_0(t,t_1)\,\hat{H}^{\text{relev.}}_{\text{INT\_X}}\,\hat{U}_0(t_1,t_0)\Big)\hat{\rho}(t_0)\Big(\int_{t_0}^{t} dt_1'\; \hat{U}_0(t,t_1')\,\hat{H}^{\text{relev.}}_{\text{INT\_X}}\,\hat{U}_0(t_1',t_0)\Big)^\dagger \hat{O}_{\mathbf{k}_f,\lambda_f}\right\}. \tag{2.17}$$

In order to process Eq. (2.17) further, we shall introduce some assumptions on $\hat{\rho}(t_0)$. To very good

[9] We want to comment on the approximations leading up to / being included in Eq. (2.17): By restricting our description of scattering—and thereby also XOWM processes—to first order contributions from $\hat{H}^{\text{relev.}}_{\text{INT\_X}}$ (as of Eq. (2.14)), we have neglected any contributions from $\mathbf{p}\cdot\mathbf{A}$-type scattering and also higher order interactions in $\mathbf{A}^2$.

The former are typically associated with resonant scattering or, for that matter, dispersive corrections. It is in line with our premise of focusing on non-resonant XOWM processes to neglect them. However, we will thereby also neglect x-ray absorption effects, which should form a natural loss channel to both in- and out-going x-rays, irrespective of any resonant condition.

approximation, the x-ray subsystem will not be correlated with the other (i.e., optical or material) degrees of freedom before the scattering process. Subsuming these parts as 'REST' below, we may factorize the initial density operator as

$$\hat{\rho}(t_0) = \hat{\rho}_{\mathrm{X}}(t_0) \otimes \hat{\rho}_{\mathrm{REST}}(t_0). \tag{2.18}$$

Using this within Eq. (2.17), we can factorize the trace over the x-ray and REST subspaces

$$\begin{aligned}\langle \hat{O}_{\mathbf{k}_f,\lambda_f} \rangle(t) = \alpha^4 \int_{t_0}^{t} dt_1 \int_{t_0}^{t} dt_1' \int d^3x \int d^3x' \\ \times \mathrm{Tr}_{\mathrm{REST}} \{ \hat{U}_0(t,t_1)\, \hat{n}(\mathbf{x})\, \hat{U}_0(t_1,t_0)\, \hat{\rho}_{\mathrm{REST}}(t_0)\, \hat{U}_0(t_0,t_1')\, \hat{n}(\mathbf{x}')\, \hat{U}_0(t_1',t)\, \hat{\mathbb{1}}_{\mathrm{REST}} \} \\ \times \mathrm{Tr}_{\mathrm{X}} \{ \hat{U}_0(t,t_1)\, \hat{\mathbf{A}}_{\mathrm{x\_in}}(\mathbf{x}) \hat{\mathbf{A}}_{\mathrm{x\_out}}(\mathbf{x})\, \hat{U}_0(t_1,t_0)\, \hat{\rho}_{\mathrm{X}}(t_0)\, \hat{U}_0(t_0,t_1')\, \hat{\mathbf{A}}_{\mathrm{x\_in}}(\mathbf{x}') \hat{\mathbf{A}}_{\mathrm{x\_out}}(\mathbf{x}')\, \hat{U}_0(t_1',t)\, \hat{\Pi}_{\mathbf{k}_f,\lambda_f} \}.\end{aligned} \tag{2.19}$$

In doing so, we implicitly understand $\hat{U}_0$, but also $\hat{\Pi}_{\mathbf{k}_f,\lambda_f}$, to be appropriately restricted to the respective subspace, upon which they are operating[10].

Next, we partition $\hat{\rho}_{\mathrm{X}}(t_0)$ analogous to the electromagnetic field in Eq. (2.13)

$$\hat{\rho}_{\mathrm{X}}(t_0) = \hat{\rho}_{\mathrm{X\_IN}}(t_0) \otimes \hat{\rho}_{\mathrm{X\_OUT}}(t_0), \tag{2.20}$$

wherein we naturally assume all scattering modes to be unoccupied initially, i.e.,

$$\hat{\rho}_{\mathrm{X\_OUT}}(t_0) = \bigotimes_{\mathbf{k},\lambda}^{out} |0\rangle \langle 0|_{\mathbf{k},\lambda}\,. \tag{2.21}$$

This allows us to further decompose the trace over all x-ray modes into:

$$\begin{aligned}\mathrm{Tr}_{\mathrm{X}} \{...\} = \mathrm{Tr}_{\mathrm{X\_IN}} \{ \hat{U}_0(t,t_1)\, (\hat{\mathbf{A}}_{\mathrm{x\_in}}(\mathbf{x}))_\rho\, \hat{U}_0(t_1,t_0)\, \hat{\rho}_{\mathrm{X\_IN}}(t_0)\, \hat{U}_0(t_0,t_1')\, (\hat{\mathbf{A}}_{\mathrm{x\_in}}(\mathbf{x}'))_\sigma\, \hat{U}_0(t_1',t)\, \hat{\mathbf{1}}_{\mathrm{X\_IN}} \} \\ \times \mathrm{Tr}_{\mathrm{X\_OUT}} \{ \hat{U}_0(t,t_1)\, (\hat{\mathbf{A}}_{\mathrm{x\_out}}(\mathbf{x}))_\rho\, \hat{U}_0(t_1,t_0)\, \hat{\rho}_{\mathrm{X\_OUT}}(t_0)\, \hat{U}_0(t_0,t_1')\, (\hat{\mathbf{A}}_{\mathrm{x\_out}}(\mathbf{x}'))_\sigma\, \hat{U}_0(t_1',t)\, \hat{\Pi}_{\mathbf{k}_f,\lambda_f} \}.\end{aligned} \tag{2.22}$$

Above and henceforth, we adhere to the convention that doubly occurring Greek indices will be summed over.

It is important to note that $\hat{U}_0$ (or $\hat{H}_0$, respectively) does not contain any x-ray-matter interaction terms, at this point—nor does it contain any other terms that could mix x-ray modes among each other. Thus, $\hat{U}_0$ merely causes the *free* evolution of all x-ray field operators. This implies, in particular, that $\hat{U}_0$ conserves the occupation number of each photonic mode. Given that the outgoing modes are initially unoccupied, this will therefore remain unchanged, *unless* a photon is created via $\hat{\mathbf{A}}_{\mathrm{x\_out}}(\mathbf{x})$.

The second point above pertains in particular to effects of multiple scattering, which we have hereby also excluded. Given the low efficiency expected for XOWM processes, this will also be justified in many cases. Nonetheless, we should expect modifications for large and mosaic sample crystals (cf. 'secondary extinction' [67]) or upon concurring, coherent diffractive effects. This is to say that, XOWM processes could be strongly modified, if the field that drives them ($\hat{\mathbf{A}}_{\mathrm{x\_in}}(\mathbf{x})$) is depleted or structured due to coincident Bragg-diffraction. Given that XOWM processes tend to occur in close proximity to regular Bragg-conditions (cf. discussion in Sec. 5.1.2.a, for instance), this interference may not always be trivial to prevent. Hereunto, a unified description of linear and nonlinear scattering in a framework akin to dynamical diffraction theory [68] would be as desirable as it is difficult.

As an overall take-away, it should be kept in mind that all of the above limits our description of XOWM, formally, to kinematical diffraction or 1st Born-approximation.

[10] We note that we will apply operators such as $\hat{U}_0$ several times in the following, always assuming that they are (implicitly) adapted to the subspace, which they operate on. We shall cease to point this out, as long as it is trivial.

Thus, it suffices to focus on the photon creation by $\hat{\mathbf{A}}_{\text{x\_out}}(\mathbf{x})$ in Eq. (2.22) and account for photon annihilation by $\hat{\mathbf{A}}_{\text{x\_in}}(\mathbf{x})$, conversely[11]. Phrasing this in terms of positive and negative frequency parts of the respective operators yields, we find

$$\begin{aligned}\mathrm{Tr}_{\mathrm{X}}\{...\} = \mathrm{Tr}_{\text{X\_IN}}\{\hat{U}_0(t,t_1)\,(\hat{\mathbf{A}}^{(+)}_{\text{x\_in}}(\mathbf{x}))_\rho\,\hat{U}_0(t_1,t_0)\,\hat{\rho}_{\text{X\_IN}}(t_0)\,\hat{U}_0(t_0,t_1')\,(\hat{\mathbf{A}}^{(-)}_{\text{x\_in}}(\mathbf{x}'))_\sigma\,\hat{U}_0(t_1',t)\,\hat{\mathbb{1}}_{\text{X\_IN}}\}\\ \times \mathrm{Tr}_{\text{X\_OUT}}\{\hat{U}_0(t,t_1)\,(\hat{\mathbf{A}}^{(-)}_{\text{x\_out}}(\mathbf{x}))_\rho\,\hat{U}_0(t_1,t_0)\,\hat{\rho}_{\text{X\_OUT}}(t_0)\,\hat{U}_0(t_0,t_1')\,(\hat{\mathbf{A}}^{(+)}_{\text{x\_out}}(\mathbf{x}'))_\sigma\,\hat{U}_0(t_1',t)\,\hat{\Pi}_{\mathbf{k}_f,\lambda_f}\}.\end{aligned} \tag{2.23}$$

Rewriting the identity of the first line above, we can resolve the incoming trace as

$$\begin{aligned}&\mathrm{Tr}_{\text{X\_IN}}\{\hat{U}_0(t,t_1)\,(\hat{\mathbf{A}}^{(+)}_{\text{x\_in}}(\mathbf{x}))_\rho\,\hat{U}_0(t_1,t_0)\,\hat{\rho}_{\text{X\_IN}}(t_0)\,\hat{U}_0(t_0,t_1')\,(\hat{\mathbf{A}}^{(-)}_{\text{x\_in}}(\mathbf{x}'))_\sigma\,\hat{U}_0(t_1',t)\,\overbrace{\hat{U}_0(t,t_0)\hat{U}_0(t_0,t)}^{\hat{\mathbb{1}}}\}\\ =&\mathrm{Tr}_{\text{X\_IN}}\{\hat{U}_0(t_0,t_1)\,(\hat{\mathbf{A}}^{(+)}_{\text{x\_in}}(\mathbf{x}))_\rho\,\hat{U}_0(t_1,t_0)\,\hat{\rho}_{\text{X\_IN}}(t_0)\,\hat{U}_0(t_0,t_1')\,(\hat{\mathbf{A}}^{(-)}_{\text{x\_in}}(\mathbf{x}'))_\sigma\,\hat{U}_0(t_1',t_0)\}\\ =&\mathrm{Tr}_{\text{X\_IN}}\{(\hat{\mathbf{A}}^{(+)}_{\text{x\_in}}(\mathbf{x},t_1,t_0))_\rho\,\hat{\rho}_{\text{X\_IN}}(t_0)\,(\hat{\mathbf{A}}^{(-)}_{\text{x\_in}}(\mathbf{x}',t_1',t_0))_\sigma\}\\ =&\mathrm{Tr}_{\text{X\_IN}}\{(\hat{\mathbf{A}}^{(+)}_{\text{x\_in}}(\mathbf{x},t_1))_\rho\,\hat{\rho}_{\text{X\_IN}}(0)\,(\hat{\mathbf{A}}^{(-)}_{\text{x\_in}}(\mathbf{x}',t_1'))_\sigma\}\\ &=: H^{(1)}_{\sigma\rho}(\mathbf{x}',t_1',\mathbf{x},t_1).\end{aligned} \tag{2.24}$$

In here, we have defined the new object $H^{(1)}_{\sigma\rho}(\mathbf{x}',t_1',\mathbf{x},t_1)$, which marks a first-order coherence function for the incoming x-ray field[12]. This definition closely follows Glauber's lead, who adopted first- (and higher-) order correlation functions to describe the coherence properties of quantized electromagnetic fields [64]. The main difference to our definition is his focus on the field variable $\hat{\mathbf{E}}(\mathbf{x},t)$, whereas we consider the vector potential $\hat{\mathbf{A}}(\mathbf{x},t)$. For more details on the description and modelling of fields via $H^{(1)}_{\sigma\rho}(\mathbf{x}',t_1',\mathbf{x},t_1)$, we refer the reader to Chpt. 4.

As a further remark on Eq. (2.24), we note the introduction of time-dependence into the field-operators. We performed this in compliance with the usual Heisenberg-picture using the definitions from App. A.1.0.b. Notably, the operators' evolution has initially (i.e., in line three of Eq. (2.24)) been referenced to the time t_0, which we have subsequently shifted to the more conventionally used $t_0 = 0$. This may freely be done, as long as the density-operator is re-referenced (i.e., translated) accordingly to $\hat{\rho}_{\text{X\_IN}}(0)$.

Turning our attention to the second trace-expression of Eq. (2.23), we notice that all components are fully determined at this point. We can evaluate it analytically by—first—applying the mode expansion (Eq. (2.1)) to $\hat{\mathbf{A}}^{(...)}_{\text{x\_out}}(...)$ and—second—using the following properties of the free evolution for any involved $\hat{a}^\dagger_{\mathbf{k},\lambda}$ ($\hat{a}_{\mathbf{k},\lambda}$):

$$\hat{U}_0(t,t_1)\,\hat{a}^\dagger_{\mathbf{k},\lambda} = \hat{a}^\dagger_{\mathbf{k},\lambda}\,e^{\mathrm{i}\,\omega_{\mathbf{k}}(t_1-t)}\,\hat{U}_0(t,t_1) \qquad \text{and} \tag{2.25}$$

$$\hat{a}_{\mathbf{k},\lambda}\,\hat{U}_0(t_1',t) = \hat{U}_0(t_1',t)\,\hat{a}_{\mathbf{k},\lambda}\,e^{-\mathrm{i}\,\omega_{\mathbf{k}}(t_1'-t)}. \tag{2.26}$$

[11] We note that this latter conclusion does not strictly follow from the mode occupation, but will manifest itself based on energy conservation for sufficiently long integration times ($t - t_0$).

[12] We note that the first order coherence function in Eq. (2.24)—more broadly speaking—corresponds to the 1-particle reduced density-matrix for the electromagnetic field.

Therewith, we write the trace-expression for the outgoing modes as

$$\begin{aligned}
&\mathrm{Tr}_{\text{X_OUT}}\{\hat{U}_0(t,t_1)\,(\hat{\mathbf{A}}^{(-)}_{\text{x_out}}(\mathbf{x}))_\rho\,\hat{U}_0(t_1,t_0)\,\hat{\rho}_{\text{X_OUT}}(t_0)\,\hat{U}_0(t_0,t_1')\,(\hat{\mathbf{A}}^{(+)}_{\text{x_out}}(\mathbf{x}'))_\sigma\,\hat{U}_0(t_1',t)\,\hat{\Pi}_{\mathbf{k}_f,\lambda_f}\}\\
=&\mathrm{Tr}_{\text{X_OUT}}\{\hat{U}_0(t,t_1)\sum_{\mathbf{k}_1,\lambda_1}\sqrt{\frac{2\pi}{V\omega_{\mathbf{k}_1}\alpha^2}}\,\hat{a}^\dagger_{\mathbf{k}_1,\lambda_1}\,(\boldsymbol{\varepsilon}^*_{\mathbf{k}_1,\lambda_1})_\rho\,e^{-\mathrm{i}\mathbf{k}_1\cdot\mathbf{x}}\,\hat{U}_0(t_1,t_0)\bigotimes_{\mathbf{k},\lambda}^{out}|0\rangle\langle 0|_{\mathbf{k},\lambda}\\
\times&\qquad\hat{U}_0(t_0,t_1')\sum_{\mathbf{k}_2,\lambda_2}\sqrt{\frac{2\pi}{V\omega_{\mathbf{k}_2}\alpha^2}}\,\hat{a}_{\mathbf{k}_2,\lambda_2}\,(\boldsymbol{\varepsilon}_{\mathbf{k}_2,\lambda_2})_\sigma\,e^{\mathrm{i}\mathbf{k}_2\cdot\mathbf{x}'}\,\hat{U}_0(t_1',t)\,\hat{\Pi}_{\mathbf{k}_f,\lambda_f}\}\\
=&\sum_{\mathbf{k}_1,\lambda_1,\mathbf{k}_2,\lambda_2}\frac{2\pi}{V\alpha^2\sqrt{\omega_{\mathbf{k}_1}\omega_{\mathbf{k}_2}}}\,(\boldsymbol{\varepsilon}^*_{\mathbf{k}_1,\lambda_1})_\rho\,(\boldsymbol{\varepsilon}_{\mathbf{k}_2,\lambda_2})_\sigma\,e^{-\mathrm{i}\mathbf{k}_1\cdot\mathbf{x}}e^{\mathrm{i}\mathbf{k}_2\cdot\mathbf{x}'}\,e^{\mathrm{i}\,\omega_{\mathbf{k}}(t_1-t)}\,e^{-\mathrm{i}\,\omega_{\mathbf{k}}(t_1'-t)}\\
\times&\mathrm{Tr}_{\text{X_OUT}}\{\hat{a}^\dagger_{\mathbf{k}_1,\lambda_1}\,\hat{U}_0(t,t_0)\bigotimes_{\mathbf{k},\lambda}^{out}|0\rangle\langle 0|_{\mathbf{k},\lambda}\,\hat{U}_0(t_0,t)\,\hat{a}_{\mathbf{k}_2,\lambda_2}\,\hat{\Pi}_{\mathbf{k}_f,\lambda_f}\}.
\end{aligned}\tag{2.27}$$

In here, the time-evolution of the vacuum yields two cancelling phase factors and—in the presence of $\hat{\Pi}_{\mathbf{k}_f,\lambda_f}$—the remaining expression is non-vanishing only, if $\mathbf{k}_1=\mathbf{k}_2=\mathbf{k}_f$ and $\lambda_1=\lambda_2=\lambda_f$. This way, the trace is resolved as

$$\mathrm{Tr}_{\text{X\_OUT}}\{...\}=\frac{2\pi}{V\alpha^2\omega_f}\,(\boldsymbol{\varepsilon}^*_f)_\rho\,(\boldsymbol{\varepsilon}_f)_\sigma e^{-\mathrm{i}\mathbf{k}_f\cdot(\mathbf{x}-\mathbf{x}')}\,e^{\mathrm{i}\,\omega_f(t_1-t_1')}.\tag{2.28}$$

As a matter of personal taste, we have switched from writing $\omega_{\mathbf{k}_f}$ to ω_f and $\boldsymbol{\varepsilon}_{\mathbf{k}_f,\lambda_f}$ to $\boldsymbol{\varepsilon}_f$.

Collecting both results from Eq. (2.24) and Eq. (2.28), we can rewrite $\langle\hat{O}_{\mathbf{k}_f,\lambda_f}\rangle(t)$ as

$$\begin{aligned}
\langle\hat{O}_{\mathbf{k}_f,\lambda_f}\rangle(t)=&\frac{2\pi\alpha^2}{V\omega_f}\int_{t_0}^t dt_1\int_{t_0}^t dt_1'\int d^3x\int d^3x'\,(\boldsymbol{\varepsilon}_f)_\sigma\,H^{(1)}_{\sigma\rho}(\mathbf{x}',t_1',\mathbf{x},t_1)\,(\boldsymbol{\varepsilon}^*_f)_\rho\,e^{-\mathrm{i}\mathbf{k}_f\cdot(\mathbf{x}-\mathbf{x}')}\,e^{\mathrm{i}\,\omega_f(t_1-t_1')}\\
&\times\mathrm{Tr}_{\text{REST}}\{\hat{U}_0(t,t_1)\,\hat{n}(\mathbf{x})\,\hat{U}_0(t_1,t_0)\,\hat{\rho}_{\text{REST}}(t_0)\,\hat{U}_0(t_0,t_1')\,\hat{n}(\mathbf{x}')\,\hat{U}_0(t_1',t)\,\hat{\mathbb{1}}_{\text{REST}}\}.
\end{aligned}\tag{2.29}$$

As a last step in this section, we shall rewrite the REST-trace slightly. We proceed analogous to Eq. (2.24) and introduce a pair of propagators $\hat{\mathbb{1}}_{\text{REST}}=\hat{U}_0(t,0)\hat{U}_0(0,t)$. Merging each with its neighbouring form of $\hat{U}_0(t_1^{(\prime)},t)$, we can eliminate the dependence of Eq. (2.29) upon t. Furthermore, we translate $\hat{\rho}_{\text{REST}}(t_0)$ to $t=0$ via

$$\hat{\rho}_{\text{REST}}(t_0)=\hat{U}_0(t_0,0)\,\hat{\rho}_{\text{REST}}(0)\,\hat{U}_0(0,t_0).\tag{2.30}$$

Thereby, we have formally lifted the dependence upon t_0 as well. The resulting observable reads

$$\begin{aligned}
\langle\hat{O}_{\mathbf{k}_f,\lambda_f}\rangle(t)=&\frac{2\pi\alpha^2}{V\omega_f}\int_{t_0}^t dt_1\int_{t_0}^t dt_1'\int d^3x\int d^3x'\,(\boldsymbol{\varepsilon}_f)_\sigma\,H^{(1)}_{\sigma\rho}(\mathbf{x}',t_1',\mathbf{x},t_1)\,(\boldsymbol{\varepsilon}^*_f)_\rho\,e^{-\mathrm{i}\mathbf{k}_f\cdot(\mathbf{x}-\mathbf{x}')}\,e^{\mathrm{i}\,\omega_f(t_1-t_1')}\\
&\times\mathrm{Tr}_{\text{REST}}\{\hat{U}_0(0,t_1)\,\hat{n}(\mathbf{x})\,\hat{U}_0(t_1,0)\,\hat{\rho}_{\text{REST}}(0)\,\hat{U}_0(0,t_1')\,\hat{n}(\mathbf{x}')\,\hat{U}_0(t_1',0)\}.
\end{aligned}\tag{2.31}$$

For this expression, we can finally perform the limits $t\to\infty$ and $t_0\to-\infty$ and thereby obtain an expres-

sion that is formally time-independent[13]

$$\langle \hat{O}_{\mathbf{k}_f,\lambda_f} \rangle = \lim_{t\to\infty} \lim_{t_0\to-\infty} \langle \hat{O}_{\mathbf{k}_f,\lambda_f} \rangle (t) = \frac{2\pi\alpha^2}{V\omega_f} \int_{-\infty}^{\infty} dt_1 \int_{-\infty}^{\infty} dt_1' \int d^3x \int d^3x' \, (\boldsymbol{\varepsilon}_f)_\sigma \, H^{(1)}_{\sigma\rho}(\mathbf{x}', t_1', \mathbf{x}, t_1) \, (\boldsymbol{\varepsilon}_f^*)_\rho$$
$$\times \, e^{-\mathrm{i}\mathbf{k}_f\cdot(\mathbf{x}-\mathbf{x}')} \, e^{\mathrm{i}\,\omega_f(t_1-t_1')} \, \mathrm{Tr}_{\mathrm{REST}} \{ \hat{n}(\mathbf{x}, t_1) \, \hat{\rho}_{\mathrm{REST}}(0) \, \hat{n}(\mathbf{x}', t_1') \} \, . \tag{2.32}$$

This expression for x-ray scattering represents the essential result of this section. Before we continue to expand upon it in the next section, we want to give some concluding comments:

- First of all, the limits in the above expression are—of course—only of formal nature. In more practical terms, we may still use a well-defined, initial state that stems from some finite time-point t_0 (in contrast to requiring an infinitely removed state to begin with). This initial state would then have to be propagated to $t = 0$, using Eq. (2.30), in order to obtain input for the above expression.

- Unsurprisingly, the above result reproduces our expectations for inelastic x-ray scattering (IXS)—just as we set out to derive from the beginning. In particular, we find that the scattering-observable is connected to an electronic density-density correlation function microscopically. This is in accordance with references, such as [59, 61, 66]. We note further that the Fourier transform of this density-density correlator (provided it is evaluated in an equilibrium state of the system) goes by the designation of 'dynamic structure factor' in the IXS-community [61].

- With regard to x-ray-optical wavemixing, we remark that the above may already be the most suitable formulation for some scenarios. In particular, if the optical light-matter coupling is strong, we would have to account for *full* time-evolution of the combined REST-system—rather than attempt further perturbative separation as in the upcoming Sec. 2.2.2. Scenarios, for which the separation of $\hat{\rho}_{\mathrm{REST}}(0)$ may be futile, include strong-field laser-driving of the sample—a case studied by Dr. Popova-Gorelova using Floquet-methods [70], for instance—but also embedding in a cavity with ensuing polaritonic effects—see Refs. [71–73] for analogies. Finally, there potentially exist hybrid cases, wherein polaritonic effects are present though their overall impact remains perturbatively weak[14]

2.2.2 Inclusion of optical admixtures

Up to this point, we have developed a rather general expression for the description of non-resonant (in)elastic x-ray scattering. This has been the result of the previous section and can be found in Eq. (2.32).

To all intents and purposes, said expression also comprises x-ray-optical wavemixing processes. This fact is not obviously apparent, however, as the optical component is fully integrated with the material degrees of freedom in the combined subsystem termed 'REST'. Apart from being slightly opaque on the conceptual side, this combined expression harbours the more crucial disadvantage of still remaining prohibitively costly to solve. In other words, it is largely impractical to obtain the *full* evolution of the combined (optical) light-matter system (REST), in order to interrogate the contained XOWM processes[15].

[13] We note that a time-independent expression like Eq. (2.32) conforms better with typical pictures of scattering. As an example, we may consider the usual S-matrix approach, wherein asymptotically unperturbed states are related via a 'short', intermediate interaction, namely the scattering process [69].

[14] For more details on what we suspect to be a case of polariton-affected XOWM, which remains within quantitative reach of perturbative treatments nonetheless, we refer the reader to Secs. 5.2.3.a and 6.1 as well as App. A.17.

[15] We want to clarify that the above statement does not extend to (highly) simplified model systems, of course. Our own Sec. 6.1 provides an example, how the coupled (optical) light-matter system may be approximated in a drastic fashion, thereby allowing its exact solution.

In an attempt to simplify the situation further, we shall, instead, resort to a perturbative separation of the coupled light-matter system again. Fully analogous to the way, in which we have separated x-ray and REST components of the problem before (cf. Sec. 2.2.1), we will now factorize REST into its optical and matter subsystems at an initial time-point t_0

$$\hat{\rho}_{\mathrm{REST}}(t_0) \approx \hat{\rho}_{\mathrm{MAT}}(t_0) \otimes \hat{\rho}_{\mathrm{OPT}}(t_0). \tag{2.33}$$

In addition, we will assume that subsequent interaction of the subsystems is weak and can be treated in terms of a perturbative expansion[16]. Setting the stage thereunto, we split the time-evolution operator[17]

$$\hat{U}_0(t,t_0) = \hat{U}_{00}(t,t_0)\,\hat{U}_{\mathrm{INT\_OPT}}(t,t_0), \tag{2.34}$$

of which we shall, later, expand the hind part to suitably low order. Alongside, we identify the respective Hamiltonians that will govern each of the above time-evolutions

$$\hat{H}_{00} = \hat{H}_{\mathrm{MAT}} + \hat{H}_{\mathrm{EM}} \tag{2.35}$$

$$\hat{H}_{\mathrm{INT\_OPT}} = \alpha \int d^3x\; \hat{\psi}^\dagger(\mathbf{x})\mathbf{p}\cdot\hat{\mathbf{A}}_{\mathrm{opt}}(\mathbf{x})\hat{\psi}(\mathbf{x}) + \frac{\alpha^2}{2}\int d^3x\; \hat{n}(\mathbf{x})\hat{\mathbf{A}}^2_{\mathrm{opt}}(\mathbf{x}). \tag{2.36}$$

These being established, we proceed to the core of our discussion. Hereunto, we pick the density-density correlator from Eq. (2.32) and use it as the basis for the following perturbative expansion

$$\begin{aligned}\langle \hat{n}(\mathbf{x}',t_1')\,\hat{n}(\mathbf{x},t_1)\rangle_{\mathrm{REST}} &:= \mathrm{Tr}_{\mathrm{REST}}\left\{\hat{n}(\mathbf{x},t_1)\,\hat{\rho}_{\mathrm{SYS}}(0)\,\hat{n}(\mathbf{x}',t_1')\right\} \\ &= \mathrm{Tr}_{\mathrm{REST}}\left\{\hat{U}_0(0,t_1)\,\hat{n}(\mathbf{x})\,\hat{U}_0(t_1,0)\,\hat{\rho}_{\mathrm{REST}}(0)\,\hat{U}_0(0,t_1')\,\hat{n}(\mathbf{x}')\,\hat{U}_0(t_1',0)\right\} \\ &= \mathrm{Tr}_{\mathrm{REST}}\left\{\hat{U}_0(t,t_1)\,\hat{n}(\mathbf{x})\,\hat{U}_0(t_1,t_0)\,\hat{\rho}_{\mathrm{REST}}(t_0)\,\hat{U}_0(t_0,t_1')\,\hat{n}(\mathbf{x}')\,\hat{U}_0(t_1',t)\right\}. \end{aligned} \tag{2.37}$$

To begin with, we have used some equivalent reformulations to re-instate the initial time t_0 as well as a 'final' time-point t. Thereby, we ensure close analogy of all procedures to Sec. 2.2.1.

Next, we implement the factorization-approximation as of Eq. (2.33)

$$\mathrm{Tr}_{\mathrm{REST}}\{...\} \approx \mathrm{Tr}_{\mathrm{OPT}}\left\{\mathrm{Tr}_{\mathrm{MAT}}\left\{\hat{U}_0(t,t_1)\,\hat{n}(\mathbf{x})\,\hat{U}_0(t_1,t_0)\left(\hat{\rho}_{\mathrm{MAT}}(t_0)\otimes\hat{\rho}_{\mathrm{OPT}}(t_0)\right)\hat{U}_0(t_0,t_1')\,\hat{n}(\mathbf{x}')\,\hat{U}_0(t_1',t)\right\}\right\}. \tag{2.38}$$

Furthermore, we introduce the reasonable assumption that the unperturbed solid is initially found in

[16] We note in terms of a caveat that our assumption to consider only weak coupling of optical light and matter may easily become dubious. This is especially true close to optical resonances but also—and less obviously at first glance—in extended (yet coherent) systems. To illustrate our point, we call to the reader's attention that optical light, which propagates through—say–a crystal, may deviate significantly from its vacuum behaviour. As it is subject to the (complex) refractive index of the medium ($n \neq 1$), it undergoes macroscopically measurable changes. These changes are the effective result of repeated absorption and re-emission on the microscopic scale, however.

This point serves to illustrate the fact that low order perturbation theory may well be *inadequate* to describe XOWM phenomena in extended systems; in other words this corresponds to the breakdown of the 1^{st} Born approximation.

In hindsight of our own later work, however, we know that a perturbative treatment *can* and *does* yield very satisfactory results—despite these initial doubts. We thus ask the reader to follow our reasoning in a temporary leap of faith.

[17] We note that in exercising the perturbative expansion in this section, we follow the logic outlined in App. A.1 once again. For more details on the general concept, the reader is referred there.

an incoherent sum of eigenstates[18]—weighted by normalized probabilities p_I

$$\hat{\rho}_{\mathrm{MAT}}(t_0) \approx \sum_I p_I \, |I\rangle\langle I| \tag{2.39}$$

Inserting this into Eq. (2.38) and using an identical reformulation of the trace in terms of the same eigenstates, i.e., $\mathrm{Tr}_{\mathrm{MAT}}\{...\} = \sum_F \langle F|...|F\rangle$, we obtain for the overall correlator

$$\begin{aligned}\mathrm{Tr}_{\mathrm{REST}}\{...\} &\approx \mathrm{Tr}_{\mathrm{OPT}}\{\sum_F \langle F|\hat{U}_0(t,t_1)\,\hat{n}(\mathbf{x})\,\hat{U}_0(t_1,t_0)\left(\sum_I p_I\,|I\rangle\langle I|\otimes\hat{\rho}_{\mathrm{OPT}}(t_0)\right)\hat{U}_0(t_0,t_1')\,\hat{n}(\mathbf{x}')\,\hat{U}_0(t_1',t)\,|F\rangle\} \\ &= \mathrm{Tr}_{\mathrm{OPT}}\{\sum_{I,F} p_I \underbrace{\langle F|\hat{U}_0(t,t_1)\,\hat{n}(\mathbf{x})\,\hat{U}_0(t_1,t_0)\,|I\rangle}_{\text{left amplitude}}\underbrace{\langle I|\otimes\hat{\rho}_{\mathrm{OPT}}(t_0)\,\hat{U}_0(t_0,t_1')\,\hat{n}(\mathbf{x}')\,\hat{U}_0(t_1',t)\,|F\rangle}_{\text{right amplitude}}\}\,.\end{aligned} \tag{2.40}$$

The expression nicely separates into two equivalent amplitudes[19], which shall save us half the work soon.

The next logical step towards a perturbative solution of Eq. (2.40) would consist in replacing any $\hat{U}_0$ via Eq. (2.34) and then expanding all occurring propagators $\hat{U}_{\mathrm{INT\_OPT}}$ in the spirit of usual TDPT. We note with caution, however, that this would result in a multitude of terms. This stands in stark contrast to our previous expansion of the x-ray diffraction process, which has been comparatively straight-forward. Before we engage with any lengthy, explicit expressions of the new kind, we shall visualize the various expansion-possibilities of the kernel $\langle F|...|F\rangle$ up to order α^2:

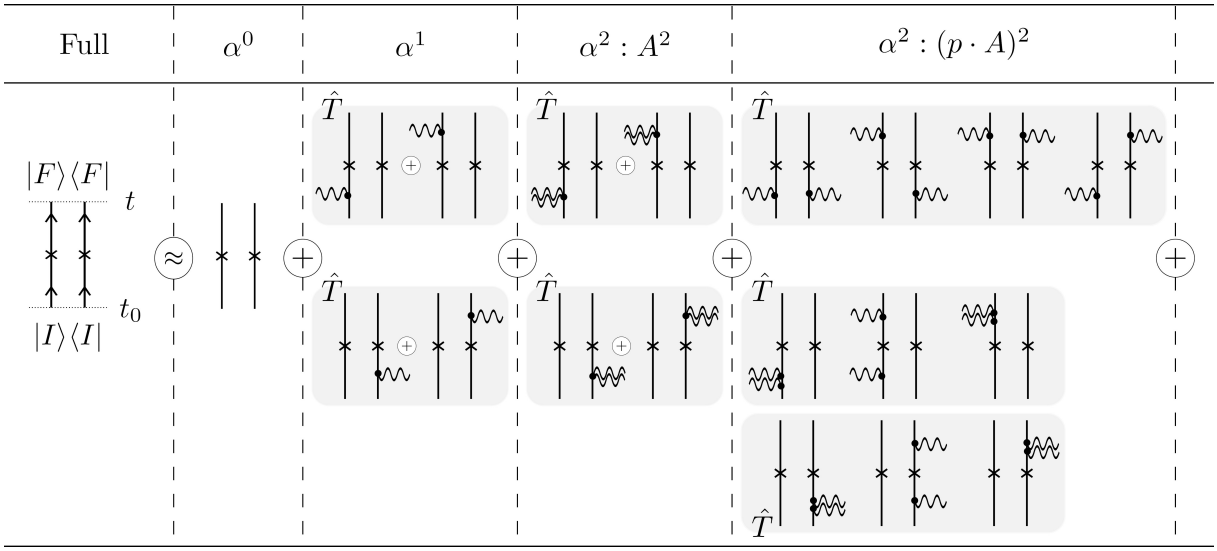

Figure 2.1: Visualization of the perturbative series that results from a low-order expansion of Eq. (2.40) in the light-matter interaction $\hat{H}_{\mathrm{INT\_OPT}}$. For an explanation of the used notation, please refer to the main text below. [We gratefully acknowledge Dr. Christina Bömer's help in rendering the above computer graphics.]

In Fig. 2.1, we represent the temporal evolution of the system in terms of primitive double-sided Feynman diagrams. We begin on the left-hand side of Fig. 2.1 by depicting the evolution of the fully coupled system (i.e., the complete REST-system). Starting symbolically from the initial state $|I\rangle\langle I|$ at

[18] We note that Eq. (2.39) does not present a considerable restriction *after* we have imposed the much more drastic decoupling of light- and matter-subsystems in Eq. (2.33) before. Left to its own devices, we would indeed expect a crystalline sample to settle either into its ground state or into a thermally excited distribution of eigenstates. Both cases can be represented in terms of Eq. (2.39).

[19] We acknowledge that, at this point, the two amplitudes do not appear to be exactly equivalent, because the right one seemingly includes $\hat{\rho}_{\mathrm{OPT}}(t_0)$. However, this is merely a consequence of the compact notation. Once expanded perturbatively, any object pertaining to the optical system may be excluded completely from *both* amplitudes.

time t_0, we employ bold arrows to depict the action of $\hat{U}_0$ leading up to the 'final' state $|F\rangle\langle F|$ at time t. In between, we mark the occurrence of the original x-ray-scattering event by an 'x'. At this point, we would find the corresponding action of the electronic density operator $\hat{n}(\mathbf{x})$ within the individual amplitudes. In all of this discussion, we suppress the optical density matrix for the sake of notational simplicity.

In expanding the 'full' propagator $\hat{U}_0$, we employ regular lines and dot-like vertices to signify the action of a propagator $\hat{U}_{00}$ and vertices from $\hat{H}_{\text{INT\_OPT}}$, respectively. These vertices may appear with a single wiggly line attached—corresponding to a $\mathbf{p}\cdot\mathbf{A}$-type interaction—or with a pair of wiggly lines attached to the same dot—corresponding to an $\mathbf{A}^2$-type interaction, conversely.

We sort the occurring terms both in the order of their expansion (i.e., powers of α) as well as their contained types of vertices. Within established categories, we furthermore group terms that are related by time-ordering within their amplitude (i.e., related by geometric re-ordering of vertices' positions along one line). The latter groups are indicated by grey-shaded boxes bearing the signature $\hat{T}$.

Solution for the *parametric* case As presumed earlier, we have found a multitude of contributing diagrams. Their evaluation would still present a formidably laborious task—even though the complexity has already been markedly reduced in comparison to the general (i.e., fully coupled) case. In order to simplify our calculations yet further, we shall restrict our discussion to so-called *parametric* wavemixing processes. These constitute the wavemixing analoga of elastic scattering, wherein the state of the matter system is not changed by the *overall* light-matter interaction. Formally, we can enforce this by setting the final state equal to the initial one, viz. $|F\rangle = |I\rangle$. Notably, we automatically fix the energy content of the matter system by imposing this constraint as well ($E_F \to E_I = E_I$). Thus, we force the XOWM process to strictly conserve energy among the involved photonic modes alone, because there is no other source (or drain) of energy left available.

Exploiting this fact, we can reduce the number of contributing diagrams significantly. To this end, we observe that all but one class of diagrams in Fig. 2.1 feature (at least) one amplitude without optical vertices. Obviously, no wave*mixing* can take place on such amplitudes and the solitary x-ray vertex is consequently forced to be elastic itself. If—by choice of the observable energy ω_f relative to the incident x-ray energies—we require an energy transfer to happen, nevertheless, the contribution from any of the aforementioned diagrams vanishes. Under such circumstances, only the four diagrams in the upper right corner of Fig. 2.1 present viable options to produce a signal, namely via XOWM[20]

[20] We note in terms of a double-caveat that both of the required conditions in this paragraph are easily imposed theoretically, but much harder to ensure experimentally.

First, we shall reconsider the desire to choose a scattered x-ray photon energy ω_f, which lies outside the bandwidth of the incoming x-ray pulse. While this condition is well-defined theoretically, it does require significant experimental effort to suppress unwanted frequency components an experimental setup. Commonly used monochromators rely on Bragg-reflection for energy filtering and en*tail* the presence of extended spectral tails. For further discussion on this subject consider Sec. 5.2.1.c as well as the more extended discussions in Refs. [51, 74] and the collected work of Dr. Bömer [75].

Concerning the parametric assumption $|F\rangle = |I\rangle$, we have to note that this can hardly be controlled experimentally, lest verified, because it is wholly unrealistic to 'probe' the final state of the matter system directly.

Not all is lost, however: It stands to be expected that a truly parametric process would show a distinct scattering *pattern* compared to non-parametric, inelastic processes. To illustrate this hypothesis, we recall the previously raised analogy that identified parametric XOWM processes as the wavemixing counterpart of elastic diffraction. Both processes leave the material system ultimately unchanged and, as such, cannot be localized through their after-effect. By extension, this allows them to proceed coherently across the full sample. For elastic scattering, this coherent diffraction gives rise to the well-known Bragg-peaks. Vice-versa, the existence of Bragg-peaks clearly indicates the presence of elastic scattering. The same should hold true in case of parametric XOWM. A coherent response across (a large volume of) the sample, will give rise to a distinct pattern, by which to identify its present retro-actively. For further discussion of such characteristic scattering signatures, the reader is referred to the explicit applications of the theory in Chpt. 5.

With these constraints in mind, we shall, now, proceed to evaluate this restricted number of diagrams explicitly. To this end, we recall Eq. (2.40) and implement the parametric approximation $|F\rangle = |I\rangle$ first

$$\begin{aligned}\mathrm{Tr}_{\mathrm{REST}}\{...\} &= \mathrm{Tr}_{\mathrm{OPT}}\{\sum_{I,F} p_I \langle F|\hat{U}_0(t,t_1)\,\hat{n}(\mathbf{x})\,\hat{U}_0(t_1,t_0)\,|I\rangle\langle I|\otimes\hat{\rho}_{\mathrm{OPT}}(t_0)\,\hat{U}_0(t_0,t_1')\,\hat{n}(\mathbf{x}')\,\hat{U}_0(t_1',t)\,|F\rangle\} \\ &\approx \mathrm{Tr}_{\mathrm{OPT}}\{\sum_{I} p_I \underbrace{\langle I|\hat{U}_0(t,t_1)\,\hat{n}(\mathbf{x})\,\hat{U}_0(t_1,t_0)\,|I\rangle}_{\text{left amplitude}\Rightarrow\text{Eq. (2.42)}}\langle I|\otimes\hat{\rho}_{\mathrm{OPT}}(t_0)\,\hat{U}_0(t_0,t_1')\,\hat{n}(\mathbf{x}')\,\hat{U}_0(t_1',t)\,|I\rangle\}\,.\end{aligned} \tag{2.41}$$

From this, we focus on a single amplitude, into which we implement the first-order expansion for $\hat{U}_{\mathrm{INT\_OPT}}$ on either side of the density operator:

$$\begin{aligned}&\langle I|\hat{U}_0(t,t_1)\,\hat{n}(\mathbf{x})\,\hat{U}_0(t_1,t_0)\,|I\rangle \\ &\approx \langle I|\hat{U}_{00}(t,t_1)\big[\hat{\mathbb{1}}-\mathrm{i}\int_{t_1}^{t}dt_2\,\hat{U}_{00}(t_1,t_2)\,\hat{H}_{\mathrm{INT\_OPT}}\,\hat{U}_{00}(t_2,t_1)\big]\,\hat{n}(\mathbf{x}) \\ &\quad\times\hat{U}_{00}(t_1,t_0)\,\big[\hat{\mathbb{1}}-\mathrm{i}\int_{t_0}^{t_1}d\tilde{t_2}\,\hat{U}_{00}(t_0,\tilde{t_2})\,\hat{H}_{\mathrm{INT\_OPT}}\,\hat{U}_{00}(\tilde{t_2},t_0)\big]\,|I\rangle \\ &= \langle I|\hat{U}_{00}(t,0)\big[\hat{\mathbb{1}}-\mathrm{i}\int_{t_1}^{t}dt_2\,\hat{H}_{\mathrm{INT\_OPT}}(t_2)\big]\,\hat{n}(\mathbf{x},t_1)\,\big[\hat{\mathbb{1}}-\mathrm{i}\int_{t_0}^{t_1}d\tilde{t_2}\,\hat{H}_{\mathrm{INT\_OPT}}(\tilde{t_2})\big]\hat{U}_{00}(0,t_0)\,|I\rangle \\ &\approx \langle I|\hat{U}_{00}(t,0)\,(-\mathrm{i})\,\alpha\Big(\int_{t_1}^{t}dt_2\int d^3y\,\hat{\mathbf{p}}(\mathbf{y},t_2)\cdot\hat{\mathbf{A}}_{\mathrm{opt}}(\mathbf{y},t_2)\,\hat{n}(\mathbf{x},t_1) \\ &\qquad\qquad+\hat{n}(\mathbf{x},t_1)\int_{t_0}^{t_1}d\tilde{t_2}\int d^3\tilde{y}\,\hat{\mathbf{p}}(\tilde{\mathbf{y}},\tilde{t_2})\cdot\hat{\mathbf{A}}_{\mathrm{opt}}(\tilde{\mathbf{y}},\tilde{t_2})\Big)\hat{U}_{00}(0,t_0)\,|I\rangle \\ &= \langle I|\hat{U}_{00}(t,0)\,(-\mathrm{i})\,\alpha\int_{t_0}^{t}dt_2\int d^3y\,\hat{T}\big[(\hat{\mathbf{p}}(\mathbf{y},t_2))_\mu\,\hat{n}(\mathbf{x},t_1)\big]\,(\hat{\mathbf{A}}_{\mathrm{opt}}(\mathbf{y},t_2))_\mu\hat{U}_{00}(0,t_0)\,|I\rangle\,.\end{aligned} \tag{2.42}$$

In the reformulation steps that we denoted as 'approximate' (viz. '$\approx$'), we have imposed the restrictions of diagrams as discussed above. First, we have limited any expansion of $\hat{U}_{\mathrm{INT\_OPT}}$ to lowest order, whereby we exclude most of the diagrams on the lower right of Fig. 2.1. Secondly, we have inserted only the $\mathbf{p}\cdot\mathbf{A}$-type interaction—eliminating any $\mathbf{A}^2$ diagrams—and dropped both the identity ($\hat{\mathbb{1}}$) and contributions at order α^2. If the same steps are applied for both amplitudes of Eq. (2.41), the result is a restriction to the previously identified diagrams in the upper right corner of Fig. 2.1.

Simplifying the notation further, we have once again introduced time-dependent operators—absorbing previously explicit time-evolution operators. In contrast to the pure x-ray case, these are defined with respect to $\hat{U}_{00}$ now, i.e., $\hat{n}(\mathbf{x},t) = \hat{U}_{00}(0,t)\,\hat{n}(\mathbf{x})\,\hat{U}_{00}(t,0)$. Apart from this, they obviously follow the same Heisenberg-picture-type logic, on which further information can be found in App. A.1.0.b.

As a novelty in the last line, we have introduced a time-ordering operator. This helps to render Eq. (2.42) more compact in simply combining two terms, which differ in nothing but their temporal arguments:

$$\begin{aligned}&\hat{T}\big[(\hat{\mathbf{p}}(\mathbf{y},t_2))_\mu\,\hat{n}(\mathbf{x},t_1)\big] \\ &= \Theta(t_2-t_1)\,(\hat{\mathbf{p}}(\mathbf{y},t_2))_\mu\,\hat{n}(\mathbf{x},t_1)+\Theta(t_1-t_2)\,\hat{n}(\mathbf{x},t_1)\,(\hat{\mathbf{p}}(\mathbf{y},t_2))_\mu\,.\end{aligned} \tag{2.43}$$

In here, $\Theta(t)$ denotes the Heaviside-function; the overall definition of $\hat{T}$ is in close alignment with typical uses thereof (cf. Ref. [69], for instance).

Using the result for a single amplitude from Eq. (2.42), we can substitute it twice into Eq. (2.41) and

thereby obtain

$$\begin{aligned}\mathrm{Tr}_{\mathrm{REST}}\{...\} &= \mathrm{Tr}_{\mathrm{OPT}}\{\sum_I p_I \langle I|\hat{U}_0(t,t_1)\,\hat{n}(\mathbf{x})\,\hat{U}_0(t_1,t_0)\,|I\rangle\,\langle I|\otimes\hat{\rho}_{\mathrm{OPT}}(t_0)\,\hat{U}_0(t_0,t_1')\,\hat{n}(\mathbf{x}')\,\hat{U}_0(t_1',t)\,|I\rangle\}\\ &\approx \alpha^2\int_{t_0}^{t}dt_2\int_{t_0}^{t}dt_2'\int d^3y\int d^3y'\;\mathrm{Tr}_{\mathrm{OPT}}\{(\hat{\mathbf{A}}_{\mathrm{opt}}(\mathbf{y},t_2))_\mu\,\hat{\rho}_{\mathrm{OPT}}(0)\,(\hat{\mathbf{A}}_{\mathrm{opt}}(\mathbf{y}',t_2'))_\nu\}\\ &\times\sum_I p_I\langle I|\,\hat{T}\left[(\hat{\mathbf{p}}(\mathbf{y},t_2))_\mu\,\hat{n}(\mathbf{x},t_1)\right]|I\rangle\left(\langle I|\,\hat{T}\left[(\hat{\mathbf{p}}(\mathbf{y}',t_2'))_\nu\,\hat{n}(\mathbf{x}',t_1')\right]|I\rangle\right)^*. \end{aligned}\tag{2.44}$$

At this point, we are in a position to, finally, close the loop back to Eq. (2.32) or Eq. (2.31) for that matter. Up to now, we have been discussing the density-density correlator (i.e., the $\mathrm{Tr}_{\mathrm{REST}}\{...\}$-object) as an independent building block, but below, we shall re-insert it into the overall scattering observable

$$\begin{aligned}\langle\hat{O}_{\mathbf{k}_f,\lambda_f}\rangle(t) &= \frac{2\pi\alpha^4}{V\omega_f}\int_{t_0}^{t}{}^{\times 4}dt_1\,dt_1'\,dt_2\,dt_2'\int^{\times 4}d^3x\,d^3x'\,d^3y\,d^3y'\,e^{-\mathrm{i}\,\mathbf{k}_f\cdot(\mathbf{x}-\mathbf{x}')}\,e^{\mathrm{i}\,\omega_f(t_1-t_1')}\\ &\times(\boldsymbol{\varepsilon}_f)_\sigma\,H^{(1)}_{\sigma\rho}(\mathbf{x}',t_1',\mathbf{x},t_1)\,(\boldsymbol{\varepsilon}_f^*)_\rho\,\mathrm{Tr}_{\mathrm{OPT}}\{\hat{\rho}_{\mathrm{OPT}}(0)\,(\hat{\mathbf{A}}_{\mathrm{opt}}(\mathbf{y}',t_2'))_\nu\,(\hat{\mathbf{A}}_{\mathrm{opt}}(\mathbf{y},t_2))_\mu\}\\ &\times\sum_I p_I\langle I|\,\hat{T}\left[(\hat{\mathbf{p}}(\mathbf{y},t_2))_\mu\,\hat{n}(\mathbf{x},t_1)\right]|I\rangle\left(\langle I|\,\hat{T}\left[(\hat{\mathbf{p}}(\mathbf{y}',t_2'))_\nu\,\hat{n}(\mathbf{x}',t_1')\right]|I\rangle\right)^*. \end{aligned}\tag{2.45}$$

We note that we have introduced a new abbreviation here, namely the superscript '$^{\times 4}$' with the integrals. This serves to indicate that there should be 4 integrals, i.e., an amount commensurate with the number of differentials, however, we forgo the notational clutter of printing all of them.

In Eq. (2.45), we have basically arrived at the main result of our derivation. The expression holds everything necessary to compute XOWM-scattering probabilities—with the paramount subsequent task being to evaluate all the required constituents. Before we do so, however, we want to engage in a few, final reformulations. Our aim here, will be to render the expression more compact and consistent.

To this end, we shall address the electronic transition amplitudes $\langle I|...|I\rangle$ first of all. These constitute the central quantity for our subsequent discussion of the nonlinear electronic response (cf. Chpt. 3) and should receive a dedicated symbolic representation. We, therefore, define the nonlinear response function

$$(\mathbf{P}_I(\mathbf{y},t_2,\mathbf{x},t_1))_\mu := \langle I|\,\hat{T}\left[(\hat{\mathbf{p}}(\mathbf{y},t_2))_\mu\,\hat{n}(\mathbf{x},t_1)\right]|I\rangle\,,\tag{2.46}$$

which captures the correlation among an electronic current-density (viz. density of the momentum operator) and a scalar electronic-density over time and space.

Having isolated and defined the material subsystem's response, we turn our attention towards the optical fields' expectation value (or correlator) from Eq. (2.45), viz.

$$\langle(\hat{\mathbf{A}}_{\mathrm{opt}}(\mathbf{y}',t_2'))_\nu\,(\hat{\mathbf{A}}_{\mathrm{opt}}(\mathbf{y},t_2))_\mu\rangle = \mathrm{Tr}_{\mathrm{OPT}}\{\hat{\rho}_{\mathrm{OPT}}(0)\,(\hat{\mathbf{A}}_{\mathrm{opt}}(\mathbf{y}',t_2'))_\nu\,(\hat{\mathbf{A}}_{\mathrm{opt}}(\mathbf{y},t_2))_\mu\}\,.\tag{2.47}$$

It would be appealing to replace this expression by another Glauber-type correlation function, as we have done for the incoming x-ray field prior. However, the above expression is more general than before (cf. Eq. (2.24)), because we have not yet restricted it to photon-emission or -absorption, i.e., we have not reduced it to negative and positive frequency parts, respectively. Seeking to retain this generality, we will opt for a different reformulation, while keeping the structural similarity to Glauber's functions intact.

Taking inspiration from the physical XOWM processes to be described, we recall that there will be laser-driven cases (such as SFG / DFG) on the one hand, contrasted with spontaneous scattering (such as XPDC) on the other. This offers reasonable ground for further distinction of the light-fields' correlator:

Accounting for both possibilities—i.e., a coherent (classical) field and a remainder of quantum-fluctuations—we split

$$\hat{\mathbf{A}}_{\text{opt}}(\mathbf{y},t) = \mathbf{A}_{\text{opt\_avg}}(\mathbf{y},t) + \hat{\mathbf{A}}_{\text{opt\_flu}}(\mathbf{y},t). \tag{2.48}$$

Herein, the average field will be defined via the expectation value of its original operator and behaves like a classical, $\mathbb{C}$-number field

$$\mathbf{A}_{\text{opt\_avg}}(\mathbf{y},t) = \langle \hat{\mathbf{A}}_{\text{opt}}(\mathbf{y},t) \rangle = \text{Tr}_{\text{OPT}} \left\{ \hat{\rho}_{\text{OPT}}(0)\, \hat{\mathbf{A}}_{\text{opt}}(\mathbf{y},t) \right\}. \tag{2.49}$$

As its complement, the remaining operator $\hat{\mathbf{A}}_{\text{opt\_flu}}(\mathbf{y},t)$ satisfies

$$\langle \hat{\mathbf{A}}_{\text{opt\_flu}}(\mathbf{y},t) \rangle = \text{Tr}_{\text{OPT}} \left\{ \hat{\rho}_{\text{OPT}}(0)\, \hat{\mathbf{A}}_{\text{opt\_flu}}(\mathbf{y},t) \right\} = 0 \tag{2.50}$$

and, therefore, captures only fluctuations *around* the average field.

The charm of this separation—while it is in itself exact—is that it provides a straight-forward avenue for approximations. Whenever a spectral region is strongly affected by an external driving laser, we can resort to its classical field alone, i.e., Eq. (2.47) becomes

$$\text{Tr}_{\text{OPT}} \left\{ \hat{\rho}_{\text{OPT}}(0)\, (\hat{\mathbf{A}}_{\text{opt}}(\mathbf{y}',t_2'))_\nu\, (\hat{\mathbf{A}}_{\text{opt}}(\mathbf{y},t_2))_\mu \right\} \approx (\mathbf{A}_{\text{opt\_avg}}(\mathbf{y}',t_2'))_\nu\, (\mathbf{A}_{\text{opt\_avg}}(\mathbf{y},t_2))_\mu. \tag{2.51}$$

Conversely when such driving is absent, we expect any fluctuations to behave as they would in the equilibrium case and write

$$\text{Tr}_{\text{OPT}} \left\{ \hat{\rho}_{\text{OPT}}(0)\, (\hat{\mathbf{A}}_{\text{opt}}(\mathbf{y}',t_2'))_\nu\, (\hat{\mathbf{A}}_{\text{opt}}(\mathbf{y},t_2))_\mu \right\} \approx \text{Tr}_{\text{OPT}} \left\{ \hat{\rho}^{equ}_{\text{OPT}} (\hat{\mathbf{A}}_{\text{opt\_flu}}(\mathbf{y}',t_2'))_\nu\, (\hat{\mathbf{A}}_{\text{opt\_flu}}(\mathbf{y},t_2))_\mu \right\}. \tag{2.52}$$

Formally, we will keep both options inside the expression

$$\begin{aligned} \text{Tr}_{\text{OPT}} \left\{ \hat{\rho}_{\text{OPT}}(0)\, (\hat{\mathbf{A}}_{\text{opt}}(\mathbf{y}',t_2'))_\nu\, (\hat{\mathbf{A}}_{\text{opt}}(\mathbf{y},t_2))_\mu \right\} &= (\mathbf{A}_{\text{opt\_avg}}(\mathbf{y}',t_2'))_\nu\, (\mathbf{A}_{\text{opt\_avg}}(\mathbf{y},t_2))_\mu \\ &\quad + \text{Tr}_{\text{OPT}} \left\{ \hat{\rho}^{equ}_{\text{OPT}} (\hat{\mathbf{A}}_{\text{opt\_flu}}(\mathbf{y}',t_2'))_\nu\, (\hat{\mathbf{A}}_{\text{opt\_flu}}(\mathbf{y},t_2))_\mu \right\}, \end{aligned} \tag{2.53}$$

and will choose either of them according to the case at hand. For further brevity, we introduce the Glauber-inspired short-hands:

$$\bar{H}^{(1)}_{\nu\mu}(\mathbf{y}',t_2',\mathbf{y},t_2) = (\mathbf{A}_{\text{opt\_avg}}(\mathbf{y}',t_2'))_\nu\, (\mathbf{A}_{\text{opt\_avg}}(\mathbf{y},t_2))_\mu \tag{2.54}$$

$$\bar{S}^{(1)}_{\nu\mu}(\mathbf{y}',t_2',\mathbf{y},t_2) = \text{Tr}_{\text{OPT}} \left\{ \hat{\rho}^{equ}_{\text{OPT}} (\hat{\mathbf{A}}_{\text{opt\_flu}}(\mathbf{y}',t_2'))_\nu\, (\hat{\mathbf{A}}_{\text{opt\_flu}}(\mathbf{y},t_2))_\mu \right\}. \tag{2.55}$$

Combining all of the above, we can write the overall observable as

$$\begin{aligned} \langle \hat{O}_{\mathbf{k}_f,\lambda_f} \rangle(t) = \frac{2\pi\alpha^4}{V\omega_f} \int_{t_0}^{t} {}^{\times 4} dt_1\, dt_1'\, dt_2\, dt_2' \int {}^{\times 4} d^3x\, d^3x'\, d^3y\, d^3y'\, e^{-\mathrm{i}\,\mathbf{k}_f\cdot(\mathbf{x}-\mathbf{x}')}\, e^{\mathrm{i}\,\omega_f(t_1-t_1')} \\ \times (\boldsymbol{\varepsilon}_f)_\sigma\, H^{(1)}_{\sigma\rho}(\mathbf{x}',t_1',\mathbf{x},t_1)\, (\boldsymbol{\varepsilon}_f^*)_\rho \left(\bar{H}^{(1)}_{\nu\mu}(\mathbf{y}',t_2',\mathbf{y},t_2) + \bar{S}^{(1)}_{\nu\mu}(\mathbf{y}',t_2',\mathbf{y},t_2) \right) \\ \times \sum_I p_I\, (\mathbf{P}_I(\mathbf{y},t_2,\mathbf{x},t_1))_\mu\, \left(\mathbf{P}_I(\mathbf{y}',t_2',\mathbf{x}',t_1') \right)^*_\nu. \end{aligned} \tag{2.56}$$

Ultimately, we invoke the same reasoning that led to Eq. (2.32) and perform the limits $t \to \infty, t_0 \to -\infty$.

Thereby, we end this section with the time-independent observable

$$\begin{aligned}\langle \hat{O}_{\mathbf{k}_f,\lambda_f}\rangle &= \lim_{t\to\infty}\lim_{t_0\to-\infty}\langle \hat{O}_{\mathbf{k}_f,\lambda_f}\rangle(t)\\ &= \frac{2\pi\alpha^4}{V\omega_f}\int^{\times 4} dt_1\,dt_1'\,dt_2\,dt_2'\int^{\times 4} d^3x\,d^3x'\,d^3y\,d^3y'\,e^{-\mathrm{i}\,\mathbf{k}_f\cdot(\mathbf{x}-\mathbf{x}')}\,e^{\mathrm{i}\,\omega_f(t_1-t_1')}\\ &\times(\boldsymbol{\varepsilon}_f)_\sigma\,H^{(1)}_{\sigma\rho}(\mathbf{x}',t_1',\mathbf{x},t_1)\,(\boldsymbol{\varepsilon}_f^*)_\rho\left(\bar{H}^{(1)}_{\nu\mu}(\mathbf{y}',t_2',\mathbf{y},t_2)+\bar{S}^{(1)}_{\nu\mu}(\mathbf{y}',t_2',\mathbf{y},t_2)\right)\\ &\times\sum_I p_I\,(\mathbf{P}_I(\mathbf{y},t_2,\mathbf{x},t_1))_\mu\,\left(\mathbf{P}_I(\mathbf{y}',t_2',\mathbf{x}',t_1')\right)^*_\nu.\end{aligned}\tag{2.57}$$

2.3 XOWM observable in reciprocal-space

As an addendum to the preceding derivation, we note that the observable Eq. (2.57) can prove decidedly more useful, if transformed into reciprocal-space. This comes as no great surprise for our intended use-case, given that crystalline samples as well as the x-ray diffraction thereof lend themselves quite naturally to a momentum-space-based point of view.

Setting out to transform our previously obtained result (Eq. (2.57)), we collect the Fourier-transformed counterparts of all involved correlation functions. These amount to[21]:

$$H^{(1)}_{\sigma\rho}(\mathbf{x}',t_1',\mathbf{x},t_1)=\frac{1}{(2\pi)^8}\int d^3k_X\int d^3k_X'\int d\omega_X\int d\omega_X'\,e^{-\mathrm{i}\,(\mathbf{k}_X'\cdot\mathbf{x}'-\omega_X't_1')}\,e^{\mathrm{i}\,(\mathbf{k}_X\cdot\mathbf{x}-\omega_Xt_1)}\,Z^{(1)}_{\sigma\rho}(\mathbf{k}_X',\omega_X',\mathbf{k}_X,\omega_X)\tag{2.58}$$

$$\bar{H}^{(1)}_{\nu\mu}(\mathbf{y}',t_2',\mathbf{y},t_2)=\frac{1}{(2\pi)^8}\int d^3k_L\int d^3k_L'\int d\omega_L\int d\omega_L'\,e^{-\mathrm{i}\,(\mathbf{k}_L'\cdot\mathbf{y}'-\omega_X't_2')}\,e^{\mathrm{i}\,(\mathbf{k}_L\cdot\mathbf{y}-\omega_Lt_2)}\,\bar{Z}^{(1)}_{\nu\mu}(\mathbf{k}_L',\omega_L',\mathbf{k}_L,\omega_L)\tag{2.59}$$

$$\bar{S}^{(1)}_{\nu\mu}(\mathbf{y}',t_2',\mathbf{y},t_2)=\frac{1}{(2\pi)^8}\int d^3k_L\int d^3k_L'\int d\omega_L\int d\omega_L'\,e^{-\mathrm{i}\,(\mathbf{k}_L'\cdot\mathbf{y}'-\omega_X't_2')}\,e^{\mathrm{i}\,(\mathbf{k}_L\cdot\mathbf{y}-\omega_Lt_2)}\,\bar{C}^{(1)}_{\nu\mu}(\mathbf{k}_L',\omega_L',\mathbf{k}_L,\omega_L)\tag{2.60}$$

$$\mathbf{P}_I(\mathbf{y},t_2,\mathbf{x},t_1)=\mathbf{P}_I(\mathbf{y},0,\mathbf{x},(t_1-t_2))=\frac{1}{(2\pi)^7}\int d^3k_1\int d^3k_2\int d\omega\,e^{\mathrm{i}\,(\mathbf{k}_1\cdot\mathbf{y}+\mathbf{k}_2\cdot\mathbf{x})}\,e^{-\mathrm{i}\,\omega(t_1-t_2)}\,\mathbf{K}_I(\mathbf{k}_1,\mathbf{k}_2,\omega).\tag{2.61}$$

In the last line, we have made use of the time-translation invariance of $\mathbf{P}_I(\mathbf{y},t_2,\mathbf{x},t_1)$ in order to reduce the number of time-arguments to be transformed effectively[22]. Substituting all of the above into Eq. (2.57),

[21] We note for reference that a collection of various Fourier relations among correlation functions may be found in App. A.8

[22] For reference, we note that the (symmetry-) properties of the nonlinear response function, among which is the time-translation invariance, are further elaborated upon in Sec. 3.1.1.

We note further that the time-translational invariance is intimately tied to the fact that $\mathbf{P}_I(\mathbf{y},t_2,\mathbf{x},t_1)$ constitutes a stationary correlation function, viz. an equilibrium Green's function of the electronic system. Similar reductions in complexity would *not* be possible for a non-stationary, non-equilibrium Green's function. By extension, a comparable reduction of time-arguments is not generally possible for the x-ray and optical fields $H^{(1)}_{\sigma\rho}(\mathbf{x}',t_1',\mathbf{x},t_1)$ or $\bar{H}^{(1)}_{\nu\mu}(\mathbf{y}',t_2',\mathbf{y},t_2)$, respectively. As long as these describe pulsed fields, they are inherently non-stationary and both of their time-arguments will have to be considered with respect to the arrival-time of the pulse. The optical fluctuations' correlator on the other hand is, in fact, assumed to be stationary again. Herewith, we could have employed the same reduction as in Eq. (2.61), but refrained in order to keep the structural symmetry with expression (2.59).

the fully expanded observable reads

$$\begin{aligned}\langle \hat{O}_{\mathbf{k}_f,\lambda_f}\rangle = &\frac{2\pi\alpha^4}{V\omega_f}\,\frac{1}{(2\pi)^{30}}\,(\boldsymbol{\varepsilon}_f)_\sigma\,(\boldsymbol{\varepsilon}_f^*)_\rho \int^{\times 4} dt_1\,dt_1'\,dt_2\,dt_2' \int^{\times 4} d^3x\,d^3x'\,d^3y\,d^3y'\; e^{-\mathrm{i}\,\mathbf{k}_f\cdot(\mathbf{x}-\mathbf{x}')}\; e^{\mathrm{i}\,\omega_f(t_1-t_1')}\\
&\times \int^{\times 2} d^3k_X\,d^3k_X' \int^{\times 2} d\omega_X\,d\omega_X'\; e^{-\mathrm{i}\,(\mathbf{k}_X'\cdot\mathbf{x}'-\omega_X't_1')}\; e^{\mathrm{i}\,(\mathbf{k}_X\cdot\mathbf{x}-\omega_X t_1)} \int^{\times 2} d^3k_L\,d^3k_L' \int^{\times 2} d\omega_L\,d\omega_L'\; e^{-\mathrm{i}\,(\mathbf{k}_L'\cdot\mathbf{y}'-\omega_X't_2')}\\
&\times e^{\mathrm{i}\,(\mathbf{k}_L\cdot\mathbf{y}-\omega_L t_2)} \int^{\times 4} d^3k_1\,d^3k_1'\,d^3k_2\,d^3k_2' \int^{\times 2} d\omega\,d\omega'\; e^{\mathrm{i}\,(\mathbf{k}_1\cdot\mathbf{y}+\mathbf{k}_2\cdot\mathbf{x})}\; e^{-\mathrm{i}\,\omega(t_1-t_2)}\; e^{-\mathrm{i}\,(\mathbf{k}_1'\cdot\mathbf{y}'+\mathbf{k}_2'\cdot\mathbf{x}')}\; e^{\mathrm{i}\,\omega(t_1'-t_2')}\\
&\times Z^{\text{X_IN}}_{\sigma\rho}(\mathbf{k}_X',\omega_X',\mathbf{k}_X,\omega_X)\,\Big(\bar{Z}^{\text{OPT}}_{\nu\mu}(\mathbf{k}_L',\omega_L',\mathbf{k}_L,\omega_L)+\bar{C}^{\text{OPT}}_{\nu\mu}(\mathbf{k}_L',\omega_L',\mathbf{k}_L,\omega_L)\Big)\\
&\times \sum_I p_I\,\Big(\mathbf{K}_I(\mathbf{k}_1,\mathbf{k}_2,\omega)\Big)_\mu\,\Big(\mathbf{K}_I(\mathbf{k}_1',\mathbf{k}_2',\omega')\Big)^*_\nu. \end{aligned} \tag{2.62}$$

Therein, we can identify several δ-function constraints, viz.

$$\int d^3x\; e^{\mathrm{i}\,(\mathbf{k}_2+\mathbf{k}_X-\mathbf{k}_f)\cdot\mathbf{x}} = (2\pi)^3\;\delta^3(\mathbf{k}_2+\mathbf{k}_X-\mathbf{k}_f) \tag{2.63}$$

$$\int d^3y\; e^{\mathrm{i}\,(\mathbf{k}_L+\mathbf{k}_1)\cdot\mathbf{y}} = (2\pi)^3\;\delta^3(\mathbf{k}_L+\mathbf{k}_1) \tag{2.64}$$

$$\int dt_1\; e^{\mathrm{i}\,(\omega_f-\omega_X-\omega)t_1} = (2\pi)\;\delta(\omega_f-\omega_X-\omega) \tag{2.65}$$

$$\int dt_2\; e^{\mathrm{i}\,(\omega-\omega_L)t_2} = (2\pi)\;\delta(\omega-\omega_L) \tag{2.66}$$

and analogous for the primed variables. Using most of these, we shorten Eq. (2.62) and obtain as an observable for XOWM processes

$$\begin{aligned}\langle \hat{O}_{\mathbf{k}_f,\lambda_f}\rangle = &\frac{2\pi\alpha^4}{V\omega_f}\,\frac{1}{(2\pi)^{14}} \int^{\times 4} d^3k_L\,d^3k_L'\,d^3k_X\,d^3k_X' \int^{\times 4} d\omega_L\,d\omega_L'\,d\omega_X\,d\omega_X'\;\delta(\omega_f-\omega_X-\omega_L)\,\delta(\omega_f-\omega_X'-\omega_L')\\
&\times (\boldsymbol{\varepsilon}_f)_\sigma\,Z^{\text{X_IN}}_{\sigma\rho}(\mathbf{k}_X',\omega_X',\mathbf{k}_X,\omega_X)\,(\boldsymbol{\varepsilon}_f^*)_\rho\,\Big(\bar{Z}^{\text{OPT}}_{\nu\mu}(\mathbf{k}_L',\omega_L',\mathbf{k}_L,\omega_L)+\bar{C}^{\text{OPT}}_{\nu\mu}(\mathbf{k}_L',\omega_L',\mathbf{k}_L,\omega_L)\Big)\\
&\times \sum_I p_I\,\Big(\mathbf{K}_I(-\mathbf{k}_L,\mathbf{k}_f-\mathbf{k}_X,\omega_L)\Big)_\mu\,\Big(\mathbf{K}_I(-\mathbf{k}_L',\mathbf{k}_f-\mathbf{k}_X',\omega_L')\Big)^*_\nu. \end{aligned} \tag{2.67}$$

This marks the final result of this chapter. We will subsequently dedicate Chpts. 3 and 4 to evaluate the constituent electronic and field correlators respectively, before we return to the above expression in Chpt. 5 again. There, we will ultimately evaluate scattering probabilities for several XOWM processes.

In closing, we want to observe two appealing aspects about Eq. (2.67):

1. As we have implied (and imposed) before, the expression indeed enforces energy conservation among the different, parametrically mixed fields. This is most prominently apparent in the respective δ-function, viz. $\delta(\omega_f-\omega_X-\omega_L)$, which we have not yet resolved.

2. Depending on the choice of ω_f in combination with the presence (or absence) of $\bar{Z}^{\text{OPT}}$, the above expression is capable of describing different XOWM processes. For instance, it describes sum-frequency generation (SFG), if a laser-drive is present and the observable photon energy is set above the input $\omega_f=\omega_X+\omega_L>\omega_X$ for (most of) the incident spectrum ω_X. Alternative choices can produce either DFG or XPDC as well. In this, we have reached our main goal to establish a theoretical framework for the description of the aforementioned XOWM processes.

Chapter 3

Nonlinear electronic response

In this chapter, we examine the previously introduced time-ordered correlation function

$$\mathbf{P}_I(\mathbf{x}_1,t_1,\mathbf{x}_2,t_2) = \langle I|\,\hat{T}\,[\hat{\mathbf{p}}(\mathbf{x}_1,t_1)\,\hat{n}(\mathbf{x}_2,t_2)]\,|I\rangle \tag{3.1}$$

or

$$\mathbf{K}_I(\mathbf{k}_1,\mathbf{k}_2,\omega) = \int d^3x_1 \int d^3x_2 \int d\tau\; e^{-\mathrm{i}\,(\mathbf{k}_1\cdot\mathbf{x}_1+\mathbf{k}_2\cdot\mathbf{x}_2)}\; e^{\mathrm{i}\,\omega\tau}\,\mathbf{P}_I(\mathbf{x}_1,0,\mathbf{x}_2,\tau). \tag{3.2}$$

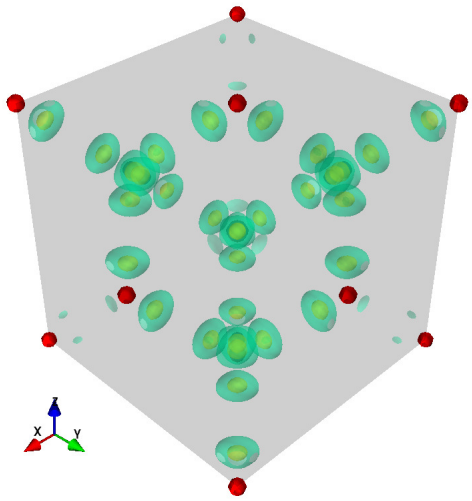

Figure 3.1: Preview of the three-dimensional distribution of the nonlinear electronic response across the conventional (cubic) unit cell of diamond. For further details, see Sec. 3.3.

We begin our discussion with a general overview of its properties in Sec. 3.1, which will cover—among other things—symmetry properties that are important for our derivations (Sec. 3.1.1) and its embedding in a periodic domain for crystal-structure calculations (Sec. 3.1.2).

Subsequently, we turn our attention towards the implementation of a mean-field model of $\mathbf{P}_I(\mathbf{x}_1,t_1,\mathbf{x}_2,t_2)$ in Sec. 3.2. This will provide the basis for later numerical evaluation of the nonlinear response and first attempts to interpret its implications (3.3).

We will close this chapter by giving an outlook onto methods *beyond* the mean-field approximation, which could be used to investigate $\mathbf{P}_I(\mathbf{x}_1,t_1,\mathbf{x}_2,t_2)$ in the future.

3.1 General properties of $\mathbf{P}_I$

The nonlinear response function $\mathbf{P}_I(\mathbf{x}_1,t_1,\mathbf{x}_2,t_2)$—being a density–current-density correlator—arises quite naturally in the context of light-matter interaction. It forms part of a more general 4×4 response tensor, which interlinks the electronic density-response with electronic current-density response functions (see, for instance, Ref. [76]). In general, $\mathbf{P}_I(\mathbf{x}_1,t_1,\mathbf{x}_2,t_2)$ is a manybody Green's function—sometimes referred to as a polarization propagator [77]—and as such it is sensitive to correlation effects within electronic manybody systems. In maintaining this important aspect, our approach differs from earlier descriptions of XOWM. Thus, we consider it to be a promising framework for in-depth investigations of (correlated) electronic dynamics beyond with novel, nonlinear probes. We emphasize in particular, that the identification of this response function also renders the inverse problem accessible, i.e., its reconstruction from measured data (cf. Secs. 3.3 and 5.1.2.d). This would allow to extract response properties of correlated systems from XOWM experiments, in order to feed them back into many-body theory—instead of enabling merely the computation of scattering patterns in forward direction.

Regarding its numerical evaluation, $\mathbf{P}_I(\mathbf{x}_1,t_1,\mathbf{x}_2,t_2)$ is amenable to a host of methods known from electronic structure theory across atomic, molecular and solid-state physics. Beyond explicit Green's function techniques (see Refs. [76, 78, 79], for examples), these include Many-Body Perturbation Theory [80–83], wave-packet propagation [84, 85], time-dependent density functional theory (TD-DFT) [86, 87] or, eventually, its phenomenologic reduction to (analytically solvable) model systems[1].

Comparison to previous electronic-structure models [21] Before we proceed to elaborate on our evaluation of $\mathbf{P}_I(\mathbf{x}_1,t_1,\mathbf{x}_2,t_2)$ in more detail, we briefly want to contrast our method with earlier approaches. Providing this context, we borrow the following discussion from our manuscript on XOWM [21] verbatim:

"In contrast, previous approaches to perturbative XOWM remained restricted to *single-particle* treatments. Most of these can be divided roughly into two classes: The first class comprises discussions such as Refs. [46, 48, 54, 55], adopting the classical current-based picture that was introduced by Eisenberger and McCall for wavemixing within the x-ray domain [27]. This captures the nonlinear electronic response at high frequencies (cf. Ref. [88]), where individual electrons interact with the driving fields like free, classical charges. However, this picture is not strictly transferable towards lower photon energies—especially if optical admixtures are involved. Then, the bound nature of the electrons becomes essential as their response is dominated by discrete, quantum-mechanical transitions. This aspect is taken more prominently into account by the second class of previously published XOWM descriptions [26, 89–94]. Herein, the quantum-mechanical nature of the response is related to single-particle wavefunctions featuring in perturbative expressions. All of these approaches can be traced to the semi-classical response formalisms presented by Armstrong et al. [95] as well as Jha et al. [96]. Despite being half a century old though, these expressions have never been evaluated in their full form for XOWM. At most, Freund has presented results for the simplified case of a 'high-frequency' limit [89], while in addition, bond-charge

[1] We note that the last evaluation option, i.e., in terms of phenomenological model systems, should not be over-rated. While they appear appealing in their simplicity, they often require significant (hidden) a-priori insight into the structure of the underlying problem, in order to reach effectiveness.

models [26] and toy-model semiconductors [94] have been considered [2]."

This being said, we will return our focus to the evaluation of $\mathbf{P}_I(\mathbf{x}_1,t_1,\mathbf{x}_2,t_2)$ for our current needs. To this end, we will first address the question of pertinent symmetries of the response. Subsequently, we shall discuss intricacies in implementing it for crystalline solids, assuming periodic boundary conditions.

3.1.1 Symmetries of $\mathbf{P}_I(\mathbf{x}_1,t_1,\mathbf{x}_2,t_2)$

The nonlinear response function $\mathbf{P}_I(\mathbf{x}_1,t_1,\mathbf{x}_2,t_2)$ exhibits a set of fundamental symmetries, which will prove important during our later work. In particular, these comprise:

- Time-translation invariance, i.e., $\mathbf{P}_I(\mathbf{x}_1,t_1,\mathbf{x}_2,t_2)=\mathbf{P}_I(\mathbf{x}_1,t_1+\tau,\mathbf{x}_2,t_2+\tau)$
- Lattice-periodicity: $\mathbf{P}_I(\mathbf{x}_1,t_1,\mathbf{x}_2,t_2)=\mathbf{P}_I(\mathbf{x}_1+\mathbf{R},t_1,\mathbf{x}_2+\mathbf{R},t_2)$ and
- Time-reversal anti-symmetry: $\mathbf{P}_I(\mathbf{x}_1,0,\mathbf{x}_2,\tau)=-\mathbf{P}_I(\mathbf{x}_1,0,\mathbf{x}_2,-\tau)$

The first two of these are easily proven using translation operators. Thus, we will not discuss them here in detail[3]. We note, however, that these properties comply with our intuitive understanding of a periodic solid resting in an energy eigenstate. That is to say, no absolute point in the lattice, nor in time for that matter, should be outstanding with respect to others. Consequentially, there should be no change in $\mathbf{P}_I(\mathbf{x}_1,t_1,\mathbf{x}_2,t_2)$, if it was translated on an absolute scale (i.e., equally in both its arguments)—neither in space nor in time. Relative changes of one argument versus the other,though, will of course entail changes in the value of $\mathbf{P}_I(\mathbf{x}_1,t_1,\mathbf{x}_2,t_2)$.

Concerning the third symmetry-property, this will requires a more involved derivation. We will present this in the upcoming section and address a (formal) issue regarding the hermiticity of the operator $\hat{\mathbf{p}}(\mathbf{x})=\hat{\psi}^\dagger(\mathbf{x})\,(-\mathrm{i}\nabla\hat{\psi}(\mathbf{x}))$ in doing so.

3.1.1.a Time-reversal (anti-)symmetry and a note on hermiticity

In the following, we will embark on the proof of time-reversal anti-symmetry of $\mathbf{P}_I(\mathbf{x}_1,t_1,\mathbf{x}_2,t_2)$. To begin with, we recall its definition and account for its two time-ordered constituents:

$$\begin{aligned}\mathbf{P}_I(\mathbf{x}_1,t_1,\mathbf{x}_2,t_2)&=\mathbf{P}_I(\mathbf{x}_1,0,\mathbf{x}_2,\tau)=\langle I|\,\hat{T}\left[\hat{\mathbf{p}}(\mathbf{x}_1,0)\,\hat{n}(\mathbf{x}_2,\tau)\right]|I\rangle\\&=\Theta(\tau)\;\langle I|\,\hat{n}(\mathbf{x}_2,\tau)\,\hat{\mathbf{p}}(\mathbf{x}_1,0)\,|I\rangle+\Theta(-\tau)\;\langle I|\,\hat{\mathbf{p}}(\mathbf{x}_1,0)\,\hat{n}(\mathbf{x}_2,\tau)\,|I\rangle\,,\end{aligned}\tag{3.3}$$

[2] It should be noted that—outside the scope of models presented here—there was a single publication by Van Vechten and Martin that also alludes to XOWM in the context of calculating local field effects in solids [97]. They conduct a full numerical evaluation of the Adler-Wiser dielectric response in random-phase approximation [98, 99] and present a result to compare with Ref. [26]. Unfortunately, they do not discuss this comparison in detail, even though their result likely presents the most elaborate computation on XOWM-related response functions to-date.

[3] We remark for the interested reader: The proof of time-translation invariance can be carried out using time-evolution operators (see also App. A.1). Rephrasing the time-dependent operators $\hat{\mathbf{p}}(\mathbf{x}_1,t_1)$ and $\hat{n}(\mathbf{x}_2,t_2)$ within the response function, we can render their 'Heisenberg-picture'-type time-dependence explicit. Afterwards, we can exploit the fact that time-evolution operators may be split or concatenated at will, to produce the desired shift by $\Delta t=\tau$. Finally, we can absorb this time-shift into the reference state(s) $\langle I|$ and $|I\rangle$, noting that the resulting phases will exactly compensate.
The proof for translational-invariance on the lattice proceed in the same fashion. However, it necessitates the definition of a sensible, spatial translation-operator first. This will obviously take on a shape very similar to $\hat{U}(t,t_0)$, whereas the generator of the translation will be the momentum rather than the energy. For an explicit reference, we recommend the discussion in Ref. [76].

where $\tau = t_2 - t_1$. In order to explore the time-reversal property of this correlator, we will follow the formalism outlined by Sachs in Ref. [100]. Before we can apply it in a convenient manner, however, we have to address a subtle issue on the (non-)hermiticity of the momentum operator above.

While it has never appeared to be a problem so far, it should not go unnoticed that the momentum density operator that is present within $\mathbf{P}_I(\mathbf{x}_1, 0, \mathbf{x}_2, \tau)$ is not actually hermitian. Using its conventional definition $\hat{\mathbf{p}}(\mathbf{x}) = \hat{\psi}^\dagger(\mathbf{x})\,(-\mathrm{i}\nabla\hat{\psi}(\mathbf{x}))$, we face the issue that

$$\Big(\hat{\mathbf{p}}(\mathbf{x})\Big)^\dagger = \Big(\hat{\psi}^\dagger(\mathbf{x})\,(-\mathrm{i}\nabla\hat{\psi}(\mathbf{x}))\Big)^\dagger = (\nabla\hat{\psi}^\dagger(\mathbf{x}))\,\mathrm{i}\hat{\psi}(\mathbf{x}) \tag{3.4}$$

is not obviously self-adjoint. Typically, this would be remedied by partial integration, because the relation

$$\nabla\hat{\psi}^\dagger(\mathbf{x})\hat{\psi}(\mathbf{x}) = (\nabla\hat{\psi}^\dagger(\mathbf{x}))\hat{\psi}(\mathbf{x}) + \hat{\psi}^\dagger(\mathbf{x})\,(\nabla\hat{\psi}(\mathbf{x})) \tag{3.5}$$

allows to trade the last term of Eq. (3.4) for the original momentum density. This holds under the provision that the surface term vanishes and there are no further complications to the integral. As a matter of fact, this simple situation is actually ensured *whilst* we introduce our correlation function $\mathbf{P}_I(\mathbf{x}_1, t_1, \mathbf{x}_2, t_2)$. Specifically in Eq. (2.44), the momentum density enters only in combination with a vector potential (stemming from a $\mathbf{p}\cdot\mathbf{A}$-type coupling term). As the derivative action vanishes on the vector potential in Coulomb gauge, we can make easy use of relation (3.5)—at this point. Later on, this is less obvious[4]. Taking unrestricted Fourier-transformations of $\mathbf{P}_I(\mathbf{x}_1, t_1, \mathbf{x}_2, t_2)$ in its isolated form (Eq. (3.3)), for instance, leaves no room to actually play the above trick and thus leaves us with a non-hermitian momentum-density for better or for worse. However, we could redefine (and should maybe do so at some point) $\mathbf{P}_I(\mathbf{x}_1, t_1, \mathbf{x}_2, t_2)$ to involve the current-density

$$\hat{\mathbf{j}}(\mathbf{x}) = \frac{1}{2\mathrm{i}}\left[\hat{\psi}^\dagger(\mathbf{x})\,(\nabla\hat{\psi}(\mathbf{x})) - (\nabla\hat{\psi}^\dagger(\mathbf{x}))\hat{\psi}(\mathbf{x})\right] \tag{3.6}$$

instead of the momentum-density. Within our initial derivation of the XOWM framework—at the stage of Eq. (2.44)—this is a one-to-one replacement, without any need for further changes. The current density is *intrinsically* hermitian, which will prove very useful in the following study of time-reversal.

Considering the constituent correlator of Eq. (3.3)—with a current density—we can insert the time-reversal operator $\hat{T}_{inv}$ as described by Sachs [100]. The resulting expression reads

$$\begin{aligned}
\langle I|\,\hat{n}(\mathbf{x}_2,\tau)\hat{\mathbf{j}}(\mathbf{x}_1,0)\,|I\rangle^* &= \langle \hat{T}_{inv} I|\,\hat{T}_{inv}\Big(\hat{n}(\mathbf{x}_2,\tau)\hat{\mathbf{j}}(\mathbf{x}_1,0)\,|I\rangle\Big) \\
&= \langle \hat{T}_{inv} I|\,\hat{T}_{inv}\hat{n}(\mathbf{x}_2,\tau)\hat{T}_{inv}^{-1}\hat{T}_{inv}\hat{\mathbf{j}}(\mathbf{x}_1,0)\,\hat{T}_{inv}^{-1}\hat{T}_{inv}\,|I\rangle \\
&= -\langle I|\,\hat{n}(\mathbf{x}_2,-\tau)\hat{\mathbf{j}}(\mathbf{x}_1,0)\,|I\rangle\,.
\end{aligned} \tag{3.7}$$

Now, using the hermiticity of both $\hat{n}$ and $\hat{\mathbf{j}}$, we can relate

$$\begin{aligned}
-\langle I|\,\hat{n}(\mathbf{x}_2,-\tau)\hat{\mathbf{j}}(\mathbf{x}_1,0)\,|I\rangle &= \langle I|\,\hat{n}(\mathbf{x}_2,\tau)\hat{\mathbf{j}}(\mathbf{x}_1,0)\,|I\rangle^* \\
&= \langle I|\,\hat{\mathbf{j}}(\mathbf{x}_1,0)\hat{n}(\mathbf{x}_2,\tau)\,|I\rangle\,.
\end{aligned} \tag{3.8}$$

[4] We suppose that one might go as far as to say less correct.

By extension to both constituents of Eq. (3.3), we can conclude

$$\begin{aligned}\mathbf{P}_I(\mathbf{x}_1,0,\mathbf{x}_2,\tau) &= \Theta(\tau)\ \langle I|\,\hat{n}(\mathbf{x}_2,\tau)\hat{\mathbf{j}}(\mathbf{x}_1,0)\,|I\rangle &&+\Theta(-\tau)\ \langle I|\,\hat{\mathbf{j}}(\mathbf{x}_1,0)\hat{n}(\mathbf{x}_2,\tau)\,|I\rangle \\ &= \Theta(\tau)\ (-1)\ \langle I|\,\hat{\mathbf{j}}(\mathbf{x}_1,0)\hat{n}(\mathbf{x}_2,-\tau)\,|I\rangle &&+\Theta(-\tau)\ (-1)\ \langle I|\,\hat{n}(\mathbf{x}_2,-\tau)\hat{\mathbf{j}}(\mathbf{x}_1,0)\,|I\rangle \\ &= -\mathbf{P}_I(\mathbf{x}_1,0,\mathbf{x}_2,-\tau). \end{aligned} \tag{3.9}$$

Thereby, we have established that the nonlinear density–current-density response function is indeed anti-symmetric upon time-reversal. We emphasize, once again, that this conclusion is only valid *strictly*, if the current-density operator is used in place of its momentum counterpart.

As a further implication of the above result, it immediately follows the Fourier-transformed response function $\mathbf{K}_I(\mathbf{k}_1,\mathbf{k}_2,\omega)$ will likewise sport an anti-symmetry. Here, it will be in its frequency dependence, i.e.,

$$\mathbf{K}_I(\mathbf{k}_1,\mathbf{k}_2,\omega) = -\mathbf{K}_I(\mathbf{k}_1,\mathbf{k}_2,-\omega). \tag{3.10}$$

We will be able to reproduce this particular anti-symmetry in our later, numerical studies of the response in Sec. 3.3.

3.1.2 The response function on a periodic domain vs. free space

In addition to the translational symmetry that comes with the lattice of a crystal, we shall further elucidate the subtleties that go along with choosing it *fully* periodic.

To begin with, we recall the Fourier-relations

$$\mathbf{K}_I(\mathbf{k}_1,\mathbf{k}_2,\omega) = \int d^3x_1 \int d^3x_2 \int d\tau\ e^{-\mathrm{i}(\mathbf{k}_1\cdot\mathbf{x}_1+\mathbf{k}_2\cdot\mathbf{x}_2)}\ e^{\mathrm{i}\omega\tau}\ \mathbf{P}_I(\mathbf{x}_1,0,\mathbf{x}_2,\tau) \tag{3.11}$$

and

$$\mathbf{P}_I(\mathbf{x}_1,0,\mathbf{x}_2,\tau) = \frac{1}{(2\pi)^7}\ \int d^3k_1 \int d^3k_2 \int d\omega\ e^{\mathrm{i}(\mathbf{k}_1\cdot\mathbf{x}_1+\mathbf{k}_2\cdot\mathbf{x}_2)}\ e^{-\mathrm{i}\omega\tau}\ \mathbf{K}_I(\mathbf{k}_1,\mathbf{k}_2,\omega), \tag{3.12}$$

which we have used so far to relate the electronic correlation function between direct and reciprocal space. In writing these infinite-domain Fourier transformations, we assume that $\mathbf{P}_I(\mathbf{x}_1,0,\mathbf{x}_2,\tau)$ pertains to a realistic system, which occupies only a finite volume within the 3-dimensional direct space. This way, the occurring spatial integrals are naturally finite as well.

However, in order to model $\mathbf{P}_I$ or $\mathbf{K}_I$ theoretically, it is often advantageous to adopt a domain that is completely filled by the 'bulk' sample and fitted with periodic boundary conditions[5] (PBC). On this alternative domain—which we will henceforth denote by the subscript $\diamond$—Fourier decompositions are discretized. A priori, this is incompatible with the previous Eqs. (3.11,3.12). Instead, we shall use

$$\mathbf{K}_{I\diamond}(\mathbf{q}+\mathbf{G}_1,-\mathbf{q}+\mathbf{G}_2,\omega) = \int_\diamond d^3x_1 \int_\diamond d^3x_2 \int d\tau\ e^{-\mathrm{i}(\mathbf{q}+\mathbf{G}_1)\cdot\mathbf{x}_1}\, e^{-\mathrm{i}(-\mathbf{q}+\mathbf{G}_2)\cdot\mathbf{x}_2}\ e^{\mathrm{i}\omega\tau}\ \mathbf{P}_{I\diamond}(\mathbf{x}_1,0,\mathbf{x}_2,\tau) \tag{3.13}$$

$$\mathbf{P}_{I\diamond}(\mathbf{x}_1,0,\mathbf{x}_2,\tau) = \frac{1}{V_\diamond^2\, 2\pi}\ \sum_{\mathbf{q}}^{\text{1. BZ rec. latt.}} \sum_{\mathbf{G}_1,\mathbf{G}_2} \int d\omega\ e^{\mathrm{i}(\mathbf{q}+\mathbf{G}_1)\cdot\mathbf{x}_1}\, e^{\mathrm{i}(-\mathbf{q}+\mathbf{G}_2)\cdot\mathbf{x}_2}\ e^{-\mathrm{i}\omega\tau}\ \mathbf{K}_{I\diamond}(\mathbf{q}+\mathbf{G}_1,-\mathbf{q}+\mathbf{G}_2,\omega). \tag{3.14}$$

[5] We note that several works of solid-state theory, refer to the aforementioned PBC more specifically in terms of 'Born-von-Karman boundary conditions' (BvK) [76, 101] following Ref. [102]. In this work, we shall use both denominations interchangeably, though.

In writing these, we have resorted to the discretized Fourier transform, which is detailed in App. A.4 and which incorporates the overall translational invariance of $\mathbf{P}_I(\mathbf{x}_1, 0, \mathbf{x}_2, \tau)$ with respect to the crystal lattice (cf. previous Sec. 3.1.1).

In order to bridge between the two descriptions, we adopt a convolution approach that is justified by the following logic:
We consider Eq. (3.11) to be our starting point, with the included $\mathbf{P}_I(\mathbf{x}_1, 0, \mathbf{x}_2, \tau)$ describing the properties of a realistic material. As such a realistic system is finite, we can introduce two window functions *around* it, which will not alter the numerical value of $\mathbf{P}_I(\mathbf{x}_1, 0, \mathbf{x}_2, \tau)$ essentially, i.e.,

$$\mathbf{P}_I(\mathbf{x}_1, 0, \mathbf{x}_2, \tau) = w(\mathbf{x}_1)\, w(\mathbf{x}_2)\, \mathbf{P}_I(\mathbf{x}_1, 0, \mathbf{x}_2, \tau). \tag{3.15}$$

These window functions are simply defined to delimit the volume of the sample

$$w(\mathbf{x}) = \begin{cases} 1 & \text{for } \mathbf{x} \text{ inside the sample} \\ 0 & \text{otherwise.} \end{cases} \tag{3.16}$$

Within these windows, we may now approximate $\mathbf{P}_I$ by $\mathbf{P}_{I\diamond}$, provided the periodic domain $\diamond$ is chosen (much) larger than the window. In this case, we essentially recover the bulk description within $w(\mathbf{x})$ and can write:

$$\begin{aligned} \mathbf{K}_I(\mathbf{k}_1, \mathbf{k}_2, \omega) \approx & \int d^3x_1 \int d^3x_2\; e^{-\mathrm{i}\,(\mathbf{k}_1\cdot\mathbf{x}_1 + \mathbf{k}_2\cdot\mathbf{x}_2)}\; w(\mathbf{x}_1)\; w(\mathbf{x}_2) \\ & \times \frac{1}{V_\diamond^2} \sum_{\mathbf{q}}^{\text{1. BZ}} \sum_{\mathbf{G}_1,\mathbf{G}_2}^{\text{rec. latt.}} e^{\mathrm{i}\,(\mathbf{q}+\mathbf{G}_1)\cdot\mathbf{x}_1}\, e^{\mathrm{i}\,(-\mathbf{q}+\mathbf{G}_2)\cdot\mathbf{x}_2}\; \mathbf{K}_{I\diamond}(\mathbf{q}+\mathbf{G}_1, -\mathbf{q}+\mathbf{G}_2, \omega). \end{aligned} \tag{3.17}$$

Next, we rewrite this further by introducing the Fourier transform of the windows $w(\mathbf{x})$ themselves:

$$w(\mathbf{x}) = \frac{1}{(2\pi)^3} \int d^3\kappa\; e^{\mathrm{i}\,\kappa\cdot\mathbf{x}}\; \tilde{w}(\kappa). \tag{3.18}$$

Thus, we obtain from Eq. (3.17):

$$\begin{aligned} \mathbf{K}_I(\mathbf{k}_1, \mathbf{k}_2, \omega) \approx & \frac{1}{V_\diamond^2} \sum_{\mathbf{q}}^{\text{1. BZ}} \sum_{\mathbf{G}_1,\mathbf{G}_2}^{\text{rec. latt.}} \int d^3\kappa_1 \int d^3\kappa_2\; \tilde{w}(\kappa_1)\, \tilde{w}(\kappa_2)\; \delta^3(\kappa_1 + \mathbf{q} + \mathbf{G}_1 - \mathbf{k}_1)\, \delta^3(\kappa_2 + \mathbf{G}_2 - \mathbf{q} - \mathbf{k}_2) \\ & \times \mathbf{K}_{I\diamond}(\mathbf{q}+\mathbf{G}_1, -\mathbf{q}+\mathbf{G}_2, \omega) \\ = & \frac{1}{V_\diamond^2} \sum_{\mathbf{q}}^{\text{1. BZ}} \sum_{\mathbf{G}_1,\mathbf{G}_2}^{\text{rec. latt.}} \tilde{w}(\mathbf{k}_1 - \mathbf{q} - \mathbf{G}_1)\, \tilde{w}(\mathbf{k}_2 + \mathbf{q} - \mathbf{G}_2)\; \mathbf{K}_{I\diamond}(\mathbf{q}+\mathbf{G}_1, -\mathbf{q}+\mathbf{G}_2, \omega), \end{aligned} \tag{3.19}$$

wherein the continuous window functions smoothly join the response function from the discretized domain $\mathbf{K}_{I\diamond}$ to its continuous counterpart $\mathbf{K}_I$. We note in closing, that comparable approaches are common practice in regular crystallography. There, the window functions are often referred to as 'form function' or 'shape function' of the crystal (see Ref. [23], for instance).

3.1.2.a Practical caveat and approximation of $\mathbf{K}_{I\diamond}$

As a caveat, we note that our previous derivation assumed $V_\diamond > V_w$. In other words, we took the bulk volume of the theoretical crystal on a domain with PBC to be larger than the actual sample. For practical,

numerical simulations, however, it will most likely be infeasible to realize such a simulation volume for a macroscopic system. Instead, numerically tractable sizes are typically much smaller ($V_{\text{num}} \ll V_w$), such that the corresponding (artificial) discretization in k-space might remain apparent despite the smoothing effect of $\tilde{w}(\boldsymbol{\kappa})$. There is no straight-forward way to resolve this issue *without* postulating any further approximations[6].

Fortunately, such approximations may not impose severe limitations on the (practical) validity of $\mathbf{K}_{I\diamond}(\mathbf{q}+\mathbf{G}_1, -\mathbf{q}+\mathbf{G}_2, \omega)$. In many cases, for instance, it may be reasonable to assume the response function to be slowly varying in $\mathbf{q}$. As such, we could interpolate it on the basis of much coarser results[7].

The simplest approximation of this kind is of 'dipole-approximation'-type, for which we shall see further motivation in the following sections. It consists in assuming that the variation of $\mathbf{K}_{I\diamond}(\mathbf{q}+\mathbf{G}_1, -\mathbf{q}+\mathbf{G}_2, \omega)$ with respect to $\mathbf{q}$—and thus the optical wave-vector of the XOWM process—is negligible:

$$\mathbf{K}_{I\diamond}(\mathbf{q}+\mathbf{G}_1, -\mathbf{q}+\mathbf{G}_2, \omega) \approx \mathbf{K}_{I\diamond}(\mathbf{G}_1, \mathbf{G}_2, \omega). \tag{3.20}$$

Thereby, we can reformulate Eq. (3.19) as:

$$\begin{aligned}
\mathbf{K}_I(\mathbf{k}_1, \mathbf{k}_2, \omega) &\approx \frac{1}{V_\diamond^2} \sum_{\mathbf{q}}^{\text{1. BZ}} \sum_{\mathbf{G}_1,\mathbf{G}_2}^{\text{rec. latt.}} \tilde{w}(\mathbf{k}_1 - \mathbf{q} - \mathbf{G}_1)\, \tilde{w}(\mathbf{k}_2 + \mathbf{q} - \mathbf{G}_2)\; \mathbf{K}_{I\diamond}(\mathbf{G}_1, \mathbf{G}_2, \omega) \\
&= \frac{1}{V_\diamond^2} \sum_{\mathbf{G}_1,\mathbf{G}_2}^{\text{rec. latt.}} \mathbf{K}_{I\diamond}(\mathbf{G}_1, \mathbf{G}_2, \omega) \sum_{\mathbf{q}}^{\text{1. BZ}} \tilde{w}(\mathbf{k}_1 - \mathbf{q} - \mathbf{G}_1)\, \tilde{w}(\mathbf{k}_2 + \mathbf{q} - \mathbf{G}_2) \\
&= \frac{1}{V_\diamond} \sum_{\mathbf{G}_1,\mathbf{G}_2}^{\text{rec. latt.}} \mathbf{K}_{I\diamond}(\mathbf{G}_1, \mathbf{G}_2, \omega)\, \frac{1}{(2\pi)^3} \int_{\text{1. BZ}} d^3q\; \tilde{w}(\mathbf{k}_1 - \mathbf{q} - \mathbf{G}_1)\, \tilde{w}(\mathbf{k}_2 + \mathbf{q} - \mathbf{G}_2).
\end{aligned} \tag{3.21}$$

In the last step, we made use of the fact that the approximated $\mathbf{K}_{I\diamond}(\mathbf{G}_1, \mathbf{G}_2, \omega)$ no longer depends on $\mathbf{q}$ explicitly. Thus, nothing forces us to stick to any numerically prescribed $\mathbf{q}$-grid any more and, instead, we can consider the respective summation in the continuum limit again. Furthermore, we can quite safely assume that $\mathbf{k}_1$, which relates to the optical field, satisfies $|\mathbf{k}_1| \ll |\mathbf{G}_1|$ for all non-trivial $\mathbf{G}_1$. These are thereby rendered meaningless within a well-defined window $\tilde{w}(\mathbf{k}_1 - \mathbf{q} - \mathbf{G}_1)$. This allows us to simplify the integral expression further

$$\int_{\text{1. BZ}} d^3q\; \tilde{w}(\mathbf{k}_1 - \mathbf{q})\, \tilde{w}(\mathbf{k}_2 + \mathbf{q} - \mathbf{G}_2) = (\tilde{w} \star \tilde{w})(\mathbf{k}_1 + \mathbf{k}_2 - \mathbf{G}_2) \tag{3.22}$$

and interpret it as a convolution. Finally, we can invoke the convolution theorem (Eq. (A.195)) and use the trivial multiplication-properties of $w(\mathbf{x})$ to simplify:

$$\begin{aligned}
(\tilde{w} \star \tilde{w}) = (FT_3(w) \star FT_3(w)) &= (2\pi)^3\, FT_3(w \cdot w) \\
&= (2\pi)^3\, FT_3(w) = (2\pi)^3\, \tilde{w}.
\end{aligned} \tag{3.23}$$

[6] We regret to point out the obvious, namely: If we want the full structure, we have to calculate the full structure. It is as simple as that.

[7] We note for caution, however, that the level of detail in $\mathbf{q}$, by which $\mathbf{K}_{I\diamond}(\mathbf{q}+\mathbf{G}_1, -\mathbf{q}+\mathbf{G}_2, \omega)$ is rasterized (i.e., $\Delta\mathbf{q}$), has to be high enough to resolve the phenomena of interest. In particular in cases of long-range (electronic) order, $|\Delta\mathbf{q}| \sim l_{\text{order}}^{-1}$ has to cover the respective length scale of the order parameter.

Implementing this result in Eq. (3.21), we obtain

$$\mathbf{K}_I(\mathbf{k}_1,\mathbf{k}_2,\omega) \approx \sum_{\mathbf{G}}^{\text{rec. latt.}} \tilde{w}(\mathbf{k}_1+\mathbf{k}_2-\mathbf{G})\ \frac{1}{V_\diamond}\,\mathbf{K}_{I\diamond}(\mathbf{0},\mathbf{G},\omega)\ , \tag{3.24}$$

for which the choice of $\mathbf{k}_2$ fixes the final $\mathbf{G}$. Note that in here, the choice of $V_\diamond$ and thus the k-space mode density does no longer influence the functional form of $\mathbf{K}_I(\mathbf{k}_1,\mathbf{k}_2,\omega)$ on the left-hand side. Thus, we can abandon the previous condition $V_\diamond > V_w$ and may simply adopt the numerically used parameter $V_{\text{num}} = V_\diamond$ for normalization[8].

[8]Note that $V_\diamond$ is seldom provided as an explicit parameter by numerical codes. Instead we may resort to the density of states in reciprocal space. Recall that the usual discretization correspondence reads: $\sum_{\mathbf{k}} \leftrightarrow V_\diamond/(2\pi)^3 \int d^3k$, where the prefactor could likewise be expressed as $V_\diamond/(2\pi)^3 = \rho_{\mathbf{k}} = (\#\text{ k-states})/(\text{k-space unit volume}) = (\#\text{ k-states in 1. BZ})/(\text{volume 1. BZ})$.

3.2 Mean-field models for the nonlinear response

In our first, and quintessential, attempt at evaluating the nonlinear response function, we shall restrict ourselves to mean-field descriptions of the underlying material systems. To do so, we approximate the fundamental Hamiltonian of the material system $\hat{H}_{\mathrm{MAT}}$ by an effectively non-interacting, single particle Hamiltonian $\hat{H}_{\mathrm{MF}}$. We take this to comprise a single-particle operator for the kinetic energy contribution and an additional one-body potential for each electron. Such an $\hat{H}_{\mathrm{MF}}$ implies the existence of a corresponding single-particle basis set, the states of which we will denote as orbitals $\varphi_p(\mathbf{x})$. They satisfy the eigenvalue equation[9]

$$\hat{H}_{\mathrm{MF}}\,\varphi_p(\mathbf{x}) = \varepsilon_p\,\varphi_p(\mathbf{x}). \tag{3.25}$$

From these single-particle orbitals, we can assemble any N-particle eigenstate of $\hat{H}_{\mathrm{MF}}$ by forming the appropriate Slater-determinant [76, 103].

Besides representing eigenstates of $\hat{H}_{\mathrm{MF}}$, we can likewise expand any electronic field-operator in this orbital basis using

$$\hat{\psi}(\mathbf{x}) = \sum_p \hat{c}_p\;\varphi_p(\mathbf{x}), \tag{3.26}$$

wherein $\hat{c}_p$ denotes the fermionic annihilation operator that corresponds to the state φ_p.

By extension, we may apply this prescription to all field-operators that are contained within $\mathbf{P}_{I\diamond}(\mathbf{x}_1,0,\mathbf{x}_2,\tau)$. We recall its overall form first

$$\begin{aligned}\mathbf{P}_{I\diamond}(\mathbf{x}_1,0,\mathbf{x}_2,\tau) &= \langle I|\,\hat{T}\,[\hat{\mathbf{p}}(\mathbf{x}_1,0)\,\hat{n}(\mathbf{x}_2,\tau)]\,|I\rangle \\ &= \Theta(\tau)\,\langle I|\,\hat{n}(\mathbf{x}_2,\tau)\,\hat{\mathbf{p}}(\mathbf{x}_1,0)\,|I\rangle + \Theta(-\tau)\,\langle I|\,\hat{\mathbf{p}}(\mathbf{x}_1,0)\,\hat{n}(\mathbf{x}_2,\tau)\,|I\rangle\end{aligned} \tag{3.27}$$

and proceed to apply Eq. (3.26) to its constituents

$$\langle I|\,\hat{n}(\mathbf{x}_2,\tau)\,\hat{\mathbf{p}}(\mathbf{x}_1,0)\,|I\rangle = \sum_{p,q,r,s}\langle I|\,\hat{c}_p^\dagger\hat{c}_q\hat{c}_r^\dagger\hat{c}_s\,|I\rangle\;\; e^{\mathrm{i}(\varepsilon_p-\varepsilon_q)\tau}\;\varphi_p^\dagger(\mathbf{x}_2)\,\varphi_q(\mathbf{x}_2)\,\varphi_r^\dagger(\mathbf{x}_1)\,(-\mathrm{i}\nabla)\,\varphi_s(\mathbf{x}_1) \tag{3.28}$$

as well as

$$\langle I|\,\hat{\mathbf{p}}(\mathbf{x}_1,0)\,\hat{n}(\mathbf{x}_2,\tau)\,|I\rangle = \sum_{p,q,r,s}\langle I|\,\hat{c}_p^\dagger\hat{c}_q\hat{c}_r^\dagger\hat{c}_s\,|I\rangle\;\; e^{\mathrm{i}(\varepsilon_r-\varepsilon_s)\tau}\;\varphi_p^\dagger(\mathbf{x}_1)\,(-\mathrm{i}\nabla)\,\varphi_q(\mathbf{x}_1)\,\varphi_r^\dagger(\mathbf{x}_2)\,\varphi_s(\mathbf{x}_2). \tag{3.29}$$

In rewriting the above, we have resolved the time-evolution of $\hat{n}(\mathbf{x}_2,\tau)$ via

$$\hat{n}(\mathbf{x}_2,\tau) = \hat{U}_{00}(0,\tau)\,\hat{n}(\mathbf{x}_2)\,\hat{U}_{00}(\tau,0) = e^{\mathrm{i}\hat{H}_{\mathrm{MAT}}\tau}\,\hat{n}(\mathbf{x}_2)\,e^{-\mathrm{i}\hat{H}_{\mathrm{MAT}}\tau} \approx e^{\mathrm{i}\hat{H}_{\mathrm{MF}}\tau}\,\hat{n}(\mathbf{x}_2)\,e^{-\mathrm{i}\hat{H}_{\mathrm{MF}}\tau}. \tag{3.30}$$

To this end, we have evaluated the action of $\hat{H}_{\mathrm{MF}}$ onto individual orbitals according to Eq. (3.25). Alongside our approximation of $\hat{H}_{\mathrm{MAT}} \approx \hat{H}_{\mathrm{MF}}$, we shall likewise assume that the initial state of the material

[9] We note two things:
a) For a finite coordinate space with periodic boundary conditions, the set of spatial eigenfunctions $\varphi_p(\mathbf{x})$ is discretized.
b) Beyond its spatial component the $\varphi_p(\mathbf{x})$ should initially be considered as a two component spinors that reflect the fermionic nature of electrons.

system $|I\rangle$ is an eigenstate of this approximate Hamiltonian[10]. This allows us to resolve the N-electron overlap $\langle I|\, \hat{c}_p^\dagger \hat{c}_q \hat{c}_r^\dagger \hat{c}_s \,|I\rangle$ straight-forwardly, namely by observing that all occurring $\hat{c}$-operators have to contract among each other. Then, and only then, will the initial state be left unchanged by the overall process. Non-vanishing contributions will therefore stem from the following three, fully-contracted classes of terms

$$\langle I|\, \overbrace{\hat{c}_p^\dagger \hat{c}_q}\, \overbrace{\hat{c}_r^\dagger \hat{c}_s}\, |I\rangle \qquad \text{with } p = q \text{ and } r = s, \text{but } p \neq r, \tag{3.31}$$

$$\langle I|\, \overbrace{\hat{c}_p^\dagger \hat{c}_q \hat{c}_r^\dagger}\, \hat{c}_s \,|I\rangle \qquad \text{with } p = s \text{ and } q = r, \text{but } p \neq q, \tag{3.32}$$

$$\langle I|\, \overbrace{\hat{c}_p^\dagger \hat{c}_q \hat{c}_r^\dagger \hat{c}_s}\, |I\rangle \qquad \text{with all indices alike.} \tag{3.33}$$

Above, we have indicated the operators, which cancel each others effect by rectangular overarches. Of the three possible classes, only the second case ($p \neq q$) features a non-trivial time-dependence due to the exponential $e^{\mathrm{i}(\varepsilon_p - \varepsilon_q)\tau}$. Thereby, it is the only class to support measurable Fourier components[11] for $\omega \neq 0$. Focusing on this, we evaluate

$$\langle I|\, \hat{c}_p^\dagger \hat{c}_q \hat{c}_r^\dagger \hat{c}_s \,|I\rangle \,\Big|_{\omega\neq 0} = \delta_{p,s}\,\delta_{q,r}\ \langle I|\, \hat{n}_p(1-\hat{n}_q)\,|I\rangle \quad \text{with } p \neq q, \tag{3.34}$$

where $\hat{n}_p = \hat{c}_p^\dagger \hat{c}_p$ denotes the number operator as usual. Note that we can drop the condition of $p \neq q$, as it will be enforced by the occupation numbers of the Slater-determinant anyway. Implementing the above in Eq. (3.28), we obtain

$$\begin{aligned}
\langle I|\, \hat{n}(\mathbf{x}_2,\tau)\,\hat{\mathbf{p}}(\mathbf{x}_1,0)\,|I\rangle &= \sum_{p,q} \langle I|\, \hat{n}_p(1-\hat{n}_q)\,|I\rangle\ e^{\mathrm{i}(\varepsilon_p-\varepsilon_q)\tau}\ \varphi_p^\dagger(\mathbf{x}_2)\,\varphi_q(\mathbf{x}_2)\,\varphi_q^\dagger(\mathbf{x}_1)\,(-\mathrm{i}\nabla)\,\varphi_p(\mathbf{x}_1) \\
&= 2\sum_{p}^{\text{occ.}}\sum_{q}^{\text{unocc.}} e^{\mathrm{i}(\varepsilon_p-\varepsilon_q)\tau}\ \underbrace{\varphi_p^*(\mathbf{x}_2)\,\varphi_q(\mathbf{x}_2)\,\varphi_q^*(\mathbf{x}_1)\,(-\mathrm{i}\nabla)\,\varphi_p(\mathbf{x}_1)}_{\mathbf{M}_{p,q}(\mathbf{x}_2,\mathbf{x}_1)},
\end{aligned} \tag{3.35}$$

where we have rephrased the expectation value of the occupation-numbers as new limits on the pertaining summations. Specifically, the sum in p traverses only orbitals that are occupied in $|I\rangle$, whereas the sum in q traverses only unoccupied ones. Moreover, we have assumed that the mean-field Hamiltonian is spin-independent, which allows us to trade the (implicitly) spinorial $\varphi_p(\mathbf{x})$ for orbitals that are merely spatial functions *and* a factor of two[12]. Furthermore, we have defined the abbreviation $\mathbf{M}_{p,q}(\mathbf{x}_2,\mathbf{x}_1)$ in an attempt to shorten upcoming formulae.

[10] We note for consistency that we had previously assumed $|I\rangle$ to be an eigenstate of the *full* Hamiltonian. In switching to the approximate Hamiltonian $\hat{H}_{\mathrm{MF}}$, we should also approximate the initial state accordingly. While we would think this to be rather self-evident, if consistency was desired, we nevertheless wanted to point out this second—maybe more subtle—approximation.

[11] We note that the contributions of terms (3.31) and (3.33) will, in fact, vanish completely. We have already established that their time-dependence restricts them to exist only for 'static' Fourier components, i.e., at $\omega = 0$. Yet in addition, we may invoke the time-reversal anti-symmetry of $\mathbf{K}_I(\mathbf{k}_1,\mathbf{k}_2,\omega)$ to conclude that at this point ($\omega = 0$) the response has to vanish exactly.

[12] We note that the assumption of a spin-independent mean-field may certainly be inappropriate for a wide range of materials. These could be magnetic systems but also materials that involve strong spin-orbit couplings and associated band-splittings. On the other hand, such systems are often ill-described by mean-field methods anyway. For the time-being, we shall stick with this most simple model. Its extension to include spin-orbitals at the end is trivial: Remove the factor of 2 and sum over orbitals of *both* spin-states explicitly.

Analogously to the above, we can reformulate Eq. (3.29) as

$$\begin{aligned}\langle I|\,\hat{\mathbf{p}}(\mathbf{x}_1,0)\,\hat{n}(\mathbf{x}_2,\tau)\,|I\rangle &= 2\sum_{p}^{\text{occ.}}\sum_{q}^{\text{unocc.}} e^{-\mathrm{i}(\varepsilon_p-\varepsilon_q)\tau}\;\varphi_p^*(\mathbf{x}_1)\,(-\mathrm{i}\nabla)\,\varphi_q(\mathbf{x}_1)\,\varphi_q^*(\mathbf{x}_2)\,\varphi_p(\mathbf{x}_2)\\ &= 2\sum_{p}^{\text{occ.}}\sum_{q}^{\text{unocc.}} e^{-\mathrm{i}(\varepsilon_p-\varepsilon_q)\tau}\;\underbrace{\varphi_q^*(\mathbf{x}_2)\,\varphi_p(\mathbf{x}_2)\,\varphi_p^*(\mathbf{x}_1)\,(-\mathrm{i}\nabla)\,\varphi_q(\mathbf{x}_1)}_{\mathbf{M}_{q,p}(\mathbf{x}_2,\mathbf{x}_1)}. \end{aligned} \tag{3.36}$$

We combine both terms in the overall correlation function and obtain

$$\mathbf{P}_{I\diamond}(\mathbf{x}_1,0,\mathbf{x}_2,\tau) = 2\sum_{p}^{\text{occ.}}\sum_{q}^{\text{unocc.}}\Big(\Theta(\tau)\,e^{\mathrm{i}(\varepsilon_p-\varepsilon_q)\tau}\,\mathbf{M}_{p,q}(\mathbf{x}_2,\mathbf{x}_1)+\Theta(-\tau)\,e^{-\mathrm{i}(\varepsilon_p-\varepsilon_q)\tau}\,\mathbf{M}_{q,p}(\mathbf{x}_2,\mathbf{x}_1)\Big), \tag{3.37}$$

which translates into the Fourier domain (following Eq. (3.13)) as:

$$\begin{aligned}\mathbf{K}_{I\diamond}(\mathbf{q}+\mathbf{G}_1,-\mathbf{q}+\mathbf{G}_2,\omega) &= 2\sum_{p}^{\text{occ.}}\sum_{q}^{\text{unocc.}}\int_\diamond d^3x_1\int_\diamond d^3x_2\,e^{-\mathrm{i}(\mathbf{q}+\mathbf{G}_1)\cdot\mathbf{x}_1}\,e^{-\mathrm{i}(-\mathbf{q}+\mathbf{G}_2)\cdot\mathbf{x}_2}\\ &\quad\times\Big(\mathbf{M}_{p,q}(\mathbf{x}_2,\mathbf{x}_1)\int_0^\infty\!\!d\tau\;e^{\mathrm{i}\omega\tau}\;e^{\mathrm{i}(\varepsilon_p-\varepsilon_q)\tau}+\mathbf{M}_{q,p}(\mathbf{x}_2,\mathbf{x}_1)\int_{-\infty}^0\!\!d\tau\;e^{\mathrm{i}\omega\tau}\;e^{-\mathrm{i}(\varepsilon_p-\varepsilon_q)\tau}\Big)\\ &= 2\sum_{p}^{\text{occ.}}\sum_{q}^{\text{unocc.}}\int_\diamond d^3x_1\int_\diamond d^3x_2\,e^{-\mathrm{i}(\mathbf{q}+\mathbf{G}_1)\cdot\mathbf{x}_1}\,e^{-\mathrm{i}(-\mathbf{q}+\mathbf{G}_2)\cdot\mathbf{x}_2}\int_0^\infty\!\!d\tau\\ &\quad\times\Big(\mathbf{M}_{p,q}(\mathbf{x}_2,\mathbf{x}_1)\,e^{\mathrm{i}(\omega-(\varepsilon_q-\varepsilon_p))\tau}+\mathbf{M}_{q,p}(\mathbf{x}_2,\mathbf{x}_1)e^{\mathrm{i}(-\omega-(\varepsilon_q-\varepsilon_p))\tau}\Big). \end{aligned} \tag{3.38}$$

We proceed to regularize the temporal integration by means of the common adiabatic switching prescription (see Ref. [57], for instance). That is, we include an infinitesimal damping factor of $e^{-\varepsilon\tau}$ and find

$$\begin{aligned}\mathbf{K}_{I\diamond}(\mathbf{q}+\mathbf{G}_1,-\mathbf{q}+\mathbf{G}_2,\omega) = \lim_{\varepsilon\to0^+}\;2\mathrm{i}\sum_{p}^{\text{occ.}}\sum_{q}^{\text{unocc.}}\Big(&\frac{\langle\varphi_p|\,e^{-\mathrm{i}(-\mathbf{q}+\mathbf{G}_2)\cdot\hat{\mathbf{x}}}\,|\varphi_q\rangle\,\langle\varphi_q|\,e^{-\mathrm{i}(\mathbf{q}+\mathbf{G}_1)\cdot\hat{\mathbf{x}}}\,\hat{\mathbf{p}}\,|\varphi_p\rangle}{\omega-(\varepsilon_q-\varepsilon_p)+\mathrm{i}\varepsilon}\\ &+\frac{\langle\varphi_p|\,e^{-\mathrm{i}(\mathbf{q}+\mathbf{G}_1)\cdot\hat{\mathbf{x}}}\,\hat{\mathbf{p}}\,|\varphi_q\rangle\,\langle\varphi_q|\,e^{-\mathrm{i}(-\mathbf{q}+\mathbf{G}_2)\cdot\hat{\mathbf{x}}}\,|\varphi_p\rangle}{-\omega-(\varepsilon_q-\varepsilon_p)+\mathrm{i}\varepsilon}\Big). \end{aligned} \tag{3.39}$$

In writing Eq. (3.39), we have adopted Dirac's notation for the inner product of wave functions on the crystalline domain, such that

$$\langle\varphi_p|\,\hat{O}\,|\varphi_q\rangle = \int_\diamond d^3x\;\varphi_p^*(\mathbf{x})\,\hat{O}\,\varphi_q(\mathbf{x}). \tag{3.40}$$

Our result (Eq. (3.39)) exhibits the familiar form of second-order perturbative expressions: It features two transition amplitudes linking initial and final state (both of which are the same here) via a set of intermediately excited states. The transition into these intermediate states comes along with a resonant denominator for each 'on-shell' transition. In particular, Eq. (3.39) bears close resemblance to the well-known Adler-Wiser response function [98, 99], which is ubiquitously used in density-response formalisms (see Ref. [104] and references therein). Notably though, the transverse nature of the response, which is implied by the momentum operator $\hat{\mathbf{p}}$ in our case would be absent, for a pure density-density response.

3.2.1 The nonlinear response for the free electron gas

Having established a general expression for the nonlinear response function $\mathbf{K}_{I\diamond}(\mathbf{q}+\mathbf{G}_1,-\mathbf{q}+\mathbf{G}_2,\omega)$ in Eq. (3.39), we aim to develop an intuition for its behaviour in terms of limiting / model cases next. As the simplemost case for the independent-particle approximation, we shall briefly consider a system of quasi-free electrons and evaluate $\mathbf{K}_{I\diamond}$ in its eigenstates. The respective wave functions can be written as plane-waves

$$\varphi_p(\mathbf{x}) = \frac{1}{\sqrt{V_\diamond}} e^{\mathrm{i}\mathbf{k}_p\cdot\mathbf{x}}, \tag{3.41}$$

where the normalization is performed with respect to the periodically-bounded crystal volume ($V_\diamond$). In accordance with our later treatment of Bloch waves, we choose to split the occurring wave-vector $\mathbf{k}_p = \mathbf{G}_p + \mathbf{q}_p$ into a portion on the reciprocal lattice of the crystal and a remainder within the first Brillouin zone, respectively. Evaluating the matrix elements from Eq. (3.39), we find:

$$\begin{aligned}
\langle\varphi_p|\, e^{-\mathrm{i}(-\mathbf{q}+\mathbf{G}_2)\cdot\hat{\mathbf{x}}}\,|\varphi_q\rangle &= \frac{1}{V_\diamond}\int_\diamond d^3x\; e^{-\mathrm{i}(\mathbf{G}_p+\mathbf{q}_p)\cdot\mathbf{x}}\, e^{-\mathrm{i}(-\mathbf{q}+\mathbf{G}_2)\cdot\hat{\mathbf{x}}}\, e^{\mathrm{i}(\mathbf{G}_q+\mathbf{q}_q)\cdot\mathbf{x}} \\
&= \frac{1}{V_\diamond}\sum_{\mathbf{R}}^{\text{dir. latt.}} e^{-\mathrm{i}(\mathbf{q}_p-\mathbf{q}-\mathbf{q}_q)\cdot\mathbf{R}} \int_{U(0)} d^3x\; e^{-\mathrm{i}(\mathbf{G}_p+\mathbf{q}_p-\mathbf{q}+\mathbf{G}_2-\mathbf{G}_q-\mathbf{q}_q)\cdot\mathbf{x}} \\
&= \frac{1}{V_\diamond} N_\text{cells} \sum_{\mathbf{G}}^{\text{rec. latt.}} \delta_{\mathbf{q}_p,\mathbf{q}+\mathbf{q}_q+\mathbf{G}} \int_{U(0)} d^3x\; e^{-\mathrm{i}(\mathbf{G}_p+\mathbf{G}_2-\mathbf{G}_q+\mathbf{G})\cdot\mathbf{x}} \\
&\approx \frac{1}{V_\diamond} N_\text{cells}\, \delta_{\mathbf{q}_p,\mathbf{q}+\mathbf{q}_q} \int_{U(0)} d^3x\; e^{-\mathrm{i}(\mathbf{G}_p+\mathbf{G}_2-\mathbf{G}_q)\cdot\mathbf{x}} \\
&= \frac{1}{V_\diamond} N_\text{cells}\, \delta_{\mathbf{q}_p,\mathbf{q}+\mathbf{q}_q}\, V_{U(0)}\, \delta_{\mathbf{G}_p,\mathbf{G}_q-\mathbf{G}_2} = \delta_{\mathbf{q}_p,\mathbf{q}+\mathbf{q}_q}\, \delta_{\mathbf{G}_p,\mathbf{G}_q-\mathbf{G}_2}
\end{aligned} \tag{3.42}$$

and analogously

$$\langle\varphi_q|\, e^{-\mathrm{i}(\mathbf{q}+\mathbf{G}_1)\cdot\hat{\mathbf{x}}}\,\hat{\mathbf{p}}\,|\varphi_p\rangle \approx \delta_{\mathbf{q}_p,\mathbf{q}+\mathbf{q}_q}\,\delta_{\mathbf{G}_p,\mathbf{G}_q+\mathbf{G}_1}\,(\mathbf{G}_p+\mathbf{q}_p). \tag{3.43}$$

In both cases, the summation $\sum_{\mathbf{R}}^{\text{dir. latt.}}\; e^{-\mathrm{i}(\mathbf{q}_p-\mathbf{q}-\mathbf{q}_q)\cdot\mathbf{R}}$ yields a non-trivial contribution, whenever the exponent $\mathbf{q}_p-\mathbf{q}-\mathbf{q}_q$ matches a reciprocal lattice vector $\mathbf{G}$. Bearing in mind that all three vectors stem from the first Brillouin zone and $\mathbf{q}$—moreover—is small even within that scope (optical photon), the most likely contribution will result from $\mathbf{q}_p-\mathbf{q}-\mathbf{q}_q=0$. Further contributions to the sum might only arise in cases, where $\mathbf{q}_p$ and $\mathbf{q}_q$ are located on opposite edges of the Brillouin zone and connect via $\mathbf{q}$ plus a corresponding reciprocal lattice vector[13]. Given that the contributing k-space volume of these edges is small, though, we shall neglect this option for the time-being.

The correlation function resulting from these matrix elements reads:

$$\begin{aligned}
\mathbf{K}_{I\diamond}(\mathbf{q}+\mathbf{G}_1,-\mathbf{q}+\mathbf{G}_2,\omega) \approx \lim_{\varepsilon\to 0^+}\; 2\mathrm{i}\sum_p^{\text{occ.}}\sum_q^{\text{unocc.}} \Big(&\frac{\delta_{\mathbf{q}_p,\mathbf{q}+\mathbf{q}_q}\,\delta_{\mathbf{G}_p,\mathbf{G}_q-\mathbf{G}_2}\,\delta_{\mathbf{G}_p,\mathbf{G}_q+\mathbf{G}_1}\,(\mathbf{G}_p+\mathbf{q}_p)}{\omega-(\varepsilon_q-\varepsilon_p)+\mathrm{i}\varepsilon} \\
&+\frac{\delta_{\mathbf{q}_q,\mathbf{q}+\mathbf{q}_p}\,\delta_{\mathbf{G}_q,\mathbf{G}_p-\mathbf{G}_2}\,\delta_{\mathbf{G}_q,\mathbf{G}_p+\mathbf{G}_1}\,(\mathbf{G}_q+\mathbf{q}_q)}{-\omega-(\varepsilon_q-\varepsilon_p)+\mathrm{i}\varepsilon}\Big),
\end{aligned} \tag{3.44}$$

where the eigenenergies of the plane waves are given by $\varepsilon_p = \mathbf{G}_p^2/2 = (\mathbf{G}_p+\mathbf{q}_p)^2/2$ as usual.

At this point, we note that the Kronecker symbols impose two conditions, which are mutually in-

[13] Note that the implied scattering 'around' the Brillouin zone amounts to a kind of 'Umklapp'-process [101].

compatible with the assumed physical reality. In particular, we find for the first term

$$\begin{aligned} \delta_{\mathbf{G}_p,\mathbf{G}_q-\mathbf{G}_2} \quad &\Rightarrow \quad \mathbf{G}_p = \mathbf{G}_q - \mathbf{G}_2 \\ \delta_{\mathbf{G}_p,\mathbf{G}_q+\mathbf{G}_1} \quad &\Rightarrow \quad \mathbf{G}_p = \mathbf{G}_q + \mathbf{G}_1 \quad \Rightarrow \quad 0 = \mathbf{G}_1 + \mathbf{G}_2 \end{aligned} \tag{3.45}$$

and an analogous condition for the second term, albeit with the indices p and q being exchanged throughout. Physically, the above condition expresses the notion that strict momentum conservation on the free electron system would require that XOWM can only take place, if the full momentum, which is transferred during the x-ray scattering, is compensated by the optical admixture (or vice versa). Given the large difference of x-ray and optical photon momenta, this could only be achieved, if x-ray scattering were to proceed in forward direction (i.e., if it induces a very low momentum transfer itself). On the contrary, however, we are interested predominantly in scattering processes at large momentum transfer, because these would enable high-resolution imaging of the sample.

Intuitively, we would expect this result: The free electron gas is a homogeneous system and, as such, does not exhibit any non-trivial short range structure. However, some kind of structure at the scale $l_{\text{structure}} \sim 1/|\mathbf{G}_2|$ would be required, in order to find corresponding non-zero signatures at finite momentum transfer ($\mathbf{G}_2$). Owing to its absence, there is no relevant information at higher-momentum components in $\mathbf{K}_{I\diamond}(\mathbf{q}+\mathbf{G}_1, -\mathbf{q}+\mathbf{G}_2, \omega)$ either.

In a closing thought, we conjecture that this reasoning should hold beyond the quasi-static case of the electron gas. In particular, it should be applicable to low-$\mathbf{q}$ excitations of the electron gas, i.e., to plasmon-oscillations [101], as well. These do not exhibit stark spatial modulations in themselves and thus we do not expect them to show pronounced signatures in XOWM either. This, in turn, casts some doubt on publications like Ref. [48], which claim to have used XPDC as a probe of this particular quasi-particle[14].

3.2.2 High-frequency limit of the nonlinear response

As a step beyond the free-electron treatment, Dr. Isaac Freund has suggested a high-frequency approximation to the description of x-ray parametric down-conversion [89]. Specifically, he has addressed the scenario, where the energy transfer ω is much larger than the characteristic binding energy of valence-electrons, yet sufficiently below any core-level threshold[15]. Under these conditions, he postulates a response that partially resembles free electrons, namely for the intermediate states. This renders his approximation reminiscent of the impulse-approximation used in the context of Compton scattering [105]. However, Freund relies on a decidedly more classical line of reasoning, despite starting out from the (single-particle) quantum description of Armstrong et al. [95].

In the following, we adapt his arguments within the framework set by our Eq. (3.39). To begin with, we impose the condition that the energy transfer is indeed much larger than the valence binding energy, viz. the band gap, $\omega \gg E_{\text{BG}}$. At the same time, we assume $\omega \ll E_{\text{core}}$, which allows us to omit deeply

[14] We note with regard to Ref. [48] that we have are other, more fundamental, objections to it as well. These will be discussed in greater length in Sec. 5.2.2.

[15] We want to note two things at this point:
First, we specify that for the case of XPDC, the energy transfer is associated with the idler photon's energy. Thus, the above conditions would translate to $E_{\text{valence}} \ll \omega_i \ll E_{\text{core}}$.
Second, we emphasize that the aforementioned conditions may *not* be achievable for many realistic systems. Notably, Freund himself has pointed out this observation alongside the very introduction of the model [89].

bound orbitals in the following summation over occupied states (p):

$$\mathbf{K}_{GS\diamond}(\mathbf{q}+\mathbf{G}_1,-\mathbf{q}+\mathbf{G}_2,\omega) = \lim_{\varepsilon\to 0^+} 2\mathrm{i} \sum_{p}^{\text{occ. val.}} \sum_{q}^{\text{unocc.}} \Big(\frac{\langle\varphi_p| e^{-\mathrm{i}(-\mathbf{q}+\mathbf{G}_2)\cdot\hat{\mathbf{x}}} |\varphi_q\rangle \langle\varphi_q| e^{-\mathrm{i}(\mathbf{q}+\mathbf{G}_1)\cdot\hat{\mathbf{x}}} \hat{\mathbf{p}} |\varphi_p\rangle}{\omega - (\varepsilon_q - \varepsilon_p) + \mathrm{i}\varepsilon} + \frac{\langle\varphi_p| e^{-\mathrm{i}(\mathbf{q}+\mathbf{G}_1)\cdot\hat{\mathbf{x}}} \hat{\mathbf{p}} |\varphi_q\rangle \langle\varphi_q| e^{-\mathrm{i}(-\mathbf{q}+\mathbf{G}_2)\cdot\hat{\mathbf{x}}} |\varphi_p\rangle}{-\omega - (\varepsilon_q - \varepsilon_p) + \mathrm{i}\varepsilon} \Big). \tag{3.46}$$

We emphasize that we will focus on a single reference state, namely the ground state $|I\rangle = |GS\rangle$, in the course of this derivation.

Moreover, we follow Freund in assuming that the dominant dielectric response stems from transitions around the band gap, i.e., from a valence band (VB) of the material into a low-lying conduction band (CB). In this case, $\varepsilon_q - \varepsilon_p \approx E_{\mathrm{BG}}$ for all relevant contributions. In addition, we still want to observe the condition $\omega \gg E_{\mathrm{BG}}$ and may thus simplify the energy denominators of Eq. (3.46) as:

$$\frac{1}{\pm\omega - (\varepsilon_q - \varepsilon_p) + \mathrm{i}\varepsilon} \approx \frac{1}{\pm\omega - E_{\mathrm{BG}} + \mathrm{i}\varepsilon} \approx \frac{1}{\pm\omega}. \tag{3.47}$$

This, in turn, renders

$$\mathbf{K}_{GS\diamond}(\mathbf{q}+\mathbf{G}_1,-\mathbf{q}+\mathbf{G}_2,\omega) \approx \frac{2\mathrm{i}}{\omega} \sum_{p}^{\mathrm{VB}} \sum_{q}^{\mathrm{CB}} \Big(\langle\varphi_p| e^{-\mathrm{i}(-\mathbf{q}+\mathbf{G}_2)\cdot\hat{\mathbf{x}}} |\varphi_q\rangle \langle\varphi_q| e^{-\mathrm{i}(\mathbf{q}+\mathbf{G}_1)\cdot\hat{\mathbf{x}}} \hat{\mathbf{p}} |\varphi_p\rangle - \langle\varphi_p| e^{-\mathrm{i}(\mathbf{q}+\mathbf{G}_1)\cdot\hat{\mathbf{x}}} \hat{\mathbf{p}} |\varphi_q\rangle \langle\varphi_q| e^{-\mathrm{i}(-\mathbf{q}+\mathbf{G}_2)\cdot\hat{\mathbf{x}}} |\varphi_p\rangle \Big). \tag{3.48}$$

For further simplification, Freund postulates that the excited electrons will respond to the high-frequency perturbation in the same way that a classical charge-density would respond to a high-frequency electromagnetic field (here: the idler field). The most straight-forward translation of this classical—respectively free—electronic behaviour into quantum-mechanical terms would consist of adopting the impulse-approximation (cf. Ref. [105]) during the intermediate-state propagation. However, this yields more involved expressions than those obtained in Ref. [89]. Instead, we have to resort to a more abstract (and also more drastic) interpretation of 'free' response. Namely, we shall consider the dynamics of an excited electron within the manifold of intermediate states to be unhindered (i.e., unobstructed by other states). Accordingly, we shall require that the projector $\sum_q^{\mathrm{CB}} |\varphi_q\rangle \langle\varphi_q|$, which is the remnant of the sum over intermediate pathways, does not impose any restrictions, i.e.,

$$\sum_{q}^{\mathrm{CB}} |\varphi_q\rangle \langle\varphi_q| \approx \sum_{q}^{\mathrm{all}} |\varphi_q\rangle \langle\varphi_q| = \mathbb{1} \qquad \Leftrightarrow \qquad 0 \approx \sum_{q}^{\mathrm{all}} |\varphi_q\rangle \langle\varphi_q| - \sum_{q}^{\mathrm{CB}} |\varphi_q\rangle \langle\varphi_q|. \tag{3.49}$$

This approximate equivalence requires two distinct conditions to be fulfilled:

- First of all, it is necessary for the restricted conduction band (CB) summation to actually represent all of the *relevant* unoccupied states of the system. Within Eq. (3.48), where those states are weighted by the transition moments, this condition is indeed implicitly incorporated, insofar as all transitions into the non-included states are weighted by ~ 0 (according to Freund's original approximation).

- The second condition is that the CB sum needs to be extended to account for all *relevant* occupied

states of the system as well. Only then can it be considered as a full resolution of the identity. This aspect has not been considered in the classical reasoning of Freund [89], though it may easily be established based on the structure of Eq. (3.48).

On the second aspect, we quickly demonstrate below that the inclusion of occupied states into the second sum does not contribute any additional terms indeed. Taking Eq. (3.48) and changing the q-summation to occupied states

$$\begin{aligned}\mathbf{K}_{GS\diamond\_correction}(\mathbf{q}+\mathbf{G}_1,-\mathbf{q}+\mathbf{G}_2,\omega) \approx \frac{2\mathrm{i}}{\omega}\sum_p^{\text{occ.}}\sum_q^{\text{occ.}}\Big(&\langle\varphi_p|e^{-\mathrm{i}(-\mathbf{q}+\mathbf{G}_2)\cdot\hat{\mathbf{x}}}|\varphi_q\rangle\,\langle\varphi_q|e^{-\mathrm{i}(\mathbf{q}+\mathbf{G}_1)\cdot\hat{\mathbf{x}}}\hat{\mathbf{p}}|\varphi_p\rangle \\ &-\langle\varphi_p|e^{-\mathrm{i}(\mathbf{q}+\mathbf{G}_1)\cdot\hat{\mathbf{x}}}\hat{\mathbf{p}}|\varphi_q\rangle\,\langle\varphi_q|e^{-\mathrm{i}(-\mathbf{q}+\mathbf{G}_2)\cdot\hat{\mathbf{x}}}|\varphi_p\rangle\Big) \\ = \frac{2\mathrm{i}}{\omega}\sum_p^{\text{occ.}}\sum_q^{\text{occ.}}\Big(&\langle\varphi_p|e^{-\mathrm{i}(-\mathbf{q}+\mathbf{G}_2)\cdot\hat{\mathbf{x}}}|\varphi_q\rangle\,\langle\varphi_q|e^{-\mathrm{i}(\mathbf{q}+\mathbf{G}_1)\cdot\hat{\mathbf{x}}}\hat{\mathbf{p}}|\varphi_p\rangle \\ &-\langle\varphi_p|e^{-\mathrm{i}(-\mathbf{q}+\mathbf{G}_2)\cdot\hat{\mathbf{x}}}|\varphi_q\rangle\,\langle\varphi_q|e^{-\mathrm{i}(\mathbf{q}+\mathbf{G}_1)\cdot\hat{\mathbf{x}}}\hat{\mathbf{p}}|\varphi_p\rangle\Big) = 0,\end{aligned} \tag{3.50}$$

the expression obviously vanishes, as both terms cancel out upon exchanging the indices in the latter.

Therefore, we may indeed employ the reformulation of the projector into a non-restricting identity (as of Eq. (3.49)) and rewrite Eq. (3.48) as follows:

$$\begin{aligned}\mathbf{K}_{GS\diamond}(0,\mathbf{G}_2,\omega) &\approx \frac{2\mathrm{i}}{\omega}\sum_p^{\text{VB}}\sum_q^{\text{all}}\Big(\langle\varphi_p|e^{-\mathrm{i}\mathbf{G}_2\cdot\hat{\mathbf{x}}}|\varphi_q\rangle\,\langle\varphi_q|\hat{\mathbf{p}}|\varphi_p\rangle-\langle\varphi_p|\hat{\mathbf{p}}|\varphi_q\rangle\,\langle\varphi_q|e^{-\mathrm{i}\mathbf{G}_2\cdot\hat{\mathbf{x}}}|\varphi_p\rangle\Big) \\ &= \frac{2\mathrm{i}}{\omega}\sum_p^{\text{VB}}\Big(\langle\varphi_p|e^{-\mathrm{i}\mathbf{G}_2\cdot\hat{\mathbf{x}}}\mathbb{1}\,\hat{\mathbf{p}}|\varphi_p\rangle-\langle\varphi_p|\hat{\mathbf{p}}\,\mathbb{1}\,e^{-\mathrm{i}\mathbf{G}_2\cdot\hat{\mathbf{x}}}|\varphi_p\rangle\Big) \\ &= \frac{2\mathrm{i}}{\omega}\sum_p^{\text{VB}}\langle\varphi_p|\left[e^{-\mathrm{i}\mathbf{G}_2\cdot\hat{\mathbf{x}}},\hat{\mathbf{p}}\right]|\varphi_p\rangle = \frac{2\mathrm{i}}{\omega}\,\mathbf{G}_2\sum_p^{\text{VB}}\langle\varphi_p|e^{-\mathrm{i}\mathbf{G}_2\cdot\hat{\mathbf{x}}}|\varphi_p\rangle \\ &= \frac{2\mathrm{i}}{\omega}\,\mathbf{G}_2\int_\diamond d^3x\,\rho^{\text{VB}}(\mathbf{x})\,e^{-\mathrm{i}\mathbf{G}_2\cdot\mathbf{x}} = \frac{2\mathrm{i}}{\omega}\,\mathbf{G}_2\,\rho^{\text{VB}}_{\mathbf{G}_2}.\end{aligned} \tag{3.51}$$

Thereby, the overall correlation function is reduced to a Fourier-component of the valence-electron density weighted by its respective reciprocal lattice vector and the inverse of the energy transfer. This provides a valuable limiting case, which we may use to cross-check more complicated approaches.

Formulation in Bloch waves In order to use, i.e., evaluate, the above result later on, we shall give an expression for it in terms of Bloch waves (cf. App. A.5):

$$\mathbf{K}_{GS\diamond}(0,\mathbf{G}_2,\omega) \approx \frac{2\mathrm{i}}{\omega}\,\mathbf{G}_2\sum_p^{\text{VB}}\sum_{\mathbf{G}}^{\text{rec. latt.}} c^*_{n_p,\mathbf{k}_p}(\mathbf{G}-\mathbf{G}_2)\,c_{n_p,\mathbf{k}_p}(\mathbf{G}). \tag{3.52}$$

This can be used in the following to evaluate the approximate correlation function numerically[16].

[16]Note that we will mainly employ the ABINIT code [106] to compute orbitals from density-functional theory (DFT). This code, in turn, relies on a Bloch-wave formulation of its orbitals.

3.2.3 The nonlinear response from Kohn-Sham orbitals

As our final, and most comprehensive, approach to resolve the single-particle response function (3.39), we combine our expression with density-functional theory (DFT) [107, 108]. DFT is a widely used methodology for performing electronic-structure calculations with broad applications to solid-state problems [109]. One of its essential benefits is to achieve reasonably accurate results at comparatively low computational cost. Its good performance is a consequence of its 'simple' mean-field nature, which can be calibrated to the problem at hand by choice of an appropriate exchange-correlation (XC) functional.

Despite its success, there is a principal caveat to be borne in mind: DFT is inherently a theory that addresses (only) the ground state of an electronic system. As such, it is not strictly valid to extract excited-state properties from this framework. Irrespective of this caveat, the Kohn-Sham formulation of DFT [108], which employs single-particle orbitals, lends itself quite naturally to an *interpretation* in terms of occupied (i.e., ground state) orbitals and unoccupied (i.e., excited or rather excitable) states. This interpretation is widely adopted, even though it entails some well-known errors—chief amongst them is the notorious underestimation of band gaps from bare DFT orbitals [110].

For our present purpose, this caveat does not constitute a major obstacle. We shall, first and foremost, use the Kohn-Sham orbitals computed for a given solid as a complete set of 'mean-field' eigenstates[17] in the sense of Eq. (3.25). Combining this with appropriate counter-measures to the band-gap problem, we may use DFT orbitals within the nonlinear response function to gain both qualitative intuition and a (rough) quantitative assessment. More so, we may achieve both in an efficient and easily transferable manner.

Subsequently, we will prepare our single-particle response function for its evaluation from Kohn-Sham orbitals, starting from

$$\begin{aligned}\mathbf{K}_{GS\diamond}(\mathbf{q}+\mathbf{G}_1,-\mathbf{q}+\mathbf{G}_2,\omega) = \lim_{\varepsilon\to 0^+} 2\mathrm{i}\sum_{p}^{\text{occ.}}\sum_{q}^{\text{unocc.}}\Big(&\frac{\langle\varphi_p|\,e^{-\mathrm{i}(-\mathbf{q}+\mathbf{G}_2)\cdot\hat{\mathbf{x}}}\,|\varphi_q\rangle\,\langle\varphi_q|\,e^{-\mathrm{i}(\mathbf{q}+\mathbf{G}_1)\cdot\hat{\mathbf{x}}}\hat{\mathbf{p}}\,|\varphi_p\rangle}{\omega-(\varepsilon_q-\varepsilon_p)+\mathrm{i}\varepsilon}\\ &+\frac{\langle\varphi_p|\,e^{-\mathrm{i}(\mathbf{q}+\mathbf{G}_1)\cdot\hat{\mathbf{x}}}\hat{\mathbf{p}}\,|\varphi_q\rangle\,\langle\varphi_q|\,e^{-\mathrm{i}(-\mathbf{q}+\mathbf{G}_2)\cdot\hat{\mathbf{x}}}\,|\varphi_p\rangle}{-\omega-(\varepsilon_q-\varepsilon_p)+\mathrm{i}\varepsilon}\Big).\end{aligned} \tag{3.53}$$

Here, we limit our reference state $|I\rangle = |GS\rangle$ to the ground state once again—which is in accordance with the ground-state reference of DFT itself.

Given our focus on lattice-periodic materials, we opt for a Bloch-wave based formulation [76, 101]. To this end, we invoke the (reasonable) assumption that the mean-field potential is itself lattice periodic[18]. In conjunction with the periodic boundary conditions on the crystal domain ($\diamond$), this allows us to identify the orbitals

$$\varphi_p(\mathbf{x}) = \varphi_{n_p,\mathbf{k}_p}(\mathbf{x}) = \frac{1}{\sqrt{V_\diamond}}\,e^{\mathrm{i}\mathbf{k}_p\cdot\mathbf{x}}\,u_{n_p,\mathbf{k}_p}(\mathbf{x}) \tag{3.54}$$

as Bloch waves (for details on these, see App. A.5).

[17] We note that the 'mean-field' pertaining to the Kohn-Sham DFT Hamiltonian may not be an ideal choice, but it is certainly a valid and, notably, affordable choice.

[18] We note that one may still pose the question, whether the potential needs to be *local* in addition to being lattice-periodic? Bloch's theorem certainly works for local potentials, including local XC-potentials like LDA. In fact, it may well be more general. However, we shall not pursue this question further at this stage.

Using this decomposition of $\varphi_p(\mathbf{x})$, we rewrite the scattering matrix element of Eq. (3.53) as

$$\begin{aligned}\langle\varphi_p|\, e^{-\mathrm{i}(-\mathbf{q}+\mathbf{G}_2)\cdot\hat{\mathbf{x}}}\,|\varphi_q\rangle &= \frac{1}{V_\diamond}\int_\diamond d^3x\; e^{-\mathrm{i}\mathbf{k}_p\cdot\mathbf{x}}\; u^*_{n_p,\mathbf{k}_p}(\mathbf{x})\; e^{-\mathrm{i}(-\mathbf{q}+\mathbf{G}_2)\cdot\hat{\mathbf{x}}}\; e^{\mathrm{i}\mathbf{k}_q\cdot\mathbf{x}}\; u_{n_q,\mathbf{k}_q}(\mathbf{x}) \\ &= \frac{1}{V_\diamond}\sum_{\mathbf{R}}^{\text{dir. latt.}} e^{-\mathrm{i}(\mathbf{k}_p-\mathbf{q}-\mathbf{k}_q)\cdot\mathbf{R}} \sum_{\mathbf{G},\mathbf{G}'}^{\text{rec. latt.}} c^*_{n_p,\mathbf{k}_p}(\mathbf{G})\, c_{n_q,\mathbf{k}_q}(\mathbf{G}')\; \int_{U(0)} d^3x\; e^{-\mathrm{i}(\mathbf{k}_p+\mathbf{G}-\mathbf{q}+\mathbf{G}_2-\mathbf{k}_q-\mathbf{G}')\cdot\mathbf{x}},\end{aligned} \tag{3.55}$$

where we have made use of the Fourier expansion for each Bloch-functions (cf. Eq. (A.51)). If we neglect contributions from Umklapp-processes[19], we obtain the simplified expression:

$$\begin{aligned}\langle\varphi_p|\, e^{-\mathrm{i}(-\mathbf{q}+\mathbf{G}_2)\cdot\hat{\mathbf{x}}}\,|\varphi_q\rangle &\approx \frac{1}{V_\diamond}\, N_{\text{cells}}\, \delta_{\mathbf{k}_p,\mathbf{q}+\mathbf{k}_q} \sum_{\mathbf{G},\mathbf{G}'}^{\text{rec. latt.}} c^*_{n_p,\mathbf{k}_p}(\mathbf{G})\, c_{n_q,\mathbf{k}_q}(\mathbf{G}')\; \int_{U(0)} d^3x\; e^{-\mathrm{i}(\mathbf{G}+\mathbf{G}_2-\mathbf{G}')\cdot\mathbf{x}} \\ &= \frac{1}{V_\diamond}\, N_{\text{cells}}\, \delta_{\mathbf{k}_p,\mathbf{q}+\mathbf{k}_q} \sum_{\mathbf{G},\mathbf{G}'}^{\text{rec. latt.}} c^*_{n_p,\mathbf{k}_p}(\mathbf{G})\, c_{n_q,\mathbf{k}_q}(\mathbf{G}')\; V_{U(0)}\, \delta_{\mathbf{G},\mathbf{G}'-\mathbf{G}_2} \\ &= \delta_{\mathbf{k}_p,\mathbf{q}+\mathbf{k}_q} \sum_{\mathbf{G}}^{\text{rec. latt.}} c^*_{n_p,\mathbf{k}_p}(\mathbf{G})\, c_{n_q,\mathbf{k}_q}(\mathbf{G}+\mathbf{G}_2).\end{aligned} \tag{3.56}$$

For the photoabsorption / -emission matrix element of Eq. (3.53), we find analogously:

$$\begin{aligned}\langle\varphi_q|\, e^{-\mathrm{i}(\mathbf{q}+\mathbf{G}_1)\cdot\hat{\mathbf{x}}}\,\hat{\mathbf{p}}\,|\varphi_p\rangle &= \frac{1}{V_\diamond}\int_\diamond d^3x\; e^{-\mathrm{i}\mathbf{k}_q\cdot\mathbf{x}}\; u^*_{n_q,\mathbf{k}_q}(\mathbf{x})\; e^{-\mathrm{i}(\mathbf{q}+\mathbf{G}_1)\cdot\hat{\mathbf{x}}}\; (-\mathrm{i}\nabla)\; e^{\mathrm{i}\mathbf{k}_p\cdot\mathbf{x}}\; u_{n_p,\mathbf{k}_p}(\mathbf{x}) \\ &\approx \frac{1}{V_\diamond}\, N_{\text{cells}}\, \delta_{\mathbf{k}_q,\mathbf{k}_p-\mathbf{q}} \sum_{\mathbf{G},\mathbf{G}'}^{\text{rec. latt.}} c^*_{n_q,\mathbf{k}_q}(\mathbf{G})\, c_{n_p,\mathbf{k}_p}(\mathbf{G}')\; V_{U(0)}\, \delta_{\mathbf{G},\mathbf{G}'-\mathbf{G}_1}\, (\mathbf{k_p}+\mathbf{G}') \\ &= \delta_{\mathbf{k}_q,\mathbf{k}_p-\mathbf{q}} \sum_{\mathbf{G}}^{\text{rec. latt.}} c^*_{n_q,\mathbf{k}_q}(\mathbf{G})\, c_{n_p,\mathbf{k}_p}(\mathbf{G}+\mathbf{G}_1)\; (\mathbf{k_p}+\mathbf{G}+\mathbf{G}_1).\end{aligned} \tag{3.57}$$

'Dipole-approximation' For practical purposes, we shall introduce one further approximation, viz. setting $\mathbf{k}_q = \mathbf{k}_p - \mathbf{q} \approx \mathbf{k}_p$. This can be justified (see also Sec. 3.1.2) by recalling that $\mathbf{q}$ will be constrained to the size of an optical photon's momentum, which is significantly smaller than the scale of the 1. Brillouin zone (BZ). For such small differences among crystal-momenta, we can assume the respective Fourier coefficients $c_{n,\mathbf{k}}(\mathbf{G})$ to be almost the same, because they vary slowly in $\mathbf{k}$[20]. Thus, evaluating both coefficients in Eqs. (3.56) or (3.57) at the same value of $\mathbf{k}_p$ should not incur a significant difference. For the basic expression of the scattering matrix element, this does not imply a large structural change—see below:

$$\langle\varphi_p|\, e^{-\mathrm{i}(-\mathbf{q}+\mathbf{G}_2)\cdot\hat{\mathbf{x}}}\,|\varphi_q\rangle \approx \delta_{\mathbf{k}_p,\mathbf{k}_q} \sum_{\mathbf{G}}^{\text{rec. latt.}} c^*_{n_p,\mathbf{k}_p}(\mathbf{G})\, c_{n_q,\mathbf{k}_p}(\mathbf{G}+\mathbf{G}_2). \tag{3.58}$$

[19] We recall from Sec. 3.2.1 that so-called Umklapp-processes arise in cases, where $\mathbf{k}_p$ and $\mathbf{k}_q$ are located on opposite edges of the Brillouin zone and connect via $\mathbf{q}$ plus a corresponding reciprocal lattice vector [101]. As the coupling thus 'flips' (german: 'umklappen') around the Brillouin zone its name was coined respectively. We note further that the contributing k-space volume at these edges of the Brillouin zone is small, which justifies neglecting Umklapp-processes for the moment.

[20] We note that many numerical approaches will opt for much coarser discretization of k-space within the 1. BZ than the scale set by an optical photon. In Ref. [111], for instance, the authors compute Kohn-Sham orbitals as well as response properties of diamond on a k-space grid with spacing of $\Delta k \approx \left|\mathbf{G}_{(100)}\right|/10$ in each direction. An optical photon's momentum, on the other hand, will be 3 to 4 orders of magnitude smaller. The neglect of its momentum transfer during transitions will therefore not make a relevant difference at all.

We note, however, that the numerical simplification obtained through the above approximation may be substantial[21]. For the momentum matrix element, we may adopt the same approximation $\mathbf{q} \approx 0$. In addition, we extend our simplifications to the exact equality $\mathbf{G}_1 = 0$ for optical photons, thereby reducing

$$\begin{aligned}\langle \varphi_q | \, e^{-\mathrm{i}(\mathbf{q}+\mathbf{G}_1)\cdot\hat{\mathbf{x}}} \, \hat{\mathbf{p}} \, | \varphi_p \rangle &\approx \delta_{\mathbf{k}_q,\mathbf{k}_p} \sum_{\mathbf{G}}^{\text{rec. latt.}} c^*_{n_q,\mathbf{k}_p}(\mathbf{G}) \, c_{n_p,\mathbf{k}_p}(\mathbf{G}) \, (\mathbf{k}_\mathbf{p} + \mathbf{G}) \\ &= \delta_{\mathbf{k}_q,\mathbf{k}_p} \sum_{\mathbf{G}}^{\text{rec. latt.}} c^*_{n_q,\mathbf{k}_p}(\mathbf{G}) \, c_{n_p,\mathbf{k}_p}(\mathbf{G}) \, \mathbf{G}. \end{aligned} \tag{3.59}$$

In the last step, we have additionally invoked Eq. (A.53) and the knowledge that occupied $(n_p, \mathbf{k}_p)$ and unoccupied $(n_q, \mathbf{k}_q)$ can not agree in both of their indices.

Finally, we have obtained all necessary ingredients to evaluate the nonlinear response function

$$\mathbf{K}_{GS\diamond}(0, \mathbf{G}, \omega) = \lim_{\varepsilon \to 0^+} 2\mathrm{i} \sum_{p}^{\text{occ.}} \sum_{q}^{\text{unocc.}} \left(\frac{\langle \varphi_p | \, e^{-\mathrm{i}\mathbf{G}\cdot\hat{\mathbf{x}}} \, | \varphi_q \rangle \, \langle \varphi_q | \, \hat{\mathbf{p}} \, | \varphi_p \rangle}{\omega - (\varepsilon_q - \varepsilon_p) + \mathrm{i}\varepsilon} + \frac{\langle \varphi_p | \, \hat{\mathbf{p}} \, | \varphi_q \rangle \, \langle \varphi_q | \, e^{-\mathrm{i}\mathbf{G}\cdot\hat{\mathbf{x}}} \, | \varphi_p \rangle}{-\omega - (\varepsilon_q - \varepsilon_p) + \mathrm{i}\varepsilon} \right). \tag{3.60}$$

In the following section, we shall discuss our numerical implementation of this expression and apply it to the example of diamond.

[21] We note with reference to the previous footnote that the discretization of numerical approaches will often be much coarser than the sampling, which is required to evaluate shifts by small $\mathbf{q}$. In order to obtain proper Bloch waves at two mildly different crystal momenta, nevertheless, we would thus require additional interpolation methods like $\mathbf{k} \cdot \mathbf{p}$-perturbation theory [101, 112]. We note that we have implemented this for testing purposes as well—just to verify its irrelevance.

3.3 Numerical evaluation of the nonlinear response

Previously, we have established the formal pre-conditions to evaluate the nonlinear response function $\mathbf{K}_{GS\diamond}(0,\mathbf{G},\omega)$ numerically. These comprise the simplified expression for the response itself (Eq. (3.60)) combined with the Bloch-wave based matrix elements in Eqs. (3.58) and (3.59).

Now, we proceed to the actual, numerical evaluation thereof. At its outset, this requires a DFT-calculation for the desired sample material, before the nonlinear response can be computed on top of the DFT-orbitals.

For the first step in this computation, we have chosen the ABINIT program [106]. As a plane-wave based DFT code, it is particularly suited to address solid-state problems—while at the same time, it is computationally fast, due to its focus on valence electrons in pseudo-potentials (for details see Ref. [106] and references therein).

The second step of our envisioned computation could not be achieve by any (openly) available software at the time of this writing. Consequentially, we have developed a computer-program of our own—`MyLiO.x`—to address this need. `MyLiO.x` implements a host of FORTRAN-routines for the evaluation of $\mathbf{K}_{GS\diamond}(0,\mathbf{G},\omega)$ as well as several related response functions. Moreover, it provides basic I/O-capabilities and, importantly, interfaces the output of ABINIT for our calculations. For more details on the program, we refer the reader to App. A.6, where we have attached our current version of the 'manual' for `MyLiO.x`.

Diamond as an example In the remainder of this section, we will apply both of the aforementioned computational codes to the exemplary case of diamond. This material exhibits a range of beneficial properties (e.g., hardness, high heat-conductivity and low optical / x-ray absorption), which make it a popular sample for x-ray wavemixing experiments (cf. both Refs. [46–48, 50, 113–115] and our own studies in Chpt. 5). As such, it is the most natural starting point for theoretical investigations as well.

For the DFT calculations that provide the basis of Kohn-Sham orbitals, we employ a basic LDA XC-potential. Within ABINIT, this is combined with a norm-conserving pseudopotential for carbon[22] and evaluated in a plane-wave basis; the cut-off energy for the latter was taken to be 15 a.u.. The real-space lattice of diamond is fixed to the cubic unit cell size of 6.741 a.u., while the Brillouin zone is initially sampled at 60 k-points (symmetry adapted) to iterate the DFT calculation. Ultimately, the result is extrapolated onto 2048 k-points spread homogeneously across the full Brillouin zone (without symmetry adaption).

Following the DFT calculation, the orbital energies of all unoccupied states are shifted upwards by a scissor correction of $\Delta E = 0.062$ a.u. (~ 1.7 eV), which we adopted from Ref. [111]. This shift is performed within `MyLiO.x` at the stage of computing the nonlinear response function and aims to correct for the incorrect band-gap energy, which we would otherwise obtain from LDA-DFT [110]. In addition, we apply a finite regularization $\varepsilon = 0.007$ a.u. (~ 0.2 eV) during the evaluation of Eq. (3.60). This replaces the original limit of $\varepsilon \to 0^+$ and parallels earlier, all-optical calculations on diamond [116] in its value.

[22] We note that we have used the standard pseudopotential that was in used for this atomic species in ABINIT in 2020.

3.3.1 Spectral properties of $\mathbf{K}_{GS\diamond}$ (in diamond)

In a first case study, we want to investigate the spectral properties of $\mathbf{K}_{GS\diamond}(0,\mathbf{G},\omega)$ in diamond. To this end, we compute the response across a spectral range of $\omega = \pm 1$ a.u. (~ 27.2 eV)—specifically for the (111) component, i.e. at $\mathbf{G} = \mathbf{G}_{(111)}$.

We notice up front that $\mathbf{K}_{GS\diamond}(0,\mathbf{G}_{(111)},\omega)$ appears to be very well aligned with $\mathbf{G}_{(111)}$ itself[23]. Considering the difference in $|\mathbf{K}_{GS\diamond}|^2 - |\hat{\mathbf{G}}_{(111)} \cdot \mathbf{K}_{GS\diamond}|^2$ as a measure[24], we find their mutual divergence to be less than $\sim 10^{-7}$ across the whole studied domain (for reference: $|\mathbf{K}_{GS\diamond}|^2 \approx 10^{-4}$).

This alignment simplifies our subsequent discussion of the response function significantly: Instead of analysing each of its vectorial components individually, we can focus on the projection $\hat{\mathbf{G}}_{(111)} \cdot \mathbf{K}_{GS\diamond}(0,\mathbf{G},\omega)$ without loss of any information. We proceed to plot its real and imaginary part in Fig. 3.2 below, further normalized to the computationally assumed crystal volume $V_\diamond$. Both real and imaginary part are shown as a solid, red curve in their respective pane of the graph. In addition, we also plot the imaginary and real part of diamond's dielectric function (blue, dashed line). This was computed via the Kubo-Greenwood formula [117] from the same Kohn-Sham orbitals as $\mathbf{K}_{GS\diamond}$ and serves for illustration and comparison[25].

As a first observation, we notice that $\mathbf{K}_{GS\diamond}(0,\mathbf{G}_{111},\omega)$ does indeed flip its sign at $\omega = 0$. We have expected this behaviour from the response function's anti-symmetry upon time-reversal (cf. Eq. (3.10) and pertaining discussion in Sec. 3.1.1).

Apart from this, we observe a prominent feature shortly below 0.5 a.u. (~ 13.6 eV). In this region, the real part of $\mathbf{K}_{I\diamond}$ comes to resemble the imaginary part of ε closely. The same holds true for the second pair (i.e., $\mathrm{Im}(\mathbf{K}_{GS\diamond})$ and $\mathrm{Re}(\varepsilon)$), respectively[26]. Such a similarity was to be expected to some degree, because both types of response functions feature an inherently similar pole-structure. This is a natural consequence of their respective origins at second order of perturbation theory, each. We could take this congruence a step further and even think of the nonlinear response function $\mathbf{K}_{I\diamond}$ as a spatially resolved view onto the material's *transverse* dielectric response in some sense[27]. As a consequence of this spatial resolution, $\mathbf{K}_{I\diamond}$ is intrinsically more sensitive to excitations at shorter length scales than the usual (macroscopic) dielectric function. This enhances the visibility of spectral features at higher energies in $\mathbf{K}_{I\diamond}$ compared to ε—see the region around ~ 1.0 a.u. (~ 27.2 eV). Such kind of enhanced sensitivity might recommend XOWM for future applications in probing localized phenomena. For instance, we could envision XOWM techniques to complement purely spectroscopic studies on orbital transitions or Frenkel excitons beyond the zero-momentum-transfer limit [118, 119].

[23] We note that the alignment of $\mathbf{K}_{GS\diamond}(0,\mathbf{G},\omega)$ along $\mathbf{G}$ is not overly surprising and could be guessed from earlier expressions already. It featured most prominently in Eq. (3.51) for the high-frequency limit of $\mathbf{K}_{GS\diamond}$. In this case, the current-/momentum-operator evaluated directly proportional to the momentum transfer of the scattering process. More broadly speaking, a specific reciprocal component of $\mathbf{K}_{GS\diamond}(0,\mathbf{G},\omega)$ will naturally resolve currents that point along the same direction, viz. $\mathbf{G}$.

[24] We note for clarity that—in the absence of quantum-mechanical operators—we employ the 'hat'-notation to signify unit vectors. As such $\hat{\mathbf{G}}_{(111)}$ denotes the unit vector parallel to $\mathbf{G}_{(111)}$.

[25] We remark that the data for $\varepsilon(\omega)$ at negative frequencies was obtained by mirroring the positive part.

[26] We note that the mildly irritating flip from real to imaginary part is probably down to our initial definition of $\mathbf{P}_I(\mathbf{x}_1,t_1,\mathbf{x}_2,t_2)$. By accident (and ignorance at the time), we did not include a factor of $-\mathrm{i}$, which appears to be commonplace in the realm of density-based response functions, though (cf. Ref. [104], for instance). As a consequence, our response function features a phase-shift by $\pi/2$. We might want to remedy this issue in the future—for the sake of broader consistency. Yet at the same time, we emphasize that this convention is fully inconsequential, when it comes to physical meaning.

[27] We note with caution that this analogy of $\mathbf{K}_{I\diamond}$ and $\varepsilon(\omega)$ should not be pushed too far—carelessly. While it is illustrative and both functions certainly pertain to related response-phenomena, they also imply important differences. In particular, we recall that the dielectric function typically describes the *longitudinal* coupling of the electronic density to a scalar potential [104]. Instead, our nonlinear response function $\mathbf{K}_{I\diamond}$ involves the *transverse* coupling of a current-density to the vector-potential $\mathbf{A}$. Yet at the same time, its spatial resolution derives from the correspondingly correlated density.

In pursuit of a more comprehensive picture of $\mathbf{K}_{I\diamond}(0, \mathbf{G}, \omega)$, we shall turn our attention towards said spatial resolution explicitly. This will feature in the upcoming Sec. 3.3.2.

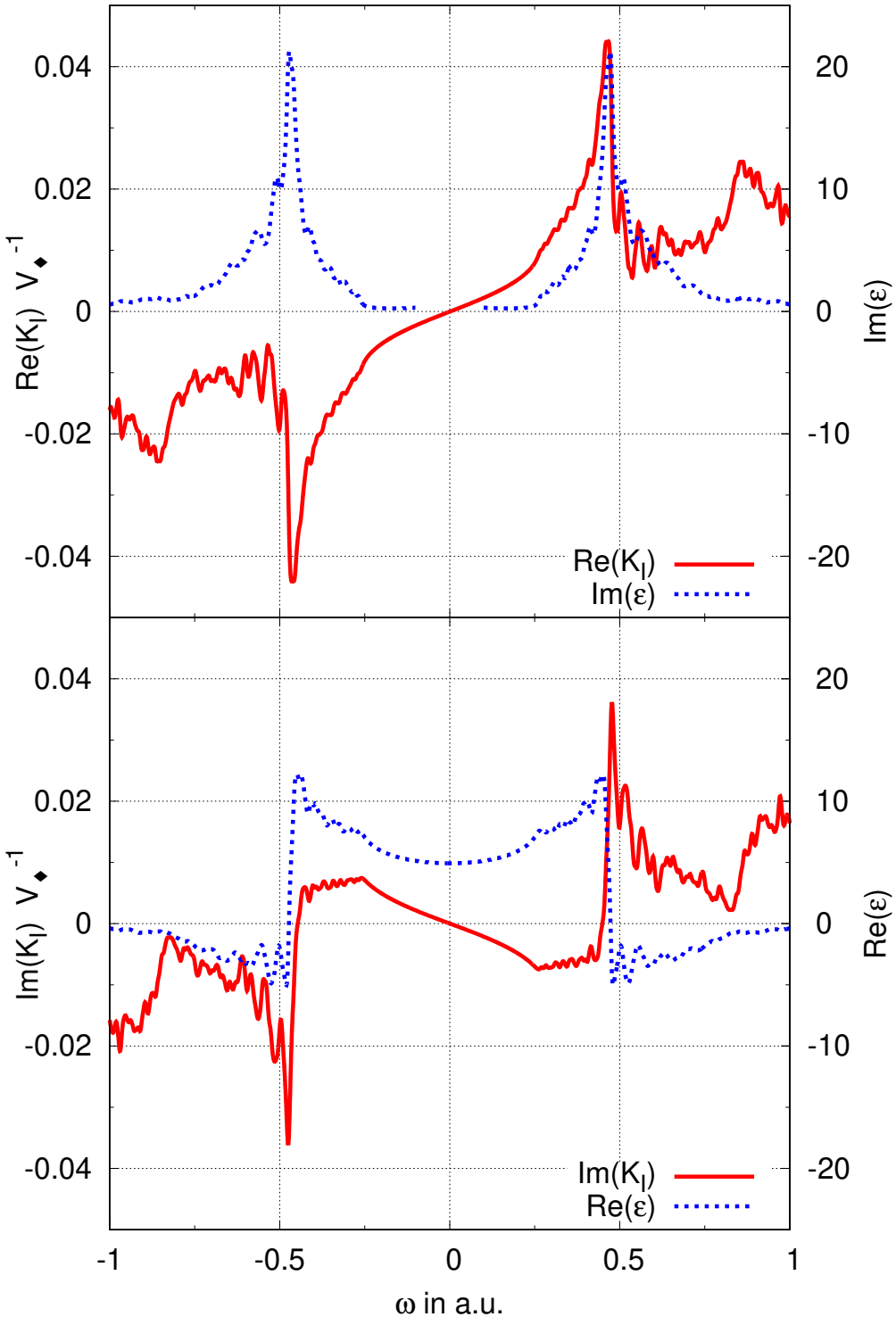

Figure 3.2: The real and imaginary part of the nonlinear response in diamond are given as red solid lines in the upper and lower section of the graph, respectively. Specifically, we show the projection of $\mathbf{K}_{GS\diamond}(0, \mathbf{G}_{111}, \omega)$ onto $\hat{\mathbf{G}}_{111}$ and normalize it by the numerical simulation volume $V_\diamond$. The nonlinear response is measured along the left-hand ordinate. For comparison, the imaginary and real part of the dielectric function are juxtaposed as blue dashed lines, respectively. They are measured along the right-hand ordinate each.

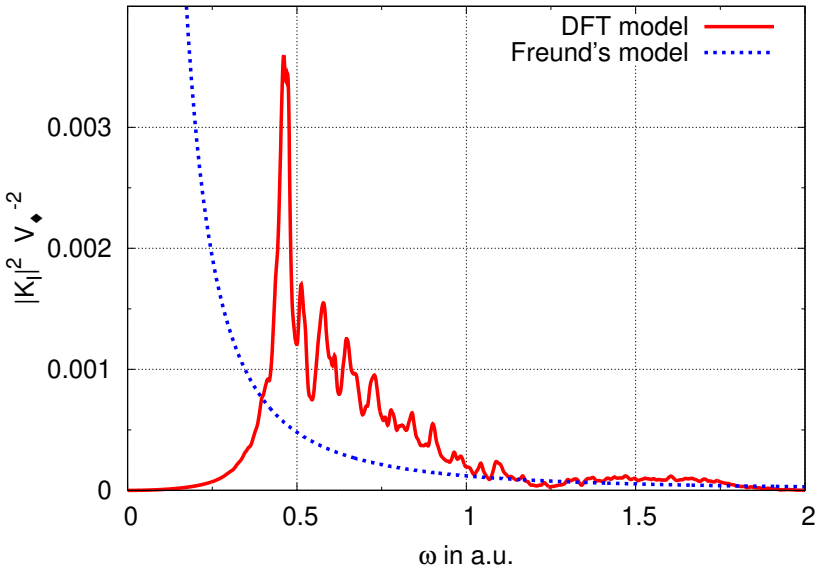

Figure 3.3: Comparison of $|\mathbf{K}_{I\diamond}(0,\mathbf{G}_{220},\omega)|^2 V_{\diamond}^{-2}$ computed from the full, DFT-model (red, solid line) versus the high-frequency approximation following Freund (blue, dashed line).

3.3.1.a Cross-check of $\mathbf{K}_{GS\diamond}$ in the high-frequency limit

Before we conclude our discussion on the spectral behaviour of the nonlinear response function, we want to address one final cross-comparison. Namely, we shall consider the high-frequency limit of $\mathbf{K}_{I\diamond}(0,\mathbf{G},\omega)$, for which we have previously obtained an approximate expression—recall Eq. (3.51) from Sec. 3.2.2

$$\mathbf{K}_{GS\diamond}(0,\mathbf{G},\omega) \approx \frac{2\mathrm{i}}{\omega}\,\mathbf{G}\,\rho_{\mathbf{G}}^{\mathrm{VB}}. \tag{3.61}$$

Using its Bloch-wave formulation, as given in Eq. (3.52), we can evaluate the approximate response function from the same DFT-orbitals as before. Thereby, we obtain a result that can be compared to our first-principles correlation function on equal footing.

Evaluating both for the (220) orientation of diamond, we find the spectra plotted in Fig. 3.3. Herein, the 'full' result according to Eq. (3.60) is shown as a red, solid line, whereas the high-frequency approximation appears in blue (dashes line). Both functions are plotted in terms of their absolute squares, as these give a direct measure of the scattering yields in XOWM. We observe that our numerical result approaches the asymptotic expression above $\omega \approx 1$ a.u. (≈ 27.2 eV). The precise point of convergence depends on the reciprocal component in question, yet generally, we find good agreement of our full correlation function with the approximate version at high energies. Observing the correct limiting behaviour of $\mathbf{K}_{I\diamond}(0,\mathbf{G},\omega)$ provides a re-assuring cross-check of our numerical implementation.

Of course, we may likewise invert our conclusion and judge Freund's approximation on this basis. As such, the above results suggest that Eq. (3.61), indeed, provides a good estimator for $\mathbf{K}_{I\diamond}(0,\mathbf{G},\omega)$ down to $\omega \approx 1$ a.u.. Even below this point, it may be used for a decent order of magnitude estimate. Nevertheless, the smooth approximation is obviously inadequate for determining any spectral features.

3.3.2 Spatial properties $\mathbf{K}_{GS\diamond}$ (in diamond)

In addition to the spectral properties of $\mathbf{K}_{GS\diamond}$, which we have discussed throughout Sec. 3.3.1, the nonlinear response during XOWM processes also offers unprecedented *spatial* insights into electronic dynamics. This distinguishes XOWM from most other probes, especially from all-optical techniques. The latter lack any microscopic resolution due to the fundamental diffraction-limit of optical wavelengths. As a case in point, we recall from Sec. 3.3.1 the (macroscopic) dielectric function, which could be probed by optical absorption-, transmission- or reflection-spectrometry, for example [120]. We have already discussed its spectral similarities with our nonlinear response function, but shall now elaborate on the additional, spatial information[28] provided by $\mathbf{K}_{GS\diamond}$.

In order to analyze the spatial information of our numerically evaluated $\mathbf{K}_{GS\diamond}(0,\mathbf{G},\omega)$, we first have to understand the impact of its approximation vis-a-vis the full response function $\mathbf{K}_{I\diamond}(\mathbf{q}+\mathbf{G}_1,-\mathbf{q}+\mathbf{G}_2,\omega)$. We recall its original Fourier relation (Eq. (3.13))

$$\mathbf{K}_{I\diamond}(\mathbf{q}+\mathbf{G}_1,-\mathbf{q}+\mathbf{G}_2,\omega)=\int_\diamond d^3x_1\int_\diamond d^3x_2\int d\tau\; e^{-\mathrm{i}(\mathbf{q}+\mathbf{G}_1)\cdot\mathbf{x}_1}\,e^{-\mathrm{i}(-\mathbf{q}+\mathbf{G}_2)\cdot\mathbf{x}_2}\;e^{\mathrm{i}\omega\tau}\;\mathbf{P}_{I\diamond}(\mathbf{x}_1,0,\mathbf{x}_2,\tau), \quad (3.62)$$

on which we shall impose the restrictions $\mathbf{q}=\mathbf{G}_1=0$ and $\mathbf{G}_2=\mathbf{G}$. Thus, we find that the approximate response function $\mathbf{K}_{GS\diamond}(0,\mathbf{G},\omega)$ corresponds to a partially averaged quantity, viz:

$$\mathbf{K}_{GS\diamond}(0,\mathbf{G},\omega)=\int_\diamond d^3x_2\int d\tau\; e^{-\mathrm{i}\mathbf{G}\mathbf{x}_2}\;e^{\mathrm{i}\omega\tau}\quad\int_\diamond d^3x_1\;\mathbf{P}_{GS\diamond}(\mathbf{x}_1,0,\mathbf{x}_2,\tau), \quad (3.63)$$

$$\text{where: }\;\mathbf{P}_{GS\diamond}(\mathbf{x}_1,0,\mathbf{x}_2,\tau)=\langle GS|\;\hat{T}\left[\hat{\mathbf{p}}(\mathbf{x}_1,0)\,\hat{n}(\mathbf{x}_2,\tau)\right]\,|GS\rangle\,. \quad (3.64)$$

In particular, we see that the first argument of the original density–current-density response function is indiscriminately averaged across the full crystalline domain. This argument pertained to the current-/momentum-contribution and mediated the optical coupling. It is fully in line with our application of a 'dipole-approximation'-type treatment on this optical coupling (cf. Sec. 3.1.2.a) that its spatial dependence is washed out.

On the other hand, we find that the spatial dependence, which is associated with the x-ray probe (here: $\mathbf{x}_2$), remains intact. From this, we can reconstruct a nonlinear response density by Fourier inversion

$$\begin{aligned}\mathbf{R}_{GS\diamond}(\mathbf{x},\omega)&=\frac{1}{V_\diamond}\sum_{\mathbf{G}}^{\text{rec. latt.}}\;e^{\mathrm{i}\mathbf{G}\cdot\mathbf{x}}\;\mathbf{K}_{GS\diamond}(0,\mathbf{G},\omega)\\&=\int d\tau\,e^{\mathrm{i}\omega\tau}\int_\diamond d^3y\;\mathbf{P}_{GS\diamond}(\mathbf{y},0,\mathbf{x},\tau).\end{aligned} \quad (3.65)$$

Building on the DFT-calculations, which we have already performed for diamond, we shall proceed to compute multiple reciprocal components of $\mathbf{K}_{GS\diamond}(0,\mathbf{G},\omega)$ and synthesize them into a real-space picture. In doing so, we focus on an optical photon energy of $\omega=0.057$ a.u. (~ 1.55 eV), because it corresponds to the cases studied in Secs. 5.1.1 and 5.1.2 later on. In Fig. 3.4 (a), we show the resulting spatial distribution of $|\mathbf{R}_{GS\diamond}(\mathbf{x},\omega)|^2$ in a $(1\bar{1}0)$-plane of diamond across the conventional (cubic) unit cell. For orientation and comparison, we show the density of valence electrons within the same plane next to it, i.e., in Fig. 3.4 (b).

As we would expect, the nonlinear response correlates with the localization of valence charges along

[28] We note for completeness that the concept of a *microscopic* dielectric function exists, which *could* provide spatial information as well. Options to probe this (or related quantities exist) but require challenging experiments in themselves; for an overview consider Refs. [61, 121].

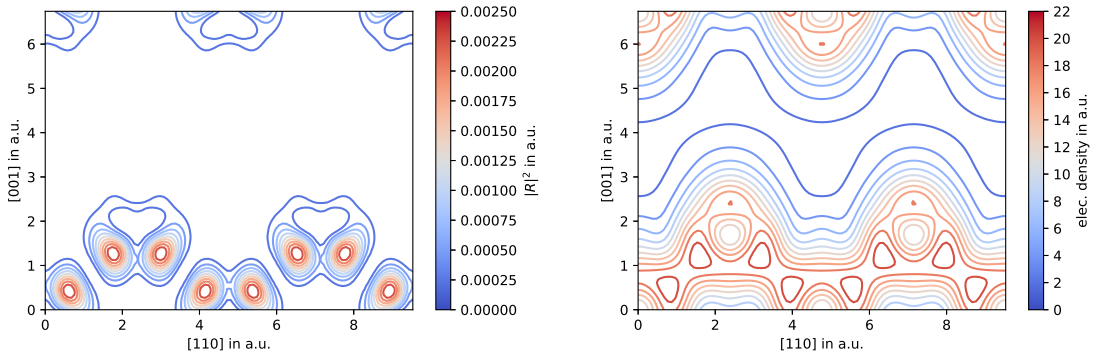

(a) **(b)**

Figure 3.4: (a) The nonlinear response of diamond is shown in terms of $|\mathbf{R}_{GS\diamond}(\mathbf{x}, 0.057)|^2$ across the $(1\bar{1}0)$-plane of its conventional (cubic) unit cell. Next to it in (b), the valence-electron density $\rho^{\mathrm{VAL}}_{GS\diamond}(\mathbf{x})$ for the ground state is given for reference.

the bonds directions, i.e., along the (111) and $(11\bar{1})$ diagonals of the plot. Yet at the same time, its distribution exhibits characteristics that clearly distinguish it from the mere ground-state density. Most notably, the nonlinear response exhibits clear nodal planes across the middle of each bond. Around these, $|\mathbf{R}_{GS\diamond}(\mathbf{x}, 0.057)|^2$ is concentrated in two pronounced maxima, thus it takes on a noticeably 'anti-bonding' shape.

By recourse to the underlying equations, we can give further intuition to this observation. Starting from the original density–current-density correlator of Eq. (3.1) or Eq. (3.64) above, we note that it incorporates *both* ground-state properties—from the bracketing states $\langle GS|$ and $|GS\rangle$—as well as properties of excited states, which are intermediately present. The latter becomes even more apparent, when looking at the prescription for our mean-field or DFT-based model of the response function in Eq. (3.60). This consists of transition-matrix elements that connect initially occupied orbitals (φ_p) to unoccupied intermediate states (φ_q). The latter are of antibonding nature and thus shape the overall transition this way. In combining contributions from ground and excited states, the nonlinear response function can be thought of as probing transition densities inside the material. We re-iterate that it is only through x-ray-optical mixing that these transition densities can be resolved microscopically, even though similar transitions would implicitly be involved in all-optical response functions as well.

In order to analyze individual transition pathways more closely, we could envision to capitalize on the spectral dependence of $\mathbf{R}_{GS\diamond}(\mathbf{x}, \omega)$. Experimentally, this would require laser sources, which can be tuned in their frequency (ω) to address selected transitions via resonant optical driving.

For the presented case of diamond, driven at $\omega = 0.057$ a.u. (~ 1.55 eV), however, we would be far off any resonance. Its nonlinear response under these circumstances reflects a weighted sum of (many) energetically distant transitions. Within this sum, those transitions with intrinsically large oscillator strength dominate, which—for diamond—are mostly localized at the pronounced spectral peak around 0.459 a.u. (~ 12.5 eV) (cf. our discussion of Fig. 3.2). The dominance of a single major transition-band leaves comparably little room for variation in the response function's shape for diamond[29]. Significantly different contours will, however, begin to appear in the high-frequency limit (see discussion in

[29] We note that this low degree of variation in the nonlinear response of diamond can also be seen by comparing Fig. 3.4 (a) to its counterpart in Ref. [51]. There, we have published a largely identical same response density in Fig. 1 (a)—albeit being evaluated at a higher energy of $\omega = 0.184$ a.u. (~ 5.0 eV), respectively. Both cases (1.55 and 5.0 eV) represent off-resonant excitations and are thus dominated by the same transition-band ultimately.

Sec. 3.3.2.a below).

In a last take on diamond's nonlinear response at $\omega = 0.057$ a.u. (~ 1.55 eV), we shall visualize it three-dimensionally. To this end, we give an extended rendering of $|\mathbf{R}_{GS\diamond}(\mathbf{x}, 0.057)|^2$ in Fig. 3.5. It provides a view of the nonlinear response across the complete conventional unit-cell of diamond—viewed along a (111)-axis. We have set the contour levels to 0.001 and 0.002 a.u. (green and yellow).

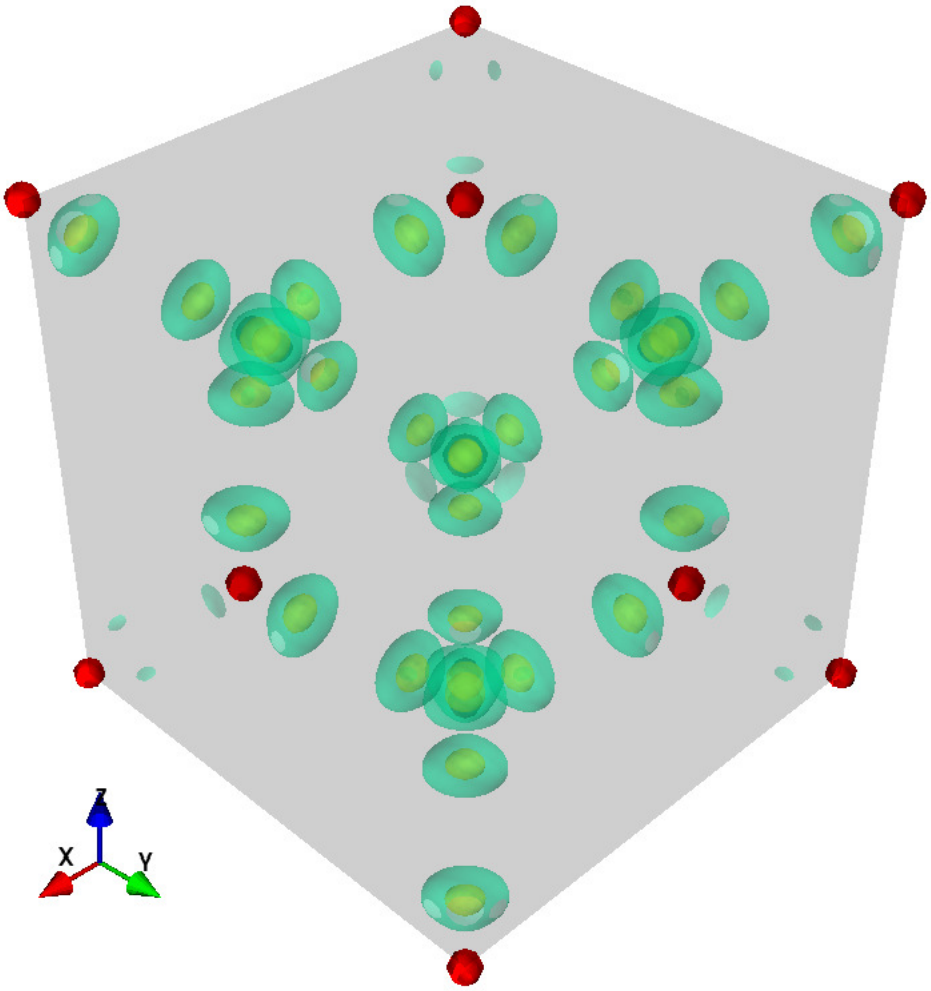

Figure 3.5: The nonlinear response of diamond is shown in terms of $|\mathbf{R}_{GS\diamond}(\mathbf{x}, 0.057)|^2$ across the conventional (cubic) unit cell. The contour levels are set at 0.001 and 0.002 a.u. for green and yellow, respectively. Additionally, red spheres are shown in place of the carbon nuclei to guide the eye.

In terms of a first assessment, we note that the three-dimensional visualization may indeed be helpful. In particular, when used in an interactive mode on a computer[30], it renders individual features of $\mathbf{R}_{GS\diamond}(\mathbf{x}, \omega)$ amenable to more intuitive analysis.

While the above graphics resulted from numerical simulations, we want to conclude on the thought that it could also be obtained from experimental datasets. Performing such a Fourier reconstruction in terms of 'nonlinear crystallography' (cf. proposal in Sec. 5.1.2.d) could open a new, visual window onto electronic phenomena. Combined with its extension to more intricate (functional) materials, we could envision to obtain interesting insights into exciton-dynamics, charge-transfer or, more generally, electronic correlation effects in bulk.

[30] We point out that our three-dimensional visualizations were obtained using the `mayavi`-package for PYTHON.

3.3.2.a Example of $\mathbf{R}_{GS\diamond}$ in the high-frequency limit

In addition to discussing the 'full' response function's spatial properties, we also include a visual example for its simplified version in the high-frequency limit (see Sec. 3.2.2 for its initial discussion). In contrast to Sec. 3.3.1.a, wherein we were still concerned with the validity of this approximation, we shall pursue no such fundamental question in the present section. Instead, the following serves purely illustrative purposes.

With a view to experimental studies on XPDC at high 'idler' photon energies (cf. Sec. 5.2.3.a), we have evaluated the high-frequency approximation of $\mathbf{K}_{GS\diamond}(0,\mathbf{G},\omega)$ at $\omega = 3.675$ a.u. (~ 100 eV) for several crystal orientations. Using these to produce a reconstruction of the approximate nonlinear response density, we obtain Fig. 3.6. Fully analogous to the previous Fig. 3.4, we use the sub-plot (a) to show the spatial distribution of $|\mathbf{R}_{GS\diamond}(\mathbf{x},\omega)|^2$ in a $(1\bar{1}0)$-plane of diamond across the conventional (cubic) unit cell. To its right, i.e., in figure-pane (b), we add the valence electron density for comparison again.

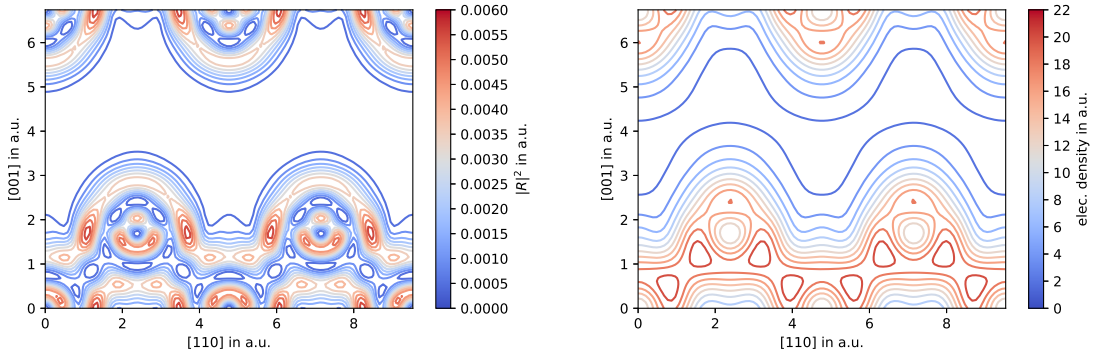

(a) **(b)**

Figure 3.6: (a) The nonlinear response of diamond is shown in terms of $|\mathbf{R}_{GS\diamond}(\mathbf{x},3.675)|^2$ across the $(1\bar{1}0)$-plane of its conventional (cubic) unit cell. Next to it in (b), the valence-electron density $\rho^{\mathrm{VAL}}_{GS\diamond}(\mathbf{x})$ for the ground state is given for reference.

We find that this approximated response density at high-frequencies resembles the neighbouring valence density much more closely than the low-frequency version did before in Fig. 3.4. Of course, this is unsurprising, given that Freund's type of approximation ended up being proportional to the reciprocal components of said valence density—recall Eq. (3.51)

$$\mathbf{K}_{GS\diamond}(0,\mathbf{G},\omega) = \frac{2\mathrm{i}}{\omega}\,\mathbf{G}\,\rho^{\mathrm{VB}}_{\mathbf{G}}. \tag{3.66}$$

The additional presence of a multiplicative factor of $\mathbf{G}$ in this (reciprocal-space) expression translates into a gradient on the real-space density. This explains, why the new response function is at its strongest *around* the actual bonds. Namely, because on this path, which approaches the binding electrons, the gradient is maximized. Conversely, where the bonds are strongest, i.e., the electronic density has maxima, the respective gradient vanishes—leaving a zero valued trace along the strongest electronic localizations.

In closing, we remark with curiosity that further investigations of the nonlinear response function in the high-energy regime—beyond mere illustration—could indeed be interesting. For instance, it would be informative to observe the cross-over from low- to high-frequency regime. At this point, we should see the nodal planes of the original function (cf. Fig. 3.4 (a))—which attest to the importance of a specific class of quantized transitions—give way to the classical continuum behaviour of intermediately free

electrons. Moreover, one could think of extending the computations even beyond the realm of valence electrons, studying the interplay of valence and (semi-)core transitions.

3.4 Beyond mean-field approaches

In a final consideration on the nonlinear response function $\mathbf{P}_{I\diamond}(\mathbf{x}_1, 0, \mathbf{x}_2, \tau)$, we want to explore options to compute this (or a related) object beyond the limits of a mean-field model.

As we have stated in the beginning of this chapter, possibilities abound for methods that *could* be used as a basis to implement our nonlinear response [76, 78–87]. However, we acknowledge that for many of the aforementioned approaches, this may require significant effort—both in terms of their ultimate computational cost but, more immediately still, in terms of initial work-load in programming. Nevertheless, we see two paths forward that could be more amenable—for different reasons.

The first option to this effect consists in implementing our density–current-density correlation function in the framework of current-density functional theory (CDFT) or its time-dependent variant TD-CDFT [104, 122], respectively. This conceptual extension of (TD)-DFT was developed to address issues arising from non-locality in the original theory. In doing so, it spawned a framework that naturally accounts for the current-density as its fundamental quantity. The regular electronic density, on the other hand, is automatically included by virtue of the continuity equation. Regarding this aspect, TD-CDFT would thus provide quite favourable conditions to implement the response function $\mathbf{P}_{I\diamond}(\mathbf{x}_1, 0, \mathbf{x}_2, \tau)$ straight-away. There is one unfortunate counter-point to TD-CDFT, however. In that it has seen far less wide-spread application than its density-based predecessor (TD-DFT). As such, there exist no general-purpose TD-CDFT codes, to our knowledge, which would be benchmarked and applicable to an extent, which compares to ABINIT, for example. Nevertheless, we could envisage possible applications of TD-CDFT in the context of XOWM in the future.

The second option, which we want to outline, is intended to achieve more immediate progress on the evaluation of $\mathbf{P}_{I\diamond}(\mathbf{x}_1, 0, \mathbf{x}_2, \tau)$. To this end, we propose to adapt existing computational capabilities from density-response formalisms. In particular, we recall that several post-DFT (or post-Hartree-Fock) methodologies involve the refinement of density-density response functions. Among others, there is TD-DFT in its widely-used linear-response formulation [104], related to which—though separately conceived—we find approaches built on the random-phase-approximation (RPA) [123], and in further addition, there are ongoing efforts to solve the Bethe-Salpeter Equation (BSE) for two-point response-functions [87, 124, 125]. All of these share the retarded density-density response function for the electronic system

$$\chi(\mathbf{x}_1, t_1, \mathbf{x}_2, t_2) = -\mathrm{i}\,\Theta(t_1 - t_2)\ \langle GS|\ [\hat{n}(\mathbf{x}_1, t_1), \hat{n}(\mathbf{x}_2, t_2)]\ |GS\rangle\,. \tag{3.67}$$

In order to utilize this for our purposes now, we would need to construct the density–current-density correlator, which governs XOWM, from this purely density-based object. This presents a conceptual problem immediately, in that the *scalar* response function of Eq. (3.67) contains less information than our *vectorial* quantity $\mathbf{P}_I(\mathbf{x}_1, t_1, \mathbf{x}_2, t_2)$—recall the definition Eq. (3.68):

$$\mathbf{P}_I(\mathbf{x}_1, t_1, \mathbf{x}_2, t_2) = \langle I|\ \hat{T}\,[\hat{\mathbf{p}}(\mathbf{x}_1, t_1)\,\hat{n}(\mathbf{x}_2, t_2)]\ |I\rangle\,. \tag{3.68}$$

In order to appreciate this problem in more fundamental terms, we can consider the continuity equation

$$\frac{\partial}{\partial t} n(\mathbf{x},t) = -\nabla \cdot \mathbf{j}(\mathbf{x},t). \tag{3.69}$$

It is quite evident from this that we should always be able to derive the dynamics of the electronic-density, if we know all three components of the current-density vector. In contrast, however, the opposite inference ($n \rightarrow \mathbf{j}$) is not generally possible[31]. Therefore, we cannot establish a general, bi-directional connection among expressions (3.67) and (3.68).

An approximate connection of χ and $\mathbf{K}_{I\diamond}$ Nevertheless, we could (and will) propose an approximate connection. Therein, we focus on the limit of vanishingly small (optical) momentum transfer, which is anyways what we have considered for $\mathbf{K}_{I\diamond}(0,\mathbf{G},\omega)$ up to now (cf. discussion of the 'Dipole-approximation' in Sec. 3.1.2.a). As a starting point for our derivations, we choose the simple Fourier transform[32]

$$\mathbf{R}_{I\diamond}(\mathbf{x},\omega) = \frac{1}{V_\diamond}\sum_{\mathbf{G}} e^{\mathrm{i}\mathbf{G}\mathbf{x}}\mathbf{K}_{I\diamond}(0,\mathbf{G},\omega) = \int d\tau\, e^{\mathrm{i}\omega\tau}\int_\diamond dy\, \mathbf{P}_{I\diamond}(\mathbf{y},0,\mathbf{x},\tau). \tag{3.70}$$

In the real-space expression $\mathbf{P}_{I\diamond}(\mathbf{x}_1,t_1,\mathbf{x}_2,t_2)$, we can identify and split two terms

$$\begin{aligned}
\mathbf{P}_{I\diamond}(\mathbf{x}_1,t_1,\mathbf{x}_2,t_2) &= \langle I|\, \hat{T}[\hat{\mathbf{p}}(\mathbf{x}_1,t_1)\hat{n}(\mathbf{x}_2,t_2)]\,|I\rangle \\
&= \underbrace{\Theta(t_1-t_2)\,\langle I|\,\hat{\mathbf{p}}(\mathbf{x}_1,t_1)\hat{n}(\mathbf{x}_2,t_2)\,|I\rangle}_{\mathbf{P}^T_{I\diamond}(\mathbf{x}_1,t_1,\mathbf{x}_2,t_2)} + \underbrace{\Theta(t_2-t_1)\,\langle I|\,\hat{n}(\mathbf{x}_2,t_2)\hat{\mathbf{p}}(\mathbf{x}_1,t_1)\,|I\rangle}_{\mathbf{P}^A_{I\diamond}(\mathbf{x}_1,t_1,\mathbf{x}_2,t_2)} \qquad (3.71)\\
&= \Theta(t_1-t_2)\;\mathrm{i}\;\mathbf{G}^{>}_{\diamond p,n}(\mathbf{x}_1,t_1,\mathbf{x}_2,t_2) + \Theta(t_2-t_1)\;(-\mathrm{i})\;\mathbf{G}^{<}_{\diamond p,n}(\mathbf{x}_1,t_1,\mathbf{x}_2,t_2). \qquad (3.72)
\end{aligned}$$

We label the two amplitudes in reminiscence of the greater and lesser Green's functions as defined in Ref. [76], for instance. In addition, we also carry some legacy notation, in form of the two half-parts of the time-ordered response function, viz. $\mathbf{P}^T_{I\diamond}$ and $\mathbf{P}^A_{I\diamond}$. In all of the above, the subscript $\diamond$ serves as a reminder that our quantities are defined on the periodic domain of the crystal.

Next, we shall simplify the individual amplitudes, starting with $\mathbf{G}^{>}_{\diamond p,n}$. We recall that, in our case, this amplitude will be integrated in $\mathbf{x}_1$ ultimately (cf. Eq. (3.70)) and thus write

$$\begin{aligned}
\int_\diamond dx_1 \mathrm{i}\;\mathbf{G}^{>}_{\diamond p,n}(\mathbf{x}_1,t_1,\mathbf{x}_2,t_2) &= \langle I|\int_\diamond d^3x_1\;\hat{\mathbf{p}}(\mathbf{x}_1,t_1)\hat{n}(\mathbf{x}_2,t_2)\,|I\rangle \\
&= \langle I|\underbrace{\int_\diamond d^3x_1 p(\mathbf{x},0)}_{\hat{\mathbf{p}}}\hat{n}(\mathbf{x}_2,\underbrace{t_2-t_1}_{\tau})\,|I\rangle \\
&= \langle I|\,\hat{\mathbf{p}}\,\hat{n}(\mathbf{x}_2,\tau)\,|I\rangle\,. \qquad (3.73)
\end{aligned}$$

Applying this integration has reduced the momentum-density operator into a simple momentum operator according to its definition $\hat{\mathbf{p}} = \int d^3x\;\hat{\psi}^\dagger(\mathbf{x})(-\mathrm{i})\nabla\hat{\psi}(\mathbf{x})$.

[31] We note that the mismatch of density- versus current-response, constitutes an extension (or an alternative facet, rather) of the problem outlined earlier in Sec. 3.3.1. Namely, that our density–current-density response function couples *transversely* to the vector-potential of the electromagnetic field, whereas many other response functions, including Eq. (3.67) above or the conventional dielectric-function $\varepsilon(\omega)$, imply *longitudinal* coupling.

[32] We note as a reminder that the absence of any optical momentum transfer ($\mathbf{q}\approx 0$) translates into the averaging integration across $\mathbf{y}$. In the original definition of $\mathbf{K}_{I\diamond}(\mathbf{q}+\mathbf{G}_1,-\mathbf{q}+\mathbf{G}_2,\omega)$ from Eq. (3.13), this integration would otherwise have been part of a second Fourier transformation.

We note that the above amplitude is still a vectorial quantity. However, it will be more convenient for our subsequent discussion to project it into a scalar. We can do so without loss of generality, as long as we keep the direction of our projection arbitrary. Hence, we define a vector $\mathbf{q}$ that points into an arbitrary direction and introduce its unit vector $\mathbf{e}_q = \mathbf{q}/|\mathbf{q}|$ with the preceding notation[33]. The projected amplitude simply becomes

$$\mathbf{e}_q \cdot \int_\diamond dx_1 \mathrm{i}\, \mathbf{G}^{>}_{\diamond p,n}(\mathbf{x}_1,t_1,\mathbf{x}_2,t_2) = \langle I|\, \mathbf{e}_q \cdot \hat{\mathbf{p}}\, \hat{n}(\mathbf{x}_2,\tau)\, |I\rangle\,. \tag{3.74}$$

In our next step, we introduce the replacement

$$\mathbf{e}_q \cdot \mathbf{p} = \lim_{q\to 0^+} \frac{1}{q} \int d^3x\, [\hat{H}, e^{\mathrm{i}\,\mathbf{qx}}\, \hat{n}(\mathbf{x})], \tag{3.75}$$

which is a variation on the better known commutator-identity $\hat{\mathbf{p}} = \mathrm{i}[\hat{H},\hat{\mathbf{x}}]$. We note that there is a second identity of similar form, which we shall introduce for later usage as well[34]:

$$\int d^3x\, [\hat{H}, e^{\mathrm{i}\,\mathbf{qx}}\, \hat{n}(\mathbf{x})] = \int d^3x\, \frac{q^2}{2}\, e^{\mathrm{i}\,\mathbf{qx}}\, \hat{n}(\mathbf{x}). \tag{3.76}$$

In both cases, we have used the notation $q = |\mathbf{q}|$ interchangeably.

Substituting Eq. (3.75) into the projected amplitude (3.74), we can rephrase it to read

$$\begin{aligned}\mathbf{e}_q \cdot \int_\diamond dx_1 \mathrm{i}\, \mathbf{G}^{>}_{\diamond p,n}(\mathbf{x}_1,t_1,\mathbf{x}_2,t_2) &= \lim_{q\to 0^+} \frac{1}{q} \int_\diamond d^3x\, \langle I|\, [\hat{H}, e^{\mathbf{iqx}}\, \hat{n}(\mathbf{x})] \hat{n}(\mathbf{x}_2,\tau)\, |I\rangle \\ &= \lim_{q\to 0^+} \frac{1}{q} \int_\diamond d^3x \Big(\langle I|\, \hat{H} e^{\mathbf{iqx}}\, \hat{n}(\mathbf{x})\, \hat{n}(\mathbf{x}_2,\tau)\, |I\rangle - \langle I|\, e^{\mathbf{iqx}}\, \hat{n}(\mathbf{x})\, \hat{H}\, \hat{n}(\mathbf{x}_2,\tau)\, |I\rangle \Big).\end{aligned} \tag{3.77}$$

In the last line, the Hamiltonian acting to the left in the first term would simply yield the energy of the initial state; its action in the second term is less obvious, however. Thus, we rephrase it using another commutator

$$\langle I|\, e^{\mathbf{iqx}}\, \hat{n}(\mathbf{x})\, \hat{H}\, \hat{n}(\mathbf{x}_2,\tau)\, |I\rangle = \langle I|\, e^{\mathbf{iqx}}\, \hat{n}(\mathbf{x})\, \hat{n}(\mathbf{x}_2,\tau)\, \hat{H}\, |I\rangle + \langle I|\, e^{\mathbf{iqx}}\, \hat{n}(\mathbf{x})\, [\hat{H}, \hat{n}(\mathbf{x}_2,\tau)]\, |I\rangle \tag{3.78}$$

and obtain for the overall amplitude

$$\begin{aligned}&\mathbf{e}_q \cdot \int_\diamond dx_1 \mathrm{i}\, \mathbf{G}^{>}_{\diamond p,n}(\mathbf{x}_1,t_1,\mathbf{x}_2,t_2) \\ &= \langle I|\, \mathbf{e}_q \cdot \hat{\mathbf{p}}\, \hat{n}(\mathbf{x}_2,\tau)\, |I\rangle \\ &= \lim_{q\to 0^+} \frac{1}{q} \int_\diamond d^3x \Big(\langle I|\, \hat{H} e^{\mathbf{iqx}} \hat{n}(\mathbf{x}) \hat{n}(\mathbf{x}_2,\tau)\, |I\rangle - \langle I|\, e^{\mathbf{iqx}} \hat{n}(\mathbf{x}) \hat{n}(\mathbf{x}_2,\tau) \hat{H}\, |I\rangle - \langle I|\, e^{\mathbf{iqx}} \hat{n}(\mathbf{x}) [\hat{H}, \hat{n}(\mathbf{x}_2,\tau)]\, |I\rangle \Big)\end{aligned} \tag{3.79}$$

Note, that the first two terms cancel, as the left and right (initial) states are equal and thus the action of $\hat{H}$ onto them yields the same energy.

[33] We note that we would usually opt for the 'hat'-notation $\hat{\mathbf{q}}$ to denote the aforementioned unit vector $\mathbf{q}/|\mathbf{q}|$, however, we consider it confusing in the presence of various operators, which sport the same type of 'hat'.

[34] We note that both identities can be derived by interpreting the commutator with the Hamiltonian in terms of the Heisenberg equations of motion, i.e., $d\hat{n}/dt = \mathrm{i}\,[\hat{H},\hat{n}]$ (cf. Sec. A.1.0.b). In addition, we can invoke the continuity equation (3.69) to combine $\hat{n}$ and $\hat{\mathbf{j}}$.

In order to evaluate the last term, let us Fourier transform the whole equation

$$\begin{aligned}
&\mathbf{e}_q \cdot \int_\diamond d^3x_2\, e^{-\mathrm{i}\mathbf{Q}_2\mathbf{x}_2} \int_\diamond d^3x_1\, \mathrm{i}\mathbf{G}^{>}_{\diamond p,n}(\mathbf{x}_1,t_1,\mathbf{x}_2,t_2) = \int_\diamond d^3x_2\, \langle I|\, \mathbf{e}_q\cdot\hat{\mathbf{p}}\,\hat{n}(\mathbf{x}_2,\tau)\,|I\rangle\; e^{-\mathrm{i}\mathbf{Q}_2\mathbf{x}_2} \\
&= \lim_{q\to 0^+} \frac{1}{q}\int_\diamond d^3x \int_\diamond d^3x_2\, (-1)\,\langle I|\, e^{\mathrm{i}\mathbf{q}\mathbf{x}}\hat{n}(\mathbf{x})[\hat{H}, e^{-\mathrm{i}\mathbf{Q}_2\mathbf{x}_2}\,\hat{n}(\mathbf{x}_2,\tau)]\,|I\rangle\,. \qquad (3.80)
\end{aligned}$$

The time dependence of $n(\mathbf{x}_2,\tau)$ commutes with $\hat{H}$, thus, we can evaluate the commutator as in Eq. (3.76):

$$\begin{aligned}
&\mathbf{e}_q \cdot \int_\diamond d^3x_2\, e^{-\mathrm{i}\mathbf{Q}_2\mathbf{x}_2} \int_\diamond d^3x_1\, \mathrm{i}\mathbf{G}^{>}_{\diamond p,n}(\mathbf{x}_1,t_1,\mathbf{x}_2,t_2) \\
&= \lim_{q\to 0^+} \frac{1}{q}\int_\diamond d^3x \int_\diamond d^3x_2 (-1)\,\langle I|\, e^{\mathrm{i}\mathbf{q}\mathbf{x}}\hat{n}(\mathbf{x})\,\frac{Q_2^2}{2} e^{-\mathrm{i}\mathbf{Q}_2\mathbf{x}_2}\,\hat{n}(\mathbf{x}_2,\tau)\,|I\rangle \\
&= \lim_{q\to 0^+} \frac{1}{q}\int_\diamond d^3x \int_\diamond d^3x_2 (-1)\frac{Q_2^2}{2}\; e^{\mathrm{i}\mathbf{q}\mathbf{x}}\, e^{-\mathrm{i}\mathbf{Q}_2\mathbf{x}_2}\,\langle I|\,\hat{n}(\mathbf{x})\,\hat{n}(\mathbf{x}_2,\tau)\,|I\rangle \quad \text{here:}\quad \tau = t_2 - t_1 < 0. \qquad (3.81)
\end{aligned}$$

Similarly, if we would have started with the other amplitude

$$(-\mathrm{i})\int_\diamond d^3x_2\, e^{-\mathrm{i}\mathbf{Q}_2\mathbf{x}_2} \int_\diamond d^3x_1\, \mathbf{G}^{<}_{\diamond p,n}(\mathbf{x}_1,t_1,\mathbf{x}_2,t_2) = \int_\diamond d^3x_2\, e^{-\mathrm{i}\mathbf{Q}_2\mathbf{x}_2}\,\langle I|\,\hat{n}(\mathbf{x},\tau)\,\hat{\mathbf{p}}\,|I\rangle \quad \text{with:}\;\; \tau = t_2 - t_1 > 0, \qquad (3.82)$$

we would arrive analogously at

$$\begin{aligned}
&\mathbf{e}_q \cdot\, (-\mathrm{i}) \int_\diamond d^3x_2\, e^{-\mathrm{i}\mathbf{Q}_2\mathbf{x}_2} \int_\diamond d^3x_1\, \mathbf{G}^{<}_{\diamond p,n}(\mathbf{x}_1,t_1,\mathbf{x}_2,t_2) \\
&= \lim_{q\to 0^+} \frac{1}{q}\int_\diamond d^3x \int_\diamond d^3x_2\, e^{-\mathrm{i}\mathbf{Q}_2\mathbf{x}_2}(-1)\frac{Q_2^2}{2}\;\langle I|\,\hat{n}(\mathbf{x}_2,\tau)\,\hat{n}(\mathbf{x})\,|I\rangle\, e^{\mathrm{i}\mathbf{q}\mathbf{x}}. \qquad (3.83)
\end{aligned}$$

By combining both amplitudes, we find that our initial time-ordered correlator of density and current-density (Eq. (3.72)) can indeed be related to a time-ordered density-density correlator[35]

$$\begin{aligned}
&\mathbf{e}_q \cdot \int_\diamond d^3x_2\, e^{-\mathrm{i}\mathbf{Q}_2\mathbf{x}_2} \int_\diamond d^3x_1\, \mathbf{P}_{I\diamond}(\mathbf{x}_1,t_1,\mathbf{x}_2,t_2) \\
&= \lim_{q\to 0^+} \frac{1}{q}\int_\diamond d^3x \int_\diamond d^3x_2\, e^{-\mathrm{i}\mathbf{Q}_2\mathbf{x}_2}(-1)\frac{Q_2^2}{2}\;\underbrace{\langle I|\,\hat{T}[\hat{n}(\mathbf{x}_1,t_1)\,\hat{n}(\mathbf{x}_2,t_2)]\,|I\rangle}_{\chi^{TO}(\mathbf{x}_1t_1,\mathbf{x}_2t_2)}\, e^{\mathrm{i}\mathbf{q}\mathbf{x}}. \qquad (3.84)
\end{aligned}$$

Finally, we need to relate the Fourier transformations above to sensibly partitioned Fourier transformations on the periodically-bounded crystalline domain $\diamond$. These need to take a form like

$$\int_\diamond d^3x \int_\diamond d^3x_2\, e^{\mathrm{i}\mathbf{q}\mathbf{x}} e^{-\mathrm{i}\mathbf{Q}_2\mathbf{x}_2} \Rightarrow \int_\diamond d^3x \int_\diamond d^3x_2\, e^{-\mathrm{i}(\mathbf{q}'+\mathbf{G}_1)\mathbf{x}} e^{-\mathrm{i}(-\mathbf{q}'+\mathbf{G}_2)\mathbf{x}_2}, \qquad (3.85)$$

wherein we have to identify the momenta $\mathbf{q}'$, $\mathbf{G}_1$ and $\mathbf{G}_2$:

- For determining $\mathbf{q}'$, we know from the definition of our discretized Fourier transforms that it should be small—specifically within the first Brillouin zone. As such, it is sensible to identify it directly with the previous $\mathbf{q}' = -\mathbf{q}$, for which the smallness is ensured via the limit $q \to 0^+$.
- With the above choice of $\mathbf{q}'$, we have already fixed $\mathbf{G}_1 = 0$ as well.

[35] We note that the definition of this density-density correlator differs from the initially outlined version (Eq. (3.67)). On the one hand, this is a time-ordered version while the initial one was retarded, but in addition, there is once again a factor of $-(i)$ differing.

- The splitting of $\mathbf{Q}_2$, finally, will prove slightly ambiguous. Applying both of the above conditions to Eq. (3.85), we would conclude $\mathbf{Q}_2 = \mathbf{G}_2 - \mathbf{q}'$ for full consistency. At the same time, we would like to approximate $\mathbf{Q}_2 \approx \mathbf{G}_2$, such that we retrieve $\mathbf{K}_{I\diamond}(0, \mathbf{G}_2, \omega)$ from the Fourier transform of Eq. (3.84). Given that the discrepancy merely amounts to the tiny momentum $\mathbf{q}$, which vanishes ultimately, we choose to apply both—formally different—identifications. That is, the former one on the right-hand side and the latter one on the left-hand side of Eq. (3.84).

Accounting for these newly identified momenta, we can rewrite Eq. (3.84)

$$\begin{aligned}
\mathbf{e}_q \cdot \mathbf{K}_{I\diamond}(0, \mathbf{G}_2, \omega) &= \mathbf{e}_q \cdot \int d\tau\, e^{\mathrm{i}\omega\tau} \int_\diamond d^3x_2\, e^{-\mathrm{i}\mathbf{G}\mathbf{x}_2} \int_\diamond d^3x_1\, \mathbf{P}_{I\diamond}(\mathbf{x}_1, t_1, \mathbf{x}_2, t_2) \\
&\approx \int d\tau\, e^{\mathrm{i}\omega\tau} \lim_{q\to 0^+} \frac{1}{q}(-1)\frac{(\mathbf{G}_2 - \mathbf{q}')^2}{2} \int_\diamond d^3x \int_\diamond d^3x_2\, e^{-\mathrm{i}(-\mathbf{q}'+\mathbf{G}_2)\mathbf{x}_2}\, e^{-\mathrm{i}\mathbf{q}'\mathbf{x}}\, \chi^{TO}(\mathbf{x}, 0, \mathbf{x}_2, \tau) \\
&\approx \lim_{q\to 0^+} \frac{-1}{q}\frac{G_2^2}{2}\, \chi^{TO}(\mathbf{q}' + 0, -\mathbf{q}' + \mathbf{G}_2, \omega) \\
&= \lim_{q\to 0^+} \frac{-1}{q}\frac{G_2^2}{2}\, \chi^{TO}(-\mathbf{q}, \mathbf{q} + \mathbf{G}_2, \omega),
\end{aligned} \tag{3.86}$$

where we have substituted our original $\mathbf{q}$ back in the last line.

In Eq. (3.86), we have achieved our main goal, i.e., we have obtained a relation that allows us to express our density–current-density correlator by means of a (time-ordered) density-density correlator. In the remainder of this section, we shall give some further remarks on its numerical evaluation. These should be understood in terms of a future outlook, however, as their computational pursuit and benchmark would extend beyond the scope of the present work.

Considering to evaluate Eq. (3.86) numerically, there is still the formal challenge to take the (numerical) limit $q \to 0^+$. In order to avoid possible convergence problems, we would suggest one last, and obvious, approximation. Namely, we suggest to settle for some finite but *small* Δq instead of an actual, infinitesimal limit[36]. Thereby, we arrive at

$$\boxed{\mathbf{e}_q \cdot \mathbf{K}_{I\diamond}(0, \mathbf{G}, \omega) \approx \frac{-1}{\Delta q}\frac{G^2}{2} \cdot \chi^{TO}(-\Delta q\, \mathbf{e}_q, \Delta q\, \mathbf{e}_q + \mathbf{G}, \omega)} \tag{3.87}$$

We consider this to be a very promising result. Except for one remaining reformulation from time-ordered to retarded response[37], this expression provides everything needed to harness the computational benefits of established density-response formalisms. In particular, it does not require any major changes to existing numerical codes. Instead, it can be evaluated in the standardized fashion, with any transformation relegated into straight-forward post-processing steps.

Thereby, we have obtained an easily applicable method that allows exploration of the nonlinear response function's properties beyond mean-field models. Even within its intrinsic limitation, i.e., its restriction to small optical momentum transfer, the expression promises a wide range of intriguing applications. Chief among these would be the investigation of (more) strongly correlated electronic systems—studying the imprints, which these correlation effects leave upon $\mathbf{K}_{I\diamond}(0, \mathbf{G}, \omega)$.

[36] We note that—as a matter of practical application—a finite remainder of Δq is always necessary, because together with $\mathbf{e}_q$ it defines the direction along which $\chi^{TO}(-\Delta q\mathbf{e}_q, \Delta q\mathbf{e}_q + \mathbf{G}, \omega)$ is evaluated. By virtue of the underlying limit, this corresponds to the projection, which is produced of $\mathbf{e}_q \cdot \mathbf{K}_{I\diamond}$.

[37] We note that the conversion from time-ordered to retarded response function can be carried out by means of few, algebraic reformulations—for the energy-range of our interest. The derivation of the respective relations proceeds largely analogous to our derivation of Eq. (A.170) in App. A.12. For more information, consider also Ref. [126].

Chapter 4

Electromagnetic fields

In this chapter, we shall concern ourselves with the electromagnetic fields that are involved in XOWM processes. Quite literally, these *x-ray* and *optical* fields constitute the essential ingredients for *x-ray-optical* wavemixing. Only in their presence may the nonlinear response of the electronic system be probed (recall Chpt. 3); and only if they are reasonably quantified can the nonlinear scattering yield be accurately predicted (see Chpt. 5). Consequently, we aim to provide a quantitative description of these fields, which integrates with our overall XOWM framework later on.

The central object, which we shall use to describe both x-ray and optical fields, will be their first-order coherence function throughout most of our work. This type of function has famously been used by Glauber to characterize the coherence of quantum fields in his seminal treatise [64]. More generally, coherence functions have played a central role in signal- and coherence-analysis, dating back to the 1930's at least [127].

In a first, introductory Sec. 4.1, we shall briefly recollect the general form of these coherence functions in our case and discuss variations on them for later applications.

Subsequently, we will dedicate Secs. 4.2 and 4.3 to individual discussions of the incident x-ray and optical fields, respectively. In both cases, we establish quantitative models[1], which will be applied in our simulations of XOWM throughout Chpt. 5.

In an additional section (4.4), we extend our model-building to include the quantitative characterization of 'vacuum'-fluctuations. This is a pre-requisite to describe spontaneous wavemixing processes, in particular XPDC, accurately.

[1] In striving for quantitative modelling on an absolute scale, our approach differs from many instances of nonlinear spectroscopy in the all-optical or XUV-domain. In these regimes, proportionality assessments and intuitive, plane-wave based modelling of the fields is often sufficient for comparison with experimental results. This is facilitated in particular, because the corresponding nonlinear processes are strong enough to be found and fitted during routine measurements. In contrast, our primary concern with many XOWM processes will be more fundamental, namely, whether they can be observed at all. Searching for them is, thus, greatly aided by quantitative predictions.

4.1 Coherence functions for x-ray and optical fields

In deriving our central expressions for XOWM processes, i.e., Eqs. 2.57 or 2.67, we found that the effect of the incident electromagnetic fields enters naturally in the form of first order coherence functions.

For the incoming x-ray field, we have identified its real-space formulation from Eq. (2.24) as

$$H^{(1)}_{\mu\nu}(\mathbf{x}_1,t_1,\mathbf{x}_2,t_2) = \mathrm{Tr}_{\mathrm{X\_IN}}\left\{\hat{\rho}_{\mathrm{X\_IN}}(0)\,(\hat{\mathbf{A}}^{(-)}_{\mathrm{x\_in}}(\mathbf{x}_1,t_1))_\mu\,(\hat{\mathbf{A}}^{(+)}_{\mathrm{x\_in}}(\mathbf{x}_2,t_2))_\nu\right\}, \tag{4.1}$$

while its Fourier-related counterpart takes on the form

$$\begin{aligned} Z^{(1)}_{\mu\nu}(\mathbf{k}_1,\omega_1,\mathbf{k}_2,\omega_2) &= \int d^3x_1 \int d^3x_2 \int dt_1 \int dt_2\; e^{\mathrm{i}\,(\mathbf{k}_1\cdot\mathbf{x}_1-\omega_1 t_1)}\; e^{-\mathrm{i}\,(\mathbf{k}_2\cdot\mathbf{x}_2-\omega_2 t_2)}\; H^{(1)}_{\mu\nu}(\mathbf{x}_1,t_1,\mathbf{x}_2,t_2) \\ &= \mathrm{Tr}_{\mathrm{X\_IN}}\left\{\hat{\rho}_{\mathrm{X\_IN}}(0)\,(\hat{\mathbf{A}}^{(+)}_{\mathrm{x\_in}}(\mathbf{k}_1,\omega_1))^\dagger_\mu\,(\hat{\mathbf{A}}^{(+)}_{\mathrm{x\_in}}(\mathbf{k}_2,\omega_2))_\nu\right\}. \end{aligned} \tag{4.2}$$

Similarly, we have found the correlation function for optical fields[2] (Eq. (2.47)) to be

$$H^{(1)\text{-full}}_{\nu\mu}(\mathbf{y}',t_2',\mathbf{y},t_2) = \mathrm{Tr}_{\mathrm{OPT}}\left\{\hat{\rho}_{\mathrm{OPT}}(0)\,(\hat{\mathbf{A}}_{\mathrm{opt}}(\mathbf{y}',t_2'))_\nu\,(\hat{\mathbf{A}}_{\mathrm{opt}}(\mathbf{y},t_2))_\mu\right\}, \tag{4.3}$$

which we have subsequently split into a classical, average part and superimposed quantum-fluctuations (recall Eqs. (2.54) and (2.55))

$$\bar{H}^{(1)}_{\nu\mu}(\mathbf{y}',t_2',\mathbf{y},t_2) = (\mathbf{A}_{\mathrm{opt\_avg}}(\mathbf{y}',t_2'))_\nu\,(\mathbf{A}_{\mathrm{opt\_avg}}(\mathbf{y},t_2))_\mu \tag{4.4}$$

$$\bar{S}^{(1)}_{\nu\mu}(\mathbf{y}',t_2',\mathbf{y},t_2) = \mathrm{Tr}_{\mathrm{OPT}}\left\{\hat{\rho}^{equ}_{\mathrm{OPT}}(\hat{\mathbf{A}}_{\mathrm{opt\_flu}}(\mathbf{y}',t_2'))_\nu\,(\hat{\mathbf{A}}_{\mathrm{opt\_flu}}(\mathbf{y},t_2))_\mu\right\}. \tag{4.5}$$

In essence, all of the above expressions are (closely) related to Glauber's first order coherence function[64]

$$G^{(1)}_{\mu\nu}(\mathbf{x}_1,t_1,\mathbf{x}_2,t_2) = \mathrm{Tr}\left\{\hat{\rho}(0)\,(\mathbf{E}^{(-)}(\mathbf{x}_1,t_1))_\mu\,(\mathbf{E}^{(+)}(\mathbf{x}_2,t_2))_\nu\right\}. \tag{4.6}$$

Their most notable difference results from the fact that we have formulated our framework on the basis of electromagnetic vector potentials $\mathbf{A}(\mathbf{x},t)$ rather than electromagnetic fields $\mathbf{E}(\mathbf{x},t)$, which underlie the majority of quantum-optics formulations (such as Refs. [53, 64, 128]). We can easily establish a connection among the two, using

$$G^{(1)}_{\mu\nu}(\mathbf{x}_1,t_1,\mathbf{x}_2,t_2) = \alpha^2\,\frac{\partial}{\partial t_1}\frac{\partial}{\partial t_2}\,H^{(1)}_{\mu\nu}(\mathbf{x}_1,t_1,\mathbf{x}_2,t_2). \tag{4.7}$$

This connection becomes all the more useful, as measurements or simulations pertaining to field coherences are regularly reported in the field-based framework—many of them [129–136] resorting to the cross-spectral density as their quantity of choice:

$$W^{(1)}_{\mu\nu}(\mathbf{x}_1,\omega_1,\mathbf{x}_2,\omega_2) = \int dt_1 \int dt_2\; e^{-\mathrm{i}\,\omega_1 t_1}\; e^{\mathrm{i}\,\omega_2 t_2}\; G^{(1)}_{\mu\nu}(\mathbf{x}_1,t_1,\mathbf{x}_2,t_2). \tag{4.8}$$

Transferring relation Eq. (4.7) into the Fourier domain, we can make immediate use of this cross spectral

[2] We point out that the optical field's correlation function differs slightly from the previous Eq. (4.1). The field-operators above have been restricted to positive and negative frequency part, each, while the optical case's expression involves full fields in both positions. This is a reflection of the fact that we consider (optical) photo-emission (DFG, XPDC) and absorption (SFG) in the same expression.

density, in that it relates to $Z^{(1)}_{\mu\nu}$:

$$Z^{(1)}_{\mu\nu}(\mathbf{k}_1,\omega_1,\mathbf{k}_2,\omega_2) = \int d^3x_1 \int d^3x_2\; e^{\mathrm{i}\mathbf{k}_1\cdot\mathbf{x}_1}\; e^{-\mathrm{i}\mathbf{k}_2\cdot\mathbf{x}_2}\; \frac{1}{\alpha^2\,\omega_1\omega_2}\; W^{(1)}_{\mu\nu}(\mathbf{x}_1,\omega_1,\mathbf{x}_2,\omega_2). \tag{4.9}$$

We note for further reference that we have collated a range of such interrelations in App. A.8.

On the basis of the coherence functions, which we have outlined above, we shall assess the x-ray and optical fields individually in the following sections. There, our aim will be to find (approximate) models for each of them, while remaining compatible to the overall framework.

4.2 Models for x-ray sources

Setting out to model the electromagnetic field correlators, which are needed to compute XOWM processes from Eqs. (2.57) or (2.67), we concern ourselves with the contribution of x-rays first. Herunto, we shall consider two conceptually different approaches:

The first will focus on so-called Gaussian Schell-model (GSM) beams. These provide a simple and therefore analytically tractable model of the first order coherence of modern x-ray sources.

While the second approach—which we shall merely outline, but not discuss in detail—considers the use of measured data or (numerical) simulation as an input for the cross spectral density.

4.2.1 Gaussian Schell-model for x-ray pulses

In our main attempt at describing the incoming x-ray-field for XOWM, we pursue a model-based formulation, which has the benefit of keeping many expressions analytically tractable. In particular, we focus on the Gaussian Schell-model (GSM)[3]. The GSM has seen wide-spread application to cases of synchrotron radiation for quite some time [131, 138–142] and—while it has known shortcomings (cf. Ref. [142])—it has also proven robust in its extension towards FEL pulses as well [129–131, 136]. As such, the model provides a well-rounded basis for our developments. In addition, we can appreciate its relative simplicity below.

In order to derive a suitable expression for $Z^{(1)}_{\mu\nu}$ in terms of pulsed GSM beams, we start from a definition of the model akin to Dr. Singer's Eq. (2.93) in Ref. [131]:

$$\begin{aligned} G^{(1)}(\mathbf{x}_1,t_1,\mathbf{x}_2,t_2) \Rightarrow G^{(1)}((\mathbf{x}_1^\perp,z_0),t_1,(\mathbf{x}_2^\perp,z_0),t_2) = G_0\; \exp\left(-\frac{(\mathbf{x}_1^\perp)^2+(\mathbf{x}_2^\perp)^2}{4\sigma^2} - \frac{(\mathbf{x}_2^\perp-\mathbf{x}_1^\perp)^2}{2\xi^2}\right) \\ \times \exp\left(-\frac{(t_1-t_0)^2+(t_2-t_0)^2}{4T^2} - \frac{(t_2-t_1)^2}{2\tau_c^2} - \mathrm{i}\omega_0\,(t_2-t_1)\right). \end{aligned} \tag{4.10}$$

We note up-front that—at this point and throughout most of the following reformulation—we will use a simplified form of $G^{(1)}(\mathbf{x}_1,t_1,\mathbf{x}_2,t_2)$ to ease the reading. In particular, we shall ignore / suppress the tensorial nature of the correlation function, which encodes the polarization properties of the field, as well as possible asymmetries of the beam profile. Both complications will be restored at the end of the discussion.

The definition above concerns Glauber's correlation function $G^{(1)}(\mathbf{x}_1,t_1,\mathbf{x}_2,t_2)$ for an x-ray beam inside a single plane at $z=z_0$. We take this plane as the source-plane of the radiation and associate it

[3] We note that the name Gaussian **Sc**hell model does *not* bear reference to the concept of a 'shell', but is instead a tribute to Dr. A. C. Schell and his instrumental treatise on antennas[137].

with the physical position of the undulator structure in a SR source or FEL. The model is parametrized through:

- σ, which measures the transverse beam profile (at the source point),
- ξ, giving the transverse coherence length (again at the source),
- T, specifying the average pulse duration,
- τ_c, which marks the temporal coherence length,
- ω_0, which gives the central photon energy of the beam and, finally,
- G_0, as a measure of the overall intensity of the field.

For a detailed discussion on how to relate these parameters to experimental observations, we refer the reader to App. A.11.

Deviating from Singer's definition, we have adapted the phase term of Eq. (4.10) to be in line with our field and Fourier-convention (cf. App. A.7). More importantly (see later discussion), we have added the parameter t_0, which can be used to calibrate the (average) arrival time of the pulse.

Converting Eq. (4.10) into the spectral domain, we write

$$\begin{aligned} W^{(1)}((\mathbf{x}_1^\perp, z_0), \omega_1, (\mathbf{x}_2^\perp, z_0), \omega_2) &= \int dt_1 \int dt_2 \; e^{-\mathrm{i}\,\omega_1 t_1} \; e^{\mathrm{i}\,\omega_2 t_2} \; G^{(1)}((\mathbf{x}_1^\perp, z_0), t_1, (\mathbf{x}_2^\perp, z_0), t_2) \\ W^{(1)}(\ldots) &= G_0 \; \exp\left(-\frac{(\mathbf{x}_1^\perp)^2 + (\mathbf{x}_2^\perp)^2}{4\sigma^2} - \frac{(\mathbf{x}_2^\perp - \mathbf{x}_1^\perp)^2}{2\xi^2} \right) e^{\mathrm{i}\, t_0 (\omega_2 - \omega_1)} \int dt_1 \int dt_2 \; e^{-\mathrm{i}\,\omega_1 t_1} \; e^{\mathrm{i}\,\omega_2 t_2} \\ &\quad \times \exp\left(-\frac{t_1^2 + t_2^2}{4T^2} - \frac{(t_2 - t_1)^2}{2\tau_c^2} - \mathrm{i}\omega_0 (t_2 - t_1) \right), \end{aligned} \tag{4.11}$$

where we have shifted both integrations by t_0 resulting in an overall phase factor. Next, we make use of the coordinate transformation

$$\Theta = (t_1 + t_2)/2, \quad \tau = t_2 - t_1 \qquad \Leftrightarrow \qquad t_1 = \Theta - \tau/2, \quad t_2 = \Theta + \tau/2, \tag{4.12}$$

which has a Jacobian of modulus 1, and find

$$\begin{aligned} W^{(1)}((\mathbf{x}_1^\perp, z_0), \omega_1, (\mathbf{x}_2^\perp, z_0), \omega_2) &= G_0 \; e^{\left(-\frac{(\mathbf{x}_1^\perp)^2 + (\mathbf{x}_2^\perp)^2}{4\sigma^2} - \frac{(\mathbf{x}_2^\perp - \mathbf{x}_1^\perp)^2}{2\xi^2}\right)} \; e^{\mathrm{i}\, t_0 (\omega_2 - \omega_1)} \int d\Theta \; e^{\mathrm{i}\,\Theta(\omega_2 - \omega_1)} \; e^{-\Theta^2/2T^2} \\ &\quad \times \int d\tau \; e^{\mathrm{i}\,\tau(\omega_1 + \omega_2)/2} \; e^{-\mathrm{i}\,\tau\omega_0} \; e^{-\tau^2/2\tau_c^2} \; e^{-\tau^2/8T^2}. \end{aligned} \tag{4.13}$$

Adopting Singer's abbreviations

$$\bar{\omega} = (\omega_1 + \omega_2)/2, \quad \Delta\omega = \omega_2 - \omega_1 \qquad \Leftrightarrow \qquad \omega_1 = \bar{\omega} - \Delta\omega/2, \quad \omega_2 = \bar{\omega} + \Delta\omega/2 \tag{4.14}$$

$$\text{as well as } \; \Omega = \sqrt{\frac{1}{4T^2} + \frac{1}{\tau_c^2}}, \tag{4.15}$$

we shorten Eq. (4.13) and solve the commonplace Gaussian integrals[4] to find:

$$W^{(1)}(\ldots) = G_0 \; e^{\left(-\frac{(\mathbf{x}_1^\perp)^2 + (\mathbf{x}_2^\perp)^2}{4\sigma^2} - \frac{(\mathbf{x}_2^\perp - \mathbf{x}_1^\perp)^2}{2\xi^2}\right)} \; e^{\mathrm{i}\, t_0 \Delta\omega} \sqrt{2\pi}\, T \; e^{-\Delta\omega^2 T^2/2} \; \sqrt{2\pi}\, \Omega^{-1} \; e^{-(\bar{\omega} - \omega_0)^2/2\Omega^2}. \tag{4.16}$$

[4] For a listing of common integrals and their solutions, see App. A.15 for integrals.

We note that the cross spectral density, as it stands above, still refers to the electromagnetic field in terms of $\mathbf{E}(\mathbf{x},t)$[5]. However, we are interested in field correlators on the level of the electromagnetic vector-potential $\mathbf{A}(\mathbf{x},t)$ instead. Thus, seeking to convert the cross spectral density of Eq. (4.16) into an equivalent expression for vector-potentials, we can extend the reasoning of Eq. (4.7) to[6]:

$$V^{(1)}(\mathbf{x}_1,\omega_1,\mathbf{x}_2,\omega_2) = \frac{1}{\alpha^2\,\omega_1\,\omega_2}\,W^{(1)}(\mathbf{x}_1,\omega_1,\mathbf{x}_2,\omega_2). \tag{4.17}$$

Applying this to Eq. (4.16), we obtain

$$\begin{aligned} V^{(1)}((\mathbf{x}_1^\perp,z_0),\omega_1,(\mathbf{x}_2^\perp,z_0),\omega_2) &= \frac{2\pi\,G_0\,T}{\alpha^2\,\omega_1\omega_2\,\Omega}\,\underbrace{e^{\left(-\frac{(\mathbf{x}_1^\perp)^2+(\mathbf{x}_2^\perp)^2}{4\sigma^2}-\frac{(\mathbf{x}_2^\perp-\mathbf{x}_1^\perp)^2}{2\xi^2}\right)}}_{J}\,e^{\mathrm{i}t_0\Delta\omega}\,\underbrace{e^{-\Delta\omega^2T^2/2}\,e^{-(\bar\omega-\omega_0)^2/2\Omega^2}}_{W} \\ &= \frac{2\pi\,G_0\,T}{\alpha^2\,\omega_1\omega_2\,\Omega}\,J(\mathbf{x}_1^\perp,\mathbf{x}_2^\perp)\,e^{\mathrm{i}t_0\Delta\omega}\,W(\omega_1,\omega_2). \end{aligned} \tag{4.18}$$

In its last line, we have introduced two sub-functions for abbreviation-purposes. These are defined largely in accordance with Ref. [136] and read[7]

$$J(\mathbf{x}_1^\perp,\mathbf{x}_2^\perp) = \exp\Big[-\frac{(\mathbf{x}_1^\perp)^2+(\mathbf{x}_2^\perp)^2}{4\sigma^2}-\frac{(\mathbf{x}_1^\perp-\mathbf{x}_2^\perp)^2}{2\xi^2}\Big] \tag{4.19}$$

$$\begin{aligned} W(\omega_1,\omega_2) &= e^{-\Delta\omega^2T^2/2}\,e^{-(\bar\omega-\omega_0)^2/2\Omega^2} \\ &= \exp\Big[-\frac{(\omega_1-\omega_0)^2+(\omega_2-\omega_0)^2}{4\Omega^2}-\frac{(\omega_1-\omega_2)^2}{2\Omega_c^2}\Big]. \end{aligned} \tag{4.20}$$

With Eq. (4.18) established, one final preparatory step is required, before we can Fourier transform the correlation function into $Z^{(1)}_{\mu\nu}$. This concerns the propagation of $V^{(1)}((\mathbf{x}_1^\perp,z_0),\omega_1,(\mathbf{x}_2^\perp,z_0),\omega_2)$ away from the source-plane at z_0. Only thereafter, would *all* coordinates of $V^{(1)}(\mathbf{x}_1,\omega_1,\mathbf{x}_2,\omega_2)$ be amenable to transformation.

For simplicity, we consider the required propagation in its simplemost case, i.e., in terms of free propagation[8]. Thereunto, we make use of the propagator derived in App. A.9 and, in particular, its application to $V^{(1)}$ as of App. A.9.5. The full result of this operation, already including the Fourier integrals, reads

$$\begin{aligned} Z^{(1)}(\mathbf{k}_1,\omega_1,\mathbf{k}_2,\omega_2) = \frac{(2\pi)^3\,G_0\,T}{\alpha^2\,\omega_1\omega_2\,\Omega}\,&\delta(k_1^{\shortparallel}-k_{1\_0}^{\shortparallel})\,\delta(k_2^{\shortparallel}-k_{2\_0}^{\shortparallel})\,e^{\mathrm{i}\,z_0(k_1^{\shortparallel}-k_2^{\shortparallel})}\,e^{\mathrm{i}t_0\Delta\omega}\,e^{-\Delta\omega^2T^2/2}\,e^{-(\bar\omega-\omega_0)^2/2\Omega^2} \\ &\times\int d^2x_1^\perp\int d^2x_2^\perp\,e^{\mathrm{i}\mathbf{k}_1^\perp\cdot\mathbf{x}_1^\perp}\,e^{-\mathrm{i}\mathbf{k}_2^\perp\cdot\mathbf{x}_2^\perp}\,e^{\left(-\frac{(\mathbf{x}_1^\perp)^2+(\mathbf{x}_2^\perp)^2}{4\sigma^2}-\frac{(\mathbf{x}_2^\perp-\mathbf{x}_1^\perp)^2}{2\xi^2}\right)}\,. \end{aligned} \tag{4.21}$$

Herein, the newly introduced, longitudinal wave vectors $k_i^{\shortparallel}$ are constrained to the condition $k_{i\_0}^{\shortparallel}=\sqrt{\alpha^2\omega_i^2-\left|\mathbf{k}_i^\perp\right|^2}$ (cf. App. A.9).

The spatial integrations can be resolved analogously to the temporal ones above. To this end, we

[5] We should specify that—strictly—the cross spectral density given in Eq. (4.16) refers to something even simpler than $\mathbf{E}(\mathbf{x},t)$, namely to a scalar version thereof. However, we think our general point is sufficiently clear in either case.

[6] We note that both relations (4.7) and (4.17) among correlation functions can, of course, be traced to the fundamental relation of $\mathbf{E}(\mathbf{x},t)=-\alpha(\partial/\partial t)\mathbf{A}(\mathbf{x},t)$ for transverse fields and vector potentials.

[7] We note with caution that—as of this writing—the definition of $W(\omega_1,\omega_2)$ differs slightly from the version used in our manuscript on XOWM [21]. There, the phase-term is included in its definition for brevity. However, the expressions turn out to be more versatile in the form of Eq. (4.20).

[8] We note that we shall extend our modelling slightly beyond the case of trivial propagation later on, as we include a monochromator's transfer function as well. Once again, we recur to the developments of App. A.9 in doing so.

introduce new variables

$$\bar{\mathbf{x}}^{\perp} = (\mathbf{x}_1^{\perp} + \mathbf{x}_2^{\perp})/2, \quad \Delta\mathbf{x} = \mathbf{x}_2^{\perp} - \mathbf{x}_1^{\perp} \qquad \Leftrightarrow \qquad \mathbf{x}_1^{\perp} = \bar{\mathbf{x}}^{\perp} - \Delta\mathbf{x}/2, \quad \mathbf{x}_2^{\perp} = \bar{\mathbf{x}}^{\perp} + \Delta\mathbf{x}^{\perp}/2, \tag{4.22}$$

thus separating the integrals

$$\begin{aligned} &\int d^2x_1^{\perp} \int d^2x_2^{\perp}\; e^{\mathrm{i}\mathbf{k}_1^{\perp}\cdot\mathbf{x}_1^{\perp}}\; e^{-\mathrm{i}\mathbf{k}_2^{\perp}\cdot\mathbf{x}_2^{\perp}}\; e^{(-\frac{(\mathbf{x}_1^{\perp})^2+(\mathbf{x}_2^{\perp})^2}{4\sigma^2} - \frac{(\mathbf{x}_2^{\perp}-\mathbf{x}_1^{\perp})^2}{2\xi^2})} \\ &= \int d^2\bar{x}^{\perp} e^{\mathrm{i}\bar{\mathbf{x}}^{\perp}(\mathbf{k}_1^{\perp}-\mathbf{k}_2^{\perp})}\; e^{-(\bar{\mathbf{x}}^{\perp})^2/2\sigma^2} \int d^2\Delta x^{\perp}\; e^{-\mathrm{i}\Delta\mathbf{x}(\mathbf{k}_1^{\perp}+\mathbf{k}_2^{\perp})}\; e^{-(\Delta\mathbf{x}^{\perp})^2/2\delta^2}\;. \end{aligned} \tag{4.23}$$

Note that we have adopted the new notation $\delta^{-1} = \sqrt{(2\sigma)^{-2} + \xi^{-2}}$, again in congruence with Singer's use in Ref. [131]. Solving the above integrations provides us with the overall expression for the field:

$$\begin{aligned} Z^{(1)}(\mathbf{k}_1,\omega_1,\mathbf{k}_2,\omega_2) = \frac{(2\pi)^5 G_0 T \sigma^2 \delta^2}{\alpha^2 \omega_1 \omega_2 \Omega}\; &\delta(k_1^{\shortparallel} - k_{1\_0}^{\shortparallel})\; \delta(k_2^{\shortparallel} - k_{2\_0}^{\shortparallel})\; e^{\mathrm{i}z_0(k_1^{\shortparallel}-k_2^{\shortparallel})}\; e^{\mathrm{i}t_0\Delta\omega}\; e^{-\Delta\omega^2 T^2/2} \\ &\times e^{-(\bar{\omega}-\omega_0)^2/2\Omega^2}\; e^{-(\mathbf{k}_2^{\perp}-\mathbf{k}_1^{\perp})^2\sigma^2/2}\; e^{-(\mathbf{k}_1^{\perp}+\mathbf{k}_2^{\perp})^2\delta^2/8}. \end{aligned} \tag{4.24}$$

This result is nicely compact and basically sufficient for our purposes. It clearly exhibits the Gaussian properties of its ancestral GSM and, thus, conserves most of its analytical simplicity.

There is one aspect in the above expression, however, which would turn out to become annoying later on—if kept unchecked. This concerns the prominent presence of the reference coordinate z_0[9]. To largely rid ourselves of its influence, we can re-base our calculation to a reference point z_r closer to the sample. In doing so, we will encounter a few opportunities to simplify the expression further and act upon them. The pertaining derivations will be outlined below.

4.2.1.a Propagation and the paraxial approximation

In this last section on the GSM for x-ray sources, we shall elaborate on the form of a propagated Gaussian beam and discuss the paraxial approximation (for $Z^{(1)}$) in the process.

As a first objective, we seek to obtain an expression for $V^{(1)}((\mathbf{x}_1^{\perp}, z_r), \omega_1, (\mathbf{x}_2^{\perp}, z_r), \omega_2)$, which no longer resides at its initial source-plane (z_0), but is instead propagated to a new 'reference'-plane z_r. Of particular interest to us, will be reference planes close to the actual sample position. There are two, equivalent, ways of reaching this expression. We may either start from the real-space expression of $V^{(1)}((\mathbf{x}_1^{\perp}, z_0), \omega_1, (\mathbf{x}_2^{\perp}, z_0), \omega_2)$ in Eq. (4.18) and explicitly propagate this using the results from App. A.9. Or alternatively, we may recall that we have effectively performed this propagation before, while deriving Eq. (4.24). As a matter of fact, this reciprocal-space expression *implies* knowledge of $V^{(1)}$ across all of

[9] We note that the expression (4.24) can be acutely sensitive to the value of z_0. This would not pose a problem, as long as its 'correct' numerical value was known; however, most sources will state only order-of-magnitude estimates on these at best. It is thus highly advisable to rid ourselves of this dependence—or reduce its influence at least.

real-space. By simply transforming back, we may thus obtain the desired

$$\begin{aligned} V^{(1)}((\mathbf{x}_1^\perp,z_r),\omega_1,(\mathbf{x}_2^\perp,z_r),\omega_2) &= \frac{1}{(2\pi)^6}\int d^3k_1\int d^3k_2\; e^{-\mathrm{i}\mathbf{k}_1^\perp\cdot\mathbf{x}_1^\perp}\, e^{-\mathrm{i}k_1^\parallel\cdot z_r}\, e^{\mathrm{i}\mathbf{k}_2^\perp\cdot\mathbf{x}_2^\perp}\, e^{\mathrm{i}k_2^\parallel\cdot z_r}\, Z^{(1)}(\mathbf{k}_1,\omega_1,\mathbf{k}_2,\omega_2) \\ &= \frac{G_0\,T\,\sigma^2\,\delta^2}{2\pi\,\alpha^2\,\omega_1\,\omega_2\,\Omega}\, W(\omega_1,\omega_2)\, e^{\mathrm{i}t_0\Delta\omega} \\ &\times\int d^2k_1^\perp\int d^2k_2^\perp\; e^{-\mathrm{i}\mathbf{k}_1^\perp\cdot\mathbf{x}_1^\perp}\; e^{\mathrm{i}\mathbf{k}_2^\perp\cdot\mathbf{x}_2^\perp}\; e^{-(\mathbf{k}_2^\perp-\mathbf{k}_1^\perp)^2\sigma^2/2}\; e^{-(\mathbf{k}_1^\perp+\mathbf{k}_2^\perp)^2\delta^2/8} \\ &\times\int dk_1^\parallel\int dk_2^\parallel\; e^{-\mathrm{i}k_1^\parallel\cdot z_r}\; e^{\mathrm{i}k_2^\parallel\cdot z_r}\; \delta(k_1^\parallel-k_{1\_0}^\parallel)\;\delta(k_2^\parallel-k_{2\_0}^\parallel)\; e^{\mathrm{i}z_0(k_1^\parallel-k_2^\parallel)}. \end{aligned} \tag{4.25}$$

Before we perform the Fourier transformations in the transverse coordinates, we shall inspect the phase-terms of the last line more closely. Combining all contributions into $\exp(\mathrm{i}(z_0-z_r)(k_{1\_0}^\parallel-k_{2\_0}^\parallel))$, we find in this a good starting point for further approximation.

More specifically, we shall employ a version of the paraxial approximation, which we will motivate below. Having used the δ-constraints, the longitudinal momenta in the phase-term are each given by

$$k_{i\_0}^\parallel=\sqrt{\frac{\omega_i^2}{c^2}-\left|\mathbf{k}_i^\perp\right|^2}\approx\frac{\omega_i}{c}\left(1-\frac{1}{2}\frac{\left|\mathbf{k}_i^\perp\right|^2}{\left|\mathbf{k}_i\right|^2}+\frac{1}{8}\frac{\left|\mathbf{k}_i^\perp\right|^4}{\left|\mathbf{k}_i\right|^4}-\ldots\right), \tag{4.26}$$

which we have further expanded into its Taylor series. For typical x-ray beams at SR sources or FELs, an early truncation of this series is a viable approximation, because their intrinsic divergence is very small, i.e., $\Theta\sim{}^{|\mathbf{k}^\perp|}/_{|\mathbf{k}|}\sim 10^{-6}\ldots10^{-4}$ (cf. Ref. [131], for instance, or parameters of Chpt. 5). In fact, the contribution of the third term is already irrelevant for the exponential expression, if we assume Singer's values for $|z_0|\approx 100\ldots1000$ m [131] in combination with even smaller values for z_r and roughly Ångström wavelength:

$$|z_0|\;\frac{\omega_i}{c}\frac{1}{8}\frac{\left|\mathbf{k}_i^\perp\right|^4}{\left|\mathbf{k}_i\right|^4}=|z_0|\;\frac{2\pi}{\lambda_i}\frac{1}{8}\frac{\left|\mathbf{k}_i^\perp\right|^4}{\left|\mathbf{k}_i\right|^4}\lesssim 1000\;\frac{2\pi}{10^{-10}}\frac{1}{8}(10^{-4})^4\ll 2\pi. \tag{4.27}$$

Employing this insight, we can write the remaining terms inside the phase-factor as

$$\begin{aligned} \exp(\mathrm{i}(z_0-z_r)(k_{1\_0}^\parallel-k_{2\_0}^\parallel)) &\approx \exp\left(\mathrm{i}(z_0-z_r)\left(\frac{\omega_1}{c}-\frac{\omega_2}{c}\right)\right)\;\exp\left(\mathrm{i}\frac{(z_0-z_r)\,c}{2}\left(\frac{(\mathbf{k}_2^\perp)^2}{\omega_2}-\frac{(\mathbf{k}_1^\perp)^2}{\omega_1}\right)\right) \\ &\approx e^{-\mathrm{i}(z_0-z_r)\,\alpha\Delta\omega}\; e^{\mathrm{i}\frac{(z_0-z_r)}{2\alpha\bar\omega}((\mathbf{k}_2^\perp)^2-(\mathbf{k}_1^\perp)^2)} \\ &= e^{-\mathrm{i}(z_0-z_r)\,\alpha\Delta\omega}\; e^{\mathrm{i}\frac{(z_0-z_r)}{\alpha\bar\omega}\bar{\mathbf{k}}^\perp\cdot\Delta\mathbf{k}^\perp}. \end{aligned} \tag{4.28}$$

In writing this paraxial approximation, we have also simplified each energy denominator to lowest order in $\bar\omega$ (see below)

$$\frac{1}{\bar\omega\pm\Delta\omega/2}=\frac{1}{\bar\omega}\left(1\mp\frac{\Delta\omega}{2\bar\omega}\pm\ldots\right). \tag{4.29}$$

Upon re-inserting Eq. (4.28) into our earlier expression for $V^{(1)}$ (Eq. (4.25)),

$$\begin{aligned} V^{(1)}((\mathbf{x}_1^\perp, z_r), \omega_1, (\mathbf{x}_2^\perp, z_r), \omega_2) = \frac{G_0\, T\, \sigma^2\, \delta^2}{2\pi\, \alpha^2\, \omega_1 \omega_2\, \Omega}\, W(\omega_1, \omega_2)\, e^{\mathrm{i} t_0 \Delta\omega} \\ \times \int d^2k_1^\perp \int d^2k_2^\perp\, e^{-\mathrm{i}\mathbf{k}_1^\perp \cdot \mathbf{x}_1^\perp}\, e^{\mathrm{i}\mathbf{k}_2^\perp \cdot \mathbf{x}_2^\perp}\, e^{-(\mathbf{k}_2^\perp - \mathbf{k}_1^\perp)^2 \sigma^2/2}\, e^{-(\mathbf{k}_1^\perp + \mathbf{k}_2^\perp)^2 \delta^2/8} \\ \times e^{-\mathrm{i}(z_0 - z_r)\, \alpha \Delta\omega}\, e^{\mathrm{i}\, \frac{(z_0 - z_r)}{\alpha \bar{\omega}} \bar{\mathbf{k}}^\perp \cdot \Delta\mathbf{k}^\perp}, \end{aligned} \tag{4.30}$$

we find the presence of *two* compatible phase-terms by now. Each of these involves $\Delta\omega$, viz. $e^{-\mathrm{i}(z_0 - z_r)\, \alpha \Delta\omega}$ and $e^{\mathrm{i}\Delta\omega t_0}$. Both are related to a choice of reference frame—specifically, they determine the spatial (z_0) or temporal (t_0) distance of the radiation source from the respective origin (0). While it will turn out to be beneficial to have the spatial origin located at the center of the scattering target (thereby fixing upstream values of $z_0 < 0$), the choice of $t = 0$ is to some degree arbitrary.

In order to simplify our expression, we may therefore choose $t_0 = z_0/c$, making the aforementioned exponentials largely cancel out[10]. Thereafter, the correlator reads

$$\begin{aligned} V^{(1)}((\mathbf{x}_1^\perp, z_r), \omega_1, (\mathbf{x}_2^\perp, z_r), \omega_2) = \frac{G_0\, T\, \sigma^2\, \delta^2}{2\pi\, \alpha^2\, \omega_1 \omega_2\, \Omega}\, W(\omega_1, \omega_2)\, e^{\mathrm{i} z_r\, \alpha \Delta\omega} \int d^2k_1^\perp \int d^2k_2^\perp\, e^{-\mathrm{i}\mathbf{k}_1^\perp \cdot \mathbf{x}_1^\perp}\, e^{\mathrm{i}\mathbf{k}_2^\perp \cdot \mathbf{x}_2^\perp} \\ \times e^{-(\mathbf{k}_2^\perp - \mathbf{k}_1^\perp)^2 \sigma^2/2}\, e^{-(\mathbf{k}_1^\perp + \mathbf{k}_2^\perp)^2 \delta^2/8}\, e^{\mathrm{i}\, \frac{(z_0 - z_r)}{\alpha \bar{\omega}} \bar{\mathbf{k}}^\perp \cdot \Delta\mathbf{k}^\perp}. \end{aligned} \tag{4.31}$$

We can resolve the remaining transformations by switching to sum- and difference coordinates once again, i.e.,

$$\bar{\mathbf{x}}^\perp = (\mathbf{x}_1^\perp + \mathbf{x}_2^\perp)/2, \quad \Delta\mathbf{x} = \mathbf{x}_2^\perp - \mathbf{x}_1^\perp \quad \Leftrightarrow \quad \mathbf{x}_1^\perp = \bar{\mathbf{x}}^\perp - \Delta\mathbf{x}/2, \quad \mathbf{x}_2^\perp = \bar{\mathbf{x}}^\perp + \Delta\mathbf{x}^\perp/2 \tag{4.32}$$

as well as

$$\bar{\mathbf{k}}^\perp = (\mathbf{k}_1^\perp + \mathbf{k}_2^\perp)/2, \quad \Delta\mathbf{k} = \mathbf{k}_2^\perp - \mathbf{k}_1^\perp \quad \Leftrightarrow \quad \mathbf{k}_1^\perp = \bar{\mathbf{k}}^\perp - \Delta\mathbf{k}/2, \quad \mathbf{k}_2^\perp = \bar{\mathbf{k}}^\perp + \Delta\mathbf{k}^\perp/2. \tag{4.33}$$

Thus, we find

$$\begin{aligned} V^{(1)}((\mathbf{x}_1^\perp, z_r), \omega_1, (\mathbf{x}_2^\perp, z_r), \omega_2) = \frac{G_0\, T\, \sigma^2\, \delta^2}{2\pi\, \alpha^2\, \omega_1 \omega_2\, \Omega}\, e^{-\Delta\omega^2 T^2/2}\, e^{-(\bar{\omega} - \omega_0)^2/2\Omega^2} e^{\mathrm{i} z_r\, \alpha \Delta\omega} \\ \times \frac{(2\pi)^2}{\delta^2\, \sigma^2\, (\Delta(z_r))^2}\, e^{-(\Delta\mathbf{x}^\perp)^2/2(\delta\Delta(z_r))^2}\, e^{\mathrm{i}\Delta\mathbf{x}^\perp \cdot \bar{\mathbf{x}}^\perp\, \alpha\, \bar{\omega}/R(z_r)} e^{-(\bar{\mathbf{x}}^\perp)^2/2(\sigma\Delta(z_r))^2} \\ = \frac{G_0\, T\, 2\pi}{\alpha^2\, \omega_1 \omega_2\, \Omega\, (\Delta(z_r))^2}\, W(\omega_1, \omega_2)\, e^{\mathrm{i} z_r\, \alpha \Delta\omega}\, e^{-(\Delta\mathbf{x}^\perp)^2/2(\delta\Delta(z_r))^2}\, e^{\mathrm{i}\Delta\mathbf{x}^\perp \cdot \bar{\mathbf{x}}^\perp\, \alpha\, \bar{\omega}/R(z_r)} e^{-(\bar{\mathbf{x}}^\perp)^2/2(\sigma\Delta(z_r))^2}. \end{aligned} \tag{4.34}$$

This result represents a Gaussian beam in itself, albeit featuring scaled parameters $\sigma \to \sigma\,\Delta(z_r)$ and $\delta \to \delta\,\Delta(z_r)$. In these, we have identified the scaling function

$$\Delta(z) = \sqrt{1 + \left(\frac{z - z_0}{z_{\mathrm{eff}}}\right)^2}, \qquad \text{where: } z_{\mathrm{eff}} = \alpha\, \bar{\omega}\, \sigma\, \delta, \tag{4.35}$$

which agrees with the definition by Singer as well [131].

[10] Note that the absolute choice of $t = 0$ is arbitrary, but the *relative* timing of external fields (and later possibly electronic excitations) has to be maintained, of course. Besides the obvious simplification, our choice also complies with the convention of scattering theory to locate the scattering event at $t = 0$. As an optional exercise, we note that the centring of the x-ray pulse's peak intensity around $t = 0$, may readily be shown using the expressions for an intensity observable derived in App. A.10. Presuming the choice $t_0 = z_0/c$, this will show x-ray pulses reaching $z = 0$ at $t = 0$.

In addition to the scaling factors, we find a spatially dependent phase term in Eq. (4.34). This is well-known as the curvature phase from regular Gaussian beams. It was naturally absent from the model, while we have been examining it merely at the source-plane (i.e., beam waist), but makes its appearance now as an effect of outwards propagation. The radius of curvature imprinted on the wavefront is given by

$$R(z) = (z - z_0)\left(1 + \left(\frac{z_{\text{eff}}}{z - z_0}\right)^2\right). \tag{4.36}$$

Having thus enhanced our understanding of the Gaussian beam-propagation within the context of our GSM. We want to transfer the incurred simplifications back into our expression for $Z^{(1)}$. Even with the new reference plane at z_r, we can obviously transform Eq. (4.34) in the same way, as we did at z_0 within Eq. (4.21), i.e., applying

$$\begin{aligned} Z^{(1)}(\mathbf{k}_1, \omega_1, \mathbf{k}_2, \omega_2) &= (2\pi)^2\, \delta(k_1^{\shortparallel} - k_{1\_0}^{\shortparallel})\, \delta(k_2^{\shortparallel} - k_{2\_0}^{\shortparallel})\, e^{\mathrm{i}\, z_r (k_1^{\shortparallel} - k_2^{\shortparallel})} \\ &\quad \times \int d^2 x_1^{\perp} \int d^2 x_2^{\perp}\, e^{\mathrm{i}\, \mathbf{k}_1^{\perp} \cdot \mathbf{x}_1^{\perp}}\, e^{-\mathrm{i}\, \mathbf{k}_2^{\perp} \cdot \mathbf{x}_2^{\perp}}\, V^{(1)}((\mathbf{x}_1^{\perp}, z_r), \omega_1, (\mathbf{x}_2^{\perp}, z_r), \omega_2). \end{aligned} \tag{4.37}$$

This leads us back to almost the same result as in Eq. (4.24), but, this time, within the newly-obtained paraxial approximation

$$\begin{aligned} &Z^{(1)}(\mathbf{k}_1, \omega_1, \mathbf{k}_2, \omega_2) \\ &\approx \frac{(2\pi)^5\, G_0\, T\, \sigma^2\, \delta^2}{\alpha^2\, \omega_1\, \omega_2\, \Omega}\, W(\omega_1, \omega_2)\, \delta(k_1^{\shortparallel} - k_{1\_0}^{\shortparallel})\, \delta(k_2^{\shortparallel} - k_{2\_0}^{\shortparallel})\, e^{-(\Delta \mathbf{k}^{\perp})^2 \sigma^2 / 2}\, e^{-(\bar{\mathbf{k}}^{\perp})^2 \delta^2 / 2} e^{\mathrm{i}\, \frac{z_0}{\alpha \bar{\omega}} \bar{\mathbf{k}}^{\perp} \cdot \Delta \mathbf{k}^{\perp}}. \end{aligned} \tag{4.38}$$

In essence, this is the main result of this section. In a final, but trivial, extension, we will generalize it slightly such as to accommodate more realistic field distributions.

Final generalizations As indicated earlier, we could easily generalize our initial GSM model to account for more realistic beam parameters. This concerns the—up to now—circular beam profile as well as the re-introduction of polarization. Neither addition would change the derivation up to this point significantly—except for inflating its notation. Instead of re-iterating the derivations with minute changes, we will, therefore, simply motivate the effects of generalizations on the basis of Eq. (4.38).

Considering an oblate beam profile first—like it is present at the SR source PETRA III in Hamburg, for example [143]—we may account for this by introducing separate Gaussian parameters for each direction: $\sigma \to \sigma^x$, σ^y and $\delta \to \delta^x$, δ^y.

Moreover, we can reintroduce the notion of polarization: Given that typical x-ray beams at SR sources or FELs are linearly polarized *and* well collimated (i.e., $k^{\shortparallel} \gg \left|\mathbf{k}^{\perp}\right|$), we can capture their polarization property by a single unit vector $\boldsymbol{\varepsilon}_X$. This can be chosen real and will be orthogonal to the main propagation-direction of the beam, which we have conventionally defined to be along z (i.e., $\boldsymbol{\varepsilon}_X \perp \mathbf{e}_z$). This choice conserves the transversality of the field to good approximation for all relevant modes of $Z^{(1)}_{\mu\nu}$. We may thus write

$$\begin{aligned} Z^{(1)}_{\mu\nu}(\mathbf{k}_1, \omega_1, \mathbf{k}_2, \omega_2) &= \frac{(2\pi)^5\, G_0\, T\, \sigma^x\, \sigma^y\, \delta^x\, \delta^y}{\alpha^2\, \omega_1\, \omega_2\, \Omega}\, (\boldsymbol{\varepsilon}_X)_{\mu}\, (\boldsymbol{\varepsilon}_X)_{\nu}\, W(\omega_1, \omega_2)\, \delta(k_1^{\shortparallel} - k_{1\_0}^{\shortparallel})\, \delta(k_2^{\shortparallel} - k_{2\_0}^{\shortparallel}) \\ &\quad \times e^{-(\Delta k^x)^2 (\sigma^x)^2 / 2}\, e^{-(\bar{k}^x)^2 (\delta^x)^2 / 2} e^{-(\Delta k^y)^2 (\sigma^y)^2 / 2}\, e^{-(\bar{k}^y)^2 (\delta^y)^2 / 2}\, e^{\mathrm{i}\, \frac{z_0}{\alpha \bar{\omega}} \bar{\mathbf{k}}^{\perp} \cdot \Delta \mathbf{k}^{\perp}}. \end{aligned} \tag{4.39}$$

In a final addition to this formula, we can include the effect of a simplified monochromator. This will prove useful during our later discussion in Chpt. 5. To this end, we should follow the scheme outlined in App. A.9 and insert an approximate transfer function[11]

$$T_m((\mathbf{x}_m^{\perp}, z_m), \omega) \approx T_m(\omega). \tag{4.40}$$

into the propagation that led to Eq. (4.39). Due to its purely spectral nature, however, $T_m(\omega)$ would commute with any propagator therein anyway. Thus, it is effectively allowed to apply it a posteriori onto Eq. (4.39) as well. The resulting expression reads:

$$\begin{aligned} Z^{(1)}_{\mu\nu}(\mathbf{k}_1, \omega_1, \mathbf{k}_2, \omega_2) = \frac{(2\pi)^5 G_0 T \sigma^x \sigma^y \delta^x \delta^y}{\alpha^2 \omega_1 \omega_2 \Omega} & (\boldsymbol{\varepsilon}_X)_\mu (\boldsymbol{\varepsilon}_X)_\nu W(\omega_1, \omega_2) \delta(k_1^{\shortparallel} - k_{1\_0}^{\shortparallel}) \delta(k_2^{\shortparallel} - k_{2\_0}^{\shortparallel}) \\ & \times e^{-(\Delta k^x)^2 (\sigma^x)^2/2} e^{-(\bar{k}^x)^2 (\delta^x)^2/2} e^{-(\Delta k^y)^2 (\sigma^y)^2/2} e^{-(\bar{k}^y)^2 (\delta^y)^2/2} e^{\mathrm{i} \frac{z_0}{\alpha\bar{\omega}} \bar{\mathbf{k}}^{\perp} \cdot \Delta\mathbf{k}^{\perp}} \\ & \times (T_m(\omega_1))^* T_m(\omega_2) \, . \end{aligned} \tag{4.41}$$

With this, we conclude our discussion of the Gaussian Schell-model for x-ray beams. For its further application and the pertaining numerical parameters, we refer the reader to Chpt. 5.

4.2.2 Measurements and simulations as input for $W^{(1)}_{\mu\nu}$

In contrast to all-analytical modelling, the recent accumulation of data on modern x-ray sources provides an alternative foundation, on which to model coherence functions numerically. Hereunto we note that, along with the increasing degree of coherence of synchrotron radiation (SR) sources and x-ray free-electron lasers (FELs), a broad range of investigations has been conducted into their respective beam properties (cf. Refs. [130, 131, 136], for some examples). Moreover, the establishment of novel sources has prompted the concomitant development of numerical tools to simulate their beams [132, 133, 135]. Facilitating a better understanding of x-ray experiments, these tools allow for the simulation, i.e., numerical propagation, of x-rays along virtual beamlines—complete with optical elements up to the envisioned target position.

Both approaches may yield data that is suitable to start the modelling of x-ray fields for XOWM processes upon. Thus, we want to consider this option as an outlook in the following. In an advanced word of caution, however, we emphasize that the required input for our simulations—which would most likely be fully numerical in this case—would have to cover a sufficiently large spatio-temporal domain. This condition may quickly result in prohibitively large data-structures—especially, if correlators like $H^{(1)}_{\mu\nu}(\mathbf{x}_1, t_1, \mathbf{x}_2, t_2)$ (cf. Eq. (4.1)) are naïvely replicated in storage[12].

Fortunately, the actual information-content of cited measurements is much smaller, yet still sufficient to characterize the field. Typical experiments, would often be restricted to the analysis of beam-properties within a single plane, perpendicular to the main propagation direction. For instance, these may yield the

[11] Note that Eq. (4.40) is obviously an approximation and not a particularly realistic one at that. In fact, the working principle of any crystalline monochromator for x-rays (namely Bragg reflection) relies quint-essentially on the coupling of spectral *and* spatial properties of the beam. Then again, for a double crystal monochromator, the ensuing dispersive effects *can* compensate to a large extent and thus the filter-model in Eq. (4.40) *may* recover some validity. At any rate, we note that having a model is better than lacking a model in this case. For better approaches consider Sec. 4.2.2 below.

[12] We note in continuation of our above comment, that the naïve implementation of $H^{(1)}_{\mu\nu}(\mathbf{x}_1, t_1, \mathbf{x}_2, t_2)$ would, obviously, require a 3×3-tensor of complex values, each of which would formally depend on 8 independent coordinates in space and time itself. If this was to be done at Å-scale resolution ($\propto$ wavelength) across the μm-scale of a sample alone, the storage and analysis of such an object would amount to a formidable computational task.

cross spectral density $W^{(1)}_{\mu\nu}((\mathbf{x}^{\perp}_1, z_0), \omega_1, (\mathbf{x}^{\perp}_2, z_0), \omega_2)$ in the plane at $z_1 = z_2 = z_0$—perpendicular to the z-direction. With this information at hand, we can propagate $W^{(1)}_{\mu\nu}$ retroactively across a certain range in z_1 and z_2 and thereby allow for an approximate Fourier transform of the data.

In the simplest scenario, we can approximate the propagation of a predominantly uni-directional beam by the free propagator—as of Eq. (A.92) in App. A.9:

$$\Big(P_{z',z}(\mathbf{x}'^{\perp}, \mathbf{x}^{\perp}, \omega)\Big)_{\mu\nu} = \frac{1}{(2\pi)^2} \int d^3k \; \delta_{\mu\nu} \; \delta(k^{\shortparallel} - k^{\shortparallel}_0) \; e^{\mathrm{i}k^{\shortparallel}(z'-z)} \; e^{\mathrm{i}\mathbf{k}^{\perp}\cdot(\mathbf{x}'^{\perp}-\mathbf{x}^{\perp})}. \tag{4.42}$$

Herein, $k^{\shortparallel}$ denotes the component of $\mathbf{k}$ along the main propagation direction, which we will—as a convention for the incoming beam—assume to be along the z-direction. The value of $k^{\shortparallel}_0$ is fixed to $k^{\shortparallel}_0 = \sqrt{\alpha^2\omega^2 - |\mathbf{k}^{\perp}|^2}$. Subsequent Fourier transformations[13] yield the field correlator $Z^{(1)}_{\mu\nu}$ in a form that is directly amenable for use in our original XOWM expression (2.67), namely

$$\begin{aligned} Z^{(1)}_{\mu\nu}(\mathbf{k}_1, \omega_1, \mathbf{k}_2, \omega_2) = \frac{(2\pi)^2}{\alpha^2 \, \omega_1 \omega_2} \; \delta(k^{\shortparallel}_1 - k^{\shortparallel}_{1\_0}) \; \delta(k^{\shortparallel}_2 - k^{\shortparallel}_{2\_0}) \; e^{\mathrm{i}z_0(k^{\shortparallel}_1 - k^{\shortparallel}_2)} \\ \times \int d^2x^{\perp}_1 \int d^2x^{\perp}_2 \; e^{\mathrm{i}\mathbf{k}^{\perp}_1\cdot\mathbf{x}^{\perp}_1} \; e^{-\mathrm{i}\mathbf{k}^{\perp}_2\cdot\mathbf{x}^{\perp}_2} \; W^{(1)}_{\mu\nu}((\mathbf{x}^{\perp}_1, z_0), \omega_1, (\mathbf{x}^{\perp}_2, z_0), \omega_2). \end{aligned} \tag{4.43}$$

With this connection being conceptually demonstrated, we note that its further pursuit extends beyond the scope of the current work. Nevertheless, we want to remark on a few additional points, thus shaping an outlook onto future efforts:

In writing Eq. (4.43) we have, so far, applied the simplest continuation at hand. It implies the unhindered propagation of $W^{(1)}_{\mu\nu}$ across all of space and therein, in particular, also the free propagation through the sample. Both aspects may be individually questionable. The first shortcoming is mostly of formal nature and could be amended straight-forwardly by applying a windowed Fourier-approach, which covers only the target-region[14]. The second shortcoming can be addressed through the use of better (or different) propagators. Instead of assuming free-space like propagation throughout the sample, these could additionally take into account its absorption or refractive corrections. For an example of such propagators on short length-scales, see App. A.9.3.

As a further step in this modelling of the beam *inside* the sample, we point to the possible presence of (self-)diffraction. This would be of particular importance, if XOWM is studied in close vicinity to elastic Bragg-conditions (cf. also our speculation on multi-beam diffraction for XOWM in Sec. 5.1.2.d).

In a final remark—which is mostly a technical comment—we want to note that the temporal origin associated with a measured or simulated cross spectral density (i.e., the definition of its frame of reference) may be quite arbitrary. As a consequence, significant, yet somewhat artificial phase-terms can arise (cf. Sec. 4.2.1). In order to interpret these correctly, it is advisable to transform $W^{(1)}_{\mu\nu}$ into the time-domain at some point and investigate its temporal structure relative to the rest of the scattering setup.

[13] For more details on field propagation, field correlation functions and their Fourier transforms, we refer the reader to Apps. A.9 and A.8, respectively. There, we give—among other relations—the free propagation of $V^{(1)}_{\mu\nu}$ (Eq. (A.117)). This can be related further to $Z^{(1)}_{\mu\nu}$ (via Eq. (A.81)) and $W^{(1)}_{\mu\nu}$ (via Eq. (A.83))—thus leading exemplarily to Eq. (4.43).

[14] We note that a windowed Fourier-approach will, to all intents and purposes, be required for actual numerical implementation anyway. While it takes care to mask the influence of unknown surroundings, its primary benefit would be the regularization and stabilization of the transformation procedure itself. In its absence, we would expect numerical artefacts to spoil more naïve Fourier transforms.

4.3 Models for optical sources

Following the establishment of a workable model for x-ray pulses, we shall shift our attention towards the description of driving, i.e., external, optical fields in this section. With regard to this specification 'external', we recall that during the course of our earlier derivations, we have actually defined *two* instances of optical fields for wavemixing. Namely, we have split the general field correlator of Eq. (2.47)

$$\mathrm{Tr}_{\mathrm{OPT}}\left\{\hat{\rho}_{\mathrm{OPT}}(0)\left(\hat{\mathbf{A}}_{\mathrm{opt}}(\mathbf{y}',t_2')\right)_\nu\left(\hat{\mathbf{A}}_{\mathrm{opt}}(\mathbf{y},t_2)\right)_\mu\right\}=\bar{H}^{(1)}_{\nu\mu}(\mathbf{y}',t_2',\mathbf{y},t_2)+\bar{S}^{(1)}_{\nu\mu}(\mathbf{y}',t_2',\mathbf{y},t_2) \tag{4.44}$$

into an average, classical contribution $\bar{H}^{(1)}_{\nu\mu}$, as of an external driving laser, and a remainder of quantum fluctuations $\bar{S}^{(1)}_{\nu\mu}$ (see later Sec. 4.4). With our focus on

$$\begin{aligned}\bar{H}^{(1)}_{\nu\mu}(\mathbf{y}',t_2',\mathbf{y},t_2)&=\left(\mathbf{A}_{\mathrm{opt\_avg}}(\mathbf{y}',t_2')\right)_\nu\left(\mathbf{A}_{\mathrm{opt\_avg}}(\mathbf{y},t_2)\right)_\mu,\\ &\text{wherein: }\mathbf{A}_{\mathrm{opt\_avg}}(...)=\mathrm{Tr}_{\mathrm{OPT}}\left\{\hat{\rho}_{\mathrm{OPT}}(0)\,\hat{\mathbf{A}}_{\mathrm{opt}}(...)\right\},\end{aligned} \tag{4.45}$$

we pursue its closer determination by considering a set of (experimental) constraints below. Subsequently, we will find that the respective conditions can be met by a Gaussian Schell-model once again.

The use of an external laser in XOWM, can be of importance for either sum- or difference-frequency generation (SFG / DFG)—within the current scope of our framework. For both cases, we have experimental references at hand, namely the demonstration of SFG by Glover and co-workers (cf. Ref. [46] and Sec. 5.1.1) as well as our own experimental campaign on DFG (cf. Sec. 5.1.3). Inferring from these scenarios, we may arrive at the following assumptions to guide our model building:

- First of all, we note that the laser-beams in both experiments have undergone mild focusing, before propagating towards the sample. In this, their case differs slightly from the previously discussed x-rays, for which the free-space propagation has been assumed as a slow expansion from the source point. Nevertheless, the optical fields exhibited only a small divergence and, as such, retained their (Gaussian) beam-like nature.

- The optical photon energy of the lasers amounted to $\hbar\omega_L = 1.55$ eV (i.e., the well-known 800 nm of Ti:Sa [144]). This ranged significantly below any electronic excitation thresholds of the respective samples (each a diamond with $E_{\text{band gap}} \approx 5.5$ eV). As a consequence, the material could not absorb the respective photons via linear processes and thus appears transparent to the laser.

- Considering the dielectric response of the material further, we note that—in the absence of absorption—there may still be refractive effects to consider. For the macroscopic propagation of the laser throughout the sample[15], these effects can be subsumed in a (real-valued) refractive index $n(\omega_L)$.

- Moreover, we shall assume the optical pulse to be sufficiently monochromatic as to allow a non-dispersive treatment of the refractive index, i.e., $n(\omega_L) = n = \text{const.}$.

- By extension, the same monochromaticity also implies a rather slowly varying pulse form.

[15] We re-iterate an important caveat at this point; namely, that the proposed macroscopic picture is founded on an arbitrary and somewhat inconsistent separation of the optical light-matter interaction into two regimes: The linear dielectric response, which we approximate macroscopically, and the nonlinear response, which is the focus of our work and results in microscopic resolution. As a future development goal, we strive for a more coherent treatment of both cases. For the time-being, however, we acknowledge—aided by hindsight—that the proposed condition will provide reasonable results.

- As a final simplification, we shall ignore refractive effects on the surfaces of the sample and instead treat the optical field as if it were inside the medium at all times. While this may appear as a drastic form of over-simplification—at first glance—we clarify that refraction could indeed be neglected in Glover's case. Here, the laser beam was adjusted for almost normal incidence on the sample, thus negating any refractive effects. For our DFG experiment, the geometry has been slightly different, yet the associated refractive effects could easily be converted into a correction of the laser-beams pointing.

4.3.1 Gaussian Schell-model for optical pulses

Constructing a suitable correlator $\bar{H}^{(1)}$ (or $\bar{Z}^{(1)}$, respectively) under these conditions, we closely follow (and reuse) our steps from the modelling of x-ray fields in Sec. 4.2.1. To begin with, we shall assume that the laser beam propagates along the same positive z-direction as the x-rays did. Later on, we can adjust this to the experimental reality. In particular, we may rotate the complete optical field distribution $\bar{Z}^{(1)}$, in order to account for any relative angles in the directions of x-ray and optical beams[16].

As in the x-ray case, we denote the position of the focal plane by $z = z_0$—noting, however, that it may well lie considerably closer to, if not within, the sample this time. Inside the focal plane, we can characterize the laser pulse by its carrier wave, its transverse spatial profile and its longitudinal, temporal profile. Choosing Gaussian models again, we write[17]

$$E^{(+)}((\mathbf{x}^{\perp}, z_0), t) = E_0 \, \exp\left(-\frac{(\mathbf{x}^{\perp})^2}{4\sigma^2}\right) \exp\left(-\frac{(t-t_0)^2}{4T^2} - \mathrm{i}\omega_0 (t-t_0) - \mathrm{i}\varphi_0\right). \tag{4.46}$$

The occurring quantities—notably without the ones related to (in)coherence—are functionally the same as in the x-ray case as well: σ measures the beam profile, T the pulse length and ω_0 gives the central frequency. In contrast to the x-ray case, however, the carrier wave and its envelope have a well defined phase relation here. This is expressed through the additional φ_0. Note further that, for such a phase-stable source, any time-translation of the pulse by t_0 has to affect *both* envelope and carrier. From Eq. (4.46), we can readily assemble a Glauber-type correlation function $\bar{G}^{(1)}$ as

$$\bar{G}^{(1)}((\mathbf{x}_1^{\perp}, z_0), t_1, (\mathbf{x}_2^{\perp}, z_0), t_2) = \Big(E^{(+)}((\mathbf{x}_1^{\perp}, z_0), t_1) + \text{c.c.}\Big)\Big(E^{(+)}((\mathbf{x}_2^{\perp}, z_0), t_2) + \text{c.c.}\Big). \tag{4.47}$$

Equivalently, we may write the cross spectral density as

$$\begin{aligned}
&\bar{W}^{(1)}((\mathbf{x}_1^{\perp}, z_0), \omega_1, (\mathbf{x}_2^{\perp}, z_0), \omega_2) = \int dt_1 \int dt_2 \; e^{-\mathrm{i}\,\omega_1 t_1} \; e^{\mathrm{i}\,\omega_2 t_2} \; \bar{G}^{(1)}((\mathbf{x}_1^{\perp}, z_0), t_1, (\mathbf{x}_2^{\perp}, z_0), t_2) \\
&= \Big(E^{(+)}((\mathbf{x}_1^{\perp}, z_0), -\omega_1) + (E^{(+)}((\mathbf{x}_1^{\perp}, z_0), \omega_1))^*\Big)\Big(E^{(+)}((\mathbf{x}_2^{\perp}, z_0), \omega_2) + (E^{(+)}((\mathbf{x}_2^{\perp}, z_0), -\omega_2))^*\Big) \\
&= \Big(E^{(+)}((\mathbf{x}_1^{\perp}, z_0), -\omega_1) + E^{(-)}((\mathbf{x}_1^{\perp}, z_0), -\omega_1)\Big)\Big(E^{(+)}((\mathbf{x}_2^{\perp}, z_0), \omega_2) + E^{(-)}((\mathbf{x}_2^{\perp}, z_0), \omega_2)\Big) \\
&= E^{(+)}((\mathbf{x}_1^{\perp}, z_0), -\omega_1) E^{(+)}((\mathbf{x}_2^{\perp}, z_0), \omega_2) + E^{(-)}((\mathbf{x}_1^{\perp}, z_0), -\omega_1) E^{(+)}((\mathbf{x}_2^{\perp}, z_0), \omega_2) \\
&+ E^{(+)}((\mathbf{x}_1^{\perp}, z_0), -\omega_1) E^{(-)}((\mathbf{x}_2^{\perp}, z_0), \omega_2) + E^{(-)}((\mathbf{x}_1^{\perp}, z_0), -\omega_1) E^{(-)}((\mathbf{x}_2^{\perp}, z_0), \omega_2).
\end{aligned} \tag{4.48}$$

[16] We note that the transformation in reciprocal-space, i.e., on $\bar{Z}^{(1)}$, which is required to rotate the field is naturally the same as it would be in real-space on $\bar{H}^{(1)}$. For reference, we have outlined the respective transformation properties of Fourier transformations in App. A.3.

[17] Note that—just as before (Sec. 4.2.1)—we initially suppress the polarization of the beam as well as its (potentially) oblate cross section.

This can be regrouped in the following way

$$\begin{aligned}
&\bar{W}^{(1)}((\mathbf{x}_1^\perp, z_0), \omega_1, (\mathbf{x}_2^\perp, z_0), \omega_2) \\
&= \underbrace{E^{(-)}((\mathbf{x}_1^\perp, z_0), -\omega_1) E^{(+)}((\mathbf{x}_2^\perp, z_0), \omega_2)}_{\text{absorption / SFG}} + \underbrace{\Big(E^{(-)}((\mathbf{x}_1^\perp, z_0), \omega_1) E^{(+)}((\mathbf{x}_2^\perp, z_0), -\omega_2)\Big)^*}_{\text{emission / DFG}} \\
&+ \int dt_1 \int dt_2 \, e^{-\mathrm{i}\,\omega_1 t_1} \, e^{\mathrm{i}\,\omega_2 t_2} \, \mathrm{Re}\Big[E^{(+)}((\mathbf{x}_1^\perp, z_0), t_1) E^{(+)}((\mathbf{x}_2^\perp, z_0), t_2)\Big],
\end{aligned} \tag{4.49}$$

where we can identify two important terms. If the above field was employed to model XOWM processes, the first of these terms would allow for the absorption of optical photons, such as needed for SFG ('up-conversion'). On the contrary, the second term could mediate the (stimulated) emission of an optical photon from the material system. Thereby, it would partake in laser-driven 'down-conversion' of x-ray photons, viz. DFG. The cross term, finally, is mostly negligible.

Comment on photon-energy selection In the following, we shall provide some further reasoning as to how and why the noted selection of photon energies comes about. As a starting point, we have to recall our initial choice of the projection observable (Eq. (2.8)) for detecting XOWM. In this, we have focused on a fixed outgoing frequency ω_f. In order to produce this frequency via XOWM—provided it is *not* included within the incident x-ray field distribution already—frequency components from the incident x-ray (ω_X) and optical fields (ω_L) have to add up (or subtract) correspondingly: $\omega_f = \omega_X \pm \omega_L$. This is reflected by the presence of δ-functions in our central wavemixing equation (2.67), which enforce the required energy balance: $\delta(\omega_f - \omega_X - \omega_L)$ and $\delta(\omega_f - \omega_X' - \omega_L')$.

In order to clarify the resulting selection of terms in Eq. (4.49), let us consider the example of a 'clean' case of SFG. That is to say, we intend to observe up-converted x-rays at a frequencies $\omega_f > \omega_X, \omega_X'$, i.e., ranging above all non-vanishing components of the incident x-ray field. By application of the above δ-functions, this implies that ω_L and ω_L' will be forced to take on positive values. At the same time, we know that positive frequencies are only included with the *positive* frequency part of the fields, by definition. It is thus easy to verify that only the first term of Eq. (4.49) can contribute to SFG in this 'clean' case.

The situation becomes more ambiguous, if the respective bandwidths of x-ray and optical fields are large and overlap with the target frequency (ω_f) in such a way, as to allow admixtures from both $E^{(+)}$ and $E^{(-)}$ to contribute to the overall result. In such cases, we may still *impose* a selection by resorting to a rotating-wave approximation[18]. On the other hand, there could be cases, for which extreme overlap is desirable in fact—cf. our amphodyne detection scheme outlined in Sec. 6.2—and thus all terms of Eqs. (4.48) or (4.49) have to be taken into account.

END OF COMMENT

For the time being, we shall focus on the first two terms of Eq. (4.49) as needed for 'clean' SFG / DFG and discuss more specialized cases when required. Performing the Fourier transform of a single

[18] We note that, for a realistic experiment, full separation of spectral components is elusive anyway. As such, there would always be a contribution from both positive and negative frequency parts, even though one of them will often be minute. In the following we shall thus make the mentioned rotating-wave approximation our implicit modus operandi.

electric field from Eq. (4.46), we can assemble each of the two terms as

$$E^{(-)}((\mathbf{x}_1^\perp, z_0), -\omega_1) E^{(+)}((\mathbf{x}_2^\perp, z_0), \omega_2) = \frac{|E_0|^2\, 2\pi T}{\Omega}\; e^{-((\mathbf{x}_1^\perp)^2+(\mathbf{x}_2^\perp)^2)/4\sigma^2}\; e^{\mathrm{i} t_0 \Delta\omega}\; e^{-\Delta\omega^2 T^2/2}\; e^{-(\bar{\omega}-\omega_0)^2/2\Omega^2} \tag{4.50}$$

and, by conjugation obviously,

$$\left(E^{(-)}((\mathbf{x}_1^\perp, z_0), \omega_1) E^{(+)}((\mathbf{x}_2^\perp, z_0), -\omega_2)\right)^* = \frac{|E_0|^2\, 2\pi T}{\Omega}\; e^{-((\mathbf{x}_1^\perp)^2+(\mathbf{x}_2^\perp)^2)/4\sigma^2}\; e^{\mathrm{i} t_0 \Delta\omega}\; e^{-\Delta\omega^2 T^2/2}\; e^{-(\bar{\omega}+\omega_0)^2/2\Omega^2}. \tag{4.51}$$

Here, we have resorted to combined variables as before

$$\bar{\omega} = (\omega_1+\omega_2)/2, \quad \Delta\omega = \omega_2 - \omega_1 \qquad \Leftrightarrow \qquad \omega_1 = \bar{\omega} - \Delta\omega/2, \quad \omega_2 = \bar{\omega} + \Delta\omega/2 \tag{4.52}$$

$$\text{as well as: } \Omega = \sqrt{\frac{1}{4T^2} + \frac{1}{\tau_c^2}}. \tag{4.53}$$

We merely note that, as a slight peculiarity, the coherence time τ_c should be considered as infinitely long for a perfectly coherent laser pulse. Its contribution to Ω thus vanishes.

We may now combine Eqs. (4.50) and (4.51) into the approximate cross spectral density

$$\begin{aligned}
&\bar{W}^{(1)}((\mathbf{x}_1^\perp, z_0), \omega_1, (\mathbf{x}_2^\perp, z_0), \omega_2) \\
&\approx E^{(-)}((\mathbf{x}_1^\perp, z_0), -\omega_1) E^{(+)}((\mathbf{x}_2^\perp, z_0), \omega_2) + \left(E^{(-)}((\mathbf{x}_1^\perp, z_0), \omega_1) E^{(+)}((\mathbf{x}_2^\perp, z_0), -\omega_2)\right)^* \\
&= \frac{|E_0|^2\, 2\pi T}{\Omega}\; e^{-((\mathbf{x}_1^\perp)^2+(\mathbf{x}_2^\perp)^2)/4\sigma^2}\; e^{\mathrm{i} t_0 \Delta\omega}\; e^{-\Delta\omega^2 T^2/2}\; \left(e^{-(\bar{\omega}-\omega_0)^2/2\Omega^2} + e^{-(\bar{\omega}+\omega_0)^2/2\Omega^2}\right).
\end{aligned} \tag{4.54}$$

Apart from accounting for *both* positive and negative frequency components, we find $\bar{W}^{(1)}$ to be equivalent to Eq. (4.16) from our x-ray discussion. Extending the analogy among the two models, we can readily obtain $\bar{Z}^{(1)}$ as of Eq. (4.24):

$$\begin{aligned}
\bar{Z}^{(1)}(\mathbf{k}_1, \omega_1, \mathbf{k}_2, \omega_2) = \frac{(2\pi)^5\, |E_0|^2\, T\, \sigma^2\, \delta^2}{\alpha^2\, \omega_1\, \omega_2\, \Omega}\; & e^{-(\mathbf{k}_2^\perp - \mathbf{k}_1^\perp)^2\sigma^2/2}\; e^{-(\mathbf{k}_1^\perp + \mathbf{k}_2^\perp)^2\delta^2/8}\; e^{-\Delta\omega^2 T^2/2}\; e^{\mathrm{i} t_0 \Delta\omega} \\
&\times \Big(e^{-(\bar{\omega}-\omega_0)^2/2\Omega^2} e^{\mathrm{i} z_0 (k_1^\parallel - k_2^\parallel)}\; \delta(k_1^\parallel - k_{1_0}^\parallel)\; \delta(k_2^\parallel - k_{2_0}^\parallel) \\
&+ e^{-(\bar{\omega}+\omega_0)^2/2\Omega^2} e^{-\mathrm{i} z_0 (k_1^\parallel - k_2^\parallel)}\; \delta(k_1^\parallel + k_{1_0}^\parallel)\; \delta(k_2^\parallel + k_{2_0}^\parallel)\Big).
\end{aligned} \tag{4.55}$$

Notably, the phase factor for the propagation of the negative frequencies is flipped with respect to the positive ones. In conjunction with this change, the second root for $k_i^\parallel$ has to be considered inside the δ-functions, such that the overall *direction* of propagation remains the same. Except for this, we can make use of the previous results including the established notation, especially $\delta^{-2} = (2\sigma)^{-2} + \xi^{-2}$. Analogous to the temporal (in-)coherence τ_c before, we may discard any spatial incoherence-effects by taking simply taking $\xi \to \infty$.

Upon considering the roots for $k_i^\parallel$ more explicitly, we encounter an additional alteration over the x-ray case. Namely, we should incorporate refraction as required by our modelling guidelines above. We recall that in the lead up to Eq. (4.24) for x-rays, we have assumed free propagation, i.e., no absorption and no refraction (really no light-matter interaction at all). Whereas in the present case, we will modify

the dispersion relation within the propagator to account for the refractive index n, viz[19]:

$$\omega = c\,|\mathbf{k}| = c_{\text{vacuum}}\,|\mathbf{k}| \qquad \rightarrow \qquad \omega = c_{\text{medium}}\,|\mathbf{k}| = c_{\text{vacuum}}\,|\mathbf{k}|\,/n. \tag{4.56}$$

By extension then, we see $k^{\shortparallel}_{i0}$ of Eq. (4.55) changing into $k^{\shortparallel}_{i0} = \sqrt{\alpha^2\omega_i^2 n^2 - \left|\mathbf{k}_i^{\perp}\right|^2}$.

This being implemented, we can continue our treatment of $\bar{Z}^{(1)}$ along the lines of Sec. 4.2.1 and generalize towards asymmetric beams besides also re-introducing the notion of polarization[20]:

$$\begin{aligned}\bar{Z}^{(1)}_{\mu\nu}(\mathbf{k}_1,\omega_1,\mathbf{k}_2,\omega_2) = {} & \frac{(2\pi)^5\,|E_0|^2\,T\,\sigma^x\sigma^y\,\delta^x\delta^y}{\alpha^2\,\omega_1\omega_2\,\Omega}\,(\boldsymbol{\varepsilon}_L)_\mu\,(\boldsymbol{\varepsilon}_L)_\nu\,e^{\mathrm{i}z_0(k^{\shortparallel}_{1\_0}-k^{\shortparallel}_{2\_0})}e^{\mathrm{i}t_0\Delta\omega}\,e^{-\Delta\omega^2T^2/2} \\ & \times e^{-(k_2^x-k_1^x)^2(\sigma^x)^2/2}\,e^{-(k_1^x+k_2^x)^2(\delta^x)^2/8}\,e^{-(k_2^y-k_1^y)^2(\sigma^y)^2/2}\,e^{-(k_1^y+k_2^y)^2(\delta^y)^2/8} \\ & \times \Big(e^{-(\bar{\omega}-\omega_0)^2/2\Omega^2}\;\delta(k^{\shortparallel}_1-k^{\shortparallel}_{1\_0})\delta(k^{\shortparallel}_2-k^{\shortparallel}_{2\_0}) + e^{-(\bar{\omega}+\omega_0)^2/2\Omega^2}\;\delta(k^{\shortparallel}_1+k^{\shortparallel}_{1\_0})\delta(k^{\shortparallel}_2+k^{\shortparallel}_{2\_0})\Big).\end{aligned} \tag{4.57}$$

Finally, we may again invoke the assumption that the laser beam is well collimated (i.e., sporting a small divergence $\Theta \approx \frac{|\mathbf{k}_L^{\perp}|}{|\mathbf{k}_L|} \ll 1$), which allows for the approximative treatment of the spatial phase term. In contrast to the x-ray case, however, we shall not remove the phase-term completely by choosing $t_0 = z_0 n/c$ this time. Instead, we include an additional time delay in $t_0 = \Delta t + z_0 n/c$. Thereby, we can accommodate either deliberate, relative time delays among x-ray and optical pulse or account for inadvertent, temporal jitter. The final expression for $\bar{Z}^{(1)}_{\mu\nu}$ now reads:

$$\begin{aligned}\bar{Z}^{(1)}_{\mu\nu}(\mathbf{k}_1,\omega_1,\mathbf{k}_2,\omega_2) = {} & \frac{(2\pi)^5\,|E_0|^2\,T\,\sigma^x\sigma^y\,\delta^x\delta^y}{\alpha^2\,\omega_1\omega_2\,\Omega}\,(\boldsymbol{\varepsilon}_L)_\mu\,(\boldsymbol{\varepsilon}_L)_\nu\,e^{-\Delta\omega^2T^2/2}\,e^{\mathrm{i}\Delta t\,\Delta\omega} \\ & \times e^{-(k_2^x-k_1^x)^2(\sigma^x)^2/2}\,e^{-(k_1^x+k_2^x)^2(\delta^x)^2/8}\,e^{-(k_2^y-k_1^y)^2(\sigma^y)^2/2}\,e^{-(k_1^y+k_2^y)^2(\delta^y)^2/8}\,e^{\mathrm{i}\frac{z_0}{\alpha|\bar{\omega}|n}\Delta\mathbf{k}^{\perp}\cdot\bar{\mathbf{k}}^{\perp}} \\ & \times \Big(e^{-(\bar{\omega}-\omega_0)^2/2\Omega^2}\;\delta(k^{\shortparallel}_1-k^{\shortparallel}_{1\_0})\delta(k^{\shortparallel}_2-k^{\shortparallel}_{2\_0}) + e^{-(\bar{\omega}+\omega_0)^2/2\Omega^2}\;\delta(k^{\shortparallel}_1+k^{\shortparallel}_{1\_0})\delta(k^{\shortparallel}_2+k^{\shortparallel}_{2\_0})\Big),\end{aligned} \tag{4.58}$$

where $k^{\shortparallel}_{i0} = \sqrt{\alpha^2\omega_i^2 n^2 - \left|\mathbf{k}_i^{\perp}\right|^2}$. All further parameters can be determined as outlined in App. A.11—accounting for $\xi^i \to \infty$ and $\tau_c \to \infty$.

Addendum on stretching There is an additional possible complication, which we will—for instance—encounter with the SFG experiment by Glover and co-workers [46]. Namely, that the laser-pulses in use can be stretched from being initially short, and thus necessarily broadband, into something long yet broadband nonetheless. In case of Ref. [46] it appears to have been reasonable to model this in terms of a linear frequency chirp (cf. methods discussion ibid.).

In order to accommodate for such stretching effect as well, we have to revisit Eq. (4.46) and change

[19] We note as a caveat that there are various ways, in which this simplified treatment of dielectric effects may be invalidated. For instance, we do not account for dispersion, i.e., broad-bandwidth pulses or rapidly varying $n(\omega)$ would pose a problem. Moreover, we discard the option of anisotropic dielectric properties (e.g., bi-refringence), which would become an issue, once we re-instate polarization properties. Furthermore, as we have already indicated before, conceptual tensions arise from this ad-hoc inclusion of linear dielectric effects vis-a-vis nonlinear light-matter interaction.

[20] Note on our generalizations, however, that we shall not go as far as to consider astigmatic beams, i.e., beams with different focal planes per transverse direction, here.

its phase behaviour

$$E^{(+)}((\mathbf{x}^{\perp},z_0),t) = E_0\ \exp\left(-\frac{(\mathbf{x}^{\perp})^2}{4\sigma^2}\right)\exp\left(-\frac{(t-t_0)^2}{4T^2} - \mathrm{i}\gamma_0\,(t-t_0)^2 - \mathrm{i}\omega_0\,(t-t_0) - \mathrm{i}\varphi_0\right). \tag{4.59}$$

We note to this end that we can think of the complex exponent as the series expansion of a general phase function

$$\begin{aligned}\phi(t-t_0) &\approx \phi(t_0) + \frac{\partial\,\phi(t)}{\partial t}\Big|_{t=t_0}(t-t_0) + \frac{1}{2}\,\frac{\partial^2\phi(t)}{\partial t^2}\Big|_{t=t_0}(t-t_0)^2 + \ldots \\ &= \varphi_0 + \omega_0\,(t-t_0) + \gamma_0\,(t-t_0)^2 + \ldots.\end{aligned} \tag{4.60}$$

wherein the second-order term describes a shift in frequency over time.

Up to this order, we can still evaluate the Fourier transform of Eq. (4.59) exactly by means of a generalized Gaussian integral (see App. A.15). The transformed field reads

$$\begin{aligned}E^{(+)}((\mathbf{x}^{\perp},z_0),\omega) &= \int dt\, e^{\mathrm{i}\,\omega t}\, E^{(+)}((\mathbf{x}^{\perp},z_0),t) \\ &= E_0\ \exp\left(-\frac{(\mathbf{x}^{\perp})^2}{4\sigma^2}\right)\int dt\, e^{\mathrm{i}\,\omega t}\,\exp\left(-\frac{(t-t_0)^2}{4T^2} - \mathrm{i}\gamma_0\,(t-t_0)^2 - \mathrm{i}\omega_0\,(t-t_0) - \mathrm{i}\varphi_0\right) \\ &= E_0\ \exp\left(-\frac{(\mathbf{x}^{\perp})^2}{4\sigma^2}\right) e^{\mathrm{i}\,\omega t_0 - \mathrm{i}\varphi_0}\int d\tau\,\exp\left(-\tau^2\left(\frac{1}{4T^2} + \mathrm{i}\gamma_0\right) - \mathrm{i}(\omega_0-\omega)\,\tau\right) \\ &= E_0\,\sqrt{\pi\,|X|}\,e^{-(\mathbf{x}^{\perp})^2/4\sigma^2}\,e^{\mathrm{i}\,\omega t_0 - \mathrm{i}\varphi_0}\,e^{-(\omega_0-\omega)^2 X/4}\,e^{\mathrm{i}\,\frac{1}{2}\arg(X^{-1})},\end{aligned} \tag{4.61}$$

where the abbreviation X is meant to denote $X = (\frac{1}{4T^2} + \mathrm{i}\gamma_0)^{-1}$. Using this result, we shall construct $\bar{Z}^{(1)}$ along the same line of reasoning as in the un-stretched case. In particular, we can write the 'absorption' and 'emission' components of $\bar{W}^{(1)}$ analogous to Eqs. (4.50) and (4.51) before

$$\begin{aligned}&E^{(-)}((\mathbf{x}_1^{\perp},z_0),-\omega_1)E^{(+)}((\mathbf{x}_2^{\perp},z_0),\omega_2) \\ &\qquad = |E_0|^2\,\pi\,|X|\,e^{-((\mathbf{x}_1^{\perp})^2+(\mathbf{x}_2^{\perp})^2)/4\sigma^2}\,e^{\mathrm{i}\,t_0(\omega_2-\omega_1)}\,e^{-(\omega_0-\omega_1)^2 X^*/4}\,e^{-(\omega_0-\omega_2)^2 X/4}\end{aligned} \tag{4.62}$$

and

$$\begin{aligned}&\Big(E^{(-)}((\mathbf{x}_1^{\perp},z_0),\omega_1)E^{(+)}((\mathbf{x}_2^{\perp},z_0),-\omega_2)\Big)^* \\ &\qquad = |E_0|^2\,\pi\,|X|\,e^{-((\mathbf{x}_1^{\perp})^2+(\mathbf{x}_2^{\perp})^2)/4\sigma^2}\,e^{\mathrm{i}\,t_0(\omega_2-\omega_1)}\,e^{-(\omega_0+\omega_1)^2 X/4}\,e^{-(\omega_0+\omega_2)^2 X^*/4}.\end{aligned} \tag{4.63}$$

We can re-write the last two exponentials into the more familiar form

$$\begin{aligned}e^{-(\omega_0-\omega_1)^2 X^*/4}\,e^{-(\omega_0-\omega_2)^2 X/4} &= \exp\Big(-\frac{(\omega_0-\omega_1)^2\,(\mathrm{Re}X - \mathrm{i}\mathrm{Im}X)}{4} - \frac{(\omega_0-\omega_2)^2\,(\mathrm{Re}X + \mathrm{i}\mathrm{Im}X)}{4}\Big) \\ &= \exp\Big(-\frac{\mathrm{Re}X}{2}\big((\omega_0-\bar{\omega})^2 + \frac{1}{4}\Delta\omega^2\big) + \frac{\mathrm{i}\mathrm{Im}X}{2}(\omega_0-\bar{\omega})\Delta\omega\Big),\end{aligned} \tag{4.64}$$

and almost the same for

$$\begin{aligned}e^{-(\omega_0+\omega_1)^2 X/4}\,e^{-(\omega_0+\omega_2)^2 X^*/4} &= \exp\Big(-\frac{(\omega_0+\omega_1)^2\,(\mathrm{Re}X + \mathrm{i}\mathrm{Im}X)}{4} - \frac{(\omega_0+\omega_2)^2\,(\mathrm{Re}X - \mathrm{i}\mathrm{Im}X)}{4}\Big) \\ &= \exp\Big(-\frac{\mathrm{Re}X}{2}\big((\omega_0+\bar{\omega})^2 + \frac{1}{4}\Delta\omega^2\big) + \frac{\mathrm{i}\mathrm{Im}X}{2}(\omega_0+\bar{\omega})\Delta\omega\Big),\end{aligned} \tag{4.65}$$

where we have made use of $\Delta\omega = \omega_2 - \omega_1$ and $\bar{\omega} = (\omega_1+\omega_2)/2$ again.

Furthermore, we can introduce new parameters

$$\tilde{T} = +\frac{1}{2}\sqrt{\mathrm{Re}X} \qquad \text{and} \quad \tilde{\Omega} = +(\sqrt{\mathrm{Re}X})^{-1} = \sqrt{\Omega^2 + 4T^2\gamma_0^2} \qquad \Rightarrow \tilde{\Omega}^2 = \frac{1}{4\tilde{T}^2} \tag{4.66}$$

and thus, highlight the similarity of the new $\bar{W}^{(1)}$ to our previous Eq. (4.54)

$$\begin{aligned}\bar{W}^{(1)}((\mathbf{x}_1^\perp, z_0), \omega_1, (\mathbf{x}_2^\perp, z_0), \omega_2) = \frac{|E_0|^2\, 2\pi T}{\tilde{\Omega}}\, e^{-((\mathbf{x}_1^\perp)^2+(\mathbf{x}_2^\perp)^2)/4\sigma^2}\, e^{\mathrm{i}t_0\Delta\omega}\, e^{-\Delta\omega^2\tilde{T}^2/2} \\ \times\left(e^{-(\bar{\omega}-\omega_0)^2/2\tilde{\Omega}^2}\, e^{-\mathrm{i}2\gamma_0 T^2\Delta\omega(\omega_0-\bar{\omega})/\tilde{\Omega}^2} + e^{-(\bar{\omega}+\omega_0)^2/2\tilde{\Omega}^2}\, e^{-\mathrm{i}2\gamma_0 T^2\Delta\omega(\omega_0+\bar{\omega})/\tilde{\Omega}^2}\right).\end{aligned} \tag{4.67}$$

The main modification compared to Eq. (4.54) is in the appearance of the additional phase terms $e^{-\mathrm{i}2\gamma_0 T^2\Delta\omega(\omega_0\mp\bar{\omega})/\tilde{\Omega}^2}$. Those aside, the functional form of $\bar{W}^{(1)}$ has not changed much.

In particular, it should be noted that it has not changed with respect to its spatial part. Therefore, we can consider the spatial propagation—wherein the spectral part plays only a parametric role—just as before. Skipping over all analogous steps, we thus infer the stretched-pulse version of Eq. (4.58) to read

$$\begin{aligned}\bar{Z}^{(1)}_{\mu\nu}(\mathbf{k}_1, \omega_1, \mathbf{k}_2, \omega_2) = \frac{(2\pi)^5\, |E_0|^2\, T\, \sigma^x\sigma^y\, \delta^x\delta^y}{\alpha^2\, \omega_1\omega_2\, \tilde{\Omega}}\, (\boldsymbol{\varepsilon}_L)_\mu\, (\boldsymbol{\varepsilon}_L)_\nu\, e^{-\Delta\omega^2\tilde{T}^2/2}\, e^{\mathrm{i}t_0\Delta\omega} \\ \times e^{-(k_2^x-k_1^x)^2(\sigma^x)^2/2}\, e^{-(k_1^x+k_2^x)^2(\delta^x)^2/8}\, e^{-(k_2^y-k_1^y)^2(\sigma^y)^2/2}\, e^{-(k_1^y+k_2^y)^2(\delta^y)^2/8} \\ \times\Big(e^{-(\bar{\omega}-\omega_0)^2/2\tilde{\Omega}^2} e^{\mathrm{i}z_0(k_1^\shortparallel-k_2^\shortparallel)}\, e^{-\mathrm{i}2\gamma_0 T^2\Delta\omega(\omega_0-\bar{\omega})/\tilde{\Omega}^2}\, \delta(k_1^\shortparallel - k_{1\_0}^\shortparallel)\, \delta(k_2^\shortparallel - k_{2\_0}^\shortparallel) \\ + e^{-(\bar{\omega}+\omega_0)^2/2\tilde{\Omega}^2} e^{-\mathrm{i}z_0(k_1^\shortparallel-k_2^\shortparallel)} e^{-\mathrm{i}2\gamma_0 T^2\Delta\omega(\omega_0+\bar{\omega})/\tilde{\Omega}^2}\, \delta(k_1^\shortparallel + k_{1\_0}^\shortparallel)\, \delta(k_2^\shortparallel + k_{2\_0}^\shortparallel)\Big).\end{aligned} \tag{4.68}$$

There is one obvious, yet nonetheless important, point to be re-called about the above expression. Namely that the described field is no longer transform limited, i.e., its product of pulse-length and bandwidth is no longer minimal. Thus, while the parameter T still controls the overall pulse length—as can be gathered from Eq. (A.130)—it is no longer the sole quantifier of the pulse's bandwidth. Focusing on the frequency resolved expressions $\bar{W}^{(1)}$ or $\bar{Z}^{(1)}$ instead, we find the relevant spectral part to read $e^{-(\bar{\omega}-\omega_0)^2/2\tilde{\Omega}^2}$, where $\tilde{\Omega}$ does define the bandwidth now.

4.4 Models for optical field-fluctuation

In contrast to laser-driven SFG or DFG, which involve an optical field in the form of its average correlator $\bar{H}^{(1)}$ (or $\bar{Z}^{(1)}$), the process of x-ray parametric down-conversion (XPDC), on the other hand, relies on the alternative term $\bar{S}^{(1)}$ (or $\bar{C}^{(1)}$) for fluctuations. For this correlator, we recall the general form from Eqs. (2.52) or (4.5)

$$\bar{S}_{\nu\mu}(\mathbf{x}',t',\mathbf{x},t) = \mathrm{Tr}_{\mathrm{OPT}}\{\hat{\rho}^{\mathrm{equ}}_{\mathrm{OPT}}\,(\hat{\mathbf{A}}_{\mathrm{opt}}(\mathbf{x}',t'))_\nu\,(\hat{\mathbf{A}}_{\mathrm{opt}}(\mathbf{x},t))_\mu\} \tag{4.69}$$

$$\text{wherein for each individual field: } \mathrm{Tr}_{\mathrm{OPT}}\{\hat{\rho}^{\mathrm{equ}}_{\mathrm{OPT}}\,(\hat{\mathbf{A}}_{\mathrm{opt}}(\mathbf{x}',t'))_\nu\} = 0. \tag{4.70}$$

In order to appreciate the impact of these fluctuation operators, we shall consider the XPDC process in more detail: During XPDC, an incident x-ray photon scatters at a net energy-loss ($\Delta\omega$), while coincidently a so-called 'idler'-photon is emitted, which takes up the energy difference of $\Delta\omega$. This 'idler' photon emerges *spontaneously* in a mode of the electromagnetic field that has previously been entirely unoccupied. Therefore, the only phenomenon capable of 'stimulating' or rather inducing this emission are quantum-fluctuations of the field. We note that the all-optical analogon of XPDC is often referred to as *spontaneous* parametric down-conversion (SPDC) [145] in view of its origin.

In the following, we present two approaches to quantify these fluctuations:
At first, we shall resort to the free-space form of the electromagnetic field (cf. Eq. (2.1)) and compute proper 'vacuum'-fluctuations on the basis of the pertaining operator algebra.
In the subsequent Sec. 4.4.2, we improve our modelling and take into account the dielectric nature of the sample.

In both cases, we will end up with expressions for the fluctuations' correlator in reciprocal-space, such that it can be implemented in Eq. (2.67). We recall the general definition of its Fourier transform below

$$\bar{C}^{\mathrm{OPT}}_{\nu\mu}(\mathbf{k}'_L,\omega'_L,\mathbf{k}_L,\omega_L) = \int^{\times 2} d^3x\,d^3x' \int^{\times 2} dt\,dt'\,e^{-\mathrm{i}\,(\mathbf{k}_L\cdot\mathbf{x}-\omega_L t)}\,e^{\mathrm{i}\,(\mathbf{k}'_L\cdot\mathbf{x}'-\omega'_L t')}\,\bar{S}_{\nu\mu}(\mathbf{x}',t',\mathbf{x},t). \tag{4.71}$$

4.4.1 Correlator of vacuum-fluctuations

If we want to obtain a first impression of the strengths and correlations among field fluctuations, we may consider as the simplemost case the fluctuations occurring in proper vacuum and at temperature $T = 0$. These can be resolved directly from the mode-expansion of the free field given in Eq. (2.1) initially. Inserting the respective expansion for $\hat{\mathbf{A}}(\mathbf{x})$ into Eq. (4.70) for the correlation function, we obtain

$$\begin{aligned}
\bar{S}_{\nu\mu}(\mathbf{x}',t',\mathbf{x},t) &= \mathrm{Tr}_{\mathrm{OPT}}\{|vac\rangle\langle vac|\,(\hat{\mathbf{A}}_{\mathrm{opt}}(\mathbf{x}',t'))_\nu\,(\hat{\mathbf{A}}_{\mathrm{opt}}(\mathbf{x},t))_\mu\} \\
&= \langle vac|\,(\hat{\mathbf{A}}_{\mathrm{opt}}(\mathbf{x}',t'))_\nu\,(\hat{\mathbf{A}}_{\mathrm{opt}}(\mathbf{x},t))_\mu\,|vac\rangle \\
&= \sum_{\mathbf{k},\lambda} \frac{2\pi}{V\alpha^2\omega_{\mathbf{k}}}\,(\boldsymbol{\varepsilon}_{\mathbf{k},\lambda})_\nu\,(\boldsymbol{\varepsilon}^*_{\mathbf{k},\lambda})_\mu\;e^{\mathrm{i}\,\mathbf{k}\cdot(\mathbf{x}'-\mathbf{x})}\,e^{-\mathrm{i}\,\omega_{\mathbf{k}}(t'-t)}\;\langle vac|\,\hat{a}_{\mathbf{k},\lambda}\hat{a}^\dagger_{\mathbf{k},\lambda}\,|vac\rangle \\
&= \sum_{\mathbf{k},\lambda} \frac{2\pi}{V\alpha^2\omega_{\mathbf{k}}}\,(\boldsymbol{\varepsilon}_{\mathbf{k},\lambda})_\nu\,(\boldsymbol{\varepsilon}^*_{\mathbf{k},\lambda})_\mu\;e^{\mathrm{i}\,\mathbf{k}\cdot(\mathbf{x}'-\mathbf{x})}\,e^{-\mathrm{i}\,\omega_{\mathbf{k}}(t'-t)}.
\end{aligned} \tag{4.72}$$

In here, we have assumed the field to be in an absolutely unoccupied state, i.e., perfect vacuum $\hat{\rho}^{\mathrm{equ}}_{\mathrm{OPT}} = |vac\rangle\langle vac|$. The free time-evolution of $\hat{a}_{\mathbf{k},\lambda}$ ($\hat{a}^\dagger_{\mathbf{k},\lambda}$) derives purely from the radiative Hamiltonian (outlined in Sec. 2.1) and can straight-forwardly be obtained from Heisenberg's equation of motion

(cf. Eq. (A.17)).

Taking the limit of large quantization volumes $V \to \infty$, we can convert the summation into an integration, by the usual prescription

$$\frac{1}{V}\sum_{\mathbf{k}} \ldots \to \frac{1}{(2\pi)^3}\int d^3k \ldots. \tag{4.73}$$

Moreover, we shall eliminate the explicit summation over polarization states in favour of the transversality constraint

$$\sum_{\lambda} (\boldsymbol{\varepsilon}_{\mathbf{k},\lambda})_\nu \, (\boldsymbol{\varepsilon}^*_{\mathbf{k},\lambda})_\mu = \delta_{\nu\mu} - \frac{(\mathbf{k})_\nu (\mathbf{k})_\mu}{|\mathbf{k}|^2}. \tag{4.74}$$

Employing both reformulations, Eq. (4.72) becomes

$$\bar{S}_{\nu\mu}(\mathbf{x}',t',\mathbf{x},t) = \int d^3k \, \frac{1}{(2\pi)^2 \alpha^2 \omega_{\mathbf{k}}} \left(\delta_{\nu\mu} - \frac{(\mathbf{k})_\nu (\mathbf{k})_\mu}{|\mathbf{k}|^2}\right) e^{\mathrm{i}\,\mathbf{k}\cdot(\mathbf{x}'-\mathbf{x})} \, e^{-\mathrm{i}\,\omega_{\mathbf{k}}(t'-t)}. \tag{4.75}$$

Finally, we also render the vacuum dispersion-relation ($\omega_{\mathbf{k}} = c\,|\mathbf{k}|$) more prominently visible. Hereunto, we introduce a formally independent integration over ω, which we constrain at the same time by an additional δ-function: $\delta(\omega - c\,|\mathbf{k}|)$. Overalls, this leads to

$$\bar{S}_{\nu\mu}(\mathbf{x}',t',\mathbf{x},t) = \int d^3k \int d\omega \; \delta(\omega - c\,|\mathbf{k}|) \, \frac{1}{(2\pi)^2 \alpha^2 \omega} \left(\delta_{\nu\mu} - \frac{(\mathbf{k})_\nu (\mathbf{k})_\mu}{|\mathbf{k}|^2}\right) e^{\mathrm{i}\,\mathbf{k}\cdot(\mathbf{x}'-\mathbf{x})} \, e^{-\mathrm{i}\,\omega(t'-t)}. \tag{4.76}$$

Its Fourier transform according to Eq. (4.71) is then easily evaluated to be

$$\bar{C}^{\mathrm{OPT}}_{\nu\mu}(\mathbf{k}'_L,\omega'_L,\mathbf{k}_L,\omega_L) = \delta^3(\mathbf{k}_L - \mathbf{k}'_L)\,\delta(\omega_L - \omega'_L)\,\delta(\omega_L + c\,|\mathbf{k}_L|)\,\frac{(2\pi)^6}{\alpha^2(-\omega_L)}\left(\delta_{\nu\mu} - \frac{(\mathbf{k}_L)_\nu (\mathbf{k}_L)_\mu}{|\mathbf{k}_L|^2}\right). \tag{4.77}$$

This result for the vacuum-case represents a solid starting point to build further intuition on the desired correlator of field-fluctuations. Moreover, it stands to be expected that even its quantitative assessment of the fluctuation-strength may be useful as a first estimation. Nevertheless, there are good reasons to go beyond the vacuum approximation as well—we shall do so below.

4.4.2 Optical field-fluctuations in dielectric materials

Having established the simplest description for the fluctuations of the optical field, we shall proceed to include the complications associated with the presence of a dielectric material—instead of vacuum.

As indicated earlier, propagation effects inside such a dielectric can significantly modify the properties of the optical photon. In the mildest case, this might be limited to refractive effects, i.e., a change of the dispersion relation

$$\omega_{\mathbf{k}} = c\,|\mathbf{k}| \to \omega_{\mathbf{k}} = \frac{c}{n}\,|\mathbf{k}|\,, \tag{4.78}$$

wherein we take n to denote a constant and real (!) refractive index for the moment. The quantization of the electromagnetic field on top of such a 'trivial' dielectric background is possible and has been discussed, for instance, by Drummond and Hillery [146]. Its most notable effect would, indeed, be the manifestation of n within the dispersion-δ-function. While seemingly innocuous, the corresponding

elongation of wave vectors $|\mathbf{k}| = \alpha\, n\, \omega_{\mathbf{k}}$ through n can already affect the scattering geometry significantly. An illustration of the phasematching-condition[21] for XPDC in Fig. 5.13, later on, highlights this difference for the example of diamond.

Beyond this geometrical effect, we point out (following Ref. [146]) the presence of a refractive index will already modify the behaviour of spontaneous emissions, in that it alters the overall density of states in the electromagnetic field. The change would be reflected in $\bar{C}^{\mathrm{OPT}}_{\nu\mu}$ as a contribution to the denominator

$$\bar{C}^{\mathrm{OPT}}_{\nu\mu}(\mathbf{k}'_L,\omega'_L,\mathbf{k}_L,\omega_L) = \delta^3(\mathbf{k}_L-\mathbf{k}'_L)\,\delta(\omega_L-\omega'_L)\,\delta(\omega_L+\frac{c}{n}\,|\mathbf{k}_L|)\frac{(2\pi)^6}{\alpha^2\,n\,(-\omega_L)}\left(\delta_{\nu\mu}-\frac{(\mathbf{k}_L)_\nu(\mathbf{k}_L)_\mu}{|\mathbf{k}_L|^2}\right). \tag{4.79}$$

For more realistic materials, we should expect to find significantly more complicated alterations being introduced. In particular, once electronic transitions may be excited by the photons involved, i.e., as soon as photoabsorption is present, we can expect non-trivial behaviour with pronounced frequency-dependence (e.g., absorption resonances).

We note that comparable effects—more broadly: the nature of quantum field-fluctuations inside matter—have received varied attention for almost a century; examples include but are not limited to Refs. [146–152].

At its core, however, we may solve the complicated quest for quantum field-fluctuations by using comparably simple insights from the realm of electrotechnics. Specifically, it was found and explained by Johnson and Nyquist, respectively, that the intrinsic noise stemming from a (linear, dissipative) circuit—most prominently grid-resistors on tube-amplifiers—can be related to the losses, which the same circuit element exhibits when driven by an external current [153, 154]. This fundamental relation of noise (i.e., fluctuations) to loss-properties (i.e., dissipation) marks the inception of the fluctuation-dissipation theorem (FDT). It has famously been extended to quantum systems by Kubo [155] and shall be used in a similar fashion towards our aims as well.

Following an elegant exposition by Landau [147], we note—first of all—that a correlator of *microscopic* fluctuations can be related to a likewise *microscopic* response function of the system[22]. Focusing for the latter on the retarded Green's function, we can formulate the respective fluctuation-dissipation theorem as (cf. Eq. (A.170) and App. A.12 more generally[23])

$$\tilde{C}_{\nu\mu}(\omega;\mathbf{x}',\mathbf{x}) = \mathrm{i}\,(1-e^{-\beta\omega})^{-1}\left(\tilde{D}^R_{\nu\mu}(\omega;\mathbf{x}',\mathbf{x}) - (\tilde{D}^R_{\mu\nu}(\omega;\mathbf{x},\mathbf{x}'))^*\right). \tag{4.80}$$

In the above, we can identify the Fourier transforms of the previously discussed fluctuation-correlator as well as the retarded Green's function

$$\tilde{C}_{\nu\mu}(\omega;\mathbf{x}',\mathbf{x}) = \int d\tau\, e^{\mathrm{i}\,\omega\tau}\,\bar{S}_{\nu\mu}(\mathbf{x}',\tau,\mathbf{x},0) \tag{4.81}$$

$$\tilde{D}^R_{\nu\mu}(\omega;\mathbf{x}',\mathbf{x}) = \int d\tau\, e^{\mathrm{i}\,\omega\tau}\,D^R_{\nu\mu}(\tau;\mathbf{x}',\mathbf{x}). \tag{4.82}$$

[21] For a conceptual discussion of 'phasematching', albeit with a focus on SFG / DFG, we refer the reader to Sec. 5.1.2.a.

[22] We note for clarification that, by use of the term 'system', we describe the electromagnetic quantum-field *in presence* of dielectric matter at this point.

[23] We note that in App. A.12, we derive the full FDT as given in Eq. (4.80) and, in addition, elaborate more broadly on the linear-response connection of micro- and macroscopic quantities therein.

The latter is defined on the microscopic scale of field-operators as

$$D^R_{\nu\mu}((t'-t);\mathbf{x}',\mathbf{x}) = -\mathrm{i}\,\theta(t'-t)\mathrm{Tr}_{\mathrm{OPT}}\left\{\hat{\rho}^{\mathrm{equ}}_{\mathrm{OPT}}\left[(\hat{\mathbf{A}}_{\mathrm{opt}}(\mathbf{x}',t'))_\nu,(\hat{\mathbf{A}}_{\mathrm{opt}}(\mathbf{x},t))_\mu\right]\right\}$$
$$= G^{\mathrm{ret}}_{A',A}(t'-t). \tag{4.83}$$

We remark that, in writing Eq. (4.83), we have adopted Landau's notation for $D^R_{\nu\mu}((t'-t);\mathbf{x}',\mathbf{x})$, which emphasizes the time-translation invariance of the response, i.e., being an equilibrium Green's function. The second line identifies the response with respect to our notation in App. A.12.

The last crucial step in obtaining a workable expression for the field fluctuations, consists in evaluating said Green's function. Rather than doing this for the microscopic response—which would be almost as difficult to calculate as the microscopic fluctuations—we identify $D^R_{\nu\mu}$ with its *macroscopic* counterpart. This identification is *approximately* valid in linear-response theory (see also Ref. [155]).

The macroscopic version of $D^R_{\nu\mu}$ can easily be obtained in reciprocal-space and reads[24]

$$D^R_{\nu\mu}(\omega;\mathbf{k}',\mathbf{k}) = \frac{4\pi}{\omega^2\,\alpha^2\,\varepsilon(|\omega|)-|\mathbf{k}|^2}(2\pi)^3\,\delta^3(\mathbf{k}'-\mathbf{k})\Big(\delta_{\nu\mu}-(\mathbf{k})_\nu(\mathbf{k})_\mu/|\mathbf{k}|^2\Big), \tag{4.84}$$

where $\varepsilon(|\omega|)$ denotes the *scalar* dielectric function of the sample. Notably, this is only valid for materials that are practically isotropic at optical wavelengths—such as diamond. Extensions thereof are obviously possible and would proceed in line with classical electrodynamics of an-isotropic or even structured materials.

For the time being, we restrict ourselves to the isotropic case and insert the above result into the fully Fourier transformed version of Eq. (4.80). Thereby, we ultimately obtain a correlator for the field-fluctuations inside dielectric matter, namely

$$\tilde{C}^{\mathrm{OPT}}_{\nu\mu}(\mathbf{k}'_L,\omega'_L,\mathbf{k}_L,\omega_L) = (2\pi)^5\,\delta^3(\mathbf{k}_L-\mathbf{k}'_L)\,\delta(\omega_L-\omega'_L)\,(1-e^{\beta\omega_L})$$
$$\Big(\delta_{\mu\nu}-\frac{(\mathbf{k}_L)_\mu(\mathbf{k}_L)_\nu}{|\mathbf{k}_L|^2}\Big)\,(-4)\,\mathrm{Im}\Big(\frac{1}{\omega_L^2\,\alpha^2\,\tilde{\varepsilon}(|\omega_L|)-|\mathbf{k}_L|^2}\Big). \tag{4.85}$$

Disregarding the thermal correction factor (which can be neglected in almost all cases), we find that the major difference with respect to the vacuum-result (Eq. (4.77)) lies in the more general dispersion relation, i.e., in the imaginary-part expression[25].

We note in closing, that the above expression implies the possibility that the dispersion may deviate around its fixed form of Eq. (4.78), viz. $\omega = \frac{c}{n}|\mathbf{k}|$. Especially, when absorption is strong (i.e., $\mathrm{Im}(\tilde{\varepsilon}(|\omega_L|)) \gg 0$), a broad range of frequencies can be associated with each wave vector. In this sense, the spatial absorption (or decay) of the 'idler'-photon introduces a line-broadening, which is otherwise known from temporal decay (cf. lifetime-broadening of resonances).

[24] We note that the macroscopic version of $D^R_{\nu\mu}$ is really just the Green's function (or propagator) for the *classical* wave equation of the electromagnetic vector potential inside a (largely) homogeneous dielectric. This dielectric, in turn, should be characterized by a macroscopic, dielectric response $\varepsilon(|\omega|)$, which could at most be augmented to feature an additional, slowly-varying dependence on its position.

[25] We note that the difference between Eq. (4.77) and Eq. (4.85), does infact vanish in the limit $\tilde{\varepsilon}(|\omega_L|) \to 1$. Thus the latter result correctly recovers our original expression. Analogously, Eq. (4.79) may be recovered, if $\tilde{\varepsilon}(|\omega_L|)$ is chosen to approach on n^2. This highlights the power of the fluctuation-dissipation theorem—it allows for a (relatively) simple inclusion of *non-perturbative* effects, despite relying on linear response theory for the micro-to-macro matching.

Chapter 5

Application to experiments

In this chapter, we will discuss applications of our XOWM framework to several experimental scenarios. Thereby, we seek to benchmark the range of its validity and—more generally—explore the burgeoning field of XOWM itself. As such, the scope of this chapter extends beyond theoretical derivations and likewise reflects the series of experiments[1], which we have conducted in close collaboration with Dr. Christina Bömer.

We begin in Sec. 5.1 by investigating x-ray-optical sum- and difference frequency generation (SFG / DFG) more closely. As a first benchmark, we employ our framework to model the landmark study of Glover et al., who demonstrated x-ray-optical SFG in 2012 [46]—see Sec. 5.1.1. Obtaining excellent agreement, we continue to generalize our findings and comment on several further use-cases in Sec. 5.1.2. Closing our discussion of laser-driven XOWM, we present an improved experimental setup in Sec. 5.1.3. This is intended to render 'nonlinear crystallography' more efficient in terms of alignment-time and was successfully tested at SwissFEL.

Subsequently, we turn our attention to scenarios of spontaneous XOWM, i.e., x-ray parametric down-conversion (XPDC)—see Sec. 5.2. For this phenomenon, we shall address two regimes: XPDC with idler photon energies below the band gap of the sample or far above it. Notably, we restrict our discussion to (mono-)crystalline semiconductors as samples. In Sec. 5.2.1, we apply our theory below the band gap of diamond and compare to a corresponding experiment of ours [51]. While both results are well compatible with each other, they jointly contradict a series of earlier reportings on XPDC. The discrepancy will be discussed separately in Sec. 5.2.2. Subsequently, we shift our focus towards the high-energy scenario in Sec. 5.2.3. Hereunto, we present both theoretical modelling of the phenomenon as well as preliminary, experimental results, which we have obtained using a novel detection scheme. Our results show good agreement with earlier, more restricted reports by Tamasaku et al., while raising an interesting conundrum. The latter will further be addressed in an 'extra' chapter 6.

We note in closing that our theoretical framework does not extend towards all-x-ray PDC at present. As such, no direct comparison with the works of Eisenberger and McCall [27] or the HASYLAB-team around Adams, Novikov and Materlik [88] could be drawn.

[1] During the course of this thesis' research, we successfully applied for 12 beamtimes at synchrotron radiation sources and XFELs. Six of these could be carried out under the constraints of the COVID-19 pandemic, viz. at Petra III: I-20190876 and I-20211074 (both at beamline P09), at the ESRF: HC-4489 and HC-4907 (both at beamline ID20), at PAL-XFEL: 2021-2nd-XSS-002 (at the FXS instrument) and at SwissFEL: 20212165 (at the Bernina endstation).

5.1 Sum- and Difference-Frequency-Generation

In this section, we shall study different cases of x-ray-optical SFG and DFG. In other words, we aim for the calculation / detection of nonlinearly scattered photons that posses as their energy either the sum ($\omega_f = \omega_X + \omega_O$) or difference ($\omega_f = \omega_X - \omega_O$) of the incident x-ray and optical frequencies. As a matter of fact, there will be no fundamental difference in their description, which is henceforth carried out in parallel in many places. Ultimately, the desired set of frequency-components can be selected through the choice of ω_f directly or the setting of an appropriate analyser transmission.

5.1.1 Benchmark – SFG experiment by Glover et al.

For the first application of our XOWM-framework, we choose to study the case of sum-frequency generation reported by Glover et al. [46]. With their quantitative, experimental results at hand, we can benchmark the performance of our theoretical description and—by extension— assess the validity of our modelling assumptions.

In their experiment, Glover et al. super-imposed an x-ray beam of 8 keV photon energy with an almost collinear optical laser, operating at 1.55 eV photon energy (i.e., 800 nm wavelength). Mixing these inside a diamond sample, they obtained a measurable SFG signal at $8000 + 1.55\,\text{eV}$ photon energy, which they discriminated for using an analyser crystal (two-bounce Si(220), channel-cut). The setup is schematically depicted in Fig. 5.1—taken from Ref. [46]—alongside the study's central results. In particular, the authors have studied the dependence of the SFG signal upon several different parameters in

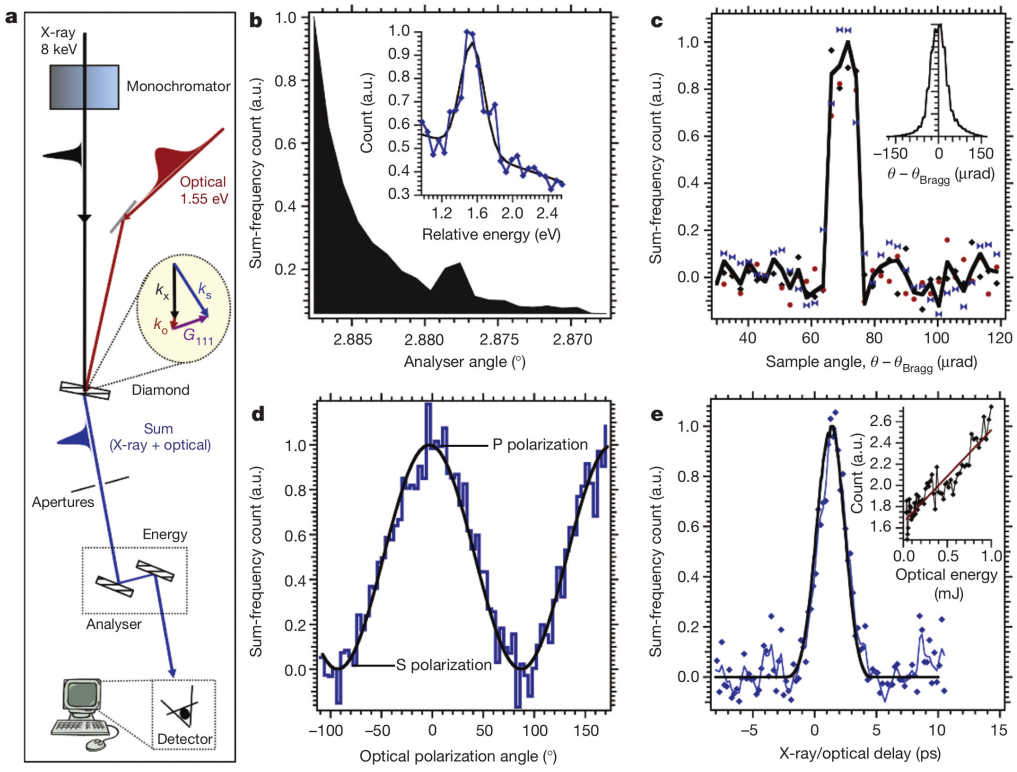

Figure 5.1: Illustration of the setup (a) used by Glover et al. to measure x-ray optical sum-frequency generation. The SFG signal was scanned for: (b)-its energy dependence, (c)-its angular dependence, (d)-its dependence upon the polarization of the laser light and (e)-the temporal correlation of x-ray and optical field. The inset of (e) further shows the scaling of the SFG signal with the laser's pulse energy. Figure reproduced from Ref. [46].

order to establish their observation conclusively. Besides the obvious scan for the signal's energetic signature (Fig. 5.1 b), they have cross-checked the rocking-behaviour, i.e., the dependence of the SFG signal upon change of the sample angle (Fig. 5.1 c). Moreover, they have rotated the laser's polarization and shifted the x-ray-optical time-delay. These resulted in a cosine-squared behaviour for the former (d) and a variation with the temporal cross-correlation for the latter scan (e). All of these results are compatible with an intuitive conception of x-ray-optical SFG and render the reported observation convincing.

Now, we aim to reproduce these findings from the theoretical side. In order to do so, we start from our general expression Eq. (2.67)

$$\begin{aligned}\langle \hat{O} \rangle =& \frac{2\pi\alpha^4}{V\omega_f}\,\frac{1}{(2\pi)^{14}}\int^{\times 4} d^3k_L d^3k'_L d^3k_X d^3k'_X \int^{\times 4} d\omega_L d\omega'_L d\omega_X d\omega'_X\; \delta(\omega_f-\omega_X-\omega_L)\,\delta(\omega_f-\omega'_X-\omega'_L)\\ &\times (\boldsymbol{\varepsilon}_f)_\sigma\,(\boldsymbol{\varepsilon}^*_f)_\rho\; Z^{\text{X\_IN}}_{\sigma\rho}(\mathbf{k}'_X,\omega'_X,\mathbf{k}_X,\omega_X)\,\bar{Z}^{\text{OPT}}_{\nu\mu}(\mathbf{k}'_L,\omega'_L,\mathbf{k}_L,\omega_L)\\ &\times \sum_I p_I \Big(\mathbf{K}_I(-\mathbf{k}_L,\mathbf{k}_f-\mathbf{k}_X,\omega_L)\Big)_\mu \Big(\mathbf{K}_I(-\mathbf{k}'_L,\mathbf{k}_f-\mathbf{k}'_X,\omega'_L)\Big)^*_\nu. \end{aligned} \tag{5.1}$$

In the following, we will specify its constituent functions to reflect the experimental situation and approximate the resulting expression such that it can easily be evaluated (semi-analytically).

We begin by modelling the x-ray field $Z^{\text{X\_IN}}_{\sigma\rho}$. This consisted of a series of XFEL pulses generated by the Linac Coherent Light Source (LCLS), which operated in SASE-mode at the time of the experiment under consideration [156, 157]. As outlined earlier, the (coherence-) properties of such a source can be modelled using a Gaussian-Schell model such as our Eq. (4.41)

$$\begin{aligned} Z^{\text{X\_IN}}_{\sigma\rho}(\mathbf{k}'_X,\omega'_X,\mathbf{k}_X,\omega_X) =& \frac{(2\pi)^5\, G_{X\_0}\, T_X\, \sigma^x_X\sigma^y_X\, \delta^x_X\delta^y_X}{\alpha^2\,\omega'_X\omega_X\,\Omega_X}\;(\boldsymbol{\varepsilon}_X)_\sigma\,(\boldsymbol{\varepsilon}_X)_\rho\;\delta(k'^{||}_X-k'^{||}_{X\_0})\,\delta(k^{||}_X-k^{||}_{X\_0})\\ &\times (T_m(\omega'_X))^*\,T_m(\omega_X)\,e^{-(\bar{\omega}_X-\omega_{X\_0})^2/2\Omega^2_X}\,e^{-\Delta\omega^2_X T^2_X/2}\\ &\times e^{-(\Delta k^x_X)^2(\sigma^x_X)^2/2}\;e^{-(\bar{k}^x_X)^2(\delta^x_X)^2/2}e^{-(\Delta k^y_X)^2(\sigma^y_X)^2/2}\;e^{-(\bar{k}^y_X)^2(\delta^y_X)^2/2}\;e^{\mathrm{i}\,\frac{z_{X\_0}}{\alpha\bar{\omega}_X}\bar{\mathbf{k}}^\perp_X\cdot\Delta\mathbf{k}^\perp_X}. \end{aligned} \tag{5.2}$$

Here, we have reserved the transmission function $T_m(\omega_X)$ to stand in for an additional monochromator. For our present purposes, it is sufficient to use a simple Gaussian monochromator model to approximate the central passwidth of the Si (111) double crystal monochromator[2] (DCM) used by Glover et al. [46]:

$$T_m(\omega_X) = e^{-(\omega_X-\omega_m)^2/(4\Omega^2_m)} \qquad \text{with: } T_m(\omega_X)T_m(\omega'_X) = e^{-(\bar{\omega}_X-\omega_m)^2/2\Omega^2_m}\,e^{-\Delta\omega^2_X/8\Omega^2_m} \tag{5.3}$$

In the two equations above, we have introduced adapted coordinates

$$\Delta\omega_X = \omega_X-\omega'_X \qquad \text{and} \qquad \bar{\omega}_X=(\omega_X+\omega'_X)/2 \qquad \Leftrightarrow \qquad \omega_X=\bar{\omega}_X+\Delta\omega_X/2, \tag{5.4}$$

$$\Delta\mathbf{k}_X = \mathbf{k}_X-\mathbf{k}'_X \qquad \text{and} \qquad \bar{\mathbf{k}}_X=(\mathbf{k}_X+\mathbf{k}'_X)/2 \qquad \Leftrightarrow \qquad \mathbf{k}_X=\bar{\mathbf{k}}_X+\Delta\mathbf{k}_X/2, \tag{5.5}$$

which denote the central frequency (or wave-vector) and deviation from it. The latter is of particular use, when establishing the range, over which the source is coherent. We can slightly rewrite $Z^{\text{X\_IN}}_{\sigma\rho}$ in terms of

[2]Note, that such a Si (111) DCM yields a spectral passwidth of $\sim 1\,\text{eV}$ (FWHM) under the given conditions, which will drive the SFG process. In addition, there will be weak, yet extended, spectral tails up to tens of eV away from the central photon energy. These will not present a problem for the case at hand, but re-emerge as a critical issue during our study of XPDC later 5.2.

the average pulse energy measured before the monochromator

$$E_{X\_p} = \frac{G_{X\_0}\, T_X\, \sigma_X^x \sigma_X^y \sqrt{\pi}}{\alpha\sqrt{2}} \tag{5.6}$$

rendering

$$Z^{\mathrm{X\_IN}}_{\sigma\rho}(\mathbf{k}'_X, \omega'_X, \mathbf{k}_X, \omega_X) = \frac{(2\pi)^4\sqrt{2\pi}\,2\,E_{X\_p}\,\delta_X^x\delta_X^y}{\alpha\,\omega'_X\,\omega_X\,\Omega_X}\,(\boldsymbol{\varepsilon}_X)_\sigma\,(\boldsymbol{\varepsilon}_X)_\rho\,\delta(k'^{\shortparallel}_X - k'^{\shortparallel}_{X\_0})\,\delta(k^{\shortparallel}_X - k^{\shortparallel}_{X\_0})\,e^{-(\bar\omega_X-\omega_{X\_0})^2\frac{\Omega_X^2+\Omega_m^2}{2\Omega_X^2\Omega_m^2}}$$
$$\times\, e^{-\Delta\omega_X^2(T_X^2+(2\Omega_m)^{-2})/2}\, e^{-(\Delta k_X^x)^2(\sigma_X^x)^2/2}\, e^{-(\bar k_X^x)^2(\delta_X^x)^2/2} e^{-(\Delta k_X^y)^2(\sigma_X^y)^2/2}\, e^{-(\bar k_X^y)^2(\delta_X^y)^2/2}\, e^{\mathrm{i}\frac{z_{X\_0}}{\alpha\bar\omega_X}\bar{\mathbf{k}}_X^\perp\cdot\Delta\mathbf{k}_X^\perp}. \tag{5.7}$$

Here, we have also assumed that $\omega_{X\_0} \approx \omega_m$, i.e., that the monochromator's central energy is roughly aligned with the intrinsic central energy of the source. This should be the natural choice, if you care not to waste flux.

Describing the laser field, with which to mix the x-rays, we implement the stretched pulse model of Eq. (4.68) for a radially symmetric beam that co-propagates with the incident x-rays:

$$\begin{aligned}\bar Z^{\mathrm{OPT}}_{\nu\mu}(\mathbf{k}'_L, \omega'_L, \mathbf{k}_L, \omega_L) = {}& \frac{(2\pi)^5\,|E_{L_0}|^2\,T_L\,\sigma_L^2\,\delta_L^2}{\alpha^2\,\omega'_L\,\omega_L\,\tilde\Omega_L}\,(\boldsymbol{\varepsilon}_L)_\nu\,(\boldsymbol{\varepsilon}_L)_\mu\, e^{-\Delta\omega_L^2\tilde T_L^2/2}\, e^{\mathrm{i}\Delta t\,\Delta\omega_L}\\
&\times e^{-(\Delta\mathbf{k}_L^\perp)^2\sigma_L^2/2}\, e^{-(\bar{\mathbf{k}}_L^\perp)^2\delta_L^2/2}\, e^{\mathrm{i}\frac{z_{L_0}}{\alpha|\bar\omega_L|^n}\bar{\mathbf{k}}_L^\perp\cdot\Delta\mathbf{k}_L^\perp}\\
&\times\Big(e^{-(\bar\omega_L-\omega_{L_0})^2/2\tilde\Omega_L^2}\, e^{-\mathrm{i}2\gamma_0 T_L^2\Delta\omega_L(\omega_{L_0}-\bar\omega_L)/\tilde\Omega_L^2}\,\delta(k'^{\shortparallel}_L - k'^{\shortparallel}_{L_0})\delta(k^{\shortparallel}_L - k^{\shortparallel}_{L_0})\\
&+ e^{-(\bar\omega_L+\omega_{L_0})^2/2\tilde\Omega_L^2}\, e^{-\mathrm{i}2\gamma_0 T_L^2\Delta\omega_L(\omega_{L_0}+\bar\omega_L)/\tilde\Omega_L^2}\,\delta(k'^{\shortparallel}_L + k'^{\shortparallel}_{L_0})\delta(k^{\shortparallel}_L + k^{\shortparallel}_{L_0})\Big).\end{aligned} \tag{5.8}$$

Here, we have again made use of reduced coordinates

$$\Delta\omega_L = \omega_L - \omega'_L \qquad \text{and} \qquad \bar\omega_L = (\omega_L + \omega'_L)/2 \qquad \Leftrightarrow \qquad \omega_L = \bar\omega_L + \Delta\omega_L/2, \tag{5.9}$$

$$\Delta\mathbf{k}_L = \mathbf{k}_L - \mathbf{k}'_L \qquad \text{and} \qquad \bar{\mathbf{k}}_L = (\mathbf{k}_L + \mathbf{k}'_L)/2 \qquad \Leftrightarrow \qquad \mathbf{k}_L = \bar{\mathbf{k}}_L + \Delta\mathbf{k}_L/2. \tag{5.10}$$

Finally, for the electronic correlation function, we disregard the sum over incoherent excitations (phonons) and consider only one ground state correlator. Furthermore, we employ the previously discussed simplification Eq. (3.24)

$$\mathbf{K}_I(-\mathbf{k}_L, \mathbf{k}_f - \mathbf{k}_X, \omega_L) \approx \tilde w(\mathbf{k}_f - \mathbf{k}_X - \mathbf{k}_L - \mathbf{G})\,\frac{1}{V_\diamond}\,\mathbf{K}_{GS\diamond}(0, \mathbf{G}, \omega_L). \tag{5.11}$$

Inserting all of these elements into Eq. (5.1), we find[3]

$$\begin{aligned}
\langle \hat{O} \rangle =& \frac{2\pi\alpha^4}{V\omega_f}\,\frac{1}{(2\pi)^{14}}\int^{\times 4} d^3k_L d^3k'_L d^3k_X d^3k'_X \int^{\times 4} d\omega_L d\omega'_L d\omega_X d\omega'_X\; \delta(\omega_f-\omega_X-\omega_L)\,\delta(\omega_f-\omega'_X-\omega'_L) \\
&\times (\boldsymbol{\varepsilon}_f)_\sigma\,(\boldsymbol{\varepsilon}^*_f)_\rho\;\frac{(2\pi)^4\sqrt{2\pi}\,2E_{X_p}\,\delta^x_X\delta^y_X}{\alpha\,\omega'_X\omega_X\,\Omega_X}\;(\boldsymbol{\varepsilon}_X)_\sigma\,(\boldsymbol{\varepsilon}_X)_\rho\,\delta(k'^{\shortparallel}_X-k'^{\shortparallel}_{X_0})\,\delta(k^{\shortparallel}_X-k^{\shortparallel}_{X_0})\,e^{-(\bar\omega_X-\omega_{X_0})^2\frac{\Omega_X^2+\Omega_m^2}{2\Omega_X^2\Omega_m^2}} \\
&\times e^{-\Delta\omega_X^2(T_X^2+(2\Omega_m)^{-2})/2}\;e^{-(\Delta k^x_X)^2(\sigma^x_X)^2/2}\;e^{-(\bar k^x_X)^2(\delta^x_X)^2/2}e^{-(\Delta k^y_X)^2(\sigma^y_X)^2/2}\;e^{-(\bar k^y_X)^2(\delta^y_X)^2/2}\;e^{\mathrm{i}\,\frac{z_{X_0}}{\alpha\bar\omega_X}\bar{\mathbf{k}}^\perp_X\cdot\Delta\mathbf{k}^\perp_X} \\
&\times \frac{(2\pi)^5\,|E_{L_0}|^2\,T_L\,\sigma_L^2\,\delta_L^2}{\alpha^2\,\omega'_L\omega_L\tilde\Omega_L}\;(\boldsymbol{\varepsilon}_L)_\nu\,(\boldsymbol{\varepsilon}_L)_\mu\,e^{-\Delta\omega_L^2\tilde T_L^2/2}\;e^{\mathrm{i}\,\Delta t\,\Delta\omega_L}\;e^{-(\Delta\mathbf{k}^\perp_L)^2\sigma_L^2/2}\;e^{-(\bar{\mathbf{k}}^\perp_L)^2\delta_L^2/2}\;e^{\mathrm{i}\,\frac{z_{L_0}}{\alpha|\bar\omega_L|^n}\bar{\mathbf{k}}^\perp_L\cdot\Delta\mathbf{k}^\perp_L} \\
&\times\Big(e^{-(\bar\omega_L-\omega_{L_0})^2/2\tilde\Omega_L^2}\,e^{-\mathrm{i}\,2\gamma_0 T_L^2\Delta\omega_L(\omega_{L_0}-\bar\omega_L)/\tilde\Omega_L^2}\,\delta(k'^{\shortparallel}_L-k'^{\shortparallel}_{L_0})\delta(k^{\shortparallel}_L-k^{\shortparallel}_{L_0}) \\
&+e^{-(\bar\omega_L+\omega_{L_0})^2/2\tilde\Omega_L{}^2}\,e^{-\mathrm{i}\,2\gamma_0 T_L^2\Delta\omega_L(\omega_{L_0}+\bar\omega_L)/\tilde\Omega_L^2}\,\delta(k'^{\shortparallel}_L+k'^{\shortparallel}_{L_0})\delta(k^{\shortparallel}_L+k^{\shortparallel}_{L_0})\Big) \\
&\times\tilde w(\mathbf{k}_f-\mathbf{k}_X-\mathbf{k}_L-\mathbf{G})\,\frac{1}{V_\diamond}\Big(\mathbf{K}_{GS\diamond}(0,\mathbf{G},\omega_L)\Big)_\mu\,(\tilde w(\mathbf{k}_f-\mathbf{k}'_X-\mathbf{k}'_L-\mathbf{G}))^*\,\frac{1}{V_\diamond}\Big(\mathbf{K}_{GS\diamond}(0,\mathbf{G},\omega'_L)\Big)^*_\nu .
\end{aligned} \tag{5.12}$$

Reordering this slightly gives

$$\begin{aligned}
\langle \hat{O} \rangle =& \frac{\sqrt{2\pi}}{(2\pi)^4}\,\frac{\alpha\,2E_{X_p}\,\delta^x_X\delta^y_X\,|E_{L_0}|^2\,T_L\,\sigma_L^2\,\delta_L^2}{V\omega_f\,\Omega_X\,\tilde\Omega_L}\,\big|\boldsymbol{\varepsilon}_f\cdot\boldsymbol{\varepsilon}_X\big|^2\int^{\times 4} d^3k_L d^3k'_L d^3k_X d^3k'_X\int^{\times 4} d\omega_L d\omega'_L d\omega_X d\omega'_X \\
&\times\delta(\omega_f-\omega_X-\omega_L)\,\delta(\omega_f-\omega'_X-\omega'_L)\frac{1}{\omega'_X\omega_X\,\omega'_L\,\omega_L}\;\delta(k'^{\shortparallel}_X-k'^{\shortparallel}_{X_0})\,\delta(k^{\shortparallel}_X-k^{\shortparallel}_{X_0})\,e^{-(\bar\omega_X-\omega_{X_0})^2\frac{\Omega_X^2+\Omega_m^2}{2\Omega_X^2\Omega_m^2}} \\
&\times e^{-\Delta\omega_X^2(T_X^2+(2\Omega_m)^{-2})/2}\;e^{-(\Delta k^x_X)^2(\sigma^x_X)^2/2}\;e^{-(\bar k^x_X)^2(\delta^x_X)^2/2}e^{-(\Delta k^y_X)^2(\sigma^y_X)^2/2}\;e^{-(\bar k^y_X)^2(\delta^y_X)^2/2}\;e^{\mathrm{i}\,\frac{z_{X_0}}{\alpha\bar\omega_X}\bar{\mathbf{k}}^\perp_X\cdot\Delta\mathbf{k}^\perp_X} \\
&\times e^{-\Delta\omega_L^2\tilde T_L^2/2}\;e^{\mathrm{i}\,\Delta t\,\Delta\omega_L}\;e^{-(\Delta\mathbf{k}^\perp_L)^2\sigma_L^2/2}\;e^{-(\bar{\mathbf{k}}^\perp_L)^2\delta_L^2/2}\;e^{\mathrm{i}\,\frac{z_{L_0}}{\alpha|\bar\omega_L|^n}\bar{\mathbf{k}}^\perp_L\cdot\Delta\mathbf{k}^\perp_L} \\
&\times\Big(e^{-(\bar\omega_L-\omega_{L_0})^2/2\tilde\Omega_L^2}\,e^{-\mathrm{i}\,2\gamma_0 T_L^2\Delta\omega_L(\omega_{L_0}-\bar\omega_L)/\tilde\Omega_L^2}\,\delta(k'^{\shortparallel}_L-k'^{\shortparallel}_{L_0})\delta(k^{\shortparallel}_L-k^{\shortparallel}_{L_0}) \\
&+e^{-(\bar\omega_L+\omega_{L_0})^2/2\tilde\Omega_L{}^2}\,e^{-\mathrm{i}\,2\gamma_0 T_L^2\Delta\omega_L(\omega_{L_0}+\bar\omega_L)/\tilde\Omega_L^2}\,\delta(k'^{\shortparallel}_L+k'^{\shortparallel}_{L_0})\delta(k^{\shortparallel}_L+k^{\shortparallel}_{L_0})\Big) \\
&\times\tilde w(\mathbf{k}_f-\mathbf{k}_X-\mathbf{k}_L-\mathbf{G})\,(\tilde w(\mathbf{k}_f-\mathbf{k}'_X-\mathbf{k}'_L-\mathbf{G}))^*\,\frac{1}{V_\diamond^2}\Big(\boldsymbol{\varepsilon}_L\cdot\mathbf{K}_{GS\diamond}(0,\mathbf{G},\omega_L)\Big)\Big(\boldsymbol{\varepsilon}_L\cdot\mathbf{K}_{GS\diamond}(0,\mathbf{G},\omega'_L)\Big)^* .
\end{aligned} \tag{5.13}$$

In this expression, we find a number of window- and δ-functions that can be simplified, before we turn towards approximations. First of all, we shall address the window functions $\tilde w(...)$. In the simplest case of an un-rotated cuboid block, the original windows factorize in real space $w(\mathbf{x}) = w(x)\cdot w(y)\cdot w(z)$. Naturally, this carries over into reciprocal space (see also App. A.15). For a *tilted* crystal, these components would be rotated among each other, however, we can neglect this minor complication for the time-being and stick with the simplemost scheme of an un-rotated box[4]. In the transverse directions, the sample may be chosen significantly larger than all relevant beam diameters. As such, the resulting

[3] Note that we employ the reduced coordinates, wherever they render the expression more compact. However, we keep the differentials d^3k and $d\omega$ in their initial form—merely for compactness of notation.

[4] Notably, Glover et al. address the (111)-reflection in a diamond sample of (100)-surface-cut. This implies that the sample only needs to be rotated by ~ 13 deg away from normal incidence. This deviation can safely be neglected in a rough description of the SFG effect, but will make a re-appearance, should the precise rocking angle be calculated.

k-space windows can be considered infinitely sharp, i.e., as δ-functions:

$$\tilde{w}(\mathbf{k}^\perp) \approx (2\pi)^2\ \delta^2(\mathbf{k}^\perp). \tag{5.14}$$

Here, the factor $(2\pi)^2$ ensures the appropriate normalization of the window—as before (cf. App. A.15). For the longitudinal component, we approximate the window function again by a Gaussian

$$\tilde{w}(k^\shortparallel) \approx l_w\ e^{-(k^\shortparallel)^2\sigma_w^2/2} \qquad \text{with} \qquad \sigma_w = \frac{l_w}{\sqrt{2\pi}}. \tag{5.15}$$

Its normalization is also chosen to accord with the integral of the original window (cf. App. A.15).

Our next step concerns the series of δ-functions, which are present in the above expression and mostly refer to the old coordinate system (ω, ω'). We shall rewrite all of them for use with the reduced coordinates. To this end, we observe the integral relation

$$\begin{aligned}
\delta(\omega_f - \omega_X - \omega_L)\,\delta(\omega_f - \omega_X' - \omega_L') &= \frac{1}{(2\pi)^2}\ \int^{\times 2} dt\,dt'\ e^{\mathrm{i}(\omega_f-\omega_X-\omega_L)t+\mathrm{i}(\omega_f-\omega_X'-\omega_L')t'} \\
&= \frac{1}{(2\pi)^2}\ \int^{\times 2} dt\,dt'\ e^{\mathrm{i}(\omega_f-\bar{\omega}_X-\bar{\omega}_L)(t+t')+\mathrm{i}(\Delta\omega_X+\Delta\omega_L)(t'-t)/2} \\
&= \frac{1}{(2\pi)^2}\ \int^{\times 2} dT\,d\tau\ e^{\mathrm{i}(\omega_f-\bar{\omega}_X-\bar{\omega}_L)T+\mathrm{i}(\Delta\omega_X+\Delta\omega_L)\tau} \\
&= \delta(\omega_f - \bar{\omega}_X - \bar{\omega}_L)\,\delta(\Delta\omega_X + \Delta\omega_L),
\end{aligned} \tag{5.16}$$

which may analogously be employed for

$$\delta(k_X'^\shortparallel - k_{X\_0}'^\shortparallel)\,\delta(k_X^\shortparallel - k_{X\_0}^\shortparallel) = \delta(\bar{k}_X'^\shortparallel - \bar{k}_{X\_0}'^\shortparallel)\,\delta(\Delta k_X^\shortparallel + \Delta k_{X\_0}^\shortparallel) \tag{5.17}$$

$$\delta(k_L'^\shortparallel - k_{L\_0}'^\shortparallel)\delta(k_L^\shortparallel - k_{L\_0}^\shortparallel) = \delta(\bar{k}_L'^\shortparallel - \bar{k}_{L\_0}'^\shortparallel)\,\delta(\Delta k_L^\shortparallel + \Delta k_{L\_0}^\shortparallel) \tag{5.18}$$

$$\delta(k_L'^\shortparallel + k_{L\_0}'^\shortparallel)\delta(k_L^\shortparallel + k_{L\_0}^\shortparallel) = \delta(\bar{k}_L'^\shortparallel + \bar{k}_{L\_0}'^\shortparallel)\,\delta(\Delta k_L^\shortparallel - \Delta k_{L\_0}^\shortparallel) \tag{5.19}$$

$$\delta^2(\mathbf{k}_f^\perp - \mathbf{k}_X^\perp - \mathbf{k}_L^\perp - \mathbf{G}^\perp)\delta^2(\mathbf{k}_f^\perp - \mathbf{k}_X'^\perp - \mathbf{k}_L'^\perp - \mathbf{G}^\perp) = \delta^2(\mathbf{k}_f^\perp - \bar{\mathbf{k}}_X^\perp - \bar{\mathbf{k}}_L^\perp - \mathbf{G}^\perp)\,\delta^2(\Delta\mathbf{k}_X^\perp + \Delta\mathbf{k}_L^\perp). \tag{5.20}$$

In the same spirit follows for the longitudinal window:

$$e^{-(k_f^\shortparallel - k_L^\shortparallel - k_X^\shortparallel - G^\shortparallel)^2\sigma_w^2/2}\,e^{-(k_f^\shortparallel - k_L'^\shortparallel - k_X'^\shortparallel - G^\shortparallel)^2\sigma_w^2/2} = e^{-(k_f^\shortparallel - \bar{k}_L^\shortparallel - \bar{k}_X^\shortparallel - G^\shortparallel)^2\sigma_w^2}\,e^{-(\Delta k_L^\shortparallel + \Delta k_X^\shortparallel)^2\sigma_w^2/4}. \tag{5.21}$$

Implementing all transformations, we obtain for the observable

$$
\begin{aligned}
\langle \hat{O} \rangle = \frac{\sqrt{2\pi}}{(2\pi)^4} \frac{\alpha\, 2 E_{X\_p}\, \delta_X^x \delta_X^y\, |E_{L\_0}|^2\, T_L\, \sigma_L^2\, \delta_L^2}{V\, \omega_f\, \Omega_X\, \tilde{\Omega}_L} \left|\boldsymbol{\varepsilon}_f \cdot \boldsymbol{\varepsilon}_X\right|^2 \int^{\times 4} d^3k_L d^3k'_L d^3k_X d^3k'_X \int^{\times 4} d\omega_L d\omega'_L d\omega_X d\omega'_X \\
\times \delta(\omega_f - \bar{\omega}_X - \bar{\omega}_L)\, \delta(\Delta\omega_X + \Delta\omega_L)\, \frac{1}{\omega'_X\, \omega_X\, \omega'_L\, \omega_L}\, \delta(\bar{k}_X^{\shortparallel} - \bar{k}_{X\_0}^{\shortparallel})\, \delta(\Delta k_X^{\shortparallel} + \Delta k_{X\_0}^{\shortparallel})\, e^{-(\bar{\omega}_X - \omega_{X\_0})^2 \frac{\Omega_X^2 + \Omega_m^2}{2\Omega_X^2 \Omega_m^2}} \\
\times e^{-\Delta\omega_X^2 (T_X^2 + (2\Omega_m)^{-2})/2}\, e^{-(\Delta k_X^x)^2 (\sigma_X^x)^2/2}\, e^{-(\bar{k}_X^x)^2 (\delta_X^x)^2/2} e^{-(\Delta k_X^y)^2 (\sigma_X^y)^2/2}\, e^{-(\bar{k}_X^y)^2 (\delta_X^y)^2/2}\, e^{\mathrm{i}\, \frac{z_{X\_0}}{\alpha\, \bar{\omega}_X} \bar{\mathbf{k}}_X^{\perp} \cdot \Delta\mathbf{k}_X^{\perp}} \\
\times e^{-\Delta\omega_L^2 \tilde{T}_L^2/2}\, e^{\mathrm{i}\, \Delta t\, \Delta\omega_L}\, e^{-(\Delta\mathbf{k}_L^{\perp})^2 \sigma_L^2/2}\, e^{-(\bar{\mathbf{k}}_L^{\perp})^2 \delta_L^2/2}\, e^{\mathrm{i}\, \frac{z_{L\_0}}{\alpha |\bar{\omega}_L|^n} \bar{\mathbf{k}}_L^{\perp} \cdot \Delta\mathbf{k}_L^{\perp}} \\
\times \Big(e^{-(\bar{\omega}_L - \omega_{L\_0})^2 / 2\tilde{\Omega}_L^2}\, e^{-\mathrm{i}\, 2\gamma_0 T_L^2 \Delta\omega_L (\omega_{L\_0} - \bar{\omega}_L)/\tilde{\Omega}_L^2}\, \delta(\bar{k}_L^{\shortparallel} - \bar{k}_{L\_0}^{\shortparallel})\, \delta(\Delta k_L^{\shortparallel} + \Delta k_{L\_0}^{\shortparallel}) \\
+ e^{-(\bar{\omega}_L + \omega_{L\_0})^2 / 2\tilde{\Omega}_L^{*2}}\, e^{-\mathrm{i}\, 2\gamma_0 T_L^2 \Delta\omega_L (\omega_{L\_0} + \bar{\omega}_L)/\tilde{\Omega}_L^2}\, \delta(\bar{k}_L^{\shortparallel} + \bar{k}_{L\_0}^{\shortparallel})\, \delta(\Delta k_L^{\shortparallel} - \Delta k_{L\_0}^{\shortparallel}) \Big) \\
\times l_w^2\, e^{-(k_f^{\shortparallel} - \bar{k}_L^{\shortparallel} - \bar{k}_X^{\shortparallel} - G^{\shortparallel})^2 \sigma_w^2}\, e^{-(\Delta k_L^{\shortparallel} + \Delta k_X^{\shortparallel})^2 \sigma_w^2/4}\, (2\pi)^4\, \delta^2(\mathbf{k}_f^{\perp} - \bar{\mathbf{k}}_X^{\perp} - \bar{\mathbf{k}}_L^{\perp} - \mathbf{G}^{\perp})\, \delta^2(\Delta\mathbf{k}_X^{\perp} + \Delta\mathbf{k}_L^{\perp}) \\
\times \frac{1}{V_\diamond^2} \Big(\boldsymbol{\varepsilon}_L \cdot \mathbf{K}_{GS\diamond}(0, \mathbf{G}, \omega_L) \Big) \Big(\boldsymbol{\varepsilon}_L \cdot \mathbf{K}_{GS\diamond}(0, \mathbf{G}, \omega'_L) \Big)^* .
\end{aligned}
\tag{5.22}
$$

Approximations In order to simplify this expression further, we shall introduce several approximations:

- Within the bandwidth of each light source, we can approximate the fraction

$$
\frac{1}{\omega'_X\, \omega_X\, \omega'_L\, \omega_L} \approx \frac{1}{\omega_{X\_0}^2\, \omega_{L\_0}^2}
\tag{5.23}
$$

  with a minor error of $\sim \Omega/\omega \sim 10^{-4} ... 10^{-2}$.

- For further spectral simplification, we take the material's response to be a slowly varying function of ω in the vicinity of the laser photon energy. In particular, this implies that we can approximate it as constant across the laser's bandwidth

$$
\mathbf{K}_{GS\diamond}(0, \mathbf{G}, \omega_L) \approx \mathbf{K}_{GS\diamond}(0, \mathbf{G}, \omega_{L\_0}) \approx \mathbf{K}_{GS\diamond}(0, \mathbf{G}, \omega'_L).
\tag{5.24}
$$

  This simplification reflects the actual behaviour of the response function below the band-gap and is consistent with our results of Chpt. 3.

- Not strictly important, but nice for conciseness: We can assume that the bandwidth after monochromatisation is significantly smaller than the intrinsic spectral width of the x-ray source[5] ($\Omega_m \ll \Omega_X$). This, in turn, allows for the more compact exponent $\frac{\Omega_X^2 + \Omega_m^2}{2\Omega_X^2 \Omega_m^2} \approx 1/2\Omega_m^2$.

- Last but not least, we can inspect the curvature phase term of the x-ray field, which holds the exponent $\frac{z_{X\_0}}{\alpha\, \bar{\omega}_X} \bar{\mathbf{k}}_X^{\perp} \cdot \Delta\mathbf{k}_X^{\perp}$. We can rewrite and estimate this as

$$
\frac{z_{X\_0} \sigma_X \delta_X}{z_{eff}} \bar{\mathbf{k}}_X^{\perp} \cdot \Delta\mathbf{k}_L^{\perp} \approx \frac{z_{X\_0} \sigma_X \delta_X}{z_{eff}} \frac{1}{\delta_X} \frac{1}{\sigma_L} \lessapprox \frac{z_{X\_0} \sigma_X \delta_X}{z_{eff}} \frac{1}{\delta_X} \frac{1}{\Delta(z=0)\sigma_X} \lessapprox 1 \ll 2\pi.
\tag{5.25}
$$

  Hereunto, we employ the notion of z_{eff} (see Sec. 4.2.1) first, before we fix $\Delta\mathbf{k}_X^{\perp}$ via one of the δ-functions in Eq. (5.22). Further, we estimate the momenta via their defining scales and observe

[5] After all, this is the reason to use a monochromator.

that the laser should cover the expanded x-ray beam at the sample position ($\sigma_L \gtrapprox \Delta(0)\sigma_X$)—for effective mixing[6]. Using the relations of z_{X_0} and z_{eff} with $\Delta(z=0)$, we obtain the final estimate—notably independent of the specific type of source and for either transverse direction! To a reasonable degree of approximation, we may thus neglect the curvature term.

Applying these simplifying assumptions to Eq. (5.22), we arrive at

$$\begin{aligned}\langle\hat{O}\rangle = \sqrt{2\pi}\,\frac{\alpha\, 2\, l_w^2\, E_{X_p}\,\delta_X^x\delta_X^y\,|E_{L_0}|^2\,T_L\,\sigma_L^2\,\delta_L^2}{V\,\omega_f\,\Omega_X\,\tilde{\Omega}_L\,\omega_{X_0}^2\,\omega_{L_0}^2}\left|\boldsymbol{\varepsilon}_f\cdot\boldsymbol{\varepsilon}_X\right|^2\frac{\left|\boldsymbol{\varepsilon}_L\cdot\mathbf{K}_{GS\diamond}(0,\mathbf{G},\omega_{L_0})\right|^2}{V_\diamond^2}\int d^3\bar{k}_L d^3\Delta k_L\int d\bar{k}_X^{\shortparallel} d\Delta k_X^{\shortparallel}\\
\times\int d\bar{\omega}_L d\Delta\omega_L\;\delta(\bar{k}_X^{\shortparallel}-\bar{k}_{X_0}^{\shortparallel})\,\delta(\Delta k_X^{\shortparallel}+\Delta k_{X_0}^{\shortparallel})\,e^{-(\omega_f-\bar{\omega}_L-\omega_{X_0})^2/2\Omega_m^2}\,e^{-\Delta\omega_L^2(T_X^2+\tilde{T}_L^2+(2\Omega_m)^{-2})/2}\,e^{\mathrm{i}\,\Delta t\,\Delta\omega_L}\\
\times e^{-(k_f^x-\bar{k}_L^x-G^x)^2(\delta_X^x)^2/2}e^{-(\bar{k}_L^x)^2\delta_L^2/2}\,e^{-(k_f^y-\bar{k}_L^y-G^y)^2(\delta_X^y)^2/2}e^{-(\bar{k}_L^y)^2\delta_L^2/2}\,e^{-(\Delta k_L^x)^2((\sigma_X^x)^2+\sigma_L^2)/2}e^{-(\Delta k_L^y)^2((\sigma_X^y)^2+\sigma_L^2)/2}\\
\times\Big(e^{-(\bar{\omega}_L-\omega_{L_0})^2/2\tilde{\Omega}_L^2}\,e^{-\mathrm{i}2\gamma_0 T_L^2\Delta\omega_L(\omega_{L_0}-\bar{\omega}_L)/\tilde{\Omega}_L^2}\,\delta(\bar{k}_L'^{\shortparallel}-\bar{k}_{L_0}'^{\shortparallel})\,\delta(\Delta k_L^{\shortparallel}+\Delta k_{L_0}^{\shortparallel})\\
+e^{-(\bar{\omega}_L+\omega_{L_0})^2/2\tilde{\Omega_L}^2}\,e^{-\mathrm{i}2\gamma_0 T_L^2\Delta\omega_L(\omega_{L_0}+\bar{\omega}_L)/\tilde{\Omega}_L^2}\,\delta(\bar{k}_L'^{\shortparallel}+\bar{k}_{L_0}'^{\shortparallel})\,\delta(\Delta k_L^{\shortparallel}-\Delta k_{L_0}^{\shortparallel})\Big)\\
\times e^{-(k_f^{\shortparallel}-\bar{k}_L^{\shortparallel}-\bar{k}_X^{\shortparallel}-G^{\shortparallel})^2\sigma_w^2}\,e^{-(\Delta k_L^{\shortparallel}+\Delta k_X^{\shortparallel})^2\sigma_w^2/4}\,e^{\mathrm{i}\,\frac{z_{L_0}}{\alpha|\bar{\omega}_L|^n}\bar{\mathbf{k}}_L^{\perp}\cdot\Delta\mathbf{k}_L^{\perp}}.\end{aligned}\tag{5.26}$$

Now, we can shorten the expression by using all longitudinal δ-functions

$$\begin{aligned}\langle\hat{O}\rangle = \sqrt{2\pi}\,\frac{\alpha\, 2\, l_w^2\, E_{X_p}\,\delta_X^x\delta_X^y\,|E_{L_0}|^2\,T_L\,\sigma_L^2\,\delta_L^2}{V\,\omega_f\,\Omega_X\,\tilde{\Omega}_L\,\omega_{X_0}^2\,\omega_{L_0}^2}\left|\boldsymbol{\varepsilon}_f\cdot\boldsymbol{\varepsilon}_X\right|^2\frac{\left|\boldsymbol{\varepsilon}_L\cdot\mathbf{K}_{GS\diamond}(0,\mathbf{G},\omega_{L_0})\right|^2}{V_\diamond^2}\int d^2\bar{k}_L^{\perp} d^3\Delta k_L^{\perp}\int d\bar{\omega}_L d\Delta\omega_L\\
\times e^{-(\omega_f-\bar{\omega}_L-\omega_{X_0})^2/2\Omega_m^2}\,e^{-\Delta\omega_L^2(T_X^2+\tilde{T}_L^2+(2\Omega_m)^{-2})/2}\,e^{\mathrm{i}\,\Delta t\,\Delta\omega_L}\,e^{-(\bar{\omega}_L\mp\omega_{L_0})^2/2\tilde{\Omega}_L^2}\,e^{-\mathrm{i}2\gamma_0 T_L^2\Delta\omega_L(\omega_{L_0}\mp\bar{\omega}_L)/\tilde{\Omega}_L^2}\\
\times e^{-(k_f^x-\bar{k}_L^x-G^x)^2(\delta_X^x)^2/2}e^{-(\bar{k}_L^x)^2\delta_L^2/2}\,e^{-(k_f^y-\bar{k}_L^y-G^y)^2(\delta_X^y)^2/2}e^{-(\bar{k}_L^y)^2\delta_L^2/2}\,e^{-(\Delta k_L^x)^2((\sigma_X^x)^2+\sigma_L^2)/2}e^{-(\Delta k_L^y)^2((\sigma_X^y)^2+\sigma_L^2)/2}\\
\times e^{-(k_f^{\shortparallel}\mp\bar{k}_{L_0}^{\shortparallel}-\bar{k}_{X_0}^{\shortparallel}-G^{\shortparallel})^2\sigma_w^2}\,e^{-(\mp\Delta k_{L_0}^{\shortparallel}-\Delta k_{X_0}^{\shortparallel})^2\sigma_w^2/4}\,e^{\mathrm{i}\,\frac{z_{L_0}}{\alpha|\bar{\omega}_L|^n}\bar{\mathbf{k}}_L^{\perp}\cdot\Delta\mathbf{k}_L^{\perp}},\end{aligned}\tag{5.27}$$

where the upper sign ($\mp$) corresponds to the SFG case and the lower one to the DFG case. Our next step concerns the remnants of the longitudinal window functions. We demonstrate in the following that—given the surrounding conditions and reasonable beam divergences—we can approximate

$$e^{-(k_f^{\shortparallel}\mp\bar{k}_{L\_0}^{\shortparallel}-\bar{k}_{X\_0}^{\shortparallel}-G^{\shortparallel})^2\sigma_w^2}\,e^{-(\mp\Delta k_{L\_0}^{\shortparallel}-\Delta k_{X\_0}^{\shortparallel})^2\sigma_w^2/4}\approx e^{-(k_f^{\shortparallel}-G^{\shortparallel}-\alpha\, n\,\bar{\omega}_L-\alpha\,\bar{\omega}_X)^2\sigma_w^2}\,e^{-(\alpha\,(n-1)\,\Delta\omega_L)^2\sigma_w^2/4}.\tag{5.28}$$

In order to resolve this, we shall expand each of the occurring $\bar{k}_{i\_0}^{\shortparallel}=(k_{i\_0}^{\shortparallel}+k_{i\_0}'^{\shortparallel})/2$ and $\Delta k_{i\_0}^{\shortparallel}=\ldots$. It is as before:

$$k_{i\_0}^{\shortparallel}=\sqrt{\frac{n_i^2\,\omega_i^2}{c^2}-\left|\mathbf{k}_i^{\perp}\right|^2}\approx\frac{n_i\,\omega_i}{c}\left(1-\frac{1}{2}\frac{\left|\mathbf{k}_i^{\perp}\right|^2}{\left|\mathbf{k}_i\right|^2}+\frac{1}{8}\frac{\left|\mathbf{k}_i^{\perp}\right|^4}{\left|\mathbf{k}_i\right|^4}-\ldots\right),\tag{5.29}$$

where we have re-introduced the absolute of the full wave-vector $|\mathbf{k}_i|^2=\alpha^2 n_i^2\,\omega_i^2$ to evoke reminiscences to the beam divergence $\Theta\approx\left|\mathbf{k}_i^{\perp}\right|/|\mathbf{k}_i|$. The refractive index is to be understood as either unity for x-rays ($i=X$) or its respective optical value for the laser-field ($i=L$).

Considering the first 'longitudinal' exponential, it becomes slightly more cumbersome to decide which terms to keep (as compared to Sec. 4.2.1), because we have to account for cross terms within the

[6]Note that we have verified this assumption later in private communication with Dr. David A. Reis.

exponents:

$$\exp\Big(-\sigma_w^2\Big(\underbrace{k_f^{\shortparallel}-G^{\shortparallel}-\frac{\bar\omega_X}{c}\mp\frac{n\,\bar\omega_L}{c}}_{m^{\shortparallel}}+\frac{1}{4}\Big(\frac{\omega_X}{c}\frac{(\mathbf{k}_X^{\perp})^2}{(\mathbf{k}_X)^2}+\frac{\omega_X'}{c}\frac{(\mathbf{k}_X'^{\perp})^2}{(\mathbf{k}_X')^2}\pm\frac{n\,\omega_L}{c}\frac{(\mathbf{k}_L^{\perp})^2}{(\mathbf{k}_L)^2}\pm\frac{n\,\omega_L'}{c}\frac{(\mathbf{k}_L'^{\perp})^2}{(\mathbf{k}_L')^2}-\ldots\Big)\Big)^2\Big).$$

In here, the pure squares of higher order terms, i.e.,

$$\sigma_w^2\Big(\frac{1}{4}\frac{\omega_X}{c}\frac{(\mathbf{k}_X^{\perp})^2}{(\mathbf{k}_X)^2}\Big)^2=\Big(\frac{l_w\sqrt{2\pi}}{4\,\lambda_X}\frac{(\mathbf{k}_X^{\perp})^2}{(\mathbf{k}_X)^2}\Big)^2\approx\Big(\frac{500\mu\mathrm{m}\sqrt{2\pi}}{4\,(1.55\text{Å})}\,(10^{-6}\mathrm{rad})^2\Big)^2\ll 1 \tag{5.30}$$

$$\sigma_w^2\Big(\frac{1}{4}\frac{n\,\omega_L}{c}\frac{(\mathbf{k}_L^{\perp})^2}{(\mathbf{k}_L)^2}\Big)^2=\Big(\frac{l_w\sqrt{2\pi}\,n}{4\,\lambda_L}\frac{(\mathbf{k}_L^{\perp})^2}{(\mathbf{k}_L)^2}\Big)^2\approx\Big(\frac{500\mu\mathrm{m}\sqrt{2\pi}\,n}{4\,(800\mathrm{nm})}\,(10^{-3}\mathrm{rad})^2\Big)^2\ll 1. \tag{5.31}$$

are negligible given the beam parameters from Ref. [46]. Therefore, we can focus on the remaining cross terms

$$\exp\left(-\sigma_w^2 m^{\shortparallel 2}\right)\exp\Big(-\frac{\sigma_w^2 m^{\shortparallel}}{2}\Big(\frac{\omega_X}{c}\frac{(\mathbf{k}_X^{\perp})^2}{(\mathbf{k}_X)^2}+\frac{\omega_X'}{c}\frac{(\mathbf{k}_X'^{\perp})^2}{(\mathbf{k}_X')^2}\pm\frac{n\,\omega_L}{c}\frac{(\mathbf{k}_L^{\perp})^2}{(\mathbf{k}_L)^2}\pm\frac{n\,\omega_L'}{c}\frac{(\mathbf{k}_L'^{\perp})^2}{(\mathbf{k}_L')^2}\Big)\Big).$$

In here, the first exponential will limit the magnitude of the longitudinal mismatch to about $|m^{\shortparallel}|\sim 1/\sigma_w$, *unless* significant contributions from the second exponential can shift this. Thus, with $|m^{\shortparallel}|/\sigma_w$ preliminarily fixed to unity, we—once again—have to estimate the expressions of Eqs. (5.30) and (5.31)—just without the overall square. Our previous conclusions remain valid, such that we may also neglect the cross terms and finally write:

$$e^{-(k_f^{\shortparallel}\mp\bar k_{L0}^{\shortparallel}-\bar k_{X0}^{\shortparallel}-G^{\shortparallel})^2\sigma_w^2}\approx e^{-(k_f^{\shortparallel}-G^{\shortparallel}-\alpha\,n\,\bar\omega_L-\alpha\,\bar\omega_X)^2\sigma_w^2}. \tag{5.32}$$

Similar arguments yield:

$$e^{-(\mp\Delta k_{L0}^{\shortparallel}-\Delta k_{X0}^{\shortparallel})^2\sigma_w^2/4}\approx e^{-(\alpha\,(n-1)\,\Delta\omega_L)^2\sigma_w^2/4}. \tag{5.33}$$

Deploying these approximations to our observable (5.27) almost leads to its factorization into spatial and spectral parts. Only the curvature phase-term of the laser-field still bears a weak frequency dependence of the form $1/|\bar\omega_L|$, the effect of which is negligible to all intents and purposes

$$\begin{aligned}\langle\hat O\rangle=\sqrt{2\pi}\,\frac{\alpha\,2\,l_w^2\,E_{X0}\,\delta_X^x\delta_X^y\,|E_{L0}|^2\,T_L\,\sigma_L^2\,\delta_L^2}{V\,\omega_f\,\Omega_X\,\tilde\Omega_L\,\omega_{X0}^2\,\omega_{L0}^2}\,\big|\boldsymbol{\varepsilon}_f\cdot\boldsymbol{\varepsilon}_X\big|^2\,\frac{1}{V_\diamond^2}\,|\boldsymbol{\varepsilon}_L\cdot\mathbf{K}_{GS\diamond}(0,\mathbf{G},\omega_{L0})|^2\int^{\times 2}d^2\bar k_L^{\perp}d^2\Delta k_L^{\perp}\\
\times e^{-(k_f^x-\bar k_L^x-G^x)^2(\delta_X^x)^2/2}e^{-(\bar k_L^x)^2\delta_L^2/2}\,e^{-(k_f^y-\bar k_L^y-G^y)^2(\delta_X^y)^2/2}e^{-(\bar k_L^y)^2\delta_L^2/2}\,e^{-(\Delta k_L^x)^2((\sigma_X^x)^2+\sigma_L^2)/2}e^{-(\Delta k_L^y)^2((\sigma_X^y)^2+\sigma_L^2)/2}\\
\times\int^{\times 2}d\bar\omega_L d\Delta\omega_L\,e^{-(\omega_f-\bar\omega_L-\omega_{X0})^2/2\Omega_m^2}e^{-\Delta\omega_L^2(T_X^2+\tilde T_L^2+(2\Omega_m)^{-2})/2}\,e^{\mathrm{i}\,\Delta t\,\Delta\omega_L}\,e^{-(\bar\omega_L\mp\omega_{L0})^2/2\tilde\Omega_L^2}\\
\times e^{-\mathrm{i}\,2\gamma_0 T_L^2\Delta\omega_L(\omega_{L0}\mp\bar\omega_L)/\tilde\Omega_L^2}e^{-(k_f^{\shortparallel}-G^{\shortparallel}-\alpha\,n\,\bar\omega_L-\alpha\,(\omega_f-\bar\omega_L))^2\sigma_w^2}e^{-(\alpha\,(n-1)\,\Delta\omega_L)^2\sigma_w^2/4}\,e^{\mathrm{i}\,\frac{z_{L0}}{\alpha\,|\bar\omega_L|^n}\bar{\mathbf{k}}_L^{\perp}\cdot\Delta\mathbf{k}_L^{\perp}}.\end{aligned} \tag{5.34}$$

Focusing on the spatial integrations, we can resolve the standard Gaussian integrals as[7]

$$\int d\Delta k\,e^{-(\Delta k)^2(\sigma_X^2+\sigma_L^2)/2}\,e^{\mathrm{i}\,\frac{z_{L0}}{\alpha\,|\bar\omega_L|^n}\bar k\cdot\Delta k}=\sqrt{\frac{2\pi}{\sigma_X^2+\sigma_L^2}}\,e^{-\frac{z_{L0}^2}{2\alpha^2\,|\bar\omega_L|^{2n}\,(\sigma_X^2+\sigma_L^2)}\bar k^2}. \tag{5.35}$$

[7]Note that we present an arbitrary (single) spatial dimension here and omit its respective superscript in order to declutter our notation. For the same reason, we omit the subscript L.

In analogy to Eq. (4.35), we can define $z_{eff} = \alpha\,|\bar{\omega}_L|\,n\,\sigma_L\,\delta_L$ for the laser beam. Capitalizing on the earlier assumption that $\sigma_L \gg \sigma_X$, the integral's result simplifies to $\sim \sqrt{2\pi}\sigma_L^{-1}\exp(-z_{L\_0}^2 z_{eff}^{-2}\bar{k}^2\delta_L^2/2)$. This may nicely be included in the remaining integration

$$\int d\bar{k}\; e^{-(k_f-G-\bar{k})^2\delta_X^2/2}\, e^{-(\bar{k})^2\delta_L^2(1+z_{L\_0}^2/z_{eff}^2)/2} = \sqrt{\frac{2\pi}{\delta_X^2+\delta_L^2\,(\Delta(z_{L\_0}))^2}}\, e^{-(k_f-G)^2\frac{\delta_X^2\,\delta_L^2(\Delta(z_{L\_0}))^2}{2(\delta_X^2+\delta_L^2(\Delta(z_{L\_0}))^2)}}, \tag{5.36}$$

with $\Delta(z_{L\_0})$ marking the scaling function known from Eq. (4.35). In the above, typically $\delta_L \gg \delta_X$, as we can see from the following estimation:

$$\delta_X\,\delta_L^{-1} \approx \frac{\lambda_X}{\Theta_X\,\pi}\,\frac{1}{2\sigma_L} \approx \frac{10^{-10}m}{10^{-6}rad\,\pi}\,\frac{1}{2\cdot 500\cdot 10^{-6}m} \approx \frac{1}{10\pi}, \tag{5.37}$$

which becomes more drastic for less ideal x-ray beams or if the effect of $z_{L\_0} \neq 0$ is included. Thus, we may simplify integral 5.36 to $\sim \sqrt{2\pi}(\delta_L\Delta(z_{L\_0}))^{-1}\exp\left(-(k_f-G)^2\delta_X^2/2\right)$. This reduces the observable to

$$\begin{aligned}
\langle\hat{O}\rangle = {} & \sqrt{2\pi}\,(2\pi)^2\,\frac{\alpha\,2\,l_w^2\,E_{X_p}\,\delta_X^x\,\delta_X^y\,|E_{L_0}|^2\,T_L\,\sigma_L^2}{V\,\omega_f\,\Omega_X\,\tilde{\Omega}_L\,\omega_{X_0}^2\,\omega_{L_0}^2\,(\sigma_L\,\Delta(z_{L_0}))^2}\,\left|\boldsymbol{\varepsilon}_f\cdot\boldsymbol{\varepsilon}_X\right|^2\,\frac{1}{V_\diamond^2}\,\left|\boldsymbol{\varepsilon}_L\cdot\mathbf{K}_{GS\diamond}(0,\mathbf{G},\omega_{L_0})\right|^2 \\
& \times e^{-(k_f^x-G^x)^2(\delta_X^x)^2/2}\,e^{-(k_f^y-G^y)^2(\delta_X^y)^2/2} \\
& \times \int^{\times 2} d\bar{\omega}_L\,d\Delta\omega_L\; e^{-(\omega_f-\bar{\omega}_L-\omega_{X_0})^2/2\Omega_m^2}\,e^{-\Delta\omega_L^2(T_X^2+\tilde{T}_L^2+(2\Omega_m)^{-2})/2}\; e^{\mathrm{i}\,\Delta t\,\Delta\omega_L}\; e^{-(\bar{\omega}_L\mp\omega_{L_0})^2/2\tilde{\Omega}_L^2} \\
& \times e^{-\mathrm{i}\,2\gamma_0 T_L^2\Delta\omega_L(\omega_{L_0}\mp\bar{\omega}_L)/\tilde{\Omega}_L^2}\,e^{-(k_f^{\shortparallel}-G^{\shortparallel}-\alpha\,n\,\bar{\omega}_L-\alpha\,(\omega_f-\bar{\omega}_L))^2\sigma_w^2}\,e^{-(\alpha\,(n-1)\Delta\omega_L)^2\sigma_w^2/4},
\end{aligned} \tag{5.38}$$

where $\sigma_L\Delta(z_{L\_0})$ gives the actual laser-beam size at the sample position. We can further simplify the frequency part

$$\begin{aligned}
& \int^{\times 2} d\bar{\omega}_L\,d\Delta\omega_L\; e^{-(\omega_f-\bar{\omega}_L-\omega_{X_0})^2/2\Omega_m^2}\,e^{-\Delta\omega_L^2(T_X^2+\tilde{T}_L^2+(2\Omega_m)^{-2})/2}\; e^{\mathrm{i}\,\Delta t\,\Delta\omega_L}\; e^{-(\bar{\omega}_L\mp\omega_{L_0})^2/2\tilde{\Omega}_L^2} \\
& \times e^{-\mathrm{i}\,2\gamma_0 T_L^2\Delta\omega_L(\omega_{L_0}\mp\bar{\omega}_L)/\tilde{\Omega}_L^2}\,e^{-(k_f^{\shortparallel}-G^{\shortparallel}-\alpha\,n\,\bar{\omega}_L-\alpha\,(\omega_f-\bar{\omega}_L))^2\sigma_w^2}\,e^{-(\alpha\,(n-1)\,\Delta\omega_L)^2\sigma_w^2/4} \\
= & \int d\,\omega_L\; e^{-(\omega_f-\omega_L\mp\omega_{L_0}-\omega_{X_0})^2/2\Omega_m^2}\,e^{-\omega_L^2/2\tilde{\Omega}_L^2}\,e^{-((ck_f^{\shortparallel}-\omega_f-cG^{\shortparallel})/(n-1)-\omega_L\mp\omega_{L_0})^2(n-1)^2\alpha^2\sigma_w^2} \\
& \times \int d\Delta\omega_L\; e^{-\Delta\omega_L^2 T_{sum}^2/2}\; e^{\mathrm{i}\,\Delta\omega_L(\Delta t-2\gamma_0 T_L^2(\mp\omega_L)/\tilde{\Omega}_L^2)} \\
= & \int d\,\omega_L\; e^{-(\omega_f-\omega_L\mp\omega_{L_0}-\omega_{X_0})^2/2\Omega_m^2}\,e^{-\omega_L^2/2\tilde{\Omega}_L^2}\,e^{-((ck_f^{\shortparallel}-\omega_f-cG^{\shortparallel})/(n-1)-\omega_L\mp\omega_{L_0})^2(n-1)^2\alpha^2\sigma_w^2} \\
& \times \frac{\sqrt{2\pi}}{T_{sum}}\; e^{-(\Delta t-2\gamma_0 T_L^2(\mp\omega_L)/\tilde{\Omega}_L^2)^2/2T_{sum}^2} \\
= & \int d\,\omega_L\; e^{-(\omega_f-\omega_L\mp\omega_{L_0}-\omega_{X_0})^2/2\Omega_m^2}\,e^{-\omega_L^2/2\tilde{\Omega}_L^2}\,e^{-((ck_f^{\shortparallel}-\omega_f-cG^{\shortparallel})/(n-1)-\omega_L\mp\omega_{L_0})^2(n-1)^2\alpha^2\sigma_w^2} \\
& \times \frac{\sqrt{2\pi}}{T_{sum}}\; e^{-(\Delta t\pm B\omega_L)^2/2T_{sum}^2},
\end{aligned} \tag{5.39}$$

where $T_{sum} = \sqrt{T_X^2+\tilde{T}_L^2+(2\Omega_m)^{-2}+\left[\alpha(n-1)\sigma_w\right]^2/2}$ and $B = 2\gamma_0 T_L^2/\tilde{\Omega}_L^2$. Note also, that we have shifted the integration in ω_L by the laser's central frequency ω_{L_0} in the second line.

Reinserting the result, the overall observable becomes

$$\begin{aligned}\langle\hat{O}\rangle = (2\pi)^3 \frac{\alpha\, 2\, l_w^2\, E_{X\_p}\, \delta_X^x \delta_X^y\, |E_{L\_0}|^2\, T_L\, \sigma_L^2}{V\, \omega_f\, \Omega_X\, \tilde{\Omega}_L\, \omega_{X\_0}^2\, \omega_{L\_0}^2\, (\sigma_L \Delta(z_{L\_0}))^2\, T_{sum}} \left|\boldsymbol{\varepsilon}_f \cdot \boldsymbol{\varepsilon}_X\right|^2 \frac{1}{V_\diamond^2} \left|\boldsymbol{\varepsilon}_L \cdot \mathbf{K}_{GS\diamond}(0, \mathbf{G}, \omega_{L\_0})\right|^2 \\ \times e^{-(k_f^x - G^x)^2 (\delta_X^x)^2/2} e^{-(k_f^y - G^y)^2 (\delta_X^y)^2/2} \\ \times \int d\omega_L\, e^{-(\omega_f - \omega_L \mp \omega_{L\_0} - \omega_{X\_0})^2/2\Omega_m^2}\, e^{-\omega_L^2/2\tilde{\Omega}_L^2}\, e^{-((ck_f^{\shortparallel} - \omega_f - cG^{\shortparallel})/(n-1) - \omega_L \mp \omega_{L\_0})^2 (n-1)^2 \alpha^2 \sigma_w^2}\, e^{-(\Delta t \pm B\omega_L)^2/2T_{sum}^2}.\end{aligned} \tag{5.40}$$

Notably, the last remaining integral is again just of Gaussian type and could be solved analytically[8]. However, we prefer to approximate the integrand a bit further and therein emphasize the physical constraints, which are at play.

We shall disregard the last exponential for the moment, as it depends on the time-delay Δt and is therefore inherently variable. Our task at hand is to identify the most restrictive of the remaining three Gaussians, which thus selects the dominant spectral contribution in ω_L:

- The monochromator's bandwidth Ω_m corresponds to ~ 1 eV for a Si (111) DCM operating at ~ 8 keV.
- The laser's bandwidth $\tilde{\Omega}_L$ is already significantly smaller, namely ~ 68 meV in the case of Glover et al., who use a pulsed (stretched) laser with a respectively broad bandwidth [46].
- Finally, the shape function of the crystal itself. This enters via the width σ_w, which represents the $\sim 500\ \mu$m thick sample.

Noting that 100 μm—if interpreted as a wavelength—corresponds to ~ 10 meV in energy, we find the last point to yield the most restrictive constraint. As such, it fixes the value of ω_L according to the root of its exponent, i.e., $\omega_L \approx \frac{ck_f^{\shortparallel} - \omega_f - cG^{\shortparallel}}{(n-1)} \mp \omega_{L\_0}$. For compactness of notation, we will treat this ω_L as a defined constant in the following. Apart from this, we need to evaluate the approximated, single Gaussian integral, which contributes an additional prefactor of $\frac{\sqrt{\pi}}{(n-1)\alpha\sigma_w}$.

We insert these findings into Eq. (5.40) and furthermore convert the observable $\langle\hat{O}\rangle$ into a double differential scattering yield[9]. To this end, we multiply by $\frac{V\alpha^3}{(2\pi)^3}\omega_f^2$ (cf. Sec. 2.1) and find

$$\begin{aligned}\frac{d^2Y}{d\omega_f\, d\Omega_f} = \frac{\alpha^4\, 2\pi\sqrt{2}\, l_w\, \omega_f\, E_{X\_p}\, \delta_X^x \delta_X^y\, |E_{L\_0}|^2\, T_L\, \sigma_L^2}{(n-1)\alpha\, \Omega_X\, \tilde{\Omega}_L\, \omega_{X\_0}^2\, \omega_{L\_0}^2\, (\sigma_L \Delta(z_{L\_0}))^2\, T_{sum}} \left|\boldsymbol{\varepsilon}_f \cdot \boldsymbol{\varepsilon}_X\right|^2 \frac{1}{V_\diamond^2} \left|\boldsymbol{\varepsilon}_L \cdot \mathbf{K}_{GS\diamond}(0, \mathbf{G}, \omega_{L\_0})\right|^2 \\ \times e^{-(k_f^x - G^x)^2 (\delta_X^x)^2/2} e^{-(k_f^y - G^y)^2 (\delta_X^y)^2/2}\, e^{-(\omega_f - \omega_L \mp \omega_{L\_0} - \omega_{X\_0})^2/2\Omega_m^2}\, e^{-\omega_L^2/2\tilde{\Omega}_L^2}\, e^{-(\Delta t \pm B\omega_L)^2/2T_{sum}^2}.\end{aligned} \tag{5.41}$$

Before we analyse this result in greater detail, we want to conduct one last reformulation. This concerns the chirp term $e^{-(\Delta t \pm B\omega_L)^2/2T_{sum}^2}$, which does not fully reflect our intuition about the SFG process, yet. In particular, we would expect—not least from Glover's results—that the SFG signal is emitted,

[8] We recall that the product of two Gaussians is again a Gaussian—merely sporting a more complicated exponent. Thus, the four separate Gaussians could be condensed into a single one and integrated, albeit with a messy result.

[9] Note that we could likewise have termed this quantity the double differential scattering probability, as is more commonly done in the context of atomic physics. However, we anticipate that the number can grow beyond unity if measured for sufficiently large samples and integrated over large solid angles. This does not invalidate the probability interpretation for each infinitesimal solid angle element, but it would nevertheless make for an awkward transition. Thus, we start out by calling it a yield directly.

when x-ray and optical pulse overlap (cf. Fig. 5.1 e). This should be reflected as $\sim e^{-\Delta t^2/2T_{cc}^2}$, where T_{cc} marks the mutual cross-correlation length of x-ray and optical pulses. It turns out that we can achieve such a form by rewriting the last two exponentials in Eq. (5.41):

$$\begin{aligned} e^{-\omega_L^2/2\tilde{\Omega}_L^2}\, e^{-(\Delta t \pm B\omega_L)^2/2T_{sum}^2} &= \exp\Big(-\frac{\omega_L^2}{2\tilde{\Omega}_L^2} - \frac{(\Delta t \pm B\omega_L)^2}{2T_{sum}^2}\Big) = \exp\Big(-\frac{\omega_L^2}{2\tilde{\Omega}_L^2} - \frac{\Delta t^2 \pm 2\Delta t B\omega_L + B^2\omega_L^2}{2T_{sum}^2}\Big) \\ &= \exp\Big(-\frac{\omega_L^2(T_{sum}^2 + \tilde{\Omega}_L^2 B^2)}{2\tilde{\Omega}_L^2 T_{sum}^2} - \frac{\Delta t^2 \pm 2\Delta t B\omega_L}{2T_{sum}^2}\Big) \\ &= \exp\Big(-\frac{\omega_L^2(T_{sum}^2 - \tilde{T}_L^2 + T_L^2)}{2\tilde{\Omega}_L^2 T_{sum}^2} - \frac{\Delta t^2 \pm 2\Delta t B\omega_L}{2T_{sum}^2}\Big). \end{aligned} \tag{5.42}$$

Intermittently, we note that $T_{sum}^2 - \tilde{T}_L^2 + T_L^2 = T_X^2 + T_L^2 + (2\Omega_m)^{-2} + \alpha^2(n-1)^2\sigma_w^2/2$ will be a useful quantity that we shall abbreviate by T_{tot}^2 henceforth[10]. Completing the square in ω_L, we arrive at

$$\begin{aligned} e^{-\omega_L^2/2\tilde{\Omega}_L^2}\, e^{-(\Delta t \pm B\omega_L)^2/2T_{sum}^2} &= \exp\Big(-[\omega_L \pm \frac{\Delta t 2\gamma_0 T_L^2}{T_{tot}^2}]^2 \frac{1}{2\tilde{\Omega}_L^2}\frac{T_{tot}^2}{T_{sum}^2} - \frac{\Delta t^2}{2T_{tot}^2}\Big) \\ &= \exp\Big(-[\omega_L \pm \frac{\Delta t 2\gamma_0 T_L^2}{T_{tot}^2}]^2 \frac{1}{2\tilde{\Omega}_L^2}\big(1 - \frac{T_L^2}{T_{tot}^2} + \frac{\tilde{T}_L^2}{T_{tot}^2}\big)^{-1} - \frac{\Delta t^2}{2T_{tot}^2}\Big) \\ &= e^{-[\omega_L \pm \Delta t C]^2 D/2\tilde{\Omega}_L^2}\, e^{-\Delta t^2/2T_{tot}^2}, \end{aligned} \tag{5.43}$$

with $C = 2\gamma_0 T_L^2/T_{tot}^2$ and $D = \big(1 - \frac{T_L^2}{T_{tot}^2} + \frac{\tilde{T}_L^2}{T_{tot}^2}\big)^{-1} = \frac{T_{tot}^2}{T_{tot}^2 - T_L^2 + \tilde{T}_L^2} = \frac{T_{tot}^2}{T_{sum}^2}$.
This result nicely reflects our intuitive expectations about the temporal behaviour of SFG/DFG. The signal is suppressed as soon as the delay Δt extends beyond the mutual overlap of x-ray ($\sim \sqrt{T_X^2 + (2\Omega_m)^{-2}}$) and optical pulse length T_L[11]. Together, they form $T_{tot} = \sqrt{T_X^2 + T_L^2 + (2\Omega_m)^{-2} + \alpha^2(n-1)^2\sigma_w^2/2}$. In addition, there is some leeway on account of the speed-of-light mismatch across the sample, given by $(n-1)\alpha\sigma_w/\sqrt{2}$. This results from the fact that optical and x-ray pulses experience different refractive indices and thus travel at different group velocities. They may therefore overlap at different delay times for different regions of the crystal—effectively broadening the overall cross-correlation condition. The other exponential in Eq. (5.43) relates to the frequency-chirp of the optical pulse. At different time-delays Δt, slightly different photon energies will be prevalent—varying across the overall bandwidth $\tilde{\Omega}_L^2$ of the original pulse. Without any chirp, this aspect will be irrelevant; the delay-controlled term will vanish as $\gamma_{L0} = 0$ inside C and consequently $T_L = \tilde{T}_L$ and $\Omega_L = \tilde{\Omega}_L$.

With the newly formulated temporal dependence, our result for the observable SFG/DFG yield (upper sign/lower sign, respectively) reads:

$$\begin{aligned} \frac{d^2Y}{d\omega_f\, d\Omega_f} = \Big(\frac{d\sigma}{d\Omega_f}\Big)_{\mathrm{Th}} &\frac{4\pi\, l_w\, \omega_f\, E_{X\_p}\, \delta_X^x \delta_X^y\, E_{L\_p}}{(n-1)\sqrt{\pi}\,\Omega_X\, \tilde{\Omega}_L\, \omega_{X\_0}^2\, \omega_{L\_0}^2\, (\sigma_L \Delta(z_{L\_0}))^2\, T_{sum}} \frac{1}{V_\diamond^2}\, |\boldsymbol{\varepsilon}_L \cdot \mathbf{K}_{GS\diamond}(0, \mathbf{G}, \omega_{L\_0})|^2 \\ &\times e^{-(k_f^x - G^x)^2(\delta_X^x)^2/2} e^{-(k_f^y - G^y)^2(\delta_X^y)^2/2}\, e^{-(\omega_f - \omega_L \mp \omega_{L\_0} - \omega_{X\_0})^2/2\Omega_m^2}\, e^{-[\omega_L \pm \Delta t C]^2 D/2\tilde{\Omega}_L^2}\, e^{-\Delta t^2/2T_{tot}^2}. \end{aligned} \tag{5.44}$$

[10] Be aware that we have previously, i.e., in a draft version of this thesis, used the symbol T_{tot} to abbreviate what is now T_{sum}—don't confuse them.

[11] Note that the x-ray pulse may effectively be elongated due to monochromatisation. While its intrinsic pulse lengths is given by T_X, the additional term $(2\Omega_m)^{-1}$ will become relevant as soon as the monochromatised bandwidth can no longer sustain a short pulse in terms of required Fourier-components. The length of the optical pulse T_L is already understood to be *after* stretching it.

Herein, we have replaced the optical pulse-intensity $|E_{L0}|^2$ with an expression for the pulse's integrated energy $E_{L\_p} = \frac{|E_{L0}|^2 T_L \sigma_L^2 \sqrt{\pi}}{\alpha\sqrt{2}}$, to highlight the symmetry of optical and x-ray input parameters. Moreover, we have abbreviated the Thomson scattering cross section $\left(\frac{d\sigma}{d\Omega_f}\right)_{\mathrm{Th}} = \alpha^4 \left|\boldsymbol{\varepsilon}_f \cdot \boldsymbol{\varepsilon}_X\right|^2$.

At this point, our result is equivalent to Eq. (38) given in our XOWM article[12] [21].
We want to emphasize that Eq. (5.44) could now be used to predict the nonlinear scattering pattern[13] for different pulse parameters, materials and chosen reciprocal components (**G**). Owing to our approximate—yet analytical—treatment it is simple to apply and cheap to evaluate. In the following, we will apply this expression in detail to the conditions of Ref. [46], before we discuss some more general features in the subsequent sections.

Evaluation In order to compare our result quantitatively to the findings of Glover et al., we shall employ their experimental parameters. Below, we give two tables that encompass all necessary values. For the x-ray pulse we extract from Ref. [46]:

	experimental value	parameter in a.u.
photon energy	8 keV	$\omega_{0X} = 294$
initial bandwidth	20 eV (FWHM)	$\Omega_X = 0.312$
monochromator passwidth	1 eV (FWHM)	$\Omega_m = 0.016$
pulse duration	80 fs (FWHM)	$T_X = 1404$
average pulse energy	$5 \cdot 10^{10}$ photons	$E_{X\_p} = 1.47 \cdot 10^{13}$
beam divergence	1.7 μrad	$\delta_X = 6.46 \cdot 10^5$

Table 5.1: X-ray pulse parameters as of Ref. [46].

The optical pulse is respectively characterized by:

	experimental value	parameter in a.u.
photon energy	1.55 eV	$\omega_{0L} = 5.7 \cdot 10^{-2}$
full bandwidth	68 meV (FWHM)	$\tilde{\Omega}_L = 1.06 \cdot 10^{-3}$
pulse duration (stretched)	2 ps (FWHM)	$T_L = 3.51 \cdot 10^5$
laser intensity	$1.5 \cdot 10^{10}$ W cm^{-2}	$I_L = 3.8 \cdot 10^{-6}$

Table 5.2: Optical pulse parameters as of Ref. [46].

Note that, in order to make use of the intensity information from Ref. [46], we have to define:

$$I_L := \frac{\bar{E}_{\mathrm{pulse\_}L}}{8\Sigma_L^2 T_L} = \frac{\bar{E}_{\mathrm{pulse\_}L}}{8\left(\sigma_L \Delta(z_{L\_0})\right)^2 T_L}. \tag{5.45}$$

On the basis of this data, we shall now investigate each of the functional dependencies that were studied by Glover et al.. Our results are graphically shown in Fig. 5.2 and may directly be compared to Fig. 5.1.

[12] This statement pertains to the draft version of the article dated to the 28$^{\mathrm{th}}$ of March 2022. To trace the equivalence of both expressions conveniently, we note the use of further re-formulations: In the article, $\sigma_L \Delta(z_{L\_0})$ was abbreviated as Σ_L, also $1/T_{sum} = \sqrt{D}/T_{tot}$ was used. The reference to DFG as a second solution was omitted in Ref. [21] and the exponentials in control of the scattering angle were condensed in vectorial notation.

[13] Note that this scattering pattern is exceedingly boring, namely just a tiny Gaussian spot. As such, we do not give an additional plot of it, but leave this visualization to the reader's imagination.

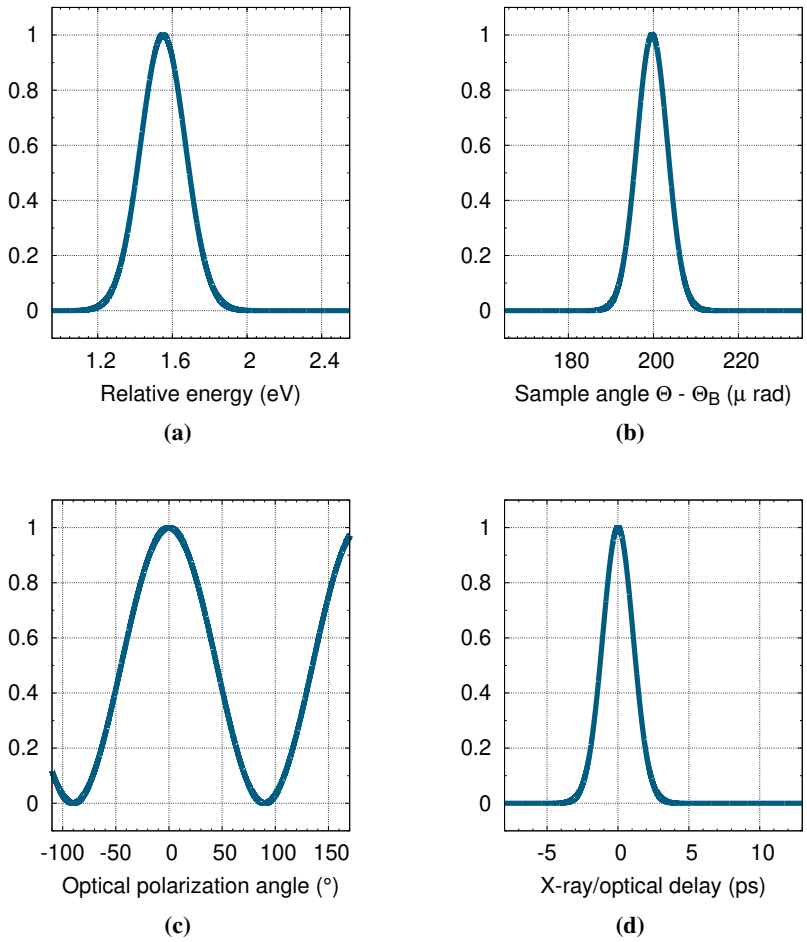

Figure 5.2: Evaluation of several parameter scans for the SFG signal on the basis of Eq. (5.44). The results can be compared to the findings of Glover et al. in Fig. 5.1. Here, the signal was scanned for: (a)-its energy dependence, (b)-its angular dependence, i.e., rocking behaviour, (c)-its dependence upon the polarization of the laser light and (d)-the temporal cross-correlation of x-ray and optical field.

Energy dependence In addressing the energy dependence of the SFG signal, we have to appreciate how Glover et al. actually discriminate SFG photons with respect to (elastic) background. Namely, they employ a crystal analyser (two-bounce Si (220), channel-cut) as an energy filter—cf. illustration of their setup in Fig. 5.1 (a). We may mimic the analyser's spectral transmission by multiplying Eq. (5.44) with an additional filter function[14] $T_a(\omega_f) = e^{-(\omega_f-\omega_a)^2/2\Omega_a^2}$.

Subsequently, we shall integrate the yield over all possible ω_f. The result will be constrained on the one hand by the physical process itself and on the other hand by the analyser's transmission. Technically, the most restrictive exponential is $e^{-[\omega_L \pm \Delta t C]^2 D/2\tilde{\Omega}_L^2}$, which incorporates the original bandwidth of the optical laser $\tilde{\Omega}_L$—further reduced by a factor of D. Performing the integration limits $\omega_L \approx 0$ and thereby fixes ω_f implicitly to $\omega_f \approx \frac{cG^{\shortparallel} \pm (n-1)\omega_{L,0}}{(\cos(\theta_f)-1)}$. Here, we neglect a tiny shift due to the chirp ΔtC, which would fall within the bandwidth of the laser at most, i.e., $\lesssim 68$ meV (FWHM). The integral also yields an overall

[14] Note that this purely spectral treatment is not ideal, as crystal optics tend to convolute spatial (read: angular) transmission properties with their wavelength dependence. In the present case, however, this simplified approach is sufficient to capture the behaviour of Glover's setup.

prefactor of $\frac{\sqrt{2\pi}(n-1)\tilde{\Omega}_L}{\sqrt{D}(2\sin^2(\theta_f/2))}$, resulting in a single differential yield of

$$\frac{dY}{d\Omega_f} \approx \left(\frac{d\sigma}{d\Omega_f}\right)_{\mathrm{Th}} \frac{2\pi\sqrt{2}\, l_w\, \omega_f\, E_{X\_p}\, \delta_X^x \delta_X^y\, E_{L\_p}}{\sin^2(\theta_f/2)\, \Omega_X\, \omega_{X\_0}^2\, \omega_{L\_0}^2\, (\sigma_L \Delta(z_{L\_0}))^2\, T_{tot}} \frac{1}{V_\diamond^2} \left|\boldsymbol{\varepsilon}_L \cdot \mathbf{K}_{GS\diamond}(0, \mathbf{G}, \omega_{L\_0})\right|^2$$
$$\times e^{-(k_f^x - G^x)^2 (\delta_X^x)^2/2} e^{-(k_f^y - G^y)^2 (\delta_X^y)^2/2} e^{-(\omega_f - \omega_a)^2/2\Omega_a^2}\, e^{-(\omega_f \mp \omega_{L\_0} - \omega_{X\_0})^2/2\Omega_m^2}\, e^{-\Delta t^2/2T_{tot}^2}. \tag{5.46}$$

Henceforth, ω_f should be considered fixed as above or—simplifying even further—approximated as $\omega_f \approx \omega_{X\_0} \pm \omega_{L\_0}$, if phase-matching is fulfilled. This will not change anything significant for the numerical value any longer.

Taking the experimental values of ~ 8 keV for the x-ray photon energy and ~ 1.55 eV for their optical counterpart, fixes $\hbar\omega_f \approx 8001.55$ eV. Obviously, the only remaining spectral dependence is then imprinted in the exponential $e^{-(\omega_f - \omega_a)^2/2\Omega_a^2}$, which models the analysers transmission function. Thus, we reproduce the analyser scan from Fig. 5.1 (b) in our Fig. 5.2 (a) by simply varying ω_a. Here, we assume the same bandwidth of the analyser as given by the authors (0.3 eV FWHM)—which unsurprisingly determines the peak width as well.

Angular dependence Subsequently, we can inspect the angular behaviour of the signal. This is set largely by the exponentials of type $e^{-(k_f^i - G^i)^2 (\delta_X^i)^2/2}$, which allow an angular spread of the same magnitude as found in the incident x-ray beam (i.e., $\sim 1/\delta_X^i$). As such, the SFG signal should have approximately the same divergence as the FEL beam, i.e., 1.7 μrad, for one fixed setting of sample and energy. Being much sharper than the analyzer acceptance, which amounts to ~ 17 μrad (FWHM), the signal is fully transmitted through the analyzer onto the detector. This is consistent with the observations by Glover et al. [46].

Next, we shall evaluate, how this confined signal beam precesses, when the sample is rocked in the scattering plane (here taken to be y). To this end, we have to follow the exponentials peak, i.e., observe the condition

$$\begin{aligned} k_f^y - G^y &\stackrel{!}{=} 0 \\ \alpha\omega_f \sin(\theta_f) - |\mathbf{G}| \cos(\Omega) &\stackrel{!}{=} 0. \end{aligned} \tag{5.47}$$

In the second line, we have parametrized k_f^y in spherical coordinates and expressed the orientation of the reciprocal lattice vector $\mathbf{G}$ via the rocking angle of the sample (Ω). We may further substitute $\omega_f \approx \frac{cG^{\shortparallel} + (n-1)\omega_{L\_0}}{(\cos(\theta_f) - 1)}$, thus using the replacement for the SFG case found above.

$$\begin{aligned} 0 &\stackrel{!}{=} \alpha \sin(\theta_f) \left(\frac{-\sin(\Omega)\, c\, |\mathbf{G}| + (n-1)\, \omega_{L\_0}}{\cos(\theta_f) - 1}\right) - |\mathbf{G}| \cos(\Omega) \\ |\mathbf{G}| \cos(\Omega) &= \frac{\sin(\theta_f)}{\cos(\theta_f) - 1} \left(-\sin(\Omega)\, |\mathbf{G}| + \alpha\, (n-1)\, \omega_{L\_0}\right) \\ \frac{\cos(\theta_f) - 1}{\sin(\theta_f)} &= \frac{\left(-\sin(\Omega)\, |\mathbf{G}| + \alpha\, (n-1)\, \omega_{L\_0}\right)}{\cos(\Omega)\, |\mathbf{G}|} = \frac{-\sin(\Omega)\, |\mathbf{G}|}{\cos(\Omega)\, |\mathbf{G}|} + \frac{\alpha\, (n-1)\, \omega_{L\_0}}{\cos(\Omega)\, |\mathbf{G}|} \\ -\tan(\frac{\theta_f}{2}) &= -\tan(\Omega) + \frac{\alpha\, (n-1)\, \omega_{L\_0}}{\cos(\Omega)\, |\mathbf{G}|}. \end{aligned} \tag{5.48}$$

As the second term on the right hand side is small compared to $\tan(\Omega)$, we may use the expansion

$\arctan(\tan(a)-x) \approx a - \cos^2(a)x + ...$ to finally obtain the rocking behaviour

$$\theta_f \approx 2\,\Omega - \frac{2\,\alpha\,(n-1)\,\omega_{L0}\cos(\Omega)}{|\mathbf{G}|}. \tag{5.49}$$

Consequently, the signal beam precesses by twice the angle that the sample is rocked ($\theta - 2\theta$-behaviour). This agrees well with the findings of Glover et al. and may be used to mimic their rocking curve scan (i.e., Fig. 5.1 c). To this end, we can assume the signal beam to be perfectly collimated compared to the angular acceptance of the analyser (1.7 μrad $\ll$ 17 μrad (FWHM)). This implies that the signal beam may be rotated within an effective rocking range of $\sim 17/2$ μrad towards either side of the central transmission without being suppressed by the analyser. This is modelled in Fig. 5.2 (b) by yet another Gaussian transmission function, the width of which corresponds well to the experimental observation.

With respect to the (absolute) position—given with reference to the Bragg angle θ_B at 8 keV in Fig. 5.2 (b)—our Eq. (5.49) is not fully accurate, though. This is unsurprising, as we have previously neglected several, albeit small, angular deviations. For instance, we have assumed the sample to be irradiated at normal incidence, instead of properly tilting it by a few degrees. Similarly, we have not accounted for the non-collinearity of x-ray and optical beams. These effects may easily compound and thus yield the absolute discrepancy of ~ 130 μrad between our Fig. 5.2 (b) and Glover's Fig. 5.1 (c).

Polarization dependence The dependence of the SFG signal on the polarization direction of the visible light (cf. Fig. 5.1 (d)) is immediately obvious from our Eq. (5.44) or Eq. (5.46). We find the SFG-yield to depend directly on the scalar product of the electronic response function $\mathbf{K}_{GS}$ with the polarization vector of the optical laser field $\boldsymbol{\varepsilon}_L$—squared. This results in a $\cos^2$-dependence for their relative angle, which we plot for completeness in Fig. 5.2 (c). There, the optical polarization is chosen to lie in the scattering plane for 0° and perpendicular to the x-ray scattering plane at $\pm 90^\circ$. The resulting curve fully reproduces the findings of Ref. [46].

Delay dependence Finally, we can obtain the dependence of the signal on the mutual delay of x-ray and optical pulse (Δt) from the temporal exponential $e^{-\Delta t^2/2T_{tot}^2}$. This allows for the SFG signal to be created as long as the mutual delay is on the order of T_{tot}. Obviously, this should yield a peak a $\Delta t = 0$, which is not fully reflected in the findings of Glover et al. (~ 1 ps offset, cf. Fig. 5.1 (e)). However, this may have various experimental reasons—let alone the definition of the absolute time delay[15].

It is more instructive (and technically robust) to investigate the width of the cross-correlation region. This marks the time-span during which (monochromatised) x-rays and optical photons overlap in some region of the sample and may thus produce a mixing signal (cf. discussion below Eq. (5.43)). As stated above, the width is given by $T_{tot} = \sqrt{T_X^2 + T_L^2 + (2\Omega_m)^{-2} + (\alpha(n-1)\sigma_w)^2/2}$, which sums up to 2.53 ps (FWHM). Our result is in excellent agreement with the experimentally determined 2.5 ps (FWHM). For completeness, we also plot the cross-correlation region as a function of Δt in Fig. 5.2 (d).

We note in closing of this paragraph that we have neglected any influence of the laser's frequency chirp in our discussion. For the given setup's broad energy distributions—both incident and accepted by the analyser—this was a valid approximation. Should, however, the setup become much more selective, then we would need to account more diligently for the exponential $e^{-[\omega_L \pm \Delta t C]^2 D/2\tilde{\Omega}_L^2}$ in Eq. (5.44). Herein,

[15] Recall, that we have defined the arrival time of each light pulse with respect to the absolute 0-position of our coordinate system. For us, this coincides with the assumed center of the sample.

variations of the photon energy are spread over the time (-delay) Δt. Correspondingly, a setup with high energy-selectivity would pick a specific temporal region, for which the energetic transmission is allowed.

Total yield In addition to the differential dependencies studied above, we may likewise benchmark our theory in terms of total SFG-counts. To this end, we would have to integrate Eq. (5.44) over both the spectral and angular degrees of freedom for the final state photon. For Eq. (5.46), respectively, wherein the spectral integration ($d\omega_f$) was already carried out, we continue to integrate over $d\Omega_f$.

$$\int d\Omega_f \, \frac{dY}{d\Omega_f} = \int d\Omega_f \, \Big(\frac{d\sigma}{d\Omega_f}\Big)_{\text{Th}} \frac{2\pi\sqrt{2}\, l_w\, \omega_f\, E_{X\_p}\, \delta_X^x \delta_X^y\, E_{L\_p}}{\sin^2(\theta_f/2)\, \Omega_X\, \omega_{X\_0}^2\, \omega_{L\_0}^2\, (\sigma_L \Delta(z_{L\_0}))^2\, T_{tot}} \frac{1}{V_\diamond^2} \, |\boldsymbol{\varepsilon}_L \cdot \mathbf{K}_{GS\diamond}(0, \mathbf{G}, \omega_{L\_0})|^2$$
$$\times\, e^{-(k_f^x - G^x)^2 (\delta_X^x)^2/2} e^{-(k_f^y - G^y)^2 (\delta_X^y)^2/2} e^{-(\omega_f - \omega_a)^2/2\Omega_a^2}\; e^{-(\omega_f \mp \omega_{L\_0} - \omega_{X\_0})^2/2\Omega_m^2}\; e^{-\Delta t^2/2T_{tot}^2}. \quad (5.50)$$

Recurring to the fact that the analyser's angular acceptance is much broader than the extent of the SFG-signal, we can simply solve[16]

$$\int d\Omega_f e^{-(k_f^x - G^x)^2 (\delta_X^x)^2/2} e^{-(k_f^y - G^y)^2 (\delta_X^y)^2/2} \approx \frac{2\pi}{\alpha^2 \omega_f^2 \cos(2\theta_B)\, \delta_X^x \delta_X^y}. \quad (5.51)$$

Here, we assume in addition that $\theta_f \approx 2\,\theta_B$—which is reasonable for x-ray optical SFG / DFG, as it occurs very close to the elastic Bragg condition for the incident x-rays. Moreover, taking all other conditions to be optimized as well, we find for the total yield

$$Y \approx \Big(\frac{d\sigma(2\theta_B)}{d\Omega}\Big)_{\text{Th}} \frac{4\pi^2\sqrt{2}\, l_w\, E_{X\_p} E_{L\_p}}{\alpha^2 \cos(2\theta_B) \sin^2(\theta_B)\, \Omega_X\, \omega_f\, \omega_{X\_0}^2\, \omega_{L\_0}^2\, (\sigma_L \Delta(z_{L\_0}))^2\, T_{tot}} \frac{1}{V_\diamond^2} \, |\boldsymbol{\varepsilon}_L \cdot \mathbf{K}_{GS\diamond}(0, \mathbf{G}, \omega_{L\_0})|^2 . \quad (5.52)$$

We note in passing, that this expression features the linear dependence on the optical pulse energy, which Glover et al. demonstrate in their inset to Fig. 5.1 (e). For our subsequent evaluation, however, we rather want to employ the optical pulse's intensity. Thus, we use our earlier definition of $I_L = \frac{\bar{E}_{L\_p}}{8\,(\sigma_L \Delta(z_{L\_0}))^2\, T_L}$ and may finally re-write the yield as

$$Y \approx \Big(\frac{d\sigma(2\theta_B)}{d\Omega}\Big)_{\text{Th}} \frac{4\pi^2\sqrt{2}\, l_w\, E_{X\_p}\, 8 I_L T_L}{\alpha^2 \cos(2\theta_B) \sin^2(\theta_B)\, \Omega_X\, \omega_f\, \omega_{X\_0}^2\, \omega_{L\_0}^2\, T_{tot}} \frac{1}{V_\diamond^2} \, |\boldsymbol{\varepsilon}_L \cdot \mathbf{K}_{GS\diamond}(0, \mathbf{G}, \omega_{L\_0})|^2 . \quad (5.53)$$

Now, we can insert all pulse parameters from Tab. 5.1 and 5.2 as well as recall that Glover et al. were using a 500 μm thick diamond crystal near a (111)-reflection. This implies a Bragg-angle of $\theta_B = 22.104$ degrees at $\hbar\omega_{X\_0} = 8$ keV. Finally, we can collect the strength of the nonlinear response function $\mathbf{K}_{GS\diamond}(0, \mathbf{G}, \omega_{L\_0})$ from our discussion in Sec. 3.3. With all of the above in place, we would predict an average yield of $Y = 4835$ SFG-photons obtainable per shot. This ranges significantly above the experimentally reported yield of $Y_{\text{exp}} = 65$, however, we have not yet accounted for the imperfect detection efficiency underlying the results of Ref. [46].

In order to obtain an estimate of the detection efficiency η_{det}, we note from Ref. [46] that Glover et al. have also measured the purely elastic rocking curve of the (111)-reflection. Starting from an incident fluence of $5 \cdot 10^{10}$ photons per pulse, they observe a maximum in reflectivity of $3 \cdot 10^7$ photons being diffracted. This marked reduction is in part ascribable to the monochromator, which reduces the incident

[16] Note that there is an important factor α^{-2} resulting from the Jacobian in this integration. Its omission has lead to erroneously small yields in early drafts of Ref. [21]—thus, we advise to be very attentive regarding constant factors.

bandwidth from 20 eV down to ~ 1 eV. Beyond this factor of 20, however, losses are inherent to the setup and may be subsumed in the detection efficiency $\eta_{\text{det}} \approx \frac{3\cdot 10^7}{5\cdot 10^{10}/20} = 0.012$.

Incorporating the detection efficiency, our theoretical result is modified to $Y \cdot \eta_{\text{det}} \approx 58$. This is in very good, quantitative agreement with the findings of Glover et al. ultimately. In combination with the successful, preceding benchmarks on differential dependencies, we can thus conclude this section on a distinctly positive note. Our XOWM theory has proven to be viable for the reproduction of experimental SFG results. This is also re-assuring with regard to the validity of the successive approximation-steps that we have undertaken during the course of our modelling endeavour.

With heightened confidence, we may now extract more general insights from our results and aim to predict (or envision) future experiments.

5.1.2 Generalizable insights on SFG / DFG

While we have focused our discussion so far on the specific case study of Ref. [46], we may further extract some generalizable insights on DFG / SFG from our above results. These comprise in order of appearance:

1. The phase-matching condition of SFG / DFG,
2. the specific intensity dependence of SFG / DFG,
3. the prospects of XOWM applications at synchrotron sources vs. XFELs,
4. the prospects of 'nonlinear crystallography' as an application of SFG /DFG for structural insights.

5.1.2.a The phase-matching condition(s)

The occurrence of an XOWM signal is predicated on fulfilling the so-called phase-matching condition. In other words, energy and momentum conservation has to be satisfied among all involved fields for the mixing-process to be allowed kinematically[17]. This condition has been built into the our scattering observable early on. Regarding energy conservation, we find it implemented as a δ-function in Eqs. (2.67) or (5.1), respectively, which sets:

$$\omega_f = \omega_X + \omega_L. \tag{5.54}$$

Momentum conservation, on the other hand, enters in disguise of the sample's shape function $\tilde{w}(\mathbf{k})$—cf. Eqs. (3.24) or (5.11) above. This is in itself (almost) δ-like and constrains all involved momenta to satisfy:

$$\mathbf{k}_f = \mathbf{k}_X + \mathbf{k}_L + \mathbf{G}, \tag{5.55}$$

where $\mathbf{G}$ denotes the reciprocal lattice vector that governs the nonlinear scattering process. Note that at this stage, both ω_L and $\mathbf{k}_L$ may be chosen positive or negative to account for SFG or DFG, respectively.

Both of these conditions are naturally transmitted into the derivation of Sec. 5.1.1, although their concrete shape is obscured at times. Thus, we want to recover them briefly and consider their more general implications thereafter.

[17] Note that the necessity to conserve energy and momentum is not fully surprising, given that their conservation laws are fundamental to all of physics. We mention it for completeness and because it allows to extract simple adjustment guidelines.

Energy conservation akin to Eq. (5.54) is still well visible above in Eq. (5.44). Herein, the exponential $e^{-(\omega_f-\omega_L\mp\omega_{L\_0}-\omega_{X\_0})^2/2\Omega_m^2}$ reproduces precisely the constraint that we would expect to find. In contrast, the information on momentum conservation is distributed across two conditions. Transverse to the incident beam, the scattered photon's momentum is determined via the exponentials $e^{-(k_f^x-G^i)^2(\delta_X^i)^2/2}$ with $i=x,y$. This fixes two components of Eq. (5.55)

$$\begin{aligned}\mathbf{k}_f^\perp &= 0+0+\mathbf{G}^\perp \\ &= \mathbf{k}_X^\perp+\mathbf{k}_L^\perp+\mathbf{G}^\perp\end{aligned} \tag{5.56}$$

under the assumption that $\mathbf{k}_X^\perp = 0 = \mathbf{k}_L^\perp$. For the longitudinal conservation of momenta, we have to look into the condition $\omega_L \approx \frac{ck_f^\parallel-\omega_f-cG^\parallel}{(n-1)} \mp \omega_{L\_0}$, which we found after integration of Eq. (5.40). If energy conservation holds, i.e., $\omega_f = \omega_{X\_0} \pm \omega_{L\_0}$ and $\omega_L \approx 0$, we can rewrite this condition as

$$\begin{aligned}\omega_L &\approx \frac{ck_f^\parallel-\omega_f-cG^\parallel}{(n-1)} \mp \omega_{L\_0} \\ 0 &\approx \frac{ck_f^\parallel-\omega_{X\_0}\mp\omega_{L\_0}-cG^\parallel}{(n-1)} \mp \omega_{L\_0} \\ 0 &\approx k_f^\parallel-\alpha\omega_{X\_0}\mp\alpha\omega_{L\_0}-G^\parallel\mp(n-1)\alpha\omega_{L\_0} \\ k_f^\parallel &\approx \underbrace{\alpha\omega_{X\_0}}_{k_{X\_0}^\parallel} \pm \underbrace{n\alpha\omega_{L\_0}}_{k_{L\_0}^\parallel}+G^\parallel\end{aligned} \tag{5.57}$$

and thereby reveal the third component of Eq. (5.55).

With these phase-matching conditions being (re-)established, we shall briefly address their usefulness: By fundamental kinematics, these conditions determine the subset of scattering conditions, for which a XOWM-signal can be created at all. As such, they allow to pre-plan an experimental setup and aim for promising positions without exercising the full calculation of Sec. 5.1.1. Notably, there may still be modulations in the scattering signal due to the strength of the nonlinear response function[18] or the (optical) polarization dependence (cf. discussion above).

In order to visualize the phase-matching condition for SFG / DFG, let us consider a two-dimensional example first: Assume that all vectors of Eq. (5.55) are constrained to lie within one plane, viz., the scattering plane. In Figs. 5.3 (a) and (b), we sketch these scenarios for SFG and DFG, respectively. For varying inclination of the reciprocal lattice vector **G**—determined by rocking the sample about an angle Ω—the momenta add up in slightly different constellations. This, in turn, affects the angle θ_f, under which the a nonlinear scattering signal may be observed. Plotting one angle against the other, we find the phase-matching conditions to line out elliptical surfaces. In Figs. 5.3 (c) and (d), we show two examples for SFG / DFG driven by incident x-rays at $\hbar\omega_X = 8$ keV and optical photons at $\hbar\omega_L = 1.55$ eV.

We note that both solutions are shifted with respect to one another, yet each envelopes the Bragg-position for elastically scattered x-rays at energy $\omega_X = c\,|\mathbf{k}_X|$, indicated as a black star at coordinate (0,0). An additional red or blue star indicates the hypothetical Bragg-position for elastically scattered radiation at $\omega_X \pm \omega_L$, respectively. In the case of Ref. [46], the authors chose a phase-matching position very close to the fundamental Bragg-peak, namely shifted by $\sim 70\ \mu$rad ≈ 0.004 deg.

Finally, we want to extend the above picture to three dimensions. To this end, we merely have to

[18] Note in particular, that there may be reciprocal components, for which the nonlinear response function vanishes completely due to crystal symmetry.

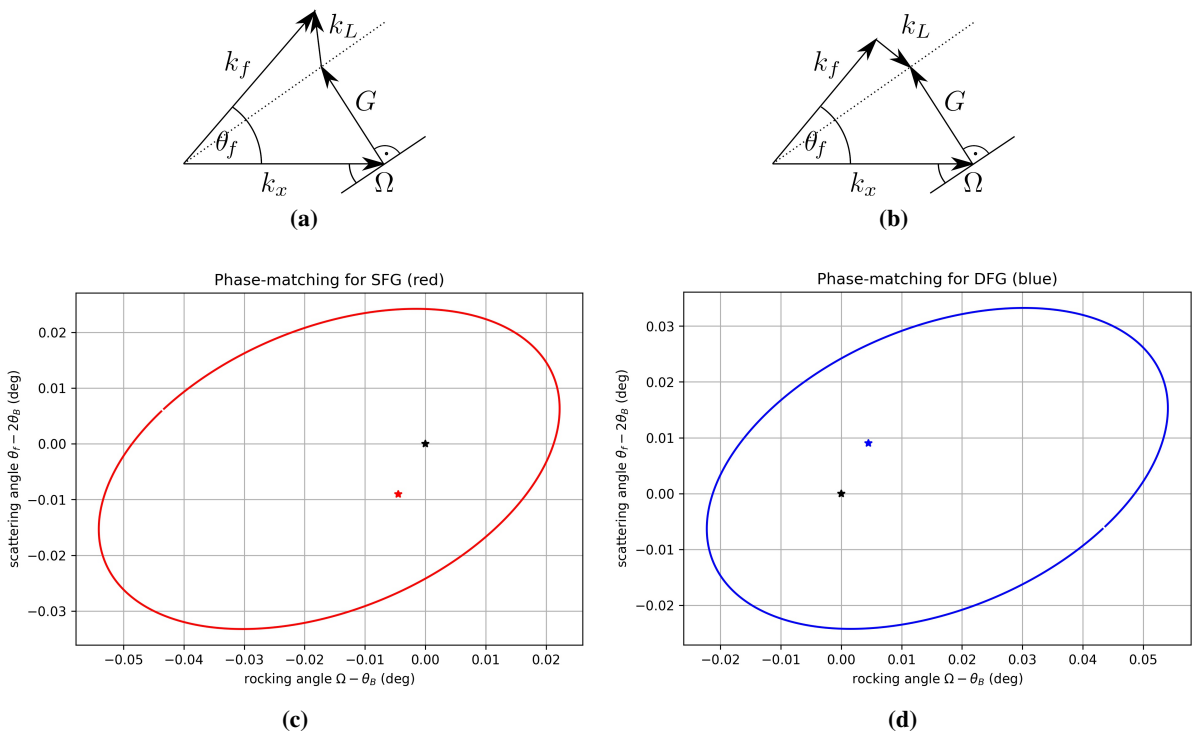

Figure 5.3: Illustration of the phase-matching conditions for SFG and DFG: Graphs (a) and (b) outline the momentum balance for the two processes, respectively. Note that each features a rotational symmetry axis (indicated as dashed line), which translates into possible scattering solutions along a circle for fixed sample position and variable laser-input. (c) and (d) outline the interrelation of the nonlinear scattering angle ω_f and the rocking angle of the sample Ω—again for SFG and DFG, respectively. [We gratefully acknowledge Dr. Christina Bömer's help in rendering the computer graphics of the sketches (a) and (b).]

recognize the inherent rotational symmetry of Figs. 5.3 (a) and (b). The combination of vectors $\mathbf{k}_f - \mathbf{k}_L$ (SFG) or $\mathbf{k}_f + \mathbf{k}_L$ (DFG) may each be rotated around the dashed axis of their respective plot. This rotation translates into circular solutions for the phase-matching condition at each sample angle. In other words, the ellipses of Figs. 5.3 (c) and (d) can trivially be extended to 3D by continuing the vertical diameter at each value of Ω into a circle that protrudes from the graphs' plane.

5.1.2.b Intensity dependence of SFG / DFG

A feature of the SFG yield Eq. (5.52), which is particularly noteworthy, comes in its is bi-linear dependence on the x-ray and optical pulse energy (or number of photons, respectively). This underlines the fact that both x-ray and optical photons are equally necessary to produce the XOWM-signal.

There is an additional, more subtle dimension to the overall dependence on photon-flux or intensity, however: The two pulse energies appear normalized to a combined time T_{tot} and cross-sectional area $(\sigma_L \Delta(z_{L\_0}))^2$. Thereby, we may define an effective intensity $I = E/(T \cdot A)$ using either one of the pulse energies. Especially in the limit of one pulse being significantly longer than the other, this effective expression recovers the physically meaningful pulse intensity of the longer pulse. We may think of this longer pulse to provide a 'homogeneous' background intensity, upon which the other pulse interacts.

This behaviour may be understood more readily from the original time-domain expression Eq. (2.57) for the XOWM-signal, if reduced only to temporal aspects:

$$\langle \hat{O} \rangle \propto \int^{\times 4} dt_1\, dt_1'\, dt_2\, dt_2'\; e^{\mathrm{i}\,\omega_f (t_1 - t_1')}\, H^{(1)}_{\mathrm{X\_IN}}(t_1', t_1)\, \bar{H}^{(1)}\mathrm{OPT}(t_2', t_2) P(t_2, t_1)\, (P(t_2', t_1'))^*. \tag{5.58}$$

For simplicity, we neglect the vectorial nature of the nonlinear response and write $\mathbf{P}_I(...,t_2,...,t_1) \to P(t_2,t_1)$ as a scalar function. Assuming further that we could collect all relevant emitted frequencies, i.e., integrate over ω_f, we produce a δ-function $\delta(t_1 - t_1')$ from the leading exponential. This assumption roughly mirrors our eventual treatment in Sec. 5.1.1. There, we had adopted yet another approximation, namely:

$$\mathbf{K}_{GS\diamond}(0,\mathbf{G},\omega_L) \approx \mathbf{K}_{GS\diamond}(0,\mathbf{G},\omega_{L\_0}) \approx \mathbf{K}_{GS\diamond}(0,\mathbf{G},\omega_L'). \tag{5.59}$$

This remains valid as long as the bandwidth of the optical field is narrow compared to the spectral variations of $\mathbf{K}_{GS\diamond}$. Transforming Eq. (5.59) back into the time domain implies:

$$\begin{aligned} P(t_2,t_1) = P(0,(t_1-t_2)) &\propto \int d\omega\, e^{-\mathrm{i}\,\omega(t_1-t_2)}\, K(\omega) \\ &\propto K(\omega_{L\_0}) \int d\omega\, e^{-\mathrm{i}\,\omega(t_1-t_2)} \\ &\propto K(\omega_{L\_0})\, \delta(t_1-t_2). \end{aligned} \tag{5.60}$$

Collecting all of the above and substituting it into Eq. (5.58), we can simplify the observable down to a single integration in dt

$$\begin{aligned} \langle \hat{O} \rangle &\propto \int^{\times 4} dt_1\, dt_1'\, dt_2\, dt_2'\;\; \delta(t_1-t_1')\, H^{(1)}_{\mathrm{X\_IN}}(t_1',t_1)\, \bar{H}^{(1)}_{\mathrm{OPT}}(t_2',t_2)\, \delta(t_1-t_2)\, \delta(t_1'-t_2')\, |K(\omega_{L\_0})|^2 \\ &\propto |K(\omega_{L\_0})|^2 \int dt\; \underbrace{H^{(1)}_{\mathrm{X\_IN}}(t,t)}_{I_{\mathrm{X\_IN}}(t)}\; \underbrace{\bar{H}^{(1)}_{\mathrm{OPT}}(t,t)}_{I_{\mathrm{OPT}}(t)}. \end{aligned} \tag{5.61}$$

The remaining expression contains an integral of the time-wise diagonal correlation functions of both involved fields. As is well-known for Glauber-type correlation functions—or can be checked in App. A.10—their time-diagonal value corresponds to the intensity of the respective field [64]. Thus, the integrated XOWM-signal ($\propto$ yield) behaves as the integral over the product of field intensities $I_{\mathrm{X\_IN}}(t) \cdot I_{\mathrm{OPT}}(t)$.

The simplified treatment of the XOWM-signal above reinforces our earlier interpretation[19]. Namely, if one pulse is much longer than the other, it forms a quasi-uniform background intensity, upon which the other pulse can contribute all its photons for mixing. Beyond this, however, Eq. (5.61) underlines a different insight: XOWM benefits from high *combined* intensities. In particular, XOWM shows an increase in yield, if a constant number of photons is forced to interact in a shorter time. In this, the process bears clear resemblence to other nonlinear phenomena, such as second harmonic generation for instance [12, 158].

Closing this discussion, we can draw a few simple conclusions:

- In order to make efficient use of all photons, the x-ray and optical pulse should be similar in length.
- Overall, shorter yet more intense pulses increase the mixing efficiency.
- As a consequence of the above, XOWM applications scale favourably at x-ray FELs compared to synchrotron radiation sources, given that the former can produce much shorter (and more intense) pulses.
- It is not advisable to try XOWM with an optical cw-laser. Even for large average power output,

[19] Note that we outline a slightly less simplified version of this derivation in App. A.16.

the achievable intensity is far inferior to pulsed sources and thus fails to optimize yield according to Eq. (5.61).

5.1.2.c Extrapolation for SFG / DFG at synchrotrons

In the previous section, we have concluded that XOWM scales favourably at FELs compared to synchrotron radiation (SR) sources. Importantly, however, it does not negate its principle viability at synchrotrons. Considering the paramount advantages of SR sources—such as high stability, high average flux[20] and sheer accessibility for users—we deem it important to conduct a dedicated case study.

For the sake of simplicity, we shall assume that the derivations from Sec. 5.1.1 roughly hold and use Eq. (5.53) as a basis for extrapolation. Obviously, we have to choose new x-ray pulse parameters. Up front, we know that SR pulses measure roughly 100 ps in length [159] compared to ~ 80 fs at an XFEL [46]. Thus, we would expect the total yield per shot to drop by roughly three orders of magnitude—all else equal being equal. Disregarding the detection efficiency, this would entail roughly 1 SFG- / DFG-photon to be available per shot.

For a complete numerical example, we closely follow our discussion from Ref. [21]. We shall assume the following parameters on the x-ray part (which may be compared to the XFEL values from Tab. 5.1):

	experimental value	parameter in a.u.
photon energy	8 keV	$\omega_{0X} = 294$
monochromator passwidth	1 eV (FWHM)	$\Omega_m = 0.016$
pulse duration	100 ps (FWHM)	$T_X = 1.76 \cdot 10^6$
average pulse energy	$4 \cdot 10^6$ photons	$E_{X\_p}^{\text{mono}} = 1.18 \cdot 10^9$
beam divergence	8 μrad	$\delta_X = 1.37 \cdot 10^5$.

Table 5.3: Exemplary x-ray pulse parameters for SFG / DFG at a synchrotron radiation source.

These parameters characterize individual x-ray pulses, i.e., the emission from single bunches, at the PETRA III synchrotron radiation source. In particular, we assume operation in the 40 bunch mode [159, 160] and generation of x-rays via the 'standard' 2 m undulator (U32) in a high-β section of the ring [161]. In contrast to the description of Sec. 5.1.1, we omit specifying an 'initial bandwidth' for this undulator[21]. Instead, we work exclusively with the monochromator's passwidth Ω_m, such that the corresponding pulse energy is to be understood *after* the monochromator. In order to apply this information properly, we have to exchange Ω_X for Ω_m in Eq. (5.53):

$$Y \approx \left(\frac{d\sigma(2\theta_B)}{d\Omega}\right)_{\text{Th}} \frac{4\pi^2\sqrt{2}\, l_w\, E_{X\_p}^{\text{mono}}\, 8\, I_L\, T_L}{\alpha^2 \cos(2\theta_B) \sin^2(\theta_B)\, \Omega_m\, \omega_f\, \omega_{X\_0}^2\, \omega_{L\_0}^2\, T_{tot}} \frac{1}{V_\diamond^2} \left|\boldsymbol{\varepsilon}_L \cdot \mathbf{K}_{GS\diamond}(0, \mathbf{G}, \omega_{L\_0})\right|^2 . \tag{5.62}$$

Beyond this, we copy the properties of the optical pulse from Tab. 5.2 in Sec. 5.1.1:

[20] Note that the lower peak intensities at SR sources may superficially be disadvantageous for the SFG / DFG-yield. However, they may anyways be necessary in order to avoid x-ray-induced sample damage. Factoring this in, it becomes a very appealing prospect to use a source that delivers weaker, yet simply *more* pulses, which spreads the load and recovers some of the yield.

[21] The overall bandwidth of radiation produced in the undulator would be rather broad and also rather irrelevant. After all, we are not interested in pink-beam usage here.

	experimental value	parameter in a.u.
photon energy	1.55 eV	$\omega_{0L} = 5.7 \cdot 10^{-2}$
full bandwidth	68 meV (FWHM)	$\tilde{\Omega}_L = 1.06 \cdot 10^{-3}$
pulse duration (stretched)	2 ps (FWHM)	$T_L = 3.51 \cdot 10^5$
laser intensity	$1.5 \cdot 10^{10}$ W cm^{-2}	$I_L = 3.8 \cdot 10^{-6}$

Table 5.4: Optical pulse parameters assumed for SFG / DFG at a synchrotron radiation source.

This simplifies our comparison. Likewise, we consider the same sample—a 500 μm-thick diamond with a (100)-surface cut—as well as the same scattering configuration, i.e., using a (111)-reflection at nominal Bragg angle of $\theta_B = 22.104°$.

Evaluating Eq. (5.62) on the basis of the above parameters, we obtain an SFG yield of $Y \approx 0.2$ photons per pulse. Very roughly, this is in line with our earlier estimate. Despite being much lower than the yield per pulse at an XFEL, the resulting number of SFG photons is reasonably measurable. In particular, we can recover a high average count-rate by capitalizing on the repetition rate of SR sources. In the case of PETRA III this amounts to ~ 5.2 MHz (timing mode) and thus a hypothetical gain of six orders of magnitude. Realistically, it may prove hard to match this repetition rate with coincident optical pulses[22], yet any subharmonic synchronization at several kilo-Hertz would already enable a significant increase in counts. Assuming 10 kHz for the sake of this argument and disregarding detection efficiencies for the moment[23], one could thus reach 2000 cts/s. Such a yield is on par with (or exceeds) linear, photon-hungry techniques, such as RIXS ($\sim$ 1000 cts/s [162]), non-resonant x-ray Raman scattering ($\sim$ 100 cts/s [163]) or nuclear resonant scattering ($\sim$ 5 cts/s [164]). Therefore, we conclude that—using efficient x-ray optics for the detection of the nonlinear signal—measuring XOWM is entirely within reach at present synchrotron radiation sources.

Beyond this, we note that further improvements of SR sources are pending. These come as upgrades towards fourth-generation, diffraction-limited storage-rings—for instance remodelling the ESRF into the ESRF-EBS [165, 166]. For PETRA III, a corresponding upgrade is planned leading to PETRA IV [167]. This ultra-low emittance storage ring will provide outstanding conditions to pursue XOWM experiments. For its latest design—using a Hybrid 6 Bend Achromat—a 40 bunch mode that is comparable to our assumptions above will feature an emittance of merely 38 pm rad (r.m.s., horz.) and 8 pm rad (r.m.s., vert.) [168]. If we aim for the same divergence as in our preceding example, i.e., 8 μrad (FWHM), this implies that we can achieve natural focal-spot sizes of ~ 26.3 μm (horz.) and ~ 5.6 μm (vert.). Compared to our starting point from Ref. [46], which measured 1 mm $\times$ 0.5 mm, this presents an improvement of more than three orders of magnitude. More importantly, this improvement can be converted into an increase in count rates, if the optical laser is focused accordingly. Thereby, both intensities increase as does the yield, which depends bi-linearly upon them (cf. previous section).
In an additional extension of the machine's capability, PETRA IV is envisioned to host five 'flagship beamlines'. These shall make use of extended insertion devices (10 m undulators) and thus provide exceptionally high brilliance—surpassing other SR sources by an order of magnitude or more [167]. At such beamlines, XOWM signal-strength could respectively be boosted even further.

Thus in conclusion, we note that XOWM does not only appear feasible at present SR sources, but

[22] Note that one should probably not even try to match the storage rings repetition rate with the rate of optical laser pulses—at least not at the given pulse energy of $\sim$ 1 mJ. After all, this would correspond to an average optical power of 1 mJ $\cdot$ 1 MHz = 1 kW, which provides a formidable thermal load on the sample.

[23] We recall that the detection efficiency in the case of Glover et al. [46] reached merely $\eta_{\text{det}} = 0.012$.

also harbours excellent prospects for upgraded storage rings. These findings raise hopes, in particular, that the ensuing application of XOWM for 'nonlinear crystallography' could be pursued routinely at SR sources in the future.

5.1.2.d Prospects for 'nonlinear crystallography'

Stepping beyond the proof-of-principle for SFG at a single orientation (cf. Ref. [46]), the more general appeal of XOWM derives from its crystallographic potential. Specifically, it allows for the (3D) reconstruction of the sample's microscopic nonlinear response. Recalling Eq. (5.53)

$$Y \approx \Big(\frac{d\sigma(2\theta_B)}{d\Omega}\Big)_{\text{Th}} \frac{4\pi^2\sqrt{2}\, l_w\, E_{X\_p}\, 8\, I_L\, T_L}{\alpha^2 \cos(2\theta_B)\sin^2(\theta_B)\, \Omega_X\, \omega_f\, \omega_{X\_0}^2\, \omega_{L\_0}^2\, T_{tot}} \frac{1}{V_\diamond^2} \left|\boldsymbol{\varepsilon}_L \cdot \mathbf{K}_{GS\diamond}(0,\mathbf{G},\omega_{L\_0})\right|^2, \tag{5.63}$$

we may think of the essential response function $\mathbf{K}_{GS\diamond}(0,\mathbf{G},\omega_{L\_0})$ in direct analogy to the structure factors of conventional (linear) crystallography $F(\mathbf{G})$. Albeit, $\mathbf{K}_{GS\diamond}$ does not only encode spatial properties via $\mathbf{G}$ but also characterizes the dynamics of the nonlinear response in terms of its spectral Fourier profile. For a more detailed discussion, we refer the reader to Chpt. 3. At this point, it suffices for us to recall that we can invert the spatial Fourier decomposition and thus obtain a response density

$$\begin{aligned}\mathbf{R}_{GS\diamond}(\mathbf{x},\omega) &= \frac{1}{V_\diamond}\sum_{\mathbf{G}}^{\text{rec.}} e^{\mathrm{i}\mathbf{G}\cdot\mathbf{x}}\, \mathbf{K}_{GS\diamond}(0,\mathbf{G},\omega) \\ &= \int d\tau\, e^{\mathrm{i}\omega\tau} \int_\diamond d^3y\, \mathbf{P}_{GS\diamond}(\mathbf{y},t_2,\mathbf{x},t_1).\end{aligned} \tag{5.64}$$

This response density provides access to a partially averaged version[24] of the density—current-density correlator $\mathbf{P}_{GS\diamond}(\mathbf{y},t_2,\mathbf{x},t_1)$ (cf. Chpt. 3) or can be used to infer the charge-density response to a specific optical pulse (cf. the upcoming M.Sc. thesis by F. Kerker [126]).

In its ideal form, i.e., at high resolution, this response density is depicted in Fig. 5.4. There, we plot both a two-dimensional view of $|\mathbf{R}_{GS\diamond}(\mathbf{x},0.057)|^2$ in the $(1\bar{1}0)$-plane and a 3D-rendering of its distribution across the conventional (cubic) unit cell of diamond—in plots (a) and (b), respectively. The presented example is based on the numerical simulations from Chpt. 3.

In order to achieve a similar reconstruction based on experimentally measured data, two major challenges have to be addressed:

1. The phase-problem has to be solved and

2. sufficiently many orientations have to be measured to reach the desired resolution.

Both issues are well known from regular crystallography.

1. Phase-problem A recent exposition of the conventional phase-problem, as well as a variety of remedies is given in Ref. [169], for instance. Analogous to the situation in regular crystallography, our Eq. (5.63) relates the scattering signal merely to the absolute value of the (nonlinear) structure factor, but crucially misses its complex phase information. Thus, the Fourier inversion of Eq. (5.64) is not strictly

[24] Note that the partial averaging, viz. the averaging over coordinate $\mathbf{y}$, is a consequence of our 'dipole-approximation'-type of treatment for the optical interaction. It is mirrored in the fact that $\mathbf{K}_{GS\diamond}(0,\mathbf{G},\omega_{L\_0})$ no longer carries any non-trivial information in its first argument, for which we assumed $\mathbf{k}_L \approx 0$. In particular, if we are interested in microscopic response properties at the level of a single unit cell, this approximation is fully adequate, as indeed $|\mathbf{k}_L|\, a_{\text{unit cell}} \ll 1$.

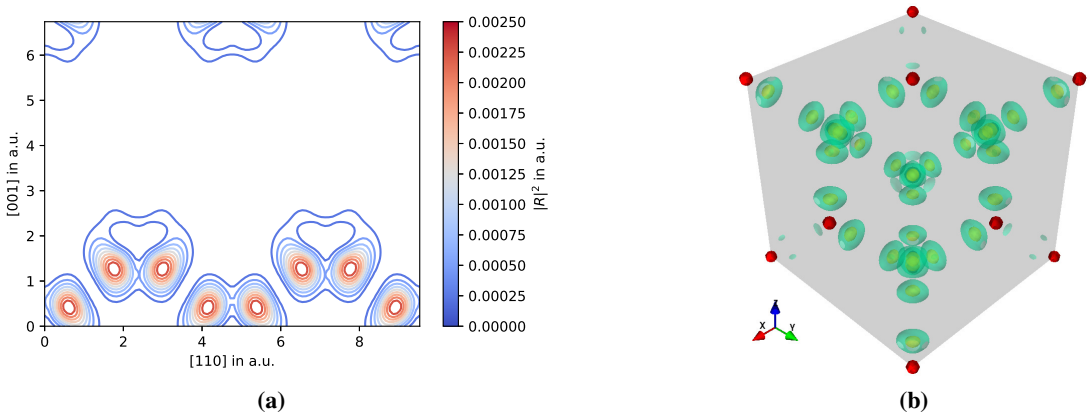

Figure 5.4: (a) The nonlinear response is shown in terms of $|\mathbf{R}_{GS\diamond}(\mathbf{x}, 0.057)|^2$ for diamond in the $(1\bar{1}0)$-plane of its conventional (cubic) unit cell. Data and interpretation correspond identically to Fig. 3.4 (a). (b) Three-dimensional rendering of the same response density; contour levels are set at 0.001 and 0.002 a.u. (green and yellow).

possible without further augmentation. Fortunately, the analogy of linear and nonlinear crystallography in this respect, allows to adopt or adapt[25] the established solutions (see again Ref. [169]).

Beyond this, more elaborate methods of phasing could be envisioned, such as phasing through multiple-beam diffraction [170]. Instead of using multiple Bragg-reflected beams though, the interdependence of the nonlinear signal beam and one Bragg-reflected beam should be monitored. We conjecture that this could work both for a 'typical' 3-beam case, where SFG / DFG proceeds close to a reciprocal lattice point $\mathbf{G}$ and another reflection is excited through $\mathbf{H} \neq \mathbf{G}$, but it could also work for the direct interplay of XOWM close to $\mathbf{G}$ with its accompanying Bragg-beam. In the latter scenario, the two distinct beams involve $\mathbf{H}_{\text{eff.}} = \mathbf{G} \pm \mathbf{k}_L$ and $\mathbf{G}$ itself, which can be excited simultaneously[26] of course (cf. Fig. 5.3 (c) or (d)).

Any detailed investigation of these phasing-options is beyond the scope of this work[27]. It is encouraging—and sufficient for the time-being—to know that viable options exist. In a pragmatic compromise, early prospective data may well be phased using the theoretical phase-information from our numerical results anyways.

2. Resolution Regarding the second challenge, we will give a brief assessment based on our numerical simulations of $\mathbf{K}_{GS\diamond}(0, \mathbf{G}, \omega_{L\_0})$ for diamond. Starting from the high-resolution data underlying Fig. 5.4, we can investigate the magnitude, and thus relevance, of individual nonlinear structure factors. In Fig. 5.5, we plot the absolute values of $\mathbf{K}_{GS\diamond}(0, \mathbf{G}, 0.057)$ against the length of their pertaining reciprocal lattice vector up to a threshold of $|\mathbf{G}| \lesssim 5.36$ a.u.. This limit corresponds to backscattering conditions at 10 keV. In addition to the reciprocal-space scale, we indicate the correspondingly achievable resolution

[25] Note that some adaptation would—for example—be required, if direct phasing algorithms were considered. In addition to the criterion of finite support, these often rely on the positivity of the electronic density. In contrast, $\mathbf{R}_{GS\diamond}(\mathbf{x}, \omega)$ may not be positive, but complex-valued in fact. Thus, a positivity constraint would be rendered meaningless. However, it is possible to re-introduce at least a reality-condition to similar effect. As we have shown in Chpt. 3, the time-dependent electronic density (response), can be expressed through $\mathbf{R}^{\text{ret}}_{GS\diamond}$ in linear response theory. Suitable linear combinations of $\mathbf{R}_{GS\diamond}$ may therefore be phased as real.

[26] As a matter of cautioning, we want to point out that the second option of 3-beam phasing may prove very challenging on the experimental side. In fact, one would rather aim to *avoid* working close to the Bragg condition for $\mathbf{G}$ in order to reduce elastic background scattering.

[27] Regarding more general, phase-sensitive scattering schemes, we want to mention our proposal for *amphodyne* detection of XOWM signals. Capitalizing on the interference of linear and nonlinear diffraction, this method would provide access to the scattering phase. For further discussion of *amphodyne* detection, we refer the reader to Chpt. 6.

in Å at the upper edge of the plot. We recall for completeness that $\omega_{L\_0} = 0.057$ a.u. corresponds to an optical photon energy of 1.55 eV.

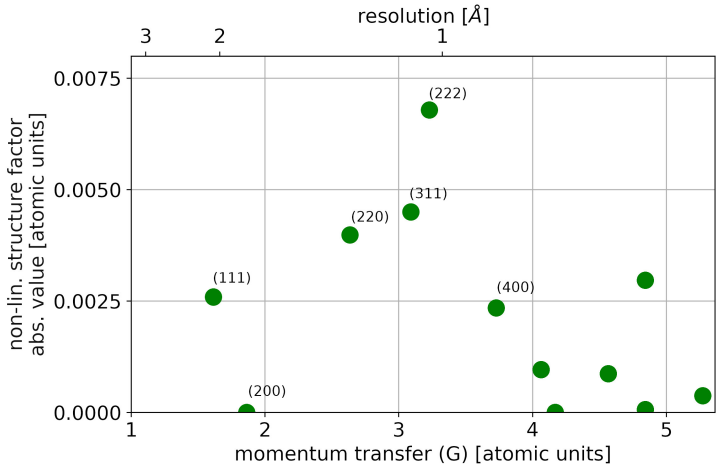

Figure 5.5: Magnitude of the nonlinear structure factors $|\mathbf{K}_{GS\diamond}(0, \mathbf{G}, 0.057)|$ for diamond. The first six components are labelled according to the conventional (cubic) system. The corresponding resolution can be read from the secondary abscissa.

In order to obtain sub-Å resolution, we find that six distinct reciprocal components are required. These are labelled explicitly in the graph above and comprise (111), (200), (220), (311), (222) as well as (400). Notably, one of them, viz. (200), is trivial for symmetry reasons[28]. Based on this list, we can model the outcome of an incomplete reconstruction. Accounting only for the six components (and all of their equivalent orientations), we perform a restricted Fourier-synthesis and thus obtain Figs. 5.6 (a) and (b). Apart from their reduced resolution, these are equivalent to Figs. 5.4 (a) and (b) and may thus be compared directly.

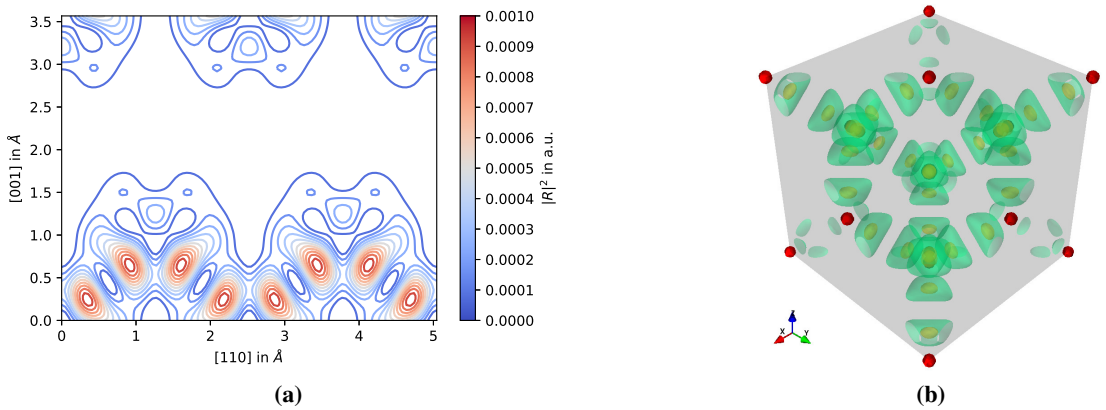

(a) **(b)**

Figure 5.6: At reduced resolution of ~ 0.89 Å, (a) the nonlinear response is shown in terms of $|\mathbf{R}_{GS\diamond}(\mathbf{x}, 0.057)|^2$ for diamond in the $(1\bar{1}0)$-plane of its conventional (cubic) unit cell. (b) Three-dimensional rendering of the same respose density; contour levels are set at 0.0004 and 0.0008 a.u. (green and yellow).

[28] As an interesting (though ancillary) observation, we note that the 'forbidden' (222) component does *not* vanish; it is in fact the strongest contribution according to Fig. 5.5. On closer inspection, this is unsurprising: The (222) reflection is strictly forbidden only for the ideal diamond structure, assuming point-like atoms at each lattice site. Extended electron distributions *in between* the lattice sites, however, result in a non-vanishing (222)-signal. This is precisely the case for diamond's valence electrons. Accordingly, the (222)-reflection could be measured in conventional crystallography—even in powders [171]. For our XOWM-signal, which originates exclusively from valence electrons, the (222)-component naturally proves to be the strongest.

While the resulting reconstructions still lack some definition compared to their high-resolution counterparts, we find the main features of $\mathbf{R}_{GS\diamond}$ to be well reproduced. In particular, we can clearly identify the two maxima of the response density along each C-C bond. Notably, these are not fully pronounced yet—with their numerical values falling a factor of 2.5 short of the reference in Fig. 5.4—but they yield an insightful picture of the valence-electronic response, nonetheless.

We want to dwell further on this notion and emphasize that 'nonlinear crystallography' can provide a valence-sensitive probe at the outlined level of detail. To this end, it requires modest measurement effort (here: six orientations) and is model-independent to a reasonable degree[29]. Increasing the complexity of these measurements, one natural step would see the incorporation of successively higher reciprocal components and thus increase the static resolution. While another path to extend the scope of the method could capitalize further on its spectroscopic selectivity. Instead of probing at a single optical frequency ω_{L0}, several data-points—even full spectra—could be acquired per reciprocal component. In particular, we note the possibility to address individual electronic transitions with spectroscopic precision and subsequently visualize them through crystallographic reconstruction. By opening such a visual window onto electronic phenomena, 'nonlinear crystallography' offers intriguing prospects for the broader study charge-transfer or -correlation effects in various bulk materials.

5.1.3 Simplified setup for 'nonlinear crystallography'

Having established the idea of 'nonlinear crystallography', we shall now proceed to scout for a (more) suitable detection setup. Recalling the approach by Glover et al. (cf. Sec. 5.1.1 and Ref. [46]), we observe that they follow a typical high-resolution x-ray diffraction scheme [172, 173]. Namely, they implement a monochromatized source in conjunction with $\Omega - 2\theta$ rotations for the sample and detector-arm, respectively (see illustration in Fig. 5.7). The detector arm further carries a channel-cut crystal

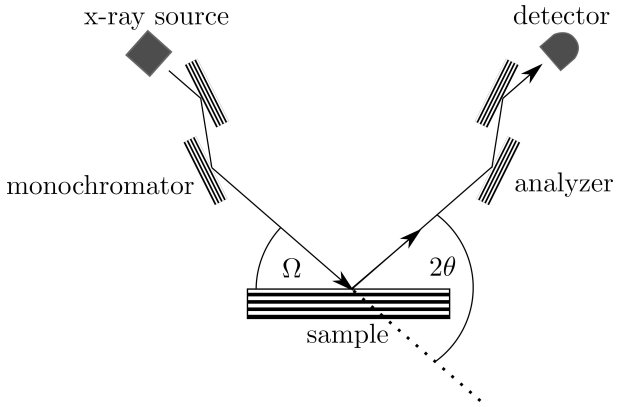

Figure 5.7: Illustration of a typical high-resolution x-ray diffraction setup—comparable to the approach by Glover et al. [46]. A monochromatised x-ray source illuminates the sample, which may be rotated about the angle Ω. The scattered signal is filtered by an analyser crystal before being measured with a detector. Both elements are mounted on an independent detector-arm, which rotates about 2θ. [We gratefully acknowledge Dr. Christina Bömer's help in rendering the above computer graphics.]

[29]Note on the aspect of model-independence that we preclude the obvious fact of requiring a XOWM-theory to link the nonlinear scattering signal to nonlinear structure factors. Once this is achieved—be it within the framework of this thesis or via other theoretical means—however, the inversion problem can be solved on the basis of crystallographic measurements alone. There is no necessity for accompanying electronic structure calculations. This is of particular importance in cases of highly complex materials, for which present simulations may be far from accurate.

analyser, which filters the scattered radiation. Notably, this does not only define an energy window for the detection, but—crucially—it also curtails the angular acceptance of the detection setup significantly. Consequently, this necessitates very precise adjustment of the detector arm for the scattering direction. Any imprecision beyond the angular acceptance of the analyser (typically $\lesssim 1$ mdeg) will result in suppression, i.e., effective loss, of the nonlinear signal. This renders it tedious to adjust the setup for the phase-matching condition of either SFG or DFG, as it effectively requires the combined optimization of three degrees of freedom (viz. sample, detector-arm and laser-direction).

While such adjustment efforts may have been bearable for the proof-of-principle study [46], they seem prohibitively time-consuming for a routine experiment—in particular, if measuring several reflections in short succession is desired. Thus, a setup for 'nonlinear crystallography' requires some fundamental simplification. This could come in the shape of a *bent-crystal analyser*:
Bent-crystal analysers can offer a significantly larger angular acceptance, thereby eliminating the necessity to adjust the detector arm at all. To this end, the curvature of the analyser's surface (i.e., its bending radius r_{bend}) has to match the scattering angle in a particular way. Following the so-called Rowland geometry [174], monochromatic x-rays emanating from a source point (S) can be refocused by the analyser into a detection point (D), if they are both located (symmetrically) on a circle of radius $r_{\text{Rowland}} = r_{\text{bend}}/2$, which is itself tangentially attached to the analyser's surface[30]. An illustration of this geometry is shown in Fig. 5.8 (a). The scattering angle on the crystal's bent lattice is approximately the same for all rays and—in order to obtain a reflection at all—has to equal the Bragg angle for the desired energy.

Analyser configurations of this kind find copious use, for instance in XES or HERFD-XAS applica-

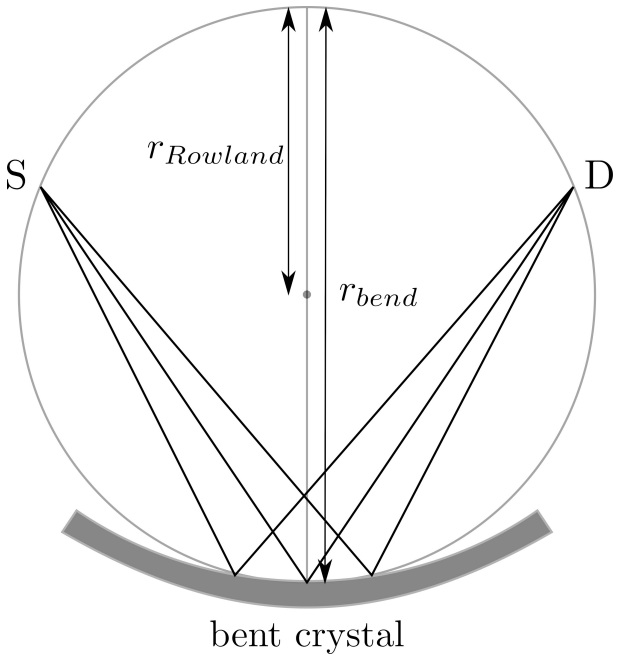

Figure 5.8: Illustration of a bent analyser crystal used in Rowland geometry: A point source (S) on the Rowland-circle is refocused into a detection point (D) via reflection at the bent crystal. [We gratefully acknowledge Dr. Christina Bömer's help in rendering the above computer graphics.]

[30]Note that the refocusing capability could only *strictly* be shown, if the reflection proceeded both specularly with respect to the lattice planes of the bent crystal *and* at the actual surface of the Rowland circle. The proof may then be carried out via the inscribed angle theorem. In reality, this condition is only met in a single point, namely, where the two circles touch tangentially (cf. Fig. 5.8). Nevertheless, the re-focusing still works quite well, but incurs the so-called Johann error from regions off the center.

tions [175, 176], for RIXS [177, 178] and also for non-resonant x-ray Raman scattering or IXS [179–181]. Of most immediate relevance at this point, however, is the fact that we have previously employed bent-crystal analysers for the detection of XPDC signals with good success (see Sec. 5.2.3.a for details). Encouraged by those results, it appears natural to try their performance in the laser-driven case as well.

For the beamtime no. 20212165 at SwissFEL [182], we thus evaluate the potential of a detection setup based on a spherically-bent Si(660) analyser[31]. A sketch of the overall experimental arrangement is given in Fig. 5.9, which comes at the courtesy of Dr. Christina Bömer.

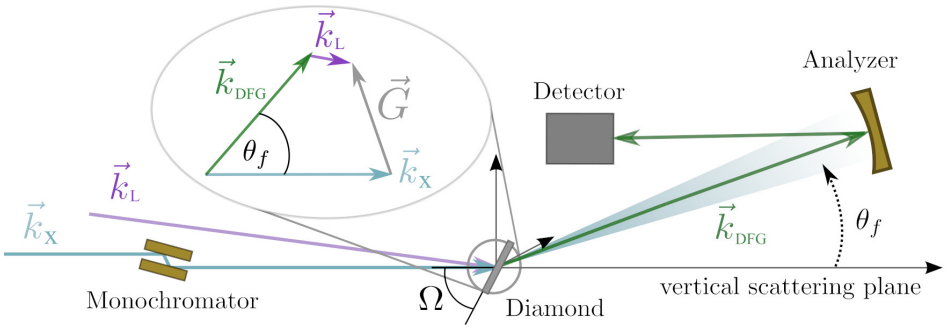

Figure 5.9: Illustration of a bent-analyser-based setup for efficient DFG detection: A monochromatised x-ray beam ($\mathbf{k}_X$) is mixed inside a diamond sample with an optical laser beam ($\mathbf{k}_L$). If adjusted for the phase-matching condition (see inset), a DFG signal ($\mathbf{k}_{DFG}$) is produced and can be captured by the bent-analyser. Note: In the actual experiment, the analyser will deflect horizontally. [Image courtesy of Dr. Christina Bömer]

It shows a diamond sample in transmission configuration (close to a Laue-diffraction condition), which is illuminated both by an optical laser ($\mathbf{k}_L$) and a monochromatised x-ray pulse ($\mathbf{k}_X$). If the phase-matching condition for DFG—which is recounted in the figure's inset—is satisfied, a respective signal beam ($\mathbf{k}_{DFG}$) is emitted from the sample. Ultimately, the signal reaches the bent-analyser and is reflected towards the detector, while concurrent (elastic) background is being suppressed. It should be noted that—for the sake of two-dimensional depiction—we show the analyser's deflection (i.e., dispersive direction) to be vertical. However, in the actual setup, we pursue horizontal deflection—thus avoiding to conflate the signal's scattering angle with the analyser's energy resolution.

Before we address the implications of this setup for our theoretical modelling of XOWM-yields, we want to conclude our discussion of bent analysers with two illustrating ray-tracing simulations[32], compiled into Fig. 5.10. In order to demonstrate the broad angular acceptance, which we have advertised above, we employ a simplified setup (see Fig. 5.10 (a)). This comprises a confined source-point ($\sim 50\ \mu$m) at 1 m distance to the Si (660) analyser, which is spherically bent at 1 m radius. First, we study the reflection of a well collimated beam (divergence 2 μrad). This scenario is close to ideal for the analyser's performance, even though it does not correspond completely to the SFG signal of Sec. 5.1.1 in terms of the beam's footprint. In Fig. 5.10 (b), we show this tiny beam propagated up to the analyser, where it covers a miniscule spot on the 10 cm large crystal. Note that we assume this signal to be spectrally homogeneous around 9.7 keV—as indicated in the colour-coded spectrogram on the figure's right side. After Bragg reflection ($\theta_B = 86.896°$), the beam emerges spectrally filtered and propagates back to the source plane, where we plot its 'detectable' cross section in Fig. 5.10 (c). From the simulated spectrogram, we can conclude that the transmitted bandwidth comprises ~ 42.9 meV (FWHM) for this

[31] Note that the particular choice of reflection, i.e., Si(660), for the analyzer setup was motivated primarily by the good performance of similar crystals at the ESRF (again, cf. Sec. 5.2.3.a). There may be several other reasonable choices, but we take the liberty to focus solely on the one at hand.

[32] All simulations and visualizations in Fig. 5.10 were performed using the XRT-package [133].

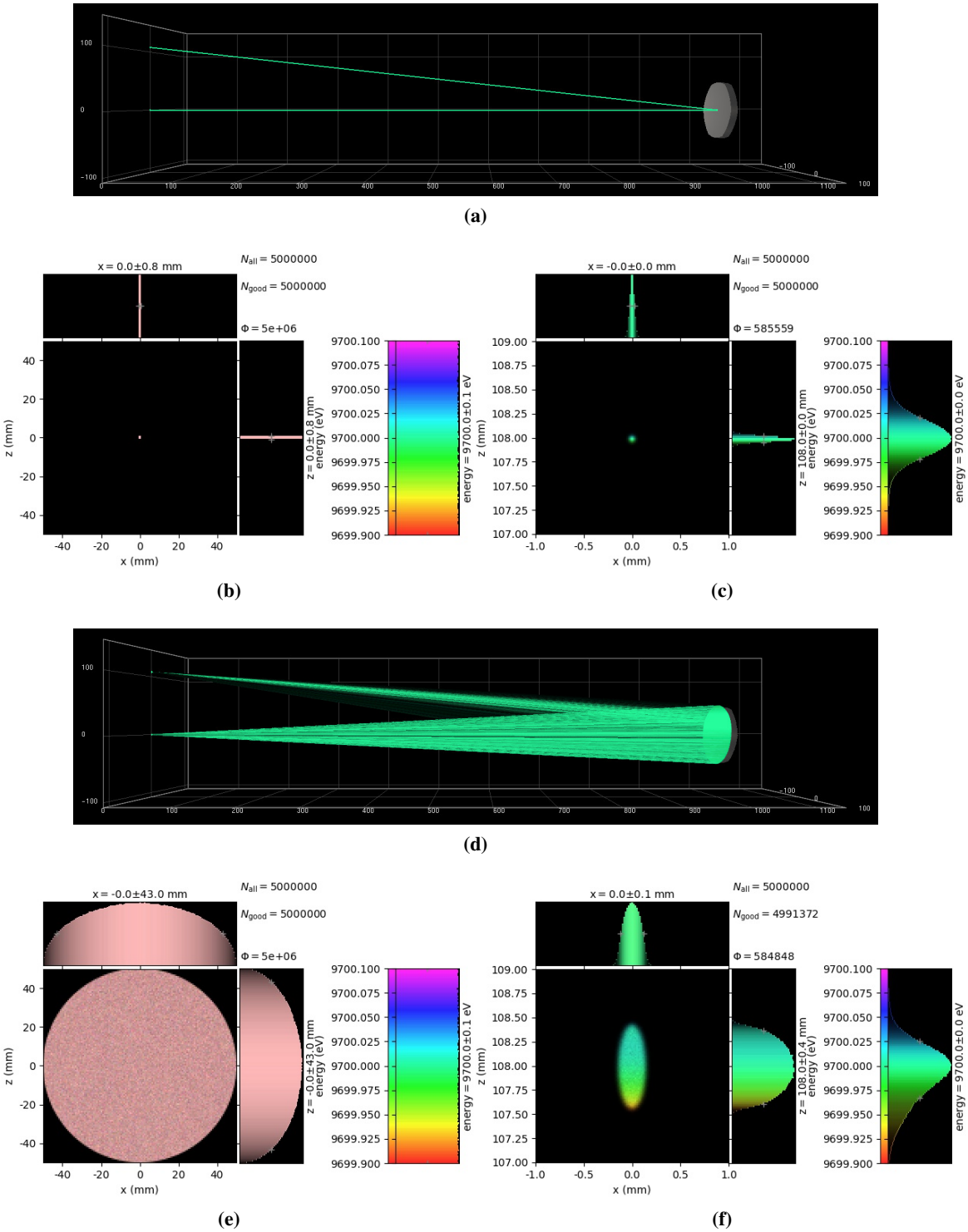

Figure 5.10: Ray-tracing simulations of the transmission across a Si (660) backscattering analyser. First, we consider a well collimated signal beam of $\sim 2\ \mu$rad divergence emanating from a confined source-point of $\sim 50\ \mu$m diameter. (a) shows this setup with all measures are given in mm. (b) gives the cross section of the beam, which illuminates the analyser with a uniform range of incident photon energies—centred at 9.7 keV (cf. coloured spectrogram); (c) shows the reflected beam measured back at the source plane. The beam is filtered in energy with a remaining bandwidth of ~ 42.9 meV (FWHM)—still centred at 9.7 keV. Starting from (d), we repeat the simulation with a highly divergent beam (100 mrad), plotting the same positions in (e) and (f) as previously in (b) and (c). The simulations and visualizations were carried out using the XRT-package [133].

scenario.

At the opposite extreme, in terms of beam divergence, we also consider a source that illuminates the complete analyser crystal of 10 cm diameter (i.e., sporting a divergence of 100 mrad). This setup is illustrated in Fig. 5.10 (d). Once again, we depict the beam on the analyzer—confirming its full coverage—in Fig. 5.10 (e), followed by the back-reflected beam's cross section in the source plane (f). The effect of spectral filtering is likewise apparent in this case—though the large angular deviations lead to a slight broadening ($\sim$ 59.6 meV (FWHM)) as well as a dispersion of the beam's footprint. Both effects are a consequence of the intrinsic Johann error and can be considered as minor; more so, as crystal imperfections and bending-strain tend to have a significantly larger impact on the analyser's resolution [183, 184].

Slight idealizations notwithstanding, our simulations confirm the initial proposition that bent-crystal analysers offer an exceedingly large angular acceptance ($\sim$ 100 mrad) compared to conventional channel-cut analysers ($\sim$ 17 μrad in case of Ref. [46]). Thus, we can positively conclude that they would prove beneficial in simplifying the detection of SFG / DFG. In particular, we recapitulate that it would indeed suffice to direct the SFG / DFG signal anywhere onto the analyser crystal in order to filter it for detection. No precise adjustment of the detector arm with the analyser on it is required.

5.1.3.a Application of bent-crystal analyzer for DFG-detection at SwissFEL

As a concrete application of our above proposal, we shall discuss the detection of DFG under the conditions of our recent SwissFEL campaign (proposal No. 20212165).

We recall with reference to Fig. 5.9 that, during this experiment, the x-ray FEL beam is monochromatised around 9.7 keV, before it is mixed inside a diamond sample with an optical laser at 1.55 eV photon energy. The resulting DFG signal at 9700 eV $-$ 1.55 eV is spectrally discriminated using a spherically-bent Si(660) analyzer and subsequently detected using a Jungfrau detector module [185, 186].

As outlined earlier, the spectral width of this analyser measures only $\sim$ 0.066 eV (FWHM) in contrast to the much broader Si(220)-reflection used by Glover et al. [46], which was reported to cover $\sim$ 0.3 eV. In order to match the incident bandwidth better to our narrow detection window, we have exchanged the beamlines standard Si(111) monochromator for a Si(311)-based setup. This resulted in pulses of $\sim$ 0.4 eV bandwidth (FWHM) with 15 μJ pulse energy on average (i.e., $\sim 10^{10}$ incident photons per shot). Notably, this input distribution will produce DFG photons across a bandwidth, which is still too broad to be fully detected by our analyser.

As a consequence, the detectable DFG yield should not blindly be extracted from *fully integrated* expressions like (5.52). Instead, one should pay closer attention to the effect of the analyser's transmission function $T_a(\omega_f) = e^{-(\omega_f-\omega_a)^2/2\Omega_a^2}$—before evaluating Eq. (5.50). Alternatively, one could refine this model at an even earlier stage. Starting from the original double-differential scattering yield Eq. (5.44), one could use the predicted scattering distribution as initial conditions for a full ray-tracing simulation through the detection setup (cf. our simulations leading to Fig. (5.10).

For simplicity, however, we shall do none of the above, but extract the detection setup's transmission function *directly* from the experiment. To do so, we consider the transmission of a Bragg reflection[33]—just like we did in Glover's case (see Sec. 5.1.1)—and obtain a combined[34] detection efficiency η_{det},

[33] Note that the Bragg reflection presents a suitable probe for the transmission of the DFG signal, as both types of scattering signals share (almost) the same divergence and bandwidth in this case.

[34] Note that—in addition to the bare analyser transmission—this detection efficiency will also account for effects, such as air absorption, self-absorption inside the sample, misalignments or the detector's (quantum) efficiency.

specifically for the case at hand. This detection efficiency can subsequently be multiplied onto the simple, integrated DFG yield (found from Eqs. like (5.52), (5.53) or (5.62)), which we had initially discarded as an option, and reduce it to the appropriate magnitude indeed. More specifically, we shall resort to the formulation of Eq. (5.62), because we have accurate knowledge of the pulse energy *after* the monochromator available:

$$Y \approx \left(\frac{d\sigma(2\theta_B)}{d\Omega}\right)_{\text{Th}} \frac{4\pi^2\sqrt{2}\, l_w\, E_{X\_p}^{\text{mono}}\, 8\, I_L\, T_L}{\alpha^2 \cos(2\theta_B)\sin^2(\theta_B)\,\Omega_m\,\omega_f\,\omega_{X\_0}^2\,\omega_{L\_0}^2\,T_{tot}} \frac{1}{V_\diamond^2}\,|\boldsymbol{\varepsilon}_L \cdot \mathbf{K}_{GS\diamond}(0,\mathbf{G},\omega_{L\_0})|^2 . \tag{5.65}$$

For our numerical example, we focus on the (111) orientation of the diamond sample. Hereunto, the fundamental Bragg angle is given by $\theta_B^{(111)} = 18.080°$, while the nonlinear response—including the polarization factor—amounts to $1/V_\diamond^2\ |\boldsymbol{\varepsilon}_L \cdot \mathbf{K}_{GS\diamond}(...)|^2 \approx 2.07 \cdot 10^{-6}$. Below, we compile further relevant beam parameters as measured or estimated for this experiment:

	experimental value	parameter in a.u.
photon energy	9.7 keV	$\omega_{0X} = 356.5$
initial bandwidth	$\sim$ 20 eV (FWHM)	$\Omega_X = 0.312$
average pulse energy	850 μJ	$E_{X\_p} = 1.95 \cdot 10^{14}$
monochromator passwidth	$\sim$ 0.4 eV (FWHM)	$\Omega_m = 6.24 \cdot 10^{-3}$
monochromatised pulse energy	15 μJ $\sim 10^{10}$ photons	$E_{X\_p} = 3.44 \cdot 10^{12}$
pulse duration	60 fs (FWHM)	$T_X = 1053$
beam divergence	$\sim$ 3.5 μrad (FWHM)	$\delta_X = 3.14 \cdot 10^5$
beam diameter	$\sim$ 450 μm (FWHM)	$\sigma_X = 3.61 \cdot 10^6$

Table 5.5: X-ray pulse parameters for SwissFEL beamtime no. 20212165

The optical pulse is respectively characterized by:

	experimental value	parameter in a.u.
photon energy	1.55 eV	$\omega_{0L} = 5.7 \cdot 10^{-2}$
full bandwidth	52 meV (FWHM)	$\tilde{\Omega}_L = 8.12 \cdot 10^{-4}$
pulse duration (stretched)	250 fs (FWHM)	$T_L = 4389$
laser intensity	$5.2 \cdot 10^{10}$ W cm^{-2}	$I_L = 8.06 \cdot 10^{-6}$

Table 5.6: Optical pulse parameters for SwissFEL beamtime no. 20212165

Using these values, we compute a potentially achievable yield of $\sim$ 29000 DFG photons/shot. In order to convert this number into detectable counts, we shall evaluate actual detection efficiency next.

Preliminary experimental results[35] As outlined before, we can infer the transmission (or detection) efficiency of the experimental setup by benchmarking on a Bragg reflection. More specifically, we shall focus on the (111)-reflection, which is both broad in its acceptances and reaches almost unit reflectivity intrinsically. Therefore, if we find significant loss of signal on this reflection, this can almost entirely be attributed to the detection setup itself.

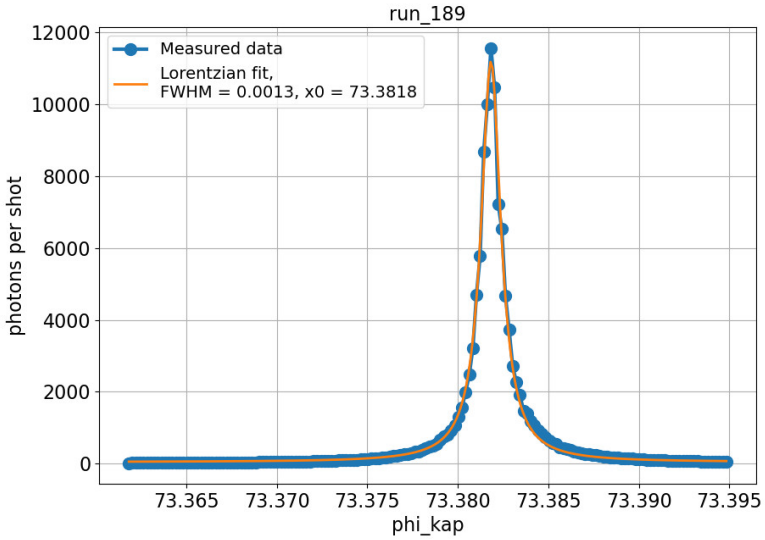

Figure 5.11: Rocking curve scan across the (111)-Bragg condition of our diamond sample at SwissFEL. Measured data is shown as blue dots on a line, while an additional, Lorentzian fit to the data is shown as an orange line. Sample angle as well as fit-parameters are given in angular degrees.

Reviewing a rocking curve scan[36] across the Bragg reflection (111) in Fig. 5.11, we find its maximum to amount to $\sim 1.15 \cdot 10^4$ cts/shot. This scan was conducted under the conditions outlined in Tab. 5.5—except for the fact the overall pulse energy was purposefully attenuated[37] by a factor of ~ 1000. Thus, the detection efficiency can be estimated as:

$$\begin{aligned} \eta_{\text{det}} &= \frac{\#\text{ detected photons}}{\#\text{ Bragg reflected photons}} \approx \frac{\#\text{ detected photons}}{1 \times \#\text{ incident photons}} \\ &= \frac{1.15 \cdot 10^4}{1 \times 10^{10} \times 10^{-3}} = 1.15 \cdot 10^{-3}. \end{aligned} \tag{5.66}$$

Combining this result with our previous prediction of the DFG yield, we would expect the *detectable*

[35] Note that there are two important points that should be borne in mind regarding this experimental section:

1. The presented results are *preliminary* in nature. This implies that data processing has not advanced far beyond the initial conversion of detector images (incl. I_0-correction) nor has any in-depth analysis of the experiment taken place at the time of this writing. As such, our findings and conclusions may be subject to changes upon later review.
2. Performing the measurements that led to the presented results has been a large, collaborative effort—far exceeding the scope of this theoretical work. Besides the invaluable collaboration with Dr. Christina Bömer in planning, organizing and conducting the experiment, further support on-site was kindly given by (in alphabetical order): Dr. Andrei Benediktovitch, Fridtjof Kerker, Daniele Ronchetti, Dr. Maria Weseloh and Lennart Wollenweber as well as the staff members of the Bernina beamline. In addition, we gratefully acknowledge countless contributions, discussions and support off-site.

[36] Note regarding terminology that, here and later on, we imply the rotation of the sample when we speak of rocking curve scans. In particular, this concerns a rotation about the axis which is itself normal to the scattering plane. The angle corresponding to this rotation is termed Ω in Fig. 5.9.

[37] Note that this attenuation is necessary in order to avoid overexposure of the detector.

fraction of the wavemixing signal to be

$$Y_{\mathrm{DFG}}^{\mathrm{detectable}} = Y_{\mathrm{DFG}} \times \eta_{\mathrm{det}} = 29 \cdot 10^{3}\ \mathrm{cts/shot} \times 1.15 \cdot 10^{-3} \approx 33\ \mathrm{cts/shot}. \tag{5.67}$$

This value may now be compared directly to our next experimental observation. In Fig. 5.12, we present another rocking curve scan—this time discriminating for the DFG signal at $\sim 9700\ \mathrm{eV} - 1.55\ \mathrm{eV}$—around the predicted phasematching condition.

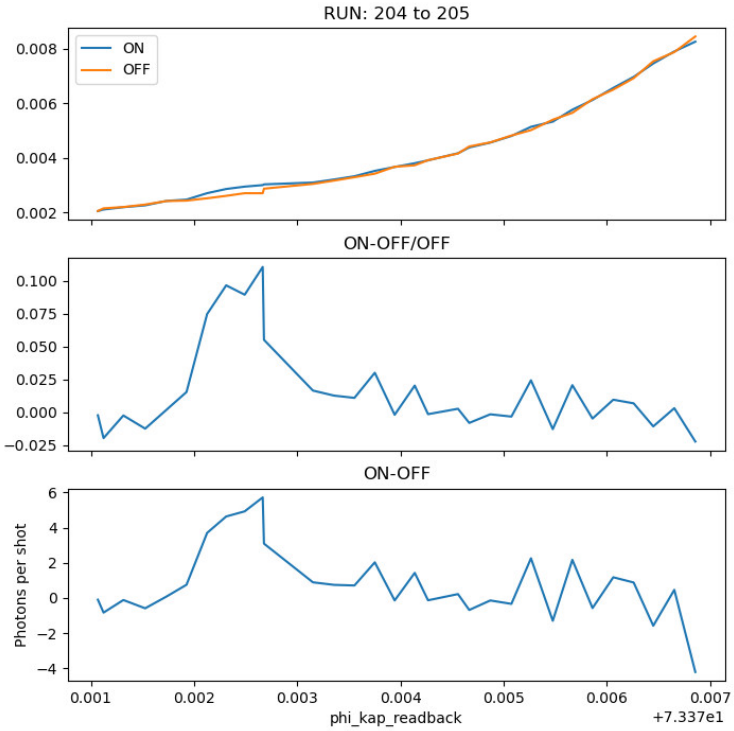

Figure 5.12: Rocking curve scan across the phasematching condition for DFG close to the (111)-Bragg condition in diamond. First pane shows (normalized) data with and without laser admixture as blue and orange lines, respectively. The DFG signal is visible as a difference of the curves around $\sim 73.3724°$. Second pane explicitly shows the difference of laser-on and laser-off signal from uppermost pane, further normalized to the background level. This difference signal is rescaled to absolute photon counts per shot in the lowest pane. Abscissa is scaled in degrees.

Here, the first pane shows the detected scattering signal in the presence of the optical laser field for wavemixing ("ON" in blue) or its absence ("OFF" in orange). Both are normalized with respect to the incident flux and thus rendered comparable. The overall trend, i.e., the increasing slope from left to right, is indicative of the nearby Bragg-remainder (elastic line at 73.3818°). The essential DFG feature, however, is the found in the difference of both curves around $\phi_{\mathrm{kap\_readback}} \approx 73.3724°$. Rendering this feature more apparent, the normalized difference of the two curves (i.e., $\frac{\text{"ON"}-\text{"OFF"}}{\text{"OFF"}}$) is plotted in the second pane of Fig. 5.12. Finally, a rescaled version of the second fills the third pane. This last one is adjusted to show the absolute difference in detected photon counts per shot, thus directly measuring the DFG yield. Its maximum amounts to ~ 6 photons/shot, which ends up being a factor of 5.5 lower than the value expected from Eq. (5.67). This presents a reasonably good agreement of theory and experiment—especially when taking the very coarse nature of our preliminary analysis into account.

In closing, we want to report that our team was able to measure a total of five different crystal orientations during the course of the SwissFEL campaign (proposal No. 20212165). These comprise the orientations (111), (220), (311), (222) and (400). By means of the pertaining data, a crystallographic reconstruction of the nonlinear response function—as envisioned in Sec. 5.1.2.d—is within reach. Notably, the use of a spherically-bent analyser has indeed provided sufficient simplification of the experimental procedure to render all of these measurements possible in short succession. This notwithstanding, further investigation of the analyser's transmission properties will be necessary to optimize the detection efficiency (far) beyond the current value of $\eta_{\mathrm{det}} = 1.15 \cdot 10^{-3}$.

5.2 X-ray parametric down-conversion

In this section, we will investigate a third class of XOWM processes, namely x-ray parametric down-conversion (XPDC). While it is closely related to the previously discussed SFG / DFG processes, it does *not* involve any external optical fields, such as the driving laser in Sec. 5.1. Instead during XPDC, an incident x-ray photon splits *spontaneously* into a pair of scattered photons through nonlinear interaction with a medium. The analogous process in the all-optical regime is therefore often termed spontaneous parametric down-conversion (SPDC) [145]. In this section, we shall adhere to the convention of calling the incident photon 'pump' (ω_p) and denoting the scattered pair by 'signal'- and 'idler'-photon (ω_s and ω_i), respectively.

As a parametric scattering process, XPDC obeys energy conservation within the photonic subsystem, i.e., $\omega_p = \omega_s + \omega_i$. This obviously coincides with the energetic constraint for DFG (cf. Sec. 5.1.2). Instead of mixing x-rays with optical photons from a laser, though, XPDC relies solely on idler-photons, which originate from the intrinsic fluctuations of the electromagnetic 'vacuum' field[38].

In this section, we adapt our general XOWM expression (2.67) to the case of XPDC and discuss its application to two different scenarios, namely: XPDC with idler-photon energies below (Sec. 5.2.1) and far above (Sec. 5.2.3) the band gap of the sample. As both scenarios share some common derivations, we shall perform those up front. For reference, note that an abbreviated version of these derivations may be found in Ref. [51].

Adaptation of Eq. (2.67) **to the general case of XPDC** We begin our derivations for XPDC by recalling the aforementioned XOWM expression from Chpt. 2:

$$\begin{aligned}\langle \hat{O} \rangle_{\mathrm{XOWM}} = \frac{2\pi\alpha^4}{V\omega_s}\,\frac{1}{(2\pi)^{14}} \int d^3k_i\, d^3k_i'\, d^3k_p\, d^3k_p' \int^{\times 4} d\omega_i\, d\omega_i'\, d\omega_p\, d\omega_p'\; \delta(\omega_s - \omega_p - \omega_i)\,\delta(\omega_s - \omega_p' - \omega_i') \\ \times (\boldsymbol{\varepsilon}_s)_\sigma\, (\boldsymbol{\varepsilon}_s^*)_\rho\; Z^{\mathrm{X\_IN}}_{\sigma\rho}(\mathbf{k}_p', \omega_p', \mathbf{k}_p, \omega_p)\; \Big(\bar{Z}^{\mathrm{OPT}}_{\nu\mu}(\mathbf{k}_i', \omega_i', \mathbf{k}_i, \omega_i) + \bar{C}^{\mathrm{OPT}}_{\nu\mu}(\mathbf{k}_i', \omega_i', \mathbf{k}_i, \omega_i) \Big) \\ \times \sum_I p_I \Big(\mathbf{K}_I(-\mathbf{k}_i, \mathbf{k}_s - \mathbf{k}_p, \omega_i) \Big)_\mu \Big(\mathbf{K}_I(-\mathbf{k}_i', \mathbf{k}_s - \mathbf{k}_p', \omega_i') \Big)^*_\nu . \end{aligned} \tag{5.68}$$

Notably, we have adapted the designation of all involved photons to comply with our new nomenclature. The identification with the original Eq. (2.67) is as follows: $\omega_X \to \omega_p$, $\omega_f \to \omega_s$ and the 'optical' $\omega_L \to \omega_i$ (analogous for the primed variables). In contrast to the laser-driven cases (SFG / DFG), we will drop the contribution due to external optical fields $\bar{Z}^{\mathrm{OPT}}_{\nu\mu}$. Instead, we keep the correlation function $\bar{C}^{\mathrm{OPT}}_{\nu\mu}$, which accounts for spontaneous fluctuations of the electromagnetic field. Drawing on our results from Sec. 4.4, we can identify these fluctuations on the basis of Eq. (4.85):

$$\begin{aligned}\bar{C}^{\mathrm{OPT}}_{\nu\mu}(\mathbf{k}_i', \omega_i', \mathbf{k}_i, \omega_i) = (2\pi)^5\, \delta^3(\mathbf{k}_i - \mathbf{k}_i')\, \delta(\omega_i - \omega_i')\, (1 - e^{\beta\omega_i}) \\ \Big(\delta_{\mu\nu} - \frac{(\mathbf{k}_i)_\mu (\mathbf{k}_i)_\nu}{|\mathbf{k}_i|^2} \Big)\, \mathrm{Im}\Big(\frac{-4}{\omega_i^2\, \alpha^2\, \tilde{\varepsilon}(|\omega_i|) - |\mathbf{k}_i|^2} \Big). \end{aligned} \tag{5.69}$$

[38] Note that our expression " 'vacuum' field" is slightly ambiguous. We imply that these fluctuations occur in a state of the photon field, which is otherwise devoid of excitations (vulgo: empty). Globally speaking, however, these fluctuations do not strictly occur in vacuo but are instead contained (and possibly shaped) by the material system, which mediates the down-conversion process.

Upon substitution into Eq. (5.68), we can simplify

$$\begin{aligned}\langle\hat{O}\rangle_{\text{XPDC}} = \frac{\alpha^4}{V\omega_s}\frac{1}{(2\pi)^8}\int^{\times 3} d^3k_i d^3k_p d^3k'_p \int^{\times 2} d\omega_i d\omega_p\; \delta(\omega_s-\omega_p-\omega_i)\,(\boldsymbol{\varepsilon}_s)_\sigma\,(\boldsymbol{\varepsilon}^*_s)_\rho\; Z^{\text{X\_IN}}_{\sigma\rho}(\mathbf{k}'_p,\omega_p,\mathbf{k}_p,\omega_p)\\ \times(1-e^{\beta\omega_i})\left(\delta_{\mu\nu}-\frac{(\mathbf{k}_i)_\mu(\mathbf{k}_i)_\nu}{|\mathbf{k}_i|^2}\right)\text{Im}\Big(\frac{-4}{\omega_i^2\,\alpha^2\,\tilde{\varepsilon}(|\omega_i|)-|\mathbf{k}_i|^2}\Big)\\ \times\sum_I p_I\left(\mathbf{K}_I(-\mathbf{k}_i,\mathbf{k}_s-\mathbf{k}_p,\omega_i)\right)_\mu\left(\mathbf{K}_I(-\mathbf{k}_i,\mathbf{k}_s-\mathbf{k}'_p,\omega_i)\right)^*_\nu.\end{aligned} \tag{5.70}$$

For our next step, we invoke the 'dipole approximation' for $\mathbf{K}_I$ as of Eq. (3.24)

$$\mathbf{K}_I(-\mathbf{k}_i,\mathbf{k}_s-\mathbf{k}_p,\omega_i)\approx\tilde{w}(\mathbf{k}_s-\mathbf{k}_p-\mathbf{k}_i-\mathbf{G})\frac{1}{V_\diamond}\mathbf{K}_{GS\diamond}(0,\mathbf{G},\omega_i), \tag{5.71}$$

which we have already made ubiquitous use of in Sec. 5.1. We re-iterate for completeness that $\tilde{w}(\mathbf{k})$ stems from the window-function that marks the extent of the crystalline sample. Furthermore, the subscript GS indicates that we restrict our analysis to the ground state contribution to the nonlinear response[39]. Thus, our XPDC observable is modified to read:

$$\begin{aligned}\langle\hat{O}\rangle_{\text{XPDC}} \approx \frac{\alpha^4}{V\omega_s}\frac{1}{(2\pi)^8}\int^{\times 3} d^3k_i d^3k_p d^3k'_p \int^{\times 2} d\omega_i d\omega_p\; \delta(\omega_s-\omega_p-\omega_i)\,(\boldsymbol{\varepsilon}_s)_\sigma\,(\boldsymbol{\varepsilon}^*_s)_\rho\; Z^{\text{X\_IN}}_{\sigma\rho}(\mathbf{k}'_p,\omega_p,\mathbf{k}_p,\omega_p)\\ \times(1-e^{\beta\omega_i})\left(\delta_{\mu\nu}-\frac{(\mathbf{k}_i)_\mu(\mathbf{k}_i)_\nu}{|\mathbf{k}_i|^2}\right)\text{Im}\Big(\frac{-4}{\omega_i^2\,\alpha^2\,\tilde{\varepsilon}(|\omega_i|)-|\mathbf{k}_i|^2}\Big)\\ \times\tilde{w}(\mathbf{k}_s-\mathbf{k}_p-\mathbf{k}_i-\mathbf{G})\frac{1}{V_\diamond}\left(\mathbf{K}_{GS\diamond}(0,\mathbf{G},\omega_i)\right)_\mu\left(\tilde{w}(\mathbf{k}_s-\mathbf{k}'_p-\mathbf{k}_i-\mathbf{G})\right)^*\frac{1}{V_\diamond}\left(\mathbf{K}_{GS\diamond}(0,\mathbf{G},\omega_i)\right)^*_\nu.\end{aligned} \tag{5.72}$$

From the above expression, we isolate the double convolution

$$J_{\sigma\rho}(\mathbf{k},\omega)=\int^{\times 2} d^3k_p d^3k'_p\, Z^{\text{X\_IN}}_{\sigma\rho}(\mathbf{k}'_p,\omega,\mathbf{k}_p,\omega)\;\tilde{w}(\mathbf{k}-\mathbf{k}_p)\left(\tilde{w}(\mathbf{k}-\mathbf{k}'_p)\right)^*, \tag{5.73}$$

which we can interpret as a generalized spectral flux. In particular, if we assume $Z^{\text{X\_IN}}_{\sigma\rho}$ to describe an x-ray pulse, then the above expression (5.73) is proportional to the pulse's total number of photons, specifying their distribution across its spectrum ($d\omega$) and wave-vector spread (d^3k). More accurately, we can define the effective[40], differential flux

$$\Phi_{\sigma\rho}(\mathbf{k},\omega)=\frac{1}{(2\pi)^{11}}\frac{\alpha\omega}{2\,l_w}\int^{\times 2} d^3k_p d^3k'_p\, Z^{\text{X\_IN}}_{\sigma\rho}(\mathbf{k}'_p,\omega,\mathbf{k}_p,\omega)\;\tilde{w}(\mathbf{k}-\mathbf{k}_p)\left(\tilde{w}(\mathbf{k}-\mathbf{k}'_p)\right)^*, \tag{5.74}$$

the diagonal of which is indeed normalized to the number of photons N_{ph} contained in the pulse[41].

[39] Phrased differently: We assume that only the ground state (GS) response function, will have a reasonably large contribution probability $p_{I=GS}\approx 1$, while all other possible initial states I will not feature significant population to begin with $p_{I\neq GS}\approx 0$.

[40] Note that the quantity $\Phi_{\sigma\rho}$ constitutes an effective flux in the sense that it does not merely describe the incident field, but also incorporates aspects of the sample geometry through $\tilde{w}(\mathbf{k})$. More specifically, it thus incorporates the phase-matching constraint. If it is evaluated sensibly, $\Phi_{\sigma\rho}$ therefore quantifies those photons, which are indeed able to partake in the XPDC process *effectively*. It remains to be seen, whether this formulation proves to be useful in the long run. For the time-being it works with all subsequent examples.

[41] We remark that one way to see the normalization of $\Phi_{\mu\mu}$ consists in transforming back into real space—analogous to Eq. (A.172). Upon integrating said expression over both $d\omega$ and d^3k, we should further assume the x-ray pulse to be reasonably narrow in bandwidth, to propagate in a beam-like fashion and to feature a cross section that is smaller than the transverse sample size (encoded in $w(\mathbf{x})$). Further helpful relations to express the integral can be found in Appendices A.8 and A.10.

Using this, we can rewrite Eq. (5.72) in a significantly more concise form:

$$\langle \hat{O} \rangle_{\mathrm{XPDC}} = \frac{2\,\alpha^3\,l_w\,(2\pi)^3}{V\,\omega_s} \int d^3k_i \int d\omega_i\; (\boldsymbol{\varepsilon}_s)_\sigma\,(\boldsymbol{\varepsilon}_s^*)_\rho\; \frac{1}{\omega_s-\omega_i}\,\Phi_{\sigma\rho}(\mathbf{k}_s-\mathbf{k}_i-\mathbf{G},\omega_s-\omega_i)\;(1-e^{\beta\omega_i}) \\ \times \mathrm{Im}\Big(\frac{-4}{\omega_i^2\,\alpha^2\,\tilde{\varepsilon}(|\omega_i|)-|\mathbf{k}_i|^2}\Big)\;\frac{1}{V_\diamond^2}\Big(\;|\mathbf{K}_{GS\diamond}(0,\mathbf{G},\omega_i)|^2\;-|\mathbf{k}_i\cdot\mathbf{K}_{GS\diamond}(0,\mathbf{G},\omega_i)|^2/\,|\mathbf{k}_i|^2\Big). \quad (5.75)$$

Here, we have not only implemented the new flux, but also evaluated the δ-function to fix $\omega_p=\omega_s-\omega_i$. Furthermore, we have contracted the summation in μ, which coupled the transversality constraint to the nonlinear response function.

Finally, we can convert our observable into a double differential scattering probability using the prescription (2.9). Thereunto, we multiply by $\frac{V\alpha^3}{(2\pi)^3}\,\omega_s^2$ and find:

$$\frac{dP_{\mathrm{XPDC}}(\mathbf{k}_s)}{d\Omega_s d\omega_s} = 2\,\alpha^6\,l_w\,\omega_s \int d^3k_i \int d\omega_i\; (\boldsymbol{\varepsilon}_s)_\sigma\,(\boldsymbol{\varepsilon}_s^*)_\rho\; \frac{1}{\omega_s-\omega_i}\,\Phi_{\sigma\rho}(\mathbf{k}_s-\mathbf{k}_i-\mathbf{G},\omega_s-\omega_i)\;(1-e^{\beta\omega_i}) \\ \times \mathrm{Im}\Big(\frac{-4}{\omega_i^2\,\alpha^2\,\tilde{\varepsilon}(|\omega_i|)-|\mathbf{k}_i|^2}\Big)\;\frac{1}{V_\diamond^2}\Big(\;|\mathbf{K}_{GS\diamond}(0,\mathbf{G},\omega_i)|^2\;-|\mathbf{k}_i\cdot\mathbf{K}_{GS\diamond}(0,\mathbf{G},\omega_i)|^2/\,|\mathbf{k}_i|^2\Big). \quad (5.76)$$

Apart from the remaining Boltzmann-factor, this result is equivalent to Eq. (7) of Ref. [51]—note the sign of ω_i though. By means of Eq. (5.76), we will be able to examine different scenarios of XPDC in the following sections.

A note on $\Phi_{\sigma\rho}$ Before we proceed further on XPDC, we shall briefly introduce a model for the differential flux $\Phi_{\sigma\rho}$. This model will be common to all subsequent case-studies—just as Eq. (5.76) itself—and thus warrants an early mention.

Building on our previous steps, the most obvious choice for $\Phi_{\sigma\rho}$ derives from the Gaussian-Schell model beams of Chpt. 4, once again. Assuming in the simplest scenario that the sample is weakly absorbing and does not significantly alter the shape of the free-propagating beam[42] $Z_{\sigma\rho}^{\text{X\_IN}}$, we can evaluate Eq. (5.74) on the basis of Eq. (4.41), for instance

$$Z_{\sigma\rho}^{\text{X\_IN}}(\mathbf{k}_1,\omega_1,\mathbf{k}_2,\omega_2) = \frac{(2\pi)^5\,G_0\,T\,\sigma^x\,\sigma^y\,\delta^x\,\delta^y}{\alpha^2\,\omega_1\omega_2\,\Omega}\;(\boldsymbol{\varepsilon}_p)_\sigma\,(\boldsymbol{\varepsilon}_p)_\rho\;W(\omega_1,\omega_2)\;(T_m(\omega_1))^*\;T_m(\omega_2)\;\delta(k_1^{\shortparallel}-k_{1\_0}^{\shortparallel}) \\ \times\,\delta(k_2^{\shortparallel}-k_{2\_0}^{\shortparallel})\;e^{-(\Delta k^x)^2(\sigma^x)^2/2}\;e^{-(\bar{k}^x)^2(\delta^x)^2/2}e^{-(\Delta k^y)^2(\sigma^y)^2/2}\;e^{-(\bar{k}^y)^2(\delta^y)^2/2}\;e^{\mathrm{i}\,\frac{z_0}{\alpha\bar{\omega}}\bar{\mathbf{k}}^{\perp}\cdot\Delta\mathbf{k}^{\perp}}. \quad (5.77)$$

Inserting the above into the definition of $\Phi_{\sigma\rho}$, we can find after some manipulation of the expression

$$\Phi_{\sigma\rho}(\mathbf{k},\omega) = \frac{N_{\mathrm{ph}}\,\delta_p^x\,\delta_p^y\,c}{(2\pi)^{3/2}\,\Omega_p}\,(\boldsymbol{\varepsilon}_p)_\sigma(\boldsymbol{\varepsilon}_p^*)_\rho\;e^{-(\omega-\omega_{p0})^2/2\Omega_p^2}\;e^{-(k^x\delta_p^x)^2/2}\;e^{-(k^y\delta_p^y)^2/2}\;\delta(\omega-c\,|\mathbf{k}|). \quad (5.78)$$

This model satisfies our normalization constraint $\int d\omega \int d^3k\,\Phi_{\sigma\sigma}=N_{\mathrm{ph}}$ and also exhibits the Gaussian shapes of spectrum and divergence, which we would intuitively expect from Eq. (5.77).

For a different—and more extendible—derivation of the above result, we refer the reader to App. A.13.

[42] We recall that neglecting the 'linear' interaction of the x-ray beam with the sample, i.e., neglecting its refraction, absorption and potentially diffraction, has been an essential approximation throughout Chpts. 4 and 5 so far. In particular for diamond samples (avoiding Bragg-reflection), this approximation has proven to be viable, but is expected to fail gradually towards heavier elements.

5.2.1 XPDC below the band gap

Having assembled all essential components for the general description of XPDC, we shall turn our attention towards the first case study. Specifically, we focus on scattering scenarios with idler photons being energetically smaller than the band gap of the sample (i.e., $\omega_i < E_{\text{band gap}}$). In an ideal experiment, these events would be selected by measuring XPDC signal-photons very close to the incoming x-ray photons' energy (i.e., $\omega_s \approx \omega_p$). Energy conservation would thus restrict the co-emitted idler photon to be small $\omega_i = \omega_p - \omega_s$.

We note that real measurements of XPDC in this regime are very challenging, due to limited fidelity in discriminating ω_s from ω_p. As a consequence, elastic background scattering tends to contaminate any detection significantly. Despite multiple attempts at measuring XPDC under these conditions, there are no verifiable observations of the effect to-date[43]. In contrast to the case of SFG, we will thus develop the theory for XPDC without definitive experimental guidance. We do command an experimental cross-check—at least to a certain degree—though. Namely, we have pursued the detection of XPDC at the (400)-orientation of diamond without positive result. This yields an upper bound on the nonlinear signal strength, which we will explore and compare in Sec. 5.2.1.c.

We begin our derivations by combining Eqs. (5.76) and (5.78) into a complete expression for the XPDC scattering probability:

$$\begin{aligned}\frac{dP_{\text{XPDC}}(\mathbf{k}_s)}{d\Omega_s d\omega_s} &= 2\,\alpha^6\, l_w\, \omega_s \int d^3k_i \int d\omega_i\, (\boldsymbol{\varepsilon}_s)_\sigma\, (\boldsymbol{\varepsilon}_s^*)_\rho\, \frac{1}{\omega_s - \omega_i}\,(1 - e^{\beta\omega_i}) \\ &\times \frac{N_{\text{ph}}\,\delta_p^x\,\delta_p^y\,c}{(2\pi)^{3/2}\,\Omega_p}\,(\boldsymbol{\varepsilon}_p)_\sigma(\boldsymbol{\varepsilon}_p^*)_\rho\; e^{-(\omega_s-\omega_i-\omega_{p0})^2/2\Omega_p^2}\; e^{-(k_s^x-k_i^x-G^x)^2(\delta_p^x)^2/2}\; e^{-(k_s^y-k_i^y-G^y)^2(\delta_p^y)^2/2} \\ &\times \delta(\omega_s - \omega_i - c\,|\mathbf{k}_s - \mathbf{k}_i - \mathbf{G}|) \\ &\times \text{Im}\Big(\frac{-4}{\omega_i^2\,\alpha^2\,\tilde{\varepsilon}(|\omega_i|) - |\mathbf{k}_i|^2}\Big)\,\frac{1}{V_\diamond^2}\,\Big(\,|\mathbf{K}_{GS\diamond}(0,\mathbf{G},\omega_i)|^2\; - |\mathbf{k}_i\cdot\mathbf{K}_{GS\diamond}(0,\mathbf{G},\omega_i)|^2\,/\,|\mathbf{k}_i|^2\,\Big).\end{aligned} \tag{5.79}$$

Here, we note a peculiarity of our expression: The idler photon's energy ω_i in the present convention is negative. This is an innate property of our underlying XOWM framework; as we aimed to treat energy increase of the scattered x-ray photon—such as in SFG—via positive admixtures (or 'idler'-energies), the opposite processes of DFG / XPDC, which involve energy loss of the scattered photon, require negative 'idler'-energies. Apart from its mildly peculiar appearance, this is of no significant consequence, though.

Our next steps are directed at some obvious simplifications of Eq. (5.79):

- We shall approximate $\frac{1}{\omega_s-\omega_i} \approx \frac{1}{\omega_{p0}}$. According to the exponential, which governs the incident spectrum, this will incur an error of $\sim \frac{\Omega_p}{\omega_{p0}}$ at most. Typically, this is on the order of $\sim 10^{-4}$ or less.
- We can neglect the Boltzmann-factor $e^{\beta\omega_i}$. Given that ω_i is negative and will have a magnitude of ~ 1 eV for band gaps of interest, the exponential is vanishingly small.
- We can merge the dot-products of $(\boldsymbol{\varepsilon}_s)_\sigma\,(\boldsymbol{\varepsilon}_s^*)_\rho ... (\boldsymbol{\varepsilon}_p)_\sigma(\boldsymbol{\varepsilon}_p^*)_\rho = |\boldsymbol{\varepsilon}_s\cdot\boldsymbol{\varepsilon}_p|^2$. Furthermore, we can combine this polarization factor with α^4 to give the differential Thomson scattering cross section

[43] Notably, there have been several claims to the observation of XPDC with low idler photon energies, however, these are likely based on a systematic misinterpretation of elastic background. We shall address this issue in more detail in the subsequent Sec. 5.2.2.

in atomic units[44]: $\left(\frac{d\sigma}{d\Omega_f}\right)_{\mathrm{Th}} = \alpha^4 \, |\boldsymbol{\varepsilon}_s \cdot \boldsymbol{\varepsilon}_p|^2$.

Applying the above leads to

$$\begin{aligned}\frac{dP_{\mathrm{XPDC}}(\mathbf{k}_s)}{d\Omega_s d\omega_s} = &\Big(\frac{d\sigma}{d\Omega_f}\Big)_{\mathrm{Th}} \frac{\omega_s}{\omega_{p0}} \, \frac{2\,\alpha\, l_w N_{\mathrm{ph}}\, \delta_p^x\, \delta_p^y}{(2\pi)^{3/2}\,\Omega_p} \int d^3k_i \int d\omega_i \; \delta(\omega_s - \omega_i - c\,|\mathbf{k}_s - \mathbf{k}_i - \mathbf{G}|) \\ &\times e^{-(\omega_s-\omega_i-\omega_{p0})^2/2\Omega_p^2} \; e^{-(k_s^x - k_i^x - G^x)^2 (\delta_p^x)^2/2} \; e^{-(k_s^y - k_i^y - G^y)^2 (\delta_p^y)^2/2} \\ &\times \mathrm{Im}\Big(\frac{-4}{\omega_i^2\,\alpha^2\,\tilde{\varepsilon}(|\omega_i|) - |\mathbf{k}_i|^2}\Big) \; \frac{1}{V_\diamond^2} \Big(|\mathbf{K}_{GS\diamond}(0,\mathbf{G},\omega_i)|^2 \; - |\mathbf{k}_i \cdot \mathbf{K}_{GS\diamond}(0,\mathbf{G},\omega_i)|^2 / |\mathbf{k}_i|^2 \Big).\end{aligned} \tag{5.80}$$

Following these technicalities, we will invoke more physical reasoning to simplify the scattering expression further. In particular, we shall make proper use of the fact that the idler energy is chosen below the band gap. In other words, $|\omega_i|$ is smaller than any relevant (electronic) transition-energies of our target crystal, which therefore appears fully transparent. Thus, its dielectric function $\tilde{\varepsilon}(|\omega_i|)$ is basically real and equals the square of the refractive index $n(|\omega_i|)$. In this limit, the imaginary-part expression can be rephrased as (cf. Eqs. (4.79,4.85)):

$$\mathrm{Im}\Big(\frac{-4}{\omega_i^2\,\alpha^2\,\tilde{\varepsilon}(|\omega_i|) - |\mathbf{k}_i|^2}\Big) \to \delta(\alpha\, n(|\omega_i|)\,\omega_i + |\mathbf{k}_i|) \; \frac{(-2\pi)}{\alpha\, n(|\omega_i|)\,\omega_i}\,. \tag{5.81}$$

In the simplemost case, where $n(|\omega_i|) = n$ is constant, we can use the equivalent

$$\delta(\alpha\, n\,\omega_i + |\mathbf{k}_i|) \; \frac{(-2\pi)}{\alpha\, n\,\omega_i} = \delta(\omega_i + \frac{c}{n}\,|\mathbf{k}_i|) \; \frac{2\pi}{\alpha\, n\,|\mathbf{k}_i|} \tag{5.82}$$

to fix ω_i. For practical purposes, it suffices that $n(|\omega_i|)$ is slowly varying within the bandwidth, which is probed by XPDC[45]. In our case, we shall approximate $n(|\omega_i|) \approx n(|\omega_f - \omega_{p0}|) = n_{\mathrm{eff}} \approx$ const. accordingly[46]. Thereby, we can employ Eq. (5.82) and rewrite our XPDC observable as:

$$\begin{aligned}\frac{dP_{\mathrm{XPDC}}(\mathbf{k}_s)}{d\Omega_s d\omega_s} = &\Big(\frac{d\sigma}{d\Omega_f}\Big)_{\mathrm{Th}} \frac{\omega_s}{\omega_{p0}} \, \frac{2\,\alpha\, l_w N_{\mathrm{ph}}\, \delta_p^x\, \delta_p^y}{(2\pi)^{3/2}\,\Omega_p} \int d^3k_i \int d\omega_i \; \delta(\omega_s - \omega_i - c\,|\mathbf{k}_s - \mathbf{k}_i - \mathbf{G}|) \\ &\times e^{-(\omega_s-\omega_i-\omega_{p0})^2/2\Omega_p^2} \; e^{-(k_s^x - k_i^x - G^x)^2 (\delta_p^x)^2/2} \; e^{-(k_s^y - k_i^y - G^y)^2 (\delta_p^y)^2/2} \\ &\times \delta(\omega_i + \frac{c}{n_{\mathrm{eff}}}\,|\mathbf{k}_i|) \; \frac{2\pi}{\alpha\, n_{\mathrm{eff}}\,|\mathbf{k}_i|} \; \frac{1}{V_\diamond^2} \Big(|\mathbf{K}_{GS\diamond}(0,\mathbf{G},\omega_i)|^2 \; - |\mathbf{k}_i \cdot \mathbf{K}_{GS\diamond}(0,\mathbf{G},\omega_i)|^2 / |\mathbf{k}_i|^2 \Big).\end{aligned} \tag{5.83}$$

Before we process this any further, we want to highlight the impact of phasematching (i.e., momentum conservation). The constraints on the transverse momentum components are already evident from the

[44] Note that there exist alternative definitions of the Thomson cross section, which incorporate an additional factor of $\omega_{\mathrm{out}}/\omega_{\mathrm{in}}$. Such definitions can be found in the IXS community, for instance [61], and—just to make matters more confusing—will be used in our Sec. 6.1. As is apparent from Eq. (5.79), this definition could just as well be employed here, given that an equivalent factor $\frac{\omega_s}{\omega_s - \omega_i}$ does already appear.

[45] Note that close to the band gap, $n(|\omega_i|)$ could vary more rapidly. Then—in order to find the proper constraint on the idler photon energy in Eq. (5.81)—one would have to resort to the general statement: $\delta(\alpha\, n(|\omega_i|)\,\omega_i + |\mathbf{k}_i|) = \delta(f(\omega_i)) = \delta(\omega_i - \omega_{\mathrm{root}})\;(|f'(\omega_i)|)^{-1}$. Here, ω_{root} labels a root of $f(\omega_i)$, i.e., it is defined by $0 = \alpha\,\omega_{\mathrm{root}}\, n(|\omega_{\mathrm{root}}|) + |\mathbf{k}_i|$. This condition can be solved (numerically) for the required range of $|\mathbf{k}_i|$. Note further, that for typical semiconductors (cf. Ref. [120]), $n(\omega)$—and thereby $f(\omega)$—is sufficiently well behaved below the bandgap to define a *unique* root. One may also see this quite generally from a simple Lorentz oscillator model for any dielectric. Below the (first) resonance (i.e., band gap), $n(\omega)$ will form the monotonous flank of a dispersion line.

[46] Note that for diamond below the band gap, this approximation is accurate to within less than 10% error.

two exponentials $e^{-(k_s^j-k_i^j-G^j)^2(\delta_p^j)^2/2}$, each of which fixes one direction of $\mathbf{k}_i^\perp \approx \mathbf{k}_{i0}^\perp = \mathbf{k}_s^\perp - \mathbf{G}^\perp$. In addition, there is $\delta(\omega_s - \omega_i - c\,|\mathbf{k}_s - \mathbf{k}_i - \mathbf{G}|)$, which holds an implicit constraint for $k_i^\shortparallel$. In order to make this more apparent, we shall use the conversion Eq. (A.89) found in our appendix A.9:

$$\delta(\omega - c\,|\mathbf{k}|) = \delta(k^\shortparallel - k_0^\shortparallel)\,\frac{|\mathbf{k}|}{ck_0^\shortparallel} \approx \alpha\,\delta(k^\shortparallel - k_0^\shortparallel) \tag{5.84}$$

with $k_0^\shortparallel = \sqrt{\omega^2/c^2 - (\mathbf{k}^\perp)^2}$ for 'forward'-propagating pump-beam. More specifically, this allows us to rewrite

$$\delta(\omega_s - \omega_i - c\,|\mathbf{k}_s - \mathbf{k}_i - \mathbf{G}|) \approx \alpha\,\delta\Big((k_s^\shortparallel - k_i^\shortparallel - G^\shortparallel) - \sqrt{(\omega_s-\omega_i)^2/c^2 - (\mathbf{k}_s^\perp - \mathbf{k}_i^\perp - \mathbf{G}^\perp)^2}\Big), \tag{5.85}$$

which determines

$$\begin{aligned} k_{i0}^\shortparallel &= k_s^\shortparallel - G^\shortparallel - \sqrt{(\omega_s-\omega_i)^2/c^2 - (\mathbf{k}_s^\perp - \mathbf{k}_i^\perp - \mathbf{G}^\perp)^2} \\ &\approx k_s^\shortparallel - G^\shortparallel - \sqrt{(\omega_s-\omega_i)^2/c^2 - 0} \\ &\approx k_s^\shortparallel - G^\shortparallel - \alpha\omega_{p0}. \end{aligned} \tag{5.86}$$

In the penultimate step, we have already approximated $\mathbf{k}_i^\perp \approx \mathbf{k}_{i0}^\perp$ to simplify the expression, before we made use of $\omega_s - \omega_i \approx \omega_{p0}$ in the last step.

Using the above on Eq. (5.83), we can simplify the expression to read

$$\begin{aligned} \frac{dP_{\mathrm{XPDC}}(\mathbf{k}_s)}{d\Omega_s d\omega_s} = \Big(\frac{d\sigma}{d\Omega_f}\Big)_{\mathrm{Th}} \frac{\omega_s}{\omega_{p0}}\,\frac{2\,\alpha\, l_w N_{\mathrm{ph}}\,\delta_p^x\,\delta_p^y}{(2\pi)^{1/2}\,\Omega_p}\,\frac{1}{n_{\mathrm{eff}}\,|\mathbf{k}_{i0}|}\; e^{-(\omega_s + \frac{c}{n_{\mathrm{eff}}}|\mathbf{k}_{i0}| - \omega_{p0})^2/2\Omega_p^2} \\ \times\,\frac{1}{V_\diamond^2}\Big(\,|\mathbf{K}_{GS\diamond}(0,\mathbf{G},-c\,|\mathbf{k}_{i0}|/n_{\mathrm{eff}})|^2\; - |\mathbf{k}_{i0}\cdot\mathbf{K}_{GS\diamond}(0,\mathbf{G},-c\,|\mathbf{k}_{i0}|/n_{\mathrm{eff}})|^2/\,|\mathbf{k}_{i0}|^2\,\Big) \\ \times\int d^2\delta k_L^\perp\; e^{-(\delta k_i^x)^2(\delta_p^x)^2/2} e^{-(\delta k_i^y)^2(\delta_p^y)^2/2}. \end{aligned} \tag{5.87}$$

In here, we have still kept the integrations of the respective remainders in $\delta\mathbf{k}_i^\perp = \mathbf{k}_i^\perp - \mathbf{k}_{i0}^\perp$, even though we assume that the main expression does not (or only weakly) depend on the explicit value of $\delta\mathbf{k}_i^\perp$. Nonetheless, it is important to include the numerical value of the integrals, viz.

$$\int d\delta k_i^j\; e^{-(\delta k_i^j)^2(\delta_p^j)^2/2} = \frac{\sqrt{2\pi}}{\delta_p^j}. \tag{5.88}$$

This finalizes our nonlinear scattering expression for XPDC below the band gap:

$$\begin{aligned} \frac{dP_{\mathrm{XPDC}}(\mathbf{k}_s)}{d\Omega_s d\omega_s} = \Big(\frac{d\sigma}{d\Omega_f}\Big)_{\mathrm{Th}} \frac{\omega_s}{\omega_{p0}}\,\frac{\sqrt{8\pi}\,\alpha\, l_w N_{\mathrm{ph}}}{\Omega_p\, n_{\mathrm{eff}}\,|\mathbf{k}_{i0}|}\; e^{-(\omega_s + \frac{c}{n_{\mathrm{eff}}}|\mathbf{k}_{i0}| - \omega_{p0})^2/2\Omega_p^2} \\ \times\,\frac{1}{V_\diamond^2}\Big(\,|\mathbf{K}_{GS\diamond}(0,\mathbf{G},-c\,|\mathbf{k}_{i0}|/n_{\mathrm{eff}})|^2\; - |\mathbf{k}_{i0}\cdot\mathbf{K}_{GS\diamond}(0,\mathbf{G},-c\,|\mathbf{k}_{i0}|/n_{\mathrm{eff}})|^2/\,|\mathbf{k}_{i0}|^2\,\Big), \end{aligned} \tag{5.89}$$

which should be used in tandem with the prescriptions:

$$k_{i0}^\shortparallel = k_s^\shortparallel - G^\shortparallel - \alpha\omega_{p0} \qquad \text{and} \qquad \mathbf{k}_{i0}^\perp = \mathbf{k}_s^\perp - \mathbf{G}^\perp. \tag{5.90}$$

Before we discuss the implications of Eq. (5.89) in more detail, let us briefly note that this result is

(almost[47]) directly analogous to Eq. (10) of our discussion in Ref. [51].

5.2.1.a Approximate evaluation of the XPDC signal

Having established Eqs. (5.89) and (5.90) to describe the XPDC signal, we want to embark on its evaluation in more detail. To begin with, we shall obtain rough estimates of both strength and shape of the signal. Thereby, we can build some intuition, ere we proceed to evaluate the full XPDC pattern numerically.

Concerning the strength of a detectable XPDC signal, we can reduce Eq. (5.89) to the following essential contributions:

$$\frac{dP_{\mathrm{XPDC}}(\mathbf{k}_s)}{d\Omega_s d\omega_s} \approx \left(\frac{d\sigma}{d\Omega_f}\right)_{\mathrm{Th}} \frac{l_w N_{\mathrm{ph}}}{\Omega_p \, |\omega_{i0}|} \; \frac{1}{V_\diamond^2} \, |\mathbf{K}_{GS\diamond}(0,\mathbf{G},\omega_{i0})|^2 \,, \tag{5.91}$$

with $|\mathbf{k}_{i0}| \approx \alpha \, |\omega_{i0}|$. Notably, the above yields a *differential* scattering probability still; thus, we need to integrate over the spectral ($d\omega_s$) and angular ($d\Omega_s$) acceptance of a hypothetical detection setup, in order to reduce Eq. (5.91) into a proper scattering probability. For simplicity, we shall assume the detection bandwidth to equal the incident bandwidth $d\omega_s \to \Delta\omega_s \approx \Omega_p$. Furthermore, we take the angular acceptance to be ~ 1 mdeg. This provides a reasonable scale[48] and corresponds to ~ 17.4 μrad. The resultant scattering probability per pulse reads

$$P_{\mathrm{XPDC}} \approx \alpha^4 \, (17.4 \cdot 10^{-6})^2 \frac{l_w N_{\mathrm{ph}}}{|\omega_{i0}|} \; \frac{1}{V_\diamond^2} \, |\mathbf{K}_{GS\diamond}(0,\mathbf{G},\omega_{i0})|^2 \,. \tag{5.92}$$

We can simplify this into a 'conversion efficiency'—which is a popular measure in the pertinent literature [28, 46, 47]—by normalizing to the incident number of photons N_{ph}. Fixing the remaining parameters, we choose a sample of length 500 μm (i.e., $l_w \approx 10^7$ a.u.), an idler photon energy at 5 eV (i.e., $\omega_{i0} \approx 0.18$ a.u.) and read the corresponding strength of $|\mathbf{K}_{GS\diamond}|^2 / V_\diamond^2$ from Fig. 3.2 for the (111) orientation of diamond: $\sim 4 \cdot 10^{-5}$. Thus, we find a conversion efficiency on the order of

$$\eta_{\mathrm{XPDC}} \approx \alpha^4 \, (17.4 \cdot 10^{-6})^2 \frac{10^7}{0.18} \, 4 \cdot 10^{-5} \approx 2 \cdot 10^{-15}. \tag{5.93}$$

This is not a particularly strong signal. Even if the details of setup, material and chosen orientation may still introduce variations around this scale, we can already conclude that the fundamental process of XPDC will be rather weak[49].

Next, we turn to the geometry of the scattering signal. We can gather a reasonable first impression hereof by studying the phase-matching condition, i.e., momentum conservation among the scattered photons. This is already laid out in Eq. (5.90)—apart from the peculiar sign convention, which renders $\mathbf{k}_{i0}$ 'negative'. Upon closer inspection of Eq. (5.89), we find this to be irrelevant anyways, as $\mathbf{k}_{i0}$ only appears in terms of its absolute value. For all intents and purposes, we may thus use the intuitive mo-

[47] The main difference in between the two expressions consists in a slightly different treatment of $k_{i0}^{\shortparallel}$ and a factor resulting from its δ-function derivative.

[48] Note that ~ 1 mdeg corresponds approximately to the angular acceptance of a Si (111)-reflection. Thus, it gives a rough scale for the angular acceptance of crystal-based analyzer setups.

[49] Note that the weakness of XPDC is largely predetermined through its proportionality to the Thomson cross section $\left(\frac{d\sigma}{d\Omega_f}\right)_{\mathrm{Th}} = \alpha^4 \approx 3 \cdot 10^{-9}$. This is a characteristic property of non-resonant x-ray scattering processes, which XPDC shares with many flavours of inelastic x-ray scattering (IXS) [61]. While many IXS signals are diffuse and benefit from large collection angles [181], however, XPDC *also* suffers from being confined to a small angular range around the phase-matching condition.

mentum balance $\mathbf{k}_{p0} + \mathbf{G} = \mathbf{k}_{i0} + \mathbf{k}_s$. This, in turn, is the same as we have found for DFG in Sec. 5.1.2, specifically in Figs. 5.3 (b) and (d). For illustration, we adapt both the momentum balance diagram and the corresponding phase-matching ellipse in Fig. 5.13 below[50].

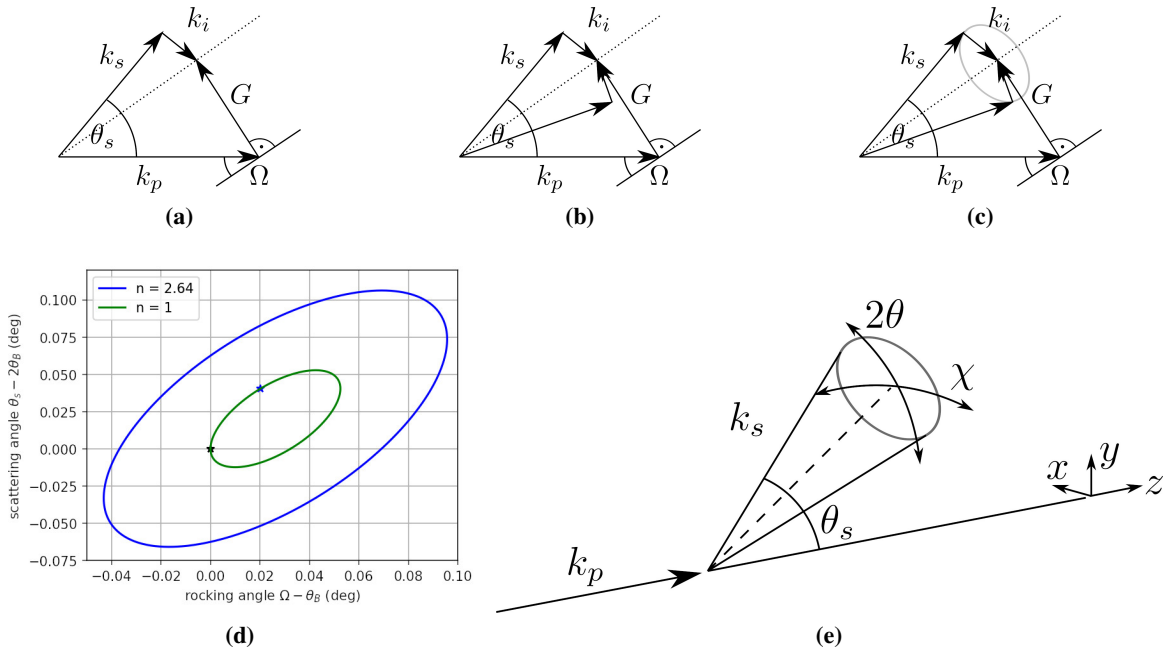

Figure 5.13: Illustration of the phase-matching conditions for XPDC: Graphs (a) through (c) outline the momentum balance for the process. Note the rotational symmetry axis (indicated as dashed line), which allows the initial configuration to be flipped (b) or indeed be rotated freely (c). This generates possible scattering solutions along a circle for any fixed sample position. The upper and lower scattering solution shown in (b) trace out an ellipse, if the sample is rocked through Ω. This is indicated in (d), for a medium with unit refractive index as well as diamond ($n = 2.64$). The circular nature of the XPDC signal becomes most apparent, if the scattering is resolved for both in- and out-of-plane scattering angles. To this end, a locally orthogonal system of coordinates 2θ, χ is defined in the three-dimensional illustration (e). [We gratefully acknowledge Dr. Christina Bömer's help in rendering the computer graphics of the sketches (a) - (c) as well as (e).]

We recall that the momentum balance has an inherent symmetry, indicated by the dashed line throughout (a) - (c). Within the scattering plane that is defined by $\mathbf{k}_{p0}$ and $\mathbf{G}$, this allows for two possible solutions: $\mathbf{k}_s$ and $\mathbf{k}_{i0}$ may form a triangle with the dashed line either from above or from below. This is shown explicitly in Fig. 5.13 (b). Rocking the sample through Ω, these solutions will be modified as the triangles adapt to the ensuing tilt of $\mathbf{G}$. Obviously, the range of admissible scattering solutions is constrained by two extremal points: Here, the triangles are either maximally stretched or maximally compressed—i.e., $\mathbf{k}_s$ and $\mathbf{k}_{i0}$ are aligned parallel or anti-parallel, respectively. Tracing across the range in between these two points, the scattering angles for XPDC (θ_s) map out an ellipse, if plotted against the rocking angle Ω. This is visualized in Fig. 5.13 (d) and occurs fully analogous to the DFG case. In contrast to DFG, however, all (or most) of these scattering solutions should indeed be observable simultaneously. While in the case of DFG, the optical laser has to be re-adjusted to phase-match at different points of the ellipse, the spontaneous idler photons of XPDC are intrinsically generated for (almost) all directions. For further reference in Fig. 5.13 (d), we indicate the elastic Bragg position of ω_{p0} by a black star and likewise show the pair of angles, for which the signal energy ($\omega_{p0} - 5$ eV) would undergo elastic diffraction (blue star). Notably, both could be found on the XPDC-ellipse, if the sample had a refractive

[50] In the present case, we choose a different orientation of diamond, viz. (400), with a view to the subsequent experimental discussion. Likewise, we employ different pump and idler photon energies at 11.216 keV and 5.0 eV, respectively.

index of unity (green line). In diamond, however, the idler photon's momentum is effectively extended through refractive corrections, such that the resulting ellipse (blue line) is larger by a factor of $n = 2.64$.

As the next step in visualizing the XPDC scattering pattern, we shall extend our view out of the scattering plane. While sketch 5.13 (b) emphasized the scattering solutions inside the plane defined by $\mathbf{k}_{p0}$ and $\mathbf{G}$, we can also rotate $\mathbf{k}_s$ out of this plane and find a matching idler photon—see illustration (c). Overall, the XPDC signal can thus be emitted on a whole cone of possible $\mathbf{k}_s$. If detected by an ideal, spatially resolving detector, this would translate into a *circular XPDC pattern* for any given orientation of the sample. This situation is further illustrated in Fig. 5.13 (e). There, we have already introduced a locally orthogonal system of angular coordinates (2θ, χ), which we can use to plot these scattering patterns later on. The in-plane scattering angle 2θ is equivalent to the polar angle θ_s for an azimuth of $\phi_s = \pi/2$, whereas χ measures the out-of-plane component.

Finally, we want to connect the circular signature of the XPDC cone (e) back to the ellipse (d). Such a cone of XPDC signal photons is emitted for each admissible rocking angle of the sample (Ω). The diameter of each cone equals the vertical dimension of the ellipse at the corresponding Ω, because they are both determined by the upper and lower solutions of sketch (b). Equivalently: If the individual XPDC patterns (i.e., circles in 2θ, χ) were stacked for different Ω into a three-dimensional shape, then, its cut in the plane of Ω-2θ would reproduce the ellipse of Fig. 5.13 (d).

5.2.1.b Numerical evaluation of the XPDC signal

Having established our expectations on the XPDC signal in the preceding discussion, we will embark on its detailed numerical investigation next. To this end, we have implemented a set of numerical routines, which—at their core—evaluate Eq. (5.89) on a two-dimensional grid of scattering angles (i.e., 2θ, χ). These routines are bundled into a PYTHON-package—correspondingly named `XPyDC`.

In the following, we shall make use of this numerical framework to study XPDC in diamond. Specifically, we will concern ourselves with the nonlinear scattering signal that is generated for the (400) orientation of the sample and its respective reciprocal component of the nonlinear response $\mathbf{K}_{GS\diamond}(0, \mathbf{G}_{(400)}, \omega_i)$. These calculations were originally performed in anticipation of an experimental campaign at the P09 beamline of PETRA III (Hamburg) [187] and published together with its findings in a joint article (see Ref. [51]). Our discussion of the scenario in this (and the next) section, will closely follow said report.

The defining beam parameters for the x-ray field—both for the simulation and for the subsequent experiment—are summarized in Tab. 5.7.

	experimental value	parameter in a.u.
photon energy	11.216 keV	$\omega_{p0} = 412.2$
monochromator passwidth	1 eV (FWHM)	$\Omega_m = \Omega_p = 0.016$
average photon 'flux'	$4 \cdot 10^{12}$ photons/s	$N_{\text{ph}} = 4 \cdot 10^{12} \times t_{\text{exposure}}$
beam divergence	8 μrad	$\delta_p = 1.37 \cdot 10^5$

Table 5.7: X-ray beam parameters for XPDC measurements at P09

Regarding the sample, we chose a $\sim 500\ \mu$m thick specimen of diamond that featured a (100)-cut surface. As such, the aimed for (400)-reciprocal component could easily be found in symmetric reflection geometry, for which the Bragg angle of regular x-ray diffraction measures $\theta_B^{(400)} = 38.304°$. Furthermore, we have focused our main effort on the detection of XPDC at an idler photon energy of 5 eV, i.e.,

shortly below the band gap of diamond. For the corresponding value of $\omega_i = 0.184$ a.u., we have evaluated the nonlinear response function $\mathbf{K}_{GS\diamond}$ numerically. Thereunto, we proceeded in an analogous fashion to previous computations, i.e., using our `MyLiO.x` code (cf. Secs. 3.3 and A.6) to obtain $\mathbf{K}_{GS\diamond}$ on the basis of Kohn-Sham orbitals. Its absolute value is found to be $\left|\mathbf{K}_{GS\diamond}(0,\mathbf{G}_{(400)},0.184)\right|^2/V_\diamond^2 \approx 5.4\cdot 10^{-6}$.

Combining these ingredients, we are—almost—in a position to evaluate Eq. (5.89) for the nonlinear scattering pattern. All that is left to do, is to specify an appropriate conversion of the average photon 'flux' from Tab. 5.7 into photon numbers[51]. Alternatively, we may simply divide Eq. (5.89) by N_{ph} and thus obtain the conversion efficiency rather than the absolute yield (or scattering probability). We have discussed this option already in the previous section (cf. discussion following Eq. (5.92)) and shall adhere to it henceforth. On this basis, we give a set of simulated scattering patterns in Fig. 5.14.

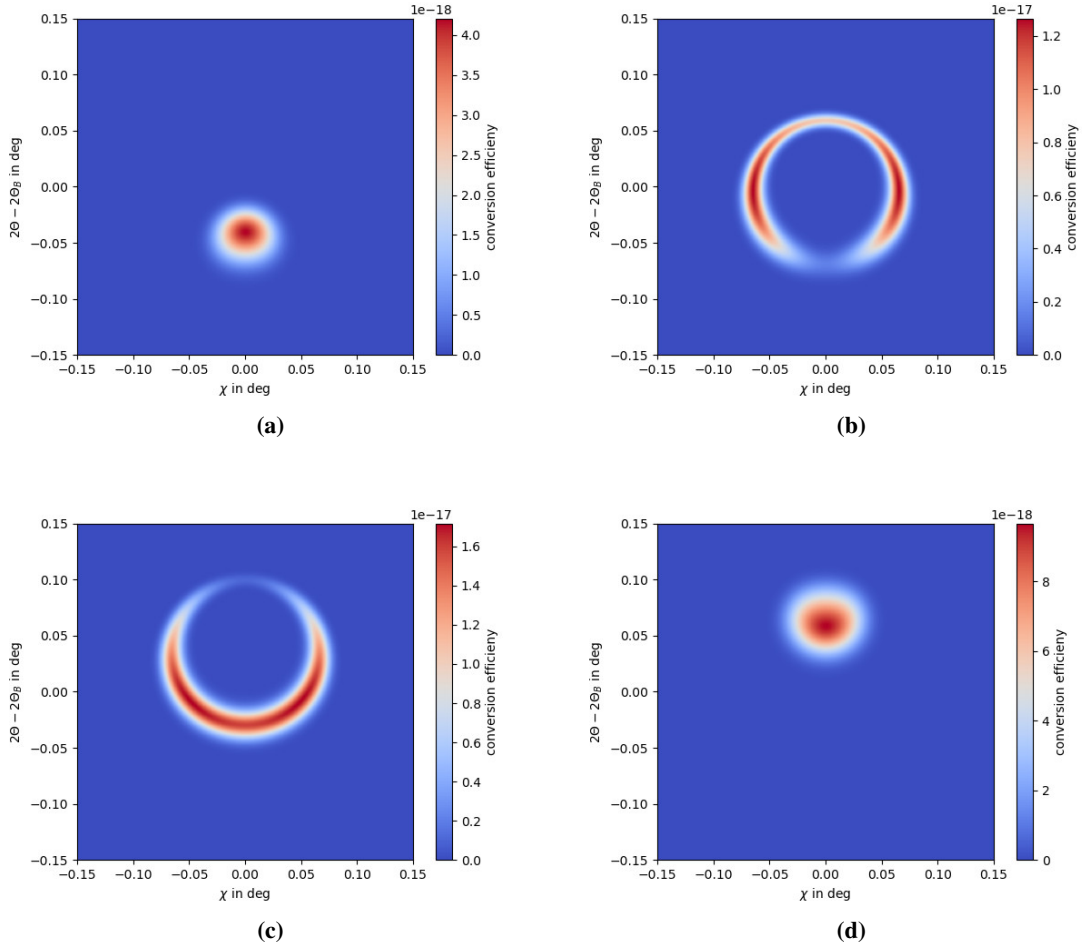

Figure 5.14: Simulated scattering patterns for XPDC at different rocking angles of the sample. Figs. (a) through (d) correspond to rocking $\Omega - \Omega_B = -50,\ 0,\ 50,\ 100$ mdeg, respectively. We take the (400) Bragg condition at the pump photon energy of $\hbar\omega_{p0} = 11.216$ keV as a reference point, fixing $\Omega_B = \theta_B$. Similarly, we center each plot around the direction of Bragg-reflection, i.e., at $2\theta = 2\theta_B$. Individual pixels correspond to a solid angle of 1 mdeg × 1 mdeg and are colour-coded to show the efficiency for down-conversion by 5 eV ± 25 meV leading to nonlinear scattering there. [The plots are equivalent to Fig. 2 of Ref. [51].]

[51] Note that we are using the term 'flux' in a somewhat colloquial fashion here. Instead of the number of photons traversing a unit-area per unit-time, which is often taken as the definition of flux, we shall use the term in quotation marks (i.e., 'flux') to subsume any kind of quantifier regarding the incident field's magnitude.

These plots pertain to different rocking angles of the sample from (a) through (d)—corresponding to settings of $\Omega - \Omega_B = -50,\ 0,\ 50,\ 100$ mdeg, respectively. For conciseness, we have referenced all angular positions to the nearby Bragg condition (i.e., $\Omega_B = \theta_B = 38.304°$) for elastic diffraction of the pump photons at an energy of $\hbar\omega_{p0} = 11.216$ keV. Each of the plots gives the distribution of normalized scattering probability (i.e., scattering efficiency) across the two-dimensional plane that is mapped out by the scattering angles 2θ and χ (cf. discussion at Fig. 5.13 (e)). The center of each plot is chosen to coincide with the hypothetical position of the Bragg-spot, provided the pump beam was diffracted elastically within the (vertical) scattering plane, i.e., at $2\theta = 2\theta_B$ and $\chi = 0°$. The individual pixels of the plots subtend an angular range of 1 mdeg $\times$ 1 mdeg, for which the integrated conversion efficiency is indicated through their colour-code. Herein, the XPDC signal is integrated for signal photon energies in the range $11.211\ \text{keV} \pm 25$ meV.

Contemplating the plots, we can immediately arrive at two important conclusions vis-a-vis our earlier estimates:

1. The conversion efficiency per pixel is even lower than we have estimated in Eq. (5.93) for the same angular range. In part, this can be attributed to $\mathbf{K}_{GS\diamond}$, which—at $\hbar\omega_i = 5$ eV—is intrinsically weaker for the (400) orientation than it was for the (111) case before. In addition, the integrated energy range (± 25 meV) for each pixel is smaller than in our earlier example.

2. The XPDC scattering pattern does indeed unfold as a circular shape in the two-dimensional 2θ-χ-plane. This agrees well with our earlier assessment in Sec. 5.2.1.a.

On further inspection, we can add to our observations that the circular scattering patterns exhibit additional modulation around the ring. As such, we find a horseshoe-shaped pattern in Fig. 5.14 (b) with two pronounced side-lobes or 'bananas'[52]. Proceeding to Fig. 5.14 (c), i.e., rocking the sample further, the opening of the horseshoe-shape has flipped downside-up, while the 'bananas' have merged into an extended crescent.

We can trace this modulation back to the difference expression $|\mathbf{K}_{GS\diamond}|^2 - \left|\hat{\mathbf{k}}_{i0} \cdot \mathbf{K}_{GS\diamond}\right|^2$ in Eq. (5.89) and—more fundamentally—to the transverse coupling of the optical field during XPDC. Starting at the former (more obvious) expression, we notice that it vanishes naturally, if $\hat{\mathbf{k}}_{i0}$ aligns parallel to $\mathbf{K}_{GS\diamond}$ such that the second term assumes the same magnitude as the first[53]. In addition, we recall that $\mathbf{K}_{GS\diamond}(0, \mathbf{G}, \omega)$ tends to align, in turn, with the reciprocal component $\mathbf{G}$, at which it is probed. In conjunction, this implies that the XPDC signal vanishes, whenever phasematching would force the idler photon's momentum $\mathbf{k}_{i0}$ to be parallel to $\mathbf{G}$. Looking back to Fig. 5.13 (b), for example, we find both upper and lower scattering solutions to be rather unfavourable in this sense. The situation changes, however, for scattering outside the vertical plane, as indicated in the neighbouring sketch 5.13 (c). For the outer extrema of the scattering circle, $\mathbf{k}_i$ would be almost perpendicular to $\mathbf{G}$ and thus harness the maximal signal strength. This behaviour gives rise to the aforementioned side-lobes or 'bananas'. It is, furthermore, quite apparent that the specific shape of this modulation will vary, depending on variations in the orientation of either $\mathbf{k}_i$ or $\mathbf{G}$. During rocking-curve scans, the latter is systematically tilted and thus traverses several possible configuration for the modulation. This is reflected in the different shapes found in Fig. 5.14.

[52] Note that we could experimentally resolve—and thus prove the existence of—these side-lobes in a later experiment (see Sec. 5.2.3.a). When faced with an early experimental image thereof, a collaborator of ours joyfully declared the discovery of the 'bananas'. In fond memory of this moment—and acknowledging the undeniable pictorial value of the expression—we shall adopt 'bananas' as equivalent terminology for XPDC side-lobes.

[53] We recall for completeness that we employ the common-place 'hat'-notation to signify unit vectors. As such $\hat{\mathbf{k}}_{i0}$ denotes the unit vector parallel to $\mathbf{k}_{i0}$.

Having established this basic understanding of the modulation from closer inspection of Eq. (5.89), we want to go one step further still. Namely, we want to highlight the origin of the difference expression $|\mathbf{K}_{GS\diamond}|^2 - |\hat{\mathbf{k}}_{i0} \cdot \mathbf{K}_{GS\diamond}|^2$. Upon review of Sec. 5.2, we find that the difference in question was embedded in the the dyadic structure of Eq. (5.69) and proliferated through our derivation from there. Fundamentally, this dyadic ensures transversality of the optical wavefield. In other words, it forces the polarization $\boldsymbol{\varepsilon}_i$ of the idler field to be perpendicular to its wavevector $\boldsymbol{\varepsilon}_i \perp \mathbf{k}_i$. This is satisfied, if the optical field's correlation function $\bar{C}^{\mathrm{OPT}}_{\nu\mu}(\mathbf{k}_i', \omega_i', \mathbf{k}_i, \omega_i)$ in Eq. (5.69) vanishes along the direction of $\mathbf{k}_i$ or $\mathbf{k}_i'$, respectively—just like the XPDC signal later on. Therefore, we are led to conclude that the origin of the modulation, which we have found in Fig. 5.14, can ultimately be traced to the transverse polarization of the idler field. It is curious to find such a profound imprint caused by a fundamental property of electromagnetic waves.

In a closing remark on this observation, we want to point out that the transversality condition may be broken in special cases. As stated, it stems from the transverse nature of the (idler) wave-field, however, this is strictly ensured only in free-space or in an isotropic, homogeneous medium. Changing to anisotropic media—featuring birefringence, for instance—we may be able to alter the polarization state via the *linear* dielectric properties of the sample. The resulting change in the field's (mode) structure could be passed onto the XPDC scattering pattern[54].

For a second observation—independent of the previous modulation aspect—we turn our attention to the edges of the rocking range, i.e., towards Figs. 5.14 (a) and (d). On these, we note that the circular scattering patterns have each collapsed into a cohesive, point-like feature. Thereby, most of the XPDC signal is concentrated into a (relatively) small solid angle of the scattering plane. These loci of concentration have previously been identified by Kleinman [188] as well as Freund and Levine [189], who have coined the term 'edge enhancement' and speculated about its usefulness in efforts to enhance XPDC-detection. It should be noted, however, that the practically achievable enhancement interdepends on the (angular) acceptance of the employed detection setup.

Post-processing for experimental comparison While the above results are fascinating in terms of their unique shapes, they boded impossible to resolve experimentally at the time. This is in part due to the minuscule conversion efficiency and in other part due to the challenge in rasterizing the two-dimensional scattering plane precisely. Thus, we have opted to search for a more integrated signal. Anticipating the analyser setup of Sec. 5.2.1.c, we expect the vertical resolution (i.e., along 2θ) to remain at ~ 1 mdeg but the horizontal acceptance (i.e., along χ) to comprise up to ~ 57 mdeg around the central $\chi = 0^\circ$ line. Similarly, we expect an energy passwidth of 1 eV (FWHM) around $\hbar\omega_s = 11.211$ keV. We can integrate and convolute our scattering patterns across these respective ranges and thereby obtain scattering distributions as 'seen' through the detection setup.

Having integrated in χ, the remaining distributions are one-dimensional lineouts along 2θ for different rocking angles of the sample (Ω). We may stack these along Ω to obtain a so-called rocking-curve map or angular space map (cf. Refs. [51, 74]). Structurally, this map covers the same ranges as the phasematching plot which we have discussed earlier (namely, Fig. 5.13 (d)). As such, it is unsurprising, that its elliptical shape re-appears here—see Fig. 5.15 below.

[54] Note that in an extension of the above proposal, cavity structures could be envisioned to modulate the XPDC pattern as well. The utility of such manipulations may be questionable, though.

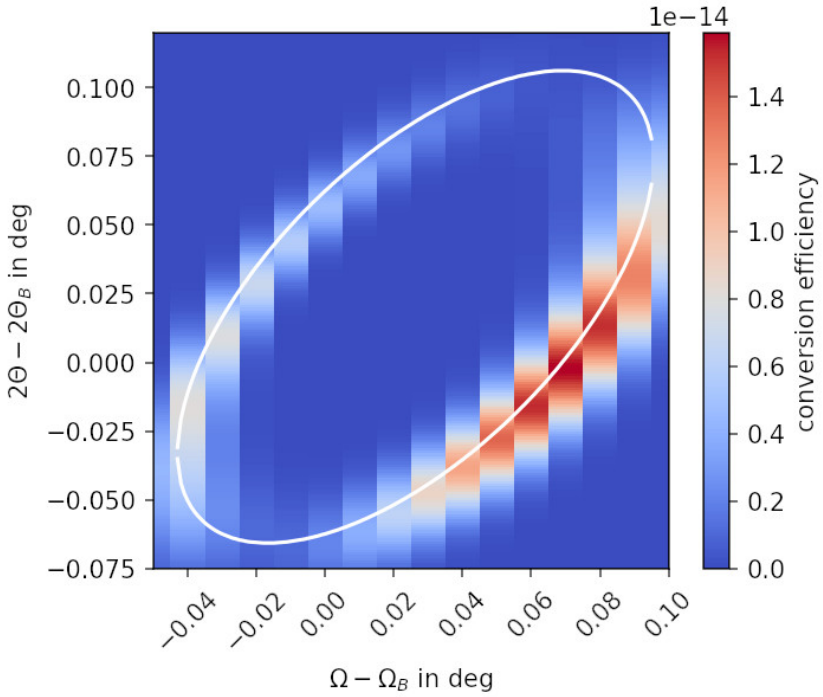

Figure 5.15: Rocking-curve map of XPDC conversion efficiency as predicted for the experimental conditions of Sec. 5.2.1.c. We take the angular acceptance to be: 57 mdeg × 1 mdeg—hor. × ver. and spectral acceptance to be 1 eV (FWHM). The signal replicates the distinct elliptical signature, which we found from our phasematching considerations in Fig. 5.13 (d) before. For direct comparison, an elliptical trace is superimposed as a solid white line. [The plot is equivalent to Fig. 3 of Ref. [51].]

This elliptical shape follows the upper and lower extrema of each phasematching circle, if sequentially aligned along an Ω-axis. Providing a rather unique signature, it can be used to detect XPDC and, in particular, *discriminate* it against other scattering effects. Despite this helpful fingerprint, however, we should expect any attempt at detecting XPDC under these conditions to remain highly challenging, due to the low conversion efficiency of $\sim 10^{-14}$. For illustration, we recall that the incident 'flux' at the P09 beamline was measured at $\sim 4 \cdot 10^{12}$ photons/s. The product of the two values implies that the total count rate for XPDC would likely remain around 0.04 counts/s. This is meagre even by the standards of photon-hungry experiments (cf. discussion in Sec. 5.1.2.c).

5.2.1.c Experimental cross-check for diamond (400)

Concomitant to our theoretical studies, we have likewise participated in an experimental investigation into XPDC. These efforts were led by Dr. Christina Bömer and aimed to detect down-conversion under the conditions outlined earlier. The experiment (proposal No.: I-20190876) was performed at the P09 beamline[55] of the synchrotron-radiation source PETRA III in Hamburg [187]. It was described in great detail in the aforementioned Ref. [51], with a full account of it far exceeding the scope of the present work.

At this point, we merely seek to summarize few important aspects of the experiment in order to contextualize our theoretical predictions. As such, we will briefly outline the setup below (Fig. 5.16),

[55] We gratefully acknowledge the immense help of Dr. Sonia Francoual and Julian Bergtholdt at the P09 beamline. Without their tireless support and open-mindedness in the face of contradicting publications (cf. our later discussion in Sec. 5.2.2) the critical work described in this section would not have been possible.

before we report on the experiment's essential finding.

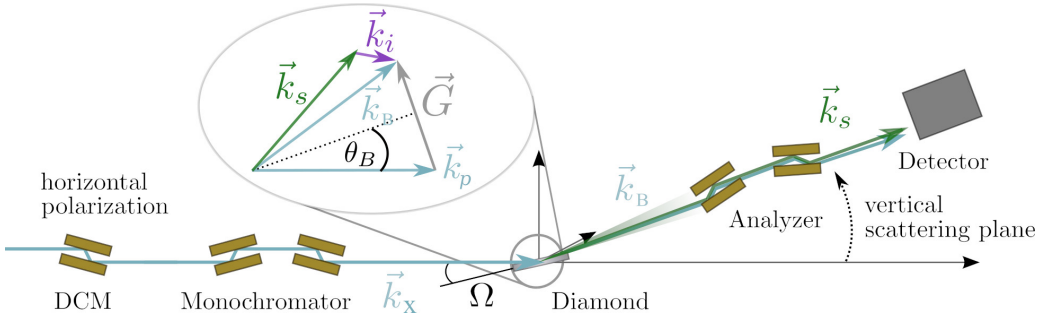

Figure 5.16: Experimental setup used in search of XPDC at PETRA III - P09. The incident beam is filtered by a Si(111) double crystal monochromator (DCM) as well as an additional 4-bounce stage. A diamond sample is adjusted close to its (400)-Bragg condition, fulfilling phasematching for XPDC (see inset graphic for illustration). The vertically scattered radiation is filtered through a 4-bounce analyser and subsequently detected. [Image courtesy of Dr. Christina Bömer. The plot is equivalent to Fig. 5 of Ref. [51].]

The setup follows a high-resolution x-ray diffraction scheme analogous to the concept outlined in Sec. 5.1.3 (Fig. 5.7). Incident radiation from an undulator is filtered through a succession of crystal-based monochromators before diffracting off the sample towards the detection side. The latter comprises a second set of crystal-optics, namely channel-cut analysers that discriminate for the desired signal energy (ω_s) prior to detection. All crystal-optics components were chosen to use Si(111) reflections, as their large bandwidth ($\sim$ 1 eV (FWHM)) conserves much of the incident flux. The large number of successive reflections ensured, in turn, high suppression of photon energies that lie outside the desired bandwidth. This is aided further by their specific arrangement in 'Bartels'-configuration [190] for both the monochromator and the analyser side. At 5 eV offset from the central pump photon energy ($\hbar\omega_p = 11.216$ keV), spectral remainders were measured to be suppressed significantly indeed—namely by $\sim 10^{-7}$.

Using this setup, we have scanned the angular range of the previously discussed rocking-curve map. The result is plotted in Fig. 5.17 and shows no sign of the XPDC signal at the expected phasematching condition.

While the scan shows a visible remainder of the elastic Bragg spot at $\Omega = \Omega_B = \theta_B^{(400)}$ and $2\theta = 2\theta_B^{(400)}$, the rest of the plane exhibits merely homogeneous background at ~ 50 counts/s. Notably, this is background is much stronger than our theoretical prediction for XPDC under these circumstances, viz. 0.04 counts/s (cf. previous section). Thus, we would not expect to observe any structure related to XPDC, unfortunately. Nevertheless, the experiments serves to provide an important experimental bound on the conversion efficiency. Normalizing for the incident 'flux' of $4 \cdot 10^{12}$ photons/s, we can specify the conversion efficiency, at which the setup *would* still be sensitive to XPDC, to be $\sim 1.25 \cdot 10^{-11}$.

The above result is easily compatible with our theoretical findings. However, it casts severe doubts on earlier reports of XPDC efficiencies which ranged much higher [47–49, 55]. This discrepancy will be the subject of a separate discussion, given in the next section (5.2.2).

5.2.2 Discrepancy towards earlier reports on XPDC

In this section, we want to address an ongoing controversy about XPDC. Specifically, this concerns a significant discrepancy in between our theoretical findings as well as experimental results, gathered under the lead of Dr. Christina Bömer, on the one hand and claims to the observation of XPDC by Dr. Sharon Shwartz and co-workers on the other (cf. Refs. [47–49, 55]). In the following, we will voice our concern on several problematic aspects of these publications.

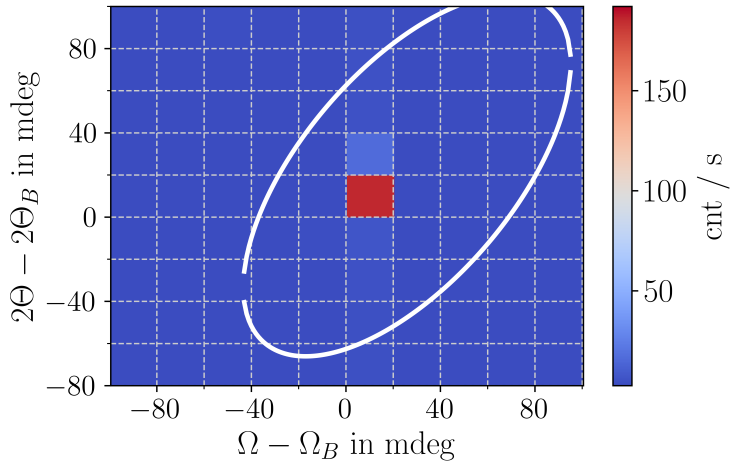

Figure 5.17: Rocking-curve map around the phasematching condition for XPDC at diamond's (400) orientation. The pump photon energy was set at $\hbar\omega_p = 11.216$ keV and detection proceeded at $\hbar\omega_s = 11.211$ keV—corresponding to idler photons of 5 eV. A white, solid line indicates the kinematically expected phasematching ellipse (cf. Figs. 5.13 and 5.15). The reference position at (0,0) is given by the elastic Bragg spot, which shows a visible remainder still. Notably, the characteristic scattering signature of XPDC is absent. [Image courtesy of Dr. Christina Bömer. The plot is equivalent to Fig. 8 of Ref. [51].]

The first—and most substantial—case for us to consider, is their claim of observing XPDC into idler photons in the optical regime (e.g., $\hbar\omega_i = 2.2 \ldots 4.4$ eV) using a diamond sample near a (220) reflection [47]. Their measurements reach count rates of 3000 counts/s (Fig. 3, ibid.[56]) and more (Fig. 4, ibid.), which the authors interpret as XPDC. These correspond to conversion efficiencies in excess of $\sim 10^{-10}$ and are thoroughly incompatible with our theoretical predictions for the given scenario.

As per our theory, the nonlinear response for diamond's (220) orientation does not differ dramatically from the (111) case, which we have analysed initially (cf. Sec. 5.2.1.a). At an idler photon energy of $\hbar\omega_i = 5$ eV, for instance, it amounts to $\left|\mathbf{K}_{GS\diamond}(0, \mathbf{G}_{(220)}, 0.184)\right|^2 / V_\diamond^2 \approx 2.9 \cdot 10^{-5}$. Using this value to repeat our estimate of Eq. (5.93) for this orientation, consequentially yields a theoretical conversion efficiency of merely $\sim 1.5 \cdot 10^{-15}$. This is, at least, *five orders of magnitude* smaller than their reported signal. Even if broader angular integration ranges were accounted for, this discrepancy could not be bridged.

We have spent significant effort—both theoretically and experimentally[57]—in order to resolve this discrepancy. Ultimately, this work culminated in the studies of Ref. [51], which we have discussed in the preceding section. Its results consistently point to much smaller count rates for XPDC.

While said study [51] provides a strong counter-indication to the claims of Shwartz and co-workers in itself, we want to extend our criticism by referencing an alternative interpretation of their 'signal' as well. This interpretation was put forward by Dr. Christina Bömer, who attempted to reproduce the findings of Shwartz and co-workers independently after participating in the measurements that led up

[56] Note that we shall refrain from reproducing any figures from the publications by Shwartz and co-workers in this work. Instead, we ask the reader to consult their data in its original context. In doing so, we seek to avoid misrepresentation of their results. We acknowledge with regret that this prevents quick, visual reference and apologize to the reader for this inconvenience. We emphasize, however, that we consider it to be instructive for any reader to acquire a first-hand impression of their work.

[57] We want to emphasize that the experimental work on this subject was primarily conducted by Dr. Christina Bömer. Large parts of it fall outside the scope of this treatise and can be reviewed from her monograph on 'Energy resolved diffraction for investigating x-ray parametric down-conversion' [75]. Nevertheless, we had the pleasure to join in later experimental campaigns and collaborated on the interpretation of some results.

to Ref. [47]. More so, she aimed to characterize the supposed XPDC signal and obtain its first two-dimensional rocking-curve map. The expected ellipse (cf. our discussion in Secs. 5.2.1.a and 5.2.1.b) would have allowed for an unequivocal identification of the down-conversion process. However, her measurements (accessible through Refs. [74, 75]) revealed linear streaks rather than the phasematching ellipse. On closer inspection, Dr. Bömer could explain these features in terms of elastic scattering, which produces background artefacts that are known from high-resolution x-ray diffraction (see, for instance, Refs. [173, 191]). Crucially, these streaks appear to coincide with the signals that Shwartz and co-workers have previously interpreted as XPDC. As such, their reports may likely be founded on a simple but fundamental misinterpretation.

Our subsequent study of Ref. [51] lends further credit to this hypothesis. Using a more refined setup, we could achieve much higher suppression of unwanted spectral components than before. As a result, the observable streaks shrank significantly—as would be expected for elastic scattering artefacts. At the same time, no evidence for XPDC could be found, even though the sensitivity of our setup ($\sim 10^{-11}$) would have covered the range reported by Shwartz and co-workers ($\gtrsim 10^{-10}$).

In a closing remark on this point, we want to note that Shwartz and co-workers have recently published further reportings on XPDC [192]. Besides claiming a dubious polarization dependence therein, they also comment on our preceding criticism. However, they remain adamant that any discrepancies would result from differences in the respective setups and that their findings of XPDC signals would indeed be valid. Most remarkable—if not ironic—about said publication is the fact that the authors *did* adopt our practise of plotting rocking-curve maps of the supposed signal (cf. Fig. 4 in Ref. [192]), whereby they find linear streaks instead of an XPDC-phasematching ellipse. Even though their plot clearly corroborates Dr. Bömer's interpretation of this 'signal' being just artefacts of elastic diffraction (recall Refs. [74, 75]), Shwartz and co-workers do not pursue any closer inspection.

Thus re-alarmed, we emphasize the need for independent reproduction of these measurements and caution against any efforts to build upon the results of Refs. [47–49, 55, 192] without prior scrutiny. Furthermore, we conclude that the first detection of parametric down-conversion from x-rays into the optical regime is—most likely—still outstanding and thus remains a challenge for future experiments to achieve.

In the following we shall briefly address three additional issues about the quoted reports, which appear questionable and call for dedicated criticism in our opinion:

Criticism on: Internal inconsistencies of earlier works In at least two cases, Shwartz and co-workers report on supposed XPDC signals in diamond, which show little to no dependence on changes in their energy-/phasematching settings. These can be found in Ref. [47], Fig. 4 and Ref. [55], Fig. 3 (a). In the former case, three instances of a 2θ-scan are presented, of which each is supposed to contain the XPDC signal for 2.2, 3.3 or 4.4 eV idler photons, respectively. Apart from variations in the strength of the residual Bragg peak, however, no significant change of the 'signal' is visible among them. This is particularly remarkable, as the authors super-impose plots of their theoretical expectations, which *do* change in position—both absolute and relative to the 'signal'.

The second example contains three—nominally different—analyzer scans, wherein the authors claim to measure XPDC at phasematching for three different idler photon energies (here: 30, 40 and 50 eV). Yet again, all three curves fall into the very same location, which is particularly obvious in this case, as

they are super-imposed directly[58].

Both reportings raise the question, why the signals—if they represented XPDC—should co-locate in the same place and shape, despite originating from a nonlinear process at considerably different phase-matching conditions. An interpretation of the signal as originating from other, linear scattering processes, on the other hand, would not necessarily suffer such inconsistencies.

Criticism on: Claim of XPDC-plasmon coupling In a separate publication [48], Shwartz and co-workers report on the parametric conversion of x-rays into the deep UV regime (i.e., involving idler photons of 28–54 eV). In addition to claiming the observation of XPDC in this regime, they claim, more specifically, to have found evidence for XPDC coupling to plasmons.

We shall not focus on their primary claim here, which we have reason to doubt in itself (viz., by extension of our previous arguments). Instead, we want to comment on the proposition that XPDC couples to plasmonic excitations from our theoretical vantage point. We deem this to be very unlikely, because the two phenomena involve mutually orthogonal types of coupling (transverse vs. longitudinal).

Expanding on this thought, we first recall from our fundamental derivation that any optical field couples to the electronic system via the $\mathbf{p}\cdot\mathbf{A}$-term of the interaction Hamiltonian (cf. Eq. (2.2)). In the coupling process, the inherently transverse nature of the electromagnetic field[59] is imprinted onto any electronic excitations, which is driven by it: A transverse field drives a transverse electronic current[60]. In the case of XPDC, this electronic current forms part of the nonlinear, current-density–density response function

$$\mathbf{P}_I(\mathbf{x}_1,t_1,\mathbf{x}_2,t_2) = \langle I|\,\hat{T}\left[\hat{\mathbf{p}}(\mathbf{x}_1,t_1)\,\hat{n}(\mathbf{x}_2,t_2)\right]|I\rangle \tag{5.94}$$

and its Fourier transform $\mathbf{K}_I$, which govern all of the wavemixing processes discussed in this work (cf. Chpt. 3 and Eq. (3.1) therein).

Plasmons[61], on the other hand, represent a longitudinally-coupled phenomenon [193]. They can be visualized as density oscillations of the (macroscopically homogeneous) electron gas of a solid. Their coupling is mediated directly through Coulomb-interaction along their line of propagation[62]. Prominent methods to excite such plasmons in bulk-materials rely on electron energy loss spectroscopy (EELS) or non-resonant x-ray Raman-scattering (i.e., IXS) [163, 194, 195], both of which probe an electronic *density–density* correlator and can in themselves be considered as longitudinally-exciting processes.

Given these fundamental differences, we reiterate our earlier assessment that we deem the coupling of XPDC to (bulk-)plasmon excitations to be very unlikely. Shwartz and co-workers could clarify this matter further, if they provided evidence that the measured phenomenon did indeed follow a plasmonic dispersion-relation—in addition to satisfying XPDC-phasematching.

[58] We note that Shwartz and co-workers do address this immobile peak, in that they conjecture, it may be the result of an underlying resonance. However, we doubt that this would invalidate phasematching. After all, phasematching dictates the position of the signal as a consequence of the fundamental principle of momentum-conservation. This should hold irrespective of any resonances—rendering their argument moot.

[59] We recall for completeness that propagating electromagnetic fields in vacuo (or inside 'simple' dielectric media) take on the form of transverse wave-fields. That is, their field vector is polarized perpendicular to their propagation direction, i.e., per each mode i, we have $\boldsymbol{\varepsilon}_i \perp \mathbf{k}_i$. In our framework of non-relativistic QED, we have made this circumstance particularly manifest through the choice of the Coulomb-gauge $\nabla\cdot\mathbf{A} = 0$.

[60] We remark for completeness that the inverse case is obviously also possible, i.e., an existing electronic current can couple to the electromagnetic field (or vacuum) thus emitting a photon rather than absorbing one. This photon will again be of transverse nature.

[61] We want to specify—as do Shwartz and co-workers in Ref. [48]—that we focus on bulk plasmons here.

[62] We note that a good analogy for such a longitudinal wave is the propagation of sound in air, namely the forward propagation of density/pressure modulations.

Criticism on: The extrapolation of nonlinear properties from the optical into the x-ray domain
In yet another publication, Shwartz and co-workers claim to have measured XPDC in Gallium-Arsenide (GaAs)—among other samples [49]. For its (111) orientation, they report an astonishing conversion efficiency of $\sim 10^{-6}$ for the XPDC process. This presents a dramatic increase compared to their own previous claim for XPDC in diamond (10^{-10}) [47] and exceeds even the measured efficiency of laser-driven wavemixing in diamond ($\sim 10^{-9}$, cf. Sec. 5.1). Shwartz and co-workers attribute the reported increase to a structural difference of GaAs over diamond, namely its lack of inversion symmetry. Motivating this proposition, they invoke an analogy with the all-optical regime. At optical frequencies, so-called 'second-order nonlinearities', which are responsible for SPDC or all-optical SFG/DFG, are known to vanish for inversion-symmetric materials (see Refs. [12–14] or similar).

However, this rule does no longer hold true at shorter wavelengths. As a matter of fact, it is only valid in conjunction with the dipole-approximation (cf. Ref. [13]) and relaxes as soon as the former loses its applicability. For x-ray-optical wavemixing, there is thus *no* reason to assume that the sample's inversion symmetry plays a relevant role—a priori.

Going beyond this general argument, we shall further review the proposition of Shwartz and co-workers against the backdrop of our theoretical XOWM framework. As we have derived this from first principles, its description of XPDC naturally takes the symmetry of the sample into account. Specifically, it does so via the nonlinear response functions $\mathbf{K}_I$ (cf. Chpt. 3): Should the inversion symmetry of diamond versus the lack thereof in GaAs imply different XPDC signal strenghts, this would be reflected in their respective magnitudes of the nonlinear response function. We will therefore proceed to compare $\mathbf{K}_I$ for both materials on the prominent (111) reciprocal component.

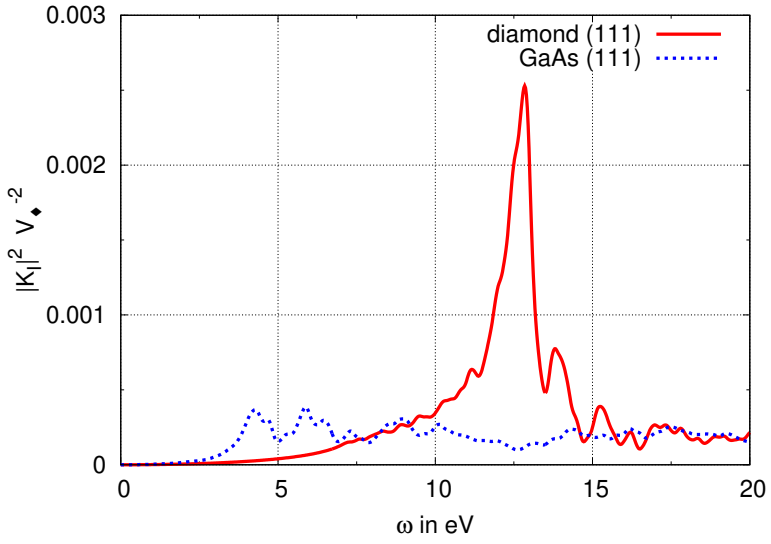

Figure 5.18: Comparison of the nonlinear response function $\mathbf{K}_I$ at the (111) orientation for diamond (red, solid line) and GaAs (blue, dashed line).

Based on Kohn-Sham DFT calculations[63], which incorporated the crystal symmetry in the construc-

[63] We note for completeness that both DFT calculations were performed with ABINIT [106] using simple LDA exchange. Both employed the norm-conserving pseudopotentials, which were standard for their atomic sub-species in ABINIT in 2020. The plane-wave basis was limited by an energy cut-off at 15 a.u.. For both crystals, the (cubic) unit cell sizes were fixed to their literature value, i.e., 6.741 a.u. for diamond and 10.6831 a.u. for GaAs. In processing the resulting band-structures with `MyLiO.x`, we implemented individual 'scissor' corrections—thereby approximating more realistic values for the respective band gaps. For diamond, the correction was taken to be $\Delta E = 0.062$ a.u. (~ 1.7 eV) adopted from Ref. [111] and for GaAs $\Delta E = 0.029$ a.u. (~ 0.8 eV) adopted from Ref. [196].

tion of their basis sets, we compute spectral outlines of the nonlinear response using our `MyLiO.x` program. The results are plotted in Fig. 5.18, with the diamond case given as a red, solid line and GaAs represented by the dashed, blue curve. Notably, both show comparable strengths at the marks of 10 eV and 20 eV, which are two points reported by Shwartz and co-workers in Ref. [49].

In conclusion, we see no indication that XPDC signals should prove (significantly) stronger in GaAs than in diamond[64]. By extension, we disagree decidedly with the more general proposition by Shwartz and co-workers that the inversion symmetry of a material would influence their nonlinear response properties for XOWM. There is neither a valid, general rule that would support this hypothesis nor do our explicit simulations back this claim for the particular case at hand.

We shall close our criticism by recalling that a characteristic signature of XPDC should be mapped out, in order to provide solid evidence of the nonlinear effect. Individual, selective measurements of photons being transmitted through a detuned analyser, on the other hand, are insufficient to prove down-conversion. We emphasize the importance of this identification especially in view of relatively strong, coincident background effects. Crucially, all of the aforementioned publications by Shwartz and co-workers fail to provide this essential evidence.

5.2.3 XPDC (far) above the band gap

As a second scenario for XPDC, we shall investigate the conversion effect far above the band gap of the sample. That is, we assume the idler photon's energy to range above any valence excitations and, moreover, to be non-resonant with any 'other' transitions admitted by the material's electronic structure. This regime of XPDC has been studied intensively by Tamasaku et al. [50, 113, 114] and thus promised to provide a good benchmark for our theory. More recently still, we succeeded in characterizing this conversion regime ourselves in two experimental campaigns (proposals No. HC-4489 and HC-4907) at beamline ID20 of the European Synchrotron Radiation Facility (ESRF) [181]. These measurements achieved the first angular-resolved view of circular XPDC scattering patterns—including the resolution of the aforementioned side-lobes ('bananas'). As such, they provide a reference that is unprecedented in its quality and shall form the guideline for our theoretical narrative.

Aiming to evaluate our theory in the outlined regime, we can resort to our earlier work and adapt it. In particular we may start out from the scattering-expression (5.76) and merge it with the effective flux model of Eq. (5.78) to arrive at Eq. (5.80), as we saw earlier:

$$\begin{aligned}\frac{dP_{\mathrm{XPDC}}(\mathbf{k}_s)}{d\Omega_s d\omega_s} = \Big(\frac{d\sigma}{d\Omega_f}\Big)_{\mathrm{Th}} \frac{\omega_s}{\omega_{p0}} \frac{2\,\alpha\, l_w N_{\mathrm{ph}}\, \delta_p^x\, \delta_p^y}{(2\pi)^{3/2}\,\Omega_p} \int d^3k_i \int d\omega_i\; \delta(\omega_s-\omega_i-c\,|\mathbf{k}_s-\mathbf{k}_i-\mathbf{G}|) \\ \times e^{-(\omega_s-\omega_i-\omega_{p0})^2/2\Omega_p^2}\; e^{-(k_s^x-k_i^x-G^x)^2(\delta_p^x)^2/2}\; e^{-(k_s^y-k_i^y-G^y)^2(\delta_p^y)^2/2} \\ \times \mathrm{Im}\Big(\frac{-4}{\omega_i^2\,\alpha^2\,\tilde{\varepsilon}(|\omega_i|)-|\mathbf{k}_i|^2}\Big)\; \frac{1}{V_\diamond^2}\Big(\,|\mathbf{K}_{GS\diamond}(0,\mathbf{G},\omega_i)|^2\; - |\mathbf{k}_i\cdot\mathbf{K}_{GS\diamond}(0,\mathbf{G},\omega_i)|^2/\,|\mathbf{k}_i|^2\Big).\end{aligned} \tag{5.95}$$

From here on, our derivation will diverge (slightly) from the path of Sec. 5.2.1. Given that the

[64] We add as a sidenote that we have evidence for the contrary, namely the XPDC signal in GaAs being weaker than in diamond, effectively. This is mainly caused by the much stronger absorption of x-rays in GaAs, which prevents illumination-depths on par with large diamond samples. We have observed this disadvantage of GaAs for XPDC at idler energies of $\hbar\omega_i \approx 100$ eV in measurements at the ESRF.

idler photon's energy is now assumed to range *above* the threshold for valence-excitations, it can suffer losses from absorption. Consequentially, it is no longer possible to rephrase the dispersion-term, i.e., Im(...), within Eq. (5.95) into the δ-function of a virtually transparent medium (cf. our reasoning at Eq. (5.81)). Instead, we will maintain its form for the moment and concentrate on simplifying other aspects of Eq. (5.95).

First of all, we impose our knowledge that the correlation function $\mathbf{K}_{GS\diamond}(0,\mathbf{G},\omega_i)$ does not exhibit much spectral structure (far) above valence excitations[65]. Ergo, we can assume it to be roughly constant around its value of $\omega_{i0} = \omega_s - \omega_{p0}$. At this point, we want to recall, once again, that our model entails *negative* idler photon energies by convention. Apart from its peculiar looks, this has no adverse consequences (cf. also discussion in Sec. 5.2.1).

As the next step for simplification, we address the exponentials, which constrain $\mathbf{k}_i^\perp$. These are very narrow on the scale of all involved momenta. As such, we can reasonably well approximate them with straight-forward δ-functions, like:

$$\frac{\delta_p^x}{\sqrt{2\pi}}\, e^{-(k_s^x - k_i^x - G^x)^2 (\delta_p^x)^2/2} \approx \delta(k_s^x - k_i^x - G^x). \tag{5.96}$$

In this—and the analogous step for the y-component—we have to bear in mind the proper normalization.

Finally, it would be convenient to convert the δ-function that represented the x-rays' dispersion relation, into a shape, where it directly impacts longitudinal momentum components. To this end, we recall from our appendix A.9 the relation Eq. (A.89):

$$\delta(\omega - c\,|\mathbf{k}|) = \delta(k^\shortparallel - k_0^\shortparallel)\,\frac{|\mathbf{k}|}{c k_0^\shortparallel} \approx \alpha\,\delta(k^\shortparallel - k_0^\shortparallel) \tag{5.97}$$

with $k_0^\shortparallel = \sqrt{\omega^2/c^2 - (\mathbf{k}^\perp)^2}$ for 'forward'-propagating pump-beam.

Combining all of the above, we find

$$\begin{aligned}\frac{dP_{\mathrm{XPDC}}(\mathbf{k}_s)}{d\Omega_s d\omega_s} \approx \Big(\frac{d\sigma}{d\Omega_f}\Big)_{\mathrm{Th}} \frac{\omega_s}{\omega_{p0}}\,\frac{2N_{ph}\,\alpha^2\,l_w}{\sqrt{2\pi}\,\Omega_p}\int d\omega_i \int d^3k_i\; e^{-(\omega_s-\omega_i-\omega_{p0})^2/2\Omega_{p0}^2} \\ \times\,\delta^2(-\mathbf{k}_i^\perp + \mathbf{k}_s^\perp - \mathbf{G}^\perp)\;\delta(-k_i^\shortparallel + k_s^\shortparallel - G^\shortparallel - k_0^\shortparallel) \\ \times\,\mathrm{Im}\Big[\frac{-4}{\omega_i^2\,\alpha^2\,\varepsilon(|\omega_i|) - |\mathbf{k}_i|^2}\Big]\;\frac{1}{V_\diamond^2}\;\Big(|\mathbf{K}_\diamond(0,\mathbf{G},\omega_{i0})|^2 - |\mathbf{k}_i\cdot\mathbf{K}_\diamond(0,\mathbf{G},\omega_{i0})|^2/\,|\mathbf{k}_i|^2\Big),\end{aligned} \tag{5.98}$$

where $k_0^\shortparallel = \sqrt{(\omega_s-\omega_i)^2/c^2 - (-\mathbf{k}_i^\perp + \mathbf{k}_s^\perp - \mathbf{G}^\perp)^2}$. Once, we make use of all δ-constraints, we can fix $\mathbf{k}_i$ in all of its components:

$$\mathbf{k}_{i0}^\perp = \mathbf{k}_s^\perp - \mathbf{G}^\perp \quad \text{and} \tag{5.99}$$

$$k_{i0}^\shortparallel = k_s^\shortparallel - G^\shortparallel - \alpha(\omega_s - \omega_i) \approx k_s^\shortparallel - G^\shortparallel - \alpha\,\omega_{p0} \tag{5.100}$$

as would be dictated by kinematical momentum conservation. In this, our results are the same as before, in fact. Even if we feed these simplifications back into our scattering probability, we are very close to

[65] We recall that in the spectral region above ~ 30 eV, the nonlinear response function for diamond is approximated quite accurately by Freund's model (cf. Sec. 3.2.2) actually. Its only spectral structure is a monotonic $1/\omega_i$-type decline. Similarly, $\mathbf{K}_{GS\diamond}(0,\mathbf{G},\omega_i)$ will be slowly varying in other materials, as long as ω_i is sufficiently far off any resonant structure.

the earlier Eq. (5.89). The main difference is in the remaining integral in ω_i:

$$\frac{dP_{\mathrm{XPDC}}(\mathbf{k}_s)}{d\Omega_s d\omega_s} \approx \left(\frac{d\sigma}{d\Omega_f}\right)_{\mathrm{Th}} \frac{\omega_s}{\omega_{p0}} \frac{2N_{ph}\,\alpha^2\,l_w}{\sqrt{2\pi}\,\Omega_p} \frac{1}{V_\diamond^2} \left(|\mathbf{K}_\diamond(0,\mathbf{G},\omega_{i0})|^2 - |\mathbf{k}_{i0}\cdot\mathbf{K}_\diamond(0,\mathbf{G},\omega_{i0})|^2 / |\mathbf{k}_{i0}|^2 \right) \times \int d\omega_i\, e^{-(\omega_s-\omega_i-\omega_{p0})^2/2\Omega_{p0}^2}\, \mathrm{Im}\left[\frac{-4}{\omega_i^2\,\alpha^2\,\varepsilon(|\omega_i|) - |\mathbf{k}_{i0}|^2}\right], \tag{5.101}$$

In the following, we will show that this integral is basically the convolution of a Gaussian with a (relativistic) Breit-Wigner profile and may be simplified into a so-called Voigt-profile for our case. To see this, we first approximate the dielectric function within the imaginary-part expression as slowly varying with energy. This step rests on the same arguments that we have invoked before when simplifying $\mathbf{K}_{GS\diamond}(0,\mathbf{G},\omega_i) \to \mathbf{K}_{GS\diamond}(0,\mathbf{G},\omega_{i0})$. Applied to $\varepsilon(|\omega_i|) \to \varepsilon(|\omega_{i0}|)$, we can rewrite

$$\mathrm{Im}\left[\frac{-4}{\omega_i^2\,\alpha^2\,\varepsilon(|\omega_i|) - |\mathbf{k}_{i0}|^2}\right] \approx \mathrm{Im}\left[\frac{-4}{\omega_i^2\,\alpha^2\,\varepsilon(|\omega_{i0}|) - |\mathbf{k}_{i0}|^2}\right] = \frac{4\,\varepsilon_i\,\omega_i^2\alpha^2}{(\omega_i^2\alpha^2\varepsilon_r - |\mathbf{k}_{i0}|^2)^2 + (\alpha^2\omega_i^2\varepsilon_i)^2}, \tag{5.102}$$

where we have used the abbreviation $\varepsilon_r = \mathrm{Re}[\varepsilon(|\omega_{i0}|)]$ and $\varepsilon_i = \mathrm{Im}[\varepsilon(|\omega_{i0}|)]$, respectively. We proceed to reformulate

$$\begin{aligned}
\frac{4\,\varepsilon_i\,\omega_i^2\alpha^2}{(\omega_i^2\alpha^2\varepsilon_r - |\mathbf{k}_{i0}|^2)^2 + (\alpha^2\omega_i^2\varepsilon_i)^2} &= \frac{4\,\varepsilon_i}{\alpha^2\,\varepsilon_r^2} \frac{\omega_i^2}{(\omega_i^2 - \underbrace{c^2\,|\mathbf{k}_{i0}|^2/\varepsilon_r}_{\bar\omega^2})^2 + (\omega_i^2\varepsilon_i/\varepsilon_r)^2} \\
&= \frac{4\,\varepsilon_i}{\alpha^2\,\varepsilon_r^2} \frac{\omega_i^2}{((\omega_i-\bar\omega)(\omega_i+\bar\omega))^2 + (\omega_i^2\varepsilon_i/\varepsilon_r)^2} \\
&\approx \frac{4\,\varepsilon_i}{\alpha^2\,\varepsilon_r^2} \frac{\bar\omega^2}{((-2\bar\omega)(\omega_i+\bar\omega))^2 + (\bar\omega^2\varepsilon_i/\varepsilon_r)^2} \\
&= \frac{\varepsilon_i}{\alpha^2\,\varepsilon_r^2} \frac{1}{(\omega_i+\bar\omega)^2 + (\bar\omega\varepsilon_i/2\varepsilon_r)^2}.
\end{aligned} \tag{5.103}$$

Herein, we have identified the two possible roots $\pm\bar\omega$, of which only the negative one is relevant at this point (recall our convention that $\omega_i < 0$ for XPDC). Furthermore, we note that we will be interested only in a small range of frequencies ω_i around the value of $\bar\omega$. Thus, we can quite safely approximate the non-resonant term with a constant value. The above already sports the appearance of a Lorentzian; subsequently, we shall re-insert this into its convolution with the Gaussian energy distribution from Eq. (5.101)

$$\begin{aligned}
&\int d\omega_i\, e^{-(\omega_s-\omega_i-\omega_{p0})^2/2\Omega_p^2}\, \mathrm{Im}\left[\frac{-4}{\omega_i^2\,\alpha^2\,\varepsilon(|\omega_i|) - |\mathbf{k}_{i0}|^2}\right] \\
\approx &\int d\omega_i\, e^{-(\omega_s-\omega_i-\omega_{p0})^2/2\Omega_p^2}\, \frac{\varepsilon_i}{\alpha^2\,\varepsilon_r^2} \frac{1}{(\omega_i+\bar\omega)^2 + (\bar\omega\varepsilon_i/2\varepsilon_r)^2} \\
= &\int d\omega_i\, e^{-(\omega_s+\omega_i-\omega_{p0})^2/2\Omega_p^2}\, \frac{\varepsilon_i}{\alpha^2\,\varepsilon_r^2} \frac{1}{(\omega_i-\bar\omega)^2 + (\bar\omega\varepsilon_i/2\varepsilon_r)^2}.
\end{aligned} \tag{5.104}$$

In the final step, we have switched the sign of the integration variable $\omega_i \to -\omega_i$, in order to ease the following identification: The convoluted expression we find in Eq. (5.104) is simply a Voigt profile:

$$V(x;\sigma,\gamma) = \int dx'\, \frac{1}{\sigma\sqrt{2\pi}}\, e^{-(x')^2/2\sigma^2}\, \frac{\gamma/\pi}{(x-x')^2+\gamma^2}. \tag{5.105}$$

More specifically adapted to our case, this reads

$$\begin{aligned}&\int d\omega_i e^{-(\omega_s+\omega_i-\omega_{p0})^2/2\Omega_p^2}\ \frac{\varepsilon_i}{\alpha^2\,\varepsilon_r^2}\,\frac{1}{(\omega_i-\bar{\omega})^2+(\bar{\omega}\varepsilon_i/2\varepsilon_r)^2}\\ =&\frac{\Omega_p\sqrt{2\pi}\,2\pi}{\alpha\sqrt{\varepsilon_r}\,|\mathbf{k}_{i0}|}\,V((\omega_s+\bar{\omega}-\omega_{p0});\Omega_p,\bar{\omega}\varepsilon_i/2\varepsilon_r).\end{aligned}\tag{5.106}$$

Using this, within our scattering expression for XPDC, finally, yields

$$\begin{aligned}\frac{dP_{\mathrm{XPDC}}(\mathbf{k}_s)}{d\Omega_s d\omega_s}\approx&\left(\frac{d\sigma}{d\Omega_f}\right)_{\mathrm{Th}}\frac{\omega_s}{\omega_{p0}}\frac{4\pi N_{ph}\,\alpha\,l_w}{\sqrt{\varepsilon_r}\,|\mathbf{k}_{i0}|}\frac{1}{V_\diamond^2}\left(|\mathbf{K}_\diamond(0,\mathbf{G},\omega_{i0})|^2-|\mathbf{k}_{i0}\cdot\mathbf{K}_\diamond(0,\mathbf{G},\omega_{i0})|^2/|\mathbf{k}_{i0}|^2\right)\\ &\times V((\omega_s+\bar{\omega}-\omega_{p0});\Omega_p,\bar{\omega}\varepsilon_i/2\varepsilon_r).\end{aligned}\tag{5.107}$$

As a brief reminder, the occurring abbreviations are: $\bar{\omega}=c\,|\mathbf{k}_{i0}|/\varepsilon_r$, $\varepsilon_r=\mathrm{Re}[\varepsilon(|\omega_{i0}|)]$ and $\varepsilon_i=\mathrm{Im}[\varepsilon(|\omega_{i0}|)]$. In addition, the components of $\mathbf{k}_{i0}$ are fixed through phasematching as:

$$\mathbf{k}_{i0}^{\perp}=\mathbf{k}_s^{\perp}-\mathbf{G}^{\perp}\qquad\text{and}\qquad k_{i0}^{\shortparallel}=k_s^{\shortparallel}-G^{\shortparallel}-\alpha\,\omega_{p0}\tag{5.108}$$

Connection to low-energy case of XPDC Notably, our above result has the same structure as our earlier scattering expression (5.89) from Sec. 5.2.1

$$\begin{aligned}\frac{dP_{\mathrm{XPDC}}(\mathbf{k}_s)}{d\Omega_s d\omega_s}=&\left(\frac{d\sigma}{d\Omega_f}\right)_{\mathrm{Th}}\frac{\omega_s}{\omega_{p0}}\,\frac{4\pi\,\alpha\,l_w N_{\mathrm{ph}}}{n_{\mathrm{eff}}\,|\mathbf{k}_{i0}|}\,\frac{1}{\Omega_p\sqrt{2\pi}}e^{-(\omega_s+\frac{c}{n_{\mathrm{eff}}}|\mathbf{k}_{i0}|-\omega_{p0})^2/2\Omega_p^2}\\ &\times\frac{1}{V_\diamond^2}\left(|\mathbf{K}_{GS\diamond}(0,\mathbf{G},-c\,|\mathbf{k}_{i0}|/n_{\mathrm{eff}})|^2-|\mathbf{k}_{i0}\cdot\mathbf{K}_{GS\diamond}(0,\mathbf{G},-c\,|\mathbf{k}_{i0}|/n_{\mathrm{eff}})|^2/|\mathbf{k}_{i0}|^2\right).\end{aligned}\tag{5.109}$$

This similarity is unsurprising, given that these two situations basically describe very similar physics. Namely, XPDC at an idler energy that is sufficiently far away from material resonances, in order for $\mathbf{K}_{GS\diamond}(0,\mathbf{G},\omega)$ to be a slowly varying function. Their distinguishing feature is the absence of absorption (of the idler photon) below the band gap. If we were to impose the same onto Eq. (5.107), i.e., prescribing $\varepsilon_i\to 0$, we would find the same result. In this case, we can simplify the Lorentzian within the Voigt-profile into a δ-function:

$$\lim_{\gamma\to 0}\frac{\gamma/\pi}{(x-x')^2+\gamma^2}=\delta(x-x')\qquad\Rightarrow\qquad\lim_{\gamma\to 0}V(x;\sigma,\gamma)=\frac{1}{\sigma\sqrt{2\pi}}\,e^{-(x)^2/2\sigma^2}\tag{5.110}$$

Thereby, its remainder reduces to a Gaussian and correspondingly Eq. (5.107) reduces directly to Eq. (5.109)—with $\sqrt{\varepsilon_r}=n_{\mathrm{eff}}$ as we would expect[66].

[66] We note for practical application: The `scipy`-implementation of Voigt-profiles seems to handle small (vanishing) γ well. As such, the more general routine from the high energy regime may be applied for the low-energy cases, too.

5.2.3.a Experimental results and numerical comparison

With positive validation of our theory on XPDC still pending at optical idler photon energies, we have, separately, attempted to detect parametric conversion of x-rays into XUV photons in the meantime. For this regime, there was reliable evidence established by Dr. Kenji Tamasaku and co-workers that scattered x-ray photons could, in fact, be detected, which were compatible with expectations for XPDC in many respects. Specifically, this concerned XPDC in the non-resonant, high-frequency limit, featuring ~ 100 eV idler photons [50, 113–115].

Notably though, the results of Tamasaku and co-workers covered only a restricted angular range of phasematching parameters, as they focused their measurements on the 'outer edge' of the phasematching ellipse. In this, they chose the region of scattering space that is furthest removed from the elastic Bragg-condition[67]. We illustrate their situation below in Fig. 5.19.

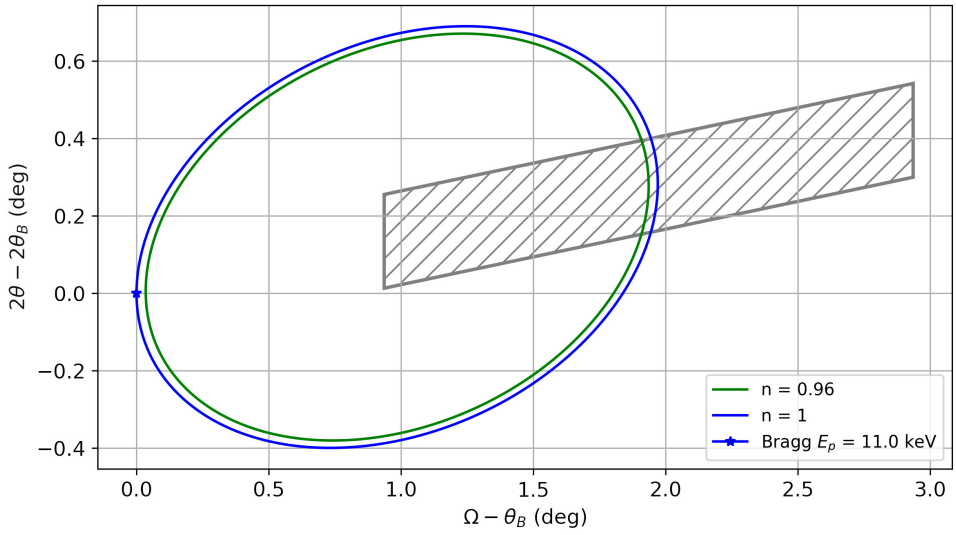

Figure 5.19: Illustration of the parameter range studied by Tamasaku and co-workers for parametric down-conversion of 11.0 keV x-rays into 100 eV idler photons: We show the complete phasematching ellipse for XPDC (green, solid line), while superimposing the scanned range of Refs. [113, 114] as a grey, hatched parallelogram. As an angular reference, we use the elastic Bragg-spot at $\theta_B^{(111)} = 15.883^\circ$ for the pump photon energy, respectively. For completeness, we note that phasematching for XPDC is expected to include refractive effects (cf. Eq. (5.107)). Nevertheless, we indicate a simplified version using $n = 1$ as well (blue, solid line).

Here, the phasematching ellipse for down-conversion into ~ 100 eV idler photons (green, solid line) is given relative to the regular Bragg-condition—the latter being marked by a blue star. The full solution of the phasematching problem takes corrections of the refractive index into account, while a reference pattern at $n = 1$ is likewise shown (blue, solid line). Finally, we indicate the angular range covered during the scans of Refs. [113, 114] by a grey, hatched parallelogram[68]. It is immediately apparent from this illustration that the approach of Tamasaku and co-workers could probe only a minute fraction of the phasematching ellipse. Moreover, their setup was integrating across both scattering angles 2θ and χ and thus lacked any resolving power that would be required to investigate two-dimensional patterns as predicted earlier (cf. Fig. 5.14 in Sec. 5.2.1.b).

[67] We note that the Bragg condition for Tamasaku's setting, i.e., using incident pump photons at an energy of $\hbar\omega_p = 11.0$ keV, the nominal Bragg angle would be $\theta_B^{(111)} = 15.883^\circ$ for a diamond (111) reflection.

[68] We note that the extent of this parallelogram was constructed on the basis of the published scan range $\sim \pm 1^\circ$ (horizontally) [113, 114] as well as a defining aperture of $\sim 0.242^\circ$ (vertically, i.e., in 2θ) [114] [augmented via private communications by Dr. Kenji Tamasaku]. The slope of the parallelogram follows the angular prescription given below Eq. (2) in Ref. [113].

In contrast, our own experiments in this regime have pioneered a new, angularly resolving setup for XPDC-studies. This setup has been implemented and refined throughout two experimental campaigns at the ESRF (proposals No. HC-4489 and HC-4907)—once again led by Dr. Christina Bömer[69]—using the x-ray Raman spectrometer at beamline ID20 [181]. At its core, the setup makes use of a single, spherically-bent crystal analyser as previously described in Sec. 5.1.3. Crucially, we have employed this analyser in an asymmetric configuration, for which the source-point was located on the Rowland circle but the detection plane was not (in contrast to Fig. 5.8 earlier). Instead, the latter was shifted inside the Rowland-circle, such that the XPDC-cone—after being reflected off the analyser—intersects the detector plane and is imaged at a *finite* diameter. We attach a sketch of the overall experimental setup below for further illustration (Fig. 5.20).

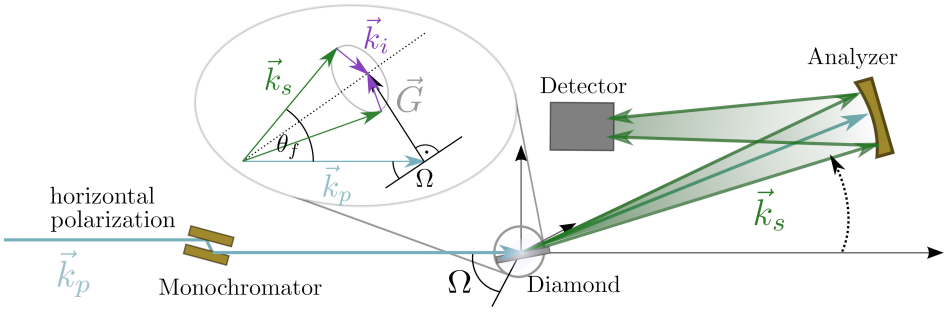

Figure 5.20: Illustration of the bent-analyser-based setup used at ID20: A monochromatised x-ray beam ($\mathbf{k}_p$) scatters vertically off a diamond sample. If adjusted for the phase-matching condition (see inset), an XPDC signal cone ($\mathbf{k}_s$) is generated, besides background scattering, and can be captured by the bent-analyser. Discriminated for its energy, the XPDC-cone (green arrows) is reflected towards the detector, where its cross section is imaged. Note: In the actual experiment (HC-4907), the analyser deflected horizontally. [Image courtesy of Dr. Christina Bömer]

It shows a diamond sample in reflection geometry (close to the symmetric (111) Bragg-condition), which is illuminated by a monochromatised x-ray 'pump' beam ($\mathbf{k}_p$). If the phasematching condition for XPDC—which is recounted in the figure's inset—is satisfied, a cone of XPDC signal photons ($\mathbf{k}_s$) is emitted from the sample. Once this signal reaches the bent analyser, it is energetically filtered, i.e., concurrent background at photon energies other than $\hbar\omega_s = \hbar\omega_p - 100$ eV is suppressed. The remaining signal is reflected towards the detector, where the cone of signal photons is imaged, before it could re-converge into a point. We note that—for the sake of two-dimensional depiction—we show the analyser's deflection (i.e., dispersive direction) to be vertical. However, in the actual setup of experiment HC-4907, we have used a horizontally deflecting analyser to detect the data shown below.

This setup allowed us to map out the two-dimensional scattering patterns of XPDC, which we have predicted before in Secs. 5.2.1.a and 5.2.1.b. Transferring these predictions to the regime of high idler-photon energies, i.e., employing Eq. (5.107), we can simulate the corresponding two-dimensional distributions of signal photons for the case at hand. To this end, we shall make use of our PYTHON-package: `XPyDC` again. Therein, we have implemented another, dedicated, subroutine for treating the high-energy dispersion. The nonlinear response function needed for these simulations was obtained in the high-frequency limit as described in Sec. 3.2.2. A first, exemplary result for the simulated scattering patterns

[69] We note that, similar to previously described experiments, the efforts involved here extended far beyond the scope of our own work—and beyond the scope of this thesis, in particular. Besides the invaluable collaboration with Dr. Christina Bömer in planning, organizing and conducting the experiment, we gratefully acknowledge the immense help and continuous inspiration provided by Dr. Blanka Detlefs and Dr. Christoph Sahle at the ID20, as well as Dr. Simo Huotari remotely. During the second campaign, our measurement efforts were further supported by Fridtjof Kerker and Dr. Maria Weseloh.

can be found in Fig. 5.21.

The defining beam parameters for the x-ray field—both for the simulation and for the subsequent experiment—are summarized in Tab. 5.8.

	experimental value	parameter in a.u.
photon energy	9.787 keV	$\omega_{p0} = 360$
monochromator passwidth	1 eV (FWHM)	$\Omega_m = \Omega_p = 0.016$
average photon 'flux'	$5 \cdot 10^{13}$ photons/s [181]	$N_{\mathrm{ph}} = 5 \cdot 10^{13} \times t_{\mathrm{exposure}}$
beam divergence	$\sim 150\ \mu$rad	$\delta_p = 7.31 \cdot 10^3$

Table 5.8: X-ray beam parameters for XPDC measurements at ID20

Regarding the sample, we have used a ~ 1.1 mm thick specimen of diamond that featured a (111)-cut surface. Its Bragg-angle for the (111) reflection at 9.787 keV amounts to $\theta_B^{(111)} = 17.914°$, which is rather shallow. This results, in turn, in a long projection of the sample's depth along the beam-path, namely ~ 3.6 mm. Given that this exceeds the absorption-length at the 'pump' photon energy, i.e., $l_{\mathrm{abs}} \approx 1.2$ mm, though, we shall rather consider the latter to delimit our effective sample length.

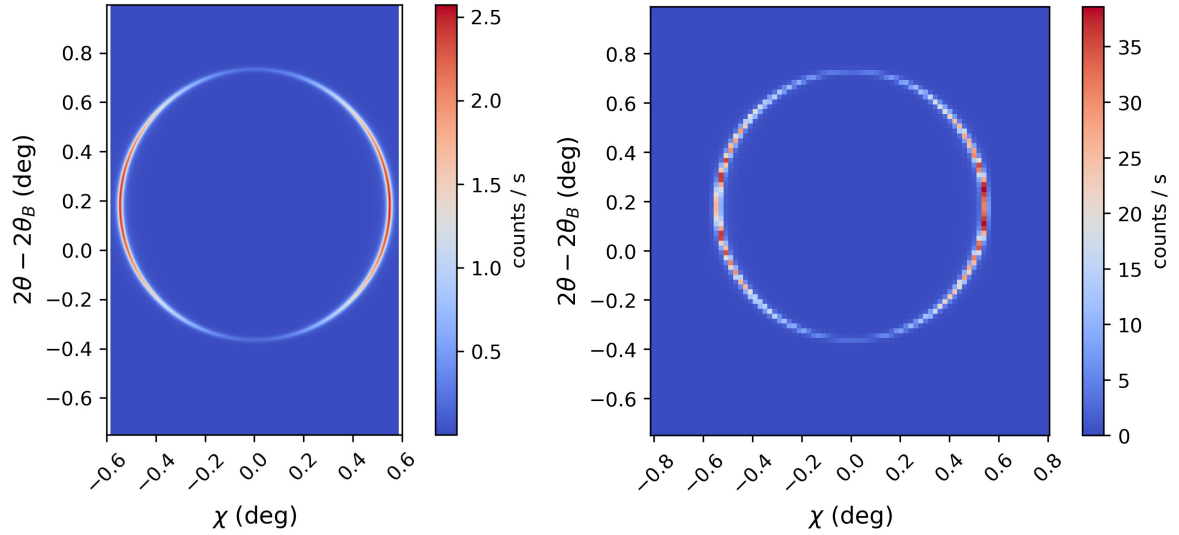

Figure 5.21: Simulated scattering patterns for XPDC at a rocking angle of $\Omega - \Omega_B = 1.0°$. For the numerical evaluation of Eq. (5.107), we have employed an angular grid at 5 mdeg pixel-spacing (a) and interpolated the observable pattern to the experimental rasterization of 20 mdeg later on (b). Using the beam parameters of Tab. 5.8, we can provide absolute count-rate estimates for the corresponding experiment. The energy acceptance on the detection side was approximated as a Gaussian window of 1.5 eV (FWHM).

Our first numerical result (Fig. 5.21) agrees well with earlier findings; the XPDC pattern is circular with an additional modulation on top. We present two versions of the same scattering scenario (i.e., sample is set for phasematching at $\Omega - \Omega_B = 1.0°$): First in Fig. 5.21 (a), we provide a fine-grained picture on an angular grid of 5 mdeg pixel-spacing, which was used for the simulation intrinsically. Second, we interpolate this to a coarser pixel size of 20 mdeg, which corresponds to the experimental situation. In both cases, we have assumed the energy acceptance of the detection setup to span 1.5 eV (FWHM), in accordance with Ref. [181], and approximated the analyser's transmission function by a Gaussian of unit peak-transmissivity.

In the next step, we shall compare our simulations to the experimental findings. These come in the form of Fig. 5.22, which has kindly been provided to us by Dr. Christina Bömer.

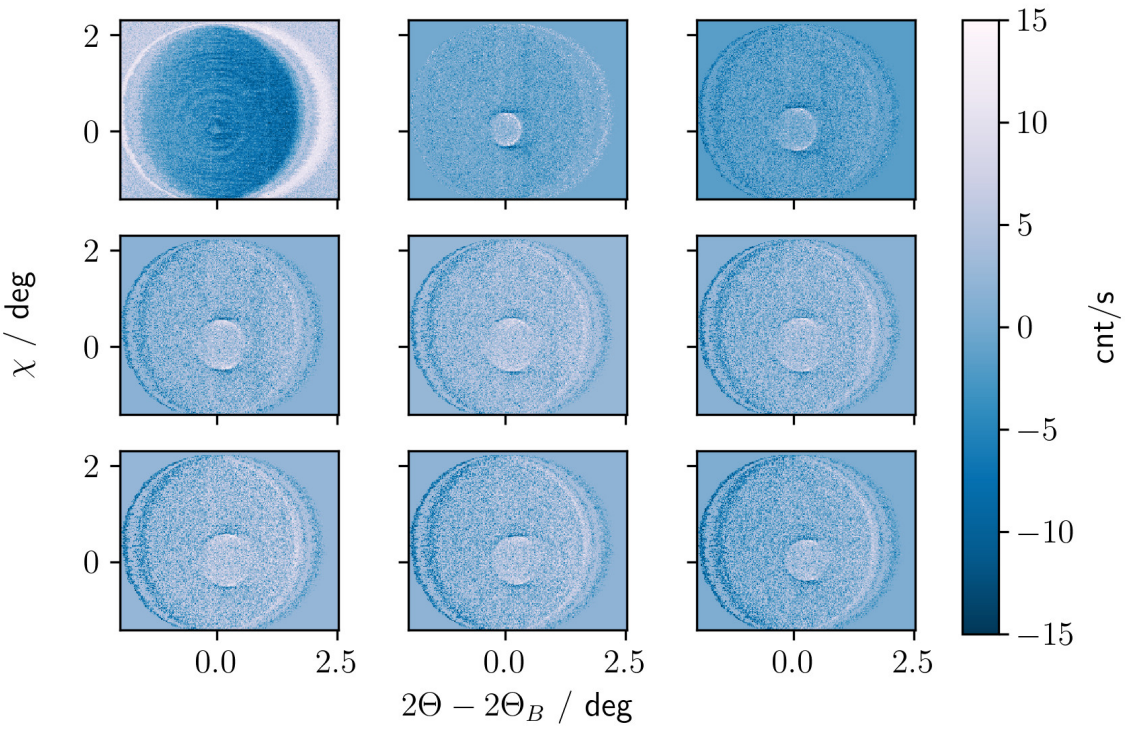

Figure 5.22: Compilation of nonlinear scattering patterns as recorded in experiment HC-4907 at ID20 (ESRF). At a pump energy of $\hbar\omega_p = 9.787$ keV and idler photon setting (i.e., energy loss) of $\hbar\omega_i = 100$ eV, the series of images covers several phasematching positions of the sample: From top left to bottom right, these traverse $\Omega - \Omega_B = 0.2^\circ$ up to 1.8° in steps of 0.2°. All images have been corrected for background scattering by subtracting a reference image from outside the phasematching condition. The contrast in the first image is insufficient to discern the nonlinear scattering signal. [Image courtesy of Dr. Christina Bömer]

In this series of pictures, we see the observable scattering patterns at several different phasematching positions of the sample: From top left to bottom right, these traverse $\Omega - \Omega_B = 0.2^\circ$ up to 1.8° in steps of 0.2°. Thus, the center-most image corresponds to $\Omega - \Omega_B = 1.0^\circ$ and can directly be compared to Fig. 5.21. We note that the experimental images appear rotated by 90 degrees (i.e., their 2θ-axis lies horizontally) as well as flipped in χ compared to Fig. 5.21. All images have been corrected for background scattering by subtraction of a reference image that was taken outside the phasematching ellipse, i.e., an image containing only homogeneous background from (inelastic) scattering.

In each of the above sub-plots, we can identify a large circular shape—which marks the (difference-) image of the complete analyser surface—as well as a smaller circular signature in the center of eight of these plots. The latter is the nonlinear scattering pattern and appears indeed in the position expected from XPDC-phasematching. For comparison, we give a plot of the corresponding theoretical simulations in the subsequent Fig. 5.23. From this comparison, we can draw four remarkable observations:

1. The positions of the individual scattering patterns (circular signatures) from the experiment agree very well with the corresponding predictions for XPDC based on our theory. Even though the diameter of the circles appears to expand and contract slightly more rapidly in the theoretical

simulations[70].

2. The scattering patterns do indeed exhibit the modulation around the circle, which we have expected from our earlier simulations and reasoning (cf. Sec. 5.2.1.b). In particular, we are able to identify well-visible XPDC side-lobes (i.e., 'bananas'[71]).

3. In stark contrast to our simulation, the experimental signature exhibits not *one* but strictly *two* circular features. More specifically, there appears a positive as well as a negative[72] pattern—concentrically aligned.

4. Apart from this qualitative difference, which is certainly significant, we note with some surprise that our theory is, nevertheless, in good quantitative agreement with the absolute scale of the effect. While the experiment shows a swing in count rates from -15 to $+15$ counts/s, the maximal value that our theory predicts ranges around ~ 35 counts/s.

Of all these observations, the alternating scattering signatures ($\pm$) are certainly the most intriguing feature. We note for reference that indications of this behaviour have been found before as well. In fact, Tamasaku and co-workers have observed the impact of the same effect on their integrated, one-dimensional scattering profiles (cf. Refs. [50, 113–115]). They proposed an interpretation in terms of XPDC interfering with the background, which consists mostly of Compton scattering. Quantum-mechanically, such an interference should be forbidden, as both processes feature distinct final states. Notably, Tamasaku and co-workers have remained critical of this explanation themselves and pointed out that "[...] the microscopic mechanism is an open question" [114].

We have pursued this question further at other points of this work. Thereby, we have arrived at the preliminary conclusion that the sustained interaction of the *idler* photon with the medium plays a crucial role for the phenomenon. We have progressed towards this conclusion in two stages:

First, we have re-considered our perturbative approach. In a derivation presented in App. A.17, we investigate at lowest order, how the 'XPDC' process is affected by the possibility that an XUV-idler photon may be readily re-absorbed by the medium. If this occurs in a coherent process, we could demonstrate that the result resembles both Compton-scattering *and* XPDC. In particular, it follows the same phase-matching condition as the latter, but does not produce a real idler photon. Most significantly, we show that its perturbative amplitude will be *subtracted* from the regular Compton background.

In a second step, we have extended our reasoning on the idler photon even further. Considering scenarios beyond a single re-absorption event, we assume the idler photon to be re-absorbed and re-emitted on a perpetual basis, instead. The hybrid system of light and matter, which arises from this perpetual coupling represents a Polariton (cf. Refs. [149, 197]). Formalising our intuition on this in

[70] We note that the slightly different behaviour in expansion of the circular scattering signature in the experiment vis-a-vis our theory could originate from several factors. On the theory side, for instance, the effects of beam-divergence have been integrated out approximately. However, they may lead to modifications of the phasematching pattern as they introduce new (and broader) angles. On the experimental side, several cross checks are themselves still outstanding and the data should be considered as *preliminary* to some degree

[71] We fondly recollect the moment during our experimental campaign HC-4489, when a first clear image of these side-lobes could be obtained. Given their unique and immediately recognizable shape, they re-assured us of the presence of nonlinear conversion and, thus, prompted relief and joy among the whole collaboration. At this moment, a collaborator of ours joyfully declared the discovery of the 'bananas'. As we have pointed out earlier already, we shall continue to employ this terminology in reminiscence of that moment.

[72] We point out that this 'negative' part of the scattering patterns is not truly negative, of course. It merely appears negative after subtracting the background. More precisely, we should say that the 'negative' features mark areas, where the scattering signal is smaller than the average background.

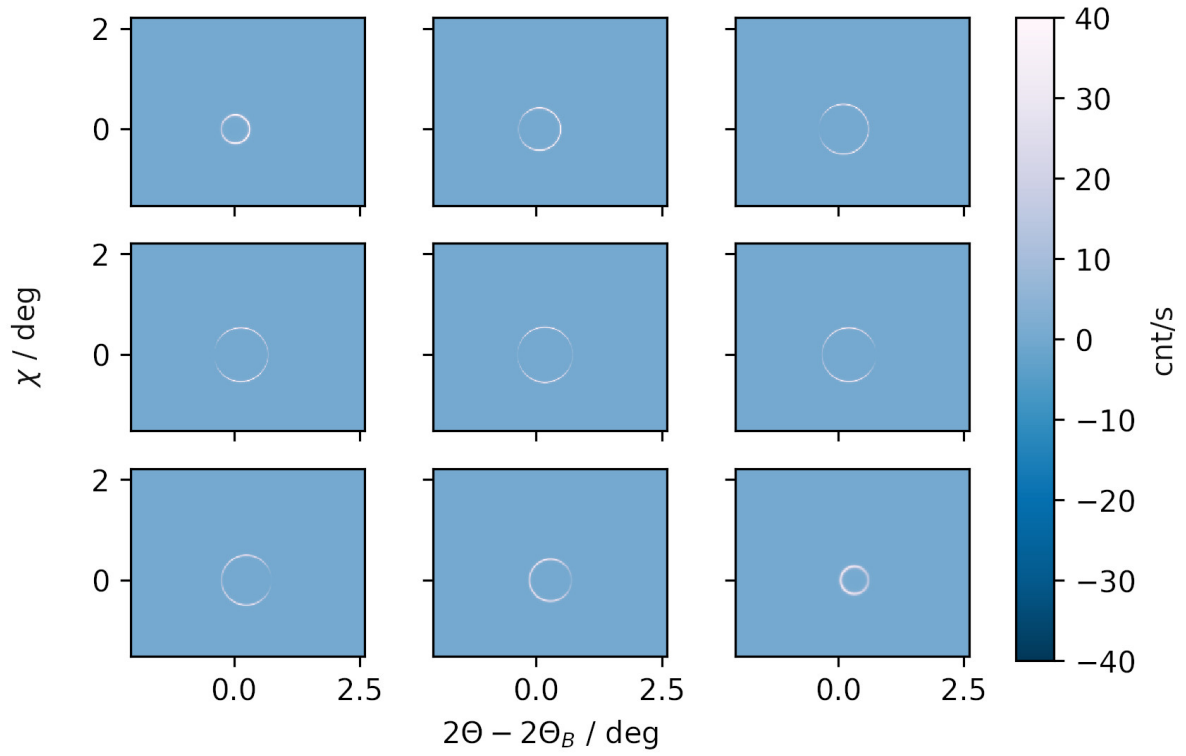

Figure 5.23: Compilation of nonlinear scattering patterns as simulated vis-a-vis Fig. 5.22. The series of images covers several phasematching positions of the sample: From top left to bottom right, these traverse $\Omega - \Omega_B = 0.2^\circ$ up to 1.8° in steps of 0.2°.

Sec. 6.1, we derive a simple model system, which allows us to explain the alternating scattering features found earlier.

With this outlook in mind, we want to conclude on the primary observation and simulations of XPDC given in this section. We remark in closing that these results have been instrumental in shaping our understanding of XOWM, specifically, and light-matter interaction, more generally[73]. By extension, further exploration of XPDC in this realm appears highly desirable and both theoretical and experimental efforts are, in fact, foreseen to this end.

[73] We note that publications pertaining to the presented results are in preparation and will elaborate further on (experimental) details and progress, which we could not cover at this point.

Chapter 6

Extras

In this chapter, we will present work that is connected to our main topic of XOWM yet, at the same time, points beyond the scope of this thesis—hence 'extra'. It draws on concepts that we have previously established and combines them with the latest insights from our thesis. The results address two outstanding issues and provide an outlook towards future research activities.

As a first topic, we concern ourselves, once again, with the intriguing scattering patterns of XPDC at high idler energies (cf. Sec. 5.2.3.a). Hereunto, we develop a simple polariton-inspired model of the scattering process, which can account for the qualitative features of our observations (see subsequent Sec. 6.1).

The second topic, which we will re-visit, is laser-driven wavemixing. In particular, we shall briefly sketch an idea how to enhance the scattering yield—drawing on inspiration from radio-technology once again (see Sec. 6.2)

6.1 A polariton picture of XPDC (and Compton scattering)

In the previous chapter, we have seen how XPDC at high idler-photon energies shows a remarkable experimental signature. Instead of the single, circular scattering pattern, which we would expect from phase-matching considerations as well as from our original perturbative approach (cf. Figs. 5.21 and 5.23), we find *two* circular features of alternating intensities in the experiment (cf. Fig. 5.22). One feature exhibits suppressed scattering (dark circular feature) and the other, inner, feature shows enhanced scattering (bright circular feature). Both are nevertheless found in the vicinity of the phase-matching condition, which suggests an intimate connection with the XPDC process. We reproduce one of the previous experimental images below for renewed reference (Fig. 6.3).

It is noteworthy that Tamasaku and co-workers have previously reported similar modulations of the scattered intensity in multiple XPDC experiments [50, 113–115]. In their cases, these modulations were observed during the course of rocking curve scans, i.e., when they rotated their sample across a range of diffraction conditions. An exemplary plot is reproduced from Ref. [114] in Fig. 6.1.

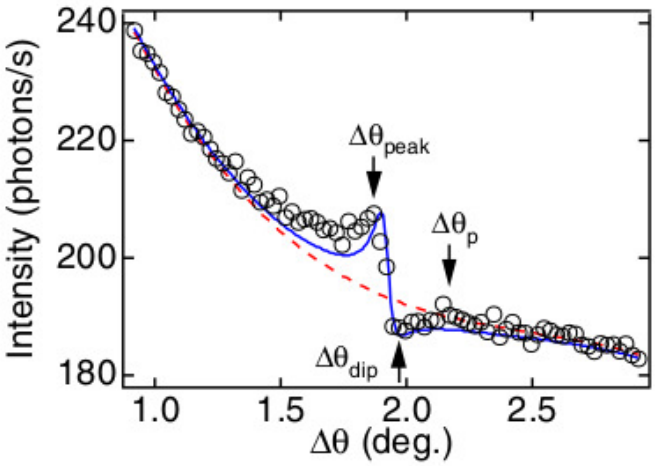

Figure 6.1: Rocking curve measured by Tamasaku and co-workers for XPDC in diamond close to the (111) reflection. The plot is reproduced from Ref. [114] and commented by the authors as: "The rocking curve of the nonlinear diffraction measured at $\Delta E - 100$ eV. Dashed line is polynomial fitting to the Compton background. The solid line is fitting with (7)."

Given that the modulation of the scattering signal resembled a Fano-profile [198], Tamasaku and co-workers sought for an interpretation that could connect to an underlying interference effect. As such, they identified inelastic (Compton) scattering and parametric conversion (XPDC) as two different channels, which would interfere. At the same time, they have noticed conceptual shortcomings with this interpretation, because the aforementionned processes have clearly distinguishable final states and therefore should not interfere at all. Instead, they conclude that the proper "[...] microscopic mechanism is an open question" [114].

Based on our q-resolved measurements, we can offer a new interpretation of the modulation—tracing it to a fundamental phenomenon of coupled light-matter systems, namely Polaritons. Polaritons constitute hybrid excitations of photonic and material degrees of freedom; they can be considered as a quasi-particle description of photons in matter or quanta of a suitably defined displacement field **D** [146, 197, 199–201]. While they occur in various forms, often enhanced through the use of optical

cavities [202], our situation is slightly different and novel for the x-ray regime[1]. In the present case, inelastic x-ray scattering (IXS—or equivalently: non-resonant x-ray Raman-scattering) excites an XUV-polariton inside the sample. This forms the precursor state for *both* XPDC and Compton scattering—see illustration 6.2.

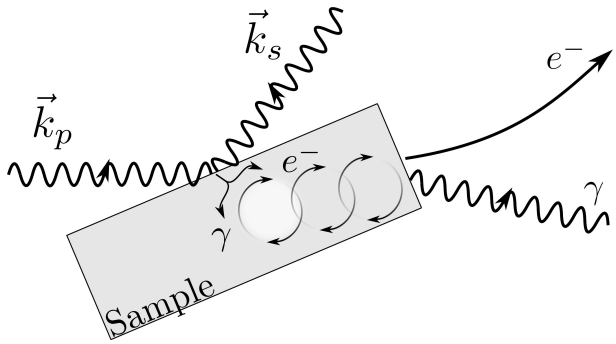

Figure 6.2: Inelastic x-ray scattering excites a polariton inside the sample, i.e., a hybrid of electronic and photonic excitation—symbolized as e^- and γ, respectively. The polariton carries the energy difference of incident pump photon ($\omega_p = c\,|\mathbf{k}_p|$) and scattered signal photon ($\omega_s = c\,|\mathbf{k}_s|$)—as well as a fraction of the transferred momentum. Upon decay of the polaritonic excitation at the sample's boundary, it may either emerges as a photon (viz., the idler photon of XPDC) or appear as an electron (viz., the remainder of Compton scattering). [We gratefully acknowledge Dr. Christina Bömer's help in rendering the above computer graphics.]

Depending on the detection setting ($\mathbf{k}_s$), different components of the polariton can be probed. As a matter of fact, our q-resolved, 2D-scattering images thus show a mapping of the polariton dispersion, with the curious modulation marking the anti-crossing of two dispersion-branches.

In the following, we will provide a simple two-level model to illustrate this proposition further. We will start from a general description of inelastic x-ray scattering (IXS) based on the dynamic structure factor[2]:

$$\frac{\mathrm{d}\sigma}{d\Omega_s d\omega_s} = \left(\frac{\mathrm{d}\sigma}{d\Omega_s}\right)_{\mathrm{Th}} \frac{\omega_s}{\omega_p}\; S(\mathbf{Q},\omega) \qquad \text{with:}\;\; \omega = \omega_p - \omega_s, \qquad \mathbf{Q} = \mathbf{k}_p - \mathbf{k}_s. \tag{6.1}$$

In this discussion, our sign convention will differ from the previous work. It is chosen in accordance with Schülke [61] and our experimental collaborators at the ESRF [163] and considers the energy transfer ω into the sample as a *positive* number. The same holds for the momentum transfer $\mathbf{Q}$ into the sample as well[3]. The dynamic structure factor of Eq. (6.1) relates to the density-density correlation function of electronic operators as

$$S(\mathbf{Q},\omega) = \frac{1}{2\pi}\int_{-\infty}^{\infty} dt\; e^{\mathrm{i}\,\omega t} \int d^3x \int d^3x'\; e^{-\mathrm{i}\,\mathbf{Q}\cdot(\mathbf{x}-\mathbf{x}')}\,\langle\, \hat{n}(\mathbf{x},t)\hat{n}(\mathbf{x}',0)\,\rangle. \tag{6.2}$$

In the following, we shall briefly discuss basic Compton scattering using this expression, before turning

[1] To our knowledge, the connection between parametric conversion and polariton scattering has likewise been noticed in the optical regime. Klyshko, for instance, reports on the subject in Ref. [149]. In this case, the polariton arises as a hybrid excitation of photon and phonon, while the parametric conversion of interest is still an electronically mediated process.

[2] Note that we could likewise use an expression akin to Eq. 2.32. As this would, however, incorporate the correlation properties of the driving x-ray field explicitly, it would prove decidedly more cumbersome to carry through these derivations. Besides this, the results would not differ significantly, as long as the x-ray field is reasonably incoherent.

[3] Note that this sign convention contrasts with the typical usage in the x-ray diffraction community, where instead the change of momentum that is imparted onto the scattered photon is measured $\Delta\mathbf{k} = \mathbf{k}_s - \mathbf{k}_p$. During our previous discussion of nonlinear diffraction for structural analysis, we have adhered to this diffraction-convention in fact.

towards our polariton model.

Compton scattering: As an initial warm-up, let us recall another—possibly more familiar—formulation of Compton scattering. Introducing explicit electronic states into Eq. (6.2), we can rewrite

$$\begin{aligned}
&\int_{-\infty}^{\infty} dt\; e^{\mathrm{i}\,\omega t}\,\langle\, \hat{n}(\mathbf{x},t)\hat{n}(\mathbf{x}',0)\,\rangle \\
&= \int_{-\infty}^{\infty} dt\; e^{\mathrm{i}\,\omega t}\,\langle I|\, \hat{U}(0,t)\hat{n}(\mathbf{x},0)\hat{U}(t,0)\hat{n}(\mathbf{x}',0)\,|I\rangle \\
&= \int_{-\infty}^{\infty} dt\; e^{\mathrm{i}\,\omega t}\, e^{\mathrm{i}E_I t}\,\langle I|\, \hat{n}(\mathbf{x},0)\sum_F |F\rangle\langle F|\,\hat{U}(t,0)\sum_{F'}|F'\rangle\langle F'|\,\hat{n}(\mathbf{x}',0)\,|I\rangle\,. \qquad (6.3)
\end{aligned}$$

Here, we take $|I\rangle$ to denote the initial eigenstate of the governing Hamiltonian $\hat{H}$, i.e., most likely the ground state. The complete sets of (final) states $|F\rangle$ and $|F'\rangle$ can likewise be taken as eigenstates of $\hat{H}$. Under these conditions, the time-evolution operator $\hat{U}(t,0)$ is diagonal. Specifically, it becomes $e^{-\mathrm{i}\hat{H}t} = e^{-\mathrm{i}E_F t}$ upon application to any $|F\rangle$. We can thus continue expression (6.3) as

$$\begin{aligned}
&\int_{-\infty}^{\infty} dt\; e^{\mathrm{i}\,\omega t}\,\langle\, \hat{n}(\mathbf{x},t)\hat{n}(\mathbf{x}',0)\,\rangle \\
&= \int_{-\infty}^{\infty} dt\; e^{\mathrm{i}\,\omega t}\, e^{\mathrm{i}E_I t}\,\langle I|\, \hat{n}(\mathbf{x},0)\sum_{F,F'} |F\rangle \underbrace{\langle F|\, e^{-\mathrm{i}E_F t}\,|F'\rangle}_{\text{diagonal}} \langle F'|\,\hat{n}(\mathbf{x}',0)\,|I\rangle \\
&= \sum_F 2\pi\;\delta(E_F - E_I - \omega)\,\langle I|\,\hat{n}(\mathbf{x},0)\,|F\rangle\,\langle F|\,\hat{n}(\mathbf{x}',0)\,|I\rangle\,. \qquad (6.4)
\end{aligned}$$

Transferring this back into the dynamic structure factor of Eq. (6.2), we obtain

$$S(\mathbf{Q},\omega) = \sum_F\;\delta(E_F - E_I - \omega)\left|\int d^3x\; e^{-\mathrm{i}\mathbf{Q}\cdot\mathbf{x}}\,\langle I|\,\hat{n}(\mathbf{x})\,|F\rangle\right|^2. \qquad (6.5)$$

In this expression, we recover the typical shape of Fermi's golden rule, featuring the square of a transition-matrix element and an associated δ-function for energy selection. Notably, this $\delta(E_F - E_I - \omega)$ implies that from the vast range of final states $|F\rangle$ only those are actually addressed, which satisfy energy conservation. Thereby, we are left with merely a handful of suitable states—quite likely a single one—per scattering condition. This will become a useful insight in the next step.

Polariton model: Now, let us extend our view and consider modelling of the polariton. In the above discussion of Compton scattering, we have implicitly assumed that the (final) states F and F' are of *electronically* excited nature. On top of this, we shall add the option that the system ends up in a *photonically* excited state. Consider for instance the case, where a previously excited electron drops back into its ground state and emits a photon in the process. This would lead to states of the form

$$|F^{\gamma}\rangle = |I^{\mathrm{el}}, \mathbf{k}_i\rangle\,, \qquad (6.6)$$

where I^{el} signifies that the electronic system has returned to its initial state, while $\mathbf{k}_i$ indicates that a photon of said momentum has been emitted. We have deliberately attached a subscript i to allude to an 'idler' photon, because this is the kind of final state, which we would expect from XPDC, in fact.

It is important to note at this point that the designation 'final state' becomes problematic. Outside of the sample, we may still identify final states asymptotically, but inside the sample, they are coupled

through light-matter interaction. Thus, they become non-stationary. Formally, we can see this notion being enforced further, if we look at Eq. (6.3) again, where F and F' actually only serve as basis states for the intermediate time-evolution.

For our polariton model, we shall take this very notion at face value. We will employ an electronically excited state $|F^{\mathrm{el}}\rangle$ and the photonically excited state $|F^{\gamma}\rangle$ as of Eq. (6.6)—both serving as mere basis states. Within this very rudimentary basis, we can write the governing Hamiltonian as a 2×2 matrix and solve the intermediate time-evolution exactly. As we will see, this procedure will provide a full, qualitative description of the curious scattering features observed in Sec. 5.2.3.a.

So, let us assemble all necessary components of the model starting from Eq. (6.3)

$$\begin{aligned}&\int_{-\infty}^{\infty}\!\!dt\; e^{\mathrm{i}\,\omega t}\,\langle\,\hat{n}(\mathbf{x},t)\hat{n}(\mathbf{x}',0)\,\rangle\\ &\approx\int_{-\infty}^{\infty}\!\!dt\; e^{\mathrm{i}\,\omega t}\,e^{\mathrm{i}\,E_I t}\,\langle I|\,\hat{n}(\mathbf{x},0)\overset{\text{two level}}{\sum_{F}}|F\rangle\langle F|\,\hat{U}(t,0)\overset{\text{two level}}{\sum_{F'}}|F'\rangle\langle F'|\,\hat{n}(\mathbf{x}',0)\,|I\rangle\,.\end{aligned}\tag{6.7}$$

The first of our two intermediate basis states is supposed to be the electronically excited $|F^{\mathrm{el}}\rangle$ with a bare energy $E_F^{\mathrm{el}}=E_I^{\mathrm{el}}+\omega_{\mathrm{exc}}$. This is composed of the ground state energy as a reference and the electronic excitation energy on top. The second basis state is $|F^{\gamma}\rangle$, for which the bare energy is also a composite

$$E_F^{\gamma}=E_I^{\mathrm{el}}+\omega_i=E_I^{\mathrm{el}}+c\,|\mathbf{k}_i|=E_I^{\mathrm{el}}+c\,|\mathbf{Q}+\mathbf{G}|\,.\tag{6.8}$$

Here, the electronic system is truely in its ground state—thus contributing E_I^{el}—whereas the energy of the co-existing photon is denoted ω_i. If we assume the vacuum dispersion relation $\omega_i=c\,|\mathbf{k}_i|$ to be valid, we can further connect this energy to the overall momentum transfer via the phasematching condition for XPDC: $\mathbf{k}_i=\mathbf{k}_p+\mathbf{G}-\mathbf{k}_s$. Identifying the two basis states with two-component column-vectors

$$|F^{\mathrm{el}}\rangle=\begin{pmatrix}1\\0\end{pmatrix}\qquad\text{and}\qquad|F^{\gamma}\rangle=\begin{pmatrix}0\\1\end{pmatrix},\tag{6.9}$$

we can write the associated Hamiltonian as

$$\hat{H}=\mathbb{1}\cdot E_I+\begin{pmatrix}\omega_{\mathrm{exc}}&0\\0&\omega_i\end{pmatrix}+\begin{pmatrix}0&V\\V^*&0\end{pmatrix}.\tag{6.10}$$

Here, V denotes the light-matter coupling and—in a more formal derivation—would be related to $\mathbf{p}\cdot\mathbf{A}$-type matrix elements $\langle F^{\mathrm{el}}|\,\mathbf{p}\cdot\mathbf{A}\,|F^{\gamma}\rangle$. This Hamiltonian can be diagonalized by a unitary transformation $\hat{S}\hat{H}\hat{S}^{\dagger}=\hat{H}_{\mathrm{diag}}$, featuring eigenenergies of the well-known form[4]

$$E_{\pm}=E_I^{\mathrm{el}}+\frac{\omega_{\mathrm{exc}}+\omega_i}{2}\pm\sqrt{\frac{1}{4}(\omega_{\mathrm{exc}}-\omega_i)^2+|V|^2}\tag{6.11}$$

for its eigenstates

$$|\phi_{\pm}\rangle=\begin{pmatrix}c_{1\pm}\\c_{2\pm}\end{pmatrix}=\frac{1}{\sqrt{1+|V|^2/(E_{\pm}-(E_I+\omega_i))^2}}\begin{pmatrix}1\\V^*/(E_{\pm}-(E_I+\omega_i))\end{pmatrix}.\tag{6.12}$$

[4]We point out that—for the reader's convenience—we have solved this rather trivial exercise of diagonalization in Appendix A.18.

Next, we embed this diagonalization in Eq. (6.7):

$$\begin{aligned}
&\int_{-\infty}^{\infty} dt\; e^{\mathrm{i}\,\omega t}\,\langle\,\hat{n}(\mathbf{x},t)\hat{n}(\mathbf{x}',0)\,\rangle \\
&\approx \int_{-\infty}^{\infty} dt\; e^{\mathrm{i}\,\omega t}\, e^{\mathrm{i}\,E_I t}\,\langle I|\,\hat{n}(\mathbf{x},0)\sum_{F}^{\text{two level}}\sum_{F'}^{\text{two level}}|F\rangle\langle F|\,\hat{S}^{\dagger}\,\underbrace{\hat{S}\hat{U}(t,0)\,\hat{S}^{\dagger}}_{e^{-\mathrm{i}\hat{H}_{\mathrm{diag}}t}}\,\hat{S}\,|F'\rangle\langle F'|\,\hat{n}(\mathbf{x}',0)\,|I\rangle\,. \qquad (6.13)
\end{aligned}$$

Besides the simplified time-evolution, we note two further aspects:

1. The transition-matrix element $\langle I|\,\hat{n}(\mathbf{x},0)\,|F\rangle$, involves an operator that is purely electronic in nature. Starting from the state $\langle I|$, which is likewise purely electronic, the state $|F\rangle$, therefore has to be restricted to $|F^{\mathrm{el}}\rangle$. In other words, no photon could be created in this step yet, rendering the sum over states superfluous.

2. The operation $\hat{S}|F^{\mathrm{el}}\rangle = \sum_i^{\pm} c_{1i}\,|\phi_i\rangle$ relates the old and new eigenstates and may therefore be expressed through the expansion coefficients found above in Eq. (6.12).

This simplifies expression (6.13) into

$$\begin{aligned}
&\int_{-\infty}^{\infty} dt\; e^{\mathrm{i}\,\omega t}\,\langle\,\hat{n}(\mathbf{x},t)\hat{n}(\mathbf{x}',0)\,\rangle \\
&\approx \int_{-\infty}^{\infty} dt\; e^{\mathrm{i}\,\omega t}\, e^{\mathrm{i}\,E_I t}\,\langle I|\,\hat{n}(\mathbf{x},0)\,|F^{\mathrm{el}}\rangle\sum_{i=\pm} c_{1i}^{*}\,\langle\phi_i|\,e^{-\mathrm{i}\hat{H}_{\mathrm{diag}}t}\sum_{j=\pm} c_{1j}\,|\phi_j\rangle\,\langle F^{\mathrm{el}}|\,\hat{n}(\mathbf{x}',0)\,|I\rangle \\
&= \int_{-\infty}^{\infty} dt\; e^{\mathrm{i}\,\omega t}\, e^{\mathrm{i}\,E_I t}\,\langle I|\,\hat{n}(\mathbf{x},0)\,|F^{\mathrm{el}}\rangle\sum_{i=\pm} |c_{1i}|^2\,\langle\phi_i|\,e^{-\mathrm{i}\,E_i t}\,|\phi_i\rangle\,\langle F^{\mathrm{el}}|\,\hat{n}(\mathbf{x}',0)\,|I\rangle \\
&= \sum_{i=\pm} |c_{1i}|^2\; 2\pi\;\delta(E_i - E_I - \omega)\;\langle I|\,\hat{n}(\mathbf{x},0)\,|F^{\mathrm{el}}\rangle\,\langle F^{\mathrm{el}}|\,\hat{n}(\mathbf{x}',0)\,|I\rangle\,. \qquad (6.14)
\end{aligned}$$

As in the Compton-case, we can transfer this result into the dynamic structure factor and obtain almost the same result (cf. Eq. (6.5)):

$$S^{\mathrm{pol}}(\mathbf{Q},\omega) = \sum_{i=\pm} |c_{1i}|^2\;\delta(E_i - E_I - \omega)\left|\int d^3x\, e^{-\mathrm{i}\,\mathbf{Q}\cdot\mathbf{x}}\,\langle I|\,\hat{n}(\mathbf{x})\,|F^{\mathrm{el}}\rangle\right|^2. \qquad (6.15)$$

The subtle difference is that the electronic final state $|F^{\mathrm{el}}\rangle$ does not emerge from a range of final states—being effectively singled out by energy conservation—but instead we have chosen it a priori by *assuming* that energy conservation will be in place. On top of this, the two branches of the polariton ($\pm$) are explicitly visible now. Crucially, they are themselves subject to energetic selection.

In order to set the overall scale of the scattering signal, we can push the analogy of Eqs. (6.5) and (6.15) even further. We note that—sufficiently far away from any phasematching condition—we would naturally expect the unmodified dynamic structure factor to show up, because these regions of scattering space are dominated by regular Compton scattering. Formalizing this intuition, we consider a detection scenario $\omega_{\mathrm{detect}} \sim \omega_{\mathrm{exc}} \ll \omega_i$. We can enforce the latter inequality by looking at scattering for large momentum transfers $\mathbf{Q} = \mathbf{k}_i - \mathbf{G}$. Pushing the optical momentum into the limit $|\mathbf{k}_i| \to \infty$ entails $\omega_i \to \infty$ on grounds of Eq. (6.8), respectively. In this limit, the two dispersion branches of the polariton (E_+ and E_-) clearly separate—sporting the asymptotic forms

$$E_+ \xrightarrow[\omega_i\to\infty]{} E_I^{\mathrm{el}} + \omega_i \qquad \text{and} \qquad E_- \xrightarrow[\omega_i\to\infty]{} E_I^{\mathrm{el}} + \omega_{\mathrm{exc}}. \qquad (6.16)$$

Simultaneously, their expansion coefficients become

$$\begin{pmatrix} c_{1+} \\ c_{2+} \end{pmatrix} \xrightarrow[\omega_i \to \infty]{} \begin{pmatrix} 0 \\ 1 \end{pmatrix} \qquad \text{and} \qquad \begin{pmatrix} c_{1-} \\ c_{2-} \end{pmatrix} \xrightarrow[\omega_i \to \infty]{} \begin{pmatrix} 1 \\ 0 \end{pmatrix} \tag{6.17}$$

and thereby, only one coefficient (viz. c_{1-}) is still relevant in expression (6.15). We can identify this remainder with regular Compton scattering, which involves only the on-shell electronic excitation. Finally, we incorporate this insight about the limiting behaviour into Eq. (6.15), by blending it with the orignal Compton-expression (Eq. (6.5)) in a slightly informal way:

$$S^{\text{pol}}(\mathbf{Q},\omega) \approx \sum_{i=\pm} |c_{1i}|^2 \; \delta(E_i - E_I - \omega)\, S(\mathbf{Q},\omega). \tag{6.18}$$

Herein, the regular dynamic structure factor $S(\mathbf{Q},\omega)$ sets the overall scale of the scattering signal. On top of this, our addition of the two polaritonic branches will introduce the circular scattering pattern of XPDC—including the alternating ($\pm$) modulation that we have observed before.

6.1.1 Comparison with experiment

If we want to compare our polariton model with the experimentally observed scattering signal, we have to engage in one further adaptation. Namely, we should relate Eq. (6.18) to an observable scattering yield. In fact, we would not *directly* observe the dynamic structure factor in any experiment, but rather the energy filtered scattering yield per element of solid angle (here: detector pixel). Modelling this, we write

$$\begin{aligned} Y_{\text{pix}} &\approx \int_{\text{pix}} d\Omega_s \int d\omega_s \; T_{\text{analyzer}}(\omega_s) \; \frac{\mathrm{d}\sigma^{\text{pol}}}{d\Omega_s d\omega_s} \; J_{\text{in}} = \int_{\text{pix}} d\Omega_s \int d\omega_s \; T_{\text{analyzer}}(\omega_s) \; \left(\frac{\mathrm{d}\sigma}{d\Omega_s}\right)_{\text{Th}} \frac{\omega_s}{\omega_p} \; S^{\text{pol}}(\mathbf{Q},\omega) \; J_{\text{in}} \\ &\approx \left(\frac{\mathrm{d}\sigma}{d\Omega_{\text{pix}}}\right)_{\text{Th}} S(\bar{\mathbf{Q}}_{\text{pix}}, \omega_{\text{detect}}) \; J_{\text{in}} \int d\omega \; e^{-(\omega-\omega_{\text{detect}})^2/2\Omega_{\text{detect}}^2} \sum_{i=\pm} \underbrace{|c_{1i}|^2 \; \delta(E_i - E_I - \omega)}_{\text{implicit dependence upon } \bar{\mathbf{Q}}_{\text{pix}}} \\ &\propto \sum_{i=\pm} |c_{1i}|^2 \; e^{-(E_i - E_I - \omega_{\text{detect}})^2/2\Omega_{\text{detect}}^2}. \end{aligned} \tag{6.19}$$

In the first line, we have used relation (6.1) to connect the dynamic structure factor to a scattering cross section. Multiplying the latter by an appropriate flux of incident photons J_{in} and considering the integration over scattered photons (subscript s) gives the sought after yield. We factor the slowly varying dependencies out of the integral and ignore them ultimately. As of Eq. (6.18), we already know that our signal will be proportional to the regular Compton background. Most importantly in this discussion, we need to specify a transmission function for the crystal analyser $T_{\text{analyzer}}(\omega_s)$. For convenience, we approximate this energy filter by a simple Gaussian as we have repeatedly done before (cf. Eq. (5.3), for instance)

$$T_{\text{analyzer}}(\omega_s) = e^{-(\omega-\omega_{\text{detect}})^2/2\Omega_{\text{detect}}^2}. \tag{6.20}$$

This transmission model considers the detection of photons at an energy transfer ω within a window of width Ω_{detect} around the central value ω_{detect}, which would be set by the experimenter.

Applying the above, we can evaluate[5] a scattering pattern as depicted in Fig. 6.3 (b). For comparison the experimental reference data at the same rocking angle $\Omega - \Omega_B = 1.0°$ is shown to its left (a). The latter is an enlarged view of the data shown in the central frame of Fig. 5.22.

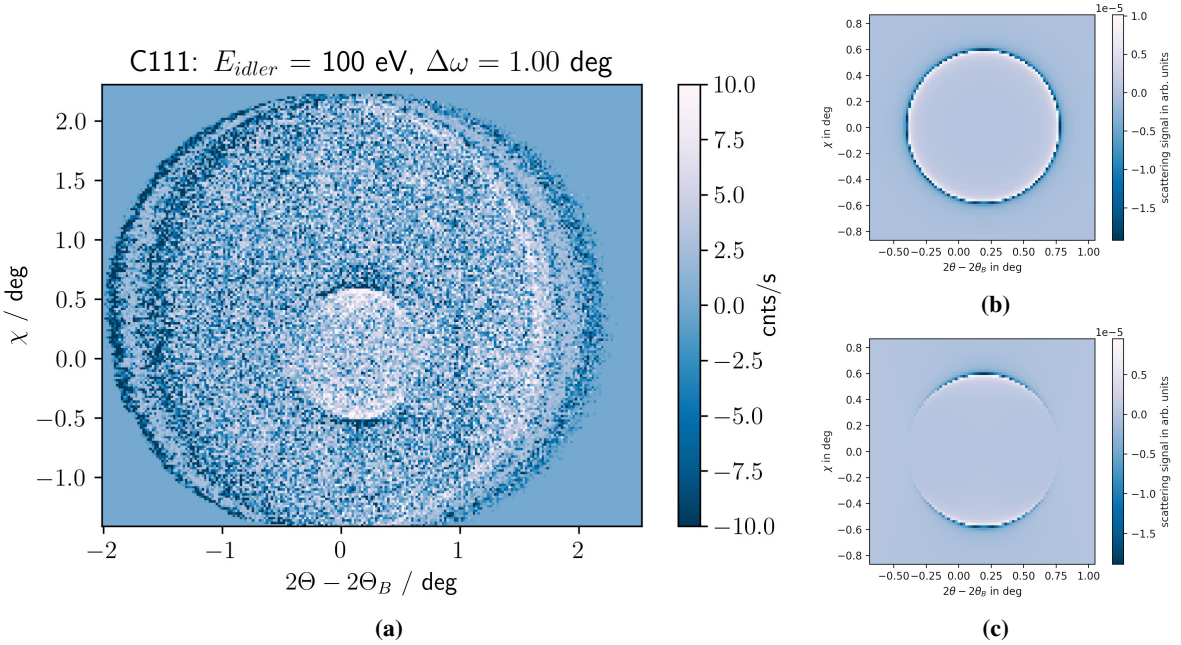

Figure 6.3: Nonlinear scattering patterns at phasematching condition for XPDC (rocking angle $\Omega - \Omega_B = 1.0°$). Experimental data (a)—taken from the central frame of Fig. 5.22—is compared to theoretical simulations within our polariton model (b) and (c). The experiment shows alternating bright and dark features (i.e., regions above and below average counts, respectively), which follow the circular phasematching condition for XPDC. Moreover, it exhibits a mirror-symmetric modulation around the circle. Our simple polariton model (b) reproduces the alternating intensities, while only the model's extension towards polarization-dependence (cf. Eq. (6.21)) captures the modulation as well—see frame (c). This final result is in good qualitative agreement with the experiment. [Image (a) courtesy of Dr. Christina Bömer]

Quite obviously, our simple approach still features an unrealistic radial symmetry. Apart from this, however, it captures the alternatingly bright and dark features nicely. In order to introduce the modulation around the circular pattern, we resort to an insight from our perturbative analysis of XPDC (see Sec. 5.2.1.b, in particular). We recall that the modulation reflects the polarization-dependence of the light-matter coupling strength: The nonlinear current-response of the material is driven by the transverse polarization of the idler photons (here the polariton)

$$\begin{aligned} \text{XPDC} \propto \sum_{\lambda}^{\substack{\text{idler} \\ \text{polarizations}}} |\boldsymbol{\varepsilon}_{i\lambda} \cdot \mathbf{K}_{GS}(0,\mathbf{G},\omega)|^2 &= |\mathbf{K}_{GS}(0,\mathbf{G},\omega)|^2 - |\mathbf{k}_i \cdot \mathbf{K}_{GS}(0,\mathbf{G},\omega)|^2 / |\mathbf{k}_i|^2 \\ &\approx |\mathbf{K}_{GS}(0,\mathbf{G},\omega)|^2 \left(1 - \frac{|\mathbf{k}_i \cdot \mathbf{G}|^2}{|\mathbf{k}_i|^2 |\mathbf{G}|^2}\right). \end{aligned} \tag{6.21}$$

We have seen the first reformulation in use throughout Sec. 5.2, whereas the last step is merely a convenient approximation for the present case, which is in line with our discussion below Fig. 5.14. Given that no definitive (nonlinear) response function is known for the polariton, we simply extend our gen-

[5] We note with respect to the simulation underlying Fig. 6.3 that we have used the following numerical parameters: $\hbar\omega_{\text{exc}} = 100$ eV, $\hbar\omega_{\text{detect}} = 100.5$ eV and $\hbar\Omega_{\text{detect}} = 0.5$ eV. We have further chosen an arbitrary coupling strength of $V = 1$ meV and fixed the pixel size to the experimental value from Sec. 5.2.3.a, i.e., 20×20 mdeg^2. The rocking position of the sample is $\Omega - \Omega_B = 0°$.

eral observation that the '**G**-component' of $\mathbf{K}_{GS}(0,\mathbf{G},\omega)$ points roughly along the eponymous vector. Transferring this insight to our polariton model, we modify the coupling strength

$$V \to V \cdot [1 - (|\mathbf{k}_i \cdot \mathbf{G}|^2)/(|\mathbf{k}_i|^2 |\mathbf{G}|^2)]. \tag{6.22}$$

Repeating the previous simulation (b) with the modified coupling yields the scattering pattern of Fig. 6.3 (c). The latter is in good overall agreement with the experimentally observed features (a).

Having validated the polariton model on our XPDC-data, we want to take a step back and consider the broader picture. In particular, we shall address the long-standing question by Tamasaku and co-workers, as to the origin of the 'Fano-type' features in their XPDC rocking-curve measurements (recall Refs. [50, 113–115]). Hereunto, we point out, first of all, that no rocking-curve scans are required to observe these 'Fano-type' features. Instead, our model exposes—in agreement with our experimental observations—that such features are already present in a single scattering pattern. We illustrate this observation in Fig. 6.4 below, where we reproduce the pattern from Fig. 6.3 (c) at higher resolution and take a line-out across its central features (lower left-hand side). This line-out clearly shows the 'Fano-type' fringes at the intersection of the line-out with each XPDC side-lobe.

However, these alternating imprints need not be interpreted as the result of interfering processes (Compton vs. XPDC). Instead, we emphasize that they should be thought of as two branches of the same phenomenon: Namely, they are the two dispersion branches of the polariton, which is excited in the system through IXS. This aspect becomes more obvious still, if the two-dimensional scattering pattern is paired explicitly with a dispersion-plot of the polaritonic eigenenergies $E_\pm$ as on the lower right-hand side of Fig. 6.4. Herein, the two energetic branches of the polariton are related to the underlying phasematching condition for the 'idler'-photon according to Eq. (6.8), parametrized via χ. As a result, we find that their characteristic anti-crossing occurs precisely at the zero-crossing of the detected signal. Thus, the scattering really just images the transition from one polariton branch to the other, giving rise to a modulation of the observable signal in the process.

By extension, we can conclude that the same effect shows during rocking-curve scans as performed by Tamasaku and co-workers—it is merely projected onto a different coordinate axis. As such, we note that our polariton model could indeed address (and solve) the conundrum posed by the results of Refs. [50, 113–115].

This elating conclusion, notwithstanding, our new-found interpretation of the phenomenon raises a host of future questions as well. On the theoretical side, there is the pre-eminent challenge to extend our polariton interpretation beyond its model character. In this, the development of a polariton-based or polariton-inspired theory from *first principles* would be highly desirable[6]. Moreover, we note that a more general application of this, i.e., to all kinds of XOWM processes, beyond the spontaneous case is conceivable.

Shared between experiment and theory, we notice the opportunity to employ XPDC in the given regime as a means to map out the full dispersion relation of XUV-polaritons in matter. In principle, we have already achieved this—considering that the assembly of patterns in Fig. 5.22 can be considered as a tomographic assembly of dispersion planes like Fig. 6.4. While their combined map might appear reasonably trivial for diamond, the extension to more complicated, even nano-structured, materials should

[6]We comment on the above notion of a fully first-principles theory that this may not require highly non-perturbative approaches. While these are common-place in many polariton-focused theories (cf. Ref. [202] for examples), the present case seems to be well within reach of perturbative methods. In particular, we recall to this effect that our perturbative simulations in Sec. 5.2.3.a could adequately capture the magnitude of the nonlinear effect.

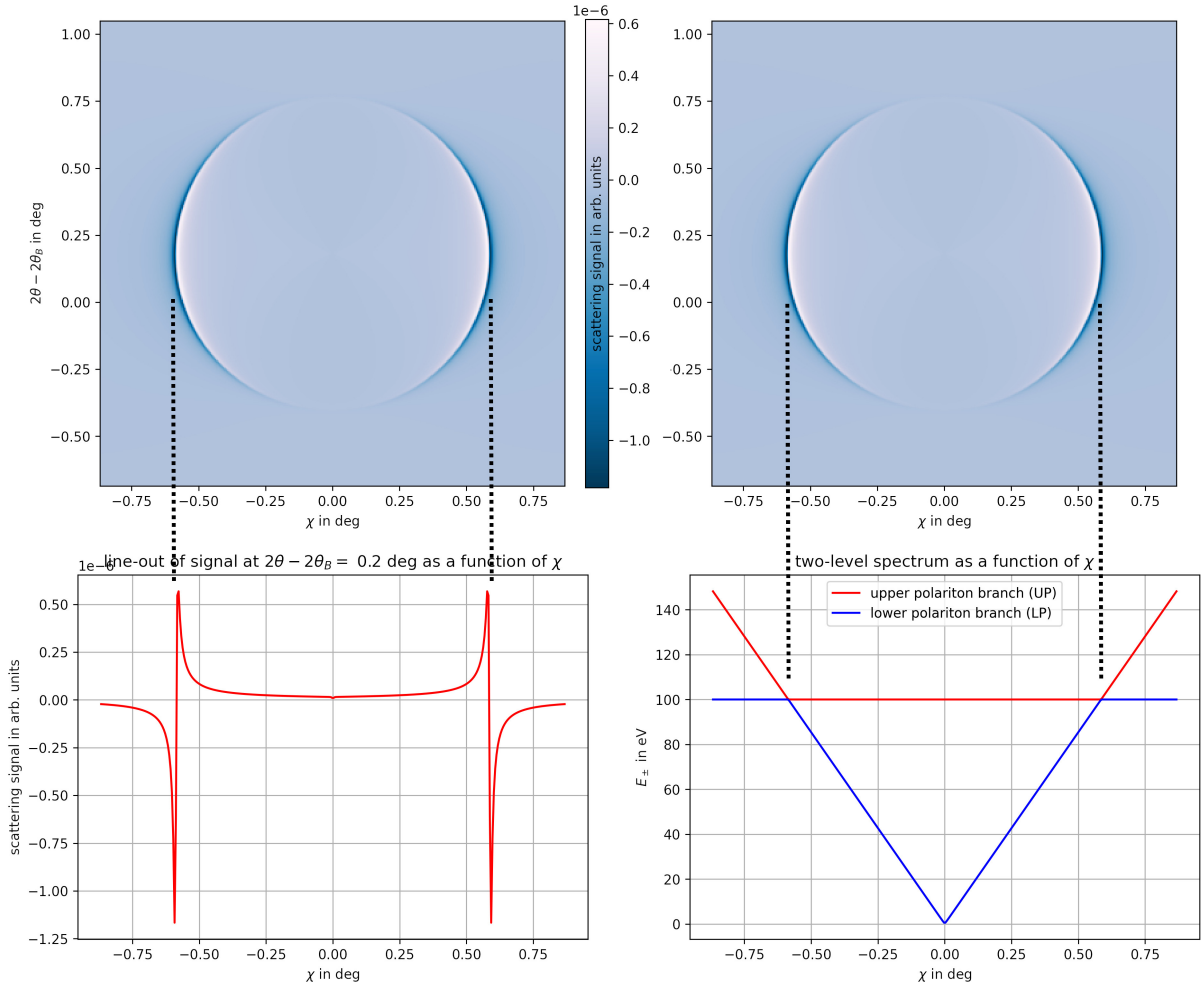

Figure 6.4: Illustration of the polaritonic imprint onto the scattering patter. Upper images show a reproduction of Fig. 6.3 (c) at higher resolution (5 mdeg). We juxtapose the scattering pattern once with a line-out of itself (lower left-hand side). At fixed $2\theta - 2\theta_B = 0.2°$, the line-out gives the scattering profile along χ; two 'Fano-type' features are visible—each corresponding to the cross section of an XPDC side-lobe (correspondence is highlighted by dashed lines). On the lower right-hand side, the same scattering pattern is juxtaposed with the underlying polariton dispersion along the same (aforementioned) line-out. Here, the zero-crossings of the scattering pattern's side-lobes are seen to correspond with the characteristic anti-crossing of the polaritonic dispersion branches.

hold very interesting discoveries.

Before addressing either of these prospects, we note in terms of a more immediate outlook, that we will apply our polariton model to the resonant case of XPDC, which Tamasaku and co-workers have investigated in Ref. [115]. Preliminary simulations to this end suggest that our model is fully capable of reproducing even the shift in line-shapes, which have been reported in Fig. 2 of cited work. Refined experimental measurements on these scenarios have been obtained in collaboration with Dr. Christina Bömer and will be published in the future[7].

[7] We also refer the interested reader to an upcoming thesis (M.Sc.) by Fridtjof Kerker, which will elaborate on some of the pertaining issues [126].

6.2 Amphodyne detection for SFG / DFG

Before we conclude our treatise on XOWM altogether, we want to entertain a final train of thought on laser-driven wavemixing. The pertaining theoretical explorations below, which have seen no experimental application yet, should be considered as a proposal for—or outlook onto—future XOWM activities.

To set the stage, we recall from Chpt. 5 that XOWM signals have been relatively weak up to now, despite gradually becoming measurable at x-ray FELs. The conversion efficiency for SFG / DFG ranges around $10^{-10}...10^{-9}$, thus requiring a large amount of incident photons to reliably detect nonlinear scattering. As a consequence, we are tempted to ask, whether there is a way to *actively* enhance this signal—other than improving the *passive* detection efficiency of our measurement setups.

In order to obtain an affirmative answer, we shall, once again, take inspiration from electro-technics—thereby coming full circle to our introductory thoughts of Sec. 1.1. As a matter of fact, radio receivers have long faced the problem of detecting and discriminating weak, high-frequency (HF) signals among a broad spectrum of competing background noises (in their case, e.g., other radio broadcasts, spark noises and various other electrical disturbances). A remarkably efficient—as well as elegant—solution to this problem has been established in the form of the *heterodyne detection* technique [1, 2], which uses a locally produced reference-wave (the so-called 'local oscillator') to enhance the detection of the desired signal.

Below, we shall illustrate the concept of heterodyne detection on electronic signals and attempt to transfer it into the realm of XOWM subsequently.

6.2.1 Heterodyne detection for electronic HF signals

Commencing to describe the detection of HF signals, let us briefly recall their model description in terms of an oscillating voltage

$$U_{\mathrm{sig}}(t) = u_s \, \sin(\omega_s t). \tag{6.23}$$

We note that—augmenting the even simpler signal of Eq. (1.1) in our exposé of wavemixing—we have introduced an explicit scale of the signal's strength u_s in the present case.

Regarding the actual detection of such HF signals, we posit that these will have to be converted into a low frequency (LF), or even DC-type, electronic output in the end. Examples of such low-end, LF-outputs could comprise the audible emission of a radio programme via loudspeaker or the (slowly varying) reading on an intensity meter, for instance. Such outputs are typically generated on the basis of the time-averaged signal power:

$$\begin{aligned} P_{\mathrm{det}} = \frac{1}{T} \int_0^T dt \; P_{\mathrm{sig}}(t) &= \frac{1}{T} \int_0^T dt \; U_{\mathrm{sig}}(t) \, I_{\mathrm{sig}}(t) \\ &= \frac{1}{T} \int_0^T dt \; U_{\mathrm{sig}}(t) \, \frac{U_{\mathrm{sig}}(t)}{R}. \end{aligned} \tag{6.24}$$

In the last line, we have applied Ohm's law, assuming that the signal's power will be detected on some kind of linear, resistive device. The most straight-forward way of demodulating an input signal $U_{\mathrm{sig}}(t)$ into such an average power, is to feed it directly into the detection circuit. In our model's terms this corresponds to substituting Eq. (6.23) directly into the above Eq. (6.24). Assuming further that the averaging interval T is much longer than a single period of the signal, i.e., $T \gg {}^{2\pi}/_{\omega_s}$, we can approximately

evaluate

$$P_{\text{det}} = \frac{1}{T}\int_0^T dt\ \frac{(U_{\text{sig}}(t))^2}{R} = \frac{1}{T}\int_0^T dt\ \frac{(u_s\sin(\omega_s t))^2}{R}$$
$$= \frac{u_s^2}{R}\frac{1}{T}\int_0^T dt\ \frac{1}{2}\big[1 - \underbrace{\cos(2\omega_s t)}_{\approx 0,\ \text{if integral averages over several periods}}\big]$$
$$\approx \frac{u_s^2}{2R}. \tag{6.25}$$

This simple detection scheme is often referred to as *homodyne*, because the signal $U_{\text{sig}}(t)$ is detected in the presence of only itself or—in some sense—in the presence of only the *same* signal. Thus the greek prefix *homo* which literally means 'the same', has been adopted for its designation. We observe that the detected power depends quadratically upon u_s and will diminish for weak signal amplitudes.

Heterodyne detection, on the other hand, will see the signal detected together with 'another' or 'different' input, which inspired the opposite prefix *hetero*[8]. To achieve this combined detection, a local oscillator is first used to produce a secondary voltage

$$U_{\text{LO}}(t) = u_{\text{LO}}\sin(\omega_{\text{LO}} t), \tag{6.26}$$

which is, subsequently, superimposed with $U_{\text{sig}}(t)$ and jointly fed into the detection circuit. Writing out their *combined* detectable power

$$P_{\text{det}} = \frac{1}{T}\int_0^T dt\ \frac{(U_{\text{sig}}(t)+U_{\text{LO}}(t))^2}{R} = \frac{1}{R}\frac{1}{T}\int_0^T dt\ \big(u_s\sin(\omega_s t)+u_{\text{LO}}\sin(\omega_{\text{LO}} t)\big)^2, \tag{6.27}$$

we recognize that its quadratic form can produce mix-terms among the two frequencies, just as the nonlinear mixer described in Eq. (1.5) of Sec. 1.1 would do. In direct correspondence to Eq. (1.5), the resultant power

$$\begin{aligned} P_{\text{det}} &= \frac{1}{R}\frac{1}{T}\int_0^T dt\ \big(u_s\sin(\omega_s t)+u_{\text{LO}}\sin(\omega_{\text{LO}} t)\big)^2 \\ &= \frac{1}{R}\frac{1}{T}\int_0^T dt\ \big((u_s\sin(\omega_s t))^2 + 2u_s u_{\text{LO}}\sin(\omega_s t)\sin(\omega_{\text{LO}} t) + (u_{\text{LO}}\sin(\omega_{\text{LO}} t))^2\big) \\ &= \frac{1}{R}\frac{1}{T}\int_0^T dt\ \Big(\frac{u_s^2}{2}\big[\underset{\text{DC}}{1} - \underbrace{\cos(2\omega_s t)}_{\text{SHG}}\big] + u_s u_{\text{LO}}\big[\underbrace{\cos((\omega_s-\omega_{\text{LO}})t)}_{\text{DFG}} - \underbrace{\cos((\omega_s+\omega_{\text{LO}})t)}_{\text{SFG}}\big] \\ &\qquad + \frac{u_{\text{LO}}^2}{2}\big[\underset{\text{DC}}{1} - \underbrace{\cos(2\omega_{\text{LO}} t)}_{\text{SHG}}\big]\Big) \end{aligned} \tag{6.28}$$

contains DC-terms, which we have identified for detection earlier (cf. remainder of Eq. (6.25)); it contains several high-frequency components (SHG or SFG), which will simply average out over the detection

[8] We note that the definition of *homo-* vs. *heterodyne* detection varies among different contexts and authors. For radio-frequency applications, there is a tendency to classify detection as *homodyne* for any scenario, wherein signals of only one (i.e., the same) frequency are detected—even though there may be superimposed waves akin to Eq. (6.27) they would all feature the same $\omega = \omega_s = \omega_{\text{LO}}$. *Heterodyne* detection would, conversely, correspond to any scheme that superimposes signals of different frequencies for detection (Ref. [203] gives an example from laser-spectroscopy, which also follows this convention).

We shall adopt a different convention—as we have already outlined—in that we consider the origin of the detected wave as a criterion for its denomination. If all detected power can be traced to the intrinsic (spontaneous) signal, i.e., it is detected in and of itself, we shall refer to the detection as *homodyne*, whereas any detection that is aided (i.e., modified or stimulated) by the admixture of a *differently*-sourced wave shall be termed *heterodyne*. This convention is closer to the use of terminology with Refs. [11, 204] and related works.

time, and—most crucially—it contains a difference-frequency contribution (DFG)

$$P_{\mathrm{DFG}} = \frac{1}{R}\,\frac{1}{T}\int_0^T dt\; u_s u_{\mathrm{LO}} \cos((\omega_s - \omega_{\mathrm{LO}})t). \tag{6.29}$$

Upon integration, this particular mix-term yields

$$\begin{aligned} P_{\mathrm{DFG}} &= \frac{u_s\,u_{\mathrm{LO}}}{R}\,\frac{1}{T}\int_0^T dt\,\cos((\omega_s - \omega_{\mathrm{LO}})t) \\ &= \frac{u_s\,u_{\mathrm{LO}}}{R}\,\frac{1}{T\,(\omega_s - \omega_{\mathrm{LO}})}\sin((\omega_s - \omega_{\mathrm{LO}})t)\,\Big|_0^T = \frac{u_s\,u_{\mathrm{LO}}}{R}\,\frac{\sin((\omega_s - \omega_{\mathrm{LO}})T)}{T\,(\omega_s - \omega_{\mathrm{LO}})} \\ &= \frac{u_s\,u_{\mathrm{LO}}}{R}\,\mathrm{sinc}((\omega_s - \omega_{\mathrm{LO}})T), \end{aligned} \tag{6.30}$$

which can contribute significantly to the overall detection, if the local oscillator is tuned close to the signal's frequency, i.e., if $\omega_s - \omega_{\mathrm{LO}} \ll \pi/2T$.

Combining the above with the non-vanishing terms of Eq. (6.28), we obtain

$$P_{\mathrm{det}} \approx \frac{u_s^2}{2R} + \frac{u_s\,u_{\mathrm{LO}}}{R}\,\mathrm{sinc}((\omega_s - \omega_{\mathrm{LO}})T) + \frac{u_{\mathrm{LO}}^2}{2R}. \tag{6.31}$$

In here, the first term marks the familiar quadratic contribution from homodyne detection[9]. Our reasoning on this remains unchanged: If the initial signal is weak, this term will yield only diminishing amounts of detectable power. There is an analogous term for the local oscillator, i.e., $u_{\mathrm{LO}}^2/2R$, for which u_{LO} is anyways known by design—thus it can be ignored (or subtracted at will). The essential novelty of Eq. (6.31) resides in the mix-term, which is linear in both u_s and u_{LO}. Thereby, it provides access to the unknown signal strength u_s at an *amplified* scale, which can be set deliberately via u_{LO}. The significance of this newly-obtained scaling property is hard to overstate; it allows for unprecedented detection efficiency, simply by ad-mixing a well-known reference signal in the detection channel.

If a transfer of this concept into the x-ray domain was possible, it could—in principle—serve to enhance our XOWM signals as well. The next section will explore this idea further and assess how 'simple' or difficult such ad-mixing of a reference would really turn out to be.

6.2.2 Transfer of the heterodyning concept to x-ray detection

In the previous section, we have illustrated how the ad-mixture of a reference wave (or local oscillator) can enhance the detection of weak HF-signals. Now, we shall explore transferring this concept into the x-ray domain.

As a first observation, we note that the overall detection observable of Eq. (6.24)—although simplified for illustration purposes—behaves analogous to typical x-ray detectors. To-date, the latter are incapable of resolving the electromagnetic vector potential $\mathbf{A}(\mathbf{x},t)$ at the time-scale of its intrinsic oscillations. Instead, any observation has to focus on the detection of (ideally individual) photons, i.e., energy quanta (cf. also our discussion in Sec. 2.1). Their measurable energy deposition is effectively the result of the detector's exposure to the irradition by the electromagnetic field integrated over a certain time T.

Analogous to Eq. (6.24), the detection of such a time-integrated intensity will depend quadratically upon the field amplitude (here: $\sim (\mathbf{A}(\mathbf{x},t))^2$ or $\sim (\mathbf{E}(\mathbf{x},t))^2$). This can most prominently be seen in the explicit intensity observable given in Eq. (A.129) of App. A.10, but may likewise be concluded from the

[9] We note that the purely *homodyne* detection scenario would obviously be recovered by Eq. (6.31), if $u_{\mathrm{LO}} \to 0$.

quadratic presence of $\hat{\mathbf{A}}_{\text{x\_out}}(\mathbf{x},t)$ within our XOWM observable in Eq. (2.27), for instance.

Given these structural similarities, in the fundamental detection, a transfer of the heterodyne detection concept towards shorter wavelength should be possible—in principle. As a matter of fact, heterodyne detection has already enjoyed a successful extension into the optical regime, where phase-stable laser-sources provide for excellent 'local oscillator'-type reference signals (cf. Refs. [203, 205, 206], for instance).

For our designated x-ray application, however, *no* stable reference source exists. While there have been some (purely theoretical) proposals of using heterodyne detection on x-ray wave mixing signals, such as Ref. [207] for SFG in molecules, these elude the *practical* question of how to achieve it. Given that the use of a secondary—let alone phase-stable—x-ray-laser seems fantastically unrealistic with today's x-ray FEL sources, we would require a reference signal of *alternative* origin to enable a quasi-heterodyne approach nonetheless.

Our proposal for such an alternative is to derive a phase-stable reference beam *in-situ* from the elastic diffraction off the sample that is produced concurrently with XOWM. In other words, we propose to use the mixed detection of linear elastic and nonlinear parametric scattering in an effort to boost the latter by help of the former. Regarding the classification of this new measurement scheme, we notice that it features elements of both *hetero-* and *homodyne* detection:
Using a reference signal (or 'local oscillator') to enhance the detection process clearly bears the hallmark of *heterodyne* detection. While at the same time, the scheme sees the 'local oscillator' being created *within* the sample. Rather than involving an explicit *external* reference, this implies, therefore, that all of the detected signals stem from a single source, which marks a key characteristic of *homodyne* detection. Accounting for this ambiguity, we shall adopt the moniker *amphodyne* detection, wherein the prefix *ampho* signifies 'both'[10].

In order to describe XOWM paired with such an *amphodyne* detection process, we—first of all—have to extend our original framework to include the description of the 'local oscillator' (i.e., linear diffraction). We shall do so in the following.

Observable for amphodyne detected XOWM In deriving an actual scattering observable for XOWM *with* the provision for amphodyne detection, we shall proceed largely analogous to Sec. 2.2.2, where we have obtained the original (homodyne) XOWM observable.

We resume the IXS-type scattering signal of Eq. (2.32) as a starting point

$$\begin{aligned}\langle \hat{O}_{\mathbf{k}_f,\lambda_f}\rangle = \lim_{t\to\infty}\lim_{t_0\to-\infty}\langle \hat{O}_{\mathbf{k}_f,\lambda_f}\rangle(t) = \frac{2\pi\alpha^2}{V\omega_f}\int_{-\infty}^{\infty}dt_1\int_{-\infty}^{\infty}dt_1'\int d^3x\int d^3x'\,(\boldsymbol{\varepsilon}_f)_\sigma H^{(1)}_{\sigma\rho}(\mathbf{x}',t_1',\mathbf{x},t_1)\,(\boldsymbol{\varepsilon}_f^*)_\rho \\ \times e^{-\mathrm{i}\mathbf{k}_f\cdot(\mathbf{x}-\mathbf{x}')}\,e^{\mathrm{i}\,\omega_f(t_1-t_1')}\,\mathrm{Tr}_{\text{REST}}\left\{\hat{n}(\mathbf{x},t_1)\,\hat{\rho}_{\text{REST}}(0)\,\hat{n}(\mathbf{x}',t_1')\right\}. \qquad (6.32)\end{aligned}$$

More specifically, we focus once again on the density-density correlator, which is contained therein

$$\begin{aligned}\langle \hat{n}(\mathbf{x}',t_1')\,\hat{n}(\mathbf{x},t_1)\rangle_{\text{REST}} &:= \mathrm{Tr}_{\text{REST}}\left\{\hat{n}(\mathbf{x},t_1)\,\hat{\rho}_{\text{SYS}}(0)\,\hat{n}(\mathbf{x}',t_1')\right\} \\ &= \mathrm{Tr}_{\text{REST}}\left\{\hat{U}_0(0,t_1)\,\hat{n}(\mathbf{x})\,\hat{U}_0(t_1,0)\,\hat{\rho}_{\text{REST}}(0)\,\hat{U}_0(0,t_1')\,\hat{n}(\mathbf{x}')\,\hat{U}_0(t_1',0)\right\} \\ &= \mathrm{Tr}_{\text{REST}}\left\{\hat{U}_0(t,t_1)\,\hat{n}(\mathbf{x})\,\hat{U}_0(t_1,t_0)\,\hat{\rho}_{\text{REST}}(t_0)\,\hat{U}_0(t_0,t_1')\,\hat{n}(\mathbf{x}')\,\hat{U}_0(t_1',t)\right\} \qquad (6.33)\end{aligned}$$

[10] We note that concepts similar to *amphodyne* detection have been proposed as 'Self-Referenced Coherent Diffraction' for molecular samples [208] or 'Self-heterodyned detection' in the context of HHG spectroscopy [209]. Its potential application to 'time-resolved Bragg peaks in crystals' has been recognized in Ref. [210].

and—following the same steps that have led up to Eqs. (2.40) and (2.41)—simplify this into two equivalent *parametric* amplitudes again

$$\begin{aligned}\mathrm{Tr}_{\mathrm{REST}}\{...\} &\approx \mathrm{Tr}_{\mathrm{OPT}}\{\sum_F \langle F|\hat{U}_0(t,t_1)\,\hat{n}(\mathbf{x})\,\hat{U}_0(t_1,t_0)\left(\sum_I p_I\,|I\rangle\langle I|\otimes\hat{\rho}_{\mathrm{OPT}}(t_0)\right)\hat{U}_0(t_0,t_1')\,\hat{n}(\mathbf{x}')\,\hat{U}_0(t_1',t)\,|F\rangle\}\\ &= \mathrm{Tr}_{\mathrm{OPT}}\{\sum_{I,F} p_I\,\langle F|\hat{U}_0(t,t_1)\,\hat{n}(\mathbf{x})\,\hat{U}_0(t_1,t_0)\,|I\rangle\langle I|\otimes\hat{\rho}_{\mathrm{OPT}}(t_0)\,\hat{U}_0(t_0,t_1')\,\hat{n}(\mathbf{x}')\,\hat{U}_0(t_1',t)\,|F\rangle\}\\ &\approx \mathrm{Tr}_{\mathrm{OPT}}\{\sum_I p_I\,\underbrace{\langle I|\hat{U}_0(t,t_1)\,\hat{n}(\mathbf{x})\,\hat{U}_0(t_1,t_0)\,|I\rangle}_{\text{left amplitude}\Rightarrow\text{Eq. (6.35)}}\langle I|\otimes\hat{\rho}_{\mathrm{OPT}}(t_0)\,\hat{U}_0(t_0,t_1')\,\hat{n}(\mathbf{x}')\,\hat{U}_0(t_1',t)\,|I\rangle\}\,.\end{aligned} \tag{6.34}$$

We recall further from Sec. 2.2.2 that our next steps consisted in partitioning the propagators $\hat{U}_0 = \hat{U}_{00}\,\hat{U}_{\mathrm{INT\_OPT}}$ (cf. Eq. (2.34)) and then expanding all resulting $\hat{U}_{\mathrm{INT\_OPT}}$ in low orders of the optical interaction. Visualizing the resulting terms, we have previously introduced a diagrammatic classification (cf. earlier Fig 2.1). We reproduce this scheme in Fig. 6.5 below[11].

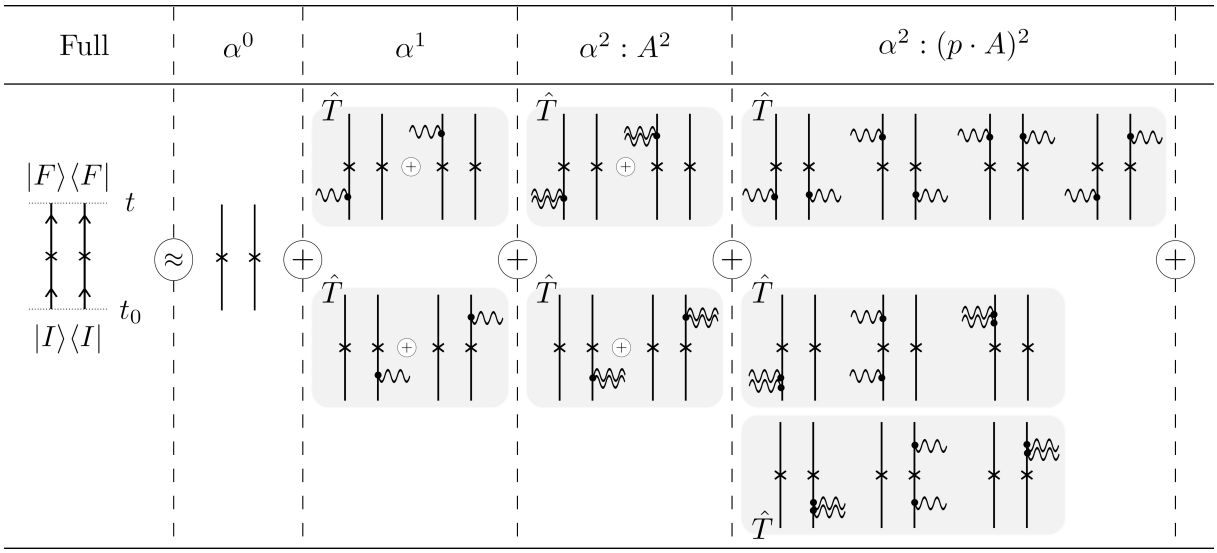

Figure 6.5: Visualization of the perturbative series that results from a low-order expansion of Eq. (6.34) in the light-matter interaction $\hat{H}_{\mathrm{INT\_OPT}}$. For an explanation of the used notation, please refer to the figure's original introduction in Sec. 2.2.2 or the pertaining footnote below. [We gratefully acknowledge Dr. Christina Bömer's help in rendering the above computer graphics.]

From this point onwards, our derivation will *deviate* from the earlier case. While we have focused on the pure (double-sided) XOWM terms, which are depicted in the upper-right corner of Fig. 6.5, during our initial discussion in Sec. 2.2.2, we shall now focus on the terms at order α^1. These diagrams involve

[11] For convenience, we also recall the construction principles underlying these diagrams from Sec. 2.2.2:
In Fig. 6.5, we represent the temporal evolution of the system in terms of primitive double-sided Feynman diagrams. We begin on the left-hand side of Fig. 6.5 by depicting the evolution of the fully coupled system (i.e., the complete REST-system). Starting symbolically from the initial state $|I\rangle\langle I|$ at time t_0, we employ bold arrows to depict the action of $\hat{U}_0$ leading up to the 'final' state $|F\rangle\langle F|$ at time t. In between, we mark the occurrence of the original x-ray-scattering event by an 'x'. At this point, we would find the corresponding action of the electronic density operator $\hat{n}(\mathbf{x})$ within the individual amplitudes. In all of this discussion, we suppress the optical density matrix for the sake of notational simplicity.

In expanding the 'full' propagator $\hat{U}_0$, we employ regular lines and dot-like vertices to signify the action of a propagator $\hat{U}_{00}$ and vertices from $\hat{H}_{\mathrm{INT\_OPT}}$, respectively. These vertices may appear with a single wiggly line attached—corresponding to a $\mathbf{p}\cdot\mathbf{A}$-type interaction—or with a pair of wiggly lines attached to the same dot—corresponding to an $\mathbf{A}^2$-type interaction, conversely.

We sort the occurring terms both in the order of their expansion (i.e., powers of α) as well as their contained types of vertices. Within established categories, we furthermore group terms that are related by time-ordering within their amplitude (i.e., related by geometric re-ordering of vertices' positions along one line). The latter groups are indicated by grey-shaded boxes bearing the signature $\hat{T}$.

one wavemixing amplitude, but also one unperturbed amplitude. The latter corresponds to a purely linear scattering event, such as we require for the generation of the 'local oscillator' in the amphodyne detection scenario.

In a seemingly minute change, we account for these linear terms in our derivation, by simply *not* neglecting the unit-contribution in Eq. (2.42), i.e.,

$$\begin{aligned}
&\langle I|\,\hat{U}_0(t,t_1)\,\hat{n}(\mathbf{x})\,\hat{U}_0(t_1,t_0)\,|I\rangle \\
&\approx \langle I|\,\hat{U}_{00}(t,t_1)\big[\hat{\mathbb{1}}-\mathrm{i}\int_{t_1}^{t}dt_2\,\hat{U}_{00}(t_1,t_2)\,\hat{H}_{\text{INT_OPT}}\,\hat{U}_{00}(t_2,t_1)\big]\,\hat{n}(\mathbf{x}) \\
&\quad\times\hat{U}_{00}(t_1,t_0)\,\big[\hat{\mathbb{1}}-\mathrm{i}\int_{t_0}^{t_1}d\tilde{t}_2\,\hat{U}_{00}(t_0,\tilde{t}_2)\,\hat{H}_{\text{INT_OPT}}\,\hat{U}_{00}(\tilde{t}_2,t_0)\big]\,|I\rangle \\
&= \langle I|\,\hat{U}_{00}(t,0)\big[\hat{\mathbb{1}}-\mathrm{i}\int_{t_1}^{t}dt_2\,\hat{H}_{\text{INT_OPT}}(t_2)\big]\,\hat{n}(\mathbf{x},t_1)\,\big[\hat{\mathbb{1}}-\mathrm{i}\int_{t_0}^{t_1}d\tilde{t}_2\,\hat{H}_{\text{INT_OPT}}(\tilde{t}_2)\big]\hat{U}_{00}(0,t_0)\,|I\rangle \\
&\approx \langle I|\,\hat{U}_{00}(t,0)\,\Big[\hat{n}(\mathbf{x},t_1)-\mathrm{i}\,\alpha\,\Big(\int_{t_1}^{t}dt_2\int d^3y\,\hat{\mathbf{p}}(\mathbf{y},t_2)\cdot\hat{\mathbf{A}}_{\text{opt}}(\mathbf{y},t_2)\,\hat{n}(\mathbf{x},t_1) \\
&\qquad\qquad +\hat{n}(\mathbf{x},t_1)\int_{t_0}^{t_1}d\tilde{t}_2\int d^3\tilde{y}\,\hat{\mathbf{p}}(\tilde{\mathbf{y}},\tilde{t}_2)\cdot\hat{\mathbf{A}}_{\text{opt}}(\tilde{\mathbf{y}},\tilde{t}_2)\Big)\Big]\hat{U}_{00}(0,t_0)\,|I\rangle \\
&= \langle I|\,\hat{U}_{00}(t,0)\,\hat{n}(\mathbf{x},t_1)\,\hat{U}_{00}(0,t_0)\,|I\rangle \\
&\quad-\langle I|\,\hat{U}_{00}(t,0)\,\mathrm{i}\,\alpha\int_{t_0}^{t}dt_2\int d^3y\,\hat{T}\big[(\hat{\mathbf{p}}(\mathbf{y},t_2))_\mu\,\hat{n}(\mathbf{x},t_1)\big]\,(\hat{\mathbf{A}}_{\text{opt}}(\mathbf{y},t_2))_\mu\hat{U}_{00}(0,t_0)\,|I\rangle\,.
\end{aligned}\tag{6.35}$$

Re-inserting this result for both amplitudes in Eq. (6.34), we shall neglect all terms beyond order α^1. For the time-being, we shall still retain the original unit-contribution. Thereby, we obtain an overall expression for the expanded correlator $\mathrm{Tr}_{\text{REST}}\{...\}$ that reads

$$\begin{aligned}
\mathrm{Tr}_{\text{REST}}\{...\} \approx \sum_I p_I\Big(&\langle I|\,\hat{n}(\mathbf{x},t_1)\,|I\rangle\,\langle I|\,\hat{n}(\mathbf{x}',t_1')\,|I\rangle \\
&+\alpha(-\mathrm{i})\int_{t_0}^{t}dt_2\int d^3y\,\langle I|\,\hat{T}\left[(\hat{\mathbf{p}}(\mathbf{y},t_2))_\mu\,\hat{n}(\mathbf{x},t_1)\right]\,|I\rangle\,(\mathbf{A}_{\text{opt_avg}}(\mathbf{y},t_2))_\mu\,\langle I|\,\hat{n}(\mathbf{x}',t_1')\,|I\rangle \\
&+\alpha(\mathrm{i})\int_{t_0}^{t}dt_2'\int d^3y'\,\langle I|\,\hat{n}(\mathbf{x},t_1)\,|I\rangle\,\underbrace{\langle I|\,\hat{T}\left[(\hat{\mathbf{p}}(\mathbf{y}',t_2'))_\nu\,\hat{n}(\mathbf{x}',t_1')\right]\,|I\rangle^*}_{(\mathbf{P}_I(\mathbf{y}',t_2',\mathbf{x}',t_1'))^*}(\mathbf{A}_{\text{opt_avg}}(\mathbf{y}',t_2'))_\nu\Big).
\end{aligned}\tag{6.36}$$

We emphasize that, in writing the above, we could already exchange $\hat{\mathbf{A}}_{\text{opt}}(\mathbf{y},t_2)$ for its classical average $\mathbf{A}_{\text{opt}}(\mathbf{y},t_2)$. This is due to the trace over the optical sub-system, which is inherent in $\mathrm{Tr}_{\text{REST}}\{...\}=\mathrm{Tr}_{\text{OPT}}\{\mathrm{Tr}_{\text{MAT}}\{...\}\}$—via Eq. (2.49) it enforces

$$\mathbf{A}_{\text{opt\_avg}}(\mathbf{y},t)=\langle\hat{\mathbf{A}}_{\text{opt}}(\mathbf{y},t)\rangle=\mathrm{Tr}_{\text{OPT}}\{\hat{\rho}_{\text{OPT}}(0)\,\hat{\mathbf{A}}_{\text{opt}}(\mathbf{y},t)\}\,.\tag{6.37}$$

Furthermore, we have identified the density–current-density response function at the heart of the XOWM contribution once again. Notably, though, the expression (6.36) is only *linear* in $\mathbf{P}_I(\mathbf{y},t_2,\mathbf{x},t_1)$.

On closer inspection of Eq. (6.36), we find that we can combine the two terms at order α^1 into a single, real-part expression

$$\begin{aligned}
\mathrm{Tr}_{\text{REST}}\{...\} \approx \sum_I p_I\Big(&\langle I|\,\hat{n}(\mathbf{x},t_1)\,|I\rangle\,\langle I|\,\hat{n}(\mathbf{x}',t_1')\,|I\rangle \\
&+\mathrm{Re}\Big\{\alpha(-\mathrm{i})\int_{t_0}^{t}dt_2\int d^3y\,(\mathbf{P}_I(\mathbf{y},t_2,\mathbf{x},t_1))_\mu\,(\mathbf{A}_{\text{opt_avg}}(\mathbf{y},t_2))_\mu\,\langle I|\,\hat{n}(\mathbf{x}',t_1')\,|I\rangle\Big\}\Big).
\end{aligned}\tag{6.38}$$

Concluding our main derivation, we substitute the above trace-expression back into the original IXS-observable (Eq. (6.32)) and obtain

$$\begin{aligned}\langle \hat{O}_{\mathbf{k}_f,\lambda_f}\rangle &= \lim_{t\to\infty}\lim_{t_0\to-\infty}\langle \hat{O}_{\mathbf{k}_f,\lambda_f}\rangle(t)\\ &\approx \frac{2\pi\alpha^2}{V\omega_f}\int_{-\infty}^{\infty}dt_1\int_{-\infty}^{\infty}dt_1'\int d^3x\int d^3x'\,(\boldsymbol{\varepsilon}_f)_\sigma\,H^{(1)}_{\sigma\rho}(\mathbf{x}',t_1',\mathbf{x},t_1)\,(\boldsymbol{\varepsilon}_f^*)_\rho\,e^{-\mathrm{i}\,\mathbf{k}_f\cdot(\mathbf{x}-\mathbf{x}')}\,e^{\mathrm{i}\,\omega_f(t_1-t_1')}\\ &\times\sum_I p_I\Big(\langle I|\,\hat{n}(\mathbf{x},t_1)\,|I\rangle\,\langle I|\,\hat{n}(\mathbf{x}',t_1')\,|I\rangle\\ &\qquad+\mathrm{Re}\Big\{\alpha(-\mathrm{i})\int_{-\infty}^{\infty}dt_2\int d^3y\,(\mathbf{P}_I(\mathbf{y},t_2,\mathbf{x},t_1))_\mu\,(\mathbf{A}_{\mathrm{opt\_avg}}(\mathbf{y},t_2))_\mu\,\langle I|\,\hat{n}(\mathbf{x}',t_1')\,|I\rangle\Big\}\Big),\end{aligned}\tag{6.39}$$

wherein we have exercised the limits $t\to\infty$ and $t_0\to-\infty$ just as we did towards the end of Sec. 2.2.2. This gives the combined observable for (elastic) background scattering, i.e., the part exclusively dependent on the density expectation values, and amphodyne detected XOWM, as of the last line.

For further simplification, we may note that any individual expectation value of the electronic density is a constant in time $\langle I|\,\hat{n}(\mathbf{x},t_1)\,|I\rangle = \langle I|\,\hat{n}(\mathbf{x},0)\,|I\rangle =: n_I(\mathbf{x})$ by way of time-translational invariance. Splitting Eq. (6.39) for background and amphodyne XOWM, we arrive at the final results in real-space:

$$\begin{aligned}\langle \hat{O}_{\mathbf{k}_f,\lambda_f}\rangle_{\mathrm{elastic}} &= \frac{2\pi\alpha^2}{V\omega_f}\int^{\times 2}dt_1\,dt_1'\int^{\times 2}d^3x\,d^3x'\,(\boldsymbol{\varepsilon}_f)_\sigma\,H^{(1)}_{\sigma\rho}(\mathbf{x}',t_1',\mathbf{x},t_1)\,(\boldsymbol{\varepsilon}_f^*)_\rho\,e^{-\mathrm{i}\,\mathbf{k}_f\cdot(\mathbf{x}-\mathbf{x}')}\,e^{\mathrm{i}\,\omega_f(t_1-t_1')}\\ &\times\sum_I p_I\,n_I(\mathbf{x})\,n_I(\mathbf{x}')\end{aligned}\tag{6.40}$$

and

$$\begin{aligned}\langle \hat{O}_{\mathbf{k}_f,\lambda_f}\rangle_{\mathrm{ampho}} &= \frac{2\pi\alpha^3}{V\omega_f}\int^{\times 3}dt_1\,dt_1'\,dt_2\int^{\times 3}d^3x\,d^3x'\,d^3y\,(\boldsymbol{\varepsilon}_f)_\sigma\,H^{(1)}_{\sigma\rho}(\mathbf{x}',t_1',\mathbf{x},t_1)\,(\boldsymbol{\varepsilon}_f^*)_\rho\,e^{-\mathrm{i}\,\mathbf{k}_f\cdot(\mathbf{x}-\mathbf{x}')}\,e^{\mathrm{i}\,\omega_f(t_1-t_1')}\\ &\times\sum_I p_I\,\mathrm{Re}\Big\{(-\mathrm{i})\,(\mathbf{P}_I(\mathbf{y},t_2,\mathbf{x},t_1))_\mu\,(\mathbf{A}_{\mathrm{opt\_avg}}(\mathbf{y},t_2))_\mu\,n_I(\mathbf{x}')\Big\}.\end{aligned}\tag{6.41}$$

At this point, we want to emphasize the importance of computing *both* the amphodyne signal and its elastic background. For contrast, we recall that we have previously omitted the explicit numerical evaluation of the latter. This was permissible on conceptual grounds, given that we could expect the scattering patterns of the XOWM signal vs. the background to be sufficiently distinguishable (at least in theory)[12].

For amphodyne detection of XOWM, the situation is *conceptually* different, however. Hereunto, the presence of elastic scattering, which produces the 'local oscillator'-type reference signal, is mandatory in order for the amphodyne detection to succeed. Thus, the elastic and amphodyne signal necessarily overlap in their occurrence and *cannot* be distinguished geometrically. Instead, we will have to rely on the same reasoning as in the radio-frequency case before, namely, knowing and subtracting the contribution that stems solely from the 'local oscillator' (cf. Eq. (6.31) and the term $u_{\mathrm{LO}}^2/2R$ therein). Therefore, we strongly advise for the explicit computation of Eq. (6.40) in this scenario.

Apart from this cautionary reminder, we have reached an expression that can serve as a basic amphodyne-XOWM observable in Eq. (6.41). In other words, we have obtained the analogue of our earlier Eq. (2.57) but for amphodyne detected wavemixing.

[12] We note as a cautioning reminder that—in spite of the conceptually clear separation between XOWM an background—contaminations from background scattering have obviously posed a considerable *practical* challenge, when trying to experimentally detect XOWM, nevertheless.

Observable for amphodyne detected XOWM in reciprocal-space Retracing our earlier steps on the original XOWM observable Eq. (2.57), we likewise want to convert the amphodyne scenario into reciprocal-space, before we close this final section. To do so, we recall all relations outlined in Eqs. (2.59) to (2.61) as well as the Fourier transform of the bare electromagnetic vector potential as given in Eq. (A.67). Using these, we can rewrite

$$\begin{aligned}\langle \hat{O}_{\mathbf{k}_f,\lambda_f}\rangle_{\text{elastic}} = \frac{2\pi\alpha^2}{V\omega_f}\int^{\times 2} dt_1\, dt_1' \int^{\times 2} d^3x\, d^3x'\, (\boldsymbol{\varepsilon}_f)_\sigma \frac{1}{(2\pi)^8}\int^{\times 2} d^3k_X\, d^3k_X' \int^{\times 2} d\omega_X\, d\omega_X'\; e^{-\mathrm{i}\,(\mathbf{k}_X'\cdot\mathbf{x}'-\omega_X' t_1')} \\ \times e^{\mathrm{i}\,(\mathbf{k}_X\cdot\mathbf{x}-\omega_X t_1)}\; Z^{(1)}_{\sigma\rho}(\mathbf{k}_X',\omega_X',\mathbf{k}_X,\omega_X)(\boldsymbol{\varepsilon}_f^*)_\rho\, e^{-\mathrm{i}\,\mathbf{k}_f\cdot(\mathbf{x}-\mathbf{x}')}\, e^{\mathrm{i}\,\omega_f(t_1-t_1')} \\ \times \sum_I p_I \frac{1}{(2\pi)^3}\int d^3k\; e^{\mathrm{i}\,\mathbf{k}\cdot\mathbf{x}}\tilde{n}_I(\mathbf{k})\frac{1}{(2\pi)^3}\int d^3k'\; e^{-\mathrm{i}\,\mathbf{k}'\cdot\mathbf{x}'}(\tilde{n}_I(\mathbf{k}'))^*\end{aligned} \tag{6.42}$$

and

$$\begin{aligned}\langle \hat{O}_{\mathbf{k}_f,\lambda_f}\rangle_{\text{ampho}} = \frac{2\pi\alpha^3}{V\omega_f}\int^{\times 3} dt_1\, dt_1'\, dt_2\; \int^{\times 3} d^3x\, d^3x'\, d^3y\; (\boldsymbol{\varepsilon}_f)_\sigma \frac{1}{(2\pi)^8}\int^{\times 2} d^3k_X\, d^3k_X' \int^{\times 2} d\omega_X\, d\omega_X'\; e^{-\mathrm{i}\,(\mathbf{k}_X'\cdot\mathbf{x}'-\omega_X' t_1')} \\ \times e^{\mathrm{i}\,(\mathbf{k}_X\cdot\mathbf{x}-\omega_X t_1)}\; Z^{(1)}_{\sigma\rho}(\mathbf{k}_X',\omega_X',\mathbf{k}_X,\omega_X)(\boldsymbol{\varepsilon}_f^*)_\rho\, e^{-\mathrm{i}\,\mathbf{k}_f\cdot(\mathbf{x}-\mathbf{x}')}\, e^{\mathrm{i}\,\omega_f(t_1-t_1')} \\ \times \sum_I p_I\, \mathrm{Re}\Big\{(-\mathrm{i})\frac{1}{(2\pi)^7}\int^{\times 2} d^3k_1\, d^3k_2 \int d\omega\; e^{\mathrm{i}\,(\mathbf{k}_1\cdot\mathbf{y}+\mathbf{k}_2\cdot\mathbf{x})}\; e^{-\mathrm{i}\,\omega(t_1-t_2)}\; (\mathbf{K}_I(\mathbf{k}_1,\mathbf{k}_2,\omega))_\mu \\ \times \frac{1}{(2\pi)^4}\int d^3k_L \int d\omega_L\; (\mathbf{A}_{\text{opt\_avg}}(\mathbf{k}_L,\omega_L))_\mu\; e^{\mathrm{i}\,(\mathbf{k}_L\cdot\mathbf{y}-\omega_L t_2)}\frac{1}{(2\pi)^3}\int d^3k'\; e^{-\mathrm{i}\,\mathbf{k}'\cdot\mathbf{x}'}(\tilde{n}_I(\mathbf{k}'))^*\Big\},\end{aligned} \tag{6.43}$$

which can be further condensed to read:

$$\begin{aligned}\langle \hat{O}_{\mathbf{k}_f,\lambda_f}\rangle_{\text{elastic}} = \frac{\alpha^2}{(2\pi)^5\, V\omega_f}\int^{\times 2} d^3k_X\, d^3k_X' \int^{\times 2} d\omega_X\, d\omega_X'\; \delta(\omega_f-\omega_X)\,\delta(\omega_f-\omega_X') \\ \times (\boldsymbol{\varepsilon}_f)_\sigma\, Z^{(1)}_{\sigma\rho}(\mathbf{k}_X',\omega_X',\mathbf{k}_X,\omega_X)(\boldsymbol{\varepsilon}_f^*)_\rho\; \sum_I p_I\, \tilde{n}_I(\mathbf{k}_f-\mathbf{k}_X)\,(\tilde{n}_I(\mathbf{k}_f-\mathbf{k}_X'))^*\end{aligned} \tag{6.44}$$

and

$$\begin{aligned}\langle \hat{O}_{\mathbf{k}_f,\lambda_f}\rangle_{\text{ampho}} = \frac{\alpha^3}{(2\pi)^9\, V\omega_f}\int^{\times 3} d^3k_X\, d^3k_X'\, d^3k_L \int^{\times 3} d\omega_X\, d\omega_X'\, d\omega_L\; \delta(\omega_f-\omega_X-\omega_L)\,\delta(\omega_f-\omega_X') \\ \times (\boldsymbol{\varepsilon}_f)_\sigma\, Z^{(1)}_{\sigma\rho}(\mathbf{k}_X',\omega_X',\mathbf{k}_X,\omega_X)(\boldsymbol{\varepsilon}_f^*)_\rho \\ \times \sum_I p_I\, \mathrm{Re}\Big\{(-\mathrm{i})\,(\mathbf{K}_I(-\mathbf{k}_L,\mathbf{k}_f-\mathbf{k}_X,\omega_L))_\mu\; (\mathbf{A}_{\text{opt\_avg}}(\mathbf{k}_L,\omega_L))_\mu (\tilde{n}_I(\mathbf{k}_f-\mathbf{k}_X'))^*\Big\}.\end{aligned} \tag{6.45}$$

In writing the above, we have employed the Fourier transform of the electronic density. However, we note that in the context of crystallography, we might as well identify its Fourier components with the more widely used structure factor, which results from the restricted transformation of a single unit cell:

$$F(\mathbf{Q}) = \int_{\text{unit cell}} d^3x\; e^{\mathrm{i}\,\mathbf{Q}\cdot\mathbf{x}}\, n_I(\mathbf{x}) = \frac{V_{\text{unit cell}}}{V_{\text{crystal}}}\,\tilde{n}_I(\mathbf{Q}). \tag{6.46}$$

Note that the last equality holds strictly only for a perfectly periodic crystal.

In terms of Eqs. (6.44) and (6.45), we have ultimately obtained two expressions, which allow for the evaluation of (nonlinear) scattering distributions in an analogous fashion to our discussions in Chpt. 5. An in-depth analysis of its features is beyond the scope of the current treatise, however. Instead, it should serve as a basis for—as well as outlook onto—future applications of XOWM.

In a first attempt at realizing the proposed methodology, we have initiated a renewed collaborative effort that seeks to implement the amphodyne detection scheme at the Linac Coherent Light Source (LCLS) in Stanford [156, 157]. For further insights on the concept, we attach the respective proposal as an Appendix (A.19) to this work[13].

With this particular outlook being hinted at already, we shall conclude our presentation of 'extra'-content and proceed to give a more general summary as well as broader outlook onto future XOWM activities in the closing chapter.

[13] We emphasize—as has been the case with previous experimental efforts—that the referenced proposal is a product of collaborative efforts despite drawing its inspiration from the above theory. To maintain this distinction from our own work, we abstain from including it directly at this point.

Chapter 7

Summary and Outlook

7.1 Summary

Theory: At the beginning of this work, we set out to formulate a description for x-ray-optical wavemixing processes.

To do so, we have started from first principles—in our case from non-relativistic Quantum-Electrodynamics—and successively simplified a general x-ray-scattering expression into a theoretical framework dedicated to parametric XOWM. Within this framework, we are capable of describing a class of popular wavemixing processes, namely sum- and difference-frequency generation as well as x-ray parametric down-conversion on equal footing. Notably, we have intended this framework to be modular in its structure and *quantitatively* predictive in its output. In pursuit of modularity, we could partition our overall XOWM-observable into constituent correlation functions, each capturing the description of a specific sub-system, i.e., the x-ray field, the optical field and the electronic response to both of the priors (cf. Chpt. 2). In our subsequent modelling of these building blocks, we have upheld our goal of reaching quantitative predictability, bearing the required realism firmly in mind (see Chpts. 3 and 4 for details).

As one of our central theoretical findings, we could identify the microscopic electronic response, which governs XOWM to lowest order. Namely, we found that this can be captured by a density–current-density correlation function of the electronic system. In this detailed insight, our theory exceeds many earlier models of x-ray wavemixing, which have often proposed ad-hoc descriptions in terms of simply a driven, i.e., time-dependent, electronic density, or others, which have argued purely on the basis of classical currents.

We have attempted to establish a better understanding of this novel correlation function by elaborating on its general properties but also studying a concrete example for the case of diamond.

Most importantly—in our opinion—we have attempted to render the density–current-density correlation function accessible for a broader community of solid-state and computational physicists by deriving expressions that are amenable to numerical implementation and evaluation. Hereunto, we have discussed two promising options at different levels of numerical cost:

1. The first option consists in a mean-field model for the nonlinear response. We have derived its formulation in single-particle orbitals within Sec. 3.2.3 and demonstrated its numerical evaluation on the basis of Kohn-Sham DFT-orbitals subsequently. Comparable implementations on the basis of wide-spread DFT-codes appear entirely feasible and, as a matter of fact, one such implementation is currently under way.

2. The second option extends beyond mean-field treatments and has been introduced in Sec. 3.4. Therein, we derive an approximate connection of our density–current-density correlation function to more commonly used density–density response functions. We appreciate the latter as a point for interfacing with alternative computational methods, as it features prominently in techniques related to RPA, (LR)-TD-DFT or BSE[1]. While the connection to any of these post-mean-field treatments could allow for new insights into (more) correlated electronic systems, we note that they also come at a significantly increased computational cost, compared to bare DFT.

Experiment Beyond deriving our XOWM framework theoretically, we could also—and more importantly in our opinion—confirm its practical viability. To do so, we have put the quantitative nature of the framework to the test and benchmarked its predictions on published data as well as on independent measurement results (cf. Chpt. 5).

In order to obtain the latter, we have proposed, promoted, organized and conducted XOWM-experiments[2] at several international x-ray sources and in different XOWM-regimes. Of these experimental campaigns, we want to highlight two essential outcomes:

1. First of all, we have been able to demonstrate the—unsurprising, yet up to that time unconfirmed—existence of x-ray-optical difference frequency generation. Moreover—going beyond a singular confirmation—we could demonstrate DFG measurements for a series of crystalline orientations in the pertaining beamtime at SwissFEL. In line with our proposal of Sec. 5.1.2.d, we have thus established the experimental proof-of-principle for ‘nonlinear crystallography’.

2. In a second noteworthy effort, we have studied x-ray parametric down-conversion in the high-energy regime of XUV-idler photons (cf. Sec. 5.2.3.a). Therein, we have re-visited earlier studies by Tamasaku and co-workers using a much improved setup. In fact, we have pioneered angle-resolved detection for XPDC and could observe its characteristic, circular scattering signature for the first time. We could further confirm our predictions of XPDC side-lobes in the resulting images as well as the intimately connected polarization-dependence of the effect.

Besides the aforementioned confirmations, however, the last experiment also raised new challenges for our theory. In particular, we could experimentally retrieve an alternating modulation of the XPDC scattering pattern, which could not be explained on the basis of our current XOWM framework alone. Closely related observations had likewise been reported by Tamasaku and co-workers about a decade earlier and remained an open question ever since. We could resolve this long-standing conundrum by developing a separate, polaritonic picture of XPDC. In its first approximate implementation as a simple model, it could reproduce all features of the remarkable scattering patterns qualitatively (cf. Sec. 6.1).

With the above in mind, we conclude that we could achieve significant progress on the description *and* application of parametric XOWM over the past years. Nevertheless, there are several open challenges, such as the re-conciliation of our framework with the polariton-picture or simply its extended application to new materials and setups—on some of which we will give an outlook below.

[1] For the convenience of readers, who have skipped the intermediate chapters, we repeatedly explicate the above abbreviations: RPA - random-phase approximation, (LR)-TD-DFT - (linear response) time-dependent density-functional theory and BSE - Bethe-Salpeter equation.

[2] We want to re-iterate our acknowledgement—at this point and for all related mentionings of experiments—that these have only been possible as *collaborative* efforts. As such, we cannot overstate our gratitude towards various collaborators for their respective support. While more detailed acknowledgements of individual contributions may be found with the respective experimental discussions, we want to highlight the singular efforts of Dr. Christina Bömer at this point again. Without her, most of the advances in this project would not have materialized in their presented form.

7.2 Outlook

Before closing this work, we want to complement our previous retrospection with an outlook into the future. As we have indicated earlier, several challenges lie ahead. Yet more importantly, we are convinced that opportunities abound for pushing XOWM research further, for consolidating our understanding of the underlying nonlinear responses and—above all—for addressing novel materials beyond elemental group-IV semiconductors.

To these effects, we will comment on several up-coming strands of research below. We loosely group these into four categories for, but note that they should be seen as mutually supporting efforts.

Numerical advances As a first big field of continuative research efforts, we identify the advancement of theoretical /numerical methods for evaluating electronic nonlinear responses. Already at the present level of mean-field DFT, there are several paths to pursue—with the extension towards more material classes being of prime importance. This could both inform future experiments but conversely also serve as a broader (and thus less biased) base for benchmarking our XOWM framework, as soon as more experimental references are available.

Beyond extending towards simply *more* computations, another logical pursuit would concern evolving towards *better* computations. Benchmarking different exchange-correlation potentials at the level of DFT would mark a first step to this end, whereas a methodical extension beyond mean-field approaches form a clear, additional goal. Once higher-order methodologies become available for XOWM calculations (cf. for example our proposal in Sec. 3.4), genuinely new insights can be expected into the nonlinear response of correlated electronic systems. A prime example—especially with a view to later polaritonic coupling—can be found in the prospective study of (band gap-) excitons and their influence on XOWM signals. Going further beyond this still, we could envision to investigate the imprints of more elaborate electronic-order phenomena as well.

In an alternative approach, we could also imagine to turn above's reasoning on its head—using the experiment to inform theory rather than the other way around. After all XOWM provides access to a nonlinear, two-particle response function of the electronic system. This could either be used directly to fit theoretical expressions at the same level of complexity or it could be integrated downwards in the spirit of hierarchical Green's function methods and thereby provide additional correlation-information at the level of one-particle observables.

Nonlinear crystallography Transitioning from theory into the experimental realm, we see the second major field of future research presenting itself in the application of (laser-driven) XOWM for nonlinear crystallography. As with the aforementioned theoretical efforts, large emphasis will be placed on the method's extension towards a broader range of samples first. These new, and likely 'less-than-perfect', crystals will entail a range of challenges. These include:

- lower scattering yields (from smaller crystals),
- higher signal-to-background ratios (from crystals of lower quality) and
- premature losses of input or output fields (in crystals featuring stronger absorption)

to name but a few. Many of these issues may be off-set, to some degree, by refining our experimental setup—both with regard to higher detection efficiency for the signal and with regard to even better

discrimination against background.

One variable of the setup, which has seen no modification yet, but would immediately recommend itself for an investigation is the driving laser. Changing—or better still—tuning its photon energy away from ~ 1.55 eV, we could explore the spectroscopic potential of XOWM on top of its spatial resolution.

On a more conceptual side, nonlinear crystallography faces an imminent challenge in achieving the spatial reconstruction of the nonlinear response density from its structure factors. This requires the solution of the well-known phase-problem (cf. our discussion in Sec. 5.1.2.d). In contrast to regular crystallography, where strong constraints on the observable density can be harnessed to simplify the problem, our nonlinear response function poses a more *complex* problem—quite literally. Irrespective of these outstanding developments, hybrid approaches—combining theoretical and experimental data—can provide us with first insights into three-dimensional responses already (see Fig. 7.1, for an example below).

In the broader context of phasing the XOWM signal, we have previously alluded to the idea of investigating multi-beam diffraction as well (similarly, see Sec. 5.1.2.d). While such delicate diffraction-phenomena may be far from the reach of our current experimental method, they certainly provide a challenging long-term outlook. At the same time, the prospect of multi-beam diffraction may already serve to inspire further theoretical studies as a near-term precursor.

Amphodyne detection In a conceptually different take on the subject of interfering beams, we have introduced the concept of 'amphodyne' detection. This marks its own route of future research, harbinging the possibility of amplifying the—otherwise often weak—wavemixing signals. At the same time, this approach faces its very own challenges: It is, in fact, sensitive to the scattering phase, which could be considered a seminal advantage. However, it would need to be implemented in the highly fluctuating environment of today's x-ray FELs. Here the effect's sensitivity to phases becomes a manifest disadvantage, as it results in the signal being washed out over the course of successive FEL-shots.

Nevertheless, we have proposed an exploratory study on 'amphodyne' detection at the LCLS and expect future developments around its concept to yield very fruitful results on the mixing process at its core.

Polariton The final cluster of research, on the prospect of which we want to comment, concerns the polaritonic imprints that we have found in XPDC (cf. Sec. 5.2.3.a). An immediate goal for its theoretical description is obviously the reconciliation with our overall XOWM framework—as stated above. Given the promising indications from our perturbative pre-study (cf. Sec. A.17), we envision a possible solution along this route—likely involving the need for renormalization techniques, though.

Retaining an explicit polariton perspective, on the other hand, we could likewise envision the development of non-perturbative approaches. These could focus on the polariton itself—in terms of an effective field theory—or consider the coupled light-matter system in a Floquet-type approach (cf. our earlier reference to Dr. Popova-Gorelova's work).

On the experimental side of research into x-ray-induced polaritons, we perceive a rich field of future applications. On the one hand, such a polariton is of fundamental interest itself—especially noting that it is *not* created by the usual cavity-coupling—on the other hand, it also harbours great potential as a secondary probe. Illustrating our latter thought further, we recall that the carrier-wavelength of a polariton at ~ 100 eV energy amounts to ~ 10 nm. Therefore, it should prove rather sensitive to nanoscopic

structures or disturbances, which are present at the same length-scale. We add to this the notion that it is possible to map the full, three-dimensional polariton-dispersion in a tomographic fashion, simply by tracing the XPDC signal across its complete phasematching range. The combination of these two aspects strongly suggests the polariton's ability to act as an in-situ diffracting nano-probe. First experimental schemes to verify this hypothesis, which should use layered and nano-structured samples, are currently being designed.

With a view to this multitude of prospective research activities, we feel confident to conclude our study of XOWM on a positive outlook. With challenging, yet potentially very insightful, questions ahead, we hope that XOWM can evolve further and form a lasting as well as meaningful contribution to the (nonlinear) toolkit of x-ray scientists and facilities.

In closing, we want to leave the reader with a literal out*look*, namely onto the first nonlinear response density, which we have reconstructed using experimental data[3].

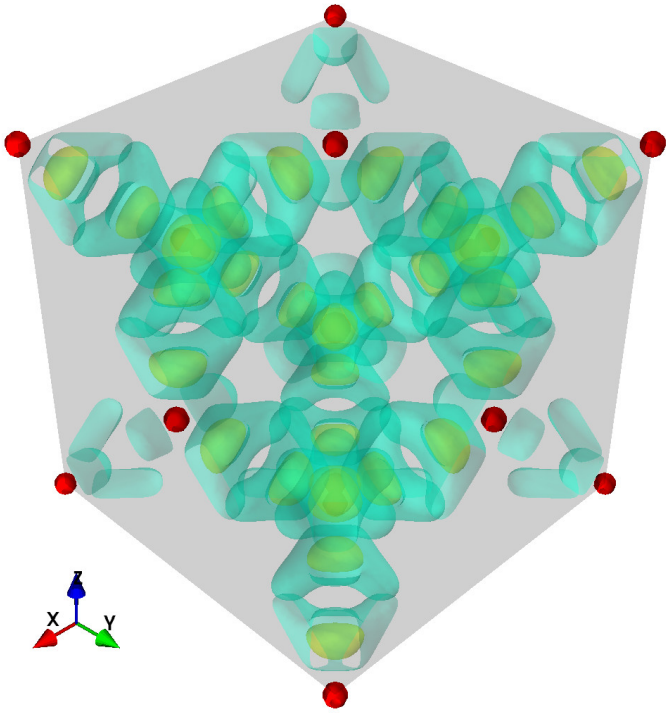

Figure 7.1: A final outlook onto the nonlinear response density $|\mathbf{R}(\mathbf{x},\omega)|^2$ as reconstructed from preliminary experimental data (cf. SwissFEL campaign of Sec. 5.1.3.a). The photon energy of the driving laser has been $\hbar\omega = 1.55$ eV and the nonlinear reflections (111), (220), (311), (222) and (400) have been used for the three-dimensional reconstruction. The resolution reaches sub-Å level and can directly be compared to our expectations in Fig. 5.6.

[3]We note that the experimental data underlying Fig. 7.1 stems from the SwissFEL campaign (proposal No. 20212165), which we have reported on in Sec. 5.1.3.a. The reconstruction relies on nonlinear scattering yields from five different reflections, viz. (111), (220), (311), (222) and (400), while for their phase information, we resorted to the theoretical values in this preliminary case. We recall, in passing, that phase-retrieval for nonlinear crystallography will remain a future challenge and outlook as well.

Appendix A

Appendices

In addition to the main body of this thesis, we have curated a set of appendices. These contain supplementary material in terms of further specifications, documentation, and derivations, which are included to act as quickly accessible references for the reader (and author). Notably, the contents of these appendices—by and large—hold no claim to novelty, but might prove convenient nonetheless.
In these appendices, the succession of topics roughly mirrors the structure of the thesis:

- At the outset, we provide further background on the quantum-mechanical time-evolution operator and underpin its perturbative expansion (as it was used in Chpt. 2).
- In addition, we briefly summarize our convention for Fourier transformations (App. A.2), before elaborating on two main blocks of topics;
- the first pertaining to electronic structure aspects (App. A.4 - App. A.6)
- and the second focusing on the electromagnetic field (App. A.7 - App. A.13).
- After these blocks, we include further appendices on miscellaneous subjects, such as a reference list of useful integrals, for instance (see App. A.15).

A.1 Fundamentals of time-evolution operators and time-dependent perturbation theory

Our theoretical description of x-ray-optical wavemixing is (mostly) formulated using time-dependent perturbation theory (TDPT). In the following, we will briefly introduce this approximative method on the basis of time-evolution operators and their equations of motion[1]. This will lead us to the well-known Dyson equation and iterative solutions thereof, viz. Dyson series (cf. Refs. [69, 211], for example).

To begin with, we recall the time-dependent Schrödinger equation (TDSE) as the governing principle of non-relativistic quantum mechanics:

$$\mathrm{i}\,\frac{\partial}{\partial t}\,|\Psi(t)\rangle = \hat{H}\,|\Psi(t)\rangle\,. \tag{A.1}$$

In here, $\hat{H}$ denotes the Hamiltonian operator pertaining to the system of interest. The TDSE prescribes the unitary evolution of a quantum state vector (vulgo: wave-function) $|\Psi(t)\rangle$ through time. In fact, its solution for $|\Psi(t)\rangle$ at any possible t is unique and fully determined through a single initial condition at some time t_0. In other words, the TDSE provides a unitary mapping

$$|\Psi(t)\rangle \quad \xleftarrow{\text{TDSE}} \quad |\Psi(t_0)\rangle \tag{A.2}$$

$$|\Psi(t)\rangle = \hat{U}(t,t_0)\,|\Psi(t_0)\rangle\,, \tag{A.3}$$

which can be expressed equivalently by using a time-evolution operator $\hat{U}(t,t_0)$. Formally, this operator incorporates all changes that the quantum state would undergo in between time t_0 and time t. Applying it to $|\Psi(t_0)\rangle$ thus propagates the wave-function through time.

In order for the resultant $|\Psi(t)\rangle$ to be a proper solution to the TDSE, the time-evolution operator *itself* has to comply with the TDSE[2]:

$$\mathrm{i}\,\frac{\partial}{\partial t}\hat{U}(t,t_0) = \hat{H}\hat{U}(t,t_0). \tag{A.4}$$

As such, $\hat{U}(t,t_0)$ is basically the Green's function of the TDSE, even though it rather goes by the name of 'time-evolution operator' or 'propagator'. It features the following intuitive—yet important—properties:

- Concatenation: $\hat{U}(t_3,t_2)\hat{U}(t_2,t_1) = \hat{U}(t_3,t_1)$
- Inversion: $(\hat{U}(t_2,t_1))^{\dagger} = (\hat{U}(t_2,t_1))^{-1} = \hat{U}(t_1,t_2)$
- Identity: $\hat{U}(t_1,t_2)\hat{U}(t_2,t_1) = \hat{U}(t_1,t_1) = \mathbb{1}$

Concluding on the general aspects of time-evolution operators, we want to emphasize that it is usually impossible to obtain their exact form for realistic problems. Just as the solution of the fundamental TDSE (Eq. (A.1)) is elusive for most cases, so likewise is its counterpart for $\hat{U}$. At this point, approximative methods are required.

[1] Note that there are many equivalent ways of phrasing TDPT in principle. However, we consider the present one, which uses time-evolution operators, to be conceptually most appealing. It provides an intuitive, yet comprehensive, picture and can be applied to wave-functions and density matrices alike.

[2] Note that Eq. (A.4) can easily be reasoned by inserting Eq. (A.3) into Eq. (A.1) and requiring that the result be valid for any arbitrary quantum state.

A.1.0.a Towards time-dependent perturbation theory

The approximative method, which we shall focus on in the following, is time-dependent perturbation theory (TDPT). It is most suited for scenarios, wherein the time-evolution of the unperturbed (e.g., static) system is known, while some additional interaction creates weak, yet possibly complicated, deviations from this evolution. A system of this kind could be described by a partitioned Hamiltonian of the form:

$$\hat{H} = \hat{H}_0 + \hat{H}_{\mathrm{INT}}. \tag{A.5}$$

Here, $\hat{H}_0$ refers to that part of the system, for which a solution to the TDSE is supposed to be known. $\hat{H}_{\mathrm{INT}}$, on the other hand, signifies the additional interaction. For example, this may be an external field driving the system or an intrinsic coupling between two subsystems of $\hat{H}_0$, which would otherwise be separated[3].

In this setting, the goal of TDPT is to simplify the general equation that governs time-evolution (i.e., Eq. (A.4)) by capitalizing on the solution for the unperturbed part, which already exists:

$$\mathrm{i}\,\frac{\partial}{\partial t}\hat{U}_0(t,t_0) = \hat{H}_0\,\hat{U}_0(t,t_0) \qquad \Rightarrow \qquad \hat{U}_0(t,t_0) = e^{-\mathrm{i}\hat{H}_0(t-t_0)}. \tag{A.6}$$

If this operator dominates the dynamics of the overall system—with small corrections from the perturbation—then, it seems sensible to account for the latter via a product-ansatz[4]:

$$\hat{U}(t,t_0) = \hat{U}_0(t,t_0)\,\hat{U}_{\mathrm{INT}}(t,t_0). \tag{A.7}$$

Using this, we can search for an equation of motion that is specific to the interaction-based time-evolution operator. To this end, we combine Eqs. (A.4), (A.5) and (A.7) and find

$$\begin{aligned}
\mathrm{i}\,\frac{\partial}{\partial t}\hat{U}(t,t_0) &= \hat{H}\,\hat{U}(t,t_0) \\
\mathrm{i}\,\frac{\partial}{\partial t}\Big(\hat{U}_0(t,t_0)\,\hat{U}_{\mathrm{INT}}(t,t_0)\Big) &= \Big(\hat{H}_0+\hat{H}_{\mathrm{INT}}\Big)\Big(\hat{U}_0(t,t_0)\,\hat{U}_{\mathrm{INT}}(t,t_0)\Big) \\
\Big(\mathrm{i}\,\frac{\partial}{\partial t}\hat{U}_0(t,t_0)\Big)\,\hat{U}_{\mathrm{INT}}(t,t_0) + \hat{U}_0(t,t_0)\,\Big(\mathrm{i}\,\frac{\partial}{\partial t}\hat{U}_{\mathrm{INT}}(t,t_0)\Big) &= \Big(\hat{H}_0+\hat{H}_{\mathrm{INT}}\Big)\Big(\hat{U}_0(t,t_0)\,\hat{U}_{\mathrm{INT}}(t,t_0)\Big) \\
\hat{H}_0\,\hat{U}_0(t,t_0)\,\hat{U}_{\mathrm{INT}}(t,t_0) + \hat{U}_0(t,t_0)\,\mathrm{i}\,\frac{\partial}{\partial t}\hat{U}_{\mathrm{INT}}(t,t_0) &= \Big(\hat{H}_0+\hat{H}_{\mathrm{INT}}\Big)\hat{U}_0(t,t_0)\,\hat{U}_{\mathrm{INT}}(t,t_0) \\
\hat{U}_0(t,t_0)\,\mathrm{i}\,\frac{\partial}{\partial t}\hat{U}_{\mathrm{INT}}(t,t_0) &= \hat{H}_{\mathrm{INT}}\,\hat{U}_0(t,t_0)\,\hat{U}_{\mathrm{INT}}(t,t_0) \\
\mathrm{i}\,\frac{\partial}{\partial t}\hat{U}_{\mathrm{INT}}(t,t_0) &= \underbrace{\hat{U}_0(t_0,t)\,\hat{H}_{\mathrm{INT}}\,\hat{U}_0(t,t_0)}_{\hat{H}^{\mathrm{I}}_{\mathrm{INT}}(t,t_0)}\,\hat{U}_{\mathrm{INT}}(t,t_0).
\end{aligned} \tag{A.8}$$

[3] Note that in principle, the interaction Hamiltonian could even be chosen to include an explicit time-dependence (i.e., $\hat{H}_{\mathrm{INT}}(t)$). In fact, this is often done in cases of external fields driving a system—think of an atom exposed to an external laser beam. However, this superficially innocuous addition poses noteworthy conceptual challenges. It formally voids energy conservation—which may be visualized on the previous example as well: There, the laser can impart energy to the atom that it did not possess originally. Effectively, this converts the originally 'closed' quantum system, which was described by $\hat{H}_0$ alone, into an 'open' quantum system. In extreme cases, this may even jeopardize the unitarity of time-evolution. With this note of caution put forth, we shall abstain from introducing an explicit time-dependence to $\hat{H}_{\mathrm{INT}}$ here. We note further, however, that it would not change the resulting equations up to and including Eq. (A.15).

[4] Note that we motivate the product-ansatz (Eq. (A.7)) in the context of small perturbative corrections, but its validity extends beyond. In fact, it is possible to factorize the time-evolution operator according to any arbitrary partitioning of the Hamiltonian—it may not be useful to do so, though.

This is once again a Schrödinger-type equation, which governs the evolution of $\hat{U}_{\mathrm{INT}}(t,t_0)$, but notably contains an effectively time-dependent Hamiltonian. In fact, this is the TDSE in the so-called 'interaction picture'—a hybrid in between the more common 'Schrödinger picture' (i.e., our starting point) and the 'Heisenberg picture' (see, for instance, Ref. [211]). The involved Hamiltonian is 'dressed' by the free time-evolution and represents the original interaction Hamiltonian *in* the interaction picture:

$$\hat{H}^{\mathrm{I}}_{\mathrm{INT}}(t,t_0) := \hat{U}_0(t_0,t)\,\hat{H}_{\mathrm{INT}}\,\hat{U}_0(t,t_0) = e^{\mathrm{i}\hat{H}_0(t-t_0)}\,\hat{H}_{\mathrm{INT}}\,e^{-\mathrm{i}\hat{H}_0(t-t_0)}. \tag{A.9}$$

Here, the second equality draws on the explicit solution of Eq. (A.6) and may be more familiar from common quantum mechanics textbooks.

Pursuing further reformulation of Eq. (A.8), we can formally integrate in time and obtain

$$\begin{aligned}\hat{U}_{\mathrm{INT}}(t,t_0) &= \mathbb{1} - \mathrm{i}\int_{t_0}^{t} dt'\;\hat{U}_0(t_0,t')\,\hat{H}_{\mathrm{INT}}\,\hat{U}_0(t',t_0)\;\hat{U}_{\mathrm{INT}}(t',t_0)\\ &= \mathbb{1} - \mathrm{i}\int_{t_0}^{t} dt'\;\hat{H}^{\mathrm{I}}_{\mathrm{INT}}(t',t_0)\;\hat{U}_{\mathrm{INT}}(t',t_0)\end{aligned} \tag{A.10}$$

or, upon including $\hat{U}_0(t_0,t)$:

$$\hat{U}(t,t_0) = \hat{U}_0(t,t_0)\hat{U}_{\mathrm{INT}}(t,t_0) = \hat{U}_0(t,t_0) - \mathrm{i}\,\hat{U}_0(t,t_0)\int_{t_0}^{t} dt'\;\hat{U}_0(t_0,t')\,\hat{H}_{\mathrm{INT}}\;\hat{U}(t',t_0). \tag{A.11}$$

These recursive expressions are known as Dyson equations and constitute the starting point for actual perturbation theory.

Instead of finding the exact solution for $\hat{U}_{\mathrm{INT}}(t,t_0)$, it often suffices to iterate Eq. (A.10) in low orders and thus find approximations as follows:

1. order:

$$\hat{U}^{(1)}_{\mathrm{INT}}(t,t_0) = \mathbb{1} - \mathrm{i}\int_{t_0}^{t} dt'\;\hat{H}^{\mathrm{I}}_{\mathrm{INT}}(t',t_0)\;\mathbb{1}, \tag{A.12}$$

2. order:

$$\begin{aligned}\hat{U}^{(2)}_{\mathrm{INT}}(t,t_0) &= \mathbb{1} - \mathrm{i}\int_{t_0}^{t} dt'\;\hat{H}^{\mathrm{I}}_{\mathrm{INT}}(t',t_0)\left(\mathbb{1} - \mathrm{i}\int_{t_0}^{t'} dt''\;\hat{H}^{\mathrm{I}}_{\mathrm{INT}}(t'',t_0)\;\mathbb{1}\right)\\ &= \mathbb{1} - \mathrm{i}\int_{t_0}^{t} dt'\;\hat{H}^{\mathrm{I}}_{\mathrm{INT}}(t',t_0) - \int_{t_0}^{t} dt'\int_{t_0}^{t'} dt''\;\hat{H}^{\mathrm{I}}_{\mathrm{INT}}(t',t_0)\,\hat{H}^{\mathrm{I}}_{\mathrm{INT}}(t'',t_0)\\ &= \mathbb{1} - \mathrm{i}\int_{t_0}^{t} dt'\;\hat{H}^{\mathrm{I}}_{\mathrm{INT}}(t',t_0) - \frac{1}{2}\int_{t_0}^{t} dt'\int_{t_0}^{t} dt''\;\hat{T}\left[\hat{H}^{\mathrm{I}}_{\mathrm{INT}}(t',t_0)\,\hat{H}^{\mathrm{I}}_{\mathrm{INT}}(t'',t_0)\right],\end{aligned} \tag{A.13}$$

3. order:

$$\begin{aligned}
\hat{U}^{(3)}_{\mathrm{INT}}(t,t_0) &= \mathbb{1} - \mathrm{i}\int_{t_0}^{t} dt'\ \hat{H}^{\mathrm{I}}_{\mathrm{INT}}(t',t_0)\Big(\mathbb{1} - \mathrm{i}\int_{t_0}^{t'} dt''\ \hat{H}^{\mathrm{I}}_{\mathrm{INT}}(t'',t_0)\Big(\mathbb{1} - \mathrm{i}\int_{t_0}^{t''} dt'''\ \hat{H}^{\mathrm{I}}_{\mathrm{INT}}(t''',t_0)\ \mathbb{1}\Big)\Big) \\
&= \mathbb{1} - \mathrm{i}\int_{t_0}^{t} dt'\ \hat{H}^{\mathrm{I}}_{\mathrm{INT}}(t',t_0) - \int_{t_0}^{t} dt' \int_{t_0}^{t'} dt''\ \hat{H}^{\mathrm{I}}_{\mathrm{INT}}(t',t_0)\,\hat{H}^{\mathrm{I}}_{\mathrm{INT}}(t'',t_0) \\
&\qquad + \mathrm{i}\int_{t_0}^{t} dt' \int_{t_0}^{t'} dt'' \int_{t_0}^{t''} dt'''\ \hat{H}^{\mathrm{I}}_{\mathrm{INT}}(t',t_0)\,\hat{H}^{\mathrm{I}}_{\mathrm{INT}}(t'',t_0)\,\hat{H}^{\mathrm{I}}_{\mathrm{INT}}(t''',t_0) \\
&= \mathbb{1} - \mathrm{i}\int_{t_0}^{t} dt'\ \hat{H}^{\mathrm{I}}_{\mathrm{INT}}(t',t_0) - \frac{1}{2}\int_{t_0}^{t} dt' \int_{t_0}^{t} dt''\ \hat{T}\left[\hat{H}^{\mathrm{I}}_{\mathrm{INT}}(t',t_0)\,\hat{H}^{\mathrm{I}}_{\mathrm{INT}}(t'',t_0)\right] \\
&\qquad + \mathrm{i}\frac{1}{6}\int_{t_0}^{t} dt' \int_{t_0}^{t} dt'' \int_{t_0}^{t} dt'''\ \hat{T}\left[\hat{H}^{\mathrm{I}}_{\mathrm{INT}}(t',t_0)\,\hat{H}^{\mathrm{I}}_{\mathrm{INT}}(t'',t_0)\,\hat{H}^{\mathrm{I}}_{\mathrm{INT}}(t''',t_0)\right]
\end{aligned} \tag{A.14}$$

and so forth.

In the last step of Eqs. (A.13) and (A.14), respectively, we have introduced the time-ordering operator $\hat{T}$ to obtain a slightly different formulation[5].

For completeness, we want to point out that the Dyson series may formally be extended ad infinitum. Re-summing it and making excessive use of $\hat{T}$ will result in a time-ordered exponential operator as the general solution

$$\hat{U}_{\mathrm{INT}}(t,t_0) = \hat{T}\left[e^{-\mathrm{i}\int_{t_0}^{t} dt'\ \hat{H}^{\mathrm{I}}_{\mathrm{INT}}(t',t_0)}\right]. \tag{A.15}$$

We should emphasize that this form is essentially analogous to the solutions for $\hat{U}(t,t_0)$ or $\hat{U}_0(t,t_0)$ (cf. Eq. (A.6)), but accounts for the additional time-dependence that each $\hat{H}^{\mathrm{I}}_{\mathrm{INT}}(t',t_0)$ carries from Eq. (A.8). In closing, we note that—despite its elegance—the compact expression above is often of little practical value, as its evaluation usually requires the re-expansion of the whole series.

A.1.0.b Remark on the Heisenberg picture and its EOM

In our above discussion, we have briefly touched upon the distinction of the Schrödinger and Heisenberg pictures of quantum-mechanical time-evolution. For completeness, we want to point out that the usage of time-evolution operators allows to convert one into the other in a straight-forward manner.

As a starting point, we recall that Heisenberg put the emphasis of his formulation of quantum-mechanics (namely, matrix-mechanics [212–214]) onto the time-evolution of operators instead of quantum states. This can be motivated from the simple observation that (time-dependent) expectation values of specific operators may be (re-)written either way:

$$\left\langle \hat{O}(t) \right\rangle = \langle \Psi(t)|\,\hat{O}\,|\Psi(t)\rangle = \langle \Psi(t_0)|\underbrace{\hat{U}(t_0,t)\,\hat{O}\,\hat{U}(t,t_0)}_{=:\hat{O}^{\mathrm{H}}(t,t_0)}|\Psi(t_0)\rangle = \langle \Psi(t_0)|\,\hat{O}^{\mathrm{H}}(t,t_0)\,|\Psi(t_0)\rangle\,. \tag{A.16}$$

Here, we have defined the operator in the Heisenberg picture $\hat{O}^{\mathrm{H}}(t,t_0)$ to incorporate the time-evolution that would otherwise (i.e., in the Schrödinger picture) have been associated with the quantum-state $|\Psi(t)\rangle$—reducing the latter to a static initial condition at $t = t_0$ (viz., $|\Psi(t_0)\rangle$).

[5] We recall that the time-ordering operator $\hat{T}[...]$ acts on all following operators, which are included by its brackets. Specifically, it sorts them according to their (first) time-argument, such that *later* operators are found further *left*. Formally, its general function can be expressed using Heaviside functions: $\hat{T}[A(t_a,t_0)B(t_b,t_0)] = \Theta(t_a - t_b)A(t_a,t_0)B(t_b,t_0) + \Theta(t_b - t_a)B(t_b,t_0)A(t_a,t_0)$.

Importantly, we keep track of the time-point, which is associated with this initial condition, by carrying t_0 as a second argument. This follows the same spirit as Eq. (A.9) earlier. For the most conventionally used case, when $t_0 = 0$ to begin with, we shall simplify this notation and drop the reference $\hat{O}^{\mathrm{H}}(t, t_0 = 0) = \hat{O}^{\mathrm{H}}(t)$

Using this definition of $\hat{O}^{\mathrm{H}}(t, t_0)$ as well as the TDSE for time-evolution operators (see Eq. (A.4) earlier), we can easily derive Heisenberg's equations of motion (EOM) for operators as follows:

$$\begin{aligned}
\frac{d}{dt}\hat{O}^{\mathrm{H}}(t,t_0) &= \frac{d}{dt}\Big(\hat{U}(t_0,t)\;\hat{O}\;\hat{U}(t,t_0)\Big) \\
&= \Big(\frac{\partial}{\partial t}\hat{U}(t_0,t)\Big)\;\hat{O}\;\hat{U}(t,t_0) + \hat{U}(t_0,t)\Big(\frac{\partial}{\partial t}\;\hat{O}\Big)\;\hat{U}(t,t_0) + \hat{U}(t_0,t)\;\hat{O}\;\Big(\frac{\partial}{\partial t}\hat{U}(t,t_0)\Big) \\
&= \Big(\frac{\partial}{\partial t}\hat{U}(t,t_0)\Big)^{\dagger}\;\hat{O}\;\hat{U}(t,t_0) + 0 + \hat{U}(t_0,t)\;\hat{O}\;\Big(\frac{\partial}{\partial t}\hat{U}(t,t_0)\Big) \\
&= \Big(-\mathrm{i}\hat{H}\hat{U}(t,t_0)\Big)^{\dagger}\;\hat{O}\;\hat{U}(t,t_0) + \hat{U}(t_0,t)\;\hat{O}\;\Big(-\mathrm{i}\hat{H}\hat{U}(t,t_0)\Big) \\
&= \mathrm{i}\hat{U}(t_0,t)\;[\hat{H},\hat{O}]\;\hat{U}(t,t_0) \\
\frac{d}{dt}\hat{O}^{\mathrm{H}}(t,t_0) &= \mathrm{i}\,[\hat{H}^{\mathrm{H}},\hat{O}^{\mathrm{H}}(t,t_0)] = \mathrm{i}\,[\hat{H},\hat{O}^{\mathrm{H}}(t,t_0)].
\end{aligned} \tag{A.17}$$

In this, we assume the operator $\hat{O}$ not to exhibit any intrinsic time-dependence in its native, Schrödinger-picture form. Similarly, we take the governing Hamiltonian to be time-independent, which allows for the last equality to be stated strictly. Otherwise, the EOM will only be valid given the exclusive use of Heisenberg-picture operators, i.e., the penultimate equality of Eq. (A.17).

A.2 Conventions for Fourier transformations

At this point, we want to briefly establish our Fourier conventions—both for the case of infinite, continuous domains and periodic, semi-discrete cases. While each scenario will be discussed in its own right later on (cf. A.7 and A.4, respectively), this section is simply intended as a quick reference.

Continuous Fourier transform In the case of an infinite, continuous domain (usually time $t \in \mathbb{R}^1$ or space $\mathbf{x} \in \mathbb{R}^3$), we concern ourselves with the Fourier transformation of complex-valued functions $f(t)$ or $f(\mathbf{x})$, which should ideally be square-integrable[6].

Considering functions of time, we apply the following Fourier relations:

$$\tilde{f}(\omega) = \int_{-\infty}^{\infty} dt\; e^{\mathrm{i}\,\omega t}\; f(t) \tag{A.18}$$

$$f(t) = \frac{1}{2\pi} \int_{-\infty}^{\infty} d\omega\; e^{-\mathrm{i}\,\omega t}\; \tilde{f}(\omega). \tag{A.19}$$

Here, we have used an additional tilde to denote the Fourier-transformed quantity.

For spatial functions, we adopt the opposite sign in the exponent, which proves convenient in the context of wave-like phenomena (see also App. A.7):

$$\tilde{f}(\mathbf{k}) = \int d^3x\; e^{-\mathrm{i}\mathbf{k}\cdot\mathbf{x}}\; f(\mathbf{x}) \tag{A.20}$$

$$f(\mathbf{x}) = \frac{1}{(2\pi)^3} \int d^3k\; e^{\mathrm{i}\mathbf{k}\cdot\mathbf{x}}\; \tilde{f}(\mathbf{k}). \tag{A.21}$$

Regarding the distribution of the $\frac{1}{(2\pi)^n}$ factors, we follow the "π goes with p"-rule, i.e., placing the factors with the momentum (frequency) space integrations in all cases.

Discrete Fourier transform In the case of a finite, but periodic domain, we employ the Fourier pair:

$$\tilde{f}(\mathbf{k}) = \int_{\diamond} d^3x\; e^{-\mathrm{i}\mathbf{k}\cdot\mathbf{x}}\; f(\mathbf{x}) \tag{A.22}$$

$$f(\mathbf{x}) = \frac{1}{V_\diamond} \sum_{\mathbf{k}}\; e^{\mathrm{i}\mathbf{k}\cdot\mathbf{x}}\; \tilde{f}(\mathbf{k}). \tag{A.23}$$

In terms of exponentials and placement of the normalization factor, these follow the same convention as their continuous counterparts above. However, the restricted domain—here indicated by $V_\diamond$ or simply $\diamond$—leads to a discretization of allowed momenta $\mathbf{k}$. This is reflected in the discrete sum in Eq. (A.23) with a mode volume per k-point of $\frac{(2\pi)^3}{V_\diamond}$.

[6] Note that we will be deliberately sloppy on this point of square-integrability, in order to accommodate for δ-'functions' and their Fourier representation without invoking distribution theory.

A.3 Spatial transformations and the Fourier transform

In the following notes, we briefly ponder the influence of spatial transformations, i.e., translations and rotations onto Fourier transformed quantities. This could be of particular use for the transformation of light-source correlation functions—from model to lab-frame.

Rotations In the course of transforming field correlators for x-ray and optical beams, we may need to account for rotations, i.e., beams at an angle. Below, we will find that spatial rotations affect real-space functions in the same way as they affect their Fourier transformed counterparts:

$$f(\mathbf{x}) = f'(\mathbf{x}') = f'(\mathbf{O}\mathbf{x}) \qquad \Leftrightarrow \qquad \tilde{f}(\mathbf{k}) = \tilde{f}'(\mathbf{k}') = \tilde{f}'(\mathbf{O}\mathbf{k}). \tag{A.24}$$

Here, the tilde indicates Fourier transformed quantities and $\mathbf{O}$ denotes a rotation matrix (orthogonal transformation[7].

In the following, we will arrive at this result for a scalar function $f(\mathbf{x})$. Its component-wise generalization to vectors etc. is straight-forward. For illustration, we imagine a situation, where a scalar field is described in two different reference frames (see Fig. A.1). Namely, we use $f(\mathbf{x})$ for the first situation (a) and $f'(\mathbf{x}')$ for the second situation (b). Now, obviously, the coordinates of physically identical points

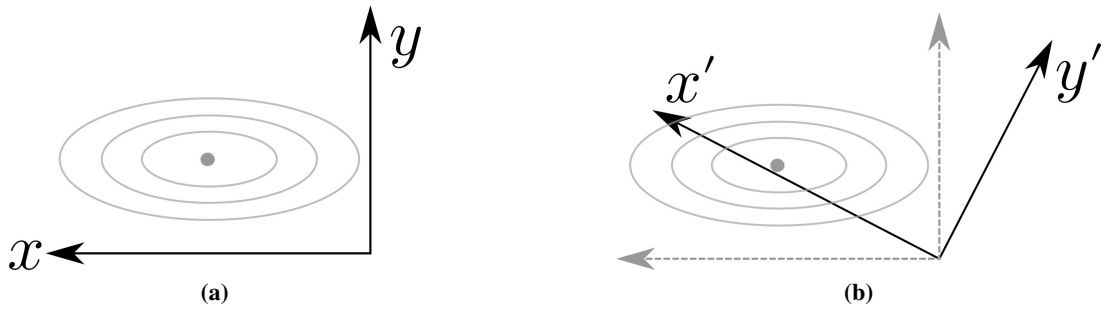

Figure A.1: Description of scalar field f in two different reference frames—namely un-primed (a) and primed (b) coordinates. [We gratefully acknowledge Dr. Christina Bömer's help in rendering the computer graphics of the above illustrations.]

must be related. Here, this is through a rotation

$$\mathbf{x}' = \mathbf{O}\mathbf{x}, \tag{A.25}$$

where $\mathbf{O}$ denotes the orthogonal rotation matrix. Moreover, the value of the field at the same physical location has to be the same, i.e.,

$$f(\mathbf{x}) = f'(\mathbf{x}') = f'(\mathbf{O}\mathbf{x}). \tag{A.26}$$

Of course, there is a Fourier transformation native to each reference frame, viz.

$$\tilde{f}(\mathbf{k}) = \int dx\, e^{-\mathrm{i}\mathbf{k}\mathbf{x}}\, f(\mathbf{x}) \qquad \text{and} \qquad \tilde{f}'(\mathbf{k}') = \int dx'\, e^{-\mathrm{i}\mathbf{k}'\mathbf{x}'}\, f'(\mathbf{x}'). \tag{A.27}$$

[7] Orthogonal transformations—as usual—obey $\mathbf{O}\mathbf{O}^T = \mathbf{1}$.

These are again related, as we can see from the replacement

$$\tilde{f}(\mathbf{k}) = \int dx\, e^{-\mathrm{i}\mathbf{kx}}\, f'(\mathbf{Ox}). \tag{A.28}$$

We can transform the coordinates $\mathbf{x} \to \mathbf{x}' = \mathbf{Ox}$ with unit Jacobian $dx \to dx'$ (due to the orthogonality of the transformation), i.e.,

$$\tilde{f}(\mathbf{k}) = \int dx\, e^{-\mathrm{i}\mathbf{kO}^T\mathbf{x}'}\, f'(\mathbf{x}'). \tag{A.29}$$

We note that the dot product implies $\mathbf{k}\cdot\mathbf{x} = \mathbf{k}^T\mathbf{x} = \mathbf{k}^T\mathbf{O}^T\mathbf{x}' = (\mathbf{Ok})^T\mathbf{x}'$ and thus follows

$$\begin{aligned}\tilde{f}(\mathbf{k}) = \int dx\, e^{-\mathrm{i}\mathbf{kO}^T\mathbf{x}'}\, f'(\mathbf{x}') &= \int dx\, e^{-\mathrm{i}(\mathbf{Ok})^T\mathbf{x}'}\, f'(\mathbf{x}') \\ &= \tilde{f}'(\mathbf{Ok}).\end{aligned} \tag{A.30}$$

Ultimately, this means that we can perform a Fourier transformation in the frame of our choice (i.e., convenience) and relate it into the coordinate frame of our needs simply by rotating its argument.

Translations The effect of spatial translations on Fourier transformations is even simpler and merely results in a phase shift:

$$f(\mathbf{x}) = f'(\mathbf{x}') = f'(\mathbf{x}+\mathbf{a}) \qquad \Leftrightarrow \qquad \tilde{f}(\mathbf{k}) = \tilde{f}'(\mathbf{k}') = e^{\mathrm{i}\mathbf{ka}}\, \tilde{f}'(\mathbf{k}). \tag{A.31}$$

Once again, we denote the Fourier transformed counterpart of a function with a tilde. The correspondence can easily be shown by simply rewriting the transformation integral with a shifted argument.

A.4 Discretized Fourier transformations

In an earlier section (A.2), we have discussed the general structure and convention for our Fourier transforms. Therein, our primary placed on "finite" (i.e., square-integrable) systems embedded in an infinite domain. These produce continuous Fourier transforms on a likewise infinite reciprocal domain and will be discussed in further detail in App. A.7.

For the description of crystalline (electronic) systems, however, it is often methodically advantageous to adopt a description on a finite domain, which is augmented by periodic boundary conditions (PBC). On this finite (periodic) domain, which we shall indicate by the symbol $\diamond$, the Fourier transform pair reads:

$$f(\mathbf{k}) = \int_{\diamond} \mathrm{d}^3x \, e^{-\mathrm{i}\mathbf{kx}} \, f(\mathbf{x}) \tag{A.32}$$

$$f(\mathbf{x}) = \frac{1}{V_\diamond} \sum_{\mathbf{k}} e^{\mathrm{i}\mathbf{kx}} \, f(\mathbf{k}), \tag{A.33}$$

where the set of allowed momenta $\mathbf{k}$ is discretized with a mode volume of $\frac{(2\pi)^3}{V_\diamond}$.

We note for consistency that the above equations will transition into our normal Fourier relations of Eqs. (A.18) and (A.19) upon relaxing the volume constraint ($V_\diamond \to \infty$). To this end, we have to impose the conventional continuum limit for the summation, i.e.,

$$\frac{(2\pi)^3}{V_\diamond} \sum_{\mathbf{k}} \xrightarrow[V_\diamond \to \infty]{} \int d^3k \tag{A.34}$$

In order to prove the inverse nature of Eqs. (A.32) and (A.33), we directly evaluate their concatenation

$$\begin{aligned} f(\mathbf{k}) = \int_{\diamond} d^3x \, e^{-\mathrm{i}\mathbf{kx}} \, f(\mathbf{x}) &= \int_{\diamond} d^3x \, e^{-\mathrm{i}\mathbf{kx}} \, \frac{1}{V_\diamond} \sum_{\mathbf{k}'} e^{\mathrm{i}\mathbf{k}'\mathbf{x}} \, f(\mathbf{k}') \\ &= \sum_{\mathbf{k}'} \left(\frac{1}{V_\diamond} \int_{\diamond} d^3x \, e^{\mathrm{i}\mathbf{x}\cdot(\mathbf{k}'-\mathbf{k})} \right) f(\mathbf{k}') = \sum_{\mathbf{k}'} \delta_{\mathbf{k},\mathbf{k}'} \, f(\mathbf{k}') = f(\mathbf{k}). \end{aligned} \tag{A.35}$$

Here, the normalized integral can be seen to yield 1, if $\mathbf{k} = \mathbf{k}'$, and 0 otherwise on grounds of periodicity; thus, it functions like, and can be represented as, a Kronecker δ.

Evaluating the opposite direction, we encounter the discrete representation of a (periodic) Dirac-δ:

$$\begin{aligned} f(\mathbf{x}) = \frac{1}{V_\diamond} \sum_{\mathbf{k}} e^{\mathrm{i}\mathbf{kx}} \, f(\mathbf{k}) &= \frac{1}{V_\diamond} \sum_{\mathbf{k}} e^{\mathrm{i}\mathbf{kx}} \int_{\diamond} d^3x' \, e^{-\mathrm{i}\mathbf{kx}'} \, f(\mathbf{x}') \\ &= \int_{\diamond} d^3x' \left(\frac{1}{V_\diamond} \sum_{\mathbf{k}} e^{\mathrm{i}\mathbf{k}\cdot(\mathbf{x}-\mathbf{x}')} \right) f(\mathbf{x}') = \int_{\diamond} d^3x' \, \delta^3_\diamond(\mathbf{x}-\mathbf{x}') \, f(\mathbf{x}') = f(\mathbf{x}). \end{aligned} \tag{A.36}$$

Analogous to the Fourier transform itself, this transitions into the conventional Dirac δ-function for $V_\diamond \to \infty$. Using Eq. (A.34), we find

$$\delta^3_\diamond(\mathbf{x}-\mathbf{x}') = \frac{1}{V_\diamond} \sum_{\mathbf{k}} e^{\mathrm{i}\mathbf{k}(\mathbf{x}-\mathbf{x}')} \xrightarrow[V_\diamond \to \infty]{} \frac{1}{(2\pi)^3} \int d^3k \, e^{\mathrm{i}\mathbf{k}(\mathbf{x}-\mathbf{x}')} = \delta^3(\mathbf{x}-\mathbf{x}'). \tag{A.37}$$

If—in addition to the PBC—there is also the notion of a lattice present (here, using real-space lattice vectors $\{\mathbf{R}\}$), we can introduce a lattice in reciprocal-space as well. The corresponding reciprocal lattice

vectors are $\{\mathbf{G}\}$ and satisfy $\mathbf{GR} = n \cdot 2\pi$ for any $\mathbf{R}$. Using these, we can re-write the Fourier transform pair as:

$$f(\mathbf{q},\mathbf{G}) = \int_{\diamond} d^3x\, e^{-\mathrm{i}(\mathbf{q}+\mathbf{G})\cdot\mathbf{x}}\, f(\mathbf{x}) \tag{A.38}$$

$$f(\mathbf{x}) = \frac{1}{V_{\diamond}} \sum_{\mathbf{q}}^{\text{1. BZ}} \sum_{\mathbf{G}}^{\text{rec. latt.}} e^{i(\mathbf{q}+\mathbf{G})\cdot\mathbf{x}}\, f(\mathbf{q},\mathbf{G}), \tag{A.39}$$

for which we have split the original momentum $\mathbf{k} = \mathbf{G} + \mathbf{q}$ into an amount captured by full reciprocal lattice vectors $\mathbf{G}$ and a remainder $\mathbf{q}$, which falls into the so-called first Brilloun zone (1. BZ) [101]. The latter momentum is—by definition—smaller than any $\mathbf{G}$.

For general $f(\mathbf{x})$, this is just an equivalent reformulation of Eqs. (A.32) and (A.33), but as soon as $f(\mathbf{x}) = f(\mathbf{x}+\mathbf{R})$ exhibits lattice periodicity, it becomes more obviously useful:

$$\begin{aligned} f(\mathbf{q},\mathbf{G}) &= \int_{\diamond} d^3x\, e^{-\mathrm{i}(\mathbf{q}+\mathbf{G})\cdot\mathbf{x}}\, f(\mathbf{x}) \\ &= \sum_{\mathbf{R}} \int_{U(0)} d^3x\, e^{-\mathrm{i}(\mathbf{q}+\mathbf{G})\cdot(\mathbf{R}+\mathbf{x})}\, f(\mathbf{R}+\mathbf{x}) \\ &= \sum_{\mathbf{R}} e^{-\mathrm{i}\mathbf{q}\mathbf{R}} \int_{U(0)} d^3x\, e^{-\mathrm{i}(\mathbf{q}+\mathbf{G})\cdot\mathbf{x}}\, f(\mathbf{x}). \end{aligned} \tag{A.40}$$

Above, $U(0)$ denotes the single unit cell of the real-space lattice which is associated with $\mathbf{R} = 0$. Given the general periodicity of the setup (recall the PBC), we can equate

$$\sum_{\mathbf{R}} e^{-\mathrm{i}\mathbf{q}\mathbf{R}} = \delta_{\mathbf{q},0}\, N_{\text{cells}} = \delta_{\mathbf{q},0} \frac{V_{\diamond}}{V_{U(0)}} \tag{A.41}$$

and thus find for Eq. (A.40) the simplification

$$\begin{aligned} f(\mathbf{q},\mathbf{G}) &= \sum_{\mathbf{R}} e^{-\mathrm{i}\mathbf{q}\mathbf{R}} \int_{U(0)} d^3x\, e^{-\mathrm{i}(\mathbf{q}+\mathbf{G})\cdot\mathbf{x}}\, f(\mathbf{x}) \\ &= \sum_{\mathbf{R}} \delta_{\mathbf{q},0} \frac{V_{\diamond}}{V_{U(0)}} \int_{U(0)} d^3x\, e^{-\mathrm{i}(\mathbf{q}+\mathbf{G})\cdot\mathbf{x}}\, f(\mathbf{x}) \\ &= \delta_{\mathbf{q},0} \int_{\diamond} d^3x\, e^{-\mathrm{i}\mathbf{G}\mathbf{x}}\, f(\mathbf{x}) \\ &= \delta_{\mathbf{q},0}\, f(0,\mathbf{G}). \end{aligned} \tag{A.42}$$

Thus, we can conclude that we can fully represent a lattice-periodic function using its reciprocal components alone.

The above reasoning can be extended to functions of several spatial arguments. For the case of simple lattice periodicity in all arguments (individually), the generalization is trivial. As a more complicated case, which is relevant for our nonlinear response function, we shall consider the scenario that translational invariance on the lattice holds only for combined shifts in two arguments (cf. symmetry discussion in Sec. 3.1.1).

To this end, we assume a function $g(\mathbf{x}_1,\mathbf{x}_2)$ that satisfies $g(\mathbf{x}_1,\mathbf{x}_2) = g(\mathbf{x}_1+\mathbf{R},\mathbf{x}_2+\mathbf{R})$ for any real-

space lattice translation $\mathbf{R}$. Its most general Fourier transform on the lattice can be written as

$$\begin{aligned}
g(\mathbf{q}_1+\mathbf{G}_1,\mathbf{q}_2+\mathbf{G}_2) &= \int_\diamond d^3x_1 \int_\diamond d^3x_2\; e^{-\mathrm{i}(\mathbf{q}_1+\mathbf{G}_1)\cdot\mathbf{x}_1}\; e^{-\mathrm{i}(\mathbf{q}_2+\mathbf{G}_2)\cdot\mathbf{x}_2}\; g(\mathbf{x}_1,\mathbf{x}_2) \\
&= \frac{1}{N_\mathrm{cells}} \sum_{\mathbf{R}} \int_\diamond d^3x_1 \int_\diamond d^3x_2\; e^{-\mathrm{i}(\mathbf{q}_1+\mathbf{G}_1)\cdot\mathbf{x}_1}\; e^{-\mathrm{i}(\mathbf{q}_2+\mathbf{G}_2)\cdot\mathbf{x}_2}\; g(\mathbf{x}_1,\mathbf{x}_2) \\
&= \frac{1}{N_\mathrm{cells}} \sum_{\mathbf{R}} \int_\diamond d^3x_1 \int_\diamond d^3x_2\; e^{-\mathrm{i}(\mathbf{q}_1+\mathbf{G}_1)\cdot\mathbf{x}_1}\; e^{-\mathrm{i}(\mathbf{q}_2+\mathbf{G}_2)\cdot\mathbf{x}_2}\; g(\mathbf{x}_1+\mathbf{R},\mathbf{x}_2+\mathbf{R}) \\
&= \frac{1}{N_\mathrm{cells}} \sum_{\mathbf{R}} \int_\diamond d^3x_1 \int_\diamond d^3x_2\; e^{-\mathrm{i}(\mathbf{q}_1+\mathbf{G}_1)\cdot(\mathbf{x}_1+\mathbf{R})}\; e^{-\mathrm{i}(\mathbf{q}_2+\mathbf{G}_2)\cdot(\mathbf{x}_2+\mathbf{R})}\; g(\mathbf{x}_1,\mathbf{x}_2) \\
&= \underbrace{\frac{1}{N_\mathrm{cells}} \sum_{\mathbf{R}} e^{-\mathrm{i}\mathbf{q}_1\mathbf{R}}\; e^{-\mathrm{i}\mathbf{q}_2\mathbf{R}}}_{\delta_{\mathbf{q}_1,-\mathbf{q}_2}} \int_\diamond d^3x_1 \int_\diamond d^3x_2\; e^{-\mathrm{i}(\mathbf{q}_1+\mathbf{G}_1)\cdot\mathbf{x}_1}\; e^{-\mathrm{i}(\mathbf{q}_2+\mathbf{G}_2)\cdot\mathbf{x}_2}\; g(\mathbf{x}_1,\mathbf{x}_2).
\end{aligned} \tag{A.43}$$

In order to expose the lattice symmetry, we have proceeded step-wise. First, we have introduced a summation over all lattice-sites, for which we normalized by dividing by the number of summands (here the number of unit-cells of the lattice N_cells). Subsequently, we have chosen to introduce a shift to the spatial arguments of g. Owing to its periodicity, this action would not change the overall expression either. Following-up on this step, we can shift each of the integration variables by $\mathbf{R}$, thus formally undoing the shift in the arguments of g. As a trade-off, we obtain two shifted exponentials. The latter can be simplified by observing that $\mathbf{GR} = n\cdot 2\pi$ and thus $e^{-\mathrm{i}\mathbf{GR}} = 1$. The remainder of the shifted exponentials can ultimately be combined with the summation and interpreted as a Kronecker-δ. In this, the last step is analogous to case for a single argument above.

Finally, we can conclude from this Kronecker-δ that the Fourier transform of a function, which exhibits lattice translational-invariance in its combined arguments, implies that we need only a single component $\mathbf{q}_1$ for its low-momentum representation.

$$\begin{aligned}
g(\mathbf{q}_1+\mathbf{G}_1,\mathbf{q}_2+\mathbf{G}_2) &= \delta_{\mathbf{q}_1,-\mathbf{q}_2} \int_\diamond d^3x_1 \int_\diamond d^3x_2\; e^{-\mathrm{i}(\mathbf{q}_1+\mathbf{G}_1)\cdot\mathbf{x}_1}\; e^{-\mathrm{i}(\mathbf{q}_2+\mathbf{G}_2)\cdot\mathbf{x}_2}\; g(\mathbf{x}_1,\mathbf{x}_2) \\
&= \delta_{\mathbf{q}_1,-\mathbf{q}_2}\; g(\mathbf{q}_1+\mathbf{G}_1,-\mathbf{q}_1+\mathbf{G}_2).
\end{aligned} \tag{A.44}$$

We remark that the extension to our nonlinear response function proceeds fully analogously. It yields the Fourier relations (cf. Eqs. (A.45) and (A.46))

$$\mathbf{K}_{I\diamond}(\mathbf{q}+\mathbf{G}_1,-\mathbf{q}+\mathbf{G}_2,\omega) = \int_\diamond d^3x_1 \int_\diamond d^3x_2 \int d\tau\; e^{-\mathrm{i}(\mathbf{q}+\mathbf{G}_1)\cdot\mathbf{x}_1}\, e^{-\mathrm{i}(-\mathbf{q}+\mathbf{G}_2)\cdot\mathbf{x}_2}\; e^{\mathrm{i}\omega\tau}\; \mathbf{P}_{I\diamond}(\mathbf{x}_1,0,\mathbf{x}_2,\tau) \tag{A.45}$$

$$\mathbf{P}_{I\diamond}(\mathbf{x}_1,0,\mathbf{x}_2,\tau) = \frac{1}{V_\diamond^2\, 2\pi} \sum_{\mathbf{q}}^{\text{1. BZ}} \sum_{\mathbf{G}_1,\mathbf{G}_2}^{\text{rec. latt.}} \int d\omega\; e^{\mathrm{i}(\mathbf{q}+\mathbf{G}_1)\cdot\mathbf{x}_1}\, e^{\mathrm{i}(-\mathbf{q}+\mathbf{G}_2)\cdot\mathbf{x}_2}\; e^{-\mathrm{i}\omega\tau}\; \mathbf{K}_{I\diamond}(\mathbf{q}+\mathbf{G}_1,-\mathbf{q}+\mathbf{G}_2,\omega). \tag{A.46}$$

A.5 Bloch waves

For a single particle Hamiltonian $\hat{h}_0$ featuring a lattice periodic potential, i.e.:

$$\hat{h}_0 = \frac{\hat{\mathbf{p}}^2}{2} + V(\mathbf{x}) \qquad \text{with} \qquad V(\mathbf{x}) = V(\mathbf{x}+\mathbf{R}), \tag{A.47}$$

all spatial eigenfunctions exhibit the following translational symmetry:

$$\varphi_{\mathbf{k}}(\mathbf{x}+\mathbf{R}) = e^{\mathrm{i}\mathbf{k}\cdot\mathbf{R}}\,\varphi_{\mathbf{k}}(\mathbf{x}). \tag{A.48}$$

This statement amounts to the well-known Bloch theorem (see, e.g., Ref. [101]) and can be confirmed along the same line of reasoning as used to establish the translational symmetry of the correlation function $\mathbf{P}_I$. As a consequence, we can rewrite these eigenfunctions in the form

$$\varphi_{n,\mathbf{k}}(\mathbf{x}) = C\, e^{\mathrm{i}\mathbf{k}\cdot\mathbf{x}}\, u_{n,\mathbf{k}}(\mathbf{x}), \tag{A.49}$$

where we restrict $\mathbf{k}$ to lie within the 1. BZ while introducing an additional band index n to compensate for this constraint. Furthermore, the function $u_{n,\mathbf{k}}(\mathbf{x})$ is understood to be fully lattice periodic and C serves as a normalization constant (to be fixed later). This particular form separates the eigenvalue problem

$$\hat{h}_0\,\varphi_{n,\mathbf{k}}(\mathbf{x}) = C\,e^{\mathrm{i}\mathbf{k}\cdot\mathbf{x}}\underbrace{\left(\frac{(\hat{\mathbf{p}}+\mathbf{k})^2}{2}+V(\mathbf{x})\right)}_{\hat{h}_{\mathbf{k}}} u_{n,\mathbf{k}}(\mathbf{x}) = \varepsilon_{n,\mathbf{k}}\,\varphi_{n,\mathbf{k}}(\mathbf{x}), \tag{A.50}$$

into independent problems per $\mathbf{k}$-point involving effective Hamiltonians $\hat{h}_{\mathbf{k}}$[8].

Given that the functions $u_{n,\mathbf{k}}(\mathbf{x})$ are assumed to be lattice periodic, we can furthermore expand them into a Fourier series on the reciprocal lattice (cf. App. A.4):

$$u_{n,\mathbf{k}}(\mathbf{x}) = \sum_{\mathbf{G}}^{\text{rec. latt.}} e^{\mathrm{i}\mathbf{G}\cdot\mathbf{x}}\, c_{n,\mathbf{k}}(\mathbf{G}). \tag{A.51}$$

With these points established, we can proceed to fix our normalization conditions—ultimately determining C: As usual, we require the overall single-particle wave functions to be normalized with respect to the inner product (on the crystal domain $\diamond$)

$$\int_{\diamond} d^3x\; \varphi^*_{n,\mathbf{k}}(\mathbf{x})\,\varphi_{n',\mathbf{k}'}(\mathbf{x}) = \delta_{n,n'}\,\delta_{\mathbf{k},\mathbf{k}'}, \tag{A.52}$$

yet in addition, we shall adopt the condition

$$\sum_{\mathbf{G}}^{\text{rec. latt.}} c^*_{n,\mathbf{k}}(\mathbf{G})\, c^*_{n',\mathbf{k}}(\mathbf{G}) = \delta_{n,n'} \tag{A.53}$$

in pragmatic congruence with the ABINIT package for DFT calculations [106]. Evaluating the l.h.s. of

[8] Note (mostly to myself): This was quite useful for shifting Bloch functions slightly or doing kp-perturbation theory.

Eq. (A.52), we find:

$$\begin{aligned}\int_{\diamond} d^3x\ \varphi^*_{n,\mathbf{k}}(\mathbf{x})\,\varphi_{n',\mathbf{k}'}(\mathbf{x}) &= |C|^2 \int_{\diamond} d^3x\ e^{-\mathrm{i}\mathbf{k}\cdot\mathbf{x}}\,u^*_{n,\mathbf{k}}(\mathbf{x})\ e^{\mathrm{i}\mathbf{k}'\cdot\mathbf{x}}\,u_{n',\mathbf{k}'}(\mathbf{x}) \\ &= |C|^2 \sum_{\mathbf{R}}^{\text{dir. latt.}} e^{\mathrm{i}(\mathbf{k}'-\mathbf{k})\cdot\mathbf{R}} \int_{U(0)} d^3x\ e^{\mathrm{i}(\mathbf{k}'-\mathbf{k})\cdot\mathbf{x}}\,u^*_{n,\mathbf{k}}(\mathbf{x})\,u_{n',\mathbf{k}'}(\mathbf{x}) \\ &= |C|^2\ N_{\text{cells}}\ \delta_{\mathbf{k},\mathbf{k}'} \int_{U(0)} d^3x\ u^*_{n,\mathbf{k}}(\mathbf{x})\,u_{n',\mathbf{k}'}(\mathbf{x}),\end{aligned} \tag{A.54}$$

where we made use of the lattice-translational invariance of the $u_{n,\mathbf{k}}(\mathbf{x})$, in order to reduce the required integration to a single unit cell (here denoted $U(0)$). This integration—in turn—can be rephrased via Eq. (A.51)

$$\begin{aligned}\int_{U(0)} d^3x\ u^*_{n,\mathbf{k}}(\mathbf{x})\,u_{n',\mathbf{k}}(\mathbf{x}) &= \int_{U(0)} d^3x \sum_{\mathbf{G}_1}^{\text{rec. latt.}} e^{-\mathrm{i}\mathbf{G}_1\cdot\mathbf{x}}\,c^*_{n,\mathbf{k}}(\mathbf{G}_1) \sum_{\mathbf{G}_2}^{\text{rec. latt.}} e^{\mathrm{i}\mathbf{G}_2\cdot\mathbf{x}}\,c_{n,\mathbf{k}}(\mathbf{G}_2) \\ &= \sum_{\mathbf{G}_1,\mathbf{G}_2}^{\text{rec. latt.}} c^*_{n,\mathbf{k}}(\mathbf{G}_1)\,c_{n,\mathbf{k}}(\mathbf{G}_2) \int_{U(0)} d^3x\ e^{\mathrm{i}(\mathbf{G}_2-\mathbf{G}_1)\cdot\mathbf{x}} \\ &= \sum_{\mathbf{G}_1,\mathbf{G}_2}^{\text{rec. latt.}} c^*_{n,\mathbf{k}}(\mathbf{G}_1)\,c_{n,\mathbf{k}}(\mathbf{G}_2)\ \delta_{\mathbf{G}_1,\mathbf{G}_2}\ V_{U(0)},\end{aligned} \tag{A.55}$$

leaving essentially the previously fixed expression A.53. Overall, we can conclude the unsurprising normalization of:

$$C = \frac{1}{\sqrt{N_{\text{cells}} V_{U(0)}}} = \frac{1}{\sqrt{V_{\diamond}}}. \tag{A.56}$$

Miscellaneous properties of Bloch functions

Among other things, Bloch waves satisfy the following relation

$$\varphi_{n,\mathbf{k}}(\mathbf{x}) = \varphi_{n,\mathbf{k}+\mathbf{G}}(\mathbf{x}). \tag{A.57}$$

This can be shown from Fourier decomposition of u.

Inspired by Jones and March [112], we want to list another relation

$$e^{-\mathrm{i}\,\boldsymbol{\kappa}\cdot\mathbf{x}}\ \varphi_{n,\mathbf{k}+\boldsymbol{\kappa}}(\mathbf{x}) = \sum_m \chi_{n,m}\ \varphi_{m,\mathbf{k}}(\mathbf{x}). \tag{A.58}$$

This connection of Bloch waves at (slightly) different momenta can be put to application when attempting to formulate $\mathbf{k}\cdot\mathbf{p}$-perturbation theory, for instance.

A.6 Introduction to MyLiO.x

In the course of this work, we have implemented numerical routines in order to evaluate the nonlinear response function $\mathbf{K}_I$. The main implementation of this kind is bundled into the Fortran-based program MyLiO.x. It works off an input of Kohn-Sham DFT orbitals for the material of interest, which have to be pre-computed using external electronic-structure codes.

In the following pages, we attach an introduction to MyLiO.x discussing both its concept, certain aspects of its programmatic implementation as well as the typical workflow for this program. Notably, this introduction has originally been written as a stand-alone document. As such the numbering scheme of its sections does not match the remainder of this work, neither are its references integrated with the overall bibliography for that matter—references are attached separately.

MyLiO.x - My Little Observable
a coarse guide to computing the current-density—density response

D. Krebs

Abstract

In this document, we will outline the working principles behind MyLiO.x. This code implements the numerical evaluation of a current-density—density response function on the basis of Kohn-Sham DFT orbitals. The response function in question is significant, as it mediates (or—depending on your point of view: is probed by) several x-ray-optical wavemixing (XOWM) processes.

1 Basics

We have recently developed a theoretical framework to describe x-ray optical wavemixing (XOWM) phenomena [1]. This was motivated by two overlapping interests: On the one hand, the unprecedented accessiblity of these processes at modern x-ray sources, viz. at synchrotron radiation sources (SR) or x-ray free-electron lasers (XFEL), prompted the interest to obtain a theoretical explanation for them. On the other hand, we were motivated to reach beyond a first, fundamental explanation and explore the intriguing prospect of using these XOWM processes as novel probes of matter. For this latter purpose, a thorough theoretical description—including structural nuances—was (and remains) imperative. In our discussion of XOWM, we focus on the related processes of x-ray optical sum- and difference-frequency generation (SFG/DFG) as well as x-ray parametric down-conversion (XPDC). All of these promise to provide diffractive imaging capabilities similar to regular x-ray diffraction, yet with additional spectroscopic selectivity that is tunable via the optical wave. Importantly, this selectivity would allow *specific* probing of valence responses or—more broadly speaking—imaging/visualizing valence electron dynamics with atomic-scale resolution.

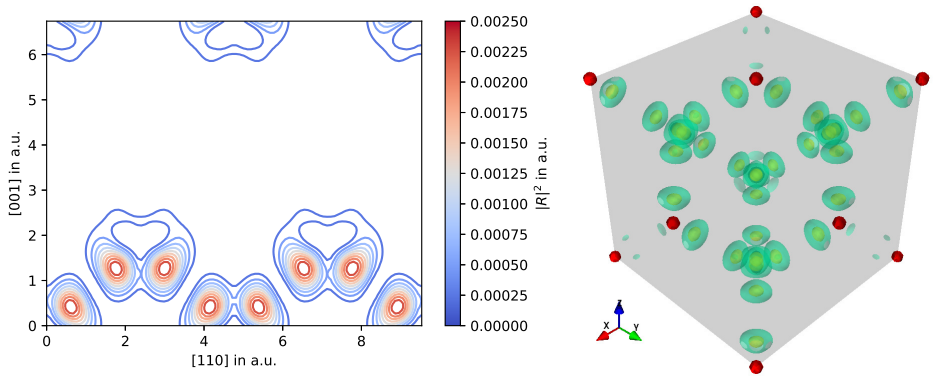

(a) (b)

Figure 1: Illustrations from Ref. [1] (a) The nonlinear response is shown in terms of $|\mathbf{R}_{GS}(\mathbf{x}, 0.057)|^2$ for diamond in the $(1\bar{1}0)$-plane of its conventional (cubic) unit cell. The DFT-model predicts a localization of the response in two maxima along each bond, reflecting transition from the ground state (bonding character) into excited states of dominantly anti-bonding character. (b) A 3D-rendering of the same response throughout the whole (cubic) unit cell.

The nonlinear electronic response is essentially captured by

$$(\mathbf{P}_I(\mathbf{y},t_2,\mathbf{x},t_1))_\mu = \langle I|\,\hat{T}\left[(\hat{\mathbf{p}}(\mathbf{y},t_2))_\mu\,\hat{n}(\mathbf{x},t_1)\right]\,|I\rangle\,, \tag{1}$$

which denotes the time-ordered correlation function of the electronic system's density $\hat{n}(\mathbf{x},t_1)$ with its current density $\hat{\mathbf{p}}(\mathbf{y},t_2) = \hat{\psi}^\dagger(\mathbf{y},t_2)\,(-\mathrm{i}\nabla)\,\hat{\psi}(\mathbf{y},t_2)$—measured in the state $|I\rangle$. This state will mostly be taken to be the ground state $|I\rangle = |GS\rangle$ only.

Presently, we evaluate this correlator on the basis of ground-state DFT. More specifically, we use the Fourier transform of $\mathbf{P}_I$ (viz. $\mathbf{K}_I = \mathrm{FT}\{\mathbf{P}_I\}$) and compute it from Kohn-Sham orbitals. Its expression in terms of single-particle matrix elements reads:

$$\mathbf{K}_{I\diamond}(\mathbf{q}+\mathbf{G}_1,-\mathbf{q}+\mathbf{G}_2,\omega) = \lim_{\eta\to 0^+}\,2\mathrm{i}\sum_p^{\text{occ.}}\sum_q^{\text{unocc.}}\Big(\frac{\langle\varphi_p|\,e^{-i(-\mathbf{q}+\mathbf{G}_2)\cdot\hat{\mathbf{x}}}\,|\varphi_q\rangle\,\langle\varphi_q|\,e^{-i(\mathbf{q}+\mathbf{G}_1)\cdot\hat{\mathbf{x}}}\,\hat{\mathbf{p}}\,|\varphi_p\rangle}{\omega-(\varepsilon_q-\varepsilon_p)+\mathrm{i}\eta} + \frac{\langle\varphi_p|\,e^{-i(\mathbf{q}+\mathbf{G}_1)\cdot\hat{\mathbf{x}}}\,\hat{\mathbf{p}}\,|\varphi_q\rangle\,\langle\varphi_q|\,e^{-i(-\mathbf{q}+\mathbf{G}_2)\cdot\hat{\mathbf{x}}}\,|\varphi_p\rangle}{-\omega-(\varepsilon_q-\varepsilon_p)+\mathrm{i}\eta}\Big). \tag{2}$$

For our current purposes, it is sufficient to consider only a simplified range of momentum transfers, namely $\mathbf{K}_I(\mathbf{0},\mathbf{G},\omega)$, where $\mathbf{G}$ are vectors of the reciprocal lattice. This reduction in complexity results from a dipole-approximation-like treatment of the optical field's interaction ($\mathbf{q}\approx 0, \mathbf{G}_1\approx 0$). From the remaining information-content of $\mathbf{K}_I$, we can nonetheless reconstruct a nonlinear response density by Fourier-synthesis:

$$\mathbf{R}_I(\mathbf{x},\omega) = \frac{1}{V_\diamond}\sum_{\mathbf{G}}^{\text{rec.}} e^{i\mathbf{G}\cdot\mathbf{x}}\,\mathbf{K}_I(0,\mathbf{G},\omega). \tag{3}$$

It is illustrated at its present numerical level (LDA-DFT) for diamond in Fig. 1.

2 The MYLIO.X code

The main purpose of the MYLIO.X code is to evaluate $\mathbf{K}_I(\mathbf{0},\mathbf{G},\omega)$ (via Eq. (2)) on the basis of Kohn-Sham DFT orbitals. Specifically, it post-processes data from the ABINIT DFT code (cf. Sec. 2.1), which takes the form of Bloch-wave states expanded into a plane-wave basis.

The code is structured as follows:
A small `main`-routine initializes the input parameters (`global_variables.f90`) for the computation and starts the required numerical routine from the module `electronic_cfct.f90`—see Fig. 2. At the same time, these three modules mark all points where user input may be processed. Notably, MYLIO.X does *not* use an explicit, human-readable input file. Instead, user-inputs are hard coded and thus implemented through re-compilation of the program[1]—see Sec. 2.1 for details.

Further routines that are involved in the operation of MYLIO.X are `read_ABINIT_files.f90`, `vec_functions.f90` and `error_handling.f90`. For all of them, the purposes are self-evident from their nomenclature. It should be borne in mind for later reference, however, that the module `read_ABINIT_files.f90` initializes the essential data structures, which are accessed during later stages of the computation. These are described in more detail in Sec. 2.2.

[1] This form of minimal I/O-operation was adopted to streamline the development process. Later conversion to more comfortable formats appears dispensable given the future transition to FHIAIMS.

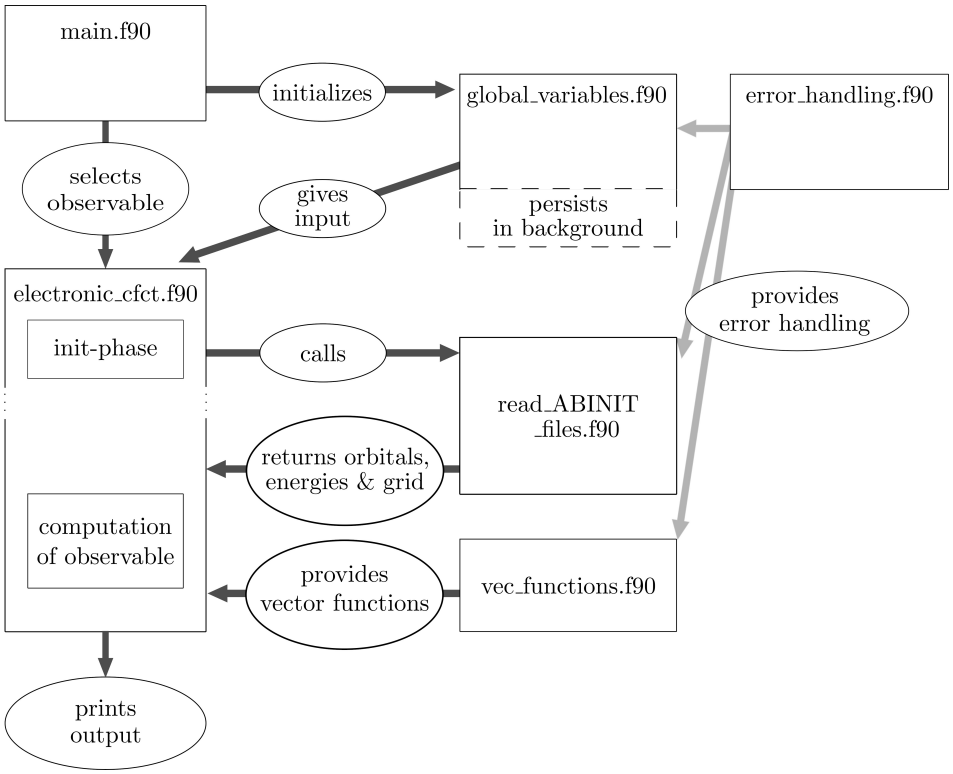

Figure 2: Overall structure of the MYLIO.X code

Observables MYLIO.X may provide several observables of the underlying electronic system.

- First and foremost, it can compute the nonlinear response function $\mathbf{K}_I(\mathbf{0},\mathbf{G},\omega)$ at DFT level. The output may be given in two distinct forms: Either as a spectral scan (ω) for a single, fixed reciprocal component $\mathbf{G}$, or as a set of reciprocal components for a fixed value of ω. The latter option is valuable for 3D-reconstruction or visualization purposes.

- In addition, a simplified version of $\mathbf{K}_I(\mathbf{0},\mathbf{G},\omega)$ can be computed. The implemented approximation reflects a high-energy limit, where the frequency ω is set far above all relevant valence-energy scales yet below core-electron excitation thresholds. It was first suggested by Freund [2] and thus, the respective routines are named accordingly inside the code (`calculate_KI_Freund`) and (`get_electronic_cfct_Freund`). While the approximation has a limited range of applications, it nevertheless proves useful from time to time (e.g., for diamond $\omega \sim 100\,\mathrm{eV}$. Output options are the same as for the regular $\mathbf{K}$.

- The (valence) electronic density $\rho(\mathbf{x}) = \langle \hat{n}(\mathbf{x}) \rangle$ can likewise be assembled using MYLIO.X. This is mostly a convenience function and had some debugging purposes. It is not strictly necessary, because ABINIT could produce this observable as well. The output is given as reciprocal components of the electron density analogous to the respective output of $\mathbf{K}$.

- Finally, the MYLIO.X code can compute the dielectric function of solid-state materials on the level of the Kubo-Greenwood formula [3]. While this does not provide outstandingly realistic results—infact it is often advisable to use tabulated dielectric functions instead—it is very helpful for cross-comparison to other numerical frameworks, which do not incorporate $\mathbf{K}$ as an observable. Moreover, this function allows us to get estimates of $\varepsilon(\omega)$ for materials without proper reference

data available. The output is given as a spectrum (ω) analogous to the respective spectral output of **K**.

2.1 Input data

In order to operate MYLIO.X, three types of input are required:

Choice of observable Inside the `main.f90`-routine, several different observables can be chosen by uncommented the respective option. The following excerpt showcases the situation for the computation of $\mathbf{K}_I(\mathbf{0},\mathbf{G},\omega)$ at fixed energy ω but for a range of reciprocal components **G**:

```
! run the calculation of observable(s)
! uncomment the task, which you need

!call print_electronic_cfct      ! Prints the spectrum of K for a fixed G
call print_cfct_structure       ! Prints K for various G but at fixed energy
                                ! nicer to use when you want to reconstruct at one energy
!call print_electronic_density   ! Prints the electronic density / its reciprocal components

!call calculate_obs_dielec       ! Computes and prints the dielectric function
                                 ! based on the Kubo-Greenwood formula

! run directly from electronic module - routines for testing
!call calculate_observable_dip_test
!call run_sig_test
```

Other possible options are likewise apparent from the excerpt—with the last two being not recommended for any production-runs, as they serve merely for debugging purposes.

Approximate observable $\mathbf{K}_{\text{Freund}}$ In case, the high-energy approximation of $\mathbf{K}_I(\mathbf{0},\mathbf{G},\omega)$ should be computed, this can also be done by choosing either of the "**K**-options" outlined above. However, it requires further modifications inside the module `electronic_cfct.f90`. Should a spectrum be generated for $\mathbf{K}_{\text{Freund}}$, the function to modify is `print_electronic_cfct`, specifically the section that determines the mode of computing **K**, obviously.

```
! allocate and fill K
allocate(K_ini(1:6,1:g_omega_n))
!call get_electronic_cfct(K_ini)
call get_electronic_cfct_Freund(K_ini)
!call get_electronic_cfct_new(K_ini)
```

Uncommenting the second of the three `get_electronic_cfct`-options gives the 'Freund'-version.

In case the reciprocal components of $\mathbf{K}_{\text{Freund}}$ at a fixed energy are desired, the function to modify is instead `get_electronic_cfct_component`.

```
! then fill the K array with K
dummy_vec = 0.d0
!K = calculate_KI(dummy_vec, dummy_vec, omega)
K = calculate_KI_Freund(dummy_vec, vecG, omega)
K = K / m_vol_crystal
```

In here, the call to either subroutine `calculate_KI` must be chosen according to need.

Global variables The majority of numerical parameters for any MYLIO.X-run is set in the `global_variables.f90`-file. In the following, we show a minimal example (for diamond) and discuss the components subsequently.

```
 ! ================================================================
  ! All system / numerical parameters follow here
  ! Some may formally be parameters, others need to be initialized
  ! (e.g., by being converted / calculated)
  ! ---------------------------------------------------------------
```

```
6   ! The following part pertains to the electronic structure calculation
7   ! i.e. ABINIT definitions / parameters for the calculation of K
8
9   ! reciprocal lattice vectors - filled by init routine
10  double precision :: g_primk_red(3,3)
11  double precision :: g_red
12
13  ! reciprocal lattice vector used for scattering - give reduced coordinates
14  ! w.r.t. the above primitive vectors
15  double precision, parameter :: g_k2tilde(1:3) = (/1.d0, 1.d0, 1.d0/)  !conventional 111
16
17  ! number of occupied bands
18  integer, parameter :: g_nocc_band=4      ! 4 for Diamond
19
20  ! frequency grid for KI calculation
21  ! note that you may choose a negative starting energy
22  double precision            :: g_omega_start = -2.0     ! in atomic units
23  double precision            :: g_omega_final = 2.0      ! in atomic units
24  ! step size
25  double precision            :: g_omega_delta = 1.0e-3
26  ! finally, there will be a number of steps associated with the above,
27  ! this is determined by the init routine
28  integer                     :: g_omega_n = 0          ! set by init routine
29
30  ! regularization parameter
31  ! can be seen as exciton lifetime
32  double precision, parameter :: g_eta = 7.0e-3  ! Benedict et al.
33
34  ! scissor correction
35  double precision, parameter :: g_scissor = 0.0
36  !double precision, parameter :: g_scissor = 0.062 ! in atomic units -> Diamond - Silvana Botti et al.
37
38  ! Addon 2020-10-15 - computation of various reciprocal components of K
39  !                    for structural reconstruction
40
41  ! optical energy at which to evaluate K
42  double precision            :: g_omega_fix = 0.057 ! in a.u. 0.057 corresponds to 1.55 eV
43
44  ! resolution up to which to evaluate
45  ! give this in terms of an incident x-ray wavelength
46  ! from this calculate Ewald's sphere - resolution = diameter
47  double precision            :: g_lambda = 1.0 ! in atomic units
48                              ! 3.347 au = 1.77 Ang / 7keV should just resolve 400 (C)
49  ! in addition, give maximal Miller indices to test
50  integer                     :: g_max_idxh = 2
51  integer                     :: g_max_idxk = 2
52  integer                     :: g_max_idxl = 2
```

In addition, there is a later section of the file, which contains the function `g_init_module` and within it the initialization of the lattice parameters.

```
1   ! reciprocal lattice vectors
2   ! these are the three primitive G vectors as used by Abinit
3   ! taken from the respective output file of my Abinit calculation
4   ! ! they satisfy G(1)*R(1) = 1 instead of the usual G(1)*R(1) = 2 pi
5
6   ! first G vector - G(1) - cartesian coordinates in Bohr**-1
7   ! Diamond
8   g_primk_red(1,1) = -0.1483536
9   g_primk_red(2,1) = 0.1483536
10  g_primk_red(3,1) = 0.1483536
11
12  g_primk_red(1,2) = 0.1483536
13  g_primk_red(2,2) = -0.1483536
14  g_primk_red(3,2) = 0.1483536
15
16  g_primk_red(1,3) = 0.1483536
17  g_primk_red(2,3) = 0.1483536
18  g_primk_red(3,3) = -0.1483536
19
20  g_red = 2.0 * 3.141592653589793  ! Use it to recover 2 pi
21                                   ! as ABINIT definition of G is without s.a.
```

2.2 Conversion of ABINIT data

In the module `read_ABINIT_files.f90`, all necessary information about the electronic structure is read in. This comprises both the actual Kohn-Sham orbitals and information on the numerical grid,

which was used to compute them in the first place (i.e., in the ABINIT-calculation).

The essential components are the single particle Kohn-Sham orbitals, which take the form of Bloch-waves in a periodic solid:

$$\varphi_{n,\mathbf{k}}(\mathbf{x}) = \frac{1}{\sqrt{V_\diamond}}\, e^{i\mathbf{k}\cdot\mathbf{x}}\, u_{n,\mathbf{k}}(\mathbf{x}). \tag{4}$$

Here we restrict $\mathbf{k}$ to lie within the 1. Brillouin-zone (BZ) while introducing an additional band index n to compensate for this constraint. Furthermore, the function $u_{n,\mathbf{k}}(\mathbf{x})$ is understood to be fully lattice periodic and normalized to the (numerical) crystal volume $V_\diamond$.

Given the periodicity of $u_{n,\mathbf{k}}(\mathbf{x})$, we can expand it into a Fourier series on the reciprocal lattice:

$$u_{n,\mathbf{k}}(\mathbf{x}) = \sum_{\mathbf{G}}^{\text{rec. latt.}} e^{i\mathbf{G}\cdot\mathbf{x}}\, c_{n,\mathbf{k}}(\mathbf{G}). \tag{5}$$

The respective data from ABINIT is stored as follows: The central object is the array of expansion coefficients $c_{n,\mathbf{k}}(\mathbf{G})$, namely `m_cg_k(i,n,G,k)`. This is a 4-dimensional array, wherein the indices correspond to

- i: ranging from 1 to 2, gives the real and imaginary part of each coefficient,
- n: ranging from 1 to `m_nband`, marks the respective band n of the Bloch-function,
- G: ranging from 1 to `m_maxnpw`, specifies which reciprocal component $\mathbf{G}$ of the Bloch-function is considered and
- k: ranging from 1 to `m_nkpt`, specifies the k-kpoint of the 1. BZ, for which the Bloch-function is evaluated.

Note that the first index is shed (converted) upon transfer into the `electronic_cftc.f90`-module, because there, a complex data-type is used. As such, the distinction of the two complex components is handled automatically.

There is a copuple of further things to note here. Obviously, there is a limited number of bands, which are numerically reproduced. This number was chosen during the ABINIT computation and is passed on via the `wfk.bin`-file to `MyLiO.x`. The respective parameter is `m_nband`. The same is the case for the number of k-points inside the 1. BZ, which is read into `m_nkpt` and a third important (range of) parameter(s), namely `m_maxnpw`. This last one specifies the number of plane-waves, i.e., $\mathbf{G}$-components, which are used at each k-point to expand the Bloch-functions. Notably, this number is non-uniform and depends on various cut-off settings chosen within ABINIT. Thus, `m_maxnpw` is actually a (one-dimensional) array indexed for each k-point from 1 to `m_nkpt`.

Next up, the $\mathbf{G}$-vectors themselves; while these could be constructed on the basis of the minimal (reciprocal) unit cell at each request, it is more economical to have their numerical values computed once and stored. This is done in the array `m_g_k(i,G,k)`, where the indexing is similar to the above

- i: ranging from 1 to 3, gives the three vector components of $\mathbf{G}$ in direct coordinates
- G: ranging from 1 to `m_maxnpw`, specifies which $\mathbf{G}$-vector is desired and
- k: ranging from 1 to `m_nkpt`, specifies the k-kpoint of the 1. BZ, for which $\mathbf{G}$ is read.

A similar data-structure exists for the numerical values of the k-points as well: `m_kpt(i,k)`. This holds the respective vectors **k** inside the 1. BZ, which formed the numerical grid of the ABINIT calculation. The indexing proceeds as expected:

- i: ranging from 1 to 3, gives the three vector components of **k** in direct coordinates and
- k: ranging from 1 to `m_nkpt`, specifies the k-kpoint of the 1. BZ, for which **k** is read.

Finally, also the eigenenergies of each Bloch-wave is stored. These are the Kohn-Sham orbital energies $\varepsilon_{n,\mathbf{k}}$, which are stored in the structure `m_eig(n,k)`. The indexing proceeds as expected:

- n: ranging from 1 to `m_nband`, marks the respective band n of the Bloch-function and
- k: ranging from 1 to `m_nkpt`, specifies the k-kpoint of the 1. BZ, for which the orbital energy is read.

Note in closing that the Bloch-waves should satisfy the following orthonormality condition at each k-point of the Brillouin zone:

$$\sum_{\mathbf{G}}^{\text{rec. latt.}} c^*_{n,\mathbf{k}}(\mathbf{G})\, c^*_{n',\mathbf{k}}(\mathbf{G}) = \delta_{n,n'}. \tag{6}$$

However, if the SCF-calculations of ABINIT did not converge properly (or other errors occurred) this condition is sometimes broken. To check this explicitly, the module `read_ABINIT_files.f90` incorporates a test function `test_wfct_orthogonality`, which is run at the end of the read-in and initialization procedure.

2.3 Implementation of matrix elements

In order to evaluate $\mathbf{K}_I$ according to Eq. (2), we essentially need to compute the matrix elements $\langle\varphi_p| e^{-i(-\mathbf{q}+\mathbf{G}_2)\cdot\hat{\mathbf{x}}} |\varphi_q\rangle$ and $\langle\varphi_q| e^{-i(\mathbf{q}+\mathbf{G}_1)\cdot\hat{\mathbf{x}}}\hat{\mathbf{p}}|\varphi_p\rangle$. This constitutes the main task of MYLIO.X and, as such, we want to specify its implementation in more detail. In particular, we shall present explicit expressions for both matrix elements when written for Bloch-functions as specified above (i.e., in Eqs. (4) and (5)). In doing so, we give the general case first, i.e., the case of full momentum dependence, before we further simplify both matrix elements along the lines of the previously mentioned dipole-approximation.

Beginning with the scattering matrix element of Eq. (2), we can write:

$$\begin{aligned}\langle\varphi_p| e^{-i(-\mathbf{q}+\mathbf{G}_2)\cdot\hat{\mathbf{x}}} |\varphi_q\rangle &= \frac{1}{V_\diamond}\int_\diamond d^3x\; e^{-i\mathbf{k}_p\cdot\mathbf{x}}\, u^*_{n_p,\mathbf{k}_p}(\mathbf{x})\; e^{-i(-\mathbf{q}+\mathbf{G}_2)\cdot\hat{\mathbf{x}}}\; e^{i\mathbf{k}_q\cdot\mathbf{x}}\, u_{n_q,\mathbf{k}_q}(\mathbf{x}) \\ &= \frac{1}{V_\diamond}\sum_{\mathbf{R}}^{\text{dir. latt.}} e^{-i(\mathbf{k}_p-\mathbf{q}-\mathbf{k}_q)\cdot\mathbf{R}} \sum_{\mathbf{G},\mathbf{G}'}^{\text{rec. latt.}} c^*_{n_p,\mathbf{k}_p}(\mathbf{G})\, c_{n_q,\mathbf{k}_q}(\mathbf{G}') \int_{U(0)} d^3x\; e^{-i(\mathbf{k}_p+\mathbf{G}-\mathbf{q}+\mathbf{G}_2-\mathbf{k}_q-\mathbf{G}')\cdot\mathbf{x}},\end{aligned} \tag{7}$$

where we have made use of the Fourier expansion of the Bloch-functions (Eq. (5)). If we neglect contri-

butions from Umklapp-processes, we obtain the simplified expression:

$$\begin{aligned}\langle\varphi_p|\, e^{-i(-\mathbf{q}+\mathbf{G}_2)\cdot\hat{\mathbf{x}}}\,|\varphi_q\rangle &\approx \frac{1}{V_\diamond}\, N_{\text{cells}}\, \delta_{\mathbf{k}_p,\mathbf{q}+\mathbf{k}_q} \sum_{\mathbf{G},\mathbf{G}'}^{\text{rec. latt.}} c^*_{n_p,\mathbf{k}_p}(\mathbf{G})\, c_{n_q,\mathbf{k}_q}(\mathbf{G}') \int_{U(0)} d^3x\; e^{-i(\mathbf{G}+\mathbf{G}_2-\mathbf{G}')\cdot\mathbf{x}} \\ &= \frac{1}{V_\diamond}\, N_{\text{cells}}\, \delta_{\mathbf{k}_p,\mathbf{q}+\mathbf{k}_q} \sum_{\mathbf{G},\mathbf{G}'}^{\text{rec. latt.}} c^*_{n_p,\mathbf{k}_p}(\mathbf{G})\, c_{n_q,\mathbf{k}_q}(\mathbf{G}')\; V_{U(0)}\, \delta_{\mathbf{G},\mathbf{G}'-\mathbf{G}_2} \\ &= \delta_{\mathbf{k}_p,\mathbf{q}+\mathbf{k}_q} \sum_{\mathbf{G}}^{\text{rec. latt.}} c^*_{n_p,\mathbf{k}_p}(\mathbf{G})\, c_{n_q,\mathbf{k}_q}(\mathbf{G}+\mathbf{G}_2). \end{aligned} \tag{8}$$

For the photoabsorption/-emission matrix element, we find analogously:

$$\begin{aligned}\langle\varphi_q|\, e^{-i(\mathbf{q}+\mathbf{G}_1)\cdot\hat{\mathbf{x}}}\,\hat{\mathbf{p}}\,|\varphi_p\rangle &= \frac{1}{V_\diamond}\int_\diamond d^3x\; e^{-i\mathbf{k}_q\cdot\mathbf{x}}\, u^*_{n_q,\mathbf{k}_q}(\mathbf{x})\; e^{-i(\mathbf{q}+\mathbf{G}_1)\cdot\hat{\mathbf{x}}}\; (-\mathrm{i}\nabla)\; e^{i\mathbf{k}_p\cdot\mathbf{x}}\, u_{n_p,\mathbf{k}_p}(\mathbf{x}) \\ &\approx \frac{1}{V_\diamond}\, N_{\text{cells}}\, \delta_{\mathbf{k}_q,\mathbf{k}_p-\mathbf{q}} \sum_{\mathbf{G},\mathbf{G}'}^{\text{rec. latt.}} c^*_{n_q,\mathbf{k}_q}(\mathbf{G})\, c_{n_p,\mathbf{k}_p}(\mathbf{G}')\; V_{U(0)}\, \delta_{\mathbf{G},\mathbf{G}'-\mathbf{G}_1}\, (\mathbf{k_p}+\mathbf{G}') \\ &= \delta_{\mathbf{k}_q,\mathbf{k}_p-\mathbf{q}} \sum_{\mathbf{G}}^{\text{rec. latt.}} c^*_{n_q,\mathbf{k}_q}(\mathbf{G})\, c_{n_p,\mathbf{k}_p}(\mathbf{G}+\mathbf{G}_1)\; (\mathbf{k_p}+\mathbf{G}+\mathbf{G}_1). \end{aligned} \tag{9}$$

Now, we proceed to apply the dipole-approximation-like treatment, which consists in setting $\mathbf{k}_q = \mathbf{k}_p - \mathbf{q} \approx \mathbf{k}_p$. This can be justified by recalling that $\mathbf{q}$ will be constrained to the size of an optical photon's momentum, which is significantly smaller than the scale of the 1. Brillouin zone (BZ). For such small differences among crystal-momenta, we can assume the respective Fourier coefficients $c_{n,\mathbf{k}}(\mathbf{G})$ to vary slowly at most[2]. Thus, evaluating both coefficients at the same value of $\mathbf{k}_p$ is not expected to incur a significant difference—neither in Eq. (8) nor in Eq. (9), respectively. For the implementation of the scattering matrix element, this does not imply a large structural change—although the numerical simplification incurred can be substantial[3]

$$\langle\varphi_p|\, e^{-i(-\mathbf{q}+\mathbf{G}_2)\cdot\hat{\mathbf{x}}}\,|\varphi_q\rangle \approx \delta_{\mathbf{k}_p,\mathbf{k}_q} \sum_{\mathbf{G}}^{\text{rec. latt.}} c^*_{n_p,\mathbf{k}_p}(\mathbf{G})\, c_{n_q,\mathbf{k}_p}(\mathbf{G}+\mathbf{G}_2). \tag{10}$$

For the momentum matrix element, we can go further than approximating $\mathbf{q} \approx 0$ and also extend to $\mathbf{G}_1 = 0$, which is an exact equality for the case of optical transitions. Its effect is

$$\begin{aligned}\langle\varphi_q|\, e^{-i(\mathbf{q}+\mathbf{G}_1)\cdot\hat{\mathbf{x}}}\,\hat{\mathbf{p}}\,|\varphi_p\rangle &\approx \delta_{\mathbf{k}_q,\mathbf{k}_p} \sum_{\mathbf{G}}^{\text{rec. latt.}} c^*_{n_q,\mathbf{k}_p}(\mathbf{G})\, c_{n_p,\mathbf{k}_p}(\mathbf{G})\; (\mathbf{k_p}+\mathbf{G}) \\ &= \delta_{\mathbf{k}_q,\mathbf{k}_p} \sum_{\mathbf{G}}^{\text{rec. latt.}} c^*_{n_q,\mathbf{k}_p}(\mathbf{G})\, c_{n_p,\mathbf{k}_p}(\mathbf{G})\; \mathbf{G}. \end{aligned} \tag{11}$$

In the last step, we have additionally invoked Eq. (6) and the knowledge that occupied $(n_p,\mathbf{k}_p)$ and unoccupied $(n_q,\mathbf{k}_q)$ can not agree in both of their indices.

Within the MYLIO.X code, the computation of these matrix elements is located in the module `electronic_cfct.f90`. Here, the function `calculate_S` pertains to the evaluation of Eq. (10)

[2] In fact, many numerical approaches will opt for much coarser discretization within the 1. BZ than the scale set by an optical photon [4]. The neglect of the optical photon's momentum transfer will often be referred to as "vertical transitions".

[3] As indicated in the previous footnote, the discretization of numerical approaches will often be much coarser than the sampling required to evaluate shifts by $\mathbf{q}$. If we wanted to obtain wavefunctions at two mildly different crystal momenta, we would therefore require additional interpolation methods like $\mathbf{k}\cdot\mathbf{p}$-perturbation theory [5]. We even implemented this at some point—just to verify its irrelevance...

and the function `calculate_gam` implements the evaluation of Eq. (11).

3 Workflow

The typical workflow when employing MYLIO.X proceeds as follows:

1. Run the (modified) ABINIT code to obtain the electronic structure of the desired crystal. In its last step, this should already produce the output `kpt.bin` and `eig.bin`.
2. Run the modified CUT3D code from the ABINIT-package to convert the wavefunction data into the `wfk.bin`-file.
3. Specify all numerical parameters for a MYLIO.X-run in the `global_variables.f90`-file and choose the desired observable (`main.f90`).
4. Recompile MYLIO.X and copy the executable into the place, where the electronic structure data (`kpt.bin`, `eig.bin` and `wfk.bin`) are located.
5. Execute MYLIO.X and redirect the output into a text-file.

References

[1] D. Krebs and N. Rohringer, *Theory of parametric x-ray optical wavemixing processes*, Phys Rev X (under review) (2022).

[2] I. Freund, *Nonlinear x-ray diffraction. determination of valence electron charge distributions*, Chemical Physics Letters, **12**, 4, 583 (1972), ISSN 0009-2614, doi:https://doi.org/10.1016/0009-2614(72)80013-7.

[3] K. Ramakrishna and J. Vorberger, *Ab initio dielectric response function of diamond and other relevant high pressure phases of carbon*, Journal of Physics: Condensed Matter, **32**, 9, 095401 (2019), doi:10.1088/1361-648x/ab558e.

[4] H. J. Monkhorst and J. D. Pack, *Special points for brillouin-zone integrations*, Phys. Rev. B, **13**, 5188 (1976), doi:10.1103/PhysRevB.13.5188.

[5] G. Czycholl, *Theoretische Festkörperphysik Band 1*, volume 1, Springer-Verlag Berlin Heidelberg (2016), doi:10.1007/978-3-662-47141-8.

A.7 Fourier transformation and the electromagnetic field

A central object of all our considerations is the electromagnetic field, which we (mostly) represent through the vector potential $\hat{\mathbf{A}}(\mathbf{x},t)$. For the non-interacting case (cf., Eq. (2.1) in Chpt. 2), we can write its operator/mode decomposition as [52, 53]:

$$\hat{\mathbf{A}}(\mathbf{x},t) = \sum_{\mathbf{k},\lambda} \sqrt{\frac{2\pi}{V\omega_{\mathbf{k}}\alpha^2}} \left(\hat{a}_{\mathbf{k},\lambda}\ \boldsymbol{\varepsilon}_{\mathbf{k},\lambda}\ e^{\mathrm{i}\mathbf{k}\cdot\mathbf{x}-\omega_{\mathbf{k}}t} + \hat{a}^{\dagger}_{\mathbf{k},\lambda}\ \boldsymbol{\varepsilon}^{*}_{\mathbf{k},\lambda}\ e^{-\mathrm{i}\mathbf{k}\cdot\mathbf{x}-\omega_{\mathbf{k}}t} \right). \tag{A.59}$$

Here, V denotes the quantization volume and $\omega_{\mathbf{k}} = c\,|\mathbf{k}| = |\mathbf{k}|/\alpha$. The $\hat{a}_{\mathbf{k},\lambda}$ ($\hat{a}^{\dagger}_{\mathbf{k},\lambda}$)—in turn—mark the annihilation or creation operators per mode. Analogous to their classical counterparts, they measure the weight of a mode within the expansion. Rendering such a mode expansion possible in the first place, is the fact that the freely propagating field $\hat{\mathbf{A}}(\mathbf{x},t)$ satisfies the wave-equation:

$$\left(\frac{1}{c^2}\frac{\partial^2}{\partial t^2} - \Delta\right)\hat{\mathbf{A}}(\mathbf{x},t) = 0. \tag{A.60}$$

This is solved by a set of independent solutions, which are generally referred to as modes—specifically, plane-waves as can be read off Eq. (A.59). For these modes, we adopt the convention [53, 128, 215] of calling the subset

$$\hat{\mathbf{A}}^{(+)}(\mathbf{x},t) = \sum_{\mathbf{k},\lambda} \sqrt{\frac{2\pi}{V\omega_{\mathbf{k}}\alpha^2}}\ \hat{a}_{\mathbf{k},\lambda}\ \boldsymbol{\varepsilon}_{\mathbf{k},\lambda}\ e^{\mathrm{i}(\mathbf{k}\cdot\mathbf{x}-\omega_{\mathbf{k}}t)} \tag{A.61}$$

the positive frequency part of $\hat{\mathbf{A}}(\mathbf{x},t)$. The remainder of Eq. (A.59) forms $\hat{\mathbf{A}}^{(-)}(\mathbf{x},t)$—the negative frequency part—respectively. On the basis of these complementary definitions, we fix our convention for the Fourier transformation. Namely, we choose

$$f(\omega) = \int_{-\infty}^{\infty} dt\ f(t)\ e^{\mathrm{i}\,\omega t} \tag{A.62}$$

$$f(t) = \frac{1}{2\pi}\int_{-\infty}^{\infty} d\omega\ f(\omega)\ e^{-\mathrm{i}\,\omega t}, \tag{A.63}$$

which ensures that the positive frequency part has indeed *positive* frequencies. For spatio-temporal Fourier transformations, we follow the wave-nature of fields and choose the $\mathbf{k}$ and ω exponents with opposite sign:

$$f(\mathbf{k},\omega) = \int_{-\infty}^{\infty} dt \int d^3x\ f(\mathbf{x},t)\ e^{-\mathrm{i}(\mathbf{k}\cdot\mathbf{x}-\omega t)} \tag{A.64}$$

$$f(\mathbf{x},t) = \frac{1}{(2\pi)^4}\int_{-\infty}^{\infty} d\omega \int d^3k\ f(\mathbf{k},\omega)\ e^{\mathrm{i}(\mathbf{k}\cdot\mathbf{x}-\omega t)}. \tag{A.65}$$

Regarding the distribution of the $\frac{1}{(2\pi)^n}$ factors, we follow the "π goes with p"-rule, i.e., placing the factors with the momentum (frequency) space integrations.

The above being said, we could likewise have chosen these Fourier conventions a priori and subsequently obtained the decomposition into positive and negative frequency parts. To this end, we remark at first that the temporal Fourier transform of $\hat{\mathbf{A}}(\mathbf{x},t)$ satisfies the Helmholtz-equation in the spectral

domain:

$$\Big(\frac{\omega^2}{c^2}+\Delta\Big)\hat{\mathbf{A}}(\mathbf{x},\omega)=0. \tag{A.66}$$

From this, we can conclude that all spectral components evolve independently, allowing us to form arbitrary superpositions. The obvious one being the Fourier recombination

$$\hat{\mathbf{A}}(\mathbf{x},t)=\frac{1}{2\pi}\int_{-\infty}^{\infty}d\omega\;\hat{\mathbf{A}}(\mathbf{x},\omega)\;e^{-\mathrm{i}\,\omega t}, \tag{A.67}$$

for which its observable (and thus hermitian) nature implies:

$$\begin{aligned}\hat{\mathbf{A}}(\mathbf{x},t)=\big(\hat{\mathbf{A}}(\mathbf{x},t)\big)^{\dagger}=\frac{1}{2\pi}\int_{-\infty}^{\infty}d\omega\;\big(\hat{\mathbf{A}}(\mathbf{x},\omega)\big)^{\dagger}\;e^{\mathrm{i}\,\omega t}=\frac{1}{2\pi}\int_{-\infty}^{\infty}d\omega\;\big(\hat{\mathbf{A}}(\mathbf{x},-\omega)\big)^{\dagger}\;e^{-\mathrm{i}\,\omega t}\\ \Rightarrow\big(\hat{\mathbf{A}}(\mathbf{x},-\omega)\big)^{\dagger}=\hat{\mathbf{A}}(\mathbf{x},\omega).\end{aligned} \tag{A.68}$$

Using two alternative mode combinations with positive (or negative) frequency content only, we can find:

$$\hat{\mathbf{A}}^{(+)}(\mathbf{x},t)=\frac{1}{2\pi}\int_{0}^{\infty}d\omega\;\hat{\mathbf{A}}(\mathbf{x},\omega)\;e^{-\mathrm{i}\,\omega t}\;\text{ and} \tag{A.69}$$

$$\hat{\mathbf{A}}^{(-)}(\mathbf{x},t)=\frac{1}{2\pi}\int_{-\infty}^{0}d\omega\;\hat{\mathbf{A}}(\mathbf{x},\omega)\;e^{-\mathrm{i}\,\omega t}, \tag{A.70}$$

fully analogous to our first approach. These two fields form a pair of hermitian adjoints

$$\hat{\mathbf{A}}^{(+)}(\mathbf{x},t)=\Big(\hat{\mathbf{A}}^{(-)}(\mathbf{x},t)\Big)^{\dagger} \tag{A.71}$$

as we can easily show by means of Eq. (A.68). Moreover, each of the two parts satisfies the wave-equation independently, i.e.,

$$\Big(\frac{1}{c^2}\frac{\partial^2}{\partial t^2}-\Delta\Big)\hat{\mathbf{A}}^{(+)}(\mathbf{x},t)=0=\Big(\frac{1}{c^2}\frac{\partial^2}{\partial t^2}-\Delta\Big)\hat{\mathbf{A}}^{(-)}(\mathbf{x},t). \tag{A.72}$$

Finally, note that we may, at times, extend the notation for the positive (or negative) frequency part into the spectral domain—by writing, e.g., $\hat{\mathbf{A}}^{(+)}(\mathbf{x},\omega)$. We take this to be the positively restricted spectral component

$$\hat{\mathbf{A}}^{(+)}(\mathbf{x},\omega)=\int_{0}^{\infty}d\omega'\;\delta(\omega-\omega')\;\hat{\mathbf{A}}(\mathbf{x},\omega') \tag{A.73}$$

and vice-versa for $\hat{\mathbf{A}}^{(-)}(\mathbf{x},\omega)$.

A.8 Correlation functions of the em-field and their Fourier relations

In this section of the Appendix, we have collated a (rather random) collection of Fourier relations among correlation functions of the electromagnetic field. As this list keeps growing and changing, we reserve an empty page for notes at its end.

To begin with, we recall the basic object of our concern

$$H^{(1)}_{\mu\nu}(\mathbf{x}_1,t_1,\mathbf{x}_2,t_2) = \mathrm{Tr}_{\mathrm{X\_IN}}\left\{\hat{\rho}_{\mathrm{X\_IN}}(0)\,(\hat{\mathbf{A}}^{(-)}_{\mathrm{x\_in}}(\mathbf{x}_1,t_1))_\mu\,(\hat{\mathbf{A}}^{(+)}_{\mathrm{x\_in}}(\mathbf{x}_2,t_2))_\nu\right\} \tag{A.74}$$

or its Fourier-related counterpart

$$\begin{aligned} Z^{(1)}_{\mu\nu}(\mathbf{k}_1,\omega_1,\mathbf{k}_2,\omega_2) &= \int d^3x_1 \int d^3x_2 \int dt_1 \int dt_2\; e^{\mathrm{i}\,(\mathbf{k}_1\cdot\mathbf{x}_1-\omega_1 t_1)}\; e^{-\mathrm{i}\,(\mathbf{k}_2\cdot\mathbf{x}_2-\omega_2 t_2)}\; H^{(1)}_{\mu\nu}(\mathbf{x}_1,t_1,\mathbf{x}_2,t_2) \\ &= \mathrm{Tr}_{\mathrm{X\_IN}}\left\{\hat{\rho}_{\mathrm{X\_IN}}(0)\,(\hat{\mathbf{A}}^{(+)}_{\mathrm{x\_in}}(\mathbf{k}_1,\omega_1))^\dagger_\mu\,(\hat{\mathbf{A}}^{(+)}_{\mathrm{x\_in}}(\mathbf{k}_2,\omega_2))_\nu\right\}. \end{aligned} \tag{A.75}$$

Further relations comprise, among others:

$$H^{(1)}_{\mu\nu}(\mathbf{x}_1,t_1,\mathbf{x}_2,t_2) = \frac{1}{(2\pi)^8}\int d^3k_1 \int d^3k_2 \int d\omega_1 \int d\omega_2\; e^{-\mathrm{i}\,(\mathbf{k}_1\cdot\mathbf{x}_1-\omega_1 t_1)}\; e^{\mathrm{i}\,(\mathbf{k}_2\cdot\mathbf{x}_2-\omega_2 t_2)}\; Z^{(1)}_{\mu\nu}(\mathbf{k}_1,\omega_1,\mathbf{k}_2,\omega_2), \tag{A.76}$$

$$W^{(1)}_{\mu\nu}(\mathbf{x}_1,\omega_1,\mathbf{x}_2,\omega_2) = \int dt_1 \int dt_2\; e^{-\mathrm{i}\,\omega_1 t_1}\; e^{\mathrm{i}\,\omega_2 t_2}\; G^{(1)}_{\mu\nu}(\mathbf{x}_1,t_1,\mathbf{x}_2,t_2), \tag{A.77}$$

$$G^{(1)}_{\mu\nu}(\mathbf{x}_1,t_1,\mathbf{x}_2,t_2) = \frac{1}{(2\pi)^2}\int d\omega_1 \int d\omega_2\; e^{\mathrm{i}\,\omega_1 t_1}\; e^{-\mathrm{i}\,\omega_2 t_2}\; W^{(1)}_{\mu\nu}(\mathbf{x}_1,\omega_1,\mathbf{x}_2,\omega_2), \tag{A.78}$$

$$G^{(1)}_{\mu\nu}(\mathbf{x}_1,t_1,\mathbf{x}_2,t_2) = \alpha^2\,\frac{\partial}{\partial t_1}\frac{\partial}{\partial t_2}\,H^{(1)}_{\mu\nu}(\mathbf{x}_1,t_1,\mathbf{x}_2,t_2), \tag{A.79}$$

$$Z^{(1)}_{\mu\nu}(\mathbf{k}_1,\omega_1,\mathbf{k}_2,\omega_2) = \int d^3x_1 \int d^3x_2\; e^{\mathrm{i}\,\mathbf{k}_1\cdot\mathbf{x}_1}\; e^{-\mathrm{i}\,\mathbf{k}_2\cdot\mathbf{x}_2}\;\frac{1}{\alpha^2\,\omega_1\omega_2}\,W^{(1)}_{\mu\nu}(\mathbf{x}_1,\omega_1,\mathbf{x}_2,\omega_2), \tag{A.80}$$

$$Z^{(1)}_{\mu\nu}(\mathbf{k}_1,\omega_1,\mathbf{k}_2,\omega_2) = \int d^3x_1 \int d^3x_2\; e^{\mathrm{i}\,\mathbf{k}_1\cdot\mathbf{x}_1}\; e^{-\mathrm{i}\,\mathbf{k}_2\cdot\mathbf{x}_2}\; V^{(1)}_{\mu\nu}(\mathbf{x}_1,\omega_1,\mathbf{x}_2,\omega_2), \tag{A.81}$$

$$V^{(1)}_{\mu\nu}(\mathbf{x}_1,\omega_1,\mathbf{x}_2,\omega_2) = \int dt_1 \int dt_2\; e^{-\mathrm{i}\,\omega_1 t_1}\; e^{\mathrm{i}\,\omega_2 t_2}\; H^{(1)}_{\mu\nu}(\mathbf{x}_1,t_1,\mathbf{x}_2,t_2), \tag{A.82}$$

$$V^{(1)}_{\mu\nu}(\mathbf{x}_1,\omega_1,\mathbf{x}_2,\omega_2) = \frac{1}{\alpha^2\,\omega_1\omega_2}\,W^{(1)}_{\mu\nu}(\mathbf{x}_1,\omega_1,\mathbf{x}_2,\omega_2), \tag{A.83}$$

$$Z^{(1)}_{\mu\nu}(\mathbf{k}_1,\omega_1,\mathbf{k}_2,\omega_2) = \int d^3x_1 \int d^3x_2\; e^{\mathrm{i}\mathbf{k}_1\cdot\mathbf{x}_1}\; e^{-\mathrm{i}\mathbf{k}_2\cdot\mathbf{x}_2}\; V^{(1)}_{\mu\nu}(\mathbf{x}_1,\omega_1,\mathbf{x}_2,\omega_2) \tag{A.84}$$
$$= \int d^3x_1 \int d^3x_2\; e^{\mathrm{i}\mathbf{k}_1\cdot\mathbf{x}_1}\; e^{-\mathrm{i}\mathbf{k}_2\cdot\mathbf{x}_2}\; \mathrm{Tr}_{\mathrm{X\_IN}}\left\{\hat{\rho}_{\mathrm{X\_IN}}(0)\,(\hat{\mathbf{A}}^{(+)}_{\mathrm{x\_in}}(\mathbf{x}_1,\omega_1))^{\dagger}_{\mu}\,(\hat{\mathbf{A}}^{(+)}_{\mathrm{x\_in}}(\mathbf{x}_2,\omega_2))_{\nu}\right\},$$

and more.

—Space for notes—

—Space for notes—

A.9 Propagation of the em-field

During our studies, we repeatedly encounter situations, wherein we happen to know the electromagnetic field of a radiation beam across a source plane—though not in the remainder of space. In order to complete our knowledge, we require a propagation formula. Focusing on the positive frequency part[9] of $\mathbf{A}(\mathbf{x},\omega)$, this would translate to:

$$\mathbf{A}^{(+)}((\mathbf{x}'^{\perp},z'),\omega) = \int d^2x^{\perp}\, P_{z',z}(\mathbf{x}'^{\perp},\mathbf{x}^{\perp},\omega)\, \mathbf{A}^{(+)}((\mathbf{x}^{\perp},z),\omega). \tag{A.85}$$

By way of our notation, we anticipate a propagation predominantly along the z-direction and a source plane perpendicular to it ($\mathbf{x}^{\perp}$). We note, furthermore, that the 'propagator' P is—in general—of tensorial nature, as it relates the three components of the source vector-potential to another three-dimensional output.

A.9.1 Free-field case / vacuum propagation

For the freely evolving field $\mathbf{A}(\mathbf{x},t)$, the above propagator may be inferred straight-forwardly from its mode-decomposition. To do so, we first recall that $\mathbf{A}(\mathbf{x},t)$ satisfies the wave equation component-wise—as does $\mathbf{A}(\mathbf{x},\omega)$ for the Helmholtz equation (cf. App. A.7). Thus, we can focus our discussion on a single (scalar) component for the time being. For this, we write the decomposition into independent solutions/modes as:

$$\begin{aligned} A^{(+)}(\mathbf{x},t) &= \int d^3k\, a(\mathbf{k})\, e^{\mathrm{i}(\mathbf{k}\cdot\mathbf{x}-\omega t)} \\ &= \int d^3k \int d\omega\, \delta(\omega - c\,|\mathbf{k}|)\, a(\mathbf{k})\, e^{\mathrm{i}(\mathbf{k}\cdot\mathbf{x}-\omega t)}, \end{aligned} \tag{A.86}$$

where in the second step, we have rendered the dispersion relation $\delta(\omega - c\,|\mathbf{k}|)$ explicit. By Fourier transformation, we obtain:

$$A^{(+)}(\mathbf{x},\omega) = \int_{-\infty}^{\infty} dt\; e^{\mathrm{i}\omega t}\, A^{(+)}(\mathbf{x},t) = 2\pi \int d^3k\, \delta(\omega - c\,|\mathbf{k}|)\, a(\mathbf{k})\, e^{\mathrm{i}\mathbf{k}\cdot\mathbf{x}}, \tag{A.87}$$

which allows for the following observation: The composition of the field (i.e., all the $a(\mathbf{k})$) is *almost* uniquely determined from the values of $A^{(+)}((\mathbf{x}^{\perp},z_0),\omega)$ in a single plane of points $\mathbf{x}^{\perp}$ at $z = z_0$ alone. In order to see this more clearly, we apply a spatial Fourier transform

$$\begin{aligned} \int d^2x^{\perp}\, e^{-\mathrm{i}\mathbf{k}'^{\perp}\cdot\mathbf{x}^{\perp}}\, A^{(+)}((\mathbf{x}^{\perp},z_0),\omega) &= \int d^2x^{\perp}\, e^{-\mathrm{i}\mathbf{k}'^{\perp}\cdot\mathbf{x}^{\perp}}\, 2\pi \int d^3k\, \delta(\omega - c\,|\mathbf{k}|)\, a(\mathbf{k})\, e^{\mathrm{i}\mathbf{k}\cdot\mathbf{x}} \\ &= 2\pi \int d^3k\, \delta(\omega - c\,|\mathbf{k}|)\, a(\mathbf{k})\, e^{\mathrm{i}k^{\parallel}z_0} \int d^2x^{\perp}\, e^{-\mathrm{i}(\mathbf{k}'^{\perp}\cdot\mathbf{x}^{\perp} - \mathbf{k}^{\perp}\cdot\mathbf{x}^{\perp})} \\ &= (2\pi)^3 \int d^3k\, \delta(\omega - c\,|\mathbf{k}|)\, a(\mathbf{k})\, e^{\mathrm{i}k^{\parallel}z_0}\, \delta^2(\mathbf{k}'^{\perp} - \mathbf{k}^{\perp}), \end{aligned} \tag{A.88}$$

[9] Note that the negative frequency part may be obtained via Eq. (A.68).

In the above, $k^{\shortparallel}$ denotes the component of $\mathbf{k}$ parallel to the z-direction and $\mathbf{k}^{\perp}$ those components perpendicular to it, respectively. Rephrasing further

$$\begin{aligned}\delta(\omega - c\,|\mathbf{k}|) &= \delta(\omega - c\sqrt{(k^{\shortparallel})^2 + (\mathbf{k}^{\perp})^2}) = \delta(f(k^{\shortparallel})) \\ &= \frac{\delta(k^{\shortparallel} - k_0^{\shortparallel})}{\left|f'(k_0^{\shortparallel})\right|} \\ &= \delta(k^{\shortparallel} - k_0^{\shortparallel})\ \frac{|\mathbf{k}|}{c k_0^{\shortparallel}},\end{aligned} \tag{A.89}$$

wherein the roots of $f(k^{\shortparallel})$ are given by $k_0^{\shortparallel} = \pm\sqrt{\omega^2/c^2 - (\mathbf{k}^{\perp})^2}$, we find the δ-functions in Eq. (A.88) capable of uniquely fixing $\mathbf{k}$ apart from the sign of the root. The latter may be deliberately chosen ($+$ in our case), if we assume beam-like propagation in only one direction (along positive z-direction in our case). Thereby, we obtain from Eq. (A.88):

$$a(\mathbf{k}) = \frac{1}{(2\pi)^3}\ \frac{c\,k^{\shortparallel}}{|\mathbf{k}|}\ e^{-\mathrm{i}\,k^{\shortparallel} z_0} \int d^2x^{\perp}\, e^{-\mathrm{i}\,\mathbf{k}^{\perp}\cdot\mathbf{x}^{\perp}}\ A^{(+)}((\mathbf{x}^{\perp}, z_0), c\,|\mathbf{k}|). \tag{A.90}$$

Reinserting the above into Eq. (A.87) and comparing to Eq. (A.85), we identify the propagator:

$$P_{z',z}(\mathbf{x}'^{\perp}, \mathbf{x}^{\perp}, \omega) = \frac{1}{(2\pi)^2}\ \int d^3k\ \delta(k^{\shortparallel} - k_0^{\shortparallel})\ e^{\mathrm{i}\,k^{\shortparallel}(z'-z)}\ e^{\mathrm{i}\,\mathbf{k}^{\perp}\cdot(\mathbf{x}'^{\perp} - \mathbf{x}^{\perp})} \tag{A.91}$$

with definite $k_0^{\shortparallel} = +\sqrt{\omega^2/c^2 - (\mathbf{k}^{\perp})^2}$.

Following the component-wise logic, the extension towards a tensorial structure is trivially given by:

$$\left(P_{z',z}(\mathbf{x}'^{\perp}, \mathbf{x}^{\perp}, \omega)\right)_{\mu\nu} = \frac{1}{(2\pi)^2}\ \int d^3k\ \delta_{\mu\nu}\ \delta(k^{\shortparallel} - k_0^{\shortparallel})\ e^{\mathrm{i}\,k^{\shortparallel}(z'-z)}\ e^{\mathrm{i}\,\mathbf{k}^{\perp}\cdot(\mathbf{x}'^{\perp} - \mathbf{x}^{\perp})}. \tag{A.92}$$

However, a note of caution is in order here: While the above is suitable for relating a *correct* initial field into an equally correct output, it is not fail-safe in the case of 'wrong' (e.g., approximate) initial fields. In particular, Eq. (A.92) does not *enforce* the transversality of an em-wave[10]. If this should be ensured additionally, it is advisable to convolute Eq. (A.92) with a transverse δ-dyadic:

$$\begin{aligned}\left(P_{z'',z}(\mathbf{x}''^{\perp}, \mathbf{x}^{\perp}, \omega)\right)_{\mu\nu} &= \int d^3x\ \delta^{\perp}_{\mu\rho}(\mathbf{x}'' - \mathbf{x}')\ \left(P_{z',z}(\mathbf{x}'^{\perp}, \mathbf{x}^{\perp}, \omega)\right)_{\rho\nu} \\ &= \frac{1}{(2\pi)^2}\ \int d^3k\ \left(\delta_{\mu\nu} - \frac{(\mathbf{k})_{\mu}(\mathbf{k})_{\nu}}{|\mathbf{k}|^2}\right)\ \delta(k^{\shortparallel} - k_0^{\shortparallel})\ e^{\mathrm{i}\,k^{\shortparallel}(z'-z)}\ e^{\mathrm{i}\,\mathbf{k}^{\perp}\cdot(\mathbf{x}'^{\perp} - \mathbf{x}^{\perp})},\end{aligned} \tag{A.93}$$

which effectively results in the replacement $\delta_{\mu\nu} \to \delta_{\mu\nu} - (\mathbf{k})_{\mu}(\mathbf{k})_{\nu}/\,|\mathbf{k}|^2$

A.9.2 Consistency checks and the Fresnel propagator

In a next step, we should make sure that our exact, plane-wave propagator behaves reasonably, if we want to use it over more commonly employed propagators. An example of the latter, established propagators is the Fresnel propagator, which is ubiquitously used in Singer's work [131], for instance. Subsequently, we shall exercise some consistency checks and actually derive the Fresnel propagator from our expression (A.92).

[10] We recall that $\nabla\hat{\mathbf{A}}(\mathbf{x}) = 0$ is explicitly set (but also required) in the Coulomb-gauge. If approximate initial conditions invalidate this condition, there is no innate correction mechanism embedded in the theory.

First of all, we require that our propagator should reproduce the trivial case of no propagation (identity). Setting $z' = z$ in Eq. (A.92), we trivially find:

$$\begin{aligned}\Big(P_{z,z}(\mathbf{x}'^{\perp},\mathbf{x}^{\perp},\omega)\Big)_{\mu\nu} &= \frac{1}{(2\pi)^2}\int d^3k\ \delta_{\mu\nu}\ \delta(k^{\shortparallel}-k_0^{\shortparallel})\ e^{\mathrm{i}k^{\shortparallel}0}\ e^{\mathrm{i}\mathbf{k}^{\perp}\cdot(\mathbf{x}'^{\perp}-\mathbf{x}^{\perp})}\\ &= \delta_{\mu\nu}\ \delta^2(\mathbf{x}'^{\perp}-\mathbf{x}^{\perp}),\end{aligned} \tag{A.94}$$

i.e., the identity operator within a $d^2x_{\perp}$-integration as of Eq. (A.85).

As a second check, we expect our propagator to exhibit a concatenation property of the kind:

$$P_{z'',z}(\mathbf{x}''^{\perp},\mathbf{x}^{\perp},\omega) = \int d^2x'^{\perp}\ P_{z'',z'}(\mathbf{x}''^{\perp},\mathbf{x}'^{\perp},\omega)\ P_{z',z}(\mathbf{x}'^{\perp},\mathbf{x}^{\perp},\omega). \tag{A.95}$$

This may easily be established via:

$$\begin{aligned}\int d^2x'^{\perp}\ P(...)P(...) &= \int d^2x'^{\perp}\ \Big(\frac{1}{(2\pi)^2}\int d^3k\ \delta(k^{\shortparallel}-k_0^{\shortparallel})\ e^{\mathrm{i}k^{\shortparallel}(z''-z')}\ e^{\mathrm{i}\mathbf{k}^{\perp}\cdot(\mathbf{x}''^{\perp}-\mathbf{x}'^{\perp})}\Big)\\ &\times\Big(\frac{1}{(2\pi)^2}\int d^3k'\ \delta(k'^{\shortparallel}-k_0'^{\shortparallel})\ e^{\mathrm{i}k'^{\shortparallel}(z'-z)}\ e^{\mathrm{i}\mathbf{k}'^{\perp}\cdot(\mathbf{x}'^{\perp}-\mathbf{x}^{\perp})}\Big)\\ &= \frac{1}{(2\pi)^2}\int d^3k\ \delta(k^{\shortparallel}-k_0^{\shortparallel})\ e^{\mathrm{i}k^{\shortparallel}(z''-z')}\int d^3k'\ \delta(k'^{\shortparallel}-k_0'^{\shortparallel})\ e^{\mathrm{i}k'^{\shortparallel}(z'-z)}\\ &\times e^{\mathrm{i}(\mathbf{k}^{\perp}\cdot\mathbf{x}''^{\perp}-\mathbf{k}'^{\perp}\cdot\mathbf{x}^{\perp})}\ \delta^2(\mathbf{k}^{\perp}-\mathbf{k}'^{\perp})\\ &= \frac{1}{(2\pi)^2}\int d^3k\ \delta(k^{\shortparallel}-k_0^{\shortparallel})\ e^{\mathrm{i}k^{\shortparallel}(z''-z)}\ e^{\mathrm{i}\mathbf{k}^{\perp}\cdot(\mathbf{x}''^{\perp}-\mathbf{x}^{\perp})}\\ &= P_{z'',z}(\mathbf{x}''^{\perp},\mathbf{x}^{\perp},\omega),\end{aligned} \tag{A.96}$$

where we made use of the occurring δ-constraints.

For a final cross check, we should be able to obtain the Fresnel propagator via approximating Eq. (A.91) (for simplicity, we focus on the scalar case again). It is:

$$\begin{aligned}P_{z',z}(\mathbf{x}'^{\perp},\mathbf{x}^{\perp},\omega) &= \frac{1}{(2\pi)^2}\int d^3k\ \delta(k^{\shortparallel}-k_0^{\shortparallel})\ e^{\mathrm{i}k^{\shortparallel}(z'-z)}\ e^{\mathrm{i}\mathbf{k}^{\perp}\cdot(\mathbf{x}'^{\perp}-\mathbf{x}^{\perp})}\\ &= \frac{1}{(2\pi)^2}\int d^3k\ \delta(k^{\shortparallel}-k_0^{\shortparallel})\ e^{\mathrm{i}k_0^{\shortparallel}(z'-z)}\ e^{\mathrm{i}\mathbf{k}^{\perp}\cdot(\mathbf{x}'^{\perp}-\mathbf{x}^{\perp})}\\ &= \frac{1}{(2\pi)^2}\int d^3k\ \delta(k^{\shortparallel}-k_0^{\shortparallel})\ e^{\mathrm{i}\sqrt{\frac{\omega^2}{c^2}-(\mathbf{k}^{\perp})^2}(z'-z)}\ e^{\mathrm{i}\mathbf{k}^{\perp}\cdot(\mathbf{x}'^{\perp}-\mathbf{x}^{\perp})}.\end{aligned} \tag{A.97}$$

Using the notion of a well-collimated beam, i.e., $\omega/c = |\mathbf{k}| \gg \left|\mathbf{k}^{\perp}\right|$, we expand:

$$\sqrt{\frac{\omega^2}{c^2}-(\mathbf{k}^{\perp})^2} \approx \frac{\omega}{c}\Big(1-\frac{1}{2}\frac{c^2\left|\mathbf{k}^{\perp}\right|^2}{\omega^2}+\frac{1}{8}\frac{c^4\left|\mathbf{k}^{\perp}\right|^4}{\omega^4}-...\Big). \tag{A.98}$$

In particular, we shall adopt the beam condition from Singer's thesis [131]:

$$\theta \approx \frac{\left|\mathbf{k}^{\perp}\right|}{|\mathbf{k}|} \ll \sqrt[4]{\frac{8\pi}{|\mathbf{k}|\,(z'-z)}} \Leftrightarrow \frac{1}{8}\frac{c^4\left|\mathbf{k}^{\perp}\right|^4}{\omega^4} \ll \frac{\pi}{|\mathbf{k}|\,(z'-z)}, \tag{A.99}$$

by which the third term in Eq. (A.98) is rendered irrelevant for the propagation. The approximate prop-

agator so far reads:

$$P_{z',z}(\mathbf{x}'^{\perp},\mathbf{x}^{\perp},\omega) \approx \frac{1}{(2\pi)^2}\, e^{\mathrm{i}(z'-z)\omega/c} \int d^2k^{\perp}\, e^{-\mathrm{i}c\left|\mathbf{k}^{\perp}\right|^2(z'-z)/2\omega}\, e^{\mathrm{i}\mathbf{k}^{\perp}\cdot(\mathbf{x}'^{\perp}-\mathbf{x}^{\perp})}. \tag{A.100}$$

For each component of $\mathbf{k}^{\perp}$, the respective integration can be solved by the method of stationary phase, which is not even an approximation in this case, as the exponent is at most quadratic[11]. The result is just:

$$P_{z',z}(\mathbf{x}'^{\perp},\mathbf{x}^{\perp},\omega) \approx \frac{1}{2\pi\,\mathrm{i}}\,\frac{\omega}{c\,(z'-z)}\, e^{\mathrm{i}(z'-z)\omega/c}\, e^{\mathrm{i}\,\omega(\mathbf{x}'^{\perp}-\mathbf{x}^{\perp})^2/2c(z'-z)}, \tag{A.101}$$

which—upon replacement of $\omega/c = k$— is the same formula as used by Singer (Eq. (2.6) in Ref. [131]).

A.9.3 Simplified propagation on short distances

Up to now, we have considered the free propagation of the radiation field—both in its general form and in the Fresnel approximation for well defined beams. In addition, we briefly want to discuss the situation, when we encounter a well defined beam *and* concern ourselves only with the propagation across rather short distances.

This will prove particularly useful, if we include the effects of weakly interacting matter, as it will allow us to describe the transmission of optically 'thin' samples. In order to do so, we modify the free-space Helmholtz-equation (A.66) to include the presence of a dielectric material through its complex refractive index $n^2(\mathbf{x},\omega)$. We assume the properties of this dielectric to vary slowly in space on the scale of the fields wavelength[12]. In doing so, we largely follow Paganin's reasoning in Ref. [216]. We begin by generalizing

$$\left(\frac{\omega^2}{c^2}\cdot n^2(\mathbf{x},\omega)+\Delta\right)\mathbf{A}^{\dagger}(\mathbf{x},\omega) = 0. \tag{A.102}$$

Next, we impose our presumption of dealing with a rather well defined beam (conventionally along coordinate z) and separate off the corresponding central phase-term of $\mathbf{A}^{\dagger}(\mathbf{x},\omega)$:

$$\mathbf{A}^{\dagger}(\mathbf{x},\omega) = e^{\mathrm{i}kz}\mathbf{A}_s^{\dagger}(\mathbf{x},\omega). \tag{A.103}$$

Here, we denote $k = \alpha\omega$. Re-inserting this—up to now exact—ansatz into Eq. A.102, we obtain

$$e^{\mathrm{i}kz}\left(\Delta + 2\mathrm{i}k_{\omega}\frac{\partial}{\partial z} + k^2(n^2-1)\right)\mathbf{A}_s^{(+)}(\mathbf{x},\omega) = 0. \tag{A.104}$$

This yields the paraxial wave equation for $\mathbf{A}_s^{\dagger}(\mathbf{x},\omega)$, wherein we have neglected the second order coupling of longitudinal and transverse propagation[13] (i.e., $(\frac{\partial}{\partial z})^2\mathbf{A}_s \approx 0$).

Then again, we may simplify Eq. A.104 even more radically, by neglecting *all* second order derivatives. For short range evolution of $\mathbf{A}_s^{\dagger}(\mathbf{x},\omega)$, such an approximation is justified, as the linear term of Eq.

[11] We note that some additional treatment of these integrals leads towards the eponymous 'Fresnel-integrals'. Their solution is listed in App. A.15.

[12] We note that in assuming the dielectric to be 'slowly-varying', we neglect its constituting microscopic properties, of course. After all, any material is still made up of atoms/electrons microscopically, which exhibit structural variation down below the Å-scale. Instead, we adopt a macroscopic view of the electromagnetic field in writing Eq. A.102.

[13] Note that this approximation closely resembles our treatment of the 'beam-propagation'-case in the previous section.

A.104 will dominate the behaviour. The resulting equation

$$\frac{\partial}{\partial z}\mathbf{A}_s^\dagger(\mathbf{x},\omega) \approx -\frac{\mathrm{i}k}{2}\left(1-n^2(\mathbf{x},\omega)\right)\mathbf{A}_s^\dagger(\mathbf{x},\omega) \tag{A.105}$$

can easily be solved by

$$\mathbf{A}_s^\dagger(\mathbf{x}^\perp z_2,\omega) \approx \exp\left(-\frac{\mathrm{i}k}{2}\int_{z_1}^{z_2} dz\,(1-n^2(\mathbf{x},\omega))\right)\mathbf{A}_s^\dagger(\mathbf{x}^\perp z_1,\omega) \tag{A.106}$$

and, thus, implies the simplified propagator

$$P_{z_2,z_1}(\mathbf{x}_2^\perp,\mathbf{x}_1^\perp,\omega) \approx e^{\mathrm{i}k(z_2-z_1)}e^{-\frac{\mathrm{i}k}{2}\int_{z_1}^{z_2} dz\,(1-n^2(\mathbf{x},\omega))}\cdot\delta^2(\mathbf{x}_2^\perp-\mathbf{x}_1^\perp). \tag{A.107}$$

For further convenience in the x-ray regime, we may rewrite the refractive index into the more conventional

$$n(\mathbf{x},\omega) = 1-\delta(\mathbf{x},\omega)+\mathrm{i}\beta(\mathbf{x},\omega) \tag{A.108}$$

and, thus, include both slight refraction and absorption[14]. For both δ and β being much smaller than 1, we can further approximate

$$1-n^2 \approx 2(\delta(\mathbf{x},\omega)-\mathrm{i}\beta(\mathbf{x},\omega)) \tag{A.109}$$

and thereby arrive ultimately at

$$P_{z_2,z_1}(\mathbf{x}_2^\perp,\mathbf{x}_1^\perp,\omega) \approx e^{\mathrm{i}k(z_2-z_1)}e^{-\mathrm{i}k\int_{z_1}^{z_2} dz\,(\delta(\mathbf{x},\omega)-\mathrm{i}\beta(\mathbf{x},\omega))}\delta^2(\mathbf{x}_2^\perp-\mathbf{x}_1^\perp). \tag{A.110}$$

A.9.4 Inclusion of optical elements

In addition to the (mostly) free propagation of radiation beams, it is sometimes desirable to include the effect of optical elements as well. These could consist of lenses, mirrors, slits/apertures, filters/ monochromators etc.. Any one of them may coarsely be modelled by the inclusion of an additional transfer function[15]. For an example, consider Fig. A.2.
The first depicted case (a) reflects the free propagation of a beam from $z=z_0$ to $z=z_f$, while the second case (b) is modified by a slit at $z=z_s$.

The corresponding propagators read:

$$\text{a)}\;\; P_{z_f,z_0}(\mathbf{x}'^\perp,\mathbf{x}^\perp,\omega) = \int d^2x_s^\perp\; P_{z_f,z_s}(\mathbf{x}'^\perp,\mathbf{x}_s^\perp,\omega)\; P_{z_s,z_0}(\mathbf{x}_s^\perp,\mathbf{x}^\perp,\omega) \tag{A.111}$$

$$\text{b)}\;\; P_{z_f,z_0}(\mathbf{x}'^\perp,\mathbf{x}^\perp,\omega) = \int d^2x_s^\perp\; P_{z_f,z_s}(\mathbf{x}'^\perp,\mathbf{x}_s^\perp,\omega)\; T_{\mathrm{slit}}(\mathbf{x}_s^\perp,\omega)\; P_{z_s,z_0}(\mathbf{x}_s^\perp,\mathbf{x}^\perp,\omega), \tag{A.112}$$

[14] Note that this absorption feature makes it all the more necessary to stick to short range propagation and—in particular—to *not* propagate backwards. This would lead to an artificial increase of the field, instead of absorption. As such, this propagator is not appropriate to generate full space fields for Fourier transforms, for instance.

[15] Here, we rely on the procedure used by Singer [131], whereto the reader is referred for further information.

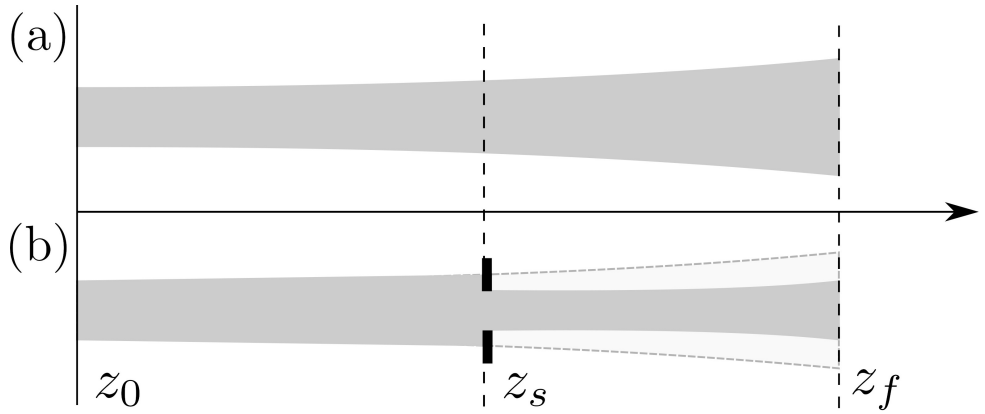

Figure A.2: Illustration of the effect of optical elements: (a) beam propagating freely from z_0 to z_f versus (b) beam traversing the same distance but being shaped (restricted) by a slit at z_s. [We gratefully acknowledge Dr. Christina Bömer's help in rendering the above computer graphics.]

where $T_{\text{slit}}(\mathbf{x}_s^{\perp}, \omega)$ denotes the transfer function of the slit. It may, for instance, be given by:

$$T_{\text{slit}}(\mathbf{x}_s^{\perp}, \omega) = \begin{cases} 1 & \text{for } |\mathbf{x}_s^x| < d = \text{const.} \\ 0 & \text{otherwise} \end{cases} \tag{A.113}$$

for a slit of width $2d$ along the y-direction. Two final remarks should be given regarding the above:

1) Depending on the degree of approximation involved in writing transfer functions, it may become increasingly more important to check/enforce the transversality of the em-field and correct for other artefacts ($\rightarrow$ stability of the propagator).

2) For more involved combinations of optical elements, useful numerical propagation routines may be found with several synchrotron radiation software packages, see Refs. [132, 133, 135].

A.9.5 Propagation of correlation functions

In this last section regarding the propagtion of em-fields, we want to extend the treatment from single fields towards correlation functions. We begin by noting that our previous construction of $P_{z'z}(...)$ relied solely on the fact that $\hat{\mathbf{A}}((\mathbf{x},t))$ satisfies the wave-equation, which allowed for our mode-decomposition. Analogously,

$$H^{(1)}_{\mu\nu}(\mathbf{x}_1,t_1,\mathbf{x}_2,t_2) = \text{Tr}_{\text{X\_IN}}\left\{\hat{\rho}_{\text{X\_IN}}(0)\,(\hat{\mathbf{A}}^{(-)}_{\text{x\_in}}(\mathbf{x}_1,t_1))^{\dagger}_{\mu}\,(\hat{\mathbf{A}}^{(+)}_{\text{x\_in}}(\mathbf{x}_2,t_2))_{\nu}\right\} \tag{A.114}$$

being composed of two fields, satisfies a wave-equation for each of its coordinate pairs:

$$\left(\frac{1}{c^2}\frac{\partial^2}{\partial t_1^2} - \Delta_1\right) H^{(1)}_{\mu\nu}(\mathbf{x}_1,t_1,\mathbf{x}_2,t_2) = 0 = \left(\frac{1}{c^2}\frac{\partial^2}{\partial t_2^2} - \Delta_2\right) H^{(1)}_{\mu\nu}(\mathbf{x}_1,t_1,\mathbf{x}_2,t_2). \tag{A.115}$$

Therefore, we may reuse our previous result as a means of propagating each pair of coordinates independently as well. For $V_{\mu\nu}(x_1,\omega_1,x_2,\omega_2)$, which we recall to be (cf. App. A.8):

$$V^{(1)}_{\mu\nu}(\mathbf{x}_1,\omega_1,\mathbf{x}_2,\omega_2) = \int dt_1 \int dt_2\; e^{-\mathrm{i}\,\omega_1 t_1}\; e^{\mathrm{i}\,\omega_2 t_2}\; H^{(1)}_{\mu\nu}(\mathbf{x}_1,t_1,\mathbf{x}_2,t_2), \tag{A.116}$$

we write accordingly

$$
\begin{aligned}
V^{(1)}_{\mu\nu}(\mathbf{x}_1,\omega_1,\mathbf{x}_2,\omega_2) &= V^{(1)}_{\mu\nu}((\mathbf{x}_1^{\perp},z_1)\omega_1,(\mathbf{x}_2^{\perp},z_2),\omega_2) \\
&= \int d^2x_1'^{\perp}\int d^2x_2'^{\perp}\left[\left(P_{z_1,z_1'}(\mathbf{x}_1^{\perp},\mathbf{x}_1'^{\perp},\omega_1)\right)_{\mu\rho}\right]^{\dagger}\left(P_{z_2,z_2'}(\mathbf{x}_2^{\perp},\mathbf{x}_2'^{\perp},\omega_2)\right)_{\nu\sigma} \\
&\times V^{(1)}_{\rho\sigma}((\mathbf{x}_1'^{\perp},z_1'),\omega_1,(\mathbf{x}_2'^{\perp},z_2'),\omega_2). \qquad \text{(A.117)}
\end{aligned}
$$

A.10 Intensity observable for the electromagnetic field

In this section, we will establish a relation between the first-order coherence function $G^{(1)}_{\mu\nu}(\mathbf{x}_1,t_1,\mathbf{x}_2,t_2)$ (or some derivation thereof) with an intensity observable. To this end, we start from the quantum-mechanical Poynting operator[16] as used by Loudon [53], for instance:

$$S_\mu(\mathbf{x},t) = \frac{1}{4\pi\alpha}\,\frac{1}{2}\left(\mathbf{E}^{(-)}(\mathbf{x},t)\times\mathbf{B}^{(+)}(\mathbf{x},t) - \mathbf{B}^{(-)}(\mathbf{x},t)\times\mathbf{E}^{(+)}(\mathbf{x},t)\right)_\mu \tag{A.118}$$

In here and below, we use Greek-style lettering to index the components of a vector or matrix. For completeness, we also recall the Fourier relations for the fields

$$\mathbf{B}^{(+)}(\mathbf{k},\omega) = \int d^3x \int dt\; e^{-\mathrm{i}(\mathbf{kx}-\omega t)}\;\mathbf{B}^{(+)}(\mathbf{x},t) \tag{A.119}$$

$$\mathbf{B}^{(+)}(\mathbf{x},t) = \frac{1}{(2\pi)^4}\int d^3k \int d\omega\; e^{i(\mathbf{kx}-\omega t)}\;\mathbf{B}^{(+)}(\mathbf{k},\omega), \tag{A.120}$$

where the same naturally holds for $\mathbf{E}^{(+)}(\mathbf{x},t)$ as well.

Next, we recall that $\mathbf{B}(\mathbf{x},\omega)$ satisfies Maxwell's equations in vacuum:

$$\nabla\times\mathbf{E}(\mathbf{x},\omega) = \frac{\mathrm{i}\omega}{c}\,\mathbf{B}(\mathbf{x},\omega), \tag{A.121}$$

which also holds independently for the positive / negative frequency part, such that

$$\Rightarrow \mathbf{B}^{(+)}(\mathbf{x},t) = \frac{1}{2\pi}\int d\omega\; e^{-\mathrm{i}\omega t}(-\frac{\mathrm{i}c}{\omega})\nabla\times\mathbf{E}^{(+)}(\mathbf{x},\omega). \tag{A.122}$$

Therewith, the Poynting-operator may be re-written as

$$\begin{aligned} S_\mu(\mathbf{x},t) = \frac{-1}{4\pi\alpha}\frac{1}{2}\Big[&\mathbf{E}^{(-)}(\mathbf{x},t)\times\Big(\frac{1}{2\pi}\int d\omega\; e^{-\mathrm{i}\omega t}(-\frac{\mathrm{i}c}{\omega})\nabla\times\mathbf{E}^{(+)}(\mathbf{x},\omega)\Big)\\ &-\Big(\frac{1}{2\pi}\int d\omega\; e^{-\mathrm{i}\omega t}(-\frac{\mathrm{i}c}{\omega})\nabla\times\mathbf{E}^{(-)}(\mathbf{x},\omega)\Big)\times\mathbf{E}^{(+)}(\mathbf{x},t)\Big]_\mu \end{aligned} \tag{A.123}$$

Next, by employing the decomposition into k-components, we can make use of

$$\nabla\times\mathbf{E}(\mathbf{x},\omega) = \nabla\times\frac{1}{(2\pi)^3}\int d^3k\; e^{\mathrm{i}\mathbf{kx}}\,\mathbf{E}(\mathbf{k},\omega) = \frac{1}{(2\pi)^3}\int d^3k\; e^{\mathrm{i}\mathbf{kx}}\mathrm{i}\,\mathbf{k}\times\mathbf{E}(\mathbf{k},\omega) \tag{A.124}$$

to reformulate S_μ further:

$$\begin{aligned} S_\mu(\mathbf{x},t) = \frac{-1}{8\pi\alpha}\frac{1}{(2\pi)^4}\int d^3k\int d\omega\;\frac{\mathrm{i}c}{\omega}e^{-\mathrm{i}\omega t}e^{\mathrm{i}\mathbf{k}\omega}\;\mathrm{i}\\ \cdot\Big[\mathbf{E}^{(-)}(\mathbf{x},t)\times(\mathbf{k}\times\mathbf{E}^{(+)}(\mathbf{k},\omega)) - (\mathbf{k}\times\mathbf{E}^{(-)}(\mathbf{k},\omega))\times\mathbf{E}^{(+)}(\mathbf{x},t)\Big]_\mu. \end{aligned} \tag{A.125}$$

Applying the identities $\mathbf{a}\times(\mathbf{b}\times\mathbf{c}) = (\mathbf{a}\cdot\mathbf{c})\mathbf{b} - (\mathbf{a}\cdot\mathbf{b})\mathbf{c}$ and $(\mathbf{a}\times\mathbf{b})\times\mathbf{c} = (\mathbf{a}\cdot\mathbf{c})\mathbf{b} - (\mathbf{b}\cdot\mathbf{c})\mathbf{a}$ this transforms

[16] We note that, in this section, we omit the 'hat'-notation on operator-valued fields. This is intended to improve the overall readability; all equations are valid for quantum- as well as classical fields.

into

$$S_\mu(\mathbf{x},t) = \frac{1}{8\pi\alpha}\frac{1}{(2\pi)^4}\int d^3k \int d\omega\ \frac{c}{\omega}\ e^{-\mathrm{i}\omega t}e^{\mathrm{i}\mathbf{k}\omega}\ \Big[(\mathbf{E}^{(-)}(\mathbf{x},t)\cdot\mathbf{E}^{(+)}(\mathbf{k},\omega))\mathbf{k} - (\mathbf{E}^{(-)}(\mathbf{x},t)\cdot\mathbf{k})\mathbf{E}^{(+)}(\mathbf{k},\omega) \\ -\mathbf{E}^{(-)}(\mathbf{k},\omega)(\mathbf{k}\cdot\mathbf{E}^{(+)}(\mathbf{x},t))) + (\mathbf{E}^{(-)}(\mathbf{k},\omega)\cdot\mathbf{E}^{(+)}(\mathbf{x},t))\mathbf{k}\Big]_\mu . \tag{A.126}$$

At this point, we note that due to the transversality of the electromagnetic field, i.e., $\mathbf{k}\perp\mathbf{E}$, terms of the type $\mathbf{k}\cdot\mathbf{E}^{(+/-)}(\mathbf{x},t)\to 0$ will vanish. This simplifies the Poynting observable into

$$S_\mu(\mathbf{x},t) = \frac{1}{8\pi\alpha}\frac{1}{(2\pi)^4}\int d^3k \int d\omega\ \frac{c}{\omega}\ e^{-\mathrm{i}\omega t}e^{\mathrm{i}\mathbf{k}x}(\mathbf{k})_\mu\ \Big[\mathbf{E}^{(-)}(\mathbf{x},t)\cdot\mathbf{E}^{(+)}(\mathbf{k},\omega) + \mathbf{E}^{(-)}(\mathbf{k},\omega)\cdot\mathbf{E}^{(+)}(\mathbf{x},t)\Big] . \tag{A.127}$$

For simplicity, we will only be interested in energy flow through a surface perpendicular to the average propagation direction $\mathbf{k}_{\mathrm{avg}}$–for which we denote the corresponding unit vector $\hat{\mathbf{k}}_{\mathrm{avg}}$.

$$\begin{aligned}
\hat{\mathbf{k}}_{\mathrm{avg}}\cdot\mathbf{S}(\mathbf{x},t) &= \frac{1}{8\pi\alpha}\frac{1}{(2\pi)^4}\int d^3k\int d\omega\ \frac{c}{\omega}\ e^{-\mathrm{i}\omega t}e^{\mathrm{i}\mathbf{k}x}\underbrace{\hat{\mathbf{k}}_{\mathrm{avg}}\cdot\mathbf{k}}_{\approx\omega/c}\Big[\mathbf{E}^{(-)}(\mathbf{x},t)\mathbf{E}^{(+)}(\mathbf{k},\omega)+\mathbf{E}^{(-)}(\mathbf{k},\omega)\mathbf{E}^{(+)}(\mathbf{x},t)\Big] \\
&\approx \frac{1}{8\pi\alpha}\frac{1}{(2\pi)^4}\int d^3k\int d\omega\ e^{-\mathrm{i}\omega t}e^{\mathrm{i}\mathbf{k}x}\ \Big[\mathbf{E}^{(-)}(\mathbf{x},t)\mathbf{E}^{(+)}(\mathbf{k},\omega)+\mathbf{E}^{(-)}(\mathbf{k},\omega)\mathbf{E}^{(+)}(\mathbf{x},t)\Big] \\
&= \frac{1}{8\pi\alpha}\Big[\mathbf{E}^{(-)}(\mathbf{x},t)\mathbf{E}^{(+)}(\mathbf{x},t)+\mathbf{E}^{(-)}(\mathbf{x},t)\mathbf{E}^{(+)}(\mathbf{x},t)\Big] \\
&= \frac{1}{4\pi\alpha}\Big[\mathbf{E}^{(-)}(\mathbf{x},t)\mathbf{E}^{(+)}(\mathbf{x},t)\Big]
\end{aligned} \tag{A.128}$$

Such that on taking the expectation value

$$\begin{aligned}
\mathrm{Tr}\{\rho(\hat{\mathbf{k}}_{\mathrm{avg}}\cdot\mathbf{S}(\mathbf{x},t))\} &= \frac{1}{4\pi\alpha}\mathrm{Tr}\{\rho\mathbf{E}^{(-)}(\mathbf{x},t)\mathbf{E}^{(+)}(\mathbf{x},t)\} \\
&= \frac{1}{4\pi\alpha}\sum_\mu G^{(1)}_{\mu\mu}(\mathbf{x}_1,t_1,\mathbf{x}_2,t_2) \\
&= \langle I(\mathbf{x},t)\rangle,
\end{aligned} \tag{A.129}$$

we find our Poynting observable to be related to the diagonal elements of Glauber's correlation function $G^{(1)}_{\mu\mu}$. We may identify this quantity with the expectation value of the field's intensity.

In addition to the above result, we also want to relate the intensity observable to some Fourier domain quantities. Starting from

$$\langle I(\mathbf{x},t)\rangle = \frac{1}{4\pi\alpha}\ G^{(1)}_{\mu\mu}(\mathbf{x},t,\mathbf{x},t), \tag{A.130}$$

we can insert the transformation to $W^{(1)}_{\mu\mu}$ as of Eq. (A.78) and obtain

$$\langle I(\mathbf{x},t)\rangle = \frac{1}{4\pi\alpha\ (2\pi)^2}\ \int d\omega_1\int d\omega_2\ e^{\mathrm{i}\,\omega_1 t}\ e^{-\mathrm{i}\,\omega_2 t}\ W^{(1)}_{\mu\mu}(\mathbf{x},\omega_1,\mathbf{x},\omega_2). \tag{A.131}$$

In particular, this can be time-integrated and gives for the resultant quantity (namely, the radiant expo-

sure)

$$H(\mathbf{x}) = \int dt \ \langle I(\mathbf{x},t)\rangle = \frac{1}{8\pi^2\alpha} \int d\omega \, W^{(1)}_{\mu\mu}(\mathbf{x},\omega,\mathbf{x},\omega). \tag{A.132}$$

We may further normalize the latter by the average photon energy and find the local fluence:

$$F(\mathbf{x}) = \frac{H(\mathbf{x})}{\omega_{\text{avg}}} = \frac{1}{8\pi^2\alpha\,\omega_{\text{avg}}} \int d\omega \, W^{(1)}_{\mu\mu}(\mathbf{x},\omega,\mathbf{x},\omega). \tag{A.133}$$

Bear in mind that all of the above quantities are supposed to be evaluated on a plane perpendicular to the beam propagation-direction $\mathbf{k}_{\text{avg}}$.

A.11 Retrieve Parameters for GSM beams

In this appendix, we will address how to relate the beam parameters used in our Gaussian Schell-models (cf. Secs. 4.2.1 and 4.3.1) to observable quantities.

The overall magnitude G_0

The most straight forward option for obtaining G_0 is via an (experimental) specification of the peak intensity. In this case, we may directly employ Eq. (A.130) in combination with Eq. (4.10) to see that

$$\begin{aligned} I_{\text{peak}} &= \langle I(\mathbf{0},0)\rangle = \frac{1}{4\pi\alpha}\, G^{(1)}_{\mu\mu}(\mathbf{0},0,\mathbf{0},0) \\ &= \frac{1}{4\pi\alpha} G_0. \end{aligned} \tag{A.134}$$

This holds, provided that the peak intensity is specified for the unfiltered / unmodified field of course.

Instead of the peak intensity, however, a more commonly found quantifier, in particular, for x-ray pulses is their average pulse energy E_{pulse}. This relates to Eq. (A.130) via time- and cross-sectional integration:

$$E_{\text{pulse}} = \int d^2\mathbf{x}^\perp \int_{\text{pulse}} dt\, \langle I(\mathbf{x},t)\rangle = \int d^2\mathbf{x}^\perp \int_{\text{pulse}} dt\, \frac{1}{4\pi\alpha}\, G^{(1)}_{\mu\mu}((\mathbf{x}^\perp,z),t,(\mathbf{x}^\perp,z),t) \tag{A.135}$$

or for the cross spectral density

$$E_{\text{pulse}} = \int d^2\mathbf{x}^\perp\, \frac{1}{8\pi^2\alpha} \int d\omega\, W^{(1)}_{\mu\mu}((\mathbf{x}^\perp,z),\omega,(\mathbf{x}^\perp,z),\omega). \tag{A.136}$$

Choosing for convenience $z = z_0$, we can employ $W^{(1)}$ similar to Eq. (4.11). Additionally, we shall account for non-cylindrical beams and include a monochromator of the form

$$T_m(\omega) = e^{-(\omega-\omega_m)^2/4\Omega_m^2}. \tag{A.137}$$

Thus, we find

$$\begin{aligned} E_{\text{pulse}} &= \int d^2\mathbf{x}^\perp \frac{1}{8\pi^2\alpha} \int d\omega\, \left| e^{-(\omega-\omega_m)^2/4\Omega_m^2} \right|^2 \frac{G_0 2\pi T}{\Omega} (\boldsymbol{\varepsilon}\cdot\boldsymbol{\varepsilon})\, e^{-(\frac{x^x}{\sigma^x})^2/2-(\frac{x^y}{\sigma^y})^2/2} e^{-(\omega-\omega_0)^2/2\Omega^2} \\ &= \frac{G_0 T}{4\pi\alpha\Omega}\, 2\pi\, \sigma^x\sigma^y \sqrt{\frac{2\pi\Omega_m^2\Omega^2}{\Omega_m^2+\Omega^2}}\, e^{-(\omega_m-\omega_0)^2/2(\Omega_m^2+\Omega^2)} \\ &= \frac{G_0 T \sigma^x\sigma^y\Omega_m\sqrt{\pi}}{\alpha\sqrt{\Omega_m^2+\Omega^2}\sqrt{2}}\, e^{-(\omega_m-\omega_0)^2/2(\Omega_m^2+\Omega^2)}. \end{aligned} \tag{A.138}$$

By inversion, we have

$$G_0 = \sqrt{\frac{2}{\pi}} \frac{\sqrt{\Omega_m^2+\Omega^2}\alpha E_{\text{pulse}}}{T\sigma^x\sigma^y\Omega_m} e^{+(\omega_m-\omega_0)^2/2(\Omega_m^2+\Omega^2)} \tag{A.139}$$

or for the simpler case of irrelevant monochromator $\Omega_m \to \infty$

$$G_0 = \sqrt{\frac{2}{\pi}} \frac{\alpha E_{\text{pulse}}}{T\sigma^x\sigma^y} \tag{A.140}$$

Also, note that $E_{\text{pulse}} = N_{\text{photon}} \cdot \omega_0$.

The temporal extent T

In order to specify the temporal extent of our GSM pulses, we consider the average intensity profile in time. Starting again from Eq. (A.130) and using the form given in Eq. (4.10), we find

$$\langle I((0,z_0),t)\rangle = G_0\, e^{-(t-t_0)^2/2T^2}, \tag{A.141}$$

where we have chosen $\mathbf{x}^\perp = 0$ on-axis and $z = z_0$ for convenience (though this is not a necessary restriction). The maximum is obviously reached at $t - t_0 = 0$, while half of it is attained for $t - t_0 = \pm\sqrt{2\ln(2)}\, T$, such that we can identify the temporal full width at half maximum (FWHM) as

$$FWHM_t = 2\sqrt{2\ln(2)}\, T \Leftrightarrow T = \frac{FWHM_t}{2\sqrt{2\ln(2)}}. \tag{A.142}$$

The spectral width Ω

By a similar reasoning as above, we arrive at a quantifier for the bandwidth Ω. Considering the spectrally resolved radiant exposure (generalizing Eq. (A.132)) and taking the expression for $W^{(1)}_{\mu\mu}$ from Eq. (4.11), we find

$$H((0,z_0),\omega) = \frac{2\pi G_0 T}{\Omega}\, e^{-(\omega_m-\omega_0)^2/2\Omega^2}. \tag{A.143}$$

Here, we have again chosen $\mathbf{x}^\perp = 0$ on axis and $z = z_0$ for convenience. Fully analogous to Eq. (A.142), we obtain the spectral FWHM as

$$FWHM_\omega = 2\sqrt{2\ln(2)}\,\Omega \Leftrightarrow \Omega = \frac{FWHM_\omega}{2\sqrt{2\ln(2)}}. \tag{A.144}$$

Note, that for chirped optical pulses as discussed in Sec. 4.3.1, Ω will be replaced by $\tilde{\Omega} = \sqrt{\Omega^2 + 4T^2\gamma_0}$.

Coherence time τ_{coh} / chirp γ_0

With both T and Ω known, we can obtain the coherence time τ_{coh} (for partially coherent fields) or the chirp parameter γ_0 (for chirped coherent fields) according to the relations

$$\Omega = \sqrt{\frac{1}{4T^2} + \frac{1}{\tau_{coh}^2}} \Leftrightarrow \tau_{coh} = \left(\sqrt{\Omega^2 - \frac{1}{4T^2}}\right)^{-1} \tag{A.145}$$

$$\tilde{\Omega} = \sqrt{\Omega^2 + 4T^2\gamma_0^2} \quad \text{and} \quad \Omega^2 = \frac{1}{4T^2} \Leftrightarrow \gamma_0 = \frac{1}{4T}\sqrt{4T^2\tilde{\Omega}^2 - 1} \tag{A.146}$$

The δ-parameter / divergence

Regarding the transverse beam parameter the situation is more complicated, as measurements are less detailed and their results typically interdependent (cf. Ref. [217], for instance). A well accessible quantity—at any rate—is given by the far-field divergence angle Θ of the beam, which is related to

δ via

$$\Theta = \frac{\lambda_0}{\delta\, 2\pi}. \tag{A.147}$$

This agrees with Singer's convention on p. 25 of Ref. [131].

For spectrally coherent beams, this (and knowledge of z_0) gives a full characterization of their transverse properties[17] Note for divergences, which have been specified with respect to vacuum propagation, that these may roughly be related to their in medio value by $\theta_{vac} = n \cdot \theta_{med}$ (for quasi-monochromatic, low dispersion beams).

The beam width σ

The beam width parameter σ of GSM beams is harder to assess than the above, because it is only directly observable in the source (/focal) plane, i.e., at $z = z_0$. There, an argument analogous to Eq. A.142 allows to refer σ from the transverse intensity profile as

$$FWHM_{trans} = 2\sqrt{2\ln(2)}\sigma \Leftrightarrow \sigma = \frac{FWHM_{trans}}{2\sqrt{2\ln(2)}}. \tag{A.148}$$

Away from this focal plane, however, the measurable beam width $\Sigma(z)$ is scaled as $\Sigma(z) = \sigma\sqrt{1 + \frac{(z-z_0)^2}{z_{eff}^2}}$, where the determination of z_{eff} will, in turn, require knowledge of ξ.

Alternatively, we may also try and refer σ directly to δ via knowledge of ξ using

$$\frac{1}{\delta^2} = \frac{1}{4\sigma^2} + \frac{1}{\xi^2} \Leftrightarrow \left(\frac{1}{\delta^2} - \frac{1}{\xi^2} = \frac{1}{4\sigma^2}\right) \tag{A.149}$$

$$\sigma^2 = \frac{1}{4}\left(\frac{1}{\delta^2} - \frac{1}{\xi^2}\right)^{-1} \tag{A.150}$$

In particular, we want to highlight the case of largely coherent FEL radiation ($\xi \sim \sigma$). Hereunto, we shall adopt Singer's notation for a q-parameter [131] and write $\xi = q\,\sigma$, i.e.,

$$\frac{1}{\delta^2} = \frac{1}{4\sigma^2} + \frac{1}{q^2\sigma^2} \Rightarrow \sigma = \delta\sqrt{\frac{1}{4} + \frac{1}{q^2}}, \tag{A.151}$$

where $q \sim 1$ for largely coherent beams.

[17] Note that $\frac{1}{\delta^2} = \frac{1}{4\sigma^2} + \frac{1}{\xi^2} \Rightarrow \frac{1}{4\sigma^2}$ determines the beam width, if $\xi \to 0$ and $2\sigma = w_0$ can be identified with the usual Gaussian beam waist.

A.12 Fluctuation-Dissipation Theorem

The fluctuation-dissipation theorem (FDT)—as the name suggests—relates the fluctuations of observables in a system to its dissipative response [153–155]. Though it may occur in various, slightly different flavours, the general principle of the FDT is always the same. Namely, it provides an algebraic reformulation of some general (often: two-point) correlation function in terms of more easily accessible response functions.

Despite this rather plain appearance, it may be profoundly useful. In particular, there exists a wide range of circumstances, for which it is actually very hard to obtain (i.e., calculate or measure) the *correlation* of two observables in general. Yet, one may well be able to get a hold of the response behaviour of any one of them with respect to the other.

For classical systems, this is all there is to it already[18]. For quantum systems on the other hand, it may still be prohibitively complicated to obtain the 'simpler' response functions, especially when dealing with macroscopically large systems. Experimentally, there is often no chance to measure a microscopic response in a macroscopic sample, while from a theoretical point of view, such macroscopic systems are typically just too large to be treated at all.

This is, where an approximation can save the day: In linear response theory, a small change of a (macroscopic) observable with respect to its unperturbed behaviour, i.e.,

$$\begin{aligned}\delta\langle\hat{A}(t)\rangle &= \langle\hat{A}(t)\rangle - \langle\hat{A}_0(t)\rangle \\ &= \mathrm{Tr}\,\{\hat{\rho}\,\hat{A}(t)\} - \mathrm{Tr}\,\{\hat{\rho}\,\hat{A}_0(t)\}\end{aligned} \tag{A.152}$$

may be identified with the desired *microscopic* response term

$$\delta\langle\hat{A}(t)\rangle \approx -\mathrm{i}\int_{-\infty}^{t} dt'\, f(t')\,\langle\big[\hat{A}_0(t),\hat{B}_0(t')\big]\rangle. \tag{A.153}$$

Here, we take the latter response to be produced under the action of[19]

$$\hat{H}_{\mathrm{INT}}(t) = f(t)\,\hat{B}, \tag{A.154}$$

wherein $f(t)$ denotes a weak driving force, which may be of macroscopic nature itself, that couples to the system through the operator $\hat{B}$.

In this way, one can set out to:

1. measure the macroscopic response behaviour,
2. use it as an approximation for the microscopic response behaviour (Eq. (A.153)) and
3. thereby obtain information about delicate quantum fluctuations ultimately[20].

[18] We emphasize further that this is already pretty awesome in its own right. The FDT has found various applications throughout electronics, stability analysis, thermodynamics and more.

[19] Note that we make use of an interaction-picture approach at this point. As such, we separate an interaction Hamiltonian $\hat{H}_{\mathrm{INT}}(t)$ off a remaining $\hat{H}_0$. The latter is understood to govern the free time-evolution—as usual. The freely evolving operators, respectively, are marked by the subscript '0', whereas those undergoing the full time-evolution remain notationally blank. The difference of the two is evaluated perturbatively. For a broader discussion of the interaction picture as well as time-dependent perturbation theory, see App. A.1.

[20] We consider this to be quite a stroke of genius actually and admit that it took us a long time to appreciate its potential—even remotely.

Next we want to develop the FDT in more detail as well as better suited to our needs (cf. Chpt. 4 Sec. 4.4.2). To this end, we start from Eq. (A.153) and note that it contains the retarded Green's function

$$G^{\mathrm{ret}}_{A,B}(t,t') = -\mathrm{i}\,\theta(t-t')\,\langle\big[\hat{A}_0(t),\hat{B}_0(t')\big]\rangle. \tag{A.155}$$

For time-independent $\hat{H}_0$ (as in our case), this is invariant under time-translations and can likewise be written using a single argument only:

$$G^{\mathrm{ret}}_{A,B}(t-t') = -\mathrm{i}\,\theta(t-t')\,\langle\big[\hat{A}_0(t-t'),\hat{B}_0(0)\big]\rangle. \tag{A.156}$$

While the above is arguably one of the most basic response functions imaginable, it is not the one, we are interested in, if we care for fluctuations. In view of our XPDC problem, we are particularly interested in a correlator of the form

$$C_{A,B}(t) = \langle\hat{A}_0(t)\hat{B}_0(0)\rangle, \tag{A.157}$$

more specifically, we can identify it with the initially introduced correlator $\bar{S}_{\nu\mu}$ (cf. Eq. (2.55)):

$$\begin{aligned} C_{A',A}(t'-t) &= \bar{S}_{\nu\mu}(\mathbf{x}',t',\mathbf{x},t) \\ &= \mathrm{Tr}_{\mathrm{OPT}}\left\{\hat{\rho}^{\mathrm{equ}}_{\mathrm{OPT}}\,(\hat{\mathbf{A}}_{\mathrm{opt}}(\mathbf{x}',t'))_\nu\,(\hat{\mathbf{A}}_{\mathrm{opt}}(\mathbf{x},t))_\mu\right\}. \end{aligned} \tag{A.158}$$

Subsequently, our attention will focus mainly on the Fourier transform of this quantity, i.e.,

$$\tilde{C}_{A,B}(\omega) = \int dt\, e^{\mathrm{i}\,\omega t}\, C_{A,B}(t). \tag{A.159}$$

Our aim is to assemble this from $G^{\mathrm{ret}}_{A,B}$, for which a good starting formulation is given by the following combination of terms

$$\begin{aligned} &\mathrm{i}\Big(G^{\mathrm{ret}}_{A,B}(t) - G^{\mathrm{ret}}_{B,A}(-t)\Big) \\ &= \mathrm{i}\Big(-\mathrm{i}\,\theta(t)\,\langle\hat{A}_0(t)\hat{B}_0(0) - \hat{B}_0(0)\hat{A}_0(t)\rangle - (-\mathrm{i})\,\theta(-t)\,\langle\hat{B}_0(-t)\hat{A}_0(0) - \hat{A}_0(0)\hat{B}_0(-t)\rangle\Big) \\ &= \theta(t)\,\langle\hat{A}_0(t)\hat{B}_0(0)\rangle + \theta(-t)\,\langle\hat{A}_0(0)\hat{B}_0(-t)\rangle - \theta(t)\,\langle\hat{B}_0(0)\hat{A}_0(t)\rangle - \theta(-t)\,\langle\hat{B}_0(-t)\hat{A}_0(0)\rangle \\ &= \underbrace{\langle\hat{A}_0(t)\hat{B}_0(0)\rangle}_{C_{A,B}(t)} - \langle\hat{B}_0(0)\hat{A}_0(t)\rangle. \end{aligned} \tag{A.160}$$

Besides simple reordering, we have essentially made use of the time translation invariance—shifting $-t \to 0$ or $0 \to t$ in some correlators. Half of the above expression already agrees with our target of finding $C_{A,B}$. This leaves only the remainder $\langle\hat{B}_0(0)\hat{A}_0(t)\rangle$ to be dealt with.

To this end, we inspect its Fourier transform in more detail

$$\int dt\, e^{\mathrm{i}\,\omega t}\,\langle\hat{B}_0(0)\hat{A}_0(t)\rangle = \int dt\, e^{\mathrm{i}\,\omega t}\,\mathrm{Tr}\left\{\hat{\rho}\,\hat{B}\hat{U}_0(0,t)\,\hat{A}\,\hat{U}_0(t,0)\right\}. \tag{A.161}$$

In order to proceed beyond this point, we have to decide upon an *actual* density operator $\hat{\rho}$. Given, that we assume equilibrium conditions for the optical field (at least for those spectral regions without laser driving—cf. Sec. 2.2.2), a thermalised ensemble is a reasonable choice. Moreover, as we are dealing

with photons, we can quite safely assume a canonical distribution[21] $\hat{\rho} = Z^{-1} e^{-\beta \hat{H}_0}$, where the precise choice of ensemble would probably be irrelevant anyway, as we are interested in photon energies ω such that $\beta\omega \gg 1$ and thermal corrections will be negligible.

With this choice and the exponential solution for $\hat{U}_0(t,0) = \exp(-\mathrm{i}\hat{H}_0 t)$, we can rewrite Eq. (A.161) as

$$\int dt\, e^{\mathrm{i}\omega t} \langle \hat{B}_0(0)\hat{A}_0(t)\rangle = \int dt\, e^{\mathrm{i}\omega t} Z^{-1} \operatorname{Tr}\{e^{-\beta\hat{H}_0}\hat{B}\, e^{\mathrm{i}\hat{H}_0 t}\hat{A}\, e^{-\mathrm{i}\hat{H}_0 t}\}. \tag{A.162}$$

Formally introducing a basis of energy eigenstates, this becomes

$$\int dt\, e^{\mathrm{i}\omega t} \langle \hat{B}_0(0)\hat{A}_0(t)\rangle = \int dt\, e^{\mathrm{i}\omega t} Z^{-1} \sum_{m,n} \langle m| e^{-\beta E_m}\hat{B}\,|n\rangle \langle n| e^{\mathrm{i}E_n t}\hat{A}\, e^{-\mathrm{i}E_m t}\,|m\rangle \tag{A.163}$$

and can be reshuffled to read

$$\begin{aligned}
\int dt\, e^{\mathrm{i}\omega t} \langle \hat{B}_0(0)\hat{A}_0(t)\rangle &= \int dt\, e^{\mathrm{i}\omega t} Z^{-1} \sum_{m,n} e^{-\beta E_m} e^{\mathrm{i}E_n t} e^{-\mathrm{i}E_m t} B_{m,n} A_{n,m} \\
&= Z^{-1} \sum_{m,n} e^{-\beta E_m} 2\pi\,\delta((\omega + E_n) - E_m)) B_{m,n} A_{n,m} \\
&= Z^{-1} \sum_{m,n} e^{-\beta(\omega+E_n)} 2\pi\,\delta((\omega + E_n) - E_m)) A_{n,m} B_{m,n} \\
&= \int dt\, e^{\mathrm{i}\omega t}\, e^{-\beta\omega} Z^{-1} \sum_{m,n} \langle n| e^{-\beta E_n} e^{\mathrm{i}E_n t}\hat{A}\, e^{-\mathrm{i}E_m t}\,|m\rangle \langle m|\hat{B}\,|n\rangle .
\end{aligned} \tag{A.164}$$

Finally, we can retract the eigenstate expansion again, condensing the above to

$$\begin{aligned}
\int dt\, e^{\mathrm{i}\omega t} \langle \hat{B}_0(0)\hat{A}_0(t)\rangle &= \int dt\, e^{\mathrm{i}\omega t}\, e^{-\beta\omega} Z^{-1} \operatorname{Tr}\{e^{-\beta\hat{H}_0}\, e^{\mathrm{i}\hat{H}_0 t}\hat{A}\, e^{-\mathrm{i}\hat{H}_0 t}\hat{B}\} \\
&= \int dt\, e^{\mathrm{i}\omega t}\, e^{-\beta\omega} \operatorname{Tr}\{\hat{\rho}\,\hat{U}_0(0,t)\hat{A}\,\hat{U}_0(t,0)\hat{B}\} \\
&= e^{-\beta\omega} \int dt\, e^{\mathrm{i}\omega t} C_{A,B}(t) = e^{-\beta\omega}\tilde{C}_{A,B}(\omega).
\end{aligned} \tag{A.165}$$

Using this result in combination with Eq. (A.160), we find

$$\begin{aligned}
\mathrm{i}\int dt\, e^{\mathrm{i}\omega t}\Big(G^{\mathrm{ret}}_{A,B}(t) - G^{\mathrm{ret}}_{B,A}(-t)\Big) &= \tilde{C}_{A,B}(\omega) - e^{-\beta\omega}\tilde{C}_{A,B}(\omega) \\
&= (1 - e^{-\beta\omega})\,\tilde{C}_{A,B}(\omega)
\end{aligned} \tag{A.166}$$

or equivalently

$$\tilde{C}_{A,B}(\omega) = \mathrm{i}(1 - e^{-\beta\omega})^{-1} \int dt\, e^{\mathrm{i}\omega t}\Big(G^{\mathrm{ret}}_{A,B}(t) - G^{\mathrm{ret}}_{B,A}(-t)\Big). \tag{A.167}$$

While we can directly identify the first term on the right-hand side with the Fourier transform of $G^{\mathrm{ret}}_{A,B}(t)$, we spend some final effort to do the same with the second. The obvious option is

$$\int dt\, e^{\mathrm{i}\omega t} G^{\mathrm{ret}}_{B,A}(-t) = \int dt\, e^{-\mathrm{i}\omega t} G^{\mathrm{ret}}_{B,A}(t) = \tilde{G}^{\mathrm{ret}}_{B,A}(-\omega). \tag{A.168}$$

[21] We note in further explanation of our above reasoning: Photons are massless bosons, i.e., there is no 'chemical potential' required in a pertaining density operator. On the other hand, we might want to bear in mind that this situation could change for polaritons or optical band gaps. Then again, the whole approach via FDT should be reconsidered first under such conditions.

We note, however, that this result could prove slightly cumbersome in application, because it requires knowledge of $\tilde{G}_{B,A}$ at two apparently different frequencies ω and $-\omega$. Instead, we continue rewriting

$$\begin{aligned}
\tilde{G}^{\mathrm{ret}}_{B,A}(-\omega) &= \int dt\, e^{-\mathrm{i}\,\omega t} G^{\mathrm{ret}}_{B,A}(t) \\
&= \int dt\, e^{-\mathrm{i}\,\omega t}\,(-\mathrm{i})\,\theta(t)\,\langle\big[\hat{B}_0(t),\hat{A}_0(0)\big]\rangle \\
&= \int dt\, \Big(e^{\mathrm{i}\,\omega t}\Big)^*\,(\mathrm{i})^*\,\theta(t)\,\langle\big[\hat{A}_0(0),\hat{B}_0(t)\big]\rangle^* \\
&= \int dt\, \Big(e^{\mathrm{i}\,\omega t}\,(\mathrm{i})\,\theta(t)\,\langle\big[\hat{A}_0(0),\hat{B}_0(t)\big]\rangle\Big)^* \\
&= \Big(\int dt\, e^{\mathrm{i}\,\omega t}\,(-\mathrm{i})\,\theta(t)\,\langle\big[\hat{B}_0(t),\hat{A}_0(0)\big]\rangle\Big)^* \\
&= \Big(\int dt\, e^{\mathrm{i}\,\omega t}\, G^{\mathrm{ret}}_{B,A}(t)\Big)^* \\
&= \Big(\tilde{G}^{\mathrm{ret}}_{B,A}(\omega)\Big)^*. \qquad \text{(A.169)}
\end{aligned}$$

Here, we have employed the identity $\langle\big[\hat{B},\hat{A}\big]\rangle^* = \langle\big[\hat{A},\hat{B}\big]\rangle$ for self-adjoint operators $\hat{A}$ and $\hat{B}$, as well as usual commutator properties.

Using Eq. (A.169) in Eq. (A.166), we can finally write the fluctuation-dissipation theorem as

$$\tilde{C}_{A,B}(\omega) = \mathrm{i}\,(1-e^{-\beta\omega})^{-1}\Big(\tilde{G}^{\mathrm{ret}}_{A,B}(\omega) - (\tilde{G}^{\mathrm{ret}}_{B,A}(\omega))^*\Big). \qquad \text{(A.170)}$$

A.13 XPDC flux-model from thin systems' propagator

During our discussion of XPDC in Chpt. 5, we have introduced an effective, differential flux for the concise description of the incident x-ray field. This quantity

$$\Phi_{\sigma\rho}(\mathbf{k},\omega) = \frac{1}{(2\pi)^{11}}\frac{\alpha\omega}{2l_w}\int^{\times 2} d^3k_p d^3k'_p\, Z^{\text{X\_IN}}_{\sigma\rho}(\mathbf{k}'_p,\omega,\mathbf{k}_p,\omega)\,\tilde{w}(\mathbf{k}-\mathbf{k}_p)\left(\tilde{w}(\mathbf{k}-\mathbf{k}'_p)\right)^*, \tag{A.171}$$

presents a convolution of field-properties with the form-factor of the sample.

While we have already introduced a model for $\Phi_{\sigma\rho}$ in Eq. (5.78), we want to use this section to give a more physical derivation of it. Moreover, this will open a perspective for further evolution. Namely, we want to obtain the same expression by tracing the actual propagation of x-rays through the sample. To this end, we shall use the thin-systems' propagator from App. A.9.3 applied to the involved correlation function (following App. A.9.5). As this requires returning to real-space, we apply the convolution theorem Eq. (A.195) once again and obtain:

$$\Phi_{\sigma\rho}(\mathbf{k},\omega) = \frac{1}{(2\pi)^{5}}\frac{\alpha\omega}{2l_w}\int^{\times 2} d^3x_1 d^3x_2\, e^{\mathrm{i}\mathbf{k}\cdot\mathbf{x}_1} e^{-\mathrm{i}\mathbf{k}\cdot\mathbf{x}_2}\, V^{\text{X\_IN}}_{\sigma\rho}(\mathbf{x}_1,\omega,\mathbf{x}_2,\omega)\, w(\mathbf{x}_1)\, w(\mathbf{x}_2)\,. \tag{A.172}$$

We can render this expression more convenient still, if we reference the integrand $V^{\text{X\_IN}}_{\sigma\rho}$ to an overall input field from outside of the integration volume. To this end, we choose a reference plane (at z_{ref})

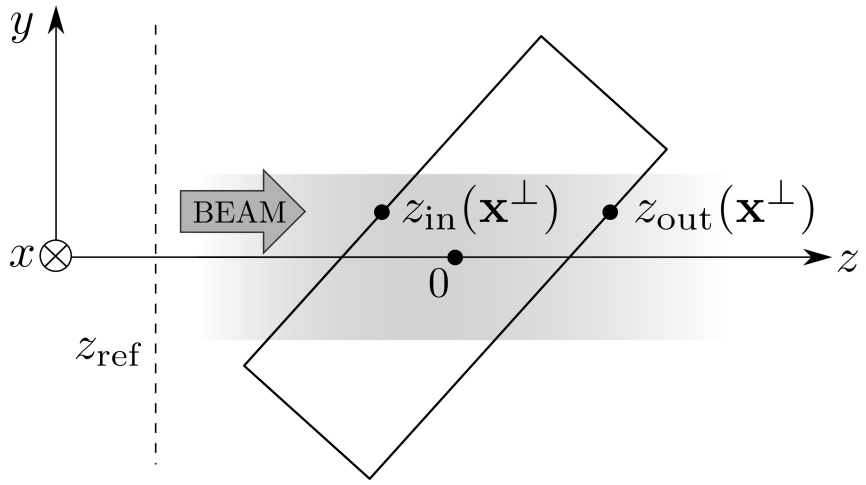

Figure A.3: Illustration of the slab geometry that underlies our reasoning in this section. An x-ray beam, which is fully characterized in a reference plane up-stream of the sample (at z_{ref}), illuminates a (possibly tilted) crystal centred at $\mathbf{x}^\perp = 0$, $z = 0$. The sample's lateral dimensions are assumed larger than the beam's diameter and for each entry-point $z_{\text{in}}(\mathbf{x}^\perp)$ of x-rays on the frontal face of the crystal, there is a corresponding exit-point $z_{\text{out}}(\mathbf{x}^\perp)$ on the same 'height' ($\mathbf{x}^\perp$) yet at the opposite face of the slab. [We gratefully acknowledge Dr. Christina Bömer's help in rendering the above computer graphics.]

outside the finite sized target crystal (cf. Fig. A.3). From this plane onwards, we can relate $V^{\text{X\_IN}}_{\sigma\rho}$ into the integration domain via the propagation relation (A.117), yielding:

$$\begin{aligned}\Phi_{\sigma\rho}(\mathbf{k},\omega) = \frac{1}{(2\pi)^{5}}\frac{\alpha\omega}{2l_w}\int^{\times 2} d^3x_1 d^3x_2\, e^{\mathrm{i}\mathbf{k}\cdot\mathbf{x}_1} e^{-\mathrm{i}\mathbf{k}\cdot\mathbf{x}_2}\, w(\mathbf{x}_1)\, w(\mathbf{x}_2)\int^{\times 2} d^2x'^\perp_1\, d^2x'^\perp_2\,\left[\left(P_{z_1,z_{\text{ref}}}(\mathbf{x}^\perp_1,\mathbf{x}'^\perp_1,\omega)\right)_{\sigma\mu}\right]^\dagger \\ \times\left(P_{z_2,z_{\text{ref}}}(\mathbf{x}^\perp_2,\mathbf{x}'^\perp_2,\omega)\right)_{\rho\nu} V^{\text{X\_IN}}_{\mu\nu}((\mathbf{x}'^\perp_1,z_{\text{ref}}),\omega,(\mathbf{x}'^\perp_2,z_{\text{ref}}),\omega).\end{aligned} \tag{A.173}$$

Given that the individual distances are rather short (∼crystal size), we can approximate the propagator

with the result from App. A.9.3 for thin systems:

$$\big(P_{z_i,z_{\rm ref}}(\mathbf{x}_i^\perp,\mathbf{x}_i'^\perp,\omega)\big)_{\mu\nu} \approx \delta_{\mu\nu}\;\delta^2(\mathbf{x}_i^\perp-\mathbf{x}_i'^\perp)\;e^{\mathrm{i}\,\alpha\,\omega\,(z_i-z_{\rm ref})}\;e^{-\mathrm{i}\,\alpha\,\omega\int_{z_{\rm ref}}^{z_i}dz\,(\delta(\mathbf{x}_i^\perp,z,\omega)-\mathrm{i}\beta(\mathbf{x}_i^\perp,z,\omega))}. \tag{A.174}$$

We assume further that our target may be well represented by a rectangular slab of constant 'optical' parameters[22] (see also sketch A.3). Thereby we can simplify the integration within the exponent of Eq. (A.174), which thus covers constant intervals only

$$\begin{aligned}\int_{z_{\rm ref}}^{z_i} dz\,(\delta(\mathbf{x}_i^\perp,z,\omega)-\mathrm{i}\beta(\mathbf{x}_i^\perp,z,\omega)) &= \int_{z_{\rm ref}}^{z_{\rm in}(\mathbf{x}_i^\perp)} dz\;0\;+\;\int_{z_{\rm in}(\mathbf{x}_i^\perp)}^{z_i} dz\,(\delta-\mathrm{i}\beta)\\ &= z_i\,(\delta-\mathrm{i}\beta)-z_{\rm in}(\mathbf{x}_i^\perp)\,(\delta-\mathrm{i}\beta).\end{aligned} \tag{A.175}$$

Next, we can re-insert this result together with Eq. (A.174) into Eq. (A.173). For improved readability, we shall focus on a single 'side' of the correlation function $V_{\sigma\rho}^{\text{X\_IN}}$, here (viz. the side with subscript 2):

$$\begin{aligned}&\int d^3x_2\,e^{-\mathrm{i}\,\mathbf{k}\cdot\mathbf{x}_2}\;w(\mathbf{x}_2)\int d^2x_2'^\perp\;\big(P_{z_2,z_{\rm ref}}(\mathbf{x}_2^\perp,\mathbf{x}_2'^\perp,\omega)\big)_{\rho\nu}\;V_{\mu\nu}^{\text{X\_IN}}(\ldots,(\mathbf{x}_2'^\perp,z_{\rm ref}),\omega)\\ \approx&\int d^3x_2\,e^{-\mathrm{i}\,\mathbf{k}\cdot\mathbf{x}_2}\;w(\mathbf{x}_2)\;e^{\mathrm{i}\,\alpha\,\omega\,(z_2-z_{\rm ref})}\;e^{-\mathrm{i}\,\alpha\,\omega\,[z_2\,(\delta-\mathrm{i}\beta)-z_{\rm in}(\mathbf{x}_2^\perp)\,(\delta-\mathrm{i}\beta)]}\;V_{\mu\rho}^{\text{X\_IN}}(\ldots,(\mathbf{x}_2^\perp,z_{\rm ref}),\omega)\\ =&\int_w d^2x_2^\perp\,e^{-\mathrm{i}\,\mathbf{k}^\perp\cdot\mathbf{x}_2^\perp}\;V_{\mu\rho}^{\text{X\_IN}}(\ldots,(\mathbf{x}_2^\perp,z_{\rm ref}),\omega)\Big(\int_{z_{\rm in}(\mathbf{x}_2^\perp)}^{z_{\rm out}(\mathbf{x}_2^\perp)}dz_2\,e^{\mathrm{i}\,z_2\,(-k^{\shortparallel}+\alpha\,\omega\,(1-\delta+\mathrm{i}\beta))}\Big)e^{-\mathrm{i}\,\alpha\,\omega\,z_{\rm ref}}\;e^{\mathrm{i}\,\alpha\,\omega\,z_{\rm in}(\mathbf{x}_2^\perp)\,(\delta-\mathrm{i}\beta)}\\ =&\int_w d^2x_2^\perp\,e^{-\mathrm{i}\,\mathbf{k}^\perp\cdot\mathbf{x}_2^\perp}\;V_{\mu\rho}^{\text{X\_IN}}(\ldots,(\mathbf{x}_2^\perp,z_{\rm ref}),\omega)\Big(\int_0^{l_w}dz_2\,e^{\mathrm{i}\,z_2\,(-k^{\shortparallel}+\alpha\,\omega\,(1-\delta+\mathrm{i}\beta))}\Big)e^{-\mathrm{i}\,\alpha\,\omega\,z_{\rm ref}}\;e^{\mathrm{i}\,z_{\rm in}(\mathbf{x}_2^\perp)\,(-k^{\shortparallel}+\alpha\,\omega)}.\end{aligned} \tag{A.176}$$

In the last line, we made use of the fact that the effective thickness of a (tilted) rectangular slab $z_{\rm out}(\mathbf{x}_2^\perp)-z_{\rm in}(\mathbf{x}_2^\perp)=l_w$ is the same for all[23] points of its cross section $\mathbf{x}_2^\perp$.

With the other side of the integration treated analogously—except for complex conjugation—we arrive at the overall expression

$$\begin{aligned}\Phi_{\sigma\rho}(\mathbf{k},\omega) = \frac{1}{(2\pi)^5}\,\frac{\alpha\omega}{2\,l_w}\,&\left|\int_0^{l_w}dz\,e^{\mathrm{i}\,z\,(-k^{\shortparallel}+\alpha\,\omega\,(1-\delta+\mathrm{i}\beta))}\right|^2\;\int_w^{\times 2}d^2x_1^\perp\,d^2x_2^\perp\;e^{\mathrm{i}\,\mathbf{k}^\perp\cdot(\mathbf{x}_1^\perp-\mathbf{x}_2^\perp)}\\ &\times V_{\sigma\rho}^{\text{X\_IN}}((\mathbf{x}_1^\perp,z_{\rm ref}),\omega,(\mathbf{x}_2^\perp,z_{\rm ref}),\omega)\;e^{\mathrm{i}\,(z_{\rm in}(\mathbf{x}_2^\perp)-z_{\rm in}(\mathbf{x}_1^\perp))\,(-k^{\shortparallel}+\alpha\,\omega)}.\end{aligned} \tag{A.177}$$

This provides a nice starting point for rather general investigations.

For the time being, however, we shall focus only on a particularly simple realization thereof. We take the crystal to be non-absorbing ($\beta=0$), oriented perpendicular to the z-axis[24] and—in its transverse

[22] Note that the constancy of δ and β is in itself a simplification, as it implies homogeneity of the sample on the scale of the probing wavelength. For x-rays this is obviously untrue and will fail spectacularly, if the crystal is tuned onto Bragg-conditions, for instance. Aside from these occurrences, it works reasonably well though and is certainly better than assuming the sample to behave like vacuum.

[23] Strictly, the effective thickness of the crystal will obviously change towards its edges (cf. Fig. A.3). However, we shall neglect this minor issue or—even more likely—assume that the beam does not reach there anyways.

[24] Note that the precise orientation is not really an issue for most of the cases that we study. It mostly affects the phasefactor, which as quite irrelevant to begin with. This can be seen from the same estimates as in Eq. (4.26).

dimensions—much larger than the relevant beam area. The above then simplifies into

$$\Phi_{\sigma\rho}(\mathbf{k},\omega) = \frac{1}{(2\pi)^5}\frac{\alpha\omega}{2\,l_w}\left|\int_0^{l_w} dz\, e^{\mathrm{i}z(-k^{\shortparallel}+\alpha\,\omega\,(1-\delta))}\right|^2 \int^{\times 2} d^2x_1^{\perp}\, d^2x_2^{\perp}\; e^{\mathrm{i}\,\mathbf{k}^{\perp}\cdot(\mathbf{x}_1^{\perp}-\mathbf{x}_2^{\perp})} \times V_{\sigma\rho}^{\text{X\_IN}}((\mathbf{x}_1^{\perp},z_{\text{ref}}),\omega,(\mathbf{x}_2^{\perp},z_{\text{ref}}),\omega), \tag{A.178}$$

wherein we can identify the integral by the sinc function and an irrelevant phase (cf. App. A.15)

$$\Phi_{\sigma\rho}(\mathbf{k},\omega) = \frac{1}{(2\pi)^5}\frac{\alpha\omega}{2\,l_w}\left|l_w\,\mathrm{sinc}((-k^{\shortparallel}+\alpha\,\omega\,(1-\delta))\,l_w/2)\right|^2 \int^{\times 2} d^2x_1^{\perp}\, d^2x_2^{\perp}\; e^{\mathrm{i}\,\mathbf{k}^{\perp}\cdot(\mathbf{x}_1^{\perp}-\mathbf{x}_2^{\perp})} \times V_{\sigma\rho}^{\text{X\_IN}}((\mathbf{x}_1^{\perp},z_{\text{ref}}),\omega,(\mathbf{x}_2^{\perp},z_{\text{ref}}),\omega). \tag{A.179}$$

Finally, we can rewrite $V_{\sigma\rho}^{\text{X\_IN}}$ through the inverse Fourier transform of $Z_{\sigma\rho}^{\text{X\_IN}}$ and find:

$$\Phi_{\sigma\rho}(\mathbf{k},\omega) = \frac{1}{(2\pi)^7}\frac{\alpha\omega}{2}\,l_w\,\mathrm{sinc}^2((-k^{\shortparallel}+\alpha\,\omega\,(1-\delta))\,l_w/2) \times \int^{\times 2} dk_1^{\shortparallel}\,dk_2^{\shortparallel}\; e^{-\mathrm{i}\,z_{\text{ref}}(k_1^{\shortparallel}-k_2^{\shortparallel})}\, Z_{\sigma\rho}^{\text{X\_IN}}((\mathbf{k}^{\perp},k_1^{\shortparallel}),\omega,(\mathbf{k}^{\perp},k_2^{\shortparallel}),\omega). \tag{A.180}$$

Note that in $Z_{\sigma\rho}^{\text{X\_IN}}$, almost all arguments are diagonal, except for $k_1^{\shortparallel}$ and $k_2^{\shortparallel}$, which are seemingly different still. Implicitly, however, these will also be fixed to the *same* value. More specifically, there will be a dispersion relation for any realistic field that $Z_{\sigma\rho}^{\text{X\_IN}}$ could describe, connecting $k_1^{\shortparallel}$ and $k_2^{\shortparallel}$ to $\mathbf{k}^{\perp}$ and ω. Thereby, the former will always be identical and we only require the diagonal component ot $Z_{\sigma\rho}^{\text{X\_IN}}$.

This observation is in line with our earlier model of the effective, differential flux. It entails that—from the overall information content of the field correlator $Z_{\sigma\rho}^{\text{X\_IN}}$—we only need to know about the distribution of the total photon number across the spectrum $\to \omega$ and its wave-vector spread $\to \mathbf{k}$. In some sense, this gives the total intensity (not field) decomposed into all plane-wave components of the pulse.

Note furthermore that the sinc-function above encodes the dispersion relation of the x-rays inside the medium. We can render this into the more familiar shape of a dispersion-delta, by taking the limit

$$\frac{a}{\pi}\,\mathrm{sinc}^2(ax) \;\xrightarrow[a\to\infty]{}\; \delta(x) \tag{A.181}$$

which corresponds to:

$$\frac{l_w}{2\pi}\,\mathrm{sinc}^2((-k^{\shortparallel}+\alpha\,\omega\,(1-\delta))\,l_w/2) \xrightarrow[l_w\to\infty]{} \delta(-k^{\shortparallel}+\alpha\,\omega\,(1-\delta)) \approx c\,\delta(\omega\,\underbrace{(1-\delta)}_{n_{\text{x-rays}}} - c\,|\mathbf{k}|). \tag{A.182}$$

In the last step, we imply that the x-ray beam ins well-collimated, such that $k^{\shortparallel} \approx |\mathbf{k}|$.

Using Eq. (A.180) or similar, propagation based expressions provides a good starting point to explore the influence of refracting or absorbing matter onto the subsequent nonlinear processes.

Consistency check Concluding this section, we briefly want to come full circle and verify that the above reproduces our initial flux model Eq. (5.78) on the basis of GSM beams. To this end, we recall

Eq. (4.41)

$$Z^{(1)}_{\mu\nu}(\mathbf{k}_1,\omega_1,\mathbf{k}_2,\omega_2) = \frac{(2\pi)^5\, G_0\, T\, \sigma^x\, \sigma^y\, \delta^x\, \delta^y}{\alpha^2\, \omega_1\, \omega_2\, \Omega}\; (\boldsymbol{\varepsilon}_X)_\mu\, (\boldsymbol{\varepsilon}_X)_\nu\, W(\omega_1,\omega_2)\; (T_m(\omega_1))^*\; T_m(\omega_2)\; \delta(k^{\shortparallel}_1 - k^{\shortparallel}_{1\_0}) \\ \times\, \delta(k^{\shortparallel}_2 - k^{\shortparallel}_{2\_0})\; e^{-(\Delta k^x)^2(\sigma^x)^2/2}\; e^{-(\bar{k}^x)^2(\delta^x)^2/2} e^{-(\Delta k^y)^2(\sigma^y)^2/2}\; e^{-(\bar{k}^y)^2(\delta^y)^2/2}\; e^{\mathrm{i}\,\frac{z_0}{\alpha\,\omega}\bar{\mathbf{k}}^\perp\cdot\Delta\mathbf{k}^\perp} \tag{A.183}$$

and insert it into Eq. (A.180). As we require only diagonal components of $Z^{\mathrm{X\_IN}}_{\sigma\rho}$, all expressions involving Δ's vanish immediately. Likewise, we can ignore any seeming differences in $k^{\shortparallel}_1 - k^{\shortparallel}_2$:

$$\Phi_{\sigma\rho}(\mathbf{k},\omega) = \frac{1}{(2\pi)^7}\,\frac{\alpha\,\omega}{2}\; l_w\; \mathrm{sinc}^2((-k^{\shortparallel} + \alpha\,\omega\,(1-\delta))\, l_w/2) \\ \times \frac{(2\pi)^5\, G_0\, T\, \sigma^x\, \sigma^y\, \delta^x\, \delta^y}{\alpha^2\, \omega^2\, \Omega} (\boldsymbol{\varepsilon}_p)_\sigma\, (\boldsymbol{\varepsilon}_p)_\rho\; W(\omega,\omega)\; |T_m(\omega_1)|^2\; e^{-(k^x)^2(\delta^x)^2/2} e^{-(k^y)^2(\delta^y)^2/2} \\ \times \int^{\times 2} dk^{\shortparallel}_1\, dk^{\shortparallel}_2\;\; \delta(k^{\shortparallel}_1 - k^{\shortparallel}_{1\_0})\delta(k^{\shortparallel}_2 - k^{\shortparallel}_{2\_0})\;. \tag{A.184}$$

Now, the last two integrals contribute merely unity. For further simplification, we ignore the transmission function of a hypothetical monochromator and simply focus on the spectral properties intrinsic to the pulse (cf. Eq. (4.20)):

$$W(\omega,\omega) = e^{-(\omega-\omega_0)^2/2\Omega^2}. \tag{A.185}$$

Furthermore, we shall render the prefactor more compact by using the average pulse energy

$$\bar{E}_{\mathrm{pulse}} = \frac{G_0\, T \sigma^x\, \sigma^y}{\alpha}\sqrt{\frac{\pi}{2}} \tag{A.186}$$

as found in App. A.11. As a result, Eq. (A.184) reduces to

$$\Phi_{\sigma\rho}(\mathbf{k},\omega) = \frac{1}{(2\pi)^{3/2}}\,\frac{\bar{E}_{\mathrm{pulse}}\,\delta^x\,\delta^y}{\omega\,\Omega}\;\frac{l_w}{2\pi}\;\mathrm{sinc}^2((-k^{\shortparallel} + \alpha\,\omega\,(1-\delta))\, l_w/2) \\ \times\, (\boldsymbol{\varepsilon}_p)_\sigma\, (\boldsymbol{\varepsilon}_p)_\rho\; e^{-(\omega-\omega_0)^2/2\Omega^2}\; e^{-(k^x)^2(\delta^x)^2/2} e^{-(k^y)^2(\delta^y)^2/2}. \tag{A.187}$$

Finally, we can employ the dispersion-delta of Eq. (A.182) and invoke the notion that $\bar{E}_{\mathrm{pulse}}/\omega = N_{\mathrm{ph}}$. Thus, we would arrive at a result, which compares identically to the model expression (5.78) used earlier.

A.14 Convolutions and the convolution theorem

At several stages throughout this thesis, we made use of convolutions or, more specifically, the convolution theorem. In this Appendix, we want to provide some background on said concept, which is intimately related to Fourier transformations.

For convolutions, we employ the usual definition:

$$(f\star g)(t) = \int_{-\infty}^{\infty} d\tau\; f(\tau)g(t-\tau) = \int_{-\infty}^{\infty} d\tau\; f(t-\tau)g(\tau) = (g\star f)(t). \tag{A.188}$$

Some general properties of the convolution are:

$$(f\star(g\star h)) = ((f\star g)\star h) \qquad \text{(associativity)} \tag{A.189}$$

$$(f\star(g+h)) = (f\star g)+(f\star h) \qquad \text{(distributivity)} \tag{A.190}$$

$$(f\star g)^* = (f^*\star g^*) \qquad \text{(conjugation)} \tag{A.191}$$

$$\frac{d}{dt}\,(f\star g)(t) = \left(f'\star g\right) = \left(f\star g'\right) \qquad \text{(differentiation)} \tag{A.192}$$

$$(f\star\delta) = f \qquad \text{(convolution with Dirac delta).} \tag{A.193}$$

All of these may simply be derived from the definition in Eq. (A.188).

Next, we shall address the convolution theorem in itself. This relates the Fourier transformations (FT) of a convolution to the simple product of the underlying Fourier transforms:

$$FT\,(f\star g) = FT\,(f)\cdot FT\,(g) \qquad FT^{-1}\,(f\star g) = 2\pi\; FT^{-1}\,(f)\cdot FT^{-1}\,(g) \tag{A.194}$$

$$2\pi\; FT\,(f\cdot g) = (FT\,(f)\star FT\,(g)) \qquad FT^{-1}\,(f\cdot g) = \left(FT^{-1}\,(f)\star FT^{-1}\,(g)\right). \tag{A.195}$$

These relations may again be proven by simply reformulating the respective definitions. For the exemplary case of Eq. (A.194)—first part—we have:

$$FT\,(f\star g) = \int_{-\infty}^{\infty} dt\; e^{\mathrm{i}\,\omega t} \int_{-\infty}^{\infty} d\tau\; f(\tau)g(t-\tau). \tag{A.196}$$

By shifting the integration from $t \to \theta = t-\tau$, we obtain directly:

$$FT\,(f\star g) = \int_{-\infty}^{\infty} d\theta\; e^{\mathrm{i}\,\omega\theta} g(\theta) \int_{-\infty}^{\infty} d\tau\; e^{\mathrm{i}\,\omega\tau} f(\tau) = FT(f)\cdot FT(g) \tag{A.197}$$

Proofs of the other identities proceed in the same fashion.

A.15 Useful integrals

In this section of the Appendix, we have collected a series of integrals and their solutions. While this content can certainly be found in the pertinent literature (cf., Ref. [9], for example), we wanted to have these results easily at hand for quick reference as well as possible reuse.

The integrals are listed in no particular order:

Gaussian exponential

$$\int_{-\infty}^{\infty} dx\, e^{\mathrm{i}ax}\, e^{-bx^2} = \sqrt{\frac{\pi}{b}}\, e^{-a^2/4b} \tag{A.198}$$

Product of Gaussian exponentials

$$\int_{-\infty}^{\infty} d\omega\, e^{-a(\omega-\Omega_a)^2}\, e^{-b(\omega-\Omega_b)^2} = \sqrt{\frac{\pi}{a+b}}\, e^{-ab(\Omega_a-\Omega_b)^2/(a+b)} \tag{A.199}$$

Proof If we want to integrate the product of two Gaussian-type exponentials, we can—of course—explicitly manipulate the exponents, such as to find a new, single quadratic form. However, we can likewise make use of the convolution theorem from App. A.14 in the following way. Starting from the l.h.s. of Eq. (A.199), we shift the integration variable such that $\omega \to \omega' = \omega - \Omega_a$ and obtain

$$\ldots = \int_{-\infty}^{\infty} d\omega'\, e^{-a(\omega')^2}\, e^{-b((\Omega_b-\Omega_a)-\omega')^2}. \tag{A.200}$$

This can be seen as the convolution of the two functions

$$f_a(\omega) = e^{-a\omega^2} \text{ and} \qquad\qquad f_b(\omega) = e^{-b\omega^2}, \tag{A.201}$$

where the outwardly apparent variable will be $X = \Omega_b - \Omega_a$

$$\ldots = \int_{-\infty}^{\infty} d\omega'\, f_a(\omega')\, f_b((\Omega_b-\Omega_a)-\omega') = (f_a \star f_b)(X). \tag{A.202}$$

Next, we use the trivial identity

$$(f_a \star f_b)(X) = FT\left(FT^{-1}\left(f_a \star f_b\right)\right), \tag{A.203}$$

in order to prepare the usage of the actual convolution theorem (cf., Eq. (A.194))

$$FT^{-1}\left(f_a \star f_b\right) = 2\pi\, FT^{-1}\left(f_a\right) \cdot FT^{-1}\left(f_b\right). \tag{A.204}$$

This renders

$$(f_a \star f_b)(X) = \int_{-\infty}^{\infty} dt e^{\mathrm{i}Xt}\, 2\pi \left(\int_{-\infty}^{\infty} \frac{d\omega}{2\pi} e^{-\mathrm{i}\,\omega t}\, e^{-a\omega^2} \cdot \int_{-\infty}^{\infty} \frac{d\omega'}{2\pi} e^{-\mathrm{i}\,\omega' t}\, e^{-b\omega'^2} \right), \tag{A.205}$$

which in turn can be simplified by using the result from Eq. (A.198) to yield

$$(f_a \star f_b)(X) = \int_{-\infty}^{\infty} dt e^{\mathrm{i}Xt}\, 2\pi\, \frac{1}{2\pi}\sqrt{\frac{\pi}{a}}\, e^{-t^2/4a} \cdot \frac{1}{2\pi}\sqrt{\frac{\pi}{b}}\, e^{-t^2/4b} = \frac{1}{2\sqrt{ab}} \int_{-\infty}^{\infty} dt\; e^{\mathrm{i}Xt}\, e^{-ct^2}. \tag{A.206}$$

Herein, $c = \frac{1}{4a} + \frac{1}{4b} = \frac{a+b}{4ab}$. Applying Eq. (A.198) again, gives the final result as of Eq. (A.199) (see above).

As a closing remark, note that there is a good-looking short report by P. A. Bromiley, which may be consulted on more general Gaussian products [218].

Product of three Gaussians

$$\int_{-\infty}^{\infty} d\omega\; e^{-a(\omega-\Omega_a)^2}\; e^{-b(\omega-\Omega_b)^2}\; e^{-c(\omega-\Omega_c)^2} = \sqrt{\frac{\pi}{a+b+c}}\, e^{-[(a+b+c)(a\Omega_a^2+b\Omega_b^2+c\Omega_c^2)-(a\Omega_a+b\Omega_b+c\Omega_c)^2]/(a+b+c)} \tag{A.207}$$

Proof via multiplication of three Gaussians, for instance.

Complex Gaussian exponential / Fresnel integrals

$$\int_{-\infty}^{\infty} dx\; e^{\mathrm{i}ax^2} = \sqrt{\frac{\pi}{|a|}}\, e^{\mathrm{sign}(a)\,\mathrm{i}\,\pi/4} \tag{A.208}$$

In the context of em-propagators, but also in the context of more general oscillatory integrals, which we might want to approximate via the stationary phase approximation, we encounter the above integral. Assuming $a > 0$ and using Euler's identity, it can be unfolded into

$$\int_{-\infty}^{\infty} dx\; e^{\mathrm{i}ax^2} = \int_{-\infty}^{\infty} dx\, \cos(ax^2) + \mathrm{i}\int_{-\infty}^{\infty} dx'\, \sin(ax'^2), \tag{A.209}$$

which, in turn, can be related to the well-known Fresnel integrals—each at the value of $\frac{1}{2}\sqrt{2\pi}$:

$$\begin{aligned} ... &= \frac{1}{\sqrt{a}}\Big(\int_{-\infty}^{\infty} ds\, \cos(s^2) + \mathrm{i}\int_{-\infty}^{\infty} ds'\, \sin(s'^2)\Big) \\ &= \frac{1}{\sqrt{a}}\Big(\frac{1}{2}\sqrt{2\pi} + \mathrm{i}\frac{1}{2}\sqrt{2\pi}\Big) \\ &= \sqrt{\frac{\pi}{2a}}\,(1+\mathrm{i}). \end{aligned} \tag{A.210}$$

For $a < 0$, we use the replacement $b = -a$ and the same reasoning as above to find:

$$... = \sqrt{\frac{\pi}{2b}}\,(1-\mathrm{i}). \tag{A.211}$$

The unified expression for both is then given by Eq. (A.208).

Sine cardinalis

$$\int dk\, \mathrm{sinc}(ak) = \frac{\pi}{a} \tag{A.212}$$

In order to see this, we first go the other way around: We note that we can obtain the sinc function as the Fourier transform of a box window with the following properties

$$w(x) = \begin{cases} 1 & \text{for } |x| \leq l/2 \\ 0 & \text{otherwise} \end{cases}. \tag{A.213}$$

Fourier transforming this window, we find

$$\begin{aligned} \tilde{w}(k) &= \int dx\, e^{-\mathrm{i}kx}\, w(x) = \int_{l/2}^{l/2} dx\, e^{-\mathrm{i}kx} = \frac{1}{-\mathrm{i}k}\left(e^{-\mathrm{i}kl/2} - e^{\mathrm{i}kl/2}\right) \\ &= \frac{2}{k}\,\sin(kl/2) = l\,\mathrm{sinc}(kl/2), \end{aligned} \tag{A.214}$$

which is the sinc function.

The inverse relation is, instead, given by

$$w(x) = \frac{1}{2\pi}\int dk\, e^{\mathrm{i}kx}\,\tilde{w}(k) = \frac{1}{2\pi}\int dk\, e^{\mathrm{i}kx}\, l\,\mathrm{sinc}(kl/2). \tag{A.215}$$

For $x = 0$ and $a = l/2$, the integral reproduces the l.h.s. of Eq. (A.212) and we find:

$$1 = w(x=0) = \frac{2a}{2\pi}\int dk\,\mathrm{sinc}(ak) \Rightarrow \int dk\,\mathrm{sinc}(ak) = \frac{\pi}{a}. \tag{A.216}$$

Approximation of the box window Regarding the use of the box-type window function as a shape-function for our crystallographic discussions, we want to comment on a particularly simple, if drastic, approximation. Namely, we can identify the central peak of the sinc-function with a Gaussian, i.e.,

$$\mathrm{sinc}(k\,l_w/2) \approx e^{-(k\,\sigma_w)^2/2} \tag{A.217}$$

with the adjustment: $\sigma_w = l_w/\sqrt{2\pi}$, to make their integrals equal. Apart from reproducing the central peak, we call for caution on this approximation, because the tails of either function are significantly different.

A second identification of this kind could be done at the level of their squares (i.e., for use in transition rates rather than amplitudes):

$$(\mathrm{sinc}(k\,l_w/2))^2 \approx e^{-(k\,\sigma_w)^2/2}. \tag{A.218}$$

Given that the integrals of sinc and sinc squared are equal, we arrive at the same adjustment for $\sigma_w = l_w/\sqrt{2\pi}$.

A.16 Derivation notes for XOWM with simplified time-dependence

Having established the overall functionality of our approach, we now want to pursue a slightly different road towards the same or similar result—hopefully. This makes use of a simplification discussed earlier, viz. around Eq. (5.58). In particular, we observe that we repeatedly have employed the approximation

$$\mathbf{K}_I(\mathbf{k}_1,\mathbf{k}_2,\omega) \approx \tilde{w}(\mathbf{k}_1+\mathbf{k}_2-\mathbf{G})\,\frac{1}{V_\diamond}\,\mathbf{K}_{I\diamond}(0,\mathbf{G},\omega) \approx \tilde{w}(\mathbf{k}_1+\mathbf{k}_2-\mathbf{G})\,\frac{1}{V_\diamond}\,\mathbf{K}_{I\diamond}(0,\mathbf{G},\omega_{L\_0}), \tag{A.219}$$

where the last simplification results from the fact that $\mathbf{K}(...)$—far off resonances—varies slowly with frequency. Consequently, it gives roughly the same response for all frequencies contained in the driving laser's pulse. This, in turn allows to simplify the Fourier-inverse (Eq. (3.2)):

$$\begin{aligned}
\mathbf{P}_I(\mathbf{x}_1,0,\mathbf{x}_2,\tau) &= \frac{1}{(2\pi)^7}\int d^3k_1 \int d^3k_2 \int d\omega\; e^{\mathrm{i}(\mathbf{k}_1\cdot\mathbf{x}_1+\mathbf{k}_2\cdot\mathbf{x}_2)}\; e^{-\mathrm{i}\,\omega\tau}\;\mathbf{K}_I(\mathbf{k}_1,\mathbf{k}_2,\omega) \\
&\approx \frac{1}{(2\pi)^7}\int d^3k_1 \int d^3k_2 \int d\omega\; e^{\mathrm{i}(\mathbf{k}_1\cdot\mathbf{x}_1+\mathbf{k}_2\cdot\mathbf{x}_2)}\; e^{-\mathrm{i}\,\omega\tau}\;\tilde{w}(\mathbf{k}_1+\mathbf{k}_2-\mathbf{G})\,\frac{1}{V_\diamond}\,\mathbf{K}_{I\diamond}(0,\mathbf{G},\omega_{L_0}) \\
&= \frac{1}{V_\diamond}\,\mathbf{K}_{I\diamond}(0,\mathbf{G},\omega_{L_0})\;\delta(\tau)\,\delta^3(\mathbf{x}_1-\mathbf{x}_2)e^{\mathrm{i}\mathbf{G}\cdot\mathbf{x}_1}\;w(\mathbf{x}_1).
\end{aligned} \tag{A.220}$$

This can now be used directly inside the real space expression of our observable (Eq. (2.57))

$$\begin{aligned}
\langle\hat{O}\rangle = \frac{2\pi\alpha^4}{V\omega_f}\int dt_1\,dt_1'\,dt_2\,dt_2' \int d^3x\,d^3x'\,d^3y\,d^3y'\,e^{-\mathrm{i}\,\mathbf{k}_f\cdot(\mathbf{x}-\mathbf{x}')}\,e^{\mathrm{i}\,\omega_f(t_1-t_1')} \\
\cdot(\boldsymbol{\varepsilon}_f)_\sigma\,H^{(1)}_{\sigma\rho}(\mathbf{x}',t_1',\mathbf{x},t_1)\,(\boldsymbol{\varepsilon}_f^*)_\rho\left(\bar{H}^{(1)}_{\nu\mu}(\mathbf{y}',t_2',\mathbf{y},t_2)+\bar{S}^{(1)}_{\nu\mu}(\mathbf{y}',t_2',\mathbf{y},t_2)\right) \\
\cdot\sum_I p_I\left(\mathbf{P}_I(\mathbf{y},t_2,\mathbf{x},t_1)\right)_\mu\left(\mathbf{P}_I(\mathbf{y}',t_2',\mathbf{x}',t_1')\right)^*_\nu.
\end{aligned} \tag{A.221}$$

Again, we assume only the ground state $I = GS$ to be relevant for our consideration and find

$$\begin{aligned}
\langle\hat{O}\rangle = \frac{2\pi\alpha^4}{V\omega_f}\int dt_1\,dt_1'\,dt_2\,dt_2' \int d^3x\,d^3x'\,d^3y\,d^3y'\,e^{-\mathrm{i}\,\mathbf{k}_f\cdot(\mathbf{x}-\mathbf{x}')}\,e^{\mathrm{i}\,\omega_f(t_1-t_1')} \\
\times(\boldsymbol{\varepsilon}_f)_\sigma\,H^{(1)}_{\sigma\rho}(\mathbf{x}',t_1',\mathbf{x},t_1)\,(\boldsymbol{\varepsilon}_f^*)_\rho\left(\bar{H}^{(1)}_{\nu\mu}(\mathbf{y}',t_2',\mathbf{y},t_2)+\bar{S}^{(1)}_{\nu\mu}(\mathbf{y}',t_2',\mathbf{y},t_2)\right) \\
\times\frac{1}{V_\diamond}\left(\mathbf{K}_{I\diamond}(0,\mathbf{G},\omega_{L_0})\right)_\mu\,\delta(t_1-t_2)\,\delta^3(\mathbf{y}-\mathbf{x})e^{\mathrm{i}\,\mathbf{G}\cdot\mathbf{x}}\,w(\mathbf{x}) \\
\times\frac{1}{V_\diamond}\left(\mathbf{K}_{I\diamond}(0,\mathbf{G},\omega_{L_0})\right)^*_\nu\,\delta(t_1'-t_2')\,\delta^3(\mathbf{y}'-\mathbf{x}')e^{-\mathrm{i}\,\mathbf{G}\cdot\mathbf{x}'}\,w(\mathbf{x}').
\end{aligned} \tag{A.222}$$

Cleaned up, this reads:

$$\begin{aligned}
\langle\hat{O}\rangle = \frac{2\pi\alpha^4}{V\omega_f}\int dt_1\,dt_1' \int d^3x\,d^3x'\;e^{-\mathrm{i}\,(\mathbf{k}_f-\mathbf{G})\cdot(\mathbf{x}-\mathbf{x}')}\,e^{\mathrm{i}\,\omega_f(t_1-t_1')}\;w(\mathbf{x})\,w(\mathbf{x}') \\
\times(\boldsymbol{\varepsilon}_f)_\sigma\,H^{(1)}_{\sigma\rho}(\mathbf{x}',t_1',\mathbf{x},t_1)\,(\boldsymbol{\varepsilon}_f^*)_\rho\left(\bar{H}^{(1)}_{\nu\mu}(\mathbf{x}',t_1',\mathbf{x},t_1)+\bar{S}^{(1)}_{\nu\mu}(\mathbf{x}',t_1',\mathbf{x},t_1)\right) \\
\times\frac{1}{V_\diamond^2}\left(\mathbf{K}_{I\diamond}(0,\mathbf{G},\omega_{L_0})\right)_\mu\left(\mathbf{K}_{I\diamond}(0,\mathbf{G},\omega_{L_0})\right)^*_\nu.
\end{aligned} \tag{A.223}$$

Note that we have carried the spontaneous optical correlator along, because we might want to use it to investigate XPDC as well. In contrast to our result Eq. (5.61), we have stopped short of simplifying the integration in ω_f, as it may well be constrained by the detection setup. In its present form, the above

may serve as a convenient starting point for more concrete derivations.

We note in closing that the particular way, in which the field correlation-functions are Fourier transformed above, lends itself to a new interpretation. Namely, these Fourier transforms are restricted to the difference coordinates $\mathbf{x}-\mathbf{x}'$ and t_1-t_1' only, while keeping the center-of-mass coordinates in real-space (or real-time, respectively). This is characteristic for so-called Wigner functions[25] [220], which have found some popularity in quantum-optics of late (for examples, cf. Refs. [221–223]. They have the intriguing property of bridging between a quantum-inspired, coherence description of the field and a more classical point of view, which may simplify all the way down to ray-optics. Further investigations along this route are foreseen in the future.

[25] We note that Ref. [219] gives a convenient introduction, adopting a perspective of (optical) signal-processing.

A.17 First perturbative model of 'negative' scattering signal

Our experimental results from the ESRF campaign(s) raised the issue of 'negative' scattering signals at the phasematching condition for XPDC with high-energy idler photons. More accurately, the scattering patterns showed circular scattering signatures, for which the count rate was smaller than the average around it (i.e., dips into the background). We raised the possibility of this being connected to the strong re-absorption of idler photons in the XUV regime. In the following, we shall elaborate further on this idea and derive an expression for the scattering signal, which supports this hypothesis to some extent.

We recall that we started our initial derivation of the XOWM signal from the IXS-type scattering expression (Eq. (2.32))

$$\langle \hat{O} \rangle = \lim_{t\to\infty} \lim_{t_0\to-\infty} \langle \hat{O} \rangle(t) = \frac{2\pi\alpha^2}{V\omega_f} \int_{-\infty}^{\infty} dt_1 \int_{-\infty}^{\infty} dt_1' \int d^3x \int d^3x' \, (\boldsymbol{\varepsilon}_f)_\sigma \, H^{(1)}_{\sigma\rho}(\mathbf{x}', t_1', \mathbf{x}, t_1) \, (\boldsymbol{\varepsilon}_f^*)_\rho$$
$$\cdot e^{-\mathrm{i}\mathbf{k}_f\cdot(\mathbf{x}-\mathbf{x}')} \, e^{\mathrm{i}\,\omega_f(t_1-t_1')} \, \mathrm{Tr}_{\mathrm{REST}} \left\{ \hat{n}(\mathbf{x}, t_1) \, \hat{\rho}_{\mathrm{REST}}(0) \, \hat{n}(\mathbf{x}', t_1') \right\}. \tag{A.224}$$

For the next order of perturbation theory—leading to XOWM—we have assumed that the optical admixture would happen symmetrically on both legs of the density matrix. Recall the set of diagrams shown in the upper right corner of Fig. 2.1—an exemplary diagram follows in Fig. A.4.

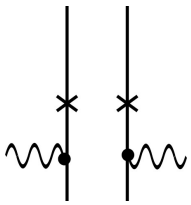

Figure A.4: The derivation of our XOWM framework in Chpt. 2 relied on diagrams, for which optical vertices (here connected to wiggly lines) appeared symmetrically on both legs. [We gratefully acknowledge Dr. Christina Bömer's help in rendering the above computer graphics.]

Regarding 'XPDC' with idler energies in the XUV-regime, however, we are potentially faced with a different situation. Given that the idler photon is quickly absorbed, we should also consider diagrams, wherein this absorption is incorporated as a second vertex on one side. In fact, it may not even be appropriate to think of the idler photon as independent—but rather consider it as a combined, polaritonic excitation of the light-matter system[26]. Just like the aforementioned scenario, we may attempt to model this situation to lowest order in terms of the emission and reabsorption of a photon. This would lead to a 'bubble-insertion' into the diagram[27] (cf. Fig. A.5).

In order to include this 'bubble' into our perturbative expression for XOWM, we start out from the density-density correlator in Eq. (A.224), which we may write as

$$\mathrm{Tr}_{\mathrm{REST}} \{ \ldots \} = \mathrm{Tr}_{\mathrm{OPT}} \left\{ \mathrm{Tr}_{\mathrm{MAT}} \left\{ \hat{U}_0(t,t_1) \, \hat{n}(\mathbf{x}) \, \hat{U}_0(t_1,t_0) \hat{\rho}_{\mathrm{REST}}(t_0) \hat{U}_0(t_0,t_1') \, \hat{n}(\mathbf{x}') \, \hat{U}_0(t_1',t) \right\} \right\}. \tag{A.225}$$

We shall, once again, factorize the initial density matrices—even though this is likely inappropriate for a

[26] Note that we followed-up on this line of thinking in Sec. 6.1. Ultimately, this proved to be very convincing.

[27] We note that we could push this thinking further by iterating the bubble—analogous to electronic RPA. Thus, we should find the polariton as a quasi-particle in the same way one would normally find the plasmon from RPA.

Figure A.5: Extending the scope of the above diagram to include re-absorption of the idler photon; notably, we remain at the same overall order of perturbative insertions, i.e., two optical vertices (here connected to wiggly lines) but spread them asymmetrically across both legs. [We gratefully acknowledge Dr. Christina Bömer's help in rendering the above computer graphics.]

polaritonic scenario:

$$\hat{\rho}_{\mathrm{REST}}(t_0) \approx \hat{\rho}_{\mathrm{MAT}}(t_0) \otimes \hat{\rho}_{\mathrm{OPT}}(t_0), \tag{A.226}$$

then, we try to capture any light-matter interaction at second order of perturbation theory. To this end, we partition the time-evolution operator as before

$$\hat{U}_0(t,t_0) = \hat{U}_{00}(t,t_0)\,\hat{U}_{\mathrm{INT\_OPT}}(t,t_0) \tag{A.227}$$

implying the following Hamiltonians for the non-interacting systems and their coupling, respectively:

$$\hat{H}_{00} = \hat{H}_{\mathrm{MAT}} + \hat{H}_{\mathrm{EM}} \tag{A.228}$$

$$\hat{H}_{\mathrm{INT\_OPT}} = \alpha \int d^3x\, \hat{\psi}^{\dagger}(\mathbf{x})\mathbf{p}\cdot\hat{\mathbf{A}}_{\mathrm{opt}}(\mathbf{x})\hat{\psi}(\mathbf{x}). \tag{A.229}$$

The object(s), which we would want to expand ultimately, are the time-evolution operators to the very left and very right in Eq. (A.225). They mark the evolution of the system *after* x-ray scattering has deposited energy in the material system. Thus, here is the chance to create a polariton. Following the splitting in Eq. (A.227), we can expand the interaction part and find to second order (cf. Eq. (A.13))

$$\begin{aligned}\hat{U}_0(t,t_0) \approx \hat{U}_{00}(t,t_0)\Big(\hat{\mathbf{1}} - \mathrm{i}\int_{t_0}^{t} dt_1\,\hat{U}_{00}(t_0,t_1)\,\hat{H}_{\mathrm{INT\_OPT}}\,\hat{U}_{00}(t_1,t_0) \\ - \int_{t_0}^{t} dt_1 \int_{t_0}^{t_1} dt_2\,\hat{U}_{00}(t_0,t_1)\,\hat{H}_{\mathrm{INT\_OPT}}\,\hat{U}_{00}(t_1,t_0)\,\hat{U}_{00}(t_0,t_2)\,\hat{H}_{\mathrm{INT\_OPT}}\,\hat{U}_{00}(t_2,t_0)\Big).\end{aligned} \tag{A.230}$$

Of this, both the identity and the second order term

$$\hat{U}_0^{(2)}(t,t_0) = \hat{U}_{00}(t,t_0)\,(-1)\int_{t_0}^{t} dt_1 \int_{t_0}^{t_1} dt_2\,\hat{U}_{00}(t_0,t_1)\,\hat{H}_{\mathrm{INT\_OPT}}\,\hat{U}_{00}(t_1,t_0)\,\hat{U}_{00}(t_0,t_2)\,\hat{H}_{\mathrm{INT\_OPT}}\,\hat{U}_{00}(t_2,t_0) \tag{A.231}$$

are relevant to us. Using them, we can identify three interesting contributions following from Eq. (A.225)

up to order α^2

$$\begin{aligned}
\mathrm{Tr}_{\mathrm{REST}}\{...\} &= \mathrm{Tr}_{\mathrm{MAT}}\{\hat{U}_{00}(t,t_1)\,\hat{n}(\mathbf{x})\,\hat{U}_{00}(t_1,t_0)\hat{\rho}_{\mathrm{MAT}}(t_0)\hat{U}_{00}(t_0,t_1')\,\hat{n}(\mathbf{x}')\,\hat{U}_{00}(t_1',t)\} \\
&+ \mathrm{Tr}_{\mathrm{OPT}}\{\mathrm{Tr}_{\mathrm{MAT}}\{\hat{U}_0^{(2)}(t,t_1)\,\hat{n}(\mathbf{x})\,\hat{U}_{00}(t_1,t_0)\Big(\hat{\rho}_{\mathrm{MAT}}(t_0)\otimes\hat{\rho}_{\mathrm{OPT}}(t_0)\Big)\,\hat{U}_{00}(t_0,t_1')\,\hat{n}(\mathbf{x}')\,\hat{U}_{00}(t_1',t)\}\} \\
&+ \mathrm{Tr}_{\mathrm{OPT}}\{\mathrm{Tr}_{\mathrm{MAT}}\{\hat{U}_{00}(t,t_1)\,\hat{n}(\mathbf{x})\,\hat{U}_{00}(t_1,t_0)\Big(\hat{\rho}_{\mathrm{MAT}}(t_0)\otimes\hat{\rho}_{\mathrm{OPT}}(t_0)\Big)\,\hat{U}_{00}(t_0,t_1')\,\hat{n}(\mathbf{x}')\,\hat{U}_0^{(2)}(t_1',t)\}\} \\
&= \mathrm{Tr}_{\mathrm{MAT}}\{\hat{U}_{00}(t,t_1)\,\hat{n}(\mathbf{x})\,\hat{U}_{00}(t_1,t_0)\hat{\rho}_{\mathrm{MAT}}(t_0)\hat{U}_{00}(t_0,t_1')\,\hat{n}(\mathbf{x}')\,\hat{U}_{00}(t_1',t)\} \\
&+ \mathrm{Tr}_{\mathrm{OPT}}\{\mathrm{Tr}_{\mathrm{MAT}}\{\hat{U}_0^{(2)}(t,t_1)\,\hat{n}(\mathbf{x})\,\hat{U}_{00}(t_1,t_0)\Big(\hat{\rho}_{\mathrm{MAT}}(t_0)\otimes\hat{\rho}_{\mathrm{OPT}}(t_0)\Big)\,\hat{U}_{00}(t_0,t_1')\,\hat{n}(\mathbf{x}')\,\hat{U}_{00}(t_1',t)\}\} \\
&+ \Big(\mathrm{Tr}_{\mathrm{OPT}}\{\mathrm{Tr}_{\mathrm{MAT}}\{\hat{U}_0^{(2)}(t,t_1')\,\hat{n}(\mathbf{x}')\,\hat{U}_{00}(t_1',t_0)\Big(\hat{\rho}_{\mathrm{MAT}}(t_0)\otimes\hat{\rho}_{\mathrm{OPT}}(t_0)\Big)\,\hat{U}_{00}(t_0,t_1)\,\hat{n}(\mathbf{x})\,\hat{U}_{00}(t_1,t)\}\}\Big)^{\dagger}.
\end{aligned} \tag{A.232}$$

Herein, the purely material part will be responsible for normal, Compton-type IXS and need not bother us in the following. Instead, we shall seek a nice reformulation of the latter two terms—which are structurally identical.

For a first simplification, we observe that the operators pertaining to the optical electromagnetic field are solely contained within the interaction Hamiltonians inside $\hat{U}_0^{(2)}(t,t_1)$. Focusing on these electromagnetic bits for the moment, we can contract the optical trace and all relevant time-translations around them:

$$\begin{aligned}
&\mathrm{Tr}_{\mathrm{OPT}}[\hat{U}_0^{(2)}(t,t_1)...\hat{U}_{00}(t_1,t_0)\hat{\rho}_{\mathrm{OPT}}(t_0)...\hat{U}_{00}(t_0,t_1')...\hat{U}_{00}(t_1',t)] \\
=&\mathrm{Tr}_{\mathrm{OPT}}[\hat{U}_{00}(t,t_1)\,(-1)\int_{t_1}^{t}dt_2\int_{t_1}^{t_2}dt_3\,\hat{U}_{00}(t_1,t_2)\,\hat{H}_{\mathrm{INT_OPT}}\,\hat{U}_{00}(t_2,t_1)\,\hat{U}_{00}(t_1,t_3)\,\hat{H}_{\mathrm{INT_OPT}}\,\hat{U}_{00}(t_3,t_1) \\
&...\hat{U}_{00}(t_1,t_0)\hat{\rho}_{\mathrm{OPT}}(t_0)...\hat{U}_{00}(t_0,t_1')...\hat{U}_{00}(t_1',t)] \\
=&\mathrm{Tr}_{\mathrm{OPT}}[\hat{U}_{00}(t,0)\,(-1)\int_{t_1}^{t}dt_2\int_{t_1}^{t_2}dt_3\,\hat{U}_{00}(0,t_2)\,...(\hat{\mathbf{A}}_{\mathrm{opt}}(\mathbf{y}_2))_\mu\,\hat{U}_{00}(t_2,0)\,\hat{U}_{00}(0,t_3)\,...(\hat{\mathbf{A}}_{\mathrm{opt}}(\mathbf{y}_3))_\nu\,\hat{U}_{00}(t_3,0) \\
&...\hat{U}_{00}(0,t_0)\hat{\rho}_{\mathrm{OPT}}(t_0)...\hat{U}_{00}(t_0,t_1')...\hat{U}_{00}(t_1',t)] \\
=&(-1)\int_{t_1}^{t}dt_2\int_{t_1}^{t_2}dt_3\mathrm{Tr}_{\mathrm{OPT}}[\hat{\rho}_{\mathrm{OPT}}(0)(\hat{\mathbf{A}}_{\mathrm{opt}}(\mathbf{y}_2,t_2))_\mu(\hat{\mathbf{A}}_{\mathrm{opt}}(\mathbf{y}_3,t_3))_\nu].
\end{aligned} \tag{A.233}$$

Here, we have made use of the Heisenberg picture defined earlier by writing $\hat{U}_{00}(0,t_2)\,(\hat{\mathbf{A}}_{\mathrm{opt}}(\mathbf{y}_2))_\mu\,\hat{U}_{00}(t_2,0) = (\hat{\mathbf{A}}_{\mathrm{opt}}(\mathbf{y}_2,t_2))_\mu$—see also below Eq. (2.44) for the same procedure. We can go even further and identify the remaining optical trace with the (spontaneous) correlation function seen in Eq. (2.55)

$$\bar{S}^{(1)}_{\mu\nu}(\mathbf{y}_2,t_2,\mathbf{y}_3,t_3) = \mathrm{Tr}_{\mathrm{OPT}}\{\hat{\rho}^{equ}_{\mathrm{OPT}}(\hat{\mathbf{A}}_{\mathrm{opt\_flu}}(\mathbf{y}_2,t_2))_\mu\,(\hat{\mathbf{A}}_{\mathrm{opt\_flu}}(\mathbf{y}_3,t_3))_\nu\}. \tag{A.234}$$

Having the optical part simplified, we return to the full expression. Herein, we reintroduce all relevant time-evolution operators as well as the electronic remainder of the interaction Hamiltonians, namely the

$\hat{\mathbf{p}}$-operators. We start from the second-to-last line of Eq. (A.232)

$$\begin{aligned}
&\mathrm{Tr}_{\mathrm{OPT}}\{\mathrm{Tr}_{\mathrm{MAT}}\{\hat{U}_0^{(2)}(t,t_1)\,\hat{n}(\mathbf{x})\,\hat{U}_{00}(t_1,t_0)\Big(\hat{\rho}_{\mathrm{MAT}}(t_0)\otimes\hat{\rho}_{\mathrm{OPT}}(t_0)\Big)\,\hat{U}_{00}(t_0,t_1')\,\hat{n}(\mathbf{x}')\,\hat{U}_{00}(t_1',t)\}\}\\
=&(-1)\mathrm{Tr}_{\mathrm{MAT}}[\hat{U}_{00}(t,t_1)\int_{t_1}^{t}dt_2\int_{t_1}^{t_2}dt_3\,\hat{U}_{00}(t_1,t_2)\,\alpha\int dy_2\,\hat{\mathbf{p}}(\mathbf{y}_2)\,\hat{U}_{00}(t_2,t_1)\,\hat{U}_{00}(t_1,t_3)\,\alpha\int dy_3\,\hat{\mathbf{p}}(\mathbf{y}_3)\,\hat{U}_{00}(t_3,t_1)\\
&\times\hat{n}(\mathbf{x})\,\hat{U}_{00}(t_1,t_0)\hat{\rho}_{\mathrm{MAT}}(t_0)\hat{U}_{00}(t_0,t_1')\,\hat{n}(\mathbf{x}')\,\hat{U}_{00}(t_1',t)]\bar{S}^{(1)}_{\mu\nu}(\mathbf{y}_2,t_2,\mathbf{y}_3,t_3)\\
=&(-1)\alpha^2\int_{t_1}^{t}dt_2\int_{t_1}^{t_2}dt_3\int dy_2\int dy_3\,\mathrm{Tr}_{\mathrm{MAT}}[\hat{\mathbf{p}}(\mathbf{y}_2,t_2)\,\hat{\mathbf{p}}(\mathbf{y}_3,t_3)\,\hat{n}(\mathbf{x},t_1)\hat{\rho}_{\mathrm{MAT}}(0)\,\hat{n}(\mathbf{x}',t_1')]\;\bar{S}^{(1)}_{\mu\nu}(\mathbf{y}_2,t_2,\mathbf{y}_3,t_3).
\end{aligned}\tag{A.235}$$

Next, we shall introduce some further simplifying assumptions. First—and not very restrictive—we shall assume our initial state to be in a set of energy eigenstates weighted by their probability (as we did in Chpt. 2)

$$\hat{\rho}_{\mathrm{MAT}}(0)\approx\sum_I p_I\;|I\rangle\langle I|\tag{A.236}$$

This is reasonable for a thermal ensemble close to the ground state. As a matter of fact, we will be focusing on said ground state alone very soon.

Starting from this initial state $|I\rangle$, the system is kicked by the action of $\hat{n}(\mathbf{x},t_1)$ into an excited state, before it de-excites by 'emitting' a photon (rather: exciting a polariton) through the coupling at $\hat{\mathbf{p}}(\mathbf{y}_3,t_3)$. In this de-excitation step, it is not unreasonable to assume that the previously created excitation vanishes completely again. Thus, the material system would return to its initial state while the virtual photon carries its excess energy. If this is true, we can insert another projector $|I\rangle\langle I|$ between the two momentum operators with impunity (cf. Fig. A.5). Doing so factorizes the above expression into a shape that is oddly familiar from the initial derivation of our XOWM expressions

$$\begin{aligned}
&(-1)\alpha^2\sum_I p_I\int_{t_1}^{t}dt_2\int_{t_1}^{t_2}dt_3\int dy_2\int dy_3\,\mathrm{Tr}_{\mathrm{MAT}}[\hat{\mathbf{p}}(\mathbf{y}_2,t_2)\;|I\rangle\langle I|\;\hat{\mathbf{p}}(\mathbf{y}_3,t_3)\,\hat{n}(\mathbf{x},t_1)\;|I\rangle\langle I|\;\hat{n}(\mathbf{x}',t_1')]\;\bar{S}^{(1)}_{\mu\nu}(\mathbf{y}_2,t_2,\mathbf{y}_3,t_3)\\
=&(-1)\alpha^2\sum_I p_I\int_{t_1}^{t}dt_2\int_{t_1}^{t_2}dt_3\int dy_2\int dy_3\;\langle I|\;\hat{n}(\mathbf{x}',t_1')\hat{\mathbf{p}}(\mathbf{y}_2,t_2)\;|I\rangle\langle I|\;\hat{\mathbf{p}}(\mathbf{y}_3,t_3)\,\hat{n}(\mathbf{x},t_1)\;|I\rangle\;\bar{S}^{(1)}_{\mu\nu}(\mathbf{y}_2,t_2,\mathbf{y}_3,t_3)\\
=&(-1)\alpha^2\sum_I p_I\int_{-\infty}^{t}dt_2\int_{-\infty}^{\infty}dt_3\int dy_2\int dy_3\Theta(t_2-t_1)\,\Theta(t_3-t_1)\,\Theta(t_2-t_3)\,\big(\langle I|\;\hat{\mathbf{p}}(\mathbf{y}_2,t_2)\hat{n}(\mathbf{x}',t_1')\;|I\rangle\big)^*\\
&\times\langle I|\;\hat{\mathbf{p}}(\mathbf{y}_3,t_3)\,\hat{n}(\mathbf{x},t_1)\;|I\rangle\;\bar{S}^{(1)}_{\mu\nu}(\mathbf{y}_2,t_2,\mathbf{y}_3,t_3).
\end{aligned}\tag{A.237}$$

Here, we have pushed the temporal interdependence of the integrals into the respective Heaviside functions $\Theta(...)$. It is noteworthy that the newly appearing correlation function *in combination* with this time constraint can actually be written in terms of our earlier (time-ordered) correlation function

$$\Theta(t_3-t_1)\;\langle I|\;\hat{\mathbf{p}}(\mathbf{y}_3,t_3)\,\hat{n}(\mathbf{x},t_1)\;|I\rangle=\Theta(t_3-t_1)\,\mathbf{P}_I(\mathbf{y}_3,t_3,\mathbf{x},t_1).\tag{A.238}$$

If we are willing to approximate a bit further, we can actually extend this to the other correlation function as well. Strictly, this will depend on t_1', for which no time-constraint is given. However, we know that t_1 and t_1' will differ only up to the coherence time of the x-ray source. Especially for synchrotron sources,

this may be small enough to justify setting $t_1 \approx t_1'$, which renders the overall expression:

$$\approx (-1)\alpha^2 \sum_I p_I \int_{-\infty}^{t} dt_2 \int_{-\infty}^{\infty} dt_3 \int dy_2 \int dy_3 \left(\Theta(t_2 - t_1')\mathbf{P}_I(\mathbf{y}_2, t_2\, \mathbf{x}', t_1')\right)^* \Theta(t_3 - t_1)\mathbf{P}_I(\mathbf{y}_3, t_3, \mathbf{x}, t_1)$$
$$\times \Theta(t_2 - t_3)\, \bar{S}^{(1)}_{\mu\nu}(\mathbf{y}_2, t_2, \mathbf{y}_3, t_3). \tag{A.239}$$

Plugging this back into our earlier expression for the perturbatively expanded IXS-correlator (Eq. (A.232)), we find the above term paired up with its adjoined counterpart

$$\begin{aligned}
&\mathrm{Tr}_{\mathrm{MAT}}\left\{\hat{n}(\mathbf{x}, t_1)\, \hat{\rho}_{\mathrm{MAT}}(0) \hat{n}(\mathbf{x}', t_1')\right\} \\
&+ (-1)\alpha^2 \sum_I p_I \int_{-\infty}^{t} dt_2 \int_{-\infty}^{\infty} dt_3 \int dy_2 \int dy_3 \left(\Theta(t_2 - t_1')\mathbf{P}_I(\mathbf{y}_2, t_2\, \mathbf{x}', t_1')\right)^* \Theta(t_3 - t_1)\mathbf{P}_I(\mathbf{y}_3, t_3, \mathbf{x}, t_1) \\
&\times \Theta(t_2 - t_3)\, \bar{S}^{(1)}_{\mu\nu}(\mathbf{y}_2, t_2, \mathbf{y}_3, t_3) \\
&+ (-1)\alpha^2 \sum_I p_I \int_{-\infty}^{t} dt_2 \int_{-\infty}^{\infty} dt_3 \int dy_2 \int dy_3\, \Theta(t_2 - t_1)\mathbf{P}_I(\mathbf{y}_2, t_2\, \mathbf{x}, t_1) \left(\Theta(t_3 - t_1')\mathbf{P}_I(\mathbf{y}_3, t_3, \mathbf{x}', t_1')\right)^* \\
&\times \left(\Theta(t_2 - t_3)\, \bar{S}^{(1)}_{\mu\nu}(\mathbf{y}_2, t_2, \mathbf{y}_3, t_3)\right)^*.
\end{aligned} \tag{A.240}$$

For a last simplification, we will rename the variables subscripted with 2 into 3 and vice versa in the last term, as well as exchanging μ and ν. Moreover we make use of the fact that

$$\left(\bar{S}^{(1)}_{\mu\nu}(\mathbf{y}_2, t_2, \mathbf{y}_3, t_3)\right)^* = \bar{S}^{(1)}_{\nu\mu}(\mathbf{y}_3, t_3, \mathbf{y}_2, t_2), \tag{A.241}$$

and combine the last two terms[28].

Now, we can re-insert this into the IXS-observable, from which we started (i.e., Eq. (A.224)) and obtain

$$\begin{aligned}
\langle \hat{O} \rangle = \lim_{t\to\infty} \lim_{t_0 \to -\infty} \langle \hat{O} \rangle(t) = \frac{2\pi\alpha^2}{V\omega_f} \int_{-\infty}^{\infty} dt_1 \int_{-\infty}^{\infty} dt_1' \int d^3x \int d^3x'\, (\boldsymbol{\varepsilon}_f)_\sigma\, H^{(1)}_{\sigma\rho}(\mathbf{x}', t_1', \mathbf{x}, t_1)\, (\boldsymbol{\varepsilon}_f^*)_\rho \\
\cdot e^{-\mathrm{i}\,\mathbf{k}_f \cdot (\mathbf{x} - \mathbf{x}')}\, e^{\mathrm{i}\,\omega_f (t_1 - t_1')} \left(\mathrm{Tr}_{\mathrm{MAT}}\left\{\hat{n}(\mathbf{x}, t_1)\, \hat{\rho}_{\mathrm{MAT}}(0) \hat{n}(\mathbf{x}', t_1')\right\} + (-1)\alpha^2 \sum_I p_I \int_{-\infty}^{\infty} dt_2 \int_{-\infty}^{\infty} dt_3 \int dy_2 \int dy_3 \right. \\
\left. \times \left(\Theta(t_2 - t_1')\mathbf{P}_I(\mathbf{y}_2, t_2\, \mathbf{x}', t_1')\right)^* \Theta(t_3 - t_1)\mathbf{P}_I(\mathbf{y}_3, t_3, \mathbf{x}, t_1)\, \bar{S}^{(1)}_{\mu\nu}(\mathbf{y}_2, t_2, \mathbf{y}_3, t_3)\right).
\end{aligned} \tag{A.242}$$

Here, the first term gives the regular (inelastic) x-ray scattering, while the second term is responsible for 'wavemixing' in the present case. Importantly, this second term is structurally equivalent to the wavemixing observable that we have obtained in the last section Eq. (2.57), i.e., for normal XPDC or SFG / DFG. The only two differences are:

- A slightly different correlation function, namely bearing a causal imprint, and
- the minus sign carried by this term since the beginning of our treatment in second order of perturbation theory.

The latter is the paramount result of this derivation. It implies—all else the same—that we will indeed end up with a term that subtracts from the regular IXS signal and thus shows a negative signature on top of the Compton background!

[28] Note that—strictly—we can not yet combine them, because the limits of the integrals are still different. However, we aim to take the limit $t \to \infty$ anyways, which will remedy this situtation.

While this result is an encouraging sign that our polariton-hypothesis may be true, we caution against pre-mature excitement. As a matter of fact, the above description likewise fails to reproduce our XPDC results at high idler energies completely. Even though it facilitates a negative component, it now lacks the positive signal. A more compelling solution to the conundrum is given in Sec. 6.1.

A.18 Diagonalization of a two-level system

In this appendix to the main thesis, we will exercise the diagonalization of a two-level system. This is in support of the earlier polariton model on XPDC (and Compton scattering)—see Sec. 6.1. The notation is largely analogous to the aforementioned section; however, we use the shorter $\omega_{\text{exc}} \to \omega_c$ and strip the homogeneous energy-offset E_I from the Hamiltonian.

As such, we start from the 2×2-matrix to be diagonalized

$$H' = \begin{pmatrix} \omega_c & V \\ V^* & \omega_i \end{pmatrix} \qquad \text{with: } \begin{pmatrix} 1 \\ 0 \end{pmatrix} \simeq |F_c^{el}\rangle \qquad \text{and: } \begin{pmatrix} 0 \\ 1 \end{pmatrix} \simeq |F^{\gamma}\rangle\,. \tag{A.243}$$

Here, the identification of basis states with 2-component vectors proceeds analogous to Sec. 6.1.

We diagonalize H' by solving the characteristic polynomial

$$H'\,|\phi_i\rangle = E_i\,|\phi_i\rangle \qquad \Rightarrow \quad (H' - \mathbb{1}E_i)\,|\phi_i\rangle = 0, \tag{A.244}$$

i.e.,

$$\begin{aligned} 0 &= \det(H' - \mathbb{1}E_i) \\ &= \det \begin{pmatrix} \omega_c - E_i & V \\ V^* & \omega_i - E_i \end{pmatrix} \\ &= (\omega_c - E_i)(\omega_i - E_i) - |V|^2 \\ &= E_i^2 - E_i(\omega_c + \omega_i) + \omega_c\omega_i - |V|^2. \end{aligned} \tag{A.245}$$

We add $|V|^2 - \omega_c\omega_i$ to both sides of the equation and obtain

$$\begin{aligned} E_i^2 - E_i \underbrace{(\omega_c + \omega_i)}_{2\bar{\omega}} &= |V|^2 - \omega_c\omega_i && \text{with: } \bar{\omega} := (\omega_c + \omega_i)/2 \\ (E_i - \bar{\omega})^2 &= |V|^2 + \frac{1}{4}(\omega_c + \omega_i)^2 - \omega_c\omega_i \\ &= |V|^2 + \frac{1}{4}(\omega_c^2 + 2\omega_c\omega_i + \omega_i^2 - 4\omega_c\omega_i) \\ &= |V|^2 + \frac{1}{4}(\omega_c - \omega_i)^2 && \text{with: } \Delta := \omega_c - \omega_i \\ E_i - \bar{\omega} &= \pm\sqrt{\frac{1}{4}(\omega_c - \omega_i)^2 + |V|^2}. \end{aligned} \tag{A.246}$$

Thus, we finally solve for E_i and find the two eigenvalues

$$\begin{aligned} E_i &= \frac{\omega_c + \omega_i}{2} \pm \sqrt{\frac{1}{4}(\omega_c - \omega_i)^2 + |V|^2} \\ &= \bar{\omega} \pm \sqrt{\frac{1}{4}\Delta^2 + |V|^2}. \end{aligned} \tag{A.247}$$

If we sketch out the energy dependence (e.g., their variation with change in ω_i) of these two solutions, we find two anti-crossing branches. Asymptotically—both at low and high energies—they will approach the energy value of one of the eigenstates of the uncoupled Hamiltonian, i.e., ω_c or ω_i, respectively. The anti-crossing in between is determined in its strength by the coupling parameter V. An illustration of this

is given below in Fig. A.6.

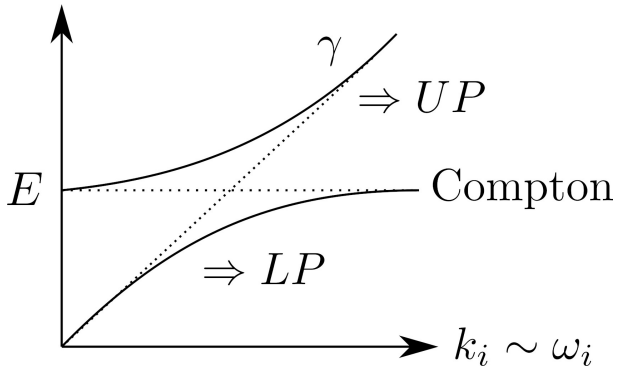

Figure A.6: Sketch of the dispersion of the eigenvalues E_i as a function of ω_i. This schematic anticipates the later use in the context of our polariton model. By (obvious) convention, the two branches are referred to as upper (UP) and lower (LP) polariton branch, respectively. The dashed lines in the background indicate the energy of the uncoupled states, with the electronic excitation ω_c pertaining to 'Compton'-scattering, while the photonic excitation of energy ω_i would pertain to an 'idler'-photon of XPDC (here labeled by γ). The essential characteristic of the polaritonic dispersion is the avoided crossing of the two branches, which is determined by the coupling strength V among the photonic and electronic states. [We gratefully acknowledge Dr. Christina Bömer's help in rendering the above computer graphics.]

In order to obtain an asymptotic identification of the two branches, we consider the limit of very small $\omega_i \to 0$:

$$E_i \approx \frac{\omega_c}{2} \pm \sqrt{\frac{1}{4}\omega_c^2 + |V|^2} \approx \frac{\omega_c}{2} \pm \frac{\omega_c}{2} \quad \begin{cases} \omega_c & : + \text{ solution} \\ \sim 0 & : - \text{ solution.} \end{cases} \tag{A.248}$$

Thus, we can identify the $+$ solution as the upper polariton branch (UP) and the $-$ solution as the lower polariton branch (LP).

Next, we find the eigenvectors of the diagonal matrix or, equivalently, the transformation coefficients to diagonalize it formally. Starting from the eigenvalue-problem

$$H' \, |\phi_i\rangle = E_i \, |\phi_i\rangle \tag{A.249}$$

once again, we can represent ϕ in the 2-component basis of Eq. (A.243) using expansion coefficients c:

$$|\phi_\pm\rangle = \begin{pmatrix} c_{1\pm} \\ c_{2\pm} \end{pmatrix}. \tag{A.250}$$

Then, the eigenvalue-problem takes on the form

$$\begin{pmatrix} \omega_c & V \\ V^* & \omega_i \end{pmatrix} \begin{pmatrix} c_{1\pm} \\ c_{2\pm} \end{pmatrix} = E_\pm \begin{pmatrix} c_{1\pm} \\ c_{2\pm} \end{pmatrix}$$
$$\begin{pmatrix} \omega_c - E_\pm & V \\ V^* & \omega_i - E_\pm \end{pmatrix} \begin{pmatrix} c_{1\pm} \\ c_{2\pm} \end{pmatrix} = 0 \tag{A.251}$$

From this set of equations, we can take a single line, for example

$$\Rightarrow (\omega_c - E_i) c_{1i} + V c_{2i} = 0,$$

and thereby fully determine c_{1i} in relation to c_{2i} or vice versa. Note that we use the index i to indicate either $+$ or $-$ here; it is not related to the label on ω_i, though.

In order to fix the overall magnitude of the coefficients, we should, furthermore, involve the normalization condition

$$1 = |c_{1i}|^2 + |c_{2i}|^2. \tag{A.252}$$

If we simply set $c_{1i} = 1$ to begin with, then we can write the *non*-normalized eigenstate as

$$\begin{pmatrix} c_{1i} \\ c_{2i} \end{pmatrix} = \begin{pmatrix} 1 \\ -(\omega_c - E_i)/V \end{pmatrix} = \begin{pmatrix} 1 \\ -V^*/(\omega_i - E_i) \end{pmatrix}. \tag{A.253}$$

In here, both forms are equivalent and merely depend on the choice of either upper or lower line of the matrix equation (A.251).

Adopting the latter version and normalizing it, we find

$$\begin{pmatrix} c_{1i} \\ c_{2i} \end{pmatrix} = \frac{1}{\sqrt{1 + \frac{|V|^2}{(E_i - \omega_i)^2}}} \begin{pmatrix} 1 \\ V^*/(E_i - \omega_i) \end{pmatrix} \tag{A.254}$$

Finally, we return to the task of specifying transformation-matrices that diagonalize H'. We recall the Hamiltonians diagonal shape as well as the mathematical fact that this diagonalization should be affected by unitary matrices (here labelled S):

$$\begin{aligned} \begin{pmatrix} E_+ & 0 \\ 0 & E_- \end{pmatrix} &= SH'S^\dagger \\ &= S \begin{pmatrix} \omega_c & V \\ V^* & \omega_i \end{pmatrix} S^\dagger \\ &= \begin{pmatrix} S_{11} & S_{12} \\ S_{21} & S_{22} \end{pmatrix} \begin{pmatrix} \omega_c & V \\ V^* & \omega_i \end{pmatrix} \begin{pmatrix} S_{11}^* & S_{21}^* \\ S_{12}^* & S_{22}^* \end{pmatrix}. \end{aligned} \tag{A.255}$$

By means of sharp observation, we conclude that

$$\begin{pmatrix} S_{11}^* \\ S_{12}^* \end{pmatrix} = \begin{pmatrix} c_{1+} \\ c_{2+} \end{pmatrix}, \tag{A.256}$$

for the symbolic "+"-eigenvector $\begin{pmatrix} 1 \\ 0 \end{pmatrix}$ to behave inside Eq. (A.255) in the same way as its original counterpart $\begin{pmatrix} c_{1+} \\ c_{2+} \end{pmatrix}$ would have behaved in the old basis, where H' was not diagonal (cf. Eq. (A.251)). Analogously, we identify

$$\begin{pmatrix} S_{21}^* \\ S_{22}^* \end{pmatrix} = \begin{pmatrix} c_{1-} \\ c_{2-} \end{pmatrix} \qquad \text{or equivalently:} \quad \begin{pmatrix} S_{11} & S_{12} \\ S_{21} & S_{22} \end{pmatrix} = \begin{pmatrix} c_{1+}^* & c_{2+}^* \\ c_{1-}^* & c_{2-}^* \end{pmatrix}. \tag{A.257}$$

A.19 Proposal for XOWM using amphodyne detection at LCLS

On the following pages, we attach our proposal for a demonstration experiment on amphodyne-detected XOWM. We note that the majority of its content derives from our theory on XOWM as well as its extension to amphodyne detection as of Sec. 6.2. Nevertheless, there have also been significant collaborative efforts entering its draft, such that we would consider it in-appropriate to present it as 'our own' within the main body of the thesis.

At this point, we acknowledge our collaborators—first and foremost—Dr. Christina Bömer as well as (in order of the proposal's name listing):

- Dr. Nina Rohringer,
- Dr. Agostino Marinelli,
- Dr. Jerome Hastings,
- Dr. David Reis and
- Dr. Diling Zhu.

Spokesperson: Christina Boemer

Upscaling nonlinear x-ray diffraction by amphodyne detection

Abstract

We propose the upscaling of weak nonlinear diffraction signals – here stemming from x-ray-optical wavemixing – by implementing an *amphodyne* detection scheme. Similar to heterodyne detection, this uses the interference of the weak signal with a stronger reference beam. In the proposed *amphodyne* case, this reference is generated *in-situ* through elastic diffraction. Detecting the nonlinear signal mixed with the reference, we expect an effective magnification by several orders of magnitude compared to conventional detection.

Successful demonstration of *amphodyne* detection will allow us to extend the scope of x-ray-optical wavemixing to a wide range of technically-relevant – but weakly scattering – samples. By magnifying the weak nonlinear signal, crystallographic application will become feasible, which allows to image valence-electron dynamics with atomic-scale resolution.

Furthermore, the *amphodyne* detection scheme can provide direct access to the scattering-phase in an ideally stable (i.e., jitter-free) scenario. In the presence of timing jitter, however, this absolute phase will be lost. Nevertheless, the x-ray-optical time-delay will be encoded in the signal's fluctuation. This opens up further avenues to develop the technique into light-by-light streaking diagnostics.

The *amphodyne* detection scheme capitalizes on ultrashort x-ray pulses with broad coherent bandwidth – only available at LCLS – and will pave the way towards broader applicability of nonlinear x-ray scattering processes.

Introduction

Nonlinear optics, specifically wavemixing processes such as sum- and difference-frequency generation (SFG, DFG) as well as parametric down-conversion (PDC) are frequently used in the optical regime. There, they find applications throughout a broad field of science and technology. However, the transfer of nonlinear optics into the x-ray regime has only succeeded for very few proof-of-principle experiments [1, 2].

Any routine application of these processes is currently prevented by their challengingly low conversion efficiencies, which can reach from $10^{-7}$for x-ray-optical SFG [1] down to 10^{-14} for PDC in similar samples [3]. Yet, precisely these x-ray-optical wavemixing (XOWM) processes would deliver unprecedented insights into matter by probing valence-charge dynamics **with** atomic-scale spatial resolution. This has been showcased experimentally in a XUV-mixing scenario [2], while recent theoretical predictions (among others by the authors) emphasize the power of nonlinear techniques with optical admixtures [4,5,6].

In order to overcome the outstanding challenge of measuring such weak nonlinear diffraction signals, we propose the implementation of an *amphodyne* detection scheme. This is a hybrid between both (hence '*ampho*') heterodyne and homodyne detection. Analogous to usual heterodyne detection, we aim to mix the weak nonlinear signal with a stronger reference field ('local oscillator'). The measurable interference of both fields effectively scales up the nonlinear component – facilitating its detection. In contrast to all-optical heterodyne setups, however, no phase-stable x-ray source exists to provide such a 'local oscillator' externally. Instead, we propose to generate a phase-stable reference beam *in-situ* from carefully tuned elastic diffraction (see illustration Fig. 1a). Overall, only scattered radiation will be used for the detection – lending the scheme a homodyne aspect as well. A similar concept has been proposed as 'Self-Referenced Coherent Diffraction' for molecular samples [7], while Mukamel et al. recognized the feasibility for 'time-resolved Bragg peaks in crystals' [8].

Specifically, for crystalline samples, the elastic diffraction can be tuned precisely enough to enable controlled interference with nonlinear scattering signals. Extending our own theoretical framework [3,6], we could identify experimental conditions and phase-matching points, for which *amphodyne* detection can be achieved. Once verified, the scheme can be generalized to a broad range of crystalline samples. This would ultimately enable routine (crystallographic) investigation of valence-charge dynamics in functional materials with atomic-scale spatial resolution.

Scientific Case and Impact of Proposed LCLS Experiments

With the proposed experiment we intend to answer the question, whether a weak x-ray-optical wavemixing signal can be scaled up by means of interference with a stronger, concurrent scattering process. As such, we propose the *amphodyne* detection scheme for nonlinear diffraction.

As outlined above, this *amphodyne* detection (ampho, Greek for 'both') combines characteristics of 'homo-' and 'heterodyne' detection methods. While it focuses on measuring scattered radiation only – as a homodyne scheme would – it likewise implements the interference of a weak signal with a stronger reference – as is typical for heterodyne schemes. The weak signal of our interest stems from x-ray-optical SFG. Specifically, from combining x-ray photons at energy $\hbar\omega_x$ = 10 keV with optical photons at $\hbar\omega_{opt}$ = 1.55 eV to yield nonlinear diffraction at $\omega_{SFG} = \omega_x + \omega_{opt}$. The corresponding scattering process is diagrammatically depicted in the upper half of Fig. 1 a). Intrinsically, this process has a low conversion efficiency ($\omega_x \rightarrow \omega_{SFG}$) of ~$\mathbf{10^{-7}}$ [1] or weaker. In order to boost the detectable signal, we aim to observe its interference with a stronger 'local oscillator'. This reference field will be generated concurrently by elastic scattering of higher energy photons ($\hbar\omega'_x$ = 10.00155 keV) from a sufficiently broad incident spectrum into the same final state $\omega_{SFG} = \omega'_x$. The corresponding linear process is depicted in the upper half of the diagram in Fig. 1 a). This establishes two scattering pathways with equivalent final state, that can interfere if the incident photons (ω_x, ω'_x.) are coherent. The required coherent bandwidth has to cover the difference $\hbar(\omega'_x - \omega_x) = \hbar\omega_{opt}$ = 1.55 eV and can be achieved at LCLS. Using ultrashort hard x-ray pulses, the transform limited nature of individual spikes (~< 1fs) automatically implies coherent bandwidth in excess of 1.55 eV [9].

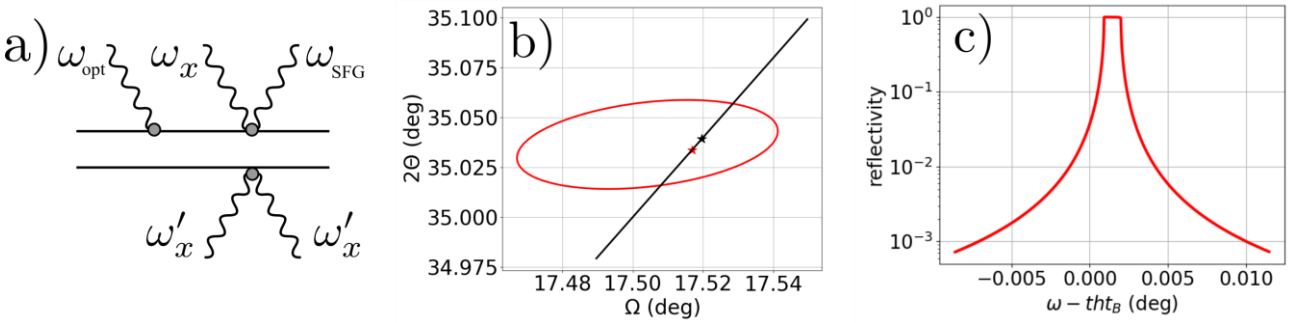

Figure 1*:* (a) Schematic principle of *amphodyne* detection: Nonlinear scattering ($\boldsymbol{\omega_x + \omega_{opt} \rightarrow \omega_{SFG}}$) interferes with linear diffraction ($\boldsymbol{\omega'_x \rightarrow \omega'_x = \omega_{SFG}}$). (b) Phase-matching conditions of elastic diffraction (black line) and the nonlinear SFG-process (red ellipse) for a diamond-(111) reflection. Positions of Bragg peaks for $\boldsymbol{\hbar\omega_x}$ = 10 keV and $\boldsymbol{\hbar\omega'_x}$. = 10.00155 keV are indicated by black and red stars, respectively. (c) Reflectivity (Darwin) curve for diamond-(111) reflection at $\boldsymbol{\hbar\omega'_x}$. = 10.00155 keV.

Beyond spectral coherence, the *amphodyne* interference process also relies critically on momentum conservation (phase-matching) for both linear and nonlinear diffraction. While linear, elastic scattering follows the well-known Ω-2θ relation (black line in Fig 1 b), the nonlinear SFG process exhibits an ellipsoidal phase-matching surface (shown in red in Fig. 1 b). Here, Ω specifies the rocking angle of the sample and 2θ denotes the angle at which the scattering signal is expected. Both diffraction conditions can be satisfied simultaneously in the vicinity of two crossing points. Notably, these points do not correspond to the actual Bragg condition for x-rays at $\boldsymbol{\omega_{SFG} = \omega'_x}$ (the Bragg spot's position is marked by a red star in Fig. 1 b). Instead, the *amphodyne* phase-matching points are detuned by $\Delta\Omega$ = -8.8 mdeg and 11.6 mdeg, respectively. Thus, the elastic diffraction, which produces the 'local oscillator' occurs in the tails of the crystal's Darwin curve – as shown in Fig. 1 c. Here, the overall reflectivity has dropped to the level of 10^{-3}, which provides a strong 'local oscillator' compared to the purely nonlinear signal at ~10^{-7}. At the same time, it also determines the most dominant background contribution.

In order to quantify both signal and background, we have derived an expression for the overall scattering yield based on non-relativistic QED. This builds upon our existing XOWM-formalism [3,6] and newly includes the

amphodyne mixing effect. As expected, we find the observable yield to consist of elastic background and a mixed contribution Y = Y_{el} + Y_{ampho}, where

$$Y_{\mathrm{ampho}}(\Omega_{\mathrm{PM}}) = \frac{(4\pi)^2\,\pi\,E_x^{\mathrm{pulse}}\,\sqrt{2\alpha}\,\sqrt{I_{\mathrm{opt}}}}{n\,\omega_{\mathrm{opt}}^2\,\omega_{\mathrm{SFG}}^2\,\omega_x\,BW_x}\,A(\Omega_{\mathrm{PM}},\phi_{\mathrm{PM}})\,S(\omega_x' = \omega_{\mathrm{SFG}})\,S(\omega_x = \omega_{\mathrm{SFG}} - \omega_{\mathrm{opt}})$$
$$\times \underbrace{\frac{1}{V_{\mathrm{unit}}}\left|F(\vec{G})\right|}_{\substack{\text{linear response}\\ \text{(structure factor / density)}}} \underbrace{\frac{1}{V_{\mathrm{unit}}}\left|\vec{\varepsilon}_{\mathrm{opt}}\cdot\vec{K}_{\mathrm{unit}}(0,\vec{G},\omega_{\mathrm{opt}})\right|}_{\substack{\text{nonlinear response function}\\ \text{(density–current-density)}}} \underbrace{e^{-(\Delta t)^2/4T_{\mathrm{opt}}^2}}_{\substack{\text{temporal}\\ \text{overlap}}} \underbrace{\sin(\omega_{\mathrm{opt}}\,\Delta t + \phi_\Sigma)}_{\substack{\text{interference}\\ \text{modulation}}} \qquad (1)$$

The *amphodyne* contribution is determined equally through linear, elastic diffraction – as connected with the sample's structure factor F(G) – and the nonlinear XOWM amplitude. The latter connects to the response function K(0, G, $\boldsymbol{\omega_{opt}}$), which is fundamentally given as a correlation function of electronic density and current-density. This correlator provides access to valence-charge dynamics beyond the static ground state density [6]. Importantly, the expression scales with two spectral dependencies S($\boldsymbol{\omega}$), which naturally require both the driving frequency for the nonlinear process ($\boldsymbol{\omega_x}$ = $\boldsymbol{\omega_{SFG}}$ – $\boldsymbol{\omega_{opt}}$) and the 'local oscillator' ($\boldsymbol{\omega'_x}$ = $\boldsymbol{\omega_{SFG}}$) to be transmitted up to the sample. Further factors include a geometric correction term A(Ω, ϕ) and an exponential that enforces temporal overlap of x-ray and optical pulses. Zero time-delay corresponds to Δt = 0. Finally, there is a sinusoidal modulation, which affirms the fact that the *amphodyne* contribution fundamentally results from interference. The phase of this modulation could only be accessed, if the jitter in the time-delay was kept below the optical field's period, i.e., Δt < 2π/$\boldsymbol{\omega_{opt}}$. As this is not currently feasible, we expect the *amphodyne* contribution to fluctuate around the elastic background level. An adequate observable for this fluctuating contribution is the overall variance of the yield:

$$\sigma_Y^2 = \langle (Y - \langle Y\rangle)^2\rangle = \sigma_{\mathrm{el}}^2 + \langle Y_{\mathrm{ampho}}^2\rangle \qquad (2)$$

To be detectable, the squared magnitude of the *amphodyne* contribution thus needs to exceed the fluctuations of the elastic background, which for Poissonian statistics corresponds to ${\sigma_{el}}^2 \sim Y_{el}$. Contrary to previous criticism by reviewers, this Poissonian approach is justified, given the independent origin of the dominant fluctuation in Y_{ampho}. We have simulated both the elastic yield (using raytracing [10]) and the *amphodyne* contribution (using our QED expression (1)) – finding $Y_{el} \sim 10^4$ and $Y_{ampho} \sim 10^3$, photons per shot, respectively. This assumed rather moderate parameters and already shows good contrast of the detectable fluctuations (${\sigma_{el}}^2 = 10^4 << \langle {Y^2}_{ampho}\rangle = 10^6$). Specifically, we have assumed x-ray pulses of 1 fs duration (i.e., 4 eV bandwidth (FWHM)), but merely 10 uJ pulse energy – before the monochromator. The simulated setup followed the scheme outlined below (experimental details). The optical laser was assumed to provide an intensity of 10^{10} W/cm² – following Ref. [1].

For future applications in more delicate samples, it is possible to decrease the laser intensity considerably. The square-root-dependence $\sqrt{I_{opt}}$ found in Eq. (1) allows this with sub-linear loss in yield. Conversely, the use of stronger x-ray pulses can be employed to (over-)compensate using the regular, linear dependence on ${E_x}^{pulse}$. Thus, the *amphodyne* detection scheme – once established – promises to enable detection of weak nonlinear scattering signals from a wide range of presently inaccessible samples. Studies of transport, charge-migration, correlation dynamics or collective excitations in functional solids can be significantly enhanced by *amphodyne*-detected XOWM signals, for instance. Their spectroscopic sensitivity combined with atomic-scale resolution can provide unprecedented insights into valence-charge dynamics and potentially enable nonlinear x-ray crystallography as a routine procedure.

Besides this, our demonstration of the *amphodyne* fluctuations would automatically confirm the presence of the phase-sensitive modulation factor sin($\boldsymbol{\omega_{opt}}$* Δt+ ϕ_Σ). Owing to the timing jitter in Δt, this cannot currently provide stable access to the scattering-phase accumulated in ϕ_Σ. However, the fluctuations of the sine can be used as a timing diagnostic, mapping the relative time-delay of x-ray and optical pulse within the period of the optical field. Effectively, this provides a light-by-light streaking mechanism based in (nonlinear) crystal optics. Choosing far-infrared driving fields in future iterations of *amphodyne* detection schemes, would enable timing-diagnostic across tens of femtoseconds. Most notably, this perturbative, nonlinear scheme would only weakly disturb the diagnosed x-ray beam.

The experiment in its proposed form is uniquely feasible at LCLS. While XOWM experiments in general require XFEL pulses to make efficient use of the wavemixing nonlinearity (cf. Ref. [6]), the *amphodyne* detection scheme additionally requires a large coherent bandwidth. At LCLS, the required coherence can be achieved by producing ultrashort pulses in the hard x-ray regime, which intrinsically feature a large coherent bandwidth within individual spikes. In addition, the XPP instrument offers the necessary synchronized optical laser and diffraction equipment as well as enormous expertise on nonlinear and pump-probe experiments among the instrument's scientists.

Experimental Details

The experimental setup basically implements a $\theta - 2\theta$ diffraction setup in the horizontal plane, which is schematically presented in Fig. 2. Using ultrashort (~1 fs) x-ray pulse of ~10 keV central energy, we expect the incident beam to provide a coherent bandwidth of up to 4 eV (FHWM) - see Fig. 2 inset (b). We employ the beamline's Si111 DCM at a slight detuning from the central energy (+0.6 eV) to filter the incident spectrum to ~1.4 eV (FWHM) – ranging from 10 keV upwards (Fig. 2, inset (c)). Importantly, the high-energy tail of the resulting spectral distribution remains coherent and contains the required energy $\hbar\boldsymbol{\omega'_x}$ = 10.00155 keV to generate the 'local oscillator' for the proposed *amphodyne* detection scheme. The collimated and filtered x-ray beam then impinges on the sample – a (111)-cut diamond crystal (500 µm thickness). Simultaneously, the synchronized optical laser pulse ($\hbar\boldsymbol{\omega_{opt}}$ = 1.55 eV) impinges on the sample. The rocking angle of the sample ($\boldsymbol{\Omega}$) as well as the incidence angle of the laser beam are adjusted to fulfill the required phase-matching conditions for *amphodyne* mixing, i.e., both linear and nonlinear diffraction conditions. A schematic representation of the momentum balance is given in Fig. 2 inset (a). As the sample is detuned from any exact Bragg condition by several millidegrees, the elastically diffracted spectrum is suppressed and reshaped further (Fig. 2, inset (c)). The elastic diffraction as well as its desired interference is detected at 2θ = $2\boldsymbol{\Omega}$ by an ePix10k module. In between the sample and detector we place a channel-cut crystal analyzer (Si 220, bandwidth of 0.5 eV) to discriminate the *amphodyne*-mixed signal from background due to the broad spectral remainder. The effective reduction is visible from the simulations in shown in Fig. 2 inset (d) transitioning to inset (e).

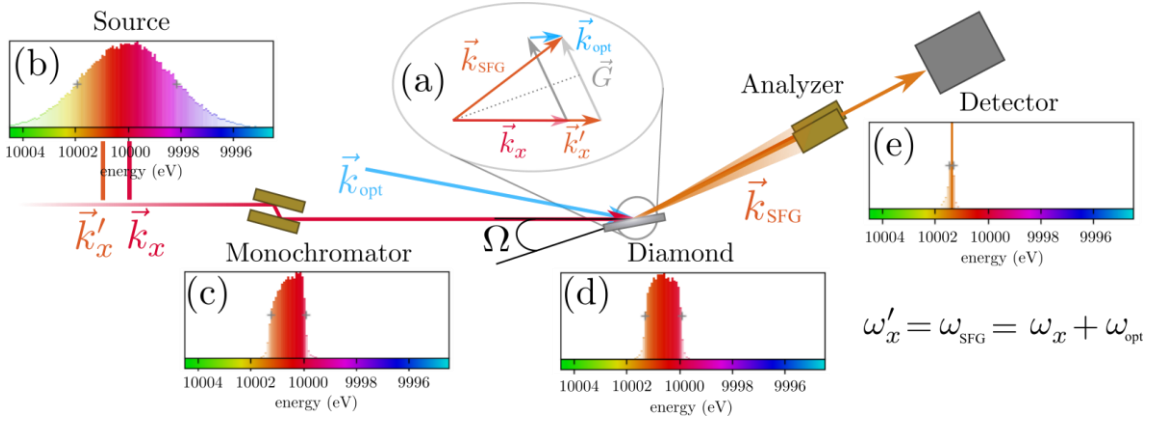

Figure 2: Experimental setup for *amphodyne* detection: The ultrashort (~1 fs) x-ray pulse with broad coherent bandwidth (b) is monochromatized (c) before it impinges on a diamond sample ((111)-oriented). Together with the optical pulse (k_{opt}) phase-matching is fulfilled for SFG, driven by x-ray photons k_x (a). Simultaneously, elastic scattering of photons k'_x into the same final wave vector k_{SFG} is possible. The interference of both scattering pathways produces the *amphodyne* mixed signal. After filtering the scattered radiation by an analyzer to reduce the elastic background from (d) to (e), the detection proceeds with a pixel detector.

In order to account for spectral jitter of the ultrashort x-ray pulses around the desired central energy, we will monitor the pulse energy before and after the monochromator on a shot-to-shot basis. Based on the transmission ratio, fitting pulses can be post-selected and the remaining fluctuations be included in the analysis. Additional spectral diagnostics downstream of the sample, such as XPP's bent crystal spectrometer [11] could provide further refinements, but are not required.

With an aligned and calibrated setup, we intend to perform several scans:

i) By rocking the sample crystal (in a range of several tens of millidegrees), we scan around both phase-matching conditions for *amphodyne* mixing. We expect sharply localized XOWM features (fluctuations) to be detectable on top of the otherwise smooth elastic background.

ii) We scan the incident laser intensity to verify the $\sqrt{I_{opt}}$-dependence of the *amphodyne* mixing signal.

iii) We scan the shift of the monochromator's central energy. Thereby, we can adjust the relative strength of x-rays driving the nonlinear process ($\boldsymbol{\omega_x}$) and 'local oscillator' for the *amphodyne* detection ($\boldsymbol{\omega'_x}$) and explore this non-trivial dependence.

iv) If time permits, we scan the dependence of the *amphodyne* mixing signal on the laser's polarization direction. We expect a cosine behavior in contrast to the cosine-square behavior of regular SFG [1].

The channel-cut crystal analyzer (Si 220) is available together with piezo-electronic motor stages for precise alignment. Both items will be brought by the experimental team. The motors are compatible with beamline electronics, appearing outwardly as conventional stepper motors.

X-ray and Laser Parameters *(or other key parameters)*
The main requirement towards the x-ray pulses is their coherent bandwidth, of at least 1.55 eV (FWHM). For more reliable *amphodyne* mixing, we propose to start from significantly broader coherent bandwidth, namely ~ 4 eV – corresponding to ~ 1 fs pulses. High pulse intensities are preferable, however, we have verified theoretically that the *amphodyne* scheme is viable for moderate pulse energies of 10 uJ (pink beam) already. We propose to conduct the experiment at 10 keV, yet any photon energy in the range of 9 – 11 keV is acceptable, especially if higher pulse energies or more reliable operation can thus be achieved. We intend to work with a collimated or lightly focused x-ray beam, with a spot size >~ 100 µm. Repetition rate is aimed to be 120 Hz, but can be adapted for beam delivery with higher pulse energy.
The central wavelength of the laser should be 800 nm (1.55 eV) with a pulse length stretched beyond the x-ray-optical timing jitter ideally (>~ 200 fs). The beam should preferably be collimated or weakly focused to a spot size of ~ 500 µm, while providing an intensity of ~10^{10} W/cm². In order to perform the laser intensity scan, the intensity should be adjustable (downwards). The repetition rate of the laser should match the x-ray repetition rate, i.e., 120 Hz.
The optical beam hits the sample collinearly to the incident x-ray beam. This configuration remains fixed for the whole experiment after initial adjustment. The laser should ideally be synchronized to the incident x-ray pulse, however, at sufficient stretching, no precise synchronization is needed. An additional timing tool for post-processing analysis with a view to the diagnostic application of *amphodyne* mixing would be interesting, but is not necessary.

Feasibility assessment
Judging from extensive simulations (see scientific case), the experiment appears feasible. Using our QED-framework [3,6], we have obtained the magnitude of the observable *amphodyne* fluctuations $\langle Y^2{}_{ampho} \rangle \sim 10^6$, which far exceed the concurrent elastic effects at $\sigma_{el}{}^2 = 10^4$. The latter has been obtained from 3D raytracing simulations [10]. Notably, both simulation results are compatible with simpler estimates derived from elastic reflectivity curves and the known efficiency of SFG [1].
Technical feasibility has likewise been established. The experimental setup geometry (θ -2θ -diffraction) in combination with a synchronized laser system is readily available at XPP – as is the Si111 DCM. Using a horizontal scattering scheme, the experiment benefits from the newly available vertical polarization of LCLS. Detection via the ePix10k is feasible at XPP as are optional beam monitoring features for spectral and temporal characterization – though not necessary. The parameters of the laser system are within the routine operation range and have been cross checked with the beamline scientists.
Finally, the ultrashort (~1fs) x-ray pulses delivering the desired coherent bandwidth are available and pulse energies exceeding 10 uJ appear feasible. These developments are discussed in close collaboration with A. Marinelli.

Experimental protocol

We request 5 shifts to conduct the experiment:

Shift 1 will be used for adjusting the machine to short pulse mode and for calibrating the setup, i.e., the monochromator alignment and the additional crystal analyzer calibration.

Shift 2: finding spatial and temporal overlap of optical and x-ray pulses, measuring various phase-matching conditions for a fixed time delay.

Shift 3: we scan the incident laser intensity to verify the $\sqrt{I_{opt}}$-dependence.

Shift 4: We scan the shift of the monochromator's central energy. Thereby, we can adjust the relative strength of x-rays driving the nonlinear process.

Shift 5: we scan the dependence of the *amphodyne* mixing signal on the laser's polarization, expecting a cosine behavior.

References

[1] T. E. Glover, et al. "X-ray and optical wave mixing." Nature 488.7413 (2012): 603-608. https://doi.org/10.1038/nature11340

[2] K. Tamasaku, et al., Nat. Phys. 7, 705–708 (2011); https://doi.org/10.1038/nphys2044

[3] C. Boemer, et al. "Towards novel probes for valence charges via X-ray optical wave mixing." Faraday discussions 228 (2021): 451-469. https://doi.org/10.1039/D0FD00130A

[4] J. R. Rouxel, et al., Phys. Rev. Lett. 120, 243902 (2018); https://doi.org/10.1103/PhysRevLett.120.243902

[5] D. Popova-Gorelova, et al., Phys. Rev. B 98, 224302 (2018); https://doi.org/10.1103/PhysRevB.98.224302

[6] Krebs, D., and Rohringer, N. "Theory of parametric x-ray optical wavemixing processes." arXiv preprint arXiv:2104.05838 (2021).

[7] J. M. Glownia, et al., Phys. Rev. Lett. 117 (2016); https://doi.org/10.1103/PhysRevLett.117.153003

[8] K. Bennett, et al., https://arxiv.org/pdf/1611.07085.pdf

[9] A. Marinelli, et al., Appl. Phys. Lett. 111, 151101 (2017); https://doi.org/10.1063/1.4990716

[10] K. Klementiev and R. Chernikov, Proc. SPIE 9209, Adv. Comp. Meth. X-Ray Optics III, 92090A (2014); https://doi.org/10.1117/12.2061400

[11] D. Zhu, et al., Appl. Phys. Lett. 101, 034103 (2012); https://doi.org/10.1063/1.4736725

Note that the experimental team list (below) and the parameter table (below) will not count against the six-page limit of the proposal.

The 'Spokesperson' is the primary point of contact for the proposed experiment

The 'Lead PI' and Co-PIs (where relevant) are the senior intellectual leaders of the proposed experiment.

Experimental team

Name	email	Project Role	Experience	Position
Prof. Nina Rohringer[1,2]	nina.rohringer@desy.de	Lead PI	A,B,C,D	Professor
Dr. Christina Boemer[1]	christina.boemer@desy.de	Spokesperson, Co-PI, Experiment, Analysis	C,D	Postdoc
Dietrich Krebs[2]	dietrich.krebs@desy.de	Co-PI, Theory, Experiment, Analysis	C,D	PhD student
Dr. Agostino Marinelli[3]	marinelli@SLAC.Stanford.EDU	Experiment, Machine coordination	A,B,C,D	Asst Professor

Prof. Jerome Hastings[3]	jerome.hastings@stanford.edu	Experiment, Analysis	A,B,C,D	Professor
Prof. David Reis[3]	dreis@stanford.edu	Experiment, Analysis	A,B,C,D	Professor
Dr. Diling Zhu[3]	dlzhu@stanford.edu	Experiment, Analysis	A,B,C,D	Senior Scientist

(1) *Deutsches Elektronen Synchrotron DESY, Notkestr. 85, 22607 Hamburg, Germany*
(2) *Universität Hamburg, Mittelweg 177, 20148 Hamburg, Germany*
(3) LCLS and *Stanford PULSE Institute, SLAC, Menlo Park, CA 94110, USA*

[A] Prior LCLS publications, [B] Prior LCLS experience, [C] Other FEL experience, [D] Synchrotron experience

Parameter Table for XPP		
Sample	Sample(S) description	Single crystal diamond
	Temperature range [C]	Room temperature
X-ray Parameters	X-ray Energy	Fixed to 10 keV
	X-ray Pulse Duration	~1 fs / short pulse mode
	X-ray Focal spot size within 10 to 200 µm	100-200 µm
Detector	Detector positioning range, List of Bragg reflections and typical scattering angles.	ePix10k Bragg reflection 111
Optical beam parameters	Wavelength [nm]	800
	Pulse duration [fs]	> 200 fs
	Maximum Pulse Energy [µJ]	Intensity ~ 10^10 W/cm²
	Focal size (FWHM) [µm]	500 µm
	Polarization requirements?	linear
	Minimum fluence on sample [mJ/cm^2]	Intensity ~ 10^10 W/cm²
	Geometry	Collinear
X-ray Beam Time	Number of shifts [1 shift = 12 hr]	5
Any additional comments		

Bibliography

[1] W. I. Orr, ed., *The Radio Handbook*, Editors and Engineers Ltd., Summerland, CA, 15 edition (1959).

[2] F. W. G. H. Meinke, ed., *Taschenbuch der Hochfrequenztechnik*, Springer Berlin, Heidelberg (1968), ISBN 978-3-662-13082-7, doi:https://doi.org/10.1007/978-3-662-13082-7.

[3] R. R. Ernst, *Multidimensional Spectroscopy: Concepts*, John Wiley & Sons, Ltd (2007), ISBN 9780470034590, doi:https://doi.org/10.1002/9780470034590.emrstm0328.

[4] F. A. A. Mulder and R. M. Scheek, *Multidimensional NMR Spectroscopy*, 1637–1646, Springer Berlin Heidelberg, Berlin, Heidelberg (2013), ISBN 978-3-642-16712-6, doi:10.1007/978-3-642-16712-6_307.

[5] P. Hamm and M. Zanni, *Concepts and Methods of 2D Infrared Spectroscopy*, Cambridge University Press (2011), doi:10.1017/CBO9780511675935.

[6] C. R. Baiz, et al., *Vibrational spectroscopic map, vibrational spectroscopy, and intermolecular interaction*, Chemical Reviews, **120**, 15, 7152 (2020), ISSN 0009-2665, doi:10.1021/acs.chemrev.9b00813.

[7] S. Mukamel, *Multidimensional femtosecond correlation spectroscopies of electronic and vibrational excitations*, Annual Review of Physical Chemistry, **51**, 1, 691 (2000), doi:10.1146/annurev.physchem.51.1.691. PMID: 11031297.

[8] T. A. A. Oliver, *Recent advances in multidimensional ultrafast spectroscopy*, R Soc Open Sci, **5**, 1, 171425 (2018).

[9] V. Z. Ilja N. Bronstejn, Konstantin A. Semendjaev, *Taschenbuch der Mathematik Für Ingenieure u. Studenten d. Techn. Hochschulen*, Teubner, Leipzig (1967).

[10] M. Bass, P. A. Franken, J. F. Ward, and G. Weinreich, *Optical rectification*, Phys. Rev. Lett., **9**, 446 (1962), doi:10.1103/PhysRevLett.9.446.

[11] S. Mukamel, *Principles of Nonlinear Optics and Spectroscopy*, volume 6 of *Oxford series in optical and imaging sciences*, Oxford University Press, New York (1995).

[12] R. W. Boyd, *Nonlinear Optics*, Academic Press (2008), ISBN 978-0-12-369470-6.

[13] Y.-R. Shen, *The Principles of Nonlinear Optics*, Wiley & Sons (2002), ISBN 978-0-471-43080-3.

[14] N. Bloembergen, *Nonlinear Optics*, WORLD SCIENTIFIC, 4th edition (1996), doi:10.1142/3046.

[15] Special Issue: Coherent Multidimensional Optical Spectroscopy, *Special issue: Coherent multidimensional optical spectroscopy*, Accounts of Chemical Research, **42**, 9, 1207 (2009), ISSN 0001-4842, doi:10.1021/ar900227m.

[16] E. Garmire, *Nonlinear optics in daily life*, Opt. Express, **21**, 25, 30532 (2013), doi:10.1364/OE.21.030532.

[17] R. K. Benninger and D. W. Piston, *Two-photon excitation microscopy for the study of living cells and tissues*, Current Protocols in Cell Biology, **59**, 1, 4.11.1 (2013), doi:https://doi.org/10.1002/0471143030.cb0411s59.

[18] J. Janušonis, T. Jansma, C. L. Chang, Q. Liu, A. Gatilova, A. M. Lomonosov, V. Shalagatskyi, T. Pezeril, V. V. Temnov, and R. I. Tobey, *Transient grating spectroscopy in magnetic thin films: Simultaneous detection of elastic and magnetic dynamics*, Scientific Reports, **6**, 1, 29143 (2016), ISSN 2045-2322, doi:10.1038/srep29143.

[19] G. Cerullo and S. De Silvestri, *Ultrafast optical parametric amplifiers*, Review of Scientific Instruments, **74**, 1, 1 (2003), doi:10.1063/1.1523642.

[20] M. E. Marhic (†), P. A. Andrekson, P. Petropoulos, S. Radic, C. Peucheret, and M. Jazayerifar, *Fiber optical parametric amplifiers in optical communication systems*, Laser & Photonics Reviews, **9**, 1, 50 (2015), doi:https://doi.org/10.1002/lpor.201400087.

[21] D. Krebs and N. Rohringer, *Theory of parametric x-ray optical wavemixing processes*, Phys Rev X (under review) (2022).

[22] W. Friedrich, P. Knipping, and M. Laue, *Interferenz-erscheinung bei roentgenstrahlen*, Sitzungsber. Bayer. Akad. der Wiss. Math. Phys. Kl., 303–322 (1912).

[23] C. Giacovazzo, H. L. Monaco, D. Viterbo, F. Scordari, G. Gilli, G. Zanotti, and M. Catti, *Fundamentals of Crystallography*, International Union of Crystallography, 1 edition (1992).

[24] M. O. Wiedorn, et al., *Megahertz serial crystallography*, Nature Communications, **9**, 1, 4025 (2018), ISSN 2041-1723, doi:10.1038/s41467-018-06156-7.

[25] P. Coppens, B. Iversen, and F. K. Larsen, *The use of synchrotron radiation in x-ray charge density analysis of coordination complexes*, Coordination Chemistry Reviews, **249**, 1, 179 (2005), ISSN 0010-8545, doi:https://doi.org/10.1016/j.ccr.2004.02.019. Synchrotron Radiation in Inorganic and Bioinorganic Chemistry.

[26] I. Freund and B. F. Levine, *Optically modulated x-ray diffraction*, Phys. Rev. Lett., **25**, 1241 (1970), doi:10.1103/PhysRevLett.25.1241.

[27] P. Eisenberger and S. L. McCall, *X-ray parametric conversion*, Phys. Rev. Lett., **26**, 684 (1971), doi:10.1103/PhysRevLett.26.684.

[28] H. Danino and I. Freund, *Parametric down conversion of x rays into the extreme ultraviolet*, Phys. Rev. Lett., **46**, 1127 (1981), doi:10.1103/PhysRevLett.46.1127.

[29] L. Young, et al., *Roadmap of ultrafast x-ray atomic and molecular physics*, Journal of Physics B: Atomic, Molecular and Optical Physics, **51**, 3, 032003 (2018), doi:10.1088/1361-6455/aa9735.

[30] C. Callegari, A. N. Grum-Grzhimailo, K. L. Ishikawa, K. C. Prince, G. Sansone, and K. Ueda, *Atomic, molecular and optical physics applications of longitudinally coherent and narrow bandwidth free-electron lasers*, Physics Reports, **904**, 1 (2021), ISSN 0370-1573, doi: https://doi.org/10.1016/j.physrep.2020.12.002. Atomic, molecular and optical physics applications of longitudinally coherent and narrow bandwidth Free-Electron Lasers.

[31] Y.-P. Sun, J.-C. Liu, C.-K. Wang, and F. Gel'mukhanov, *Propagation of a strong x-ray pulse: Pulse compression, stimulated raman scattering, amplified spontaneous emission, lasing without inversion, and four-wave mixing*, Phys. Rev. A, **81**, 013812 (2010), doi:10.1103/PhysRevA.81.013812.

[32] C. Weninger, M. Purvis, D. Ryan, R. A. London, J. D. Bozek, C. Bostedt, A. Graf, G. Brown, J. J. Rocca, and N. Rohringer, *Stimulated electronic x-ray raman scattering*, Phys. Rev. Lett., **111**, 233902 (2013), doi:10.1103/PhysRevLett.111.233902.

[33] V. Kimberg, A. Sanchez-Gonzalez, L. Mercadier, C. Weninger, A. Lutman, D. Ratner, R. Coffee, M. Bucher, M. Mucke, M. Agåker, C. Såthe, C. Bostedt, J. Nordgren, J. E. Rubensson, and N. Rohringer, *Stimulated x-ray raman scattering – a critical assessment of the building block of nonlinear x-ray spectroscopy*, Faraday Discuss., **194**, 305 (2016), doi:10.1039/C6FD00103C.

[34] M. Hollstein and N. Rohringer, *Stimulated resonant inelastic x-ray scattering with chirped, broadband pulses*, Phys. Rev. A, **99**, 013425 (2019), doi:10.1103/PhysRevA.99.013425.

[35] S. B. Zhang, V. Kimberg, and N. Rohringer, *Nonlinear resonant auger spectroscopy in co using an x-ray pump-control scheme*, Phys. Rev. A, **94**, 063413 (2016), doi:10.1103/PhysRevA.94.063413.

[36] F. Gel'mukhanov, M. Odelius, S. P. Polyutov, A. Föhlisch, and V. Kimberg, *Dynamics of resonant x-ray and auger scattering*, Rev. Mod. Phys., **93**, 035001 (2021), doi: 10.1103/RevModPhys.93.035001.

[37] G. Doumy, et al., *Nonlinear atomic response to intense ultrashort x rays*, Phys. Rev. Lett., **106**, 083002 (2011), doi:10.1103/PhysRevLett.106.083002.

[38] E. P. Kanter, et al., *Unveiling and driving hidden resonances with high-fluence, high-intensity x-ray pulses*, Phys. Rev. Lett., **107**, 233001 (2011), doi:10.1103/PhysRevLett.107.233001.

[39] Y.-P. Sun, Z. Rinkevicius, C.-K. Wang, S. Carniato, M. Simon, R. Taïeb, and F. Gel'mukhanov, *Two-photon-induced x-ray emission in neon atoms*, Phys. Rev. A, **82**, 043430 (2010), doi: 10.1103/PhysRevA.82.043430.

[40] S. B. Zhang and N. Rohringer, *Photoemission spectroscopy with high-intensity short-wavelength lasers*, Phys. Rev. A, **89**, 013407 (2014), doi:10.1103/PhysRevA.89.013407.

[41] A. N. Hopersky and A. M. Nadolinsky, *X-ray quadrupole emission in the scattering of two photons by a multicharged atomic ion*, JETP Letters, **109**, 10, 638 (2019), ISSN 1090-6487, doi: 10.1134/S0021364019100102.

[42] A. Nazarkin, S. Podorov, I. Uschmann, E. Förster, and R. Sauerbrey, *Nonlinear optics in the angstrom regime: Hard-x-ray frequency doubling in perfect crystals*, Phys. Rev. A, **67**, 041804 (2003), doi:10.1103/PhysRevA.67.041804.

[43] J.-C. Liu, C. Miron, H. Ågren, S. Polyutov, and F. Gel'mukhanov, *Resonant x-ray second-harmonic generation in atomic gases*, Phys. Rev. A, **100**, 063403 (2019), doi: 10.1103/PhysRevA.100.063403.

[44] S. Mukamel, *Multiple core-hole coherence in x-ray four-wave-mixing spectroscopies*, Phys. Rev. B, **72**, 235110 (2005), doi:10.1103/PhysRevB.72.235110.

[45] F. Bencivenga, et al., *Four-wave mixing experiments with extreme ultraviolet transient gratings*, Nature, **520**, 7546, 205 (2015), ISSN 1476-4687, doi:10.1038/nature14341.

[46] T. E. Glover, et al., *X-ray and optical wave mixing*, Nature, **488**, 7413, 603 (2012), ISSN 1476-4687, doi:10.1038/nature11340.

[47] A. Schori, C. Bömer, D. Borodin, S. P. Collins, B. Detlefs, M. Moretti Sala, S. Yudovich, and S. Shwartz, *Parametric down-conversion of x rays into the optical regime*, Phys. Rev. Lett., **119**, 253902 (2017), doi:10.1103/PhysRevLett.119.253902.

[48] D. Borodin, A. Schori, J.-P. Rueff, J. M. Ablett, and S. Shwartz, *Evidence for collective nonlinear interactions in x ray into ultraviolet parametric down-conversion*, Phys. Rev. Lett., **122**, 023902 (2019), doi:10.1103/PhysRevLett.122.023902.

[49] S. Sofer, O. Sefi, E. Strizhevsky, H. Aknin, S. P. Collins, G. Nisbet, B. Detlefs, C. J. Sahle, and S. Shwartz, *Observation of strong nonlinear interactions in parametric down-conversion of x-rays into ultraviolet radiation*, Nature Communications, **10**, 1, 5673 (2019), ISSN 2041-1723, doi:10.1038/s41467-019-13629-w.

[50] K. Tamasaku, K. Sawada, E. Nishibori, and T. Ishikawa, *Visualizing the local optical response to extreme-ultraviolet radiation with a resolution of l/380*, Nature Physics, **7**, 9, 705 (2011), ISSN 1745-2481, doi:10.1038/nphys2044.

[51] C. Boemer, D. Krebs, A. Benediktovitch, E. Rossi, S. Huotari, and N. Rohringer, *Towards novel probes for valence charges via x-ray optical wave mixing*, Faraday Discuss., **228**, 451 (2021), doi:10.1039/D0FD00130A.

[52] D. P. Craig and T. Thirunamachandran, *Molecular Quantum Electrodynamics*, Dover (1998).

[53] R. Loudon, *The Quantum Theory of Light*, Oxford University Press (1983).

[54] Z. Li, N. Medvedev, H. N. Chapman, and Y. Shih, *Radiation damage free ghost diffraction with atomic resolution*, Journal of Physics B: Atomic, Molecular and Optical Physics, **51**, 2, 025503 (2017), doi:10.1088/1361-6455/aa9737.

[55] D. Borodin, S. Levy, and S. Shwartz, *High energy-resolution measurements of x-ray into ultraviolet parametric down-conversion with an x-ray tube source*, Applied Physics Letters, **110**, 13, 131101 (2017), doi:10.1063/1.4979413.

[56] N. Rohringer and R. Santra, *X-ray nonlinear optical processes using a self-amplified spontaneous emission free-electron laser*, Phys. Rev. A, **76**, 033416 (2007), doi:10.1103/PhysRevA.76.033416.

[57] R. Santra, *Concepts in x-ray physics*, Journal of Physics B: Atomic, Molecular and Optical Physics, **42**, 2, 023001 (2009).

[58] J. M. Slowik, *Quantum effects in nonresonant x-ray scattering*, Ph.D. thesis, DESY (2015).

[59] D. Popova-Gorelova, *Imaging electron dynamics with ultrashort light pulses: A theory perspective*, Applied Sciences, **8**, 3 (2018), ISSN 2076-3417, doi:10.3390/app8030318.

[60] D. Krebs, D. A. Reis, and R. Santra, *Time-dependent qed approach to x-ray nonlinear compton scattering*, Phys. Rev. A, **99**, 022120 (2019), doi:10.1103/PhysRevA.99.022120.

[61] W. Schuelke, *Electron Dynamics by Inelastic X-Ray Scattering*, Oxford University Press (2007).

[62] J. Als-Nielsen and D. McMorrow, *Elements of Modern X-ray Physics*, John Wiley & Sons, Ltd., 2 edition (2011), ISBN 9780470973950, doi:10.1002/9781119998365.

[63] P. J. Ho and R. Santra, *Theory of x-ray diffraction from laser-aligned symmetric-top molecules*, Phys. Rev. A, **78**, 053409 (2008), doi:10.1103/PhysRevA.78.053409.

[64] R. J. Glauber, *The quantum theory of optical coherence*, Phys. Rev., **130**, 2529 (1963), doi:10.1103/PhysRev.130.2529.

[65] T. C. Lohrmann, *Perturbative analysis of multiple x-ray photon-matter interactions*, M.Sc. thesis at University of Hamburg (2018).

[66] G. Dixit, O. Vendrell, and R. Santra, *Imaging electronic quantum motion with light*, Proceedings of the National Academy of Sciences, **109**, 29, 11636 (2012), ISSN 0027-8424, doi:10.1073/pnas.1202226109.

[67] S. Chandrasekhar, *Extinction in x-ray crystallography*, Advances in Physics, **9**, 36, 363 (1960), doi:10.1080/00018736000101219.

[68] A. Authier, *Dynamical Theory of X-Ray Diffraction*, Oxford University Press (2003), ISBN 9780198528920, doi:10.1093/acprof:oso/9780198528920.001.0001.

[69] M. E. Peskin and D. V. Schroeder, *Quantum Field Theory*, Perseus Books Publishing, L.L.C. (1995).

[70] D. Popova-Gorelova, D. A. Reis, and R. Santra, *Theory of x-ray scattering from laser-driven electronic systems*, Phys. Rev. B, **98**, 224302 (2018), doi:10.1103/PhysRevB.98.224302.

[71] I. V. Tokatly, *Time-dependent density functional theory for many-electron systems interacting with cavity photons*, Phys. Rev. Lett., **110**, 233001 (2013), doi:10.1103/PhysRevLett.110.233001.

[72] J. Flick, M. Ruggenthaler, H. Appel, and A. Rubio, *Atoms and molecules in cavities, from weak to strong coupling in quantum-electrodynamics (qed) chemistry*, Proceedings of the National Academy of Sciences, **114**, 12, 3026 (2017), ISSN 0027-8424, doi:10.1073/pnas.1615509114.

[73] M. A. Sentef, M. Ruggenthaler, and A. Rubio, *Cavity quantum-electrodynamical polaritonically enhanced electron-phonon coupling and its influence on superconductivity*, Science Advances, **4**, 11 (2018), doi:10.1126/sciadv.aau6969.

[74] C. Boemer, D. Krebs, M. Diez, N. Rohringer, A. Galler, and C. Bressler, *X-ray parametric down-conversion: Challenging previous findings on the basis of improved experimental methods*, arXiv, , 2002.12822 (2020).

[75] C. Bömer, *Energy resolved diffraction for investigating x-ray parametric down-conversion*, Ph.D. thesis, Universität Hamburg (2020).

[76] G. Stefanucci and R. van Leeuwen, *Nonequilibrium Many-Body Theory of Quantum Systems: A Modern Introduction*, Cambridge University Press (2013), doi:10.1017/CBO9781139023979.

[77] J. Oddershede, P. Jørgensen, and D. L. Yeager, *Polarization propagator methods in atomic and molecular calculations*, Computer Physics Reports, **2**, 2, 33 (1984), ISSN 0167-7977, doi: https://doi.org/10.1016/0167-7977(84)90003-0.

[78] L. P. Kadanoff and G. Baym, *Quantum Statistical Mechanics*, CRC Press, 1 edition (1962), doi: 10.1201/9780429493218.

[79] G. Kotliar, S. Y. Savrasov, K. Haule, V. S. Oudovenko, O. Parcollet, and C. A. Marianetti, *Electronic structure calculations with dynamical mean-field theory*, Rev. Mod. Phys., **78**, 865 (2006), doi:10.1103/RevModPhys.78.865.

[80] J. Schirmer, *Beyond the random-phase approximation: A new approximation scheme for the polarization propagator*, Phys. Rev. A, **26**, 2395 (1982), doi:10.1103/PhysRevA.26.2395.

[81] J. Schirmer and A. B. Trofimov, *Intermediate state representation approach to physical properties of electronically excited molecules*, The Journal of Chemical Physics, **120**, 24, 11449 (2004), doi:10.1063/1.1752875.

[82] E. S. Nielsen, P. Jo/rgensen, and J. Oddershede, *Transition moments and dynamic polarizabilities in a second order polarization propagator approach*, The Journal of Chemical Physics, **73**, 12, 6238 (1980), doi:10.1063/1.440119.

[83] S. P. Sauer, H. F. Pitzner-Frydendahl, M. Buse, H. J. A. Jensen, and W. Thiel, *Performance of soppa-based methods in the calculation of vertical excitation energies and oscillator strengths*, Molecular Physics, **113**, 13-14, 2026 (2015), doi:10.1080/00268976.2015.1048320.

[84] G. H. Booth, A. Grüneis, G. Kresse, and A. Alavi, *Towards an exact description of electronic wavefunctions in real solids*, Nature, **493**, 7432, 365 (2013), ISSN 1476-4687, doi: 10.1038/nature11770.

[85] X. Wang and T. C. Berkelbach, *Excitons in solids from periodic equation-of-motion coupled-cluster theory*, Journal of Chemical Theory and Computation, **16**, 5, 3095 (2020), ISSN 1549-9618, doi:10.1021/acs.jctc.0c00101.

[86] E. Gross and W. Kohn, *Time-dependent density-functional theory*, in P.-O. Löwdin, ed., *Density Functional Theory of Many-Fermion Systems*, volume 21 of *Advances in Quantum Chemistry*, 255–291, Academic Press (1990), doi:https://doi.org/10.1016/S0065-3276(08)60600-0.

[87] G. Onida, L. Reining, and A. Rubio, *Electronic excitations: density-functional versus many-body green's-function approaches*, Rev. Mod. Phys., **74**, 601 (2002), doi:10.1103/RevModPhys.74.601.

[88] B. Adams, P. Fernandez, W.-K. Lee, G. Materlik, D. M. Mills, and D. V. Novikov, *Parametric down conversion of x-ray photons*, Journal of Synchrotron Radiation, **7**, 2, 81 (2000), doi: 10.1107/S0909049599015113.

[89] I. Freund, *Nonlinear x-ray diffraction. determination of valence electron charge distributions*, Chemical Physics Letters, **12**, 4, 583 (1972), ISSN 0009-2614, doi:https://doi.org/10.1016/0009-2614(72)80013-7.

[90] P. M. Eisenberger and S. L. McCall, *Mixing of x-ray and optical photons*, Phys. Rev. A, **3**, 1145 (1971), doi:10.1103/PhysRevA.3.1145.

[91] J. W. F. Woo and S. S. Jha, *Inelastic scattering of x rays from optically induced charge-density oscillations*, Phys. Rev. B, **6**, 4081 (1972), doi:10.1103/PhysRevB.6.4081.

[92] S. S. Jha and J. W. F. Woo, *Nonlinear response of bound electrons to x rays*, Phys. Rev. B, **5**, 4210 (1972), doi:10.1103/PhysRevB.5.4210.

[93] S. S. Jha and J. W. F. Woo, *Nonlinear response of electrons in a solid to x-rays*, Il Nuovo Cimento B (1971-1996), **10**, 1, 229 (1972), ISSN 1826-9877, doi:10.1007/BF02911422.

[94] R. Cohen and S. Shwartz, *Theory of nonlinear interactions between x rays and optical radiation in crystals*, Phys. Rev. Research, **1**, 033133 (2019), doi:10.1103/PhysRevResearch.1.033133.

[95] J. A. Armstrong, N. Bloembergen, J. Ducuing, and P. S. Pershan, *Interactions between light waves in a nonlinear dielectric*, Phys. Rev., **127**, 1918 (1962), doi:10.1103/PhysRev.127.1918.

[96] S. S. Jha and C. S. Warke, *Nonlinear electromagnetic response of bloch electrons in a magnetic field*, Il Nuovo Cimento B (1965-1970), **53**, 1, 120 (1968), ISSN 1826-9877, doi:10.1007/BF02710966.

[97] J. A. Van Vechten and R. M. Martin, *Calculation of local effective fields: Optical spectrum of diamond*, Phys. Rev. Lett., **28**, 446 (1972), doi:10.1103/PhysRevLett.28.446.

[98] S. L. Adler, *Quantum theory of the dielectric constant in real solids*, Phys. Rev., **126**, 413 (1962), doi:10.1103/PhysRev.126.413.

[99] N. Wiser, *Dielectric constant with local field effects included*, Phys. Rev., **129**, 62 (1963), doi:10.1103/PhysRev.129.62.

[100] R. G. Sachs, *The Physics of Time Reversal*, Chicago University Press, Chicago and London (1996).

[101] G. Czycholl, *Theoretische Festkörperphysik Band 1*, volume 1, Springer-Verlag Berlin Heidelberg (2016), doi:10.1007/978-3-662-47141-8.

[102] M. Born and T. von Karman, *Ueber schwingungen im raumgitter*, Physikalische Zeitschrift, **13**, 297 (1912).

[103] A. Szabo and N. S. Ostlund, *Modern Quantum Chemistry*, Dover Publication Inc., Mineola, NY (1996).

[104] M. A. Marques, N. T. Maitra, F. Nogueira, E. K. U. Gross, and A. Rubio, eds., *Fundamentals of Time-Dependent Density Functional Theory*, volume 837 of *Lecture Notes in Physics*, Springer Berlin Heidelberg, Berlin, Heidelberg (2012), ISBN 978-3-642-23517-7.

[105] P. Eisenberger and P. M. Platzman, *Compton scattering of x rays from bound electrons*, Phys. Rev. A, **2**, 415 (1970), doi:10.1103/PhysRevA.2.415.

[106] X. Gonze, et al., *The abinitproject: Impact, environment and recent developments*, Computer Physics Communications, **248**, 107042 (2020), ISSN 0010-4655, doi: https://doi.org/10.1016/j.cpc.2019.107042.

[107] P. Hohenberg and W. Kohn, *Inhomogeneous electron gas*, Phys. Rev., **136**, B864 (1964), doi: 10.1103/PhysRev.136.B864.

[108] W. Kohn and L. J. Sham, *Self-consistent equations including exchange and correlation effects*, Phys. Rev., **140**, A1133 (1965), doi:10.1103/PhysRev.140.A1133.

[109] P. J. Hasnip, K. Refson, M. I. J. Probert, J. R. Yates, S. J. Clark, and C. J. Pickard, *Density functional theory in the solid state*, Philosophical Transactions of the Royal Society A: Mathematical, Physical and Engineering Sciences, **372**, 2011, 20130270 (2014), doi:10.1098/rsta.2013.0270.

[110] J. P. Perdew, *Density functional theory and the band gap problem*, International Journal of Quantum Chemistry, **28**, S19, 497 (1985), doi:10.1002/qua.560280846.

[111] S. Botti, F. Sottile, N. Vast, V. Olevano, L. Reining, H.-C. Weissker, A. Rubio, G. Onida, R. Del Sole, and R. W. Godby, *Long-range contribution to the exchange-correlation kernel of time-dependent density functional theory*, Phys. Rev. B, **69**, 155112 (2004), doi: 10.1103/PhysRevB.69.155112.

[112] W. Jones and N. March, *Theoretical Solid State Physics*, number Bd. 1 in Dover books on physics and chemistry, Wiley-Interscience (1973), ISBN 9780471449003.

[113] K. Tamasaku and T. Ishikawa, *Idler energy dependence of nonlinear diffraction in $X \rightarrow X +$ EUV parametric down-conversion*, Acta Crystallographica Section A, **63**, 5, 437 (2007), doi: 10.1107/S0108767307032680.

[114] K. Tamasaku and T. Ishikawa, *Interference between compton scattering and x-ray parametric down-conversion*, Phys. Rev. Lett., **98**, 244801 (2007), doi:10.1103/PhysRevLett.98.244801.

[115] K. Tamasaku, K. Sawada, and T. Ishikawa, *Determining x-ray nonlinear susceptibility of diamond by the optical fano effect*, Phys. Rev. Lett., **103**, 254801 (2009), doi: 10.1103/PhysRevLett.103.254801.

[116] L. X. Benedict, E. L. Shirley, and R. B. Bohn, *Theory of optical absorption in diamond, si, ge, and gaas*, Phys. Rev. B, **57**, R9385 (1998), doi:10.1103/PhysRevB.57.R9385.

[117] K. Ramakrishna and J. Vorberger, *Ab initio dielectric response function of diamond and other relevant high pressure phases of carbon*, Journal of Physics: Condensed Matter, **32**, 9, 095401 (2019), doi:10.1088/1361-648x/ab558e.

[118] D. Qi, H. Su, M. Bastjan, O. D. Jurchescu, T. M. Palstra, A. T. S. Wee, M. Rübhausen, and A. Rusydi, *Observation of frenkel and charge transfer excitons in pentacene single crystals using spectroscopic generalized ellipsometry*, Applied Physics Letters, **103**, 11, 113303 (2013), doi: 10.1063/1.4811758.

[119] P. Cudazzo, M. Gatti, A. Rubio, and F. Sottile, *Frenkel versus charge-transfer exciton dispersion in molecular crystals*, Phys. Rev. B, **88**, 195152 (2013), doi:10.1103/PhysRevB.88.195152.

[120] S. Adachi, *Optical Constants of Crystalline and Amorphous Semiconductors*, Springer Science+Business Media, New York (1999).

[121] S. Huotari, *Fundamentals of Time-Dependent Density Functional Theory*, volume 837 of *Lecture Notes in Physics*, chapter Spectroscopy in the Frequency Domain, 15–28, Springer Berlin Heidelberg, Berlin, Heidelberg (2012), ISBN 978-3-642-23517-7.

[122] G. Vignale, *Current Density Functional Theory*, 75–91, Springer Berlin Heidelberg, Berlin, Heidelberg (2006), ISBN 978-3-540-35426-0, doi:10.1007/3-540-35426-3_5.

[123] X. Ren, P. Rinke, C. Joas, and M. Scheffler, *Random-phase approximation and its applications in computational chemistry and materials science*, Journal of Materials Science, **47**, 21, 7447 (2012), ISSN 1573-4803, doi:10.1007/s10853-012-6570-4.

[124] M. Palummo, O. Pulci, R. D. Sole, A. Marini, P. Hahn, W. G. Schmidt, and F. Bechstedt, *The bethe–salpeter equation: a first-principles approach for calculating surface optical spectra*, Journal of Physics: Condensed Matter, **16**, 39, S4313 (2004), doi:10.1088/0953-8984/16/39/006.

[125] L. Adamska and P. Umari, *Bethe-salpeter equation approach with electron-phonon coupling for exciton binding energies*, Phys. Rev. B, **103**, 075201 (2021), doi:10.1103/PhysRevB.103.075201.

[126] F. Kerker, *tbd* (2023).

[127] F. Zernike, *The concept of degree of coherence and its application to optical problems*, Physica, **5**, 8, 785 (1938), ISSN 0031-8914, doi:https://doi.org/10.1016/S0031-8914(38)80203-2.

[128] M. O. Scully and M. S. Zubairy, *Quantum Optics*, Cambridge University Press (1997), doi:10.1017/CBO9780511813993.

[129] G. Geloni, E. Saldin, L. Samoylova, E. Schneidmiller, H. Sinn, T. Tschentscher, and M. Yurkov, *Coherence properties of the european XFEL*, New Journal of Physics, **12**, 3, 035021 (2010), doi:10.1088/1367-2630/12/3/035021.

[130] I. A. Vartanyants, et al., *Coherence properties of individual femtosecond pulses of an x-ray free-electron laser*, Phys. Rev. Lett., **107**, 144801 (2011), doi:10.1103/PhysRevLett.107.144801.

[131] A. Singer, *Coherence properties of third and fourth generation x-ray sources. Theory and experiment*, Ph.D. thesis, University of Hamburg (2012).

[132] O. Chubar, A. Fluerasu, L. Berman, K. Kaznatcheev, and L. Wiegart, *Wavefront propagation simulations for beamlines and experiments with "synchrotron radiation workshop"*, Journal of Physics: Conference Series, **425**, 16, 162001 (2013), doi:10.1088/1742-6596/425/16/162001.

[133] K. Klementiev and R. Chernikov, *Powerful scriptable ray tracing package xrt*, in M. S. del Rio and O. Chubar, eds., *Advances in Computational Methods for X-Ray Optics III*, volume 9209, 60 – 75, International Society for Optics and Photonics, SPIE (2014), doi:10.1117/12.2061400.

[134] R. R. Lindberg and K.-J. Kim, *Compact representations of partially coherent undulator radiation suitable for wave propagation*, Phys. Rev. ST Accel. Beams, **18**, 090702 (2015), doi: 10.1103/PhysRevSTAB.18.090702.

[135] L. Samoylova, A. Buzmakov, O. Chubar, and H. Sinn, *WavePropaGator: interactive framework for X-ray free-electron laser optics design and simulations*, Journal of Applied Crystallography, **49**, 4, 1347 (2016), doi:10.1107/S160057671600995X.

[136] O. Y. Gorobtsov, G. Mercurio, G. Brenner, U. Lorenz, N. Gerasimova, R. P. Kurta, F. Hieke, P. Skopintsev, I. Zaluzhnyy, S. Lazarev, D. Dzhigaev, M. Rose, A. Singer, W. Wurth, and I. A. Vartanyants, *Statistical properties of a free-electron laser revealed by hanbury brown–twiss interferometry*, Phys. Rev. A, **95**, 023843 (2017), doi:10.1103/PhysRevA.95.023843.

[137] A. C. Schell, *The multiple plate antenna*, Ph.D. thesis, Massachusetts Institute of Technology (1961).

[138] M. R. Howells and B. M. Kincaid, *The Properties of Undulator Radiation*, 315–358, Springer Netherlands, Dordrecht (1994), ISBN 978-94-011-0868-3, doi:10.1007/978-94-011-0868-3_13.

[139] R. Coïsson, *Spatial coherence of synchrotron radiation*, Appl. Opt., **34**, 5, 904 (1995), doi: 10.1364/AO.34.000904.

[140] R. Coïsson and S. Marchesini, *Gauss–Schell Sources as Models for Synchrotron Radiation*, Journal of Synchrotron Radiation, **4**, 5, 263 (1997), doi:10.1107/S0909049597008169.

[141] Y. Takayama, N. Takaya, T. Miyahara, S. Kamada, W. Okamoto, T. Hatano, R. Tai, and Y. Kagoshima, *Spatial coherence of undulator radiation beyond the van cittert–zernike theorem*, Nuclear Instruments and Methods in Physics Research Section A: Accelerators, Spectrometers, Detectors and Associated Equipment, **441**, 3, 565 (2000), ISSN 0168-9002, doi: https://doi.org/10.1016/S0168-9002(99)00988-2.

[142] G. Geloni, E. Saldin, E. Schneidmiller, and M. Yurkov, *Transverse coherence properties of x-ray beams in third-generation synchrotron radiation sources*, Nuclear Instruments and Methods in Physics Research Section A: Accelerators, Spectrometers, Detectors and Associated Equipment, **588**, 3, 463 (2008), ISSN 0168-9002, doi:https://doi.org/10.1016/j.nima.2008.01.089.

[143] M. T. Price, G. A. Blair, G. Boorman, S. T. Boogert, A. Bosco, S. Malton, T. Kamps, K. Balewski, E. Elsen, V. Gharibyan, H.-C. Lewin, F. Poirier, S. Schreiber, N. Walker, and K. Wittenburg, *Beam profile measurements with the 2-d laser-wire at petra*, in *2007 IEEE Particle Accelerator Conference (PAC)*, 4303–4305 (2007), doi:10.1109/PAC.2007.4439998.

[144] P. F. Moulton, *Spectroscopic and laser characteristics of ti:al2o3*, J. Opt. Soc. Am. B, **3**, 1, 125 (1986), doi:10.1364/JOSAB.3.000125.

[145] O. Slattery, L. Ma, K. Zong, and X. Tang, *Background and review of cavity-enhanced spontaneous parametric down-conversion*, Journal of Research (NIST JRES), , 124 (2019), doi: https://doi.org/10.6028/jres.124.019.

[146] P. D. Drummond and M. Hillery, *The Quantum Theory of Nonlinear Optics*, Cambridge University Press (2014), doi:10.1017/CBO9780511783616.

[147] L. D. Landau and E. M. Lifshitz, *Course of Theoretical Physics*, volume 9, Pergamon Press, Oxford (1980).

[148] H. B. G. Casimir and D. Polder, *The influence of retardation on the london-van der waals forces*, Phys. Rev., **73**, 360 (1948), doi:10.1103/PhysRev.73.360.

[149] D. N. Klyshko, *Photons and Nonlinear Optics*, CRC Press (1988).

[150] S. M. Barnett, B. Huttner, and R. Loudon, *Spontaneous emission in absorbing dielectric media*, Phys. Rev. Lett., **68**, 3698 (1992), doi:10.1103/PhysRevLett.68.3698.

[151] S. Y. Buhmann, *Dispersion Forces I*, Springer Berlin, Heidelberg (2012), doi: https://doi.org/10.1007/978-3-642-32484-0.

[152] S. Y. Buhmann, *Dispersion Forces II*, Springer Berlin, Heidelberg (2012), doi: https://doi.org/10.1007/978-3-642-32466-6.

[153] J. B. Johnson, *Thermal agitation of electricity in conductors*, Phys. Rev., **32**, 97 (1928), doi: 10.1103/PhysRev.32.97.

[154] H. Nyquist, *Thermal agitation of electric charge in conductors*, Phys. Rev., **32**, 110 (1928), doi: 10.1103/PhysRev.32.110.

[155] R. Kubo, *The fluctuation-dissipation theorem*, Reports on Progress in Physics, **29**, 1, 255 (1966), doi:10.1088/0034-4885/29/1/306.

[156] P. Emma, et al., *First lasing and operation of an angstrom-wavelength free-electron laser*, Nat Photon, **4**, 9, 641 (2010), ISSN 1749-4885, doi:10.1038/nphoton.2010.176.

[157] C. Bostedt, S. Boutet, D. M. Fritz, Z. Huang, H. J. Lee, H. T. Lemke, A. Robert, W. F. Schlotter, J. J. Turner, and G. J. Williams, *Linac coherent light source: The first five years*, Rev. Mod. Phys., **88**, 015007 (2016), doi:10.1103/RevModPhys.88.015007.

[158] P. A. Franken, A. E. Hill, C. W. Peters, and G. Weinreich, *Generation of optical harmonics*, Phys. Rev. Lett., **7**, 118 (1961), doi:10.1103/PhysRevLett.7.118.

[159] H.-C. Schröder, A. Affeldt, H. Gausepohl, G. Kube, and G. Priebe, *Bunch length measurement for petra iii light source storage ring*, in *Proc. of the 10th European Workshop on Beam Diagnostics and Instrumentation for Particle Accelerators (DIPAC2011), Hamburg, Germany, 16-18 May, 2011*, Beam Diagnostics and Instrumentation for Particle Accelerators, 113–115, JACoW, Geneva, Switzerland (2011). Http://accelconf.web.cern.ch/DIPAC2011/papers/mopd30.pdf.

[160] M. Bieler, I. Agapov, H. Ehrlichmann, J. Keil, G. Sahoo, and R. Wanzenberg, *PETRA III Operation*, in *Proc. of International Particle Accelerator Conference (IPAC'17), Copenhagen, Denmark, 14-19 May, 2017*, number 8 in International Particle Accelerator Conference, 2589–2591, JACoW, Geneva, Switzerland (2017), ISBN 978-3-95450-182-3, doi:https://doi.org/10.18429/JACoW-IPAC2017-WEPAB014. Https://doi.org/10.18429/JACoW-IPAC2017-WEPAB014.

[161] A. Schöps, P. Vagin, and M. Tischer, *Properties of the insertion devices for petra iii and its extension*, AIP Conference Proceedings, **1741**, 1, 020019 (2016), doi:10.1063/1.4952798.

[162] L. J. P. Ament, M. van Veenendaal, T. P. Devereaux, J. P. Hill, and J. van den Brink, *Resonant inelastic x-ray scattering studies of elementary excitations*, Rev. Mod. Phys., **83**, 705 (2011), doi: 10.1103/RevModPhys.83.705.

[163] C. J. Sahle, A. Mirone, J. Niskanen, J. Inkinen, M. Krisch, and S. Huotari, *Planning, performing and analyzing X-ray Raman scattering experiments*, Journal of Synchrotron Radiation, **22**, 2, 400 (2015), doi:10.1107/S1600577514027581.

[164] P. Alexeev, O. Leupold, I. Sergueev, M. Herlitschke, D. F. McMorrow, R. S. Perry, E. C. Hunter, R. Röhlsberger, and H.-C. Wille, *Nuclear resonant scattering from 193ir as a probe of the electronic and magnetic properties of iridates*, Scientific Reports, **9**, 1, 5097 (2019), ISSN 2045-2322, doi:10.1038/s41598-019-41130-3.

[165] P. Raimondi, *Esrf-ebs: The extremely brilliant source project*, Synchrotron Radiation News, **29**, 6, 8 (2016), doi:10.1080/08940886.2016.1244462.

[166] P. Raimondi, L. Farvacque, G. L. Bec, J.-C. Biasci, J.-F. Bouteille, J. Jacob, J.-M. Chaize, K. Scheidt, J. Chavanne, T. Perron, S. White, M. Hahn, and D. Martin, *ESRF – EBS Design Report* (2018).

[167] C. G. Schroer and H. DESY Dt. Elektr.-Synchr., *PETRA IV: upgrade of PETRA III to the Ultimate 3D X-ray microscope. Conceptual Design Report*, Deutsches Elektronen-Synchrotron DESY, Hamburg (2019), ISBN 9783945931264, doi:10.3204/PUBDB-2019-03613.

[168] C. G. Schroer, *Petra iv - new dimensions*, Workshop Presentation (2021).

[169] G. Taylor, *The phase problem*, Acta Crystallographica Section D, **59**, 11, 1881 (2003), doi: 10.1107/S0907444903017815.

[170] E. Weckert and K. Hümmer, *Multiple-Beam X-ray Diffraction for Physical Determination of Reflection Phases and its Applications*, Acta Crystallographica Section A, **53**, 2, 108 (1997), doi: 10.1107/S0108767396011117.

[171] E. Nishibori, E. Sunaoshi, A. Yoshida, S. Aoyagi, K. Kato, M. Takata, and M. Sakata, *Accurate structure factors and experimental charge densities from synchrotron X-ray powder diffraction data at SPring-8*, Acta Crystallographica Section A, **63**, 1, 43 (2007), doi: 10.1107/S0108767306047210.

[172] D. K. Bowen and B. K. Tanner, *High Resolution X-Ray Diffractometry And Topography*, Taylor and Francis (1998).

[173] U. Pietsch, V. Holy, and T. Baumbach, *High-Resolution X-Ray Scattering*, Springer, New York, NY (2004).

[174] P. H. Rowland, *Lxi. preliminary notice of the results accomplished in the manufacture and theory of gratings for optical purposes*, The London, Edinburgh, and Dublin Philosophical Magazine and Journal of Science, **13**, 84, 469 (1882), doi:10.1080/14786448208627217.

[175] E. Welter, P. Machek, G. Dräger, U. Brüggmann, and M. Fröba, *A new X-ray spectrometer with large focusing crystal analyzer*, Journal of Synchrotron Radiation, **12**, 4, 448 (2005), doi: 10.1107/S0909049505007843.

[176] S. Hayama, R. Boada, J. Chaboy, A. Birt, G. Duller, L. Cahill, A. Freeman, M. Amboage, L. Keenan, and S. Diaz-Moreno, *Photon-in/photon-out spectroscopy at the i20-scanning beamline at diamond light source*, Journal of Physics: Condensed Matter, **33**, 28, 284003 (2021), doi: 10.1088/1361-648x/abfe93.

[177] G. Dräger, T. Kirchner, S. Bocharov, and C.-C. Kao, *Spin-resolved NEXAFS from resonant X-ray scattering (RXS)*, Journal of Synchrotron Radiation, **8**, 2, 398 (2001), doi: 10.1107/S0909049500017234.

[178] M. Moretti Sala, K. Martel, C. Henriquet, A. Al Zein, L. Simonelli, C. J. Sahle, H. Gonzalez, M.-C. Lagier, C. Ponchut, S. Huotari, R. Verbeni, M. Krisch, and G. Monaco, *A high-energy-resolution resonant inelastic X-ray scattering spectrometer at ID20 of the European Synchrotron Radiation Facility*, Journal of Synchrotron Radiation, **25**, 2, 580 (2018), doi: 10.1107/S1600577518001200.

[179] E. Burkel, *Ultrahigh-energy-resolution inelastic x-ray scattering spectroscopy*, Zeitschrift für Naturforschung A, **48**, 1-2, 289 (1993), doi:doi:10.1515/zna-1993-1-254.

[180] J. R. Schmitz, H. Schulte-Schrepping, A. Berthold, S. Mourikis, and W. Schülke, *Performance of the compton spectrometer at harwi/hasylab*, Zeitschrift für Naturforschung A, **48**, 1-2, 279 (1993), doi:doi:10.1515/zna-1993-1-252.

[181] S. Huotari, C. J. Sahle, C. Henriquet, A. Al-Zein, K. Martel, L. Simonelli, R. Verbeni, H. Gonzalez, M.-C. Lagier, C. Ponchut, M. Moretti Sala, M. Krisch, and G. Monaco, *A large-solid-angle X-ray Raman scattering spectrometer at ID20 of the European Synchrotron Radiation Facility*, Journal of Synchrotron Radiation, **24**, 2, 521 (2017), doi:10.1107/S1600577516020579.

[182] C. J. Milne, et al., *Swissfel: The swiss x-ray free electron laser*, Applied Sciences, **7**, 7 (2017), ISSN 2076-3417, doi:10.3390/app7070720.

[183] A.-P. Honkanen, R. Verbeni, L. Simonelli, M. Moretti Sala, A. Al-Zein, M. Krisch, G. Monaco, and S. Huotari, *Improving the energy resolution of bent crystal X-ray spectrometers with position-sensitive detectors*, Journal of Synchrotron Radiation, **21**, 4, 762 (2014), doi: 10.1107/S1600577514011163.

[184] A.-P. Honkanen, R. Verbeni, L. Simonelli, M. Moretti Sala, G. Monaco, and S. Huotari, *Study on the reflectivity properties of spherically bent analyser crystals*, Journal of Synchrotron Radiation, **21**, 1, 104 (2014), doi:10.1107/S160057751302242X.

[185] A. Mozzanica, A. Bergamaschi, M. Brueckner, S. Cartier, R. Dinapoli, D. Greiffenberg, J. Jungmann-Smith, D. Maliakal, D. Mezza, M. Ramilli, C. Ruder, L. Schaedler, B. Schmitt, X. Shi, and G. Tinti, *Characterization results of the JUNGFRAU full scale readout ASIC*, Journal of Instrumentation, **11**, 02, C02047 (2016), doi:10.1088/1748-0221/11/02/c02047.

[186] S. Redford, et al., *Operation and performance of the JUNGFRAU photon detector during first FEL and synchrotron experiments*, Journal of Instrumentation, **13**, 11, C11006 (2018), doi: 10.1088/1748-0221/13/11/c11006.

[187] J. Strempfer, S. Francoual, D. Reuther, D. K. Shukla, A. Skaugen, H. Schulte-Schrepping, T. Kracht, and H. Franz, *Resonant scattering and diffraction beamline p09 at petra iii*, Journal of Synchrotron Radiation, **20**, 4, 541 (2013), doi:https://doi.org/10.1107/S0909049513009011.

[188] D. A. Kleinman, *Theory of optical parametric noise*, Phys. Rev., **174**, 1027 (1968), doi: 10.1103/PhysRev.174.1027.

[189] I. Freund and B. F. Levine, *Parametric conversion of x rays*, Phys. Rev. Lett., **23**, 854 (1969), doi:10.1103/PhysRevLett.23.854.

[190] W. J. Bartels, *Characterization of thin layers on perfect crystals with a multipurpose high resolution x-ray diffractometer*, Journal of Vacuum Science & Technology B: Microelectronics Processing and Phenomena, **1**, 2, 338 (1983), doi:10.1116/1.582553.

[191] A. Mikhalychev, A. Benediktovitch, T. Ulyanenkova, and A. Ulyanenkov, *Ab initio simulation of diffractometer instrumental function for high-resolution x-ray diffraction*, J. Appl. Crystallogr., **48**, Pt 3, 679 (2015).

[192] S. Sofer, O. Sefi, A. G. A. Nisbet, and S. Shwartz, *Measurements of polarization dependencies in parametric down-conversion of x rays into ultraviolet radiation*, Phys. Rev. B, **104**, 085207 (2021), doi:10.1103/PhysRevB.104.085207.

[193] C. Kittel, *Introduction to solid state physics*, Wiley, Hoboken, NJ, 8 edition (2005), ISBN 978-0-471-68057-4.

[194] H. Raether, *Volume plasmons*, 4–13, Springer Berlin Heidelberg, Berlin, Heidelberg (1980), ISBN 978-3-540-34716-3, doi:10.1007/BFb0045953.

[195] H.-C. Weissker, J. Serrano, S. Huotari, E. Luppi, M. Cazzaniga, F. Bruneval, F. Sottile, G. Monaco, V. Olevano, and L. Reining, *Dynamic structure factor and dielectric function of silicon for finite momentum transfer: Inelastic x-ray scattering experiments and ab initio calculations*, Phys. Rev. B, **81**, 085104 (2010), doi:10.1103/PhysRevB.81.085104.

[196] S. Botti, *Semi-empirical and ab-initio calculations of optical properties in semiconductor superlattices*, Ph.D. thesis, Universita degli studi di Pavia (2002).

[197] J. J. Hopfield, *Theory of the contribution of excitons to the complex dielectric constant of crystals*, Phys. Rev., **112**, 1555 (1958), doi:10.1103/PhysRev.112.1555.

[198] U. Fano, *Effects of configuration interaction on intensities and phase shifts*, Phys. Rev., **124**, 1866 (1961), doi:10.1103/PhysRev.124.1866.

[199] K. HUANG, *Lattice vibrations and optical waves in ionic crystals*, Nature, **167**, 4254, 779 (1951), ISSN 1476-4687, doi:10.1038/167779b0.

[200] U. Fano, *Atomic theory of electromagnetic interactions in dense materials*, Phys. Rev., **103**, 1202 (1956), doi:10.1103/PhysRev.103.1202.

[201] B. Huttner and S. M. Barnett, *Quantization of the electromagnetic field in dielectrics*, Phys. Rev. A, **46**, 4306 (1992), doi:10.1103/PhysRevA.46.4306.

[202] D. N. Basov, A. Asenjo-Garcia, P. J. Schuck, X. Zhu, and A. Rubio, *Polariton panorama*, Nanophotonics, **10**, 1, 549 (2021), doi:doi:10.1515/nanoph-2020-0449.

[203] M. Collett, R. Loudon, and C. Gardiner, *Quantum theory of optical homodyne and heterodyne detection*, Journal of Modern Optics, **34**, 6-7, 881 (1987), doi:10.1080/09500348714550811.

[204] C. A. Marx, U. Harbola, and S. Mukamel, *Nonlinear optical spectroscopy of single, few, and many molecules: Nonequilibrium green's function qed approach*, Phys. Rev. A, **77**, 022110 (2008), doi:10.1103/PhysRevA.77.022110.

[205] O. E. DeLange, *Optical heterodyne detection*, IEEE Spectrum, **5**, 10, 77 (1968), doi:10.1109/MSPEC.1968.5215385.

[206] S. M. Gallagher, A. W. Albrecht, J. D. Hybl, B. L. Landin, B. Rajaram, and D. M. Jonas, *Heterodyne detection of the complete electric field of femtosecond four-wave mixing signals*, J. Opt. Soc. Am. B, **15**, 8, 2338 (1998), doi:10.1364/JOSAB.15.002338.

[207] J. R. Rouxel, M. Kowalewski, K. Bennett, and S. Mukamel, *X-ray sum frequency diffraction for direct imaging of ultrafast electron dynamics*, Phys. Rev. Lett., **120**, 243902 (2018), doi:10.1103/PhysRevLett.120.243902.

[208] J. M. Glownia, A. Natan, J. P. Cryan, R. Hartsock, M. Kozina, M. P. Minitti, S. Nelson, J. Robinson, T. Sato, T. van Driel, G. Welch, C. Weninger, D. Zhu, and P. H. Bucksbaum, *Self-referenced coherent diffraction x-ray movie of ångstrom- and femtosecond-scale atomic motion*, Phys. Rev. Lett., **117**, 153003 (2016), doi:10.1103/PhysRevLett.117.153003.

[209] A. P. Fidler, E. R. Warrick, H. J. B. Marroux, E. Bloch, D. M. Neumark, and S. R. Leone, *Self-heterodyned detection of dressed state coherences in helium by noncollinear extreme ultraviolet wave mixing with attosecond pulses*, Journal of Physics: Photonics, **2**, 3, 034003 (2020), doi:10.1088/2515-7647/ab869c.

[210] K. Bennett, M. Kowalewski, and S. Mukamel, *Heterodyne-detected ultrafast x-ray diffraction and scattering from nonstationary states*, arXiv (2018).

[211] J. J. Sakurai and J. Napolitano, *Modern Quantum Mechanics*, Cambridge University Press, 2 edition (2017), doi:10.1017/9781108499996.

[212] W. Heisenberg, *Über quantentheoretische umdeutung kinematischer und mechanischer beziehungen.*, Zeitschrift für Physik, **33**, 1, 879 (1925), ISSN 0044-3328, doi:10.1007/BF01328377.

[213] M. Born and P. Jordan, *Zur quantenmechanik*, Zeitschrift für Physik, **34**, 1, 858 (1925), ISSN 0044-3328, doi:10.1007/BF01328531.

[214] M. Born, W. Heisenberg, and P. Jordan, *Zur quantenmechanik. ii.*, Zeitschrift für Physik, **35**, 8, 557 (1926), ISSN 0044-3328, doi:10.1007/BF01379806.

[215] L. Mandel and E. Wolf, *Optical Coherence and Quantum Optics*, Cambridge University Press (1995), doi:10.1017/CBO9781139644105.

[216] D. Paganin, *Coherent X-Ray Optics*, Oxford Series on Synchrotron Radiation, Oxford University Press, Oxford (2013), ISBN 9780199673865.

[217] A. T. Friberg and R. J. Sudol, *Propagation parameters of gaussian schell-model beams*, Optics Communications, **41**, 6, 383 (1982), ISSN 0030-4018, doi:https://doi.org/10.1016/0030-4018(82)90161-4.

[218] P. A. Bromiley, *Products and convolutions of gaussian probability density functions*, Tina Memo No. 2003-003, Internal Report (2003).

[219] M. J. Bastiaans, *Wigner distribution function and its application to first-order optics*, J. Opt. Soc. Am., **69**, 12, 1710 (1979), doi:10.1364/JOSA.69.001710.

[220] E. Wigner, *On the quantum correction for thermodynamic equilibrium*, Phys. Rev., **40**, 749 (1932), doi:10.1103/PhysRev.40.749.

[221] J. Weinbub and D. K. Ferry, *Recent advances in wigner function approaches*, Applied Physics Reviews, **5**, 4, 041104 (2018), doi:10.1063/1.5046663.

[222] P. Yang, I. F. Valtierra, A. B. Klimov, S.-T. Wu, R.-K. Lee, L. L. Sánchez-Soto, and G. Leuchs, *The wigner flow on the sphere*, Physica Scripta, **94**, 4, 044001 (2019), doi:10.1088/1402-4896/aaf91b.

[223] U. Seyfarth, A. B. Klimov, H. d. Guise, G. Leuchs, and L. L. Sanchez-Soto, *Wigner function for SU(1,1)*, Quantum, **4**, 317 (2020), ISSN 2521-327X, doi:10.22331/q-2020-09-07-317.

Acknowledgements

In a final—decidedly more personal—retrospection, we want to express our gratitude to several collaborators, colleagues and friends, without whom this thesis would never have assumed its present form. Emphasizing the distinction between the scientific reporting above and the personal account to follow, we shall proceed to phrase this retrospection in the first person singular.

First of all, I want to express my immense gratitude towards, and appreciation of, Dr. Nina Rohringer. Acknowledging her merely as the 'supervisor' of my thesis, however, would hardly do justice to the variegated interplay of worries and joys, patience and impatience, quarrels and support, which marked our common journey. In order to fathom this unique, almost familial, bond, I would much rather resort to the German language, which is endowed with the more appropriate term 'Doktormutter'. Despite all our differences, I could not wish for a better academic parent than Nina.

As the second referee of my thesis, I thank Dr. Mariana Rossi for her generous offer to repeatedly read and review my work. More importantly, though, I want to thank her for the inspiring collaboration on electronic structure theory applied to wavemixing. Her enthusiasm to work across disciplines has not only provided momentary motivation to me, but serves as an aspirational model in general.

Broadening my retrospection, I look back at a wonderful time at DESY that has been rendered all the more enjoyable because of my dear colleagues and friends at FS-TUX(S). Apart from the obvious (and plentiful) scientific discussions, I have relished the countless coffee-breaks and cake-parties at our offices (of which we occupied various over time, actually). It has been a recurring pleasure to pursue intellectual excursions into literature, film, politics and various other topics within this lively company. Beyond this, we have enjoyed our fair share of common adventures, be it canoeing, skiing or—of course—the collective madness of beamtimes. During the latter, the unwavering support of the group has been a key-factor in obtaining our wavemixing results and was deeply appreciated.

While I could hardly single out any particular colleague for a specific acknowledgement—given my comprehensive appreciation of the group as a whole—I want to give a special mention to my long-term office mate Dr. Andrei Benediktovitch nevertheless. Throughout several relocations and a pandemic shut-down, I have enjoyed his company and fondly remember the days, when we would have silent, hurried lunch, in order to afford more time for scientific discussions afterwards.

Turning my focus to the experiments, which I have engaged in during this thesis work, I want to repeat an earlier acknowledgement: Namely, that these efforts have been largely collaborative and their success was enabled in no small part through the help and support of committed people in various places.

At the beamlines themselves, I want express my gratitude first of all to Dr. Sonia Francoual and Julian Bergtholdt, whose tireless support at P09 (PETRA III) made our first high-resolution experiment on XPDC possible. At the ID20 (ESRF), I want to acknowledge and thank Dr. Blanka Detlefs and Dr. Christoph Sahle as well as Florent Gerbon for all their help during our experiments in Grenoble and their often ingenious modifications of the involved setups. This list of collaborators at ID20 would be

woefully incomplete without mentioning Dr. Simo Huotari, who—unfortunately—could only join our efforts remotely, but remained unabatedly committed to eradicate any background contamination from afar. For our experiments at SwissFEL, I am grateful to the whole Bernina team, headed by Dr. Henrik Lemke. Their steady support has enabled our demonstration of DFG at their beamline and sustained our momentum to collect a whole crystallographic series of measurements. In conjunction with the beamline team, I want to mention and thank Lennart Wollenweber, who joined our campaign and has been of great help throughout.

In addition to the on-site support, I want to thank several colleagues and collaborators for their enormous help in enabling or preparing our experiments. Chief among these are Dr. Horst Schulte-Schrepping and Manfred Spiwek at DESY, who have advised us on the design of our first high-resolution XPDC experiment and manufactured parts of the crystal optics needed therefore. Both their expertise and their encouragement of our efforts have given us an invaluable boost, for which I thank them very much. Similarly, I am deeply grateful to Dr. Berit Marx-Glowna and Dr. Ingo Uschmann from the University of Jena, who likewise supported our quest for crystal optics on multiple occasions. Yet (again), their support has far exceeded material contributions; in addition to countless discussions, I want to thank the two of them—exemplarily for all their help—for the long hours of work invested into our BMBF proposal. It has been a great joy to find such kind and amicable collaborators in an all too often contentious scientific environment. The same holds true for Dr. Ralf Röhlsberger, who established our contact to Jena in the first place. I would like to re-iterate my gratitude to him explicitly, though, given all of his support to our wavemixing project as well as his considerate mentorship over the last years.

A very special mention and reverence is due for Dr. Dmitri Novikov. From the early days of our ambitious, yet at times seemingly futile, wavemixing project, he has been a staunch supporter of our endeavours. I want to thank him dearly for bolstering our resolve through his unwavering belief in the value of fundamental science and his emphatic encouragement to keep trying.

Regarding our overseas collaborations, I first want to acknowledge Dr. David Reis, with whom I had the fortune to share a passion for nonlinear x-ray phenomena since our research on nonlinear Compton scattering. Further invigorated by Dr. Jerome Hastings, our respective wavemixing efforts have seen prolific advances through extensive discussions, some friendly competition and various shared efforts. Throughout this time, working with Jerry and David has often been inspirational, leading all of us to seek unconventional solutions and push experimental (as well as theoretical) boundaries.

Working at very different wavelengths, yet hardly less creative, I want to further acknowledge Dr. Michael Zürch and Dr. Craig Schwartz. In addition to their general support of our endeavours and being inspiring collaborators, who motivated us to look for wavemixing ‘outside of our comfort zone’, they have also presented admirable role models—both in their very own ways. Summarily, I am grateful to have made their acquaintances through this work.

Considering all of the aforementioned colleagues and collaborators, I want to emphasize—without distinction—that it has been a privilege to work with so many brilliant people for such a long time. For this opportunity in itself, I am invariably grateful.

Reaching much further back than present scientific collaborations, I also want to include my parents in this list of commemorations. They have always encouraged me to be curious and open-minded, thus laying the foundation for scientific work early on. For this and for their steady support of my peculiar passion for physics, I thank them dearly.

Last, but certainly not least, I want to thank Dr. Christina Bömer for her partnership throughout much

of the wavemixing endeavour. Without her, this thesis would have taken a very different form. Far beyond her immediate help in rendering many of the thesis' illustrations and proof-reading its content, she has been instrumental in shaping (and advancing) our wavemixing project into the form documented in the previous chapters. Our experimental successes—and by extension many of the corresponding theoretical developments—would have never materialised without her bold initiative as well as passionate pursuit. It has been most remarkable and inspiring—albeit unnerving at times—to experience Christina's incredible optimism and motivation in spite of (experimental) hardships and exhaustion. I consider myself very fortunate to have met such an admirable person, scientist and friend and I am grateful for all the time, we could spend together, as well as the fun, we had doing so.

Eidesstattliche Versicherung / Declaration on oath

Hiermit versichere ich an Eides statt, die vorliegende Dissertationsschrift selbst verfasst und keine anderen als die angegebenen Hilfsmittel und Quellen benutzt zu haben.

Hamburg, den 15.08.2022

Unterschrift des Doktoranden